Volume 7 Issue 4 (2021) · ISSN 2424-7723

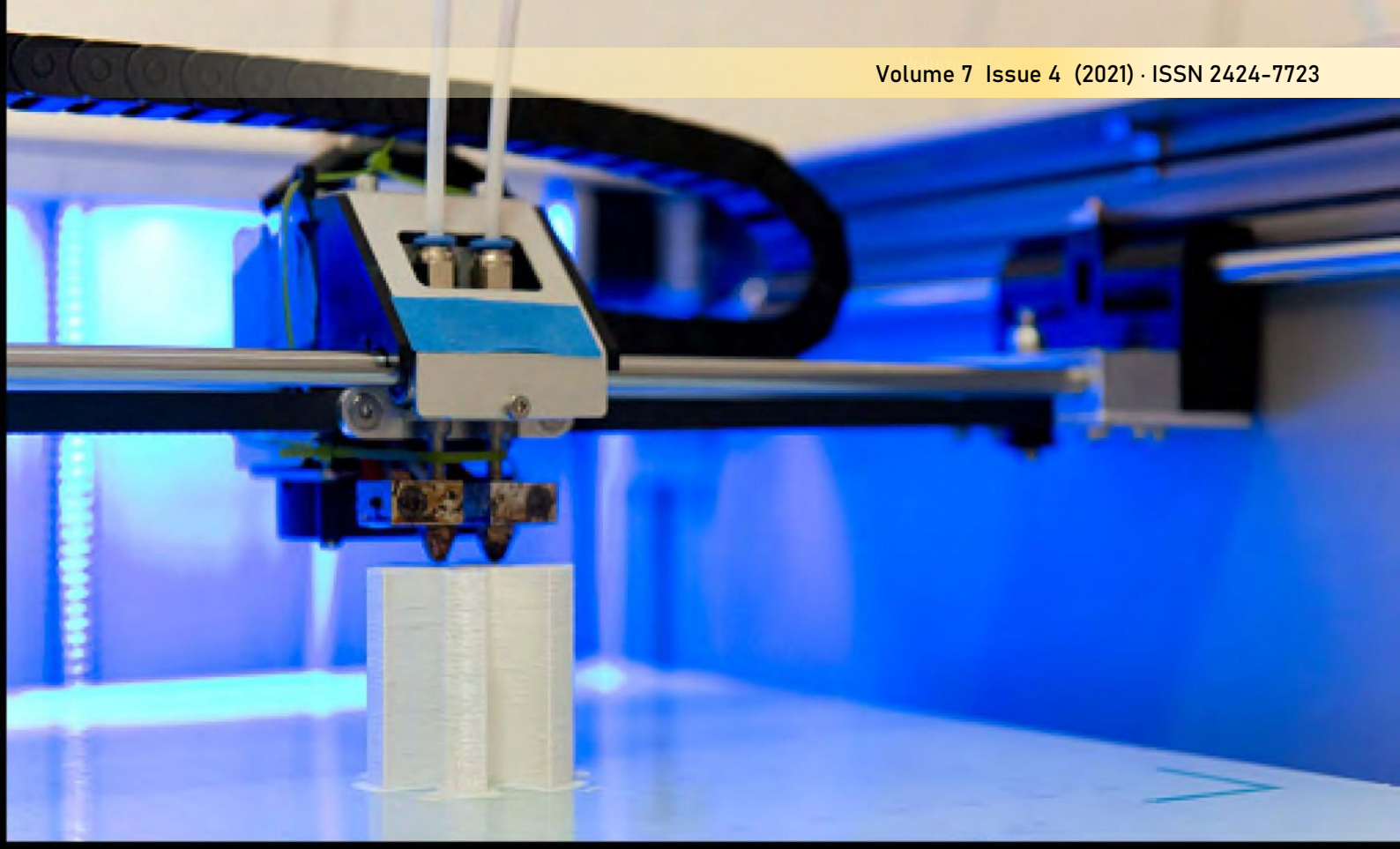

INTERNATIONAL JOURNAL OF BIOPRINTING

WHIOCE PUBLISHING PTE. LTD.
PROVIDING
FIRST-CLASS SCIENTIFIC INFORMATION
FOR TOP SCHOLARS

Volume 7 Issue 4 • 2021
ISSN 2424-7723 (print) ISSN 2424-8002 (online)

INTERNATIONAL JOURNAL OF BIOPRINTING

Editor-in-Chief

Chee Kai Chua

Singapore University of Technology and Design, Singapore

WHIOCE PUBLISHING PTE. LTD.

Volume 7 | Issue 4 | 2021 | Page 1 – 189 |

International Journal of Bioprinting

https://ijb.whioce.com/index.php/int-j-bioprinting

CONTENTS

REVIEW ARTICLE

Using Spheroids as Building Blocks Towards 3D Bioprinting of Tumor Microenvironment

Pei Zhuang, Yi-Hua Chiang, Maria Serafim Fernanda, Mei He*

Department of Pharmaceutics, University of Florida, Gainesville, Florida, 32610, USA

Abstract: Cancer still ranks as a leading cause of mortality worldwide. Although considerable efforts have been dedicated to anticancer therapeutics, progress is still slow, partially due to the absence of robust prediction models. Multicellular tumor spheroids, as a major three-dimensional (3D) culture model exhibiting features of avascular tumors, gained great popularity in pathophysiological studies and high throughput drug screening. However, limited control over cellular and structural organization is still the key challenge in achieving *in vivo* like tissue microenvironment. 3D bioprinting has made great strides toward tissue/organ mimicry, due to its outstanding spatial control through combining both cells and materials, scalability, and reproducibility. Prospectively, harnessing the power from both 3D bioprinting and multicellular spheroids would likely generate more faithful tumor models and advance our understanding on the mechanism of tumor progression. In this review, the emerging concept on using spheroids as a building block in 3D bioprinting for tumor modeling is illustrated. We begin by describing the context of the tumor microenvironment, followed by an introduction of various methodologies for tumor spheroid formation, with their specific merits and drawbacks. Thereafter, we present an overview of existing 3D printed tumor models using spheroids as a focus. We provide a compilation of the contemporary literature sources and summarize the overall advancements in technology and possibilities of using spheroids as building blocks in 3D printed tissue modeling, with a particular emphasis on tumor models. Future outlooks about the wonderous advancements of integrated 3D spheroidal printing conclude this review.

Keywords: 3D bioprinting; Tumor microenvironment; Spheroid

*Correspondence to: Mei He, at the Department of Pharmaceutics, University of Florida, Gainesville, Florida, 32610, USA; mhe@cop.ufl.edu

Received: September 6, 2021; **Accepted:** October 2, 2021; **Published Online:** October 21, 2021

Citation: Zhuang P, Chiang YH, Fernanda MS, *et al*., 2021, Using Spheroids as Building Blocks Towards 3D Bioprinting of Tumor Microenvironment. *Int J Bioprint*, 7(4):444. http://doi.org/10.18063/ijb.v7i4.444

1. Introduction

Cancer accounts for about 1 in every 6 deaths and is the second leading cause of deaths worldwide. In 2020, cancer was estimably affecting 18.3 million people globally, causing nearly 10 million deaths[1]. Despite the soaring investment in the development of anticancer therapeutics in past decades, positive outcomes are still far from satisfactory. The journey of an anticancer drug from lab-to-shelf could take years (~15 years): Before entering a clinical trial, drugs are heavily interrogated through required sets of *in vivo* and *in vitro* tests. However, a reliable *in vitro* model for accurate prediction of drug responses is lacking. Such shortfalls directly result in increased cost and time on developmental study, and overuse of animal models with slackening drug discovery processes. Addressing these issues requires a wide range of tumor models, including *in vivo*, *ex vivo*, and *in vitro* (two-dimensional [2D] and three-dimensional [3D]) models with various complexities, developed specifically for studying cancer pathology and progressing with anticancer therapeutics.

Various types of mouse models, including cancer cell line-derived and patient-derived tumor xenograft (PDX) models, have been generated by transplanting cell lines, or a fraction of human tumors heterotopically and/or orthotopically to immunocompromised mice. Cancer cell line-derived models fail in fully capturing the histopathological features exhibited in a clinical setting, although PDXs models largely preserves the genetic and epigenetic abnormalities of the original tumors when compared to patients in clinical trials[2]. Despite

this great potential of PDX models within an aspect of precision medicine, the outcomes were compromised by notably the insufficient relevant tissue-specific microenvironment support[3]. Often after engraftment, the stromal components in tumors undergo remodeling with embedded stromal cells which are gradually replaced by host stroma. The use of immunodeficient mice also leads to incompetent PDX models in immunotherapy-relevant studies which currently is a widespread concern[4]. Other problems, such as low engraftment rate[5], have also been frequently raised as a part of the key challenges.

On the other hand, *in vitro* models are speculated as promising platforms to interrogatively extrapolate *in vivo* conditions. 2D culture models lack cell-to-cell and cell-to-extracellular matrix (ECM) interactions rendered in 2D culture platforms, which are incompetent in recapitulating the heterogeneous features characteristically shown in the tumor microenvironment (TME). Substantial evidence has revealed that 3D culture is more physiologically relevant in comparison to planar culture[6,7]. The essential differences between cell behaviors, gene and protein expressions, and drug responses in 2D versus 3D cell culture systems are driving communal adoption of 3D culture toward more faithful and sophisticated tumor models. Thereafter, a series of 3D *in vitro* tumor models with diverse configurations and various complexities have been investigated for cancer research, drug discovery and have become a promising complimentary tool in bridging the *in vitro, in vivo,* and clinical investigations[8,9].

Spheroids have been recognized as classic 3D culture models for pathophysiological studies, which mimics the aggregation of one or multiple types of tumor and tumor tissue microenvironment relevant cells grown in suspension or in a 3D matrix. Spheroids are formed by boosting the cell-to-cell interaction while minimizing the cell-to-matrix adhesion[10]. Cells initially aggregate to form loose bonds by integrin-mediated attachment to ECM, which substantiates the upregulation of cadherin. This accumulation of cadherin on the cell membrane facilitates the compact spheroid formation[11], as opposed to individual cells, spheroids possess an non-apical cell morphology with stronger cell-to-cell, and cell-to-ECM interactions. Spheroids with increased cell survival rates, higher levels of ECM proteins secretion, and a more stable morphology have been reported in comparison to 2D culture[12]. Diffusion limit (~250 μm) enables ordered gradient proliferation rates observed in a large size of spheroids over 500 μm[13], which exhibit different zones with varied cell conditions delineated by the proliferation zone in the outer layer, quiescent zone in the middle layer, and necrotic zone in the center core[11]. Cells presenting in the outer layer receive abundant oxygen and culture medium, thus displaying much higher proliferation rate and viability. In contrast, cells in the core tend to be quiescent or hypoxic due to the limited supply of oxygen and nutrient delivery[14]. On the other hand, the oxygen-depleted cells anaerobically convert pyruvate to lactic acid, in an effort to produce an acidic core within spheroids. Above-mentioned observations reflect *in vivo* features of avascular tumors, in terms of cell morphology, growing kinetics, hypoxia, metabolism, nutrient gradient, and gene expression, which represent a promising platform for a better understanding of cancer biology and drug discovery *ex vivo*.

In the past few decades, 3D bioprinting has garnered extensive attention[15-17]. 3D bioprinting possesses superior flexibility and controllability on the spatial arrangement of biomaterials and cells, which has been expansively applied to tumor-related studies including TME mimicking, tumor angiogenesis, tumor metastasis, and antitumor drug screening using individual cells and miscellaneous biomaterials[18-21]. Nevertheless, individually dispersed cells within the hydrogel matrix are insufficient in faithfully recapitulating specific disease states either indicating fibrosis or tumor propagation[22]. In contrast, spheroids could be a perfect alternative and implementable approach. Despite the high potential in building tissue constructs by combining 3D bioprinting and spheroidal assembly, 3D printing or positioning spheroids with high precision remains challenging.

Herein, we review state-of-the-art status of using spheroids for mimicking tumor tissue microenvironment and their potential as building blocks in 3D bioprinting technology. We first concisely describe the context of the TME, followed by an introduction of various methodologies for spheroid formation, including the comparison of their merits and drawbacks. We then compile contemporary literature sources, providing a compelling overview of recent progress of using spheroids as building blocks for 3D printed tissue modeling, with a particular emphasis on tumor models. Finally, we discuss the future potential and challenges on spheroid formation, 3D bioprinting and their combination thereof utilized for advancing cancer research.

2. TME

Tumorigenesis is a dynamically complicated process involving its initiation, progression, and metastasis. It is governed by not only malignant tumor cells but also the constantly interacting, surrounding stroma, which is referred to as TME[23]. During tumorigenesis, the interplay between tumor cells and associated TME, reciprocally remodeling the ECM and their subsequent competition, determines whether tumorigenesis proceeds[24]. The TME is a highly heterogeneous, stage- and localization- dependent, and individually specific to its origination[25]. Only a small fraction of the tumor is comprised of tumor cells, while the larger,

non-tumor fraction houses stromal cells mainly including fibroblasts and myofibrolasts, adipocyte, blood and lymphatic vascular networks, infiltrating immune cells, and the non-cellular ECM[23], as shown in **Figure 1**. The major cell types in TME include immune cells, stromal cells, and tumor endothelial cells (TECs). Immune cells such as macrophages, dendritic cells (DCs), myeloid-derived suppressor cells (MDSCs), CD4/CD8 T cells, and regulatory T cells (Tregs) play a key role in tumor immune evasion[26]. These immune cells in TME present the resistance to immunosurveillance which recognizes and destroys foreign pathogens. Moreover, tumor-associated macrophages (TAMs) also promote angiogenesis and metastasis by producing multiple cytokines, including vascular endothelial growth factor A (VEGF-A), tumor necrosis factor α (TNFα), and interleukin 6 (IL-6)[24]. Stromal cells, including cancer-associated fibroblasts (CAFs), mesenchymal stromal cells (MSCs), and pericytes contribute to the structure of TME and promote growth, invasion, as well as metastasis of tumors. MSCs in TME, a kind of multipotent progenitor cells, can differentiate into multiple connective tissues to exacerbate tumor desmoplasia, proliferation, and angiogenesis[27]. Pericytes, along with endothelial cells, act as a physical barrier involving basement membrane remodeling during tumor angiogenesis and tumorigenesis. In addition, pericytes also regulate leukocytes transmigration and elicit phagocytic activity[28]. In addition, TECs, with irregular shape and size, build up the inner layer of blood vessels of the tumor and involve in tumor angiogenesis, progression, metastasis, and chemo drugs resistance[29]. Through providing a leaking vascular system, impaired blood flow, as well as a high-interstitial-fluid-pressure, hypoxia, and acidic environment, the disorganized TECs are key factors of tumor progression[24]. The ECM is a 3D network of extracellular macromolecules composed of collagen, laminin, fibronectin, hyaluronan, proteoglycan, and other biopolymers with varied concentrations and organizations (**Figure 1**); therefore, the ECM exists in various elasticities and dimensional stiffness.

It is well documented that stiffness of tumor is higher than that of the normal tissue and will vary across tumor grade[30]. On tissue damage, an increasing number of CAFs are detected within the tumor. These myofibroblasts are thought to be "activated" fibroblasts and will engage to promote the tumor progression[31]. Specifically, breast tumor has shown a stiffer microenvironment (4 kPa) compared to the healthy breast tissue (150~200 Pa). In

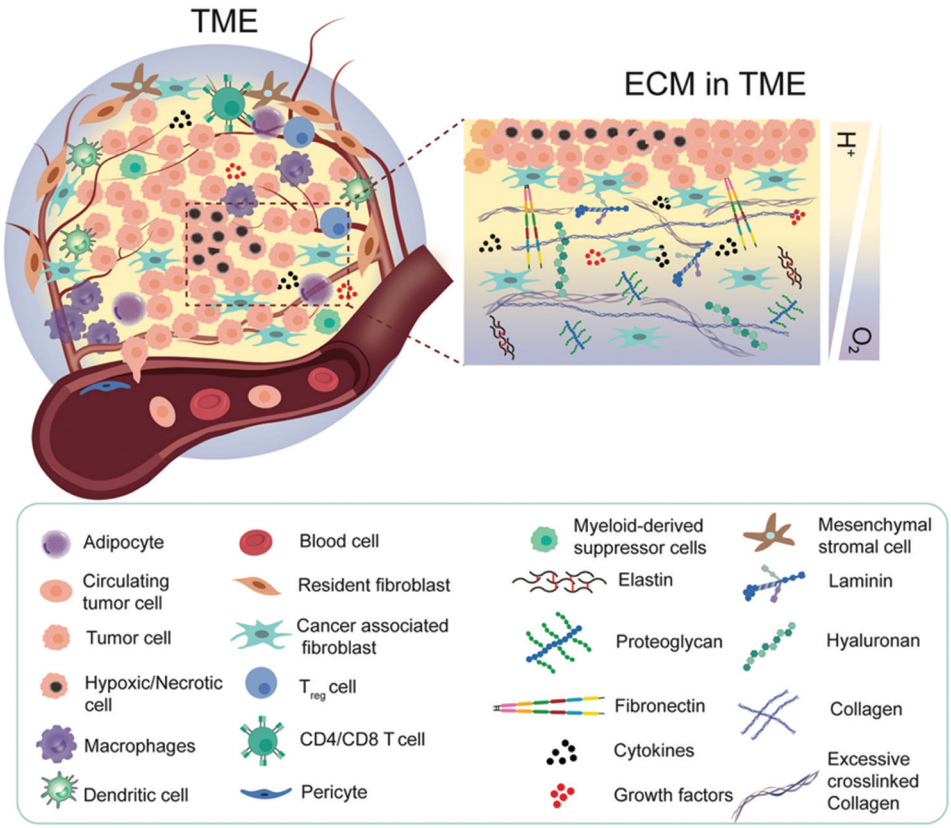

Figure 1. A schematic view of cellular components and extracellular matrix compositions of tumor microenvironment (TME). TME not only houses tumor cells but also includes stromal cells and infiltrating immune cells. Limited perfusion and tumor expansion establish a gradient of oxygen availability from the blood vessels to the adjacent tumor cells in the acidic environment.

addition, both the stroma surrounding the tumor and the tumor vasculature exhibit increased stiffness (E = ~800 – 1000 Pa and ~450 Pa, respectively) compared with healthy mammary tissue and vasculature (E = ~200 Pa) [32]. Similarly, healthy brain tissue has extremely low stiffness, typically range from 100 to 1000 Pa, whereas the increased secretion and remodeling of fibrous ECM proteins in tumor niche leads to increased tissue stiffness up to 26 kPa[33].

Hypoxia is recognized to be one of the hallmarks of the malignant tumors[34]. As tumor cells expand, the oxygen transportation to cells in the central zone is compromised due to the fact that the diffusion limit of oxygen in tissue is about 250 μm[35]. Hence, the increased metabolic rate in the external cell proliferating region and the limited access to oxygen in the core establish a gradient of oxygen availability from the blood vessels to the adjacent tumor cells. Hypoxia-inducible factor (HIF-) 1 plays a pivotal role in regulating oxygen homeostasis within cells. The hypoxic tumor cells with the upregulation of HIF-1 strive to secret VEGF, fibroblast growth factor (FGF), and other proangiogenic factors to recruit endothelial cells and facilitate capillary network formation, which is also referred to as "tumor angiogenesis"[36]. However, due to the perturbed cell-to-cell and cell-to-ECM interactions and remodeled ECM, the tumor blood vessels are chaotic and highly differed from normal host vascular network. Such leaky and highly disorganized neovasculature leads to limited oxygen diffusion and are in correlation with the ability of tumor invasion and metastasis. In the process of tumor metastasis, tumor cells travel through a series of microenvironment with changing matrix stiffness, including stroma, circulating system, endothelium, and finally the tissues at a secondary site[37].

3. Spheroid generation methods

Spheroids have found great potential in anticancer pharmaceutical development, because they are able to resemble the main features of humanoid tumors in many aspects; for instance, structural organization, and metabolic and proliferative gradients[13]. A spheroid's size could be tailored to specific applications. In general, cellular types, seeding density, and culture period are working synergistically in appropriating the size of spheroids. Uniformity of the spheroids is of utmost importance because the relevant size and shape dictate therapeutic efficacy and clinical reproducibility. Numerous strategies have been reported in attempting to form spheroids with desired size and uniformity, including hanging drop[38-40], agitation-based techniques[41,42], liquid overlay technique (LOT)[43], hydrogel microwells[44,45], external-force-driven (magnetic, electric, acoustic) techniques[46-48], microfluidics[49,50], and 3D bioprinting[51] (**Figure 2**).

3.1. Hanging drop technique

Hanging drop technique is a straightforward and well-established method for spheroid preparation, which is also the most frequently used method, due to its ease in handling and user-friendliness without needs of specialized instrumentation. Briefly, small droplets of cells are deposited on a lidded surface of a polystyrene tissue culture plate (**Figure 2A-a**).

Driven by gravity, cells in the droplet start to aggregate and eventually form spheroids at the bottom of the droplets[52]. By adjusting the diameter of the contact area (3, 5 and 7 mm) and droplet volume (10 – 153 μL), Gao *et al*. have developed a hanging drop platform with controlled geometry to investigate the effects of droplet curvature, spreading area and cell density on spheroid formation using β-TC-6 islet cells. These results demonstrated that at a fixed volume, the radius of drop curvature was proportional to the diameter of the guiding circle, and a small radius of curvature yielded spheroids with better aggregation and compactness. A guiding circle with a selected diameter of 5 mm exhibited the highest efficient spheroid formation. The selected cell density of 105 cells/mL gave rise to spheroids with a diameter of 400 – 500 μm, which was well aligned with native islet size[53]. Notably, the optimized spheroids made of islet cells exhibited similar morphology and function to primary islets as compared to 2D culture, which indicates the superior role of 3D culture.

Optimizations were conducted and reported on these hanging drop methods for promoting spheroid formation[38]. Due to a higher hydrophobic nature and a selected droplet contact angle of 99°, polydimethylsiloxane (PDMS) was demonstrated to be superior to polystyrene in generating more uniformly compacted spheroids[52]. Notably, the supplement of collagen fibril at 500 μg/ml in the hanging droplet greatly accelerated the spheroid formation within 24 h. In addition, other additives, such as poly (N-isopropylacrylamide) and methylcellulose, have also been promising in aiding uniformly compact spheroid formation[54,55]. Industrial scale-up strategies regarding the manufacturing of spheroids in a high-throughput manner are reported (**Figure 2A-a$_1$**). A hanging drop spheroid culture array plate that could give rise to up to 384 spheroids had been developed[39,40]. These corresponding results displayed that the osmolality could be maintained at a desired culture range, requiring 30% of culture medium exchanged every other day. Taken together, the hanging drop method displays excellent control on the size and shape of spheroids, yet is unstable and laborious. Medium exchange as well as the drug administration can be time-consuming and challenging. Inappropriate practice might disturb the spheroids and result in a compromised integrity. Moreover, accurate monitoring of growth with regard to the spheroids, in real-time, is difficult to achieve.

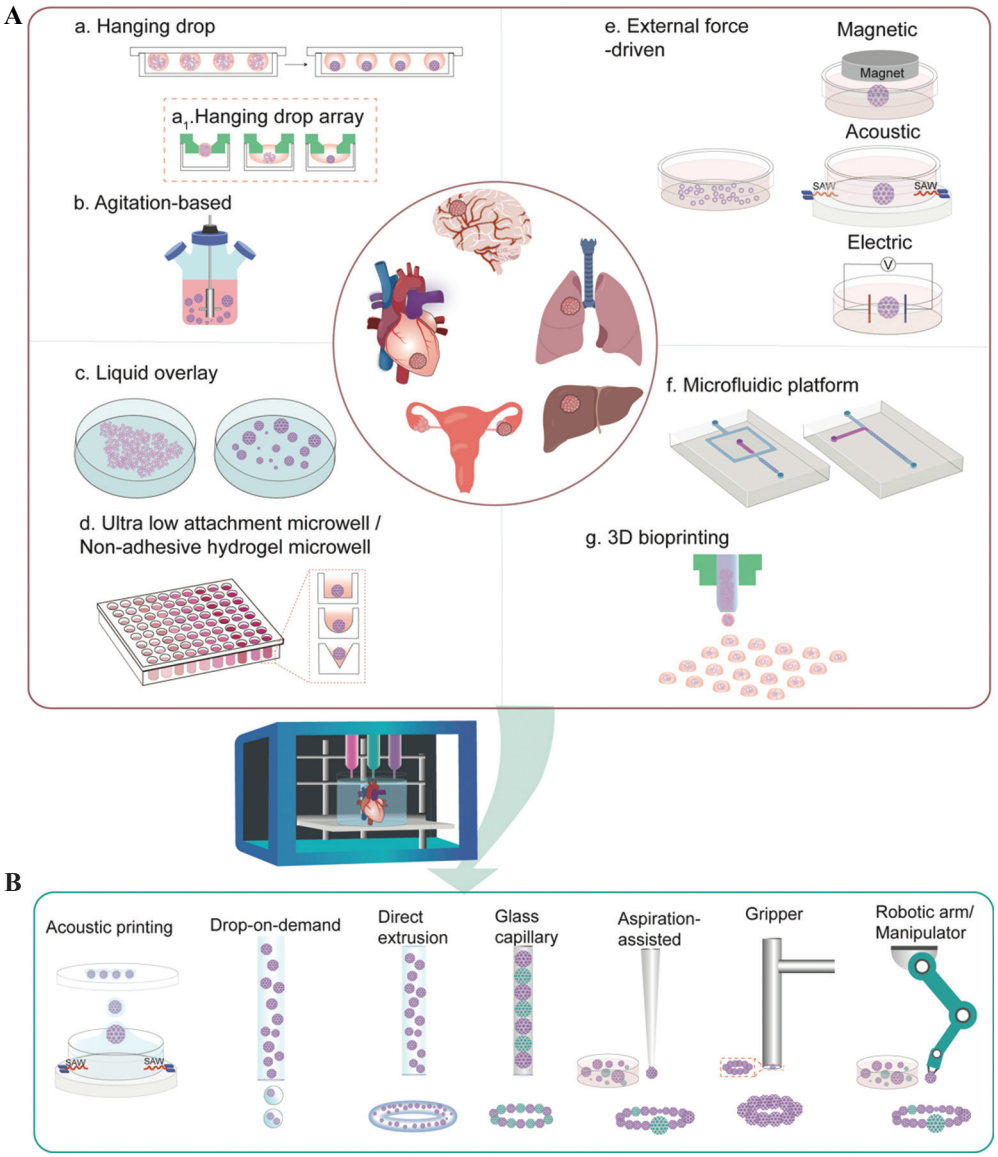

Figure 2. Schematic illustration of using spheroids as building blocks in 3D bioprinting for healthy/disease tissue construction. (A) Overview of spheroid formation techniques. (B) 3D Printing and its adaptions in assisting spheroid assembly.

3.2. Agitation-based methods

Agitation-based methods promote spheroid formation by maintaining cells in suspension using specialized equipment, such as spinner flasks, roller bottles, gyratory shakers, or a NASA bioreactors through continuous stirring by an impeller(s) or magnetic stirrer(s)[41,56-59]. This approach enables mass production of spheroids with long-term culture, while also allows tracking of these spheroids during constant culture (**Figure 2A-b**). In particular, using a bioreactor facilitates the control over pH, oxygenation and nutrient concentration[60]. However, these spheroids are generated in a single compartment, resulting in poor control over size and uniformity. The stirring rate and the culture time need to be constantly monitored. The combined stirrer's mechanical stress coupled with the fluid's shear stress generated from the high stirring rate may cause cell damage and reduce the spheroid formation, whereas a low stirring rate may not be able to prevent cell sedimentation.

3.3. LOT

Different from agitation-based technique (subjecting cells to high shear stress), LOT is a static technique that suspends cell culture on non-adhesive surfaces, prevents cell-to-substrate adhesion, and promotes cell-to-cell interaction, advantageously with low shear stress (**Figure 2A-c**). Typically, this non-adhesive surface is achieved by pre-coating with biocompatible materials such as agarose[61-63] and poly-2-hydroxyethyl methacrylate (polyHEMA)[64-66]

on any commercially available cell culture plate. Among them, agarose is the most widely utilized material due to its cost-effectiveness and ease of handling. Agarose could be simply prepared, sterilized by autoclave, and solidified in only a few minutes after coating. In addition, polyHEMA is recognized as an effective alternative for spheroid formation. Briefly, a homogeneous polyHEMA solution can be obtained by dissolving polyHEMA powder in 95% ethanol at 65°C overnight, followed by a drying process at room temperature and ethanol evaporation at temperature up to 37°C. The drying process could take days to weeks according to different protocols[66-68]. Regardless of the preparation time, polyHEMA solutions can be stored at 4°C for up to 2 months[68], whereas agarose solution cannot be lengthily stored because repeated heating impairs the properties of agarose.

Like agitation-based techniques, spheroids generated by LOT on flat surfaces are revealed as irregularly shaped and disorganized. Optimizations have been attempted in increasing amenability to high-throughput applications. Ivascu *et al*. had conducted a systematic parametric study about optimal spheroid formation on polyHEMA-coated surface in terms of cell types, cell density, medium additives, plate type (round bottom and conical shaped bottom), and the presence of horizontal stirring[69]. Twenty tumor cell lines of different lineages were examined. A series of medium additives with varied concentrations have been systematically screened for optimal spheroid formation, including reconstituted basement membrane (rBM), collagen type I and type IV, laminin, fibronectin, heparan sulphate proteoglycan and chondroitin sulphate. Interestingly, the results reported the compact spheroid formation for all the cell lines with the addition of 2.5% rBM. In addition to ECM-related components, methylcellulose is also validated as an additive support for compact, unisized spheroid formation[70].

3.4. Non-adhesive hydrogel microwell

Micro-molded microwells using non-adhesive hydrogels have been proven as an effective alternative for spheroid formation. Similar to the LOT, non-adhesive materials are used in preventing cell adhesion to the bottom of the microwell. A series of materials have been explored, such as agarose[71], polyethylene glycol diacrylate (PEGDA)[72], and PDMS[73]. Among them, agarose is most prevalently used for micro-molding[74-76]. Briefly, a microfeature mold is fabricated through soft lithography or rapid prototyping, a PDMS-negative replicate could be achieved subsequently. Thereafter, the agarose micro-mold could be obtained by casting into the PDMS replicate[75]. Micro-molds with an array of various patterns, for instance, flat surface or a conical shape with a rounded bottom and hemispherical shape, have been demonstrated in promoting spheroid formation (**Figure 2A-d**)[75,77]. Evidenced by their successful fabrications of micro-molded non-adhesive agarose hydrogels composed of 822 concave recesses (800 μm deep × 400 μm wide)[78], this technique is relatively high throughput with effortless scale up capabilities. Spheroid growth becomes easily accessible during culture. In contrast to the hanging drop method, cell medium change and drug administration are more convenient to accomplish without the risk of disturbing the spheroids using LOT and non-adhesive hydrogel microwells.

3.5. External force-driven methods

External forces, such as electromagnetic and acoustic forces, have been applied in generating spheroids (**Figure 2A-e**). The utilization of dielectrophoresis (DEP), in the development of multicellular aggregation, was successfully demonstrated and optimized[48]. DEP functions by producing an external force on a dielectric particle when it is subjected to a non-uniform electric field, analogous to piezoelectric materials. Cells could be guided by dielectrophoretic forces to form clusters; however, the clusters could be damaged by mechanical or hydrodynamic forces after the removal of electric field. Hence, a range of biomaterials, including but not limit to collagen, PEGDA, agarose, pluronic, and PuraMatrix, have been introduced for immobilizing and stabilizing the cell aggregates[79-81].

Magnetized cells could be obtained by cell internalization. Magnetic nanoparticles, including magnetoferritin, superparamagnetic iron oxide nanoparticles and its cousin, gold, could be internalized into cell cytoplasm through endocytosis, or by surface functionalization[82]. As an example of surface functionalization, magneto-functionalized cell membrane was readily achieved with a combination of poly-L-lysine mixed gold or iron oxide nanoparticles[83]. Leveraging this newly embedded magnetic capability, magnetized cells could be levitated and agglomerated to form spheroids when magnets are placed on the culture dish or using a magnetic lid[46,82,84]. Spheroids formed with magnetized cells demonstrated a negligible adverse effect on cell viability while accelerating spheroidization time. Diverse structures and sizes of 3D cellular aggregates could be achieved through the adjustment a magnetic field configuration[85]. Urbanczyk *et al*. have investigated the interaction of pancreatic β-cells with vascular endothelial cells in heterotypic pancreatic spheroid models using magnetic levitation in three different configurations. The results identified that human umbilical vein endothelial cells (HUVECs), which disassembles from the spheroids over time, spontaneously formed spheroids, highlighting this significant role of magnetic levitation. Magnetic levitation could enhance the stability of heterotypic spheroids, facilitating HUVEC integration[83].

Integrating acoustics with microfluidics and acoustic fluidics have found many applications in cell sorting and separation[86]. This acoustic-based cell manipulation technique is non-invasive and label-free. By guiding surface acoustic waves (SAW) to a microfluidic chamber, Chen *et al*. had demonstrated spheroid formation, while simultaneously patterning through a designed 3D acoustic tweezer platform[47]. Guo *et al*. had developed a high-throughput acoustic fluidic platform for large-scale spheroid formation[87]. By acoustically assembling cancer cells, this platform enables high throughput fabrication of 6000 tumor spheroids per batch within 24 h.

3.6. Microfluidic platforms

By manipulating fluid flow between micro- and nano-scales within microchannels, microfluidic platforms have evolved as powerful tools that could possibly miniaturize significant experimental processes onto a microfluidic chip less than the size of a finger[88]. Droplet-based microfluidics, which generates discrete droplets via immiscible multiphase flows inside microfluidic devices, have gained substantial interest in past decades. Through adjustments to the flow rate of immiscible fluids, this method enables generation of highly monodispersed droplets with a production speed spanning from 10-1000 droplets per second[89]. Typically, there are 3 types of microfluidic configurations for passive droplet generation: cross-flowing/T junction[90,91], flow-focusing[92-95], and co-flowing droplet formation[96]. Flow-focusing with single-, double-, and multiple-emulsion designs have been extensively utilized (**Figure 2A-f**)[97-99]. As a result, cell-encapsulated capsules with a template of water-in-oil (w/o), oil-in-water-in-oil (o/w/o), water-in-water-in-oil (w/w/o), and water-in-oil-in-water (w/o/w) could be produced[100,101]. By assigning different materials and/or cells to replace each individual phase, microcapsules displaying varied cell/material arrangements could be tailored for diverse applications[102]. For instance, with a double-emulsion, flow-focusing microfluidic device, Agarwal *et al*. had developed core-shell microcapsules with embryonic stem cell-laden carboxymethyl cellulose and alginate in the core and shell, respectively. Other than alginate[98], hydrogels such as chitosan, thermosensitive gelatin, agarose, Matrigel, collagen, P(NIPAM-AA), photoinitiative gelatin methacrylate (gelMA), PEGDA, and hyaluronic acid-MA have all been examined for facilitating spheroid formation and growth[94]. In addition to droplet-based microfludics, lab-on-a-chip technology also can integrate hanging drop networks[103-105], microwell[50,106], U-shape microstructure, or micropillar into the platforms for spheroid formation and on-chip culture. Microfluidic platforms outperform conventional static culture methods through the introduction of a perfusion flow that could improve oxygen and nutrient transportation, sustaining long-term cell culture[107,108].

These continuous flow-based microfluidic platforms frequently use and require syringe pumps, whereas digital microfluidic platforms can optimally dispense pico- to micro-liter droplets on an electromechanical apparatus; therefore, digital microfluidic platform are more portable and cost-effective[109-111]. Through tight control over fluidic flow, microfluidic platforms allow the generation of monodispersed droplets with uniform spheroid formation coupling a high throughput production output[112,113].

3.7. 3D Bioprinting techniques

Despite the broad utilization of extrusion-based bioprinting in building 3D tissue constructs, strong interests in inkjet-based bioprinting have been growing substantially in recent decades. The capability of a "drop-on-demand" style printing to accurately dispense discrete spheroids makes this technique appealing for high-throughput spheroid formation (**Figure 2A-g**). By dispensing the cell droplets into an alginate hydrogel matrix residing within a 96-well plate, through microvalve-based printing, Utama *et al*. had successfully generated spheroids using 3 different cell types, including neuroblastoma (SK-N-BE(2)), non-small cell lung cancer (H460), and glioblastoma (U87vIII) cells[114]. The size of these printed spheroids was controlled by adjusting the initial printing cell density and incubation time, as well as the confinement of the printed hydrogel matrix. Evidenced by the expression of Ki67, HIF-1α, and apoptotic marker cleaved caspase-3, the 3D-printed SK-N-BE(2) spheroids exhibited similar tumor-like characteristics that resemble manually formed spheroids. Similar level of CD133 expression was found in both 3D printed and manually generated neuroblastoma spheroids, indicating a similar preservation of cancer stemness between both types of spheroids. Therapeutic efficacy was also examined by doxorubicin (DOX) treatment for 2 h. DOX penetration was found on the periphery of both types of prepared spheroids, which are also frequently observed in tumors. These results collectively demonstrated the capability of 3D printed spheroids in recapitulating the biological features of tumors.

Taking advantage of the thermal property of gelatin hydrogel, Ling *et al*. had fabricated concave wells molded from a polyethylene glycol-dimethacrylate (PEG-DMA) array, with *in situ* seeding of human breast cancer cell-laden gelatin for cellular spheroid formation on a chip[115]. However, challenges associated with droplet inconsistency, low cell density, easy nozzle blockage, and physical stresses on cells limit the range of this technique's applicability. Alternatively, laser-based bioprinting also enables droplet-based printing for single cell manipulation or 3D spheroid formation[116,117].

Using the platform, laser direct-write, Kingsley *et al*. had generated size and shape controllable chitosan-shelled alginate structures with human breast cancer cells and mouse embryonic stem cells encapsulated, respectively[51]. Adjusting the beam diameter of the laser enables control over the printed aggregate sizer ranging from 200 μm and 400 μm. These obtained microbeads were further washed in chitosan solution, forming a core-shell structure that could constrain the aggregate geometry. Over a 14-day culture period, both cells showed high cell viability. Notably, both cell types self-assembled into 3D aggregates to match the corresponding geometry of their printed constructs. Similarly, with the laser-assisted bioprinting, Hakobyan *et al*. had created 3D pancreatic cell spheroid arrays using the AR42J-B-13 rat acinar cell line for studying the initial stages of pancreatic ductal adenocarcinoma development[118]. The printed spheroids were observed with a diameter around 30-40 μm. Taken together, this nozzle-free, laser-assisted method allows spheroid generation with a high resolution and density, but rather financially taxing in usage[115]. In addition, although extrusion-based bioprinting is not as capable in generating droplets, they have been utilized to print 3D microtissue inserts[119], or hanging drippers[40], availing toward a high-throughput spheroid formation.

4. 3D printing-assisted spheroid assembly

Despite the great efforts that have been devoted to 3D-printed TME, the progress is limited by many reasons including the incompliant mechanical stiffness of the bio-inks and thus compromised cell-to-cell, cell-to-ECM interactions. Spheroid is recognized as a physiologically relevant 3D model that could capture the key characteristics of both healthy and disease tissues. Given the high cell density, increased deposition of ECM and accelerated proliferation rate, spheroids-based model could greatly reduce the tissue maturation time. Such densely packed spheroid is thus proposed as building blocks for either healthy or diseased tissue modeling. However, the spheroid growth and fusion are highly disorganized, which would ultimately affect the consistency in therapeutic outcomes. To impose spatial control and guide the spheroid fusion and arrangement, several strategies such as direct fusion and magnetic-driven assembly have been explored for manipulating spheroids. However, major issues, such as poor positioning resolution, simple structures, and the requirement of specialized instruments, are yet to be addressed. Given the capability of bioprinting in spatial control, several 3D printing strategies and its adaptions have been investigated for their potentiality in spheroid assembly. The software programs for converting digital files to real 3D printing can be as complex as AutoCAD and SolidWorks or 3ds Max and Maya, or as simple as TinkecCAD or OpenSCAD. G-code is the standard program used by outputting from slicing software and setting instructions for 3D printers to move the stage and printer nozzles in x-, y-, and z-axes along with bio-ink extrusion.

Finally, the embedded software that runs on the printer itself takes the G-code and turns it into electrical signals for running various motors. This is usually done in C/C++ but could also be written in anything that fits on the printer's hardware.

4.1. Direct extrusion-based printing

Swaminathan *et al*. investigated the bioprinting of pre-formed breast epithelial spheroids in alginate-based bio-ink co-culture with endothelial cells[120,121], and demonstrated that the printed pre-formed spheroids exhibited high cell viability and maintained their spheroid morphology after bioprinting, either in monoculture or co-culture with HUVECs. Moreover, the 3D-printed spheroids were shown to be more resistant to the paclitaxel treatment as compared to 3D-printed individual cells, highlighting that the spheroids have preserved their function after being extruded. This study has validated the capability of printing spheroids directly using extrusion-based bioprinting. To maintain the integrity and avoid spheroid aggregation in printing cartridge and nozzle clogging, the size of the spheroids was confined to ~70 μm.

Recently, Horder *et al*. have interrogated the interaction between adipose-derived stromal cell (ASC) and breast cancer cells in a 3D-printed co-culture model[122]. The model was composed of directly printed ASC spheroids in hyaluronic acid (HA)-rich hydrogel. The printability of ASC spheroids (228 ± 22 μm) was assessed using 2 different needle sizes, 250 and 330 μm, with a corresponding pressure at 5 bar and 1 bar. Printing with the 330 μm needle caused 9% damage on the integrity of the printed spheroids, while the damage and cell death was dramatically increased to 56% using the 250 μm needle. Over a 21-day differentiation culture, the printed ASC spheroids showed substantial and sustained adipogenesis. Comparable levels of triglyceride, the expression of both early markers (PPAR and C/EBP) and late marker (fatty acid-binding protein 4 (FABP4)) of adipogenic differentiation, and the secretion of adiponectin were demonstrated in both printed and non-printed spheroids, indicating that the printing process have negligible effects on the cellular differentiation. Evidenced by Oil Red O staining and quantitative analysis of intracellular triglycerides, a considerable reduction on lipid content in co-culture constructs was observed as compared to ASCs monoculture model. Moreover, the immunostaining for the major ECM components collagen I, IV, and VI, laminin, and fibronectin revealed the ECM remodeling in the co-culture model. These features reflected what was observed *in vivo*, highlighting

the physiological relevance of the printed co-culture model. Taken together, extrusion-based printing enables the direct spheroid printing without any modification to the printing setup. However, the resolution of extrusion-based printing is needle size-dependent, thus limiting the size and density of the spheroids. The integrity of large spheroids will be compromised, and the high spheroid density is liable to induce nozzle blockage.

Interestingly, utilizing a capillary micropipette with a defined diameter at 300 or 500 μm in bio-printer, Jakab *et al*. have successfully delivered multicellular spheroids to collagen type I substrate and formed certain structures, such as ring, sheets, and cylinders[123]. Interestingly, the spheroids were formed by a rapid centrifugation, incubation, and a cutting process to secure the size consistency in obtained spheroids. The spheroids were then aspirated into a capillary micropipette as a printing cartridge and extruded from the cartridge through the positive displacement of a piston within the micropipette. This printing technique was subsequently applied to engineer vessels of distinct shapes and hierarchical trees with diameters spanning from 900 μm to 2.5 mm. Agarose was used as temporary support to facilitate the construction of hanging features. The deposited discrete spheroids underwent post-printing fusion and formed single-layer and double-layer tubular structures. Notably, with the adapted capillary micropipette as printing cartridge, this scaffold-free approach circumvents some shortcomings associated with exogeneous biomaterials and provides much better control over the spheroid geometry and position, therefore greatly improving the reproducibility and scalability as compared to the non-adapted extrusion-based printing.

4.2. Droplet-based bioprinting

Apart from extrusion-based printing, other bioprinting modalities such as microvalve-based printing[124], laser-assisted printing[125], and acoustic printing[126] have also been explored for their capability in printing spheroid aggregates. By adopting an open cartridge, Chen *et al*. introduced a nozzle-free, contact-free acoustic-driven bioprinting that allows both cell and spheroid ejection[126]. Cell encapsulating GelMA droplets were ejected onto a receiving substrate in a pre-designed arrangement, followed by UV crosslinking that stabilizes the structure. The authors had generated a co-culture TME with the tumor spheroid in the central zone and the CAFs in the periphery. Over a 7-day culture period, increased tumor spheroid invasion area and distance was observed in co-culture model as compared to monoculture, suggesting that CAFs may promote morphological changes within tumor cells. Such a nozzle-free printing approach holds great potential for constructing tissue models with low cell damage, although the resolution is limited and only suitable for bio-inks with low viscosity. This method alleviates heat or mechanical damage exerted by the bioprinting nozzle on the cells/spheroids, enabling printing with high cell densities (>10^8 cells/mL).

4.3. Kenzan method

Proposed by Prof. Koich Nakayama, Kenzan method has been frequently used in constructing tissue models with scaffold-free bio-inks. Kenzan, which is also referred to as a microneedle-based method, using stainless-steel needle arrays that function as temporary support for spheroids and allow the *in-situ* fusion of the spheroids to form a macro-tissue[127]. The spheroids are picked up by a mobile nozzle arm from well plates and moved on the top of the microneedle array. By switching the negative pneumatic pressure to slightly positive, the spheroids are released into the substrate. The process is repeated until the entire construct is completed and left on the microneedle array for continuous culture.

Upon fusion, the needle arrays are retracted, and the obtained tissue could be perfused and cultured for further maturation[128,129]. Kenzan method has found its application in many tissues, including blood vessel, tracheal, heart, liver, and urinary bladder[130]. In a seminal study, van Pel *et al*. investigated glioma cell invasion into neural-like tissues using Kenzan method[131]. Eight neurospheres formed from induced pluripotent stem cells (iPSC)-derived human neural progenitor cells were robotically placed in the micro-needle arrays and cultured for 3 weeks for fusion and maturation into a neural organoid. U118 human glioma cell spheroids were subsequently printed on the top of the neural organoid and cultured for up to 4 weeks. Revealed by cryosectioning and confocal imaging, GFP^+ U118 cells were found within the human neural organoid, which confirmed the glioma cell invasion. However, no gliosis was observed surrounding the tumor or invading cells, which was different from the previous observations. In summary, the Kenzan method has greatly facilitated the scaffold-free fabrication from various cell types into complex structures, particular tubular constructs but the fixed distance between needles (~400 μm) requires the size-consistent spheroids with a diameter approximate to ~600 μm to ensure their direct contact with one another[132], which significantly restrains the size of usable spheroids and highly relys on spheroid preparation, especially when a large quantity of spheroids is needed. Besides, the mechanical interruption could induce the structural damage to the spheroids, particularly the smaller ones.

4.4. Gripper and manipulator

In addition, gripper or micromanipulator has also been introduced to assemble the spheroids. Notably, inspired by electronics manufacturing, an instrument named Bio-Pick, Place, and Perfuse (Bio-P3) was introduced

to assist the large-scale tissue block translocation[133,134]. Using polycarbonate track-etched membrane-integrated cell culture inserts as the gripper and a peristaltic pump to generate fluid suction through the nozzle's membrane, the nozzle could pick-up, transfer and release the spheroids/microtissues with minimized damage to the living cells, while perfusing the parts in an aqueous environment. As a proof-of-concept, a series of features including spheroids, toroids, and honeycombs with sizes range from 600 μm to 3.4 mm was created to validate the capability of the instrument. A stack of 16 donut ring constructs and 4 honeycombs have been successfully assembled and fused over a 48 h-period for culture to form a single tissue[134]. In a lateral study, the optimization on the system enabled the stacking of 20 honeycomb-shaped structures with improved alignment accuracy[133]. Such strategies have offered an effective alternative for assembling spheroids as building blocks, though with limited precision and prolonged fabrication period.

4.5. Aspiration-assisted bioprinting (AAB)

Harnessing the strength of aspiration forces, Ayan *et al*. have developed an AAB technique that enables to pick and print spheroids with a broader range of sizes from 80 μm to 600 μm in a high precision manner. The printer was adapted from a low-cost commercial printer and equipped with a custom-made tapered pipette (diameter ~80 μm)[135]. Coupling with conventional micro-valve printing, the spheroids could be either printed on hydrogel-based substrate or without scaffold. To demonstrate the capability of the printing strategy, spheroids with different viscoelastic surface tension properties and varied size ranges from 200-600 μm were prepared from a wide range of cell types, including HUVECs, mouse fibroblast cell line (3T3), mouse mammary carcinoma line (4T1), human mesenchymal stem cells (MSCs), HUVECs/MSCs, and human dermal fibroblasts. A heterogeneous pyramid construct was printed using spheroids with different sizes and types, indicating that the technique allows the printing of non-uniform spheroids. The printing accuracy was reported to be ~11% with respect to the spheroid size. The printed spheroids exhibited an overall moderate viability over 80%. Further, in combination with Freeform Reversible Embedding of Suspended Hydrogels (FRESH) printing, they have further extended the versatility of AAB by precisely positioning spheroids in self-healing yield-stress hydrogels to achieve more complicated tissue structures[136]. Both Carbopol with varied concentrations at 0.8%, 1.2%, 1.6% and 0.5% alginate microparticles were investigated for their potentiality as supporting bath for spheroids printing using AAB in terms of positional accuracy and cell viability post printing. As demonstrated, the positional accuracy for 0.8%, 1.2%, and 1.6% concentrations of Carbopol and alginate microparticles were ~97%, 22%, 12%, and 34%, respectively. Notably, over a 3-day culture period, spheroids cultured in 1.2% Carbopol showed a reduced viability around 74%, while maintaining a 93% survival rate in alginate microparticles. Similarly, Daly *et al*. have also printed spheroids in a modified HA-enriched hydrogel supporting bath with a ~10% with respect to spheroid size positional precision[137]. Conclusively, the AAB technique offered an effective alternative to position spheroids in a highly reproducible and precise fashion, therefore giving rise to reliable and robust 3D *in vitro* models for disease modeling. The overall reported methods for generating spheroids were summarized in below **Table 1**.

5. Progress in establishing 3D tumor models via 3D bioprinting

Conventional 3D models, such as spheroids and scaffold-based constructs, offer limited control over cell organization and ascribe poor vascularization. Such shortfalls leave us with oversimplified tumor models, which are incompetent for understanding tumor biology and fail to predict accurate therapeutic response. In recent years, 3D bioprinting technology has undergone rapid development and evolution[141]. The outstanding spatial control over cells and materials, coupled with an integration of vascular networks into the platform, could give rise to higher fidelity 3D tumor models with greatly increased complexity.

To date, bioprinting technologies can be categorized into extrusion-based[142], inkjet-based[143], laser-based[144], and stereolithography techniques[145]. Each technique has its own merits and drawbacks and requires bio-inks with specific properties[146-148]. Indeed, the critical role of bio-inks is embedding a mechanical property that regulates the cellular response. Particularly, in extrusion-based bioprinting, the major stumbling block is the imbalance of printability and the mechanical property of the selected bio-ink[149]. With the development of FRESH printing, where a semisolid suspension bath is used to print into, the resolution of printing intricate hierarchical features such as vascular networks could be significantly improved. Furthermore, this newfound capability of generating soft matrices from low viscous bio-ink provides excitingly tailorable elicitations of any desired cellular response, thus boosting the cell proliferation[150]. Through the aid of bioprinting technologies, a variety of 3D printed models have been created, producing significant advances toward mimicking *in vivo* tumor structure and cell growth behavior as summarized in **Figure 3**. Accumulating studies were reported, describing the use of 3D bioprinting platforms with increased complexity and key features for mimicking tumor progression in an architecturally relevant manners, such as tumor heterogeneity[151-154], tumor angiogenesis[155-157], metastasis[158-160], and anti-

Table 1. 3D printing assisted spheroid assembly

Printing strategy	Target tissue	Spheroid generation method	Materials	Cell type (density)	Spheroid size/ spheroidization time (ST)/ fusion time (FT)	Feature	Ref
Extrusion-based printing	Breast cancer	Falcon 8 chamber polystyrene vessel	Matrigel, gelatin-alginate, collagen-alginate	MCF10A, MCF10A-NeuN, MDA-MB-231, MCF7	5000 cells/well Size~100 μm ST: MCF10A cells, 8–10 d; MCF-7, MDA-MB-231, MCF10A-NeuN, 5–6 d FT: N.A.	• High cell viability in mono- and co-culture • More resistant to paclitaxel than individual cells • Size limitation of spheroid • Limited control over spheroid arrangement	[121]
Extrusion-based printing	Breast cancer	8-well chamber slide	Matrigel	MCF10A MDA-MB-231 (10000 cells/well) HUVECs	Size<70 μm ST: MCF10A, 8 d; MDA-MB-231, 5 d FT: N.A.	• MDA-MB-231 migrates out of spheroids in co-culture with HUVECs • Limited control on bioprinted spheroid location and number • Size limitation of spheroid	[120]
Extrusion-based bioprinting	Breast cancer	Agarose molds cast in MicroTissues®3D Petri Dishes®	Thiol-modified HA, unmodified high concentration HA,	ASCs (2500 cells/ spheroid) MDA-MB-231	4800 spheroids/mL Size: 228 ± 22 μm ST: 2 d FT: N.A.	• Reduction of the lipid content • Increased fibronectin, collagen I and collagen VI expression • Limited control over spheroid arrangement • Size limitation of spheroid	[122]
Extrusion-based printing (capillary micropipette)	Cardiac tissue	Pellet centrifugation	Collagen type I (Bio-paper)	Cardiac and endothelial cells, VEGF	Size: 300/500 μm ST: A few minutes FT: 70 h	• Synchronously beating after 90 h • Size-consistent spheroids • Weak spheroids	[123]

(Contd...)

Table 1. *(Continued)*

Printing strategy	Target tissue	Spheroid generation method	Materials	Cell type (density)	Spheroid size/ spheroidization time (ST)/ fusion time (FT)	Feature	Ref
Extrusion-based printing (capillary micropipette)	Vascular	Pellet centrifugation	Agarose as temporary support	Chinese Hamster Ovary cell, Human umbilical vein smooth muscle cells, Human skin fibroblasts, porcine aortic smooth muscle cells	Size: 300/500 μm ST: 1-2 h FT: 5-7 d	• Size consistent spheroids • Long fusion time • Large quantity of spheroids preparation is time consuming • Non-uniform structure • Weak spheroids	[138]
Multifunctional Fabion 3D bioprinter with the turnstile system	Thyroid gland	Hanging drop	Collagen	Individual thyroid explants and allantoides	Size: thyroid, 388.2 μm±45.3; Allantoide, 493.6 μm±114.3 ST: 18-24 h	• Turnstile allows the deposition of spheroid one at a time • Improved vascularization	[139]
Scaffold-free bioprinter/ Regenova/kenzan method	Glioblastoma	96-well U-bottom plates	N.A.	iPSC-derived human neural progenitor cells (40,000 cells/well), U118 human glioma cells (10,000 cells/well)	Size: 500 μm ST: 48 h FT: 3 weeks	• Mechanical damage to the integrity of spheroids • Fixed spacing between needles • High cost	[131]
Aspiration-assisted bioprinting	Post-myocardial infarction (MI) scarring	Ultra-low attachment 96-well round-bottom plates	HA modified with either adamantane (Ad) or β-cyclodextrin (CD)	Human MSCs, Human cardiac fibroblasts Human iPSC-CM	Size: 5000 cells/200 μm 10000 cells/400 μm ST: 96h FT: 4d	• High resolution positioning (~10% spheroid size) • High density micro-tissue • High cell viability	[137]
Aspiration-assisted bioprinting	/	U-bottom 96-well microplate	Fibrin	3T3, mouse mammary carcinoma line 4T1, HUVECs/MSCs, HDF, electrocytes 2500-10,000 cells/ well	80-800 μm (~30 s/spheroid) ST: 24h	• ~11%with respect to the spheroid size --position accuracy • Non-uniform spheroids printing	[135]

(Contd...)

Table 1. *(Continued)*

Printing strategy	Target tissue	Spheroid generation method	Materials	Cell type (density)	Spheroid size/ spheroidization time (ST)/ fusion time (FT)	Feature	Ref
Aspiration-assisted bioprinting	Osteogenic tissues, cartilage	96-well plate	Carbopol, alginate microparticles	Human MSC spheroids	Osteogenic spheroid, 20000 cells/well; chondrogenic spheroids, 50000 cells/well	• Alginate microparticles: ~34% positional accuracy	[136]
Bio-P3 instrument	Tumor	Nonadhesive agarose micro-mold	N.A.	Rat hepatoma (H35), human ovarian granulosa (KGN), human breast cancer (MCF-7) cells	1250 cells/ spheroid feature, 25,000–40,000 cells/toroid feature, and 250,000 cells/ honeycomb feature ST: spheroid and toroids, 18-24 h; honeycomb, 48 h FT: 48 h	• Allow large microtissue pick-up • Manually operated • Long fabrication time • Limited gripper size available • Optical clarity required	[134]
	Hepatoma	Nonadhesive agarose micro-mold	N.A.	HepG2	375 000 cells/ honeycomb mold ST: 24 h	• Syringe pump-better flow control • Allow large part pick-up • Long fabrication time • Optical clarity required	[133]
Micro-manipulator	/	Non-adhesive round-bottom 96-well plate	N.A.	NIH/3T3 spheroids	3000 cells/well	• Spheroid size >300 μm	[140]
Microvalve printing	Breast cancer	Culture in Matrigel for 7 days (0.5 million cells/mL)	Elastin-like protein-RGD hydrogels	Human premalignant breast epithelial cells (MCF10ATs) spheroid	~ 50 μm	• Maintained morphology and size	[124]
Laser direct-write	Breast cancer	High-voltage electric field-driven microbead fabrication	Alginate/collagen Alginate/gelatin	MDA-MB231, MCF-7, or mixed MDA-MB-231/ MCF-7 breast cancer cells	Size: 300–400 μm	• Real-time video monitoring • Microbead shifting • Limited resolution	[125]
Acoustic droplet printing	Oral cancer	Hanging-drop method	GelMA	Oral squamous cell carcinoma (OSCC) cell line CAL27 spheroids, CAF	600 cells/spheroid, Size ~ 150 μm	• Nozzle-free • Contact-free • Low cell damage	[126]

cancer drug screening[161,162]. Those notable reports also detailed the challenges of current existing technologies for assembling cell-favorable biomaterials with multiple cell types in complex tissue microenvironment as we summarized in **Figure 3**.

Using spheroids as building blocks in facile macro-sized tissue construction has been proposed[163], the most straightforward method in assembling these spheroids is spontaneous fusion[164-167]. Fleming *et al*. had reported a spheroidal fusion between unilluminated vascular spheroids through liquid-like coalescence. Specifically, 2 juxtaposed spheroids were fused when positioned close enough, forming a larger spheroid with preserved composite structural characteristics[168]. These features have legitimized a notion of suitability for using spheroids as building modules in engineering large-scale tissues for tissue regeneration and/or disease modeling. Early studies have also demonstrated the feasibility of assembling spheroids through directed fusion, achieving microtissues with prescribed patterns including honeycomb, rods, and tori[169,170]. Briefly, spheroids are manually placed in a pre-designed mold/template containing the prescribed topography. These spheroids will then gradually fuse together and achieve the specified pattern over time. This manual processing has shed light on a great possibility of generating tissue constructs by spheroidal modular assembly, despite its limited control and low throughput. For overcoming such challenge, several bioengineering strategies have been exploited for spheroid assembly, potentiating its large-scale functional tissue manufacturing with improvements in accuracy through a high-throughput manner.

Leveraging magnetic force, spheroids that are functionalized with magnetic nano/microparticles can be assembled into specific patterns by imposing temporary magnetic fields[171-176]. An applied magnetic field could accelerate the cell aggregation process, but the topology of the constructs is highly dependent on the magnetic template[172,173]. In addition, the association of magnetic particles is inevitable, and the linker involved may engender safety issues. The effects of magnetic nanoparticles on cell physiology and function, other than fundamental cell viability and proliferation, should be considered before further involvement. Instead of magnetically labeling cells, an alternative usage is paramagnetizing the cells. Alahough a paramagnetic

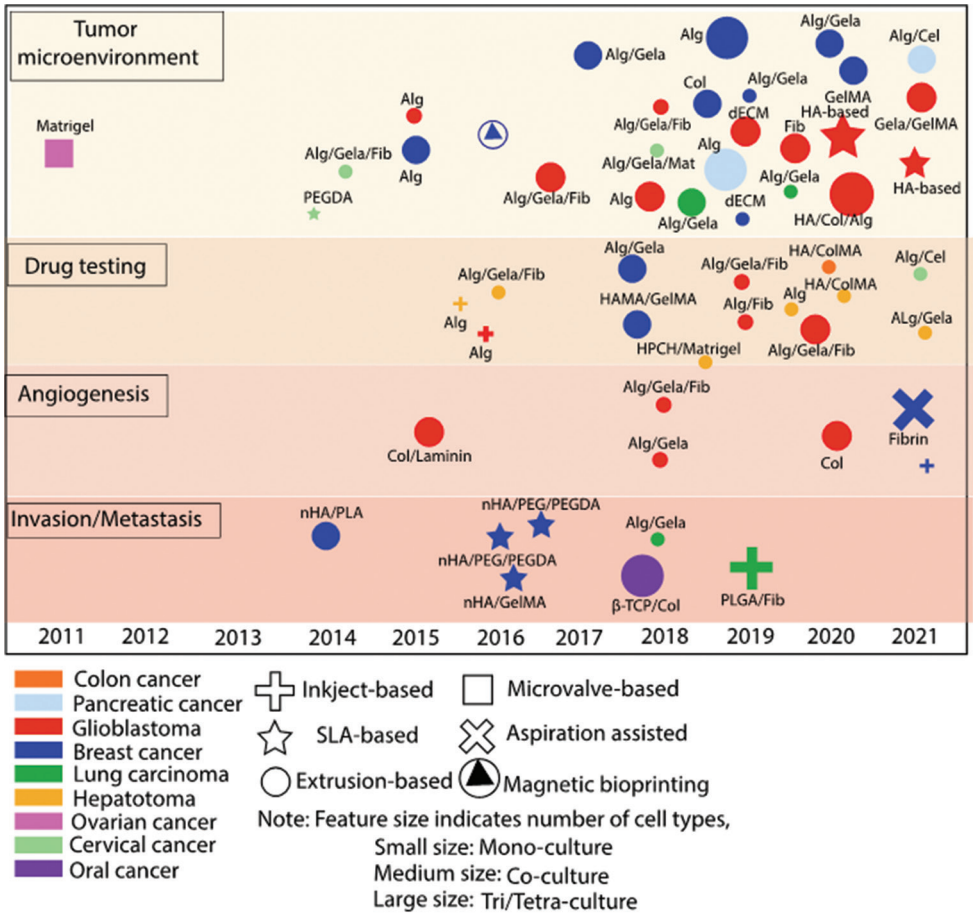

Figure 3. Progress in establishing 3D tumor models via 3D bioprinting.

agent could be removed after spheroidal construction, these paramagnetic agents, at high concentration, could be detrimental to cell survival. Comparatively, another label-free alternative using acoustic wave has also been investigated. By applying non-destructive SAW, Chen *et al*. assembled large amounts of cell spheroids in a fluidic environment, forming various patterns within a couple of seconds[177]. By altering the acoustic wave frequency, several geometric patterns ranging from circle, square, and line to complex geometries could be obtained. A complete fusion of fibroblast spheroids, HUVEC spheroids, and co-cultured spheroids were observed within 72h. To explore this versatility and modularity, the selected strategy was further applied to generate densely packed hepatic tissue constructs from fibroblast, HUVECs and primary rat hepatocytes. Notably, the formation of bile canaliculi was observed at the hepatic junctions over a 6-day culture. The results highlighted a remarkable effectiveness of this contactless, biocompatible, and label-free method in assembling spheroids through a highly efficient process. Interestingly, Parfenov *et al*. recently reported a hybrid magnetoacoustic bioassembly method that allowed rapid assembly of 3D tissue construction from spheroids within a medium, with a relatively low concentration of paramagnetic agent (gadolinium salt)[178]. Harnessing the strength from both magnetic waves and acoustic sounds, this method not only circumvents a challenge from a potentially adverse effect stemming from the paramagnetic agent, but also imparts more flexibility on the assembled structure.

The major challenge associated with replicating tumor models is simulating the heterogeneity of cellular components and ECM. Dynamic interactions between cells and the ECM contribute to tumor initiation, progression, and metastasis through biophysiochemical cues. For instance, macrophages are a heterogeneous population of cells that are crucial to the detection, phagocytosis, and destruction of pathogens. However, when recruited to tumor cells, the TAMs polarize differently and do not display an anti-inflammatory role but rather facilitate tumor growth and angiogenesis. In understanding the crosstalk between glioblastoma cells and macrophages, Heinrich *et al*. generated a 3D-bioprinted mini-brain with GelMA/gelatin encapsulating mouse glioblastoma cells (GL261) in the core of a mouse macrophage cell line (RAW264.7)-enriched at the peripheral[179]. Over a 4-day culture, active migration of macrophages toward tumor cells was observed, while tumors also displayed migration behavior toward macrophages, albeit less dramatic, indicating that macrophages could be actively recruited by tumor cells and polarized into a Glioblastoma-associated macrophages (GAMs) specific phenotype.

Another notable study on interrogating the functional dependencies and cellular interactions in the brain tumor was conducted by Tang *et al*. They developed a 3D-printed glioblastoma (GBM) model consisting of patient-derived glioblastoma stem cells (GSCs), astrocytes, and neural stem cells (NSCs), with or without the presence of macrophages in a blended GelMA and glycidyl methacrylate-HA hydrogel through digital light processed-based bioprinting[180]. The printed construct was composed of 2 regions: (i) GSC or mixed GSC/macrophage encapsulated tumor cores, (ii) surrounded by a non-neoplastic region enriched with NSCs and astrocytes. The upregulation of the glioblastoma tissue-specific gene sets, as compared to 2D and GSC spheres, suggested a better dynamic viewing window of transcriptional states than *ex vivo*-derived glioblastoma tissues. Further, the inclusion of macrophages resulted in upregulation of hypoxic response and glycolic metabolism, eliciting invasiveness signatures in the tetra-culture brain tumor model. This significantly indicated that the 3D-printed GBM model, to a higher extent, resembled the pathologic conditions *in vivo*.

The TME comprises numerous signaling molecules and resulting pathways that influence the angiogenic response. Achieving a durable and efficient antiangiogenic response will require approaches that simultaneously and/or sequentially target multiple aspects of the TME[181]. Dey *et al*. developed a 3D-vascularized breast cancer micro-environment that consists of HUVECs, metastatic MDA-MB-231 cells, and fibroblasts-laden fibrin gel as the tumor stroma to investigate the interactions between cellular and acellular components in a TME[182]. Given the critical role of matrix stiffness in regulating tumorigenesis, matrix density affecting angiogenesis and invasion was investigated by varying the fibrinogen and thrombin concentration. The impact of fibroblasts was examined by embedding the pre-vascularized spheroids into a fibrin matrix, which was pre-loaded with fibroblasts in a serial density from 0.25 million to 2 million cells/mL. Interestingly, an increase in total vessel length and branching index was observed with increasing fibroblast densities ranging from 0.25 million to 1 million cells/mL, indicating enhanced angiogenesis. Furthermore, to mimic a vascularized TME, HUVECs were introduced into the fibrin matrix with fibroblasts in a 2:1 ratio to create a vascular bed for tumor cells. Over a 7-day culture period, HUVECs that sprouted from the laden tumor spheroid anastomosed with the vascularized fibrin matrix, organizing into a wide range of capillaries. Cancer cells were observed within capillary networks, indicating their intravasation. Taken together, these multicellular bioprinted tumor models, with exquisite control on both cellular and acellular components, serving as promising platforms to interrogate cellular crosstalk, cell-to-

ECM, as well as tumor-immune interactions in a more physiologically relevant microenvironment.

Recent progress in bioprinting techniques, biomaterial science and cell biology have generated 3D tumor models with greatly enhanced robustness and physiological relevance. Such models with higher fidelity hold great potential not only in unraveling the underlying mechanism, but also facilitating the anticancer drug screening before entering clinical trials. For instance, to validate the reliability of the printed co-culture platform in the above-mentioned study[183], immunotoxins EGF4KDEL and CD22KDEL which target EGFR-overexpressing A549s and an off-target parallel control, respectively, were introduced through the vascular conduit. Specifically, EGF4KDEL greatly suppressed the tumor growth, invasion, and migration, while negligible effect was observed with the treatment of CD22KDEL. By interlacing cancer cells, stromal cells, and vascular networks, this bioprinted model was reminiscent of the native TME, providing a valuable reference for anticancer drug screening. Similarly, several models displaying varied complexities have been constructed for anticancer drug testing[184-187]; yet, the majority were utilizing animal cells or immortal human cell lines, which could be less effective in therapeutic prediction. Notably, in a recently published study, Xie *et al*. generated a patient-derived hepatocellular carcinoma (HCC) model using cell-laden gelatin/alginate as bio-ink[188]. Immunofluorescence staining revealed the stabilized expression of α-fetoprotein in HCC model over a 2-week culture period. In addition, evidenced by whole-exome sequencing and RNA-sequencing; a high level of concordance for single nucleotide variants was observed between 3D printed HCC model and the corresponding original HCC tissue, indicating the retained genetic alterations and expression profiles. Overall, the results demonstrated that the 3D-printed HCC model could preserve the features of the original tumor during long-term culture. The printed models were subsequently subjected to the treatments with 4 commonly used, dose-dependent targeting drugs. The patient-specific response suggested the potentiality of the 3D-printed model as a drug prediction model for personalized medicine.

6. Outlooks and challenges

TME is now recognized as a highly dynamic and heterogeneous environment with reciprocal interactions between cellular and acellular components. Although massive efforts have been dedicated to emulating the key features of TME, the majority of these studies are focusing on a single aspect within TME, i.e. a true-to-life tumor model. This golden model could recapitulate all the essential characteristics of TME, but currently, its construction is restricted by technological limitations. Given its potentiality in recapitulating the key features of the avascular tumor *in vivo*, spheroids have been identified as a promising tool for understanding tumor biology and anticancer therapeutic development. However, the random structural organization yields inconsistent therapeutic outcomes, which greatly precludes the model from translational clinical applications. Featuring with excellent control system, bioprinting has been greatly beneficial to the tissue engineering field. The existing 3D printed models are serving as promising platforms, providing deeper insights into some critical aspects of tumor progression, including but not limited to tumor heterogeneity resemblance, tumor angiogenesis, metastasis, and anticancer therapeutic development. However, the major issue in the current 3D printed models is balancing the mechanical properties of exogeneous bio-inks with the biological functions of sportingly involved cellular components. To this end, there is a growing interest in adopting spheroids as building blocks within 3D bioprinting, possibly achieving large-scale tissue construction. Harnessing the power from spheroids and 3D bioprinting would likely circumvent associated shortcomings from using foreign bio-inks (mismatched mechanical stiffness and degradation rate, etc.), while maintaining structural guidance for spheroid growth. Therefore, tumor models with increased authenticity, including well-organized structure, maximized cell-to-cell interaction, cell-secreted ECM, and multicellular environment, could be fabricated in a high-throughput manner. Although, promising progresses have been achieved in 3D printing spheroids so far, current existing technologies could not accurately position the spheroids. In addition, spheroid processing (including spheroidization, assembly process, tissue fusion, and maturation) is time consuming. Using spheroids as tissue building blocks in 3D bioprinting is still in its infancy.

Conventional spheroid generation strategies have offered wealthy information on parameters that affect spheroid formation but are not scalable. For instance, 96-well U bottom well plate are very expensive, and worsens when a large amount of spheroids are required -a large amount of spheroids require more 96 well plates, which is very expensive[189]. Recent advent of microfluidic platforms and drop-on-demand bioprinting are promising on improving the high throughput fabrication of spheroids, yet the spheroid uniformity is far from satisfactory. New methods, such as machine learning, bring emerging solutions by integrating imaging and screening of functional modules into the current systems for spheroid selection through morphological feature analysis. A fully automated system can significantly improve the fabrication performance and lessen the time. Lee *et al*. integrated a machine learning model using least general generalization algorithm combined with

yield stress, viscoelasticity, and shape fidelity from using various type I collagen-based bio-inks[190]. By separating the class variables into shape fidelity and extrusion, the machine learning algorithm effectively optimized the composite bio-ink material fraction and subsequent printing performance[191,192]. Current applications of 3D bioprinting based machine learning algorithms are currently geared towards using regressive models such as LASSO; however, a potential avenue of integrating advanced learning systems using generative ensembles or Bayesian approaches in producing highest performing inks of spheroidal assembly remains completely untapped. Current existing technologies are challenged by spheroid precision positioning coupled with an assembly process lasting tediously for a simple structure, not even including the spheroid production and the post-printing tissue maturation. Apart from technical improvements on the printer, biomaterials such as nanofibers, nanoparticles, hydrogels could be designed and incorporated, and could instruct accelerated spheroidal formative growth and tissue maturation. Scaffold-free spheroid printing could overcome the shortcomings of exogeneous biomaterials, while functional bio-inks with appropriate mechanical property hold great potential to improve the position accuracy. Further, vascular networks and lymphatic systems are essential components that are associated with tumor angiogenesis and metastasis. To present a strong reminiscence of the native TME, both blood vessels and lymphatic vessels should be involved. Co-cultured spheroids have also been generated from various types of cells, such as fibroblast and HUVECs, to replicate the complexity of the tissue microenvironment[13,193,194]. Particularly, in the presence of endothelial cells, capillary-like network formations have been achieved by co-cultured spheroids. Moor *et al*. had generated tri-cultured spheroids composed of HUVECs, human foreskin fibroblasts and adipose tissue-derived MSCs using a non-adhesive agarose microwell, and reported optimized culture ratio and cell density through which endothelial cells underwent self-sorting and formed capillary-like networks within these spheroids[195]. Prospectively, prevascularized spheroids could serve as promising building units for fabricating large-scale tissue models that require proper vascularization[196]. In addition, the incorporation of printing with sacrificial material or in supporting bath to create hollow channels for vascularization would likely help to achieve better vascularization. Notably, adopting the sacrificial writing into functional tissue approach, Skylar-Scott *et al*. created perusable vascular networks in the organ building blocks' bath through embedded 3D bioprinting[189]. The great potential of 3D bioprinting is harnessing a strategy to print patient-specific human tissues with patient-derived cells. Future works focusing on using patient-derived cells are likely to provide deeper insights into the stage-dependent, patient-specific tumor cell behavior, further elucidating tumor progression dynamics, and thus facilitating stronger anticancer therapeutic development.

Acknowledgments

The authors would like to thank funding support by NIH NIGMS MIRA award 1R35GM133794 to Dr. Mei He

Conflicts of interest

The authors declare no conflict of interest.

References

1. Sung H, Ferlay J, Siegel RL, *et al*., 2021, Global Cancer Statistics 2020: GLOBOCAN Estimates of Incidence and Mortality Worldwide for 36 Cancers in 185 Countries. rtd*CA Cancer J Clin*, 71:209–49. https://doi.org/10.3322/caac.21660.
2. Jackson SJ, Thomas GJ, 2017, Human Tissue Models in Cancer Research: Looking Beyond the Mouse. *Dis Model Mech*, 10:939–42. https://doi.org/10.1242/dmm.031260
3. Yoshida GJ, 2020, Applications of Patient-derived Tumor Xenograft Models and Tumor Organoids. *J Hematol Oncol*, 13: 4. https://doi.org/10.1186/s13045-019-0829-z
4. Goto T, 2020, Patient-Derived Tumor Xenograft Models: Toward the Establishment of Precision Cancer Medicine. *J Pers Med*, 10:64. https://doi.org/10.3390/jpm10030064
5. Lai Y, Wei X, Lin S, *et al*., 2017, Current Status and Perspectives of Patient-derived Xenograft Models in Cancer Research. *J Hematol Oncol*, 10:106. https://doi.org/10.1186/s13045-017-0470-7
6. Ozturk MS, Lee VK, Zou H, *et al*., 2020, High-resolution Tomographic Analysis of *In Vitro* 3D Glioblastoma Tumor Model under Long-term Drug Treatment. *Sci Adv*, 6:eaay7513. https://doi.org/10.1126/sciadv.aay7513
7. Rijal G, Li W, 2017, A Versatile 3D Tissue Matrix Scaffold System for Tumor Modeling and Drug Screening. *Sci Adv*, 3:e1700764. https://doi.org/10.1126/sciadv.1700764
8. Ferreira LP, Gaspar VM, Mano JF, 2018, Design of Spherically Structured 3D *In Vitro* Tumor Models Advances and Prospects. *Acta Biomater*, 75:11–34. https://doi.org/10.1016/j.actbio.2018.05.034

9. Stock K, Estrada MF, Vidic S, *et al*., 2016, Graeser, Capturing Tumor Complexity *In Vitro*: Comparative Analysis of 2D and 3D Tumor Models for Drug Discovery. *Sci Rep*., 6:28951. https://doi.org/10.1038/srep28951
10. Laschke MW, Menger MD, 2017, Life is 3D: Boosting Spheroid Function for Tissue Engineering. *Trends Biotechnol*, 35:133–44. https://doi.org/10.1016/j.tibtech.2016.08.004
11. Cui X, Hartanto Y, Zhang H, 2017, Advances in Multicellular Spheroids Formation. *J R Soc Interface*, 14:20160877. https://doi.org/10.1098/rsif.2016.0877
12. Achilli TM, Meyer J, Morgan JR, 2012, Advances in the Formation, Use and Understanding of Multi-cellular Spheroids. *Expert Opin Biol Ther*, 12:1347–60. https://doi.org/10.1517/14712598.2012.707181
13. Nunes AS, Barros AS, Costa EC, *et al*., 2019, 3D Tumor Spheroids as *In Vitro* Models to Mimic *In Vivo* Human Solid Tumors Resistance to Therapeutic Drugs. *Biotechnol Bioeng*, 116:206–26. https://doi.org/10.1002/bit.26845
14. Edmondson R, Broglie JJ, Adcock AF, *et al*., 2014, Three-dimensional Cell Culture Systems and their Applications in Drug Discovery and Cell-based Biosensors. *Assay Drug Dev Technol*., 12:207–18. https://doi.org/10.1089/adt.2014.573
15. Zhuang P, Sun AX, An J, *et al*., 2018, 3D Neural Tissue Models: From Spheroids to Bioprinting. *Biomaterials*, 154:113–33. https://doi.org/10.1016/j.biomaterials.2017.10.002
16. Zhuang P, An J, Chua CK, *et al*., 2020, Bioprinting of 3D *In Vitro* Skeletal Muscle Models: A Review. *Mater Des*, 193:108794. https://doi.org/10.1016/j.matdes.2020.108794
17. Shin YJ, Shafranek RT, Tsui JH, *et al*., 2021, 3D Bioprinting of Mechanically Tuned Bioinks Derived from Cardiac Decellularized Extracellular Matrix. *Acta Biomater*, 119:75–88. https://doi.org/10.1016/j.actbio.2020.11.006
18. Ma X, Liu J, Zhu W, *et al*., 2018, 3D Bioprinting of Functional Tissue Models for Personalized Drug Screening and *In Vitro* Disease Modeling. *Adv Drug Deliv Rev*, 132:235–51. https://doi.org/10.1016/j.addr.2018.06.011
19. Kang Y, Datta P, Shanmughapriya S, *et al*., 2020, 3D Bioprinting of Tumor Models for Cancer Research. *ACS Appl Bio Mater*, 3:5552–73. https://doi.org/10.1021/acsabm.0c00791
20. Zhang YS, Duchamp M, Oklu R, *et al*., 2016, Bioprinting the Cancer Microenvironment. *ACS Biomater Sci Eng*, 2:1710–21. https://doi.org/10.1021/acsbiomaterials.6b00246
21. Albritton JL, Miller JS, 2017, 3D Bioprinting: Improving *In Vitro* Models of Metastasis with Heterogeneous Tumor Microenvironments. *Dis Model Mech*, 10:3–14. https://doi.org/10.1242/dmm.025049
22. Tang M, Rich JN, Chen S, 2021, Biomaterials and 3D Bioprinting Strategies to Model Glioblastoma and the Blood Brain Barrier. *Adv Mater*, 33:2004776. https://doi.org/10.1002/adma.202004776
23. Wang M, Zhao J, Zhang L, *et al*., 2017, Role of Tumor Microenvironment in Tumorigenesis. *J Cancer*, 8:761–73. https://doi.org/10.7150/jca.17648
24. Baghban R, Roshangar L, Jahanban-Esfahlan R, *et al*., 2020, Tumor Microenvironment Complexity and Therapeutic Implications at a Glance. *Cell Commun Signal*, 18:59. https://doi.org/10.1186/s12964-020-0530-4
25. Winkler J, Abisoye-Ogunniyan A, Metcalf KJ, *et al*., 2020, Concepts of Extracellular Matrix Remodelling in Tumour Progression and Metastasis. *Nat Commun*, 11:5120. https://doi.org/10.1038/s41467-020-18794-x
26. Anderson NM, Simon MC, 2020, The Tumor Microenvironment. *Curr Biol*, 30:R921–R925. https://doi.org/10.1016/j.cub.2020.06.081
27. Cuiffo BG, Karnoub AE, 2012, Mesenchymal Stem Cells in Tumor Development: Emerging Roles and Concepts. *Cell Adh Migr*, 46:220–30. https://doi.org/10.4161/cam.20875
28. Ribeiro AL, Okamoto OK, 2015, Combined Effects of Pericytes in the Tumor Microenvironment. *Stem Cells Int*, 2015:868475. https://doi.org/10.1155/2015/868475
29. Nagl L, Horvath L, Pircher A, *et al*., 2020, Tumor Endothelial Cells (TECs) as Potential Immune Directors of the Tumor Microenvironment New Findings and Future Perspectives. *Front Cell Dev Biol*, 8:766. https://doi.org/10.3389/fcell.2020.00766
30. Wullkopf L, West AK, Leijnse N, *et al*., 2018, Cancer Cells' Ability to Mechanically Adjust to Extracellular Matrix Stiffness Correlates with their Invasive Potential. *Mol Biol Cell*, 29:2378–85. https://doi.org/10.1091/mbc.E18-05-0319
31. Kalli M, Stylianopoulos T, 2018, Defining the Role of Solid Stress and Matrix Stiffness in Cancer Cell Proliferation and Metastasis. *Front Oncol*, 8:55. https://doi.org/10.3389/fonc.2018.00055
32. Bahcecioglu G, Basara G, Ellis BW, *et al*., 2020, Breast

Cancer Models: Engineering the Tumor Microenvironment. *Acta Biomater*, 106:1-21. https://doi.org/10.1016/j.actbio.2020.02.006

33. Wang C, Sinha S, Jiang X, *et al*., 2021, Matrix Stiffness Modulates Patient-Derived Glioblastoma Cell Fates in Three-Dimensional Hydrogels. *Tissue Eng Part A*, 27:390–401. https://doi.org/10.1089/ten.TEA.2020.0110
34. Muz B, de la Puente P, Azab F, *et al*., 2015, The Role of Hypoxia in Cancer Progression, Angiogenesis, Metastasis, and Resistance to Therapy. *Hypoxia* (*Auckland, NZ*), 3:83–92. https://doi.org/10.2147/HP.S93413
35. Vajda J, Milojević M, Maver U, *et al*., 2021, Microvascular Tissue Engineering a Review. *Biomedicines*, 9:589. https://doi.org/10.3390/biomedicines9060589
36. Chen L, Endler A, Shibasaki F, 2009, Hypoxia and Angiogenesis: Regulation of Hypoxia-inducible Factors Via Novel Binding Factors. *Exp Mol Med*, 41:849–57. https://doi.org/10.3858/emm.2009.41.12.103
37. Peela N, Truong D, Saini H, *et al*., 2017, Advanced Biomaterials and Microengineering Technologies to Recapitulate the Stepwise Process of Cancer Metastasis. *Biomaterials*, 133:176–207. https://doi.org/10.1016/j.biomaterials.2017.04.017
38. Oliveira MB, Neto AI, Correia CR, *et al*., 2014, Superhydrophobic Chips for Cell Spheroids High-Throughput Generation and Drug Screening. *ACS Appl Mater Interfaces*, 6:9488–95. https://doi.org/10.1021/am5018607
39. Tung YC, Hsiao AY, Allen SG, *et al*., 2011, High-throughput 3D Spheroid Culture and Drug Testing Using a 384 Hanging Drop Array. *Analyst*, 136:473–8. https://doi.org/10.1039/c0an00609b
40. Zhao L, Xiu J, Liu Y, *et al*., 2019, A 3D Printed Hanging Drop Dripper for Tumor Spheroids Analysis Without Recovery. *Sci Rep*, 9:19717. https://doi.org/10.1038/s41598-019-56241-0
41. Massai D, Isu G, Madeddu D, *et al*., A Versatile Bioreactor for Dynamic Suspension Cell Culture. Application to the Culture of Cancer Cell Spheroids. *PLoS One*, 11:e0154610. https://doi.org/10.1371/journal.pone.0154610
42. Franchi-Mendes T, Lopes N, Brito C, 2021, Heterotypic Tumor Spheroids in Agitation-Based Cultures: A Scaffold-Free Cell Model That Sustains Long-Term Survival of Endothelial Cells. *Front Bioeng Biotechnol*, 9:447. https://doi.org/10.3389/fbioe.2021.649949
43. Costa EC, de Melo-Diogo D, Moreira AF, *et al*., 2018, Spheroids Formation on Non-Adhesive Surfaces by Liquid Overlay Technique: Considerations and Practical Approaches. *Biotechnol J*, 13:417. https://doi.org/10.1002/biot.201700417
44. Lee JM, Park DY, Yang L, *et al*., 2018, Generation of Uniform-sized Multicellular Tumor Spheroids Using Hydrogel Microwells for Advanced Drug Screening. *Sci Rep*, 8:17145. https://doi.org/10.1038/s41598-018-35216-7
45. Tu TY, Wang Z, Bai J, *et al*, 2014, Rapid Prototyping of Concave Microwells for the Formation of 3D Multicellular Cancer Aggregates for Drug Screening. *Adv Healthc Mater*, 3:609–16. https://doi.org/10.1002/adhm.201300151
46. Kim JA, Choi JH, Kim M, *et al*, 2013, High-throughput Generation of Spheroids Using Magnetic Nanoparticles for Three-dimensional Cell Culture. *Biomaterials*, 34:8555–63. https://doi.org/10.1016/j.biomaterials.2013.07.056
47. Chen K, Wu M, Guo F, *et al*., 2016, Rapid Formation of Size-controllable Multicellular Spheroids Via 3D Acoustic Tweezers. *Lab Chip*, 16:2636–43. https://doi.org/10.1039/C6LC00444J
48. Sebastian A, Buckle AM, Markx GH, 2007, Tissue Engineering with Electric Fields: Immobilization of Mammalian Cells in multilayer Aggregates Using Dielectrophoresis. *Biotechnol Bioeng*, 98:694–700. https://doi.org/10.1002/bit.21416
49. Wu Z, Gong Z, Ao Z, *et al*., 2020, Rapid Microfluidic Formation of Uniform Patient-Derived Breast Tumor Spheroids. *ACS Appl Bio Mater*, 3:6273–83. https://doi.org/10.1021/acsabm.0c00768
50. Ruppen J, Wildhaber FD, Strub C, *et al*., 2015, Towards Personalized Medicine: Chemosensitivity Assays of Patient Lung Cancer Cell Spheroids in a Perfused Microfluidic Platform. *Lab Chip*, 15:3076–85. https://doi.org/10.1039/C5LC00454C
51. Kingsley DM, Roberge CL, Rudkouskaya A, *et al*., 2019, Laser-based 3D Bioprinting for Spatial and Size Control of Tumor Spheroids and Embryoid Bodies. *Acta Biomater*, 95:357–70. https://doi.org/10.1016/j.actbio.2019.02.014
52. Kuo CT, Wang JY, Lin YF, *et al*, 2017, Three-dimensional Spheroid Culture Targeting Versatile Tissue Bioassays Using a PDMS-based Hanging Drop Array. *Sci Rep*, 7:4363. https://doi.org/10.1038/s41598-017-04718-1
53. Gao B, Jing C, Ng K, *et al*., 2019, Fabrication of Three-dimensional Islet Models by the Geometry-controlled Hanging-drop Method. *Acta Mech Sin*, 35:329–37.

https://doi.org/10.1007/s10409-019-00856-z

54. Ware MJ, Colbert K, Keshishian V, *et al*., 2016, Generation of Homogenous Three-Dimensional Pancreatic Cancer Cell Spheroids Using an Improved Hanging Drop Technique. *Tissue Eng Part C Methods*, 22:312–21. https://doi.org/10.1089/ten.TEC.2015.0280
55. Vignesh RA, Kumari S, Poddar P, *et al*., 2020, Poly(N-isopropylacrylamide)-Based Polymers as Additive for Rapid Generation of Spheroid via Hanging Drop Method. *Macromol Biosci*, 20:2000180. https://doi.org/10.1002/mabi.202000180
56. He H, He Q, Xu F, *et al*., 2019, Dynamic Formation of Cellular Aggregates of Chondrocytes and Mesenchymal Stem Cells in Spinner Flask. *Cell Prolif*, 52:e12587. https://doi.org/10.1111/cpr.12587
57. Shi W, Kwon J, Huang Y, *et al*., 2018, Facile Tumor Spheroids Formation in Large Quantity with Controllable Size and High Uniformity. *Sci Rep*, 8:6837. https://doi.org/10.1038/s41598-018-25203-3
58. Lancaster MA, Knoblich JA, 2014, Generation of Cerebral Organoids from Human Pluripotent Stem Cells. *Nat Protoc*, 9:2329–40. https://doi.org/10.1038/nprot.2014.158
59. Lei X, Ning L, Cao Y, *et al*., 2011, NASA-Approved Rotary Bioreactor Enhances Proliferation of Human Epidermal Stem Cells and Supports Formation of 3D Epidermis-Like Structure. *PLoS One*, 6:e26603. https://doi.org/10.1371/journal.pone.0026603
60. Salehi-Nik N, Amoabediny G, Pouran B, *et al*., 2013, Engineering Parameters in Bioreactor's Design: A Critical Aspect in Tissue Engineering. *Biomed Res Int*, 2013:762132. https://doi.org/10.1155/2013/762132
61. Lei KF, Lin BY, Tsang NM, 2017, Real-time and Label-free Impedimetric Analysis of the Formation and Drug Testing of Tumor Spheroids Formed via the Liquid Overlay Technique. *RSC Adv*, 7:13939–46. https://doi.org/10.1039/C7RA00209B
62. Gaskell H, Sharma P, Colley HE, *et al*., 2016, Characterization of a Functional C3A Liver Spheroid Model. *Toxicol Res* (*Camb*), 5:1053–65. https://doi.org/10.1039/c6tx00101g
63. Costa EC, Gaspar VM, Coutinho P, *et al*., 2014, Optimization of Liquid Overlay Technique to Formulate Heterogenic 3D Co-cultures Models. *Biotechnol Bioeng*, 111:1672–85. https://doi.org/10.1002/bit.25210
64. Chen YC, Lou X, Zhang Z, *et al*., 2015, High-Throughput Cancer Cell Sphere Formation for Characterizing the Efficacy of Photo Dynamic Therapy in 3D Cell Cultures. *Sci Rep*, 5:12175. https://doi.org/10.1038/srep12175
65. Kim JH, Lim IR, Joo HJ, *et al*., 2015, Sphere Formation of Adipose Stem Cell Engineered by Poly-2-hydroxyethyl Methacrylate Induces *In Vitro* Angiogenesis through Fibroblast Growth Factor 2. *Biochem Biophys Res Commun*, 468:372–9. https://doi.org/10.1016/j.bbrc.2015.10.083
66. Lawrenson K, Grun B, Gayther SA, 2012, Heterotypic Three-dimensional *In Vitro* Modeling of Stromal-epithelial Interactions during Ovarian Cancer Initiation and Progression. *J Vis Exp*, 66:e4206. https://doi.org/10.3791/4206
67. Phung YT, Barbone D, Broaddus VC, *et al*., 2011, Rapid Generation of *In Vitro* Multicellular Spheroids for the Study of Monoclonal Antibody Therapy. *J Cancer*, 2:507–14. https://doi.org/10.7150/jca.2.507
68. Kuroda Y, Wakao S, Kitada M, *et al*., 2013, Isolation, Culture and Evaluation of Multilineage-differentiating Stress-enduring (Muse) cells. *Nat Protoc*, 8:1391–415. https://doi.org/10.1038/nprot.2013.076
69. Ivascu A, Kubbies M, 2006, Rapid Generation of Single-tumor Spheroids for High-throughput Cell Function and toxicity Analysis. *J Biomol Screen*, 11:922–32. https://doi.org/10.1177/1087057106292763
70. Bilandzic M, Stenvers KL, 2014, Assessment of Ovarian Cancer Spheroid Attachment and Invasion of Mesothelial Cells in Real Time. *J Vis Exp*, 87:51655. https://doi.org/10.3791/51655
71. Huang Z, Yu P, Tang J, 2020, Characterization of Triple-Negative Breast Cancer MDA-MB-231 Cell Spheroid Model. *Onco Targets Ther*, 13:5395–405. https://doi.org/10.2147/OTT.S249756
72. Fan Y, Avci NG, Nguyen DT, *et al*., 2015, Engineering a High-Throughput 3-D *In Vitro* Glioblastoma Model. *IEEE J Transl Eng Health Med*, 3:4300108. https://doi.org/10.1109/JTEHM.2015.2410277
73. Lee D, Pathak S, Jeong JH, 2019, Design and Manufacture of 3D Cell Culture Plate for Mass Production of Cell-Spheroids. *Sci Rep*, 9:13976. https://doi.org/10.1038/s41598-019-50186-0
74. Gong X, Lin C, Cheng J, *et al*., 2015, Generation of Multicellular Tumor Spheroids with Microwell-Based Agarose Scaffolds for Drug Testing. *PLoS One*, 10:e0130348. https://doi.org/10.1371/journal.pone.0130348
75. Chao C, Ngo LP, Engelward BP, 2020, SpheroidChip:

Patterned Agarose Microwell Compartments Harboring HepG2 Spheroids are Compatible with Genotoxicity Testing. *ACS Biomater Sci Eng*, 6:2427–39. https://doi.org/10.1021/acsbiomaterials.9b01951

76. Mirab F, Kang YJ, Majd S, 2019, Preparation and Characterization of Size-controlled Glioma Spheroids Using Agarose hydrogel Microwells. *PLoS One*, 14:e0211078. https://doi.org/10.1371/journal.pone.0211078
77. Thomsen AR, Aldrian C, Bronsert P, *et al*., 2018, A Deep Conical Agarose Microwell Array for Adhesion Independent Three-dimensional Cell Culture and Dynamic Volume Measurement. *Lab Chip*, 18:179–89. https://doi.org/10.1039/C7LC00832E
78. Desroches BR, Zhang P, Choi BR, *et al*., 2012, Functional Scaffold-free 3-D Cardiac Microtissues: A Novel Model for the Investigation of Heart Cells. *Am J Physiol Heart Circ Physiol*, 302:H2031–42. https://doi.org/10.1152/ajpheart.00743.2011
79. Henslee EA, Dunlop CM, de Mel CM, *et al*., 2020, DEP-Dots for 3D Cell Culture: Low-cost, High-repeatability, Effective 3D Cell Culture in Multiple Gel Systems. *Sci Rep*, 10:14603. https://doi.org/10.1038/s41598-020-71265-7
80. Albrecht DR, Tsang VL, Sah RL, *et al*., Photo- and electropatterning of hydrogel-encapsulated living cell arrays. *Lab Chip*, 5:111–8. https://doi.org/10.1039/b406953f
81. Agarwal S, Sebastian A, Forrester LM, *et al*., 2012, Formation of Embryoid Bodies Using Dielectrophoresis. *Biomicrofluidics*, 6:24101–11. https://doi.org/10.1063/1.3699969
82. Jafari J, Han X, Palmer J, *et al*., 2019, Remote Control in Formation of 3D Multicellular Assemblies Using Magnetic Forces. *ACS Biomater Sci Eng*, 5:2532–42. https://doi.org/10.1021/acsbiomaterials.9b00297
83. Urbanczyk M, Zbinden A, Layland SL, *et al*., Controlled Heterotypic Pseudo-Islet Assembly of Human β-Cells and Human Umbilical Vein Endothelial Cells Using Magnetic Levitation. *Tissue Eng Part A*, 26:387–99. https://doi.org/10.1089/ten.TEA.2019.0158
84. Lewis NS, El Lewis E, Mullin M, *et al*., 2017, Magnetically levitated mesenchymal stem cell spheroids cultured with a collagen gel maintain phenotype and quiescence. *J Tissue Eng*, 8:2041731417704428. https://doi.org/10.1177/2041731417704428
85. Tseng H, Gage JA, Shen T, *et al*., 2015, A Spheroid Toxicity Assay Using Magnetic 3D Bioprinting and Real-time Mobile Device-based Imaging. *Sci Rep*, 5:13987. https://doi.org/10.1038/srep13987
86. Wu M, Ozcelik A, Rufo J, *et al*., 2019, Acoustofluidic Separation of Cells and Particles. *Microsyst Nanoeng*, 5:32. https://doi.org/10.1038/s41378-019-0064-3
87. Chen B, Wu Y, Ao Z, *et al*., 2019, High-throughput Acoustofluidic Fabrication of Tumor Spheroids. *Lab Chip*, 19:1755–63. https://doi.org/10.1039/C9LC00135B
88. Ota H, Miki N, 2011, Microfluidic Experimental Platform for Producing Size-controlled Three-dimensional Spheroids. *Sens Actuat A Phys*, 169:266–73. https://doi.org/10.1016/j.sna.2011.03.051
89. Hong S, Hsu HJ, Kaunas R, *et al*., 2012, Collagen Microsphere Production on a Chip. *Lab Chip*, 12:3277–80. https://doi.org/10.1039/C2LC40558J
90. Damiati S, Kompella UB, Damiati SA, *et al*., 2018, Microfluidic Devices for Drug Delivery Systems and Drug Screening. *Genes* (*Basel*), 9:103. https://doi.org/10.3390/genes9020103
91. McMillan KS, McCluskey AG, Sorensen A, *et al*., 2016, Emulsion Technologies for Multicellular Tumour Spheroid Radiation Assays. *Analyst*, 141:100–10. https://doi.org/10.1039/c5an01382h
92. Lee JM, Choi JW, Ahrberg CD, *et al*., 2020, Generation of Tumor Spheroids Using a Droplet-based Microfluidic Device for Photothermal Therapy. *Microsyst Nanoeng*, 6:52. https://doi.org/10.1038/s41378-020-0167-x
93. Lee D, Cha C, 2018, The Combined Effects of Co-Culture and Substrate Mechanics on 3D Tumor Spheroid Formation within Microgels Prepared via Flow-Focusing Microfluidic Fabrication. *Pharmaceutics*, 10:229. https://doi.org/10.3390/pharmaceutics10040229
94. Cui X, Liu Y, Hartanto Y, *et al*., 2016, Multicellular Spheroids Formation and Recovery in Microfluidics-generated Thermoresponsive Microgel Droplets. *Colloid Interface Sci Commun*, 14:4–7. https://doi.org/10.1016/j.colcom.2016.09.001
95. Zeng W, Xiang D, Fu H, 2019, Prediction of Droplet Production Speed by Measuring the Droplet Spacing Fluctuations in a Flow-Focusing Microdroplet Generator. *Micromachines*, 10:812. https://doi.org/10.3390/mi10120812
96. Kong T, Wu J, Yeung KW, *et al*., 2013, Microfluidic Fabrication of Polymeric Core-shell Microspheres for Controlled Release Applications. *Biomicrofluidics*, 7:44128. https://doi.org/10.1063/1.4819274
97. Tran TM, Lan F, Thompson CS, *et al*., 2013, From Tubes to

Drops: Droplet-based Microfluidics for Ultrahigh-throughput Biology. *J Phys D Appl Phys*, 46:114004. https://doi.org/10.1088/0022-3727/46/11/114004

98. Chan HF, Zhang Y, Ho YP, *et al*., 2013, Rapid Formation of Multicellular Spheroids in Double-emulsion Droplets with Controllable Microenvironment. *Sci Rep*, 3:3462. https://doi.org/10.1038/srep03462
99. Kim C, Chung S, Kim YE, *et al*., 2011, Generation of Core-shell Microcapsules with Three-dimensional Focusing Device for Efficient Formation of Cell Spheroid. *Lab Chip*, 11:246–52. https://doi.org/10.1039/C0LC00036A
100. Grist SM, Nasseri SS, Laplatine L, *et al*., 2019, Long-term Monitoring in a Microfluidic System to Study Tumour Spheroid Response to Chronic and Cycling Hypoxia. *Sci Rep*, 9:17782. https://doi.org/10.1038/s41598-019-54001-8
101. Wang Y, Zhao L, Tian C, *et al*., 2015, Geometrically Controlled Preparation of Various Cell Aggregates by Droplet-based Microfluidics. *Anal Methods*, 7:10040–51. https://doi.org/10.1039/C5AY02466H
102. Sun Q, Tan SH, Chen Q, *et al*., 2018, Microfluidic Formation of Coculture Tumor Spheroids with Stromal Cells As a Novel 3D Tumor Model for Drug Testing. *ACS Biomater Sci Eng*, 4:4425–33. https://doi.org/10.1021/acsbiomaterials.8b00904
103. Yazdi SR, Shadmani A, Bürgel SC, *et al*., Adding the "Heart" to Hanging Drop Networks for Microphysiological Multi-tissue Experiments. *Lab Chip*, 15:4138–47. https://doi.org/10.1039/c5lc01000d
104. Frey O, Misun PM, Fluri DA, *et al*., 2014, Reconfigurable Microfluidic Hanging Drop Network for Multi-tissue Interaction and Analysis. *Nat Commun*, 5:4250. https://doi.org/10.1038/ncomms5250
105. Wu HW, Hsiao YH, Chen CC, *et al*., 2016, A PDMS-Based Microfluidic Hanging Drop Chip for Embryoid Body Formation. *Molecules*, 21:882. https://doi.org/10.3390/molecules21070882
106. Dadgar N, Gonzalez-Suarez AM, Fattahi P, *et al*., 2020, A Microfluidic Platform for Cultivating Ovarian Cancer Spheroids and Testing their Responses to Chemotherapies. *Microsyst Nanoeng*, 6:93. https://doi.org/10.1038/s41378-020-00201-6
107. Chen SY, Hung PJ, Lee PJ, 2011, Microfluidic Array for Three-dimensional Perfusion Culture of Human Mammary Epithelial Cells. *Biomed Microdev*, 13:753–8. https://doi.org/10.1007/s10544-011-9545-3
108. Lee K, Kim C, Yang JY, *et al*., 2012, Gravity-oriented Microfluidic Device for Uniform and Massive Cell Spheroid Formation. *Biomicrofluidics*, 6:14114–47. https://doi.org/10.1063/1.3687409
109. Fiddes LK, Luk VN, Au SH, *et al*., 2012, Hydrogel Discs for Digital Microfluidics. *Biomicrofluidics*, 6:14112–211. https://doi.org/10.1063/1.3687381
110. Eydelnant IA, Li BB, Wheeler AR, 2014, Microgels on-demand. *Nat Commun*, 5:3355. https://doi.org/10.1038/ncomms4355
111. Aijian AP, Garrell RL, 2015, Digital Microfluidics for Automated Hanging Drop Cell Spheroid Culture. *J Lab Autom*, 20:283–95. https://doi.org/10.1177/2211068214562002
112. Vadivelu RK, Kamble H, Shiddiky MJ, *et al*., 2017, Microfluidic Technology for the Generation of Cell Spheroids and Their Applications. *Micromachines*, 8:94. https://doi.org/10.3390/mi8040094
113. Moshksayan K, Kashaninejad N, Warkiani ME, *et al*., 2018, Spheroids-on-a-chip: Recent Advances and Design Considerations in Microfluidic Platforms for Spheroid Formation and Culture. *Sens Actuat B Chem*, 263:151–76. https://doi.org/10.1016/j.snb.2018.01.223
114. Utama RH, Atapattu L, O'Mahony AP, *et al*., 2020, A 3D Bioprinter Specifically Designed for the High-Throughput Production of Matrix-Embedded Multicellular Spheroids. *IScience*, 23:101621. https://doi.org/10.1016/j.isci.2020.101621
115. Ling K, Huang G, Liu J, *et al*., 2015, Bioprinting-Based High-Throughput Fabrication of Three-Dimensional MCF-7 Human Breast Cancer Cellular Spheroids. *Engineering*, 1:269–74. https://doi.org/10.15302/J-ENG-2015062
116. Vinson BT, Sklare SC, Chrisey DB, 2017, Laser-based Cell Printing Techniques for Additive Biomanufacturing. *Curr Opin Biomed Eng*, 2:14–21. https://doi.org/10.1016/j.cobme.2017.05.005
117. Armon N, Greenberg E, Edri E, *et al*., 2021, Laser-Based Printing: From Liquids to Microstructures. *Adv Funct Mater*, 31:2008547. https://doi.org/10.1002/adfm.202008547
118. Hakobyan D, Médina C, Dusserre N, *et al*., 2020, Laser-assisted 3D Bioprinting of Exocrine Pancreas Spheroid Models for Cancer Initiation Study. *Biofabrication*, 12:35001. https://doi.org/10.1088/1758-5090/ab7cb8
119. Boyer CJ, Ballard DH, Barzegar M, *et al*., 2018, High-throughput Scaffold-free Microtissues through 3D Printing.

3D Print Med, 4:9.
https://doi.org/10.1186/s41205-018-0029-4

120. Swaminathan S, Clyne AM, 2020, Direct Bioprinting of 3D Multicellular Breast Spheroids onto Endothelial Networks. *J Vis Exp*, 165:61791.
https://doi.org/10.3791/61791
121. Swaminathan S, Hamid Q, Sun W, *et al*., 2019, Bioprinting of 3D Breast Epithelial Spheroids for Human Cancer Models. *Biofabrication*, 11:25003.
https://doi.org/10.1088/1758-5090/aafc49
122. Horder H, Lasheras MG, Grummel N, *et al*., 2021, Bioprinting and Differentiation of Adipose-Derived Stromal Cell Spheroids for a 3D Breast Cancer-Adipose Tissue Model. *Cells*, 10:803.
https://doi.org/10.3390/cells10040803
123. Jakab K, Norotte C, Damon B, *et al*., 2008, Tissue Engineering by Self-assembly of Cells Printed into Topologically Defined Structures. *Tissue Eng Part A*, 14:413–21.
https://doi.org/10.1089/tea.2007.0173
124. Campos DF, Lindsay CD, Roth JG, *et al*., 2020, Bioprinting Cell-and Spheroid-Laden Protein-Engineered Hydrogels as Tissue-on-Chip Platforms. *Front Bioeng Biotechnol*, 8:374.
https://doi.org/10.3389/fbioe.2020.00374
125. Vinson BT, Phamduy TB, Shipman J, *et al*., 2017, Laser Direct-write Based Fabrication of a Spatially-defined, Biomimetic Construct as a Potential Model for Breast Cancer Cell Invasion into Adipose Tissue. *Biofabrication*, 9:25013.
https://doi.org/10.1088/1758-5090/aa6bad
126. Chen K, Jiang E, Wei X, *et al*., 2021, The Acoustic Droplet Printing of Functional Tumor Microenvironments. *Lab Chip*, 21:1604–12.
https://doi.org/10.1039/D1LC00003A
127. Moldovan NI, Hibino N, Nakayama K, 2017, Principles of the Kenzan Method for Robotic Cell Spheroid-Based Three-Dimensional Bioprinting. *Tissue Eng Part B Rev*, 23:237–44.
https://doi.org/10.1089/ten.TEB.2016.0322
128. Arai K, Murata D, Verissimo AR, *et al*., 2018, Fabrication of Scaffold-free Tubular Cardiac Constructs Using a Bio-3D Printer. *PLoS One*, 13:e0209162.
https://doi.org/10.1371/journal.pone.0209162
129. LaBarge W, Morales A, Pretorius D, *et al*., 2019, Scaffold-Free Bioprinter Utilizing Layer-By-Layer Printing of Cellular Spheroids. *Micromachines*, 10:570.
https://doi.org/10.3390/mi10090570
130. Murata D, Arai K, Nakayama K, 2020, Scaffold-Free Bio-3D Printing Using Spheroids as "Bio-Inks" for Tissue (Re-) Construction and Drug Response Tests. *Adv Healthc Mater*, 9:e1901831.
https://doi.org/10.1002/adhm.201901831
131. van Pel DM, Harada K, Song D, *et al*., 2018, Modelling Glioma Invasion Using 3D Bioprinting and Scaffold-free 3D Culture. *J Cell Commun Signal*, 12:723–30.
https://doi.org/10.1007/s12079-018-0469-z
132. Kizawa H, Nagao E, Shimamura M, *et al*., 2017, Scaffold-free 3D Bio-printed Human Liver Tissue Stably Maintains Metabolic Functions Useful for Drug Discovery. *Biochem Biophys Reports*, 10:186–91.
https://doi.org/10.1016/j.bbrep.2017.04.004
133. Ip BC, Cui F, Tripathi A, *et al*., 2016, The Bio-gripper: A Fluid-driven Micro-Manipulator of Living Tissue Constructs for Additive Bio-manufacturing. *Biofabrication*, 8:25015.
https://doi.org/10.1088/1758-5090/8/2/025015
134. Blakely AM, Manning KL, Tripathi A, *et al*., 2015, Bio-Pick, Place, and Perfuse: A New Instrument for Three-Dimensional Tissue Engineering. *Tissue Eng Part C Methods*, 21:737–46.
https://doi.org/10.1089/ten.TEC.2014.0439
135. Ayan B, Heo DN, Zhang Z, *et al*., 2020., Aspiration-assisted Bioprinting for Precise Positioning of Biologics. *Sci Adv*, 6:eaaw5111.
https://doi.org/10.1126/sciadv.aaw5111
136. Ayan B, Celik N, Zhang Z, *et al*., 2020, Aspiration-assisted Freeform Bioprinting of Pre-fabricated Tissue Spheroids in a Yield-stress Gel. *Commun Phys*, 3:183.
https://doi.org/10.1038/s42005-020-00449-4
137. Daly AC, Davidson MD, Burdick JA, 2021, 3D Bioprinting of High Cell-density Heterogeneous Tissue Models through Spheroid Fusion within Self-healing Hydrogels. *Nat Commun*, 12:753.
https://doi.org/10.1038/s41467-021-21029-2
138. Norotte C, Marga FS, Niklason LE, *et al*., 2009, Scaffold-free Vascular Tissue Engineering Using Bioprinting. *Biomaterials*, 30:5910–7.
https://doi.org/10.1016/j.biomaterials.2009.06.034
139. Bulanova EA, Koudan EV, Degosserie J, *et al*., 2017, Bioprinting of a Functional Vascularized Mouse Thyroid Gland Construct. *Biofabrication*, 9:34105.
https://doi.org/10.1088/1758-5090/aa7fdd
140. Kozaki S, Moritoki Y, Furukawa T, *et al*., 2020, Additive Manufacturing of Micromanipulator Mounted on a Glass Capillary for Biological Applications. *Micromachines*, 11:174.
https://doi.org/10.3390/mi11020174
141. Zhuang P, An J, Tan LP, *et al*., 2018, The Current Status of 3D Bioprinting for Neural Tissue Models. 2018:183–8.

https://doi.org/10.25341/D4688F

142. Zhuang P, Ng WL, An J, *et al*., 2019, Layer-by-layer Ultraviolet Assisted Extrusion-based (UAE) Bioprinting of Hydrogel Constructs with High Aspect Ratio for Soft Tissue Engineering Applications. *PLoS One*, 14:e0216776. https://doi.org/10.1371/journal.pone.0216776
143. Li X, Liu B, Pei B, *et al*., 2020, Inkjet Bioprinting of Biomaterials. *Chem Rev*, 120:10793–833. https://doi.org/10.1021/acs.chemrev.0c00008
144. Koch L, Gruene M, Unger C, *et al*., 2013, Laser Assisted Cell Printing. *Curr Pharm Biotechnol*, 14:91–7.
145. Grigoryan B, Sazer DW, Avila A, *et al*., 2021, Development, Characterization, and Applications of Multi-Material Stereolithography Bioprinting. *Sci Rep*, 11:3171. https://doi.org/10.1038/s41598-021-82102-w
146. Matai I, Kaur G, Seyedsalehi A, *et al*., 2020, Progress in 3D Bioprinting Technology for Tissue/Organ Regenerative Engineering. *Biomaterials*, 226:119536. https://doi.org/10.1016/j.biomaterials.2019.119536
147. Murphy SV, De Coppi P, Atala A, 2020, Opportunities and Challenges of Translational 3D Bioprinting. *Nat Biomed Eng*, 4:370–80. https://doi.org/10.1038/s41551-019-0471-7
148. Cui X, Li J, Hartanto Y, *et al*., 2020, Advances in Extrusion 3D Bioprinting: A Focus on Multicomponent Hydrogel-Based Bioinks. *Adv Healthc Mater*, 9:1901648. https://doi.org/10.1002/adhm.201901648
149. Zhuang P, Greenberg Z, He M, 2021, Biologically Enhanced Starch Bio-Ink for Promoting 3D Cell Growth. *Adv Mater Technol*, 2021:2100551. https://doi.org/10.1002/admt.202100551
150. McCormack A, Highley CB, Leslie NR, *et al*., 2020, 3D Printing in Suspension Baths: Keeping the Promises of Bioprinting Afloat. *Trends Biotechnol*, 38:584–93. https://doi.org/10.1016/j.tibtech.2019.12.020
151. Hermida MA, Kumar JD, Schwarz D, *et al*., 2020, Three Dimensional *In Vitro* Models of Cancer: Bioprinting Multilineage Glioblastoma Models. *Adv Biol Regul*, 75:100658. https://doi.org/10.1016/j.jbior.2019.100658
152. Dai X, Liu L, Ouyang J, *et al*., 2017, Coaxial 3D Bioprinting of Self-assembled Multicellular Heterogeneous Tumor Fibers. *Sci Rep*, 7:1457. https://doi.org/10.1038/s41598-017-01581-y
153. Wang X, Li X, Dai X, *et al*., 2018, Coaxial Extrusion Bioprinted Shell-core Hydrogel Microfibers Mimic Glioma Microenvironment and Enhance the Drug Resistance of Cancer Cells. *Colloids Surf B Biointerfaces*, 171:291–9. https://doi.org/10.1016/j.colsurfb.2018.07.042
154. Yi HG, Jeong YH, Kim Y, *et al*., 2019, A Bioprinted Human-glioblastoma-on-a-Chip for the Identification of Patient-specific Responses to Chemoradiotherapy. *Nat Biomed Eng*, 3:509–19. https://doi.org/10.1038/s41551-019-0363-x
155. Wang X, Li X, Ding J, *et al*., 2021, 3D Bioprinted Glioma Microenvironment for Glioma Vascularization. *J Biomed Mater Res Part A*, 109:915–25. https://doi.org/10.1002/jbm.a.37082
156. Wang X, Li X, Dai X, *et al*., 2018, Bioprinting of Glioma Stem Cells Improves their Endotheliogenic Potential. *Colloids Surf B Biointerfaces*, 171:629–37. https://doi.org/10.1016/j.colsurfb.2018.08.006
157. Lee VK, Dai G, Zou H, *et al*., 2015, Generation of 3-D Glioblastoma-vascular Niche Using 3-D Bioprinting. In: 2015 41st Annual Northeast Biomedical Engineering Conference, p1-2. https://doi.org/10.1109/NEBEC.2015.7117111
158. Wang X, Zhang X, Dai X, *et al*., 2018, Tumor-like Lung Cancer Model Based on 3D Bioprinting. *3 Biotech*, 8:501. https://doi.org/10.1007/s13205-018-1519-1
159. Zhou X, Zhu W, Nowicki M, *et al*., 2016, 3D Bioprinting a Cell-Laden Bone Matrix for Breast Cancer Metastasis Study. *ACS Appl Mater Interfaces*, 8:30017–26. https://doi.org/10.1021/acsami.6b10673
160. Zhu W, Holmes B, Glazer RI, *et al*., 2016, 3D Printed Nanocomposite Matrix for the Study of Breast Cancer Bone Metastasis. *Nanomedicine*, 12:69–79. https://doi.org/10.1016/j.nano.2015.09.010
161. Han S, Kim S, Chen Z, *et al*., 2020, 3D Bioprinted Vascularized Tumour for Drug Testing. *Int J Mol Sci*, 21:2993. https://doi.org/10.3390/ijms21082993
162. Smits IP, Blaschuk OW, Willerth SM, 2020, Novel N-cadherin Antagonist Causes Glioblastoma Cell Death in a 3D Bioprinted Co-culture Model. *Biochem Biophys Res Commun*, 529:162–8. https://doi.org/10.1016/j.bbrc.2020.06.001
163. Mironov V, Visconti RP, Kasyanov V, *et al*., 2009, Organ Printing: Tissue Spheroids as Building Blocks. *Biomaterials*, 30:2164–74. https://doi.org/10.1016/j.biomaterials.2008.12.084
164. Ahmad T, Shin HJ, Lee J, *et al*., 2018, Fabrication of *In Vitro* 3D Mineralized Tissue by Fusion of Composite Spheroids Incorporating Biomineral-coated Nanofibers and Human Adipose-derived Stem Cells. *Acta Biomater*, 74:464–77.

https://doi.org/10.1016/j.actbio.2018.05.035

165. Kelm JM, Lorber V, Snedeker JG, *et al*., 2010, A Novel Concept for Scaffold-free Vessel Tissue Engineering: Self-assembly of Microtissue Building Blocks. *J Biotechnol*, 148:46–55. https://doi.org/10.1016/j.jbiotec.2010.03.002
166. Birey F, Andersen J, Makinson CD, *et al*., 2017, Assembly of Functionally Integrated human Forebrain Spheroids. *Nature*, 545:54–9. https://doi.org/10.1038/nature22330
167. Kato-Negishi M, Morimoto Y, Onoe H, *et al*., 2013, Millimeter-Sized Neural Building Blocks for 3D Heterogeneous Neural Network Assembly. *Adv Healthc Mater*, 2:1564–70. https://doi.org/10.1002/adhm.201300052
168. Fleming PA, Argraves WS, Gentile C, *et al*., 2010, Fusion of Uniluminal Vascular Spheroids: A Model for Assembly of Blood Vessels. *Dev Dyn*, 239:398–406. https://doi.org/10.1002/dvdy.22161
169. Dean DM, Napolitano AP, Youssef J, *et al*., 2007, Rods, Tori, and Honeycombs: The Directed Self-assembly of Microtissues with Prescribed Microscale Geometries. *FASEB J*, 21:4005–12. https://doi.org/10.1096/fj.07-8710com
170. Luo J, Meng J, Gu Z, *et al*., 2019, Topography-Induced Cell Self-Organization from Simple to Complex Aggregates. *Small*, 15:1900030. https://doi.org/10.1002/smll.201900030
171. Olsen TR, Mattix B, Casco M, *et al*., 2015, Manipulation of Cellular Spheroid Composition and the Effects on Vascular Tissue Fusion. *Acta Biomater*, 13:188–98. https://doi.org/10.1016/j.actbio.2014.11.024
172. Mattix B, Olsen TR, Gu Y, *et al*., 2014, Biological Magnetic Cellular Spheroids as Building Blocks for Tissue Engineering. *Acta Biomater*, 10:623–9. https://doi.org/10.1016/j.actbio.2013.10.021
173. Whatley BR, Li X, Zhang N, *et al*., 2014, Magnetic-directed Patterning of cell Spheroids. *J Biomed Mater Res A*, 102:1537–47. https://doi.org/10.1002/jbm.a.34797
174. Lin RZ, Chu WC, Chiang CC, *et al*., 2008, Magnetic Reconstruction of Three-Dimensional Tissues from Multicellular Spheroids. *Tissue Eng Part C Methods*, 14:197–205. https://doi.org/10.1089/ten.tec.2008.0061
175. Bratt-Leal AM, Kepple KL, Carpenedo RL, *et al*., 2011, Magnetic Manipulation and Spatial Patterning of Multi-cellular Stem Cell Aggregates. *Integr Biol* (*Camb*), 3:1224–32. https://doi.org/10.1039/c1ib00064k
176. Fayol D, Frasca G, Le Visage C, *et al*., 2013, Use of Magnetic Forces to Promote Stem Cell Aggregation During Differentiation, and Cartilage Tissue Modeling. *Adv Mater*, 25:2611–6. https://doi.org/10.1002/adma.201300342
177. Chen P, Güven S, Usta OB, *et al*., 2015, Biotunable Acoustic Node Assembly of Organoids. *Adv Healthc Mater*, 4:1937–43. https://doi.org/10.1002/adhm.201500279
178. Parfenov VA, Koudan EV, Krokhmal AA, *et al*., 2020, Biofabrication of a Functional Tubular Construct from Tissue Spheroids Using Magnetoacoustic Levitational Directed Assembly. *Adv Healthc Mater*, 9:2000721. https://doi.org/10.1002/adhm.202000721
179. Heinrich MA, Bansal R, Lammers T, *et al*., 2019, 3D-Bioprinted Mini-Brain: A Glioblastoma Model to Study Cellular Interactions and Therapeutics. *Adv Mater*, 31:e1806590. https://doi.org/10.1002/adma.201806590
180. Tang M, Xie Q, Gimple RC, *et al*., 2020, Three-dimensional Bioprinted Glioblastoma Microenvironments Model Cellular Dependencies and Immune Interactions. *Cell Res*., 30:833–53. https://doi.org/10.1038/s41422-020-0338-1
181. Weis SM, Cheresh DA, 2011, Tumor Angiogenesis: Molecular Pathways and Therapeutic Targets. *Nat Med*, 17:1359–70. https://doi.org/10.1038/nm.2537
182. Dey M, Ayan B, Yurieva M, *et al*., 2021, Studying Tumor Angiogenesis and Cancer Invasion in a Three-Dimensional Vascularized Breast Cancer Micro-Environment. *Adv Biol*, 2021:e2100090. https://doi.org/10.1002/adbi.202100090
183. Meng F, Meyer CM, Joung D, *et al*., 2019, 3D Bioprinted *In Vitro* Metastatic Models via Reconstruction of Tumor Microenvironments. *Adv Mater*, 31:e1806899. https://doi.org/10.1002/adma.201806899
184. Maloney E, Clark C, Sivakumar H, *et al*., 2020, Immersion Bioprinting of Tumor Organoids in Multi-Well Plates for Increasing Chemotherapy Screening Throughput. *Micromachines*, 11:208. https://doi.org/10.3390/mi11020208
185. Li Y, Zhang T, Pang Y, *et al*., 2019, 3D Bioprinting of Hepatoma Cells and application with microfluidics for pharmacodynamic test of Metuzumab. *Biofabrication*, 11:34102. https://doi.org/10.1088/1758-5090/ab256c
186. Sun L, Yang H, Wang Y, *et al*., 2020, Application of a 3D Bioprinted Hepatocellular Carcinoma Cell Model in

Antitumor Drug Research. *Front Oncol*, 10:878. https://doi.org/10.3389/fonc.2020.00878

187. Zhang J, Chen F, He Z, *et al*., 2016, A Novel Approach for Precisely Controlled Multiple Cell Patterning in Microfluidic Chips by Inkjet Printing and the Detection of Drug Metabolism and Diffusion. *Analyst*, 141:2940–7. https://doi.org/10.1039/C6AN00395H
188. Xie F, Sun L, Pang Y, *et al*., 2021, Three-dimensional Bio-printing of Primary Human Hepatocellular Carcinoma for Personalized Medicine. *Biomaterials*, 265:120416. https://doi.org/10.1016/j.biomaterials.2020.120416
189. Skylar-Scott MA, Uzel SG, Nam LL, *et al*., 2019, Biomanufacturing of Organ-Specific Tissues with High Cellular Density and Embedded Vascular Channels. *Sci Adv*, 5:eaaw2459. https://doi.org/10.1126/sciadv.aaw2459
190. Lee J, Oh SJ, An SH, *et al*., 2020, Machine Learning-based Design Strategy for 3D Printable Bioink: Elastic Modulus and Yield Stress Determine Printability. *Biofabrication*, 12:35018. https://doi.org/10.1088/1758-5090/ab8707
191. Yin R, Luo Z, Zhuang P, *et al*., 2021, VirPreNet: A Weighted Ensemble Convolutional Neural Network for the Virulence Prediction of Influenza A Virus Using All Eight Segments. *Bioinformatics*, 37:737–43. https://doi.org/10.1093/bioinformatics/btaa901
192. Yin R, Zhou X, Rashid S, *et al*., 2020, HopPER: An Adaptive Model for Probability Estimation of Influenza Reassortment through Host Prediction. *BMC Med Genomics*, 13:9. https://doi.org/10.1186/s12920-019-0656-7
193. Lazzari G, Nicolas V, Matsusaki M, *et al*., 2018, Multicellular Spheroid Based on a Triple Co-culture: A Novel 3D Model to Mimic Pancreatic Tumor Complexity. *Acta Biomater*, 78:296–307. https://doi.org/10.1016/j.actbio.2018.08.008
194. Meier-Hubberten JC, Sanderson MP, 2019, Establishment and Analysis of a 3D Co-Culture Spheroid Model of Pancreatic Adenocarcinoma for Application in Drug Discovery. *Methods Mol Biol*, 1953:163–79. https://doi.org/10.1007/978-1-4939-9145-7_11
195. De Moor L, Merovci I, Baetens S, *et al*., 2018, High-throughput Fabrication of Vascularized Spheroids for Bioprinting. *Biofabrication*, 10:35009. https://doi.org/10.1088/1758-5090/aac7e6
196. Noguchi R, Nakayama K, Itoh M, *et al*., 2016, Development of a Three-Dimensional Pre-vascularized Scaffold-free Contractile Cardiac Patch for Treating Heart Disease. *J Heart Lung Transplant*, 35:137–45. https://doi.org/10.1016/j.healun.2015.06.001

REVIEW ARTICLE

3D Printing Polymer-based Bolus Used for Radiotherapy

Ying Lu[1,2], Jianbo Song[2], Xiaohong Yao[1], Meiwen An[3]*, Qinying Shi[2], Xiaobo Huang[1]*

[1]Laboratory of Biomaterial Surface and Interface, School of Materials Science and Engineering, Taiyuan University of Technology, Taiyuan 030024, Shanxi Province, China
[2]Shanxi Bethune Hospital, Shanxi Academy of Medical Sciences, Taiyuan 030032, Shanxi Province, China
[3]Institute of Applied Mechanics and Biomedical Engineering, Taiyuan University of Technology, Taiyuan 030024, Shanxi Province, China

Abstract: Bolus is a kind of auxiliary device used in radiotherapy for the treatment of superficial lesions such as skin cancer. It is commonly used to increase skin dose and overcome the skin-sparing effect. Despite the availability of various commercial boluses, there is currently no bolus that can form full contact with irregular surface of patients' skin, and incomplete contact would result in air gaps. The resulting air gaps can reduce the surface radiation dose, leading to a discrepancy between the delivered dose and planned dose. To avoid this limitation, the customized bolus processed by three-dimensional (3D) printing holds tremendous potential for making radiotherapy more efficient than ever before. This review mainly summarized the recent development of polymers used for processing bolus, 3D printing technologies suitable for polymers, and customization of 3D printing bolus. An ideal material for customizing bolus should not only have the feature of 3D printability for customization, but also possess radiotherapy adjuvant performance as well as other multiple compound properties, including tissue equivalence, biocompatibility, antibacterial activity, and antiphlogosis.

Keywords: Radiotherapy; Bolus; 3D printing; Soft polymers; Hydrogel

*Correspondence to: Xiaobo, Huang, Laboratory of Biomaterial Surface and Interface, School of Materials Science and Engineering, Taiyuan University of Technology, Taiyuan 030024, Shanxi Province, China; huangtyut@163.com

Received: June 15, 2021; **Accepted:** July 21, 2021; **Published Online:** September 22, 2021

Citation: Lu Y, Song J, Yao X, *et al.*, 2021, 3D Printing Polymer-based Bolus Used for Radiotherapy. *Int J Bioprint*, 7(4):414. http://doi.org/10.18063/ijb.v7i4.414

1. Introduction

Radiotherapy is an effective way used for the treatment of tumors, especially in areas where surgery is not possible. Almost half of cancer patients receive radiotherapy at certain point of treatment[1]. To provide a sufficient radiation dose to the tumor, the types of radiation that target tumor location should be selected. Conventionally, electron is used to kill tumors of superficial lesions, such as breast cancer, skin cancer, and nasopharyngeal cancer; however, the dose distribution is inhomogeneous and the target coverage is inadequate. It is widely recommended that the target area should receive at least 95% of the predesigned dose when administering radiotherapy[2]. However, because of the skin sparing effect of high-energy photon beams, the superficial lesions cannot receive a sufficient dose. To solve this problem, a build-up material called bolus, is often placed on the surface of the skin to maximize the radiation dose of subcutaneous tissues so as to achieve the desired dose at target position while reducing the dose in deep tissues[3]. Bolus acts as a layer of skin tissues to provide a more effective treatment to the superficial lesions[4] (**Figure 1**).

Despite the availability of commercial bolus, there are still some problems with bolus during radiotherapy. Most commercial boluses are in a flaky structure that does not form adequate contact with the irregular surface of patients' skin, such as the ear, nose, and scalp, resulting in air gaps between the bolus and the irregular skin[5]. The resulting air gap is very harmful to obtaining the expected distribution of radiation dose at planning target volume (PTV) for achieving a desired therapeutic outcome[6]. The

conventional flat bolus with a uniform size can hardly match the patient's unique body geometry and allow for repeatable setup for treatment[7,8]. Therefore, it is an urgent desire to customize a bolus for fitting any skin contour perfectly in radiotherapy[9-12] (**Figure 2**).

Presently, three-dimensional (3D) printing is one of the ideal means to achieve the customization of various complex structure, especially the personalized medical device[13,14]. At present, some personalized boluses processed by 3D printing have begun to be used in radiotherapy.

Compared to the commercial flat bolus, the 3D-printed bolus allows for a closer match to a patient's skin surface[15,16]. The patient-personalized boluses processed by 3D printing have proven to be close to the skin and have good efficacy in radiotherapy, but have been limited in practical use due to the shortcomings, including the immaturity of printed materials, inconvenient preparation, and time-consuming preparation.

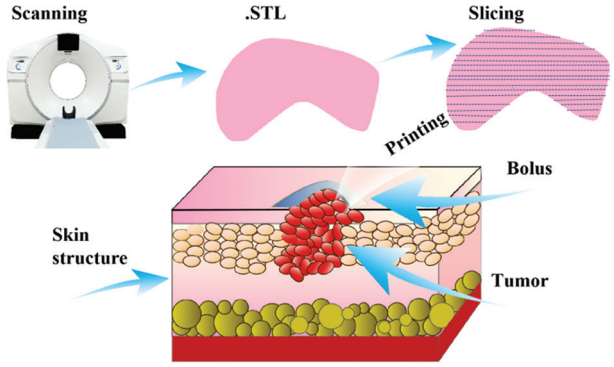

Figure 1. Illustration of bolus for the treatment of superficial tumors by radiotherapy. The tumor (red) is located in the subcutaneous tissues. Bolus (blue) is used to increase skin dose and overcome the skin-sparing effect.

This review mainly focuses on the very recent advances in the development of 3D printed bolus, which has significant potential in radiotherapy. A systematic searching was performed within PubMed, EMBASE, ScienceDirect, and Scopus investigating terms (3D printing OR 3-dimensional printing OR three-dimensional printing OR rapid prototyping OR additive manufacturing) And (bolus OR polymers) with a careful selection and deep analysis. Only papers published in English between January 2000 and December 2020 were included in the study. This review was organized as follows: the first part shows the main soft polymers used for processing bolus; the second part describes the current 3D printing technologies suitable for processing soft polymer materials; the third part discusses the research status of 3D printing bolus; and the last part presents our perspective and outlook on the development of the 3D printing bolus.

2. Soft polymers used for creating bolus

The use of bolus originally reported as early as 1920 still finds its way in the current radiotherapy[17]. In the history of radiotherapy, various materials, such as water, wet gauze, paraffin, beeswax, and Vaseline, have been used to create bolus[18]. However, there are still many problems in the practical application of most bolus materials, mainly because they have poor fit to skin contour and are uneasy

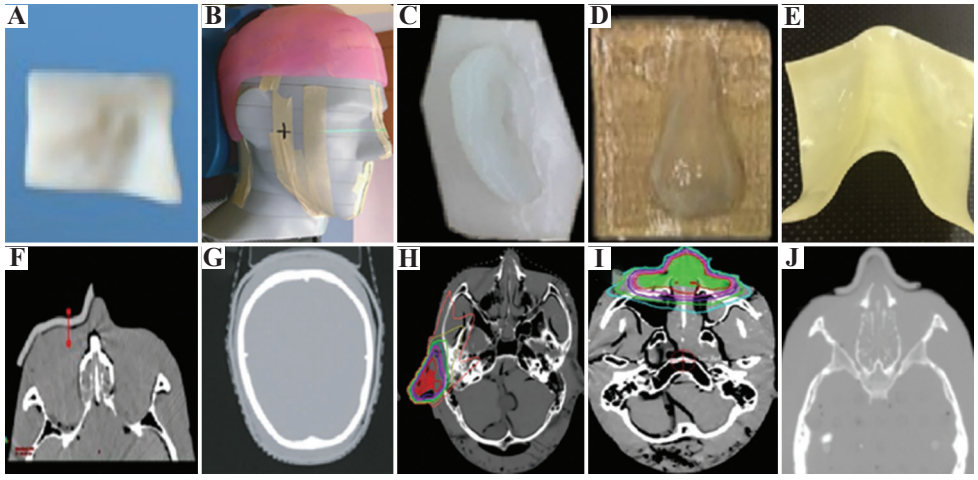

Figure 2. Different boluses and their cross-sectional computed tomography (CT) images. Acrylonitrile butadiene styrene (ABS) bolus (A) and its CT image (B) for head radiotherapy (Reproduced from Ref[8] licensed under Creative Commons Attribution 4.0 license). Agilus-60 bolus (C) and its CT image (D) for head radiotherapy (Reproduced from Ref[9] licensed under Creative Commons Attribution 4.0 license). Silicon bolus (E) and its CT image (F) for ear radiotherapy (Reproduced from Ref[10] licensed under Creative Commons Attribution 4.0 license). Hydrogel bolus (G) and its CT image (H) for nose radiotherapy (Reproduced from Ref[10] licensed under Creative Commons Attribution 4.0 license). PCL bolus (I) and its CT image (J) for nose radiotherapy (Reproduced from Ref[12] licensed under Creative Commons Attribution 4.0 license).

to fabricate. With the development of technology, the modern bolus based on polymers has begun to appear in the field of radiotherapy. Compared to other materials, soft polymers are more suitable for constructing the modern bolus due to their unique physical properties, such as toughness, flexibility, and viscoelasticity. Young's modulus is a key parameter used for defining soft and rigid materials. Human soft tissues, such as skin or muscle tissues, exhibit a modulus of 10^4 – 10^9 Pa[19] (**Figure 3**); thus, we believe that soft polymers with a modulus in the range of soft tissues have the quality and can be used to construct modern bolus.

Sheet-type boluses are now popular in radiotherapy and are generally used to cover large areas that do not need customization. Superflab is one of the most commonly used commercial boluses due to its excellent tissue equivalency, but they are not moldable[20]. Besides, various soft polymers, such as plastics (resins), hydrogels, silicone elastomers, TangoPlus, and polyurethane (PU), have been used for processing the tissue-equivalent modern bolus. From the viewpoint of materials' physicochemical properties, the application of various polymers in bolus is reviewed in **Table 1**.

2.1. Plastic-based boluses used in radiotherapy

Plastic is a kind of macromolecular polymer, which has been widely used in industry and many fields. Synthetic resin is the most important component in plastics, and thus, the nature of plastic is often determined by the resin due to its large content. According to the physicochemical properties of various plastics, they can be divided into two types: thermosetting plastics and thermoplastics. Thermoplastics melt when heated, cure when cooled, and melt again when heated. Up to now, several thermoplastics including polystyrene, acrylonitrile butadiene styrene (ABS), polycaprolactone (PCL), polylactic acid (PLA), and polyethylene terephthalate–glycol-modified (PETG) have been used for creating bolus.

In radiotherapy, polystyrene is generally considered the gold standard (solid water) in bolus material[21]. It has been reported that a shape memory bolus was designed by tetra-branch PCL with acrylate end groups. The PCL-based bolus shows good adhesion to the body surface and can be processed in a short time[12]. As a form of ABS resin, ABS-M30 (Stratasys, Eden Prairie, MN) resin and ABSplus thermoplastic have also been used to process boluses[22,23]. Park *et al.* reported a PLA-based bolus used for breast cancer radiation therapy[24]. Since the plastic is commonly stiffer than the skin tissues, the poor comfort can cause pain for patients during therapy and air gaps, resulting in the failure of radiotherapy. To improve the fit of bolus to skin contour, the plastic-based boluses were usually customized by the 3D printing technology, especially the fused deposition modeling (FDM) method (the detailed content about 3D printing plastic-based bolus will be discussed in the later parts).

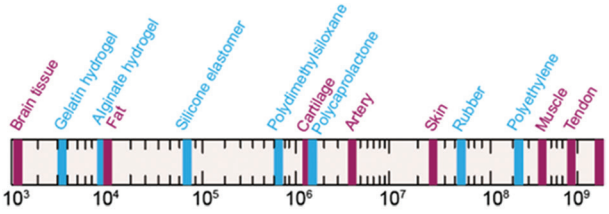

Figure 3. Young's modulus of selected soft polymers (blue) and human tissues (red).

2.2. Elastomer-based boluses used in radiotherapy

The elastomer materials used for creating bolus mainly include silicone and polyurethane (PU). The silicone elastomer refers to a straight chain polymer, whose main chain is composed of silicon atoms and oxygen atoms alternately, and the silicon atoms are usually connected with two organic groups. Compared with the plastic, the silicone elastomers have the flexibility and elasticity

Table 1. Polymer materials used for processing bolus

Categories	Typical materials	Density (g/cm³)	Youngty modulus (Pa)	Advantages	Disadvantages	References
Plastic	PCL Polystyrene ABS PLA PETG	1.03 – 1.30	10^6 – 10^7	Suitable for processing	Stiff; discomfortable for patients	[12,21-24]
Elastomer	TPU Silicone	1.05 – 1.25	10^4 – 10^9	Flexible; elastic; biocompatible	Air gaps between bolus and skin	[15,25,26]
Hydrogel	TPU/PAM Methacrylic acid Nanocellulose	1.05 – 1.32	10^2 – 10^4	Tunable physicochemical property; tissue equivalence; adhesion	Poor mechanical properties	[7,10,27]

closer to the skin tissue. As a representative silicone, polydimethylsiloxane, which is colorless, odorless, transparent and does not cause skin irritation, can be developed into commercial bolus[25]. The polymer has excellent shear resistance, which can ensure its repeated use in radiotherapy. In addition, other silicone elastomers used for processing boluses were also reported. For example, a silicone elastomer based on dihydroxypolysioxane and ethyl polysilicate as the crosslinking agent was synthesized to construct a bolus[10]. Chiu *et al.* have constructed a silicone-based bolus through casting the liquid silicone (EcoFlex 00-30, Smooth-on Inc.)[26]. Due to their chemical stability, excellent biocompatibility, and good mechanical properties, silicone elastomers have great advantages in preparing bolus, but their density (1.1 – 1.2 g/cm^3) being slightly different from the skin tissue may lead to a decrease of tissue equivalence. No matter how good the performance of the silicone elastomers, the sheet structure of bolus will always cause air gaps in the treatment of irregular surface of patients' skin.

PU, also known as polycarbamate, is a kind of polymer containing repeated structural units of -O-CO-NH- bonds in its molecular chains. Due to its excellent biocompatibility and flexibility, PU has been widely used to construct medical devices, such as catheters, cardiac aid devices, medical films, artificial skin, and so on[28]. PU-based polymers can be developed by incorporating soft segments (e.g. lactides, caprolactone, and poly(ethylene glycol) [PEG]) or chain extenders in PU backbone. Recently, PU as a bolus material has entered the view of researchers. For example, Zhao *et al.* have used a kind of thermoplastic PU (TPU) to create a bolus for adjuvant treating a recurrent squamous cell carcinoma at the nasal septum[15]. Hou *et al.* have developed a PU-based bolus with multi-functions, including excellent mechanics and adhesive properties, which make it fit closely to the patient's skin with irregular surface[7]. The mechanical properties of PU can be tailor-made according to the structure-property relationship. Therefore, PU is likely to be processed into a bolus with good tissue equivalence. Besides, TangoPlus is another kind of commercial elastomer used to print tissue-equivalent bolus[29].

2.3.Hydrogel-based boluses used in radiotherapy

Hydrogel is a kind of 3D network consisting of hydrophilic polymer chains, which are crosslinked to matrix with high water content. Due to its excellent characteristics, including tunable physicochemical and bioactive properties, versatility in fabrication, high biocompatibility, and similarity to native extracellular matrix, the hydrogel has widely used as promising biomaterials in the biomedical field[30]. Up to now, different hydrogels from both synthetic and natural hydrogels have been developed in various applications, such as tissue engineering, cell therapy, regenerative medicine, and stem cell and cancer research[31,32]. Synthetic hydrogels, such as poly(vinyl alcohol), polyacrylamide (PAM), and PEG, generally possess precise controllable performance and show high mechanical properties, but lack biological moieties[33-35]. On the other hand, natural hydrogels, such as chitosan, collagen, alginate, gelatin, and hyaluronic acid (HA), have received wide attention due to their bioactive properties. However, their deficiencies include uncontrollable degradation, potential immunogenicity, and low mechanical properties[36-38]. Due to the distinct performance of each of the hydrogel classes, it can be selectively used in various fields according to the application requirements.

Among various materials, hydrogels have the best tissue equivalence due to their similar density and structure to soft tissues. In recent years, hydrogel-based boluses have been studied in the radiotherapy. For example, Kong *et al.* fabricated a bolus composed of methacrylic acid hydrogel, which not only showed good dose parameters in intensity modulated radiation therapy plans, but also had a high degree of comfort and repeatability[10]. Chiozzini *et al.* reported a hydrogel-based bolus consisting of the bacterial nanocellulose, which is made up of D-glucose monomers and produced by several kinds of bacteria[27]. Compared to the commercial bolus, this bolus showed superiority in relation to the radiotherapy parameters, including the radiation attenuation potential and radiological density.

To the best of our knowledge, hydrogel has many advantages including flexibility, odorlessness, nontoxicity, and high transparence, but up to now, it has not been widely used as a bolus in clinical setting. The reason is the quality of losing water easily and the nature of being fragile for the traditional hydrogel. Due to the high-water content (>85%), hydrogels tend to lose water and undergo shrinkage or deformation, which greatly limits their application in radiotherapy. To solve this problem, a water-resisting layer, such as polyol PU membrane or silicone oil, can be used to cover the hydrogel surface to prevent dehydration of hydrogels[10]. An alternate approach is to replace the water in the gel with glycerine, maintaining the structure of hydrogels.

In fact, the main problem limiting the wide application of traditional hydrogels is their poor mechanical behavior, including low stretchability, low toughness, and notch-sensitiveness. For example, the alginate hydrogel is easily ruptured when just stretched to 1.2 times of its original length. Most traditional hydrogels with a fracture energy of about 10 J/m^{-2}, are more brittle than the cartilage with ~1000 J/m^{-2} and natural rubbers with 10,000 J/m^{-2}. When the hydrogels contain notches, the strength and stretchability of samples can be markedly decreased. To solve this problem, various types

of composite hydrogels, including slide-ring hydrogels, double network hydrogels, and nanocomposite hydrogels, have been developed by introducing an effective energy dissipation mechanism[39,40]. For example, a nanocomposite hydrogel composed of hectorite clay and N-isopropylacrylamide has an elongation of up to 1300%. A tough and stretchable hydrogel with double networks was created by mixing covalently crosslinked PAM and ionically crosslinked alginate. The resulting composite hydrogel can be stretched more than 20 times of its original length. It also showed excellent notch-insensitive and self-recovery performance[41]. Hou *et al.* have reported a composite hydrogel (PU/PAM) composed of PU and PAM as bolus. This novel hydrogel with excellent mechanical, self-healing and adhesive properties, can provide an optimal dose distribution for radiotherapy[7]. Over the past decade, major breakthroughs have been made in the research of composite hydrogels with strengthened mechanics. We believe that these advances will lead to a framework that helps construct an ideal bolus in radiotherapy through rational design of hydrogels. Therefore, with the development of hydrogel research, more and more hydrogels will be developed to construct boluses used for radiotherapy in the future.

In this section, we mainly review the current soft polymers used to prepare boluses and analyze the physicochemical properties of these materials as boluses. Compared with plastics, elastomers, and hydrogels with excellent flexibility and tissue equivalence are more suitable to construct boluses. The properties of the material play an important role in radiotherapy, but to form full contact with the irregular surface of patients' skin, the structure of the bolus needs to be customized.

3. 3D printing technology suitable for processing polymers

As a promising additive manufacturing, 3D printing has become a versatile technology for manufacturing 3D structures composed of different materials, such as ceramics, metals, and polymers[42]. According to the digital data of 3D models, the designed 3D objects can be processed layer-by-layer. Different from traditional manufacturing methods, 3D printing can rapidly turn digital-aided designs into 3D complex objects without wasting any materials. According to the printing materials and the principles, print heads or laser optics are generally used to deposit one layer of 3D objects. During the process of printing, the deposited regions are crosslinked or solidified to yield entities[43]. In addition, the ability of 3D printing to quickly produce products on demand has greatly boosted the academic research and the industrial production[44]. Up to now, based on different principles and materials, over dozen types of 3D printing technologies that meet the nature of different materials have been developed[45]. Especially for polymer materials with various polymerization characteristics, four printing techniques are mainly used, including powder bed fusion, material extrusion, material jetting, and vat polymerization (**Figure 4**). The performance of different printing technologies is listed in **Table 2**.

3.1. Powder bed fusion

As a kind of additive manufacturing process, power bed fusion makes use of a laser to sinter powdered materials. It is also called selective laser sintering (SLS) according to the phase states of powder bonding[46]. With the help of lasers that automatically aim at points in space manipulated by a 3D control system, the powdered materials are bonded together to form a solid structure. The manufacturing process of SLS consists of three repeated steps[47]. First, the powdered materials are uniformly distributed as a printing layer by scraping or rolling. Second, the powder is selectively fused to form a solid structure by scanning the laser. Third, to print the next layer, the build platform descends one layer. These three steps are repeated until the SLS process is finished. Compared to other 3D printing, SLS does not require additional supporting materials. In addition, the powder in the non-molten region can be recycled after printing, resulting in a material utilization rate of close to 100%.

The resolution of SLS printed parts is largely dependent on the particle size: the larger the particle and the lower the spatial resolution. However, for the sake of safety, cost efficiency and process ability, the size of powder particles is usually limited to a range of 10 – 100 μ. Up to now, the resolution of SLS can reach 100 μm under optimal conditions[48].

In general, powdered materials used in SLS should possess several properties, such as compactness, good fluidity, and thermal stability. During the first step of SLS process, good fluidity and compactness are the key factors to ensure proper coalescence in the subsequent sintering. In addition, the most crucial requirement for SLS powders is the thermal properties that allow the powders to solidify uniformly during melting and sintering[49]. As for soft polymer materials used for SLS, these requirements are extraordinarily harsh. At present, few soft polymer powders are processed using SLS, such as polycarbonate (PC), PCL, and thermoplastic elastomers (TPEs). There is a popular view that the biomedical fields are the most active areas for SLS using soft polymer materials[50]; however, SLS is not well suited for processing soft bolus with good softness and tissue equivalence due to its strict requirements for materials.

3.2. Material extrusion

In extrusion printing, the polymer materials are extruded through a nozzle to form a continuous filament, which

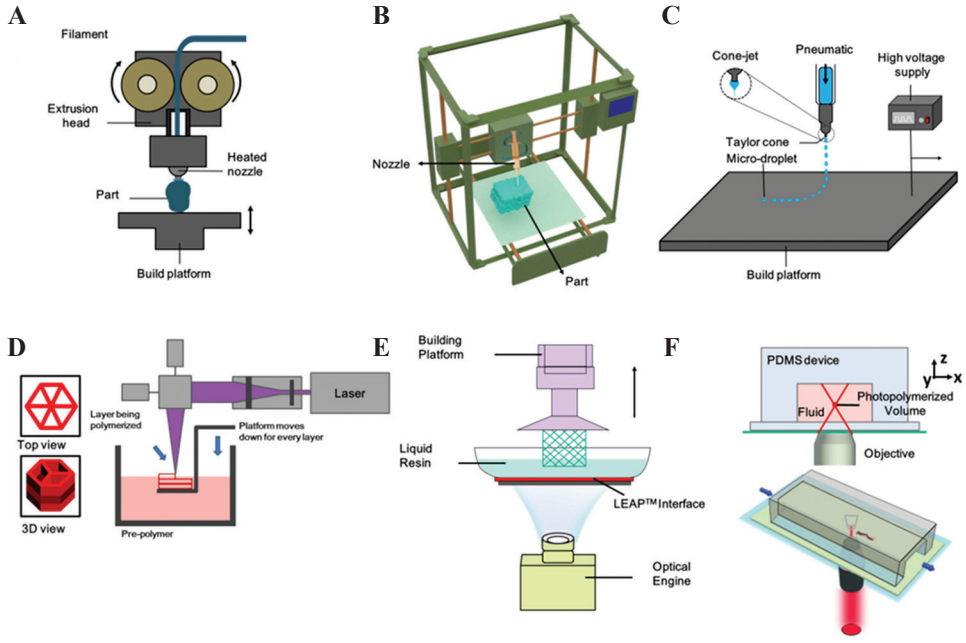

Figure 4. Schematic illustrations of different 3D printing technologies. (A) Fused deposition modeling printing. (B) Direct ink writing printing. (C) Inkjet printing. (D) Stereolithography printing. (E) Digital projection lithography printing. (F) Two-photon polymerization printing.

is deposited to build the target entity. The extruded filament is deposited at the designed position through the movement of the XY axis to complete the pattern of one layer. After finishing one layer, the build platform moves down to deposit the next layer. These steps are repeated until the designed objects are completed[51].

At present, the extrusion printing mainly includes FDM and direct ink writing (DIW). As for the FDM, thermoplastic filaments are liquefied into their semi-molten state using a heated nozzle. The liquefied materials are then solidified when they are cooled below their glass transition temperature. Due to the high viscosity and the swelling of the melted polymer, the resolution of printed structures is greatly reduced to a few 100 μ[52]. In addition to the basic thermoplasticity, the printed materials must maintain a balance between the mechanical performance and the rheological properties, which greatly limits the variety of printable materials. Up to now, several thermoplastic polymers have been used in the FDM, including PCL, ABS, PLA, and other thermoplastics[53]. However, inhomogeneity associated with an FDM printed bolus may also impact the use in radiotherapy.

The DIW method is mainly used to print viscoelastic materials. Compared with the FDM using a heated nozzle, DIW utilizes a common needle to extrude the printed materials[54]. After deposition, the curing processes, including cooling curing and photopolymerization, are used to solidify the printed structures. The viscoelasticity of material is critical for DIW, which requires the rheological property of printed materials to ensure the printing fidelity and continuity, including yield point and shear thinning[55]. The extrusion of viscoelastic material is considered a transient shear process, which allows the extrusion to be smooth and ensures the deposited filaments retain their shapes. When the inks are extruded from the nozzle, such viscoelastic liquids can recover their initial storage modulus and viscosity. Compared to other printing methods, the DIW process can accept a larger variety of materials that possess such rheological properties. Therefore, a large number of polymer materials can be printed using the DIW, including silicone elastomer, PU, and hydrogels[56]. The main disadvantages of the DIW technology are its slow building speed and low resolution. At present, it has been reported that the resolution of DIW can just reach a few 100 μ and the highest printing speed of DIW is only 100 mm/s, which is greatly less than that of photopolymerization printing[57].

3.3. Material jetting

Inkjet printing is an additive manufacturing technology through which innumerable droplets of printed materials are deposited layer-by-layer to form the target entity[58]. The typical setup of inkjet printing is generally composed of a motion platform with jetting heads, an X-Y-Z three axis, and auxiliary curing devices. Low-viscosity liquids are ejected from the jetting heads to form the droplets, which are deposited on the building platform and then solidified[59]. The inkjet printing needs to meet two basic

Table 2. Comparison of printing methods for bolus

Categories	Methods	Resolution	Building speed	Suitable materials	Potential to print bolus	Advantages	Disadvantages	References
Powder bed fusion	SLS	>100 μ1	**	Powdered materials	Poor	High material utilization rate; no support material required	Material limitation; few soft polymer powders	[46-50]
Material extrusion	FDM	>100 μ1	**	Thermoplastic polymers	Poor	High simplicity; capability to print compositional gradients	Low speed; low resolution	[51-57]
	DIW	1-100 μ-	**	Pseudoplastic polymer fluids	Poor			
Material jetting	Inkjet printing	>10 μ1	***	Polymer fluids with low viscosity	Poor	Applicable for wide range of biomaterials; ability to print multi-material	Clogging of the printing head; expensive setup	[58-62]
Photopolymerization	SLA	>5 μ5	***	Photopolymers with low viscosity including photoresin and photohydrogen	Fair	High resolution; suitable for many photocurable polymers; raw material base is fluid	Material limitation; require an UV source	[63-72]
	TPP	>100 nm	*		Poor			
	DLP	>5 μ5	****		Good			
	CLIP	>100 μ1	*****		Good			

requirements, namely, the fluid suitable for ink jetting and the ability to solidify into an entity. As a key process of inkjet printing, the generation of droplets is mainly dependent on both the fluid performance and the 3D printing parameters[60]. The former includes dynamic viscosity (η), fluid density (ρ) and surface tension (γ), and the latter encompasses the velocity of the ejected fluid (ν), the droplet length (*l*), and the nozzle diameter (*d*). The inkjet printing can be achieved only when these parameters are controlled in an appropriate processing condition[61].

The dimensionless *Z* parameter is generally used to determine whether the liquids can be ejected stably. As for the high values of *Z*, the ejected droplets are easily to splash into multiple satellite droplets, whereas at low values of *Z*, the droplet ejection will be prevented by viscous dissipation. In general, stable jetting can be generated when *Z* is controlled between 1 and 10[62].

Due to such stringent requirements, few polymers can be printed by inkjet printing. Among these polymers, because many hydrogels have excellent inkjet printing performance, inkjet printing hydrogels have become a very hot topic[60]. Nowadays, the advanced inkjet printing technology possesses a powerful ability to rapidly construct complex 3D structures using multi-nozzle arrays, which can eject more than 100 million droplets per second[42]. In fact, it is difficult to eject complex fluids without clogging, limiting the diversity of printable polymers.

3.4. Vat polymerization

As a kind of additive manufacturing process with great potential, photocuring printing uses ultraviolet (UV) light to selectively solidify liquid photosensitive polymers by photocuring layer-by-layer to obtain the target object[63,64]. Up to now, the photopolymerization printing technology mainly includes stereolithography (SLA), digital projection lithography (DLP), two-photon polymerization (TPP), and computed axial lithography (CAL).

SLA is the first photocuring printing developed in the early 1980s. The SLA uses a point light source (e.g. laser) to irradiate only one voxel at a time and prints patterns with the movement of the beam. After one layer is completed, the building plate moves by one-layer thickness and a new layer of liquid photosensitive polymers turns into the printing regions to print the next layer. These procedures are repeated layer-by-layer until the printing of the desired object entity is accomplished[65,66]. In general, the photocuring resin is mainly used as the printed material of SLA to fabricate 3D objects with large size in the manufacturing industry.

In TPP, two laser pulses with high wavelengths intersect to generate a single pulse with a low wavelength, which stimulates the polymerization[67]. Compared to the SLA possessing a focal plane, the TPP gets a focal spot. Thus, the accuracy of TPP is generally higher than SLA. It is reported that the optimal printing resolution of the TPP so far is around 100 nm[68]. TPP is normally used to fabricate 3D sophisticated objects within several micrometers, but the printing dimensions are very small, usually limited in 1 cm^3. For example, using this method, PEGDA gels were processed into 3D helix-shaped constructs in micron grade[69]. In summary, these two laser-based prototyping techniques possess the characteristic of high precision and resolution. However, the processing speed of SLA and TPP is relatively slow, which may make 3D printing bolus challenging.

To increase the manufacturing speed of photopolymerization, researchers have developed the DLP technology[70], which makes an entire pattern on the focal plane to be crosslinked simultaneously. In this method, a dynamic pattern can be projected by using a liquid crystal display or a digital micro-mirror device[43,71]. Therefore, the printing speed of DLP is significantly improved in comparison to the point light technology. Recently, continuous liquid interface production (CLIP) technology, which is an advanced DLP technology with higher printing speed has been developed. The CLIP can achieve the continuity of printing by forming a polymerization "dead zone," which allows the 3D objects to be printed in minutes instead of hours[42].

Recently, a novel photocuring printing technology named CAL was developed. By irradiating a rotating volume of photosensitive polymers with a dynamically changing light pattern, CAL can obtain the concurrent printing of all points within a 3D object[71]. The conventional photocuring printing, such as DLP, prints objects layer-by-layer, whereas the CAL delivers light energy to the material volume in the form of a series of 2D images. Each image projection is propagated through the material volume at a different angle. The superposition of light energy causes the whole entity to solidify at 1 time in accordance with the designed geometry. It has been reported that the printing time for a centimeter-scale object just needed about 30 – 120 s, which is greatly faster than the layer-by-layer printing method. However, the resolution of CAL is limited to sub-millimeters[72].

In summary, polymers suitable for most photopolymerization printing should obtain two basic characteristics: good fluidity and photocurable ability[73]. The photopolymers should be liquid with low viscosity so that the polymers can be evenly spread within the printable area. In general, the photopolymers have a specific group, which can be induced to undergo photo crosslinking reactions triggered by the initiators. In addition to the initiators and the photopolymers, other additives are also used to improve the printing quality,

including light absorbers, radical inhibitors, and diluents. The light absorbers can restrain the curing depth, the radical inhibitors can prevent premature solidification of liquids, and the diluents can decrease the liquid viscosity[74]. Compared to the large polymer family, the variety of photopolymers is relatively small. Novel photopolymers can be developed by grafting specific photosensitive groups with normal polymers. Up to now, various photopolymers have been used for photocuring printing, including photocuring resins, hydrogels, and silicone elastomers[75].

4. Customization of bolus through 3D printing

With the improvement of 3D printing technology, it has been widely used in various fields, especially the biomedical field requiring customization of medical devices. 3D printing is currently a promising approach to achieve the customization of bolus. Compared to the commonly used flat bolus, the 3D-printed bolus allows for a more match to a patient's skin surface and shows desirable curative effect of radiotherapy (**Figure 5**). However, 3D printing bolus still stays in the early stages of development due to shortcomings of printable and appropriate materials. Reviewing the research progress of 3D printing bolus in recent years, we divide the current 3D printing bolus into two main categories: indirect printing and direct printing. The former is to first print a shell of the bolus and then fill it with other polymers, and the latter is to print a bolus directly with a 3D printing technique.

4.1. Indirect printing bolus (casting)

As the name suggests, the indirect printing means that it takes at least two steps to produce a customized bolus. The typical workflow to make bolus by the indirect printing is shown in **Figure 6A**. In this method, the bolus shells are first printed by 3D printing technology, then the materials were cast into the chamber of shells. After demolding, a customized bolus is obtained. To be precise, this method should be called casting, which is suitable for processing most of hydrogels and some elastomers with low melting point. Up to now, various polymers have been widely processed as customized bolus using this method. For example, Kong *et al.* printed a shell of bolus using the PLA and then filled it with silicone rubber and hydrogels for non-melanoma skin cancer radiotherapy[10]. Park *et al.* casted a urethane liquid rubber and liquid silicon compound into the mold to make the customized boluses[81]. Resins are commonly used to print mold shells due to their high stiffness, low swellability, and low flexibility. Compared to the commonly used sheet bolus, the bolus cast by this method can contact closer with the body, greatly

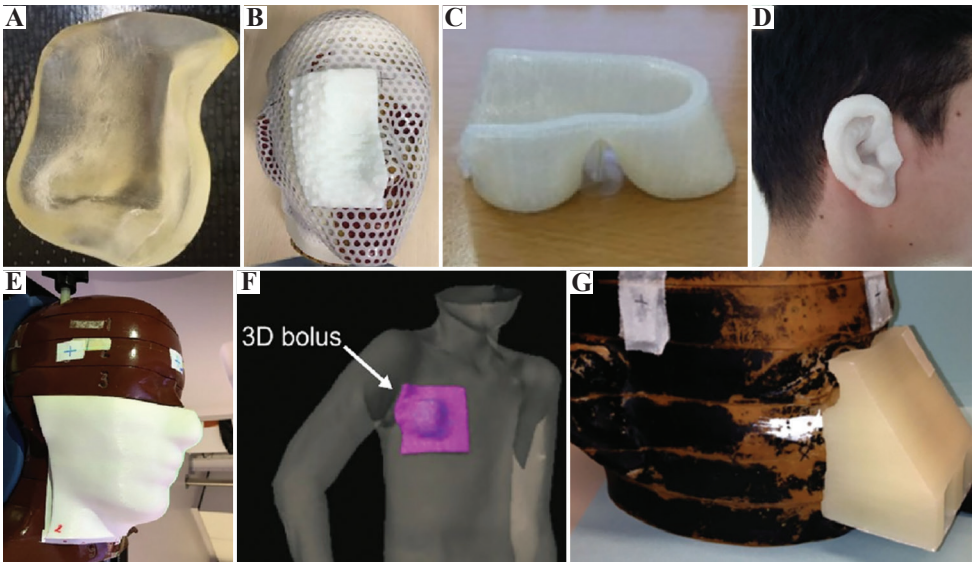

Figure 5. Some 3D-printed boluses reported in the literature. (A) A nose bolus printed with Tangoplus (Reproduced from Ref[76] licensed under Creative Commons Attribution 4.0 license). (B) A bolus printed with ABS on the head phantom surface (Reproduced from Ref[77] licensed under Creative Commons Attribution 4.0 license). (C) 3D-printed bolus of the 4th and 5th knuckle (Reproduced from Ref[8] licensed under Creative Commons Attribution 4.0 license). (D) 3D-printed bolus fitting the ear of a volunteer (Reproduced from Ref[8] licensed under Creative Commons Attribution 4.0 license). (E) 3D-printed Ninjaflex bolus covering the right-hand side of the head phantom (Reproduced from Ref[78] licensed under Creative Commons Attribution 4.0 license). (F) 3D-printed breast bolus (Reproduced from Ref[79] licensed under Creative Commons Attribution 4.0 license). (G) Bolus printed with PLA on the Alderson RANDO phantom (Reproduced from Ref[80] licensed under Creative Commons Attribution 4.0 license).

reducing the air gap and improving the efficiency of radiotherapy.

However, the indirect printing method is complicated and time-consuming, and the accuracy of this method is relatively low. The process of this method mainly includes molding and casting, which determines the preparing efficiency of customized bolus. Chiu *et al.* have constructed a silicone bolus using this method for head-and-neck radiotherapy. The time taken for construction including mold printing and fillers casting is about 2 days depending on bolus surface area, complexity and volume[26]. In this method, two pieces of mold shells including a positive and a negative are first printed and then put together to form a chamber for casting fillers. The accuracy of the bolus is seriously influenced by the thickness of mold shells. This method is suitable for the preparation of bolus with a large size used for breast or head radiotherapy, but not for small bolus with complex structures used for ear or nose. In a word, although the indirect printing method enables the customization of bolus and improves the efficiency of radiotherapy to some extent, the complicated and time-consuming process will greatly limit the commercialization of this technology in the field of radiotherapy.

4.2. Direct printing bolus

Direct printing means that 3D objects can be directly realized from CAD models by means of computer numerical control printers. CAD models are translated into computer-readable formats (usually standard tessellation language file), and then sliced into control codes which can control printers to solidify material in a layer-by-layer manner[76] (**Figure 6B**). With the rapid development of 3D printing technology, increasing researchers from different backgrounds have started to manufacture devices or structures with high complexity using this powerful technology[8,77,78]. In recent years, the customized bolus directly processed using 3D printing has also attracted wide attention of doctors and scholars in the field of radiotherapy.

Up to now, various polymers have been used to fabricate bolus using different 3D printing technologies, mainly including FDM, inkjet and SLA[79,80]. FDM is one of the earliest 3D printing technologies used to print bolus. For example, Kim *et al.* have used the FDM method to print a nose bolus using ABS resins as the printing material[22]. Using ABSplus thermoplastic as printing materials, Park *et al.* have fabricated a customized ear bolus by applying the FDM method[82]. A customized breast bolus composed of PLA was also printed by means of this method[24]. Through this method, a semi-flexible TPU was processed into a customized leg bolus used for treating the primary cutaneous lymphoma[83]. In the current study, the thermoplastic polymers were mainly used to process customized bolus based on the printing principle of FDM technology. Compared with both the commercial sheet bolus and the indirectly printed bolus, the customized bolus processed by FDM has a better fit to the irregular body skin. However, these thermoplastic polymers used for FDM are stiffer than the soft tissues. It inevitably results in the patient experiencing pain and air gaps, influencing the efficiency of radiotherapy. In addition, the time required for preparing a customized bolus using this method was relatively long due to the time-consuming process of FDM. Consequently, a more malleable and printable polymer should be used to process customized bolus.

Recently, some other 3D printing technologies suitable for processing soft polymers have begun to be used to produce customized bolus. Park *et al.* used an inkjet printing technology to print a nose bolus composed of a malleable rubber-like material[76]. Using the same method, Baltz *et al.* also made a customized bolus cap composed of a rubber-like photopolymer resin used for

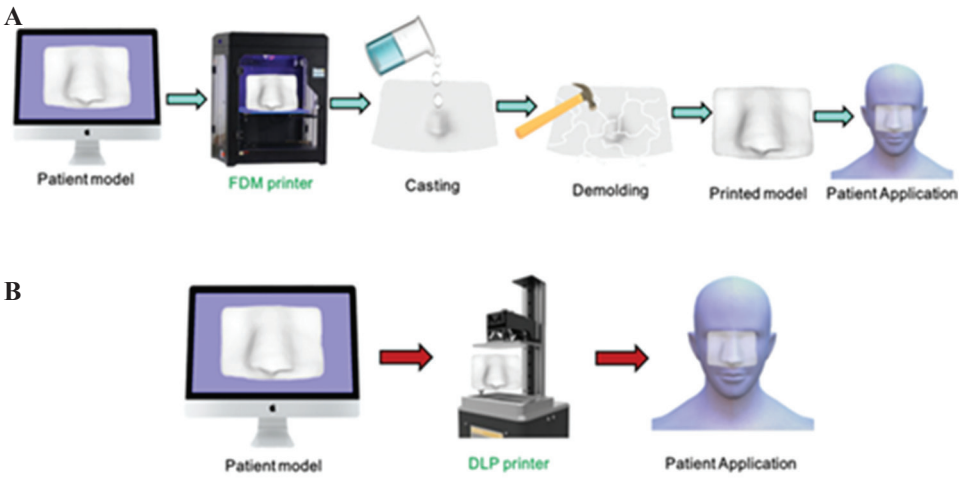

Figure 6. (A) Indirect printing workflow of bolus. (B) Direct printing workflow of bolus.

total scalp irradiation[9]. In addition, Munoz *et al.* used SLA method to create a customized nose bolus composed of elastomeric materials, which showed compliant, elastic, and water equivalent properties[84]. Compared to the rigid bolus, the soft bolus created by these two methods greatly reduces the patient discomfort and unwanted air gaps. It suggests that the customization of bolus is not only related with the selection of 3D printing methods, but also dependent on the properties of printed materials.

Direct printing is a promising approach to rapidly achieve the customization of bolus, but 3D printing of bolus using soft polymers is still in the early stage of development. An ideal bolus should not only provide a close contact with the patients' irregular surface, but also possess excellent properties, such as flexibility, biocompatibility, and adhesion. The 3D printing methods determine the printing speed and printing accuracy of bolus, while the printed materials mainly influence the performance of bolus. With the current 3D printing technology, the bottleneck restricting the application of 3D printed bolus is mainly the deficient development of printable polymer materials. The advances in materials science and 3D printing technology lead to the development of more printable polymers, which will be used for 3D printing of bolus.

5. Summary and outlook

Various materials that are able to be processed into bolus have been used in radiation therapy, but the development of customized bolus prepared by 3D printing of polymers is still in its infancy. To achieve the personalized customization of bolus, this review aims at providing comprehensive insights into the 3D printing bolus. How to choose an appropriate 3D printing technique and to design a suitable printable polymer is an urgent issue to be solved in customizing bolus. We focus on three points: (i) polymer materials used for fabricating bolus, (ii) 3D printing techniques suitable for processing polymer materials, and (iii) personalized customization of bolus through 3D printing technology.

Various 3D printing techniques utilizing different principle to pattern are suitable for different materials. The choice of 3D printing methods is mainly determined by the actual requirements of application[85]. A 3D printing technique suitable for processing bolus should have the following three characteristics: rapid printing speed (<1 h), medium printing scale (X-Y-Z three axis ≤30 cm), and general printing accuracy (≤200 μm). The extrusion printing and the inkjet printing utilize a nozzle to deliver the polymers to the designed position and solidify the polymers by a curing process. As for the nozzle-based printing techniques, most polymers can be printed as long as they have suitable rheological properties. However, the point-to-point printing mode results in a slow printing speed, which will greatly limit the manufacturing efficiency of personalized bolus. In contrast, photocuring printing can selectively solidify the polymers from a liquid tank, which can perform the patterning process and curing process at the same time. Especially for the DLP- and CLIP-based layer-by-layer printing mode, these photocuring printing methods enable the direct and rapid construction of bolus. As an emerging photocuring printing technology, the CAL shows a faster patterning speed in comparison to the DLP method. However, this technology is premature, costly, and the printing precision is still relatively low. Therefore, among different 3D printing techniques, the DLP and CLIP methods based on layer photocuring are probably the most ideal technology to print personalized bolus at present.

Up to now, the printable materials suitable for DLP-based photocuring printing are mainly photosensitive resins, which have the basic characteristic of photocurability[86]. Photosensitive resins are a class of relatively mature photocurable prepolymers with low molecular weights, which mainly include esterified acrylate epoxy resin, unsaturated polyester, PU, and polymercaptan/polyene photocurable resin systems[87]. Although the photo-resins (Young modulus, ~GPa) have been widely used in the manufacturing industry, they are not suitable for constructing bolus by DLP-based printing due to their higher hardness compared to patients' skin tissues (~KPa). The mismatching in hardness between bolus and skin tissues will inevitably lead to the failure of radiotherapy. Besides, the potential toxicity of photo-resin makes it even less likely to be used in clinic. Therefore, it is urgent to develop a kind of material that can not only be used for DLP printing, but also has an elastic modulus equivalent to skin tissues.

Hydrogels and silicon gels have an elastic modulus close to that of human skin tissue, while most of these materials cannot be directly used for photocuring printing due to a lack of photosensitive properties. To endow the gels with photocurable ability, some photopolymerizable functional groups have been grafted onto the molecular chain of the gels. The modified gels with both photocurable ability and bionic hardness will be a kind of ideal materials for constructing bolus. In addition, it has been recognized that the bolus-assisted radiotherapy can efficiently control the recurrence of subcutaneous tumor, but it also causes some side effects. For example, it is likely to damage the normal tissues around tumors and cause dermatitis in the exposed areas. More severely, inflamed areas are susceptible to bacterial infection, which may prevent irradiated skin from healing and even aggravate skin necrosis. Therefore, to improve the curative effect of radiotherapy, it is urgent and necessary to design a new-type bolus with combined features, including printability,

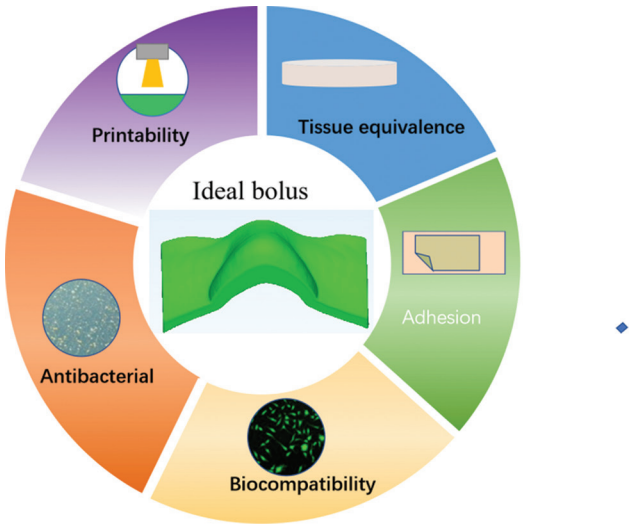

Figure 7. An ideal soft polymer suitable for customized bolus should have combined features, including printability, tissue equivalence, biocompatibility, flexibility, and antibacterial properties.

biocompatibility, good-fit to skin contour as well as antibacterial and antiphlogosis properties (**Figure 7**).

In brief, there has been impressive progress in the application of 3D printing technology in many areas. However, as an emerging technology used in radiotherapy, 3D printing still faces numerous challenges before practical applications, including printing methods, printable materials, and boluses' design. Through reviewing the 3D printing techniques and polymers suitable for processing bolus, we anticipate this review could help readers choose suitable printing methods and design printable polymer materials to achieve the customization of bolus.

An ideal 3D-printed bolus for radiotherapy is an auxiliary device that should integrate multiple properties, including customizable dimensions, appropriate physicochemical performance, and favorable compatibility and antibacterial activity. (i) The customizable dimension is the primary feature of the 3D printed bolus. The conventional bolus is usually a kind of square film with uniform thickness (5 mm), while the 3D printed bolus is an irregular membrane tailored to the characteristics of the patient's skin surface. Compared to the conventional bolus, the 3D printed bolus allows for a more match to the human body, such as the head, breast, and facial parts, and ensures the expected dose distribution at PTV. (ii) The appropriate physicochemical properties of 3D printed bolus mainly include the tissue equivalence, transparency, mechanical performance, and bioadhesion. The bolus is considered a kind of tissue equivalence, which can simulate the absorption and scattering properties of skin tissues for a given irradiation. Although transparency does not normally affect the effects of radiation, good transparency (≥50%) will help to facilitate the accurate and repeatable placement of bolus. Good mechanical performance means that the bolus not only has an elastic modulus similar to the skin tissues, but also good toughness to prevent it from being torn in repeated use. The bioadhesive performance enables the 3D printed bolus to fit well with the irregular human skin, ensuring the accuracy of radiation dose. (iii) The favorable compatibility means that an ideal 3D-printed bolus should not generate any adverse effects in contact with human body. Besides, antibacterial properties can inhibit the occurrence of inflammation caused by the side effect of radiotherapy. Therefore, to obtain an ideal 3D printed bolus, the convergence of versatility in the soft polymers is inevitable in the future, and is thought to accelerate the outcome of radiotherapy.

Acknowledgments

This work was supported by the National Natural Science Foundation of China (31300808), the Natural Science Foundation of Shanxi Province (201801D121094), the Open Research Fund Program of Collaborative Innovation Center for Molecular Imaging of Precision Medicine, No. 2020-ZD02.

Conflicts of Interest

The authors declare that they have no known competing financial interests or personal relationships that could have appeared to influence the work reported in this paper.

Author contributions

Y.L. collected information and drafted the manuscript. J.S. advised the organization of the main contents. X.Y. and M.A. reviewed the manuscript. Q.S. collected the detailed research results. X.H. conceived the ideas and edited the manuscript.

References

1. Baskar R, Lee KA, Yeo R, *et al.*, 2012, Cancer and Radiation Therapy: Current Advances and Future Directions. *Int J Med Sci*, 9:193–9.
2. Hodapp N, 2012, The ICRU Report 83: Prescribing, Recording and Reporting Photon-Beam Intensity-Modulated Radiation Therapy (IMRT). *Strahlenther Onkol*, 188:97–9. https://doi.org/10.1093/jicru_ndq002
3. Babic S, Kerr A T, Westerland M, *et al.*, 2002, Examination of Jeltrate Plus as a Tissue Equivalent Bolus Material. *J Appl Clin Med Phys*, 3:170–5. https://doi.org/10.1120/1.1471552
4. Hsu SH, Roberson PL, Chen Y, *et al.*, 2008, Assessment of Skin Dose for Breast Chest Wall Radiotherapy as a Function

of Bolus Material. *Phys Med Biol*, 53:2593–606. https://doi.org/10.1088/0031-9155/53/10/010

5. Aras S, Tanzer İO, 2020, Dosimetric comparison of superflab and specially prepared bolus materials used in radiotherapy practice. *Eur J Breast Health*, 16:167–70. https://doi.org/10.5152/ejbh.2020.5041
6. Khan Y, Villarreal-Barajas JE, Udowicz M, *et al.*, 2013, Clinical and Dosimetric Implications of Air Gaps between Bolus and Skin Surface during Radiation Therapy. *J Cancer Ther*, 4:1251–5. https://doi.org/10.4236/jct.2013.47147
7. Hou Y, Song Y, Sun X, *et al.*, 2020, Multifunctional Composite Hydrogel Bolus with Combined Self-Healing, Antibacterial and Adhesive Functions for Radiotherapy. *J Mater Chem B*, 8:2627–35. https://doi.org/10.1039/c9tb02967b
8. Dipasquale G, Poirier A, Sprunger Y, *et al.*, 2018, Improving 3D-Printing of Megavoltage X-Rays Radiotherapy Bolus with Surface-Scanner. *Radiat Oncol*, 13:203. https://doi.org/10.1186/s13014-018-1148-1
9. Baltz GC, Chi PM, Wong PF, *et al.*, 2019, Development and Validation of a 3D-Printed Bolus Cap for Total Scalp Irradiation. *J Appl Clin Med Phys*, 20:89–96. https://doi.org/10.1002/acm2.12552
10. Kong Y, Yan T, Sun Y, *et al.*, 2019, A Dosimetric Study on the Use of 3D-Printed Customized Boluses in Photon Therapy: A Hydrogel and Silica Gel Study. *J Appl Clin Med Phys*, 20:348–55. https://doi.org/10.1002/acm2.12489
11. Robar JL, Moran K, Allan J, *et al.*, 2018, Intrapatient Study Comparing 3D Printed Bolus Versus Standard Vinyl Gel Sheet Bolus for Postmastectomy Chest Wall Radiation Therapy. *Pract Radiat Oncol*, 8:221–9. https://doi.org/10.1016/j.prro.2017.12.008
12. Aoyama T, Uto K, Shimizu H, *et al.*, 2020, Physical and Dosimetric Characterization of Thermoset Shape Memory Bolus Developed for Radiotherapy. *Med Phys*, 47:6103–12. https://doi.org/10.1002/mp.14516
13. Asfia A, Novak JI, Mohammed MI, *et al.*, 2020, A Review of 3D Printed Patient Specific Immobilisation Devices in Radiotherapy. *Phys Imaging Radiat Oncol*, 13:30–5. https://doi.org/10.1016/j.phro.2020.03.003
14. Zemnick C, Woodhouse SA, Gewanter RM, *et al.*, 2007, Rapid Prototyping Technique for Creating a Radiation Shield. *J Prosthet Dent*, 97:236–41. https://doi.org/10.1016/j.prosdent.2007.02.005
15. Zhao Y, Moran K, Yewondwossen M, *et al.*, 2017, Clinical Applications of 3-Dimensional Printing in Radiation Therapy. *Med Dosim*, 42:150–5.
16. Tino R, Leary M, Yeo A, *et al.*, 2020, Additive Manufacturing in Radiation Oncology: A Review of Clinical Practice, Emerging Trends and Research Opportunities. *Int J Extrem Manuf*, 2:012003. https://doi.org/10.1088/2631-7990/ab70af
17. Walker M, Cohen N, Menchaca D, 2005, Play-Doh and Water-Soaked Gauze Sponges as Alternative Bolus Material For Cobalt-60 Teletherapy. *Vet Radiol Ultrasound*, 46:179–81. https://doi.org/10.1111/j.1740-8261.2005.00033.x
18. Vyas V, Palmer L, Mudge R, *et al.*, 2013, On Bolus for Megavoltage Photon and Electron Radiation Therapy. *Med Dosim*, 38:268–73. https://doi.org/10.1016/j.meddos.2013.02.007
19. Rus D, Tolley MT, 2015, Design, Fabrication and Control of soft Robots. *Nature*, 521:467–75. https://doi.org/10.1038/nature14543
20. Benoit J, Pruitt AF, Thrall DE, 2009, Effect of Wetness Level on the Suitability of Wet Gauze as a Substitute for Superflab as a Bolus Material for use with 6mv Photons. *Vet Radiol Ultrasound*, 50:555–9. https://doi.org/10.1111/j.1740-8261.2009.01573.x
21. Reft CS, 1989, Output Calibration in Solid Water for High Energy Photon Beams. *Med Phys*, 16:299–301. https://doi.org/10.1118/1.596423
22. Kim SW, Shin HJ, Kay CS, *et al.*, 2014, A customized Bolus Produced Using a 3-Dimensional Printer for Radiotherapy. *PLoS One*, 9:e110746. https://doi.org/10.1371/journal.pone.0110746
23. Lukowiak M, Jezierska K, Boehlke M, *et al.*, 2017, Utilization of a 3D Printer to Fabricate Boluses used for Electron Therapy of Skin Lesions of the Eye Canthi. *J Appl Clin Med Phys*, 18:76–81.
24. Park SY, Choi CH, Park JM, *et al.*, 2016, A Patient-Specific Polylactic Acid Bolus Made by a 3D Printer for Breast Cancer Radiation Therapy. *PLoS One*, 11:e0168063. https://doi.org/10.1371/journal.pone.0168063
25. Banerjee SL, Samanta S, Sarkar S, *et al.*, 2020, A Self-Healable and Antifouling Hydrogel Based on PDMS Centered ABA Tri-Block Copolymer Polymersomes: A Potential Material for Therapeutic Contact Lenses. *J Mater Chem B*, 8:226–43. https://doi.org/10.1039/c9tb00949c
26. Chiu T, Tan J, Brenner M, *et al.*, 2018, Three-Dimensional Printer-Aided Casting of Soft, Custom Silicone Boluses (SCSBs) for Head and Neck Radiation Therapy. *Pract Radiat*

Oncol, 8:e167–4.
https://doi.org/10.1016/j.prro.2017.11.001

27. Chiozzini GC, Mendes GP, Vanni FP, *et al.*, 2020, Bacterial nanocellulose membrane as bolus in radiotherapy: "Proof of concept". *Cellulose*, 28:607–13.
https://doi.org/10.1007/s10570-020-03579-8
28. Cooke SL, Whittington AR, 2016, Influence of Therapeutic Radiation on Polycaprolactone and Polyurethane Biomaterials. *Mater Sci Eng C Mater Biol Appl*, 60:78–83.
29. Bil M, Kijeńska-Gawrońska E, Głodkowska-Mrówka E, *et al.*, 2020, Design and *In Vitro* Evaluation of Electrospun Shape Memory Polyurethanes for Self-Fitting Tissue Engineering Grafts and Drug Delivery Systems. *Mater Sci Eng C Mater Biol Appl*, 110:110675.
https://doi.org/10.1016/j.msec.2020.110675
30. Eslahi N, Abdorahim M, Simchi A, 2016, Smart Polymeric Hydrogels for Cartilage Tissue Engineering: A Review on the Chemistry and Biological Functions. *Biomacromolecules*, 17:3441–63.
https://doi.org/10.1021/acs.biomac.6b01235
31. Ng WL, Chua CK, Shen YF, 2019, Print Me An Organ! Why We Are Not There Yet. *Prog Polym Sci*, 97:101145.
https://doi.org/10.1016/j.progpolymsci.2019.101145
32. Askari M, Naniz MA, Kouhi M, *et al.*, 2021, Recent Progress in Extrusion 3D Bioprinting of Hydrogel Biomaterials for Tissue Regeneration: A Comprehensive Review with Focus on Advanced Fabrication Techniques. *Biomater Sci*, 9:535–73.
https://doi.org/10.1039/d0bm00973c
33. Tao G, Wang Y, Cai R, *et al.*, 2019, Design and Performance of Sericin/Poly(Vinyl Alcohol) Hydrogel as a Drug Delivery Carrier for Potential Wound Dressing Application. *Mater Sci Eng C Mater Biol Appl*, 101:341–51.
https://doi.org/10.1016/j.msec.2019.03.111
34. Wang T, Qu G, Wang C, *et al.*, 2019, Importance of Polyacrylamide Hydrogel Diverse Chains and Cross-Linking Density for Cell Proliferation, Aging, and Death. *Langmuir*, 35:13999–4006.
https://doi.org/10.1021/acs.langmuir.9b02799.s001
35. An H, Zhu L, Shen J, *et al.*, 2020, Self-Healing PEG-Poly (Aspartic Acid) Hydrogel with Rapid Shape Recovery and Drug Release. *Colloids Surf B Biointerfaces*, 185:110601.
https://doi.org/10.1016/j.colsurfb.2019.110601
36. Hussain Z, Thu HE, Shuid AN, *et al.*, 2018, Recent Advances in Polymer-based Wound Dressings for the Treatment of Diabetic Foot Ulcer: An Overview of State-of-the-Art. *Curr Drug Targets*, 19:527–50.
https://doi.org/10.2174/1389450118666170704132523
37. Bonani W, Cagol N, Maniglio D, 2020, Alginate Hydrogels: A Tool for 3D Cell Encapsulation, Tissue Engineering, and Biofabrication. *Adv Exp Med Biol*, 1250:49–61.
https://doi.org/10.1007/978-981-15-3262-7_4
38. Xu J, Zheng S, Hu X, 2020, Advances in the Research of Bioinks Based on Natural Collagen, Polysaccharide and Their Derivatives for Skin 3D Bioprinting. *Polymers* (*Basel*), 12:1237.
https://doi.org/10.3390/polym12061237
39. Haq MA, Su Y, Wang D, 2017, Mechanical Properties of PNIPAM Based Hydrogels: A Review. *Mater Sci Eng C Mater Biol Appl*, 70:842–55.
40. Zhang B, Li S, Hingorani H, *et al.*, 2018, Highly Stretchable Hydrogels for UV Curing Based High-Resolution Multimaterial 3D Printing. *J Mater Chem B*, 6:3246–53.
https://doi.org/10.1039/c8tb00673c
41. Sun JY, Zhao X, Illeperuma WR, *et al.*, 2012, Highly Stretchable and Tough Hydrogels. *Nature*, 489:133–6.
42. Truby RL, Lewis JA, 2016, Printing Soft Matter in Three Dimensions. *Nature*, 540:371–8.
https://doi.org/10.1038/nature21003
43. Zhu W, Ma X, Gou M, *et al.*, 2016, 3D Printing of Functional Biomaterials for Tissue Engineering. *Curr Opin Biotechnol*, 40:103–12.
44. Murphy SV, Atala A, 2014, 3D Bioprinting of Tissues and Organs. *Nat Biotechnol*, 32:773–85.
https://doi.org/10.1038/nbt.2958
45. Zhou LY, Fu J, He Y, 2020, A Review of 3D Printing Technologies for Soft Polymer Materials. *Adv Funct Mater*, 30:2000187.
https://doi.org/10.1002/adfm.202000187
46. Kinstlinger IS, Bastian A, Paulsen SJ, *et al.*, 2016, Open-Source Selective Laser Sintering (OpenSLS) of Nylon and Biocompatible Polycaprolactone. *PLoS One*, 11:e0147399.
https://doi.org/10.1371/journal.pone.0147399
47. Soe SP, Eyers DR, Setchi R, 2013, Assessment of Non-Uniform Shrinkage in the Laser Sintering of Polymer Materials. *Int J Adv Manuf Technol*, 68:111–25.
https://doi.org/10.1007/s00170-012-4712-0
48. Liu K, Sun H, Tan Y, *et al.*, 2016, Additive Manufacturing of Traditional Ceramic Powder Via Selective Laser Sintering with Cold Isostatic Pressing. *Int J Adv Manuf Technol*, 90:945–52.
https://doi.org/10.1007/s00170-016-9441-3
49. Novitsky TF, Mathias LJ, Osborn S, *et al.*, 2012, Synthesis and Thermal Behavior of Polyamide 12, T Random and

Block Copolymers. *Macromol Symp*, 313–314:90–9. https://doi.org/10.1002/masy.201250310

50. Gu D, Wang H, Zhang G, 2014, Selective Laser Melting Additive Manufacturing of Ti-Based Nanocomposites: The Role of Nanopowder. *Metall Mater Trans A*, 45:464–76. https://doi.org/10.1007/s11661-013-1968-4
51. Ramanath HS, Chua CK, Leong KF, *et al.*, 2008, Melt Flow Behaviour of Poly-Epsilon-Caprolactone in Fused Deposition Modelling. *J Mater Sci Mater Med*, 19:2541–50. https://doi.org/10.1007/s10856-007-3203-6
52. Heras ES, Haro FB, 2018, Filament Advance Detection Sensor for Fused Deposition Modelling 3D Printers. *Sensors* (*Basel*), 18:1495. https://doi.org/10.3390/s18051495
53. Hrynevich A, Elçi B, Haigh JN, *et al.*, 2018, Dimension-Based Design of Melt Electrowritten Scaffolds. *Small*, 14:e1800232. https://doi.org/10.1002/smll.201800232
54. Cheng Y, Chan KH, Wang XQ, *et al.*, 2019, Direct-Ink-Write 3D Printing of Hydrogels into Biomimetic Soft Robots. *ACS Nano*, 13:13176–84. https://doi.org/10.1021/acsnano.9b06144
55. Paxton N, Smolan W, Böck T, *et al.*, 2017, Proposal to Assess Printability of Bioinks for Extrusion-Based Bioprinting and Evaluation of Rheological Properties Governing Bioprintability. *Biofabrication*, 9:044107. https://doi.org/10.1088/1758-5090/aa8dd8
56. Zhou LY, 2019, Multimaterial 3D Printing of Highly Stretchable Silicone Elastomers. *ACS Appl Mater Interfaces*, 11:23573–83. https://doi.org/10.1021/acsami.9b04873
57. Kim Y, Yuk H, Zhao R, *et al.*, 2018, Printing Ferromagnetic Domains for Untethered Fast-Transforming Soft Materials. *Nature*, 558:274–9. https://doi.org/10.1038/s41586-018-0185-0
58. Kuang M, Wang L, Song Y, 2014, Controllable Printing Droplets for High-Resolution Patterns. *Adv Mater*, 26:6950–8. https://doi.org/10.1002/adma.201305416
59. Scoutaris N, Ross S, Douroumis D, 2016, Current Trends on Medical and Pharmaceutical Applications of Inkjet Printing Technology. *Pharm Res*, 33:1799–816. https://doi.org/10.1007/s11095-016-1931-3
60. Negro A, Cherbuin Tm Lutolf MP, 2018, 3D Inkjet Printing of Complex, Cell-Laden Hydrogel Structures. *Sci Rep*, 8:17099. https://doi.org/10.1038/s41598-018-35504-2
61. Ehtezazi T, Dempster NM, Martin GD, *et al.*, 2014, Development of High-Throughput Glass Inkjet Devices for Pharmaceutical Applications. *J Pharm Sci*, 103:3733–42. https://doi.org/10.1002/jps.24192
62. Poozesh S, Saito K, Akafuah NK, *et al.*, 2016, Comprehensive Examination of a New Mechanism to Produce Small Droplets in Drop-on-Demand Inkjet Technology. *Appl Phys A*, 122:110. https://doi.org/10.1007/s00339-016-9630-9
63. Li W, Mille LS, Robledo JA, *et al.*, 2020, Recent Advances in Formulating and Processing Biomaterial Inks for Vat Polymerization-Based 3D Printing. *Adv Healthc Mater*, 9:2000156. https://doi.org/10.1002/adhm.202000156
64. Ng WL, Lee JM, Zhou M, *et al.*, 2020, Vat Polymerization-Based Bioprinting-Process, Materials, Applications and Regulatory Challenges. *Biofabrication*, 12:022001. https://doi.org/10.1088/1758-5090/ab6034
65. Melchels FP, Feijen J, Grijpma DW, 2010, A Review on Stereolithography and its Applications in Biomedical Engineering. *Biomaterials*, 31:6121–30. https://doi.org/10.1016/j.biomaterials.2010.04.050
66. Kumar H, Kim K, 2020, Stereolithography 3D Bioprinting. *Methods Mol Biol*, 2140:93–108.
67. Laza SC, Polo M, Neves AA, *et al.*, 2012, Two-Photon Continuous Flow Lithography. *Adv Mater*, 24:1304–8. https://doi.org/10.1002/adma.201103357
68. Annabi N, Tamayol A, Uquillas JA, *et al.*, 2014, 25th Anniversary Article: Rational Design and Applications of Hydrogels in Regenerative Medicine. *Adv Mater*, 26:85–123. https://doi.org/10.1002/adma.201303233
69. Ho CM, Mishra A, Hu K, *et al.*, 2017, Femtosecond-Laser-Based 3D Printing for Tissue Engineering and Cell Biology Applications. *ACS Biomater Sci Eng*, 3:2198–214. https://doi.org/10.1021/acsbiomaterials.7b00438
70. Gauvin R, Chen YC, Lee JW, *et al.*, 2012, Microfabrication of Complex Porous Tissue Engineering Scaffolds using 3D Projection Stereolithography. *Biomaterials*, 33:3824–34. https://doi.org/10.1016/j.biomaterials.2012.01.048
71. Kelly BE, Bhattacharya I, 2019, Volumetric Additive Manufacturing Via Tomographic Reconstruction. *Science*, 363:1075–9.
72. Raman R, Bhaduri B, Mir M, *et al.*, 2016, High-Resolution Projection Microstereolithography for Patterning of Neovasculature. *Adv Healthc Mater*, 5:610–9. https://doi.org/10.1002/adhm.201500721
73. Xu X, Awad A, Robles-Martinez P, *et al.*, 2021, Vat Photopolymerization 3D Printing for Advanced Drug

Delivery and Medical Device Applications. *J Control Release*, 329:743–57.
https://doi.org/10.1016/j.jconrel.2020.10.008

74. Mostafa KG, Arshad M, Ullah A, *et al.*, 2020, Concurrent Modelling and Experimental Investigation of Material Properties and Geometries Produced by Projection Microstereolithography. *Polymers* (*Basel*), 12:506.
https://doi.org/10.3390/polym12030506

75. Ligon SC, Liska R, 2017, Polymers for 3D Printing and Customized Additive Manufacturing. *Chem Rev*, 117:10212–90.
https://doi.org/10.1021/acs.chemrev.7b00074

76. Park JW, Oh SA, Yea JW, *et al.*, 2017, Fabrication of Malleable Three-Dimensional-Printed Customized Bolus Using Three-Dimensional Scanner. *PLoS One*, 12:e0177562.
https://doi.org/10.1371/journal.pone.0177562

77. Kang D, Wang B, Peng Y, *et al.*, 2020, Low-Cost iPhone-Assisted Processing to Obtain Radiotherapy Bolus Using Optical Surface Reconstruction and 3D-Printing. *Sci Rep*, 10:8016.
https://doi.org/10.1038/s41598-020-64967-5

78. Robertson FM, Couper MB, Kinniburgh M, *et al.*, 2021, Ninjaflex vs Superflab: A Comparison of Dosimetric Properties, Conformity to the Skin Surface, Planning Target Volume Coverage and Positional Reproducibility for External Beam Radiotherapy. *J Appl Clin Med Phys*, 22:26–33.
https://doi.org/10.1002/acm2.13147

79. An HJ, Kim MS, Kim J, *et al.*, 2019, Geometric Evaluation of Patient-Specific 3D Bolus from 3D Printed Mold and Casting Method for Radiation Therapy. *Prog Med Phys*, 30:32.
https://doi.org/10.14316/pmp.2019.30.1.32

80. Burleson S, Baker J, Hsia AT, *et al.*, 2015, Use of 3D Printers to Create a Patient-Specific 3D Bolus for External Beam Therapy. *J Appl Clin Med Phys*, 16:5247.
https://doi.org/10.1118/1.4889472

81. Park JM, Son J, An HJ, *et al.*, 2019, Bio-Compatible Patient-Specific Elastic Bolus for Clinical Implementation. *Phys Med Biol*, 64:105006.
https://doi.org/10.1088/1361-6560/ab1c93

82. Park JW, Yea JW, 2016, Three-Dimensional Customized Bolus for Intensity-Modulated Radiotherapy in a Patient with Kimura's Disease Involving the Auricle. *Cancer Radiother*, 20:205–9.
https://doi.org/10.1016/j.canrad.2015.11.003

83. Obeid JP, Gutkin PM, Lewis J, *et al.*, 2019, Volumetric Modulated Arc Therapy and 3-Dimensional Printed Bolus in the Treatment of Refractory Primary Cutaneous Gamma Delta Lymphoma of the Bilateral Legs. *Pract Radiat Oncol*, 9:220–5.
https://doi.org/10.1016/j.prro.2019.02.016

84. Munoz L, Rijken J, Hunter M, *et al.*, 2020, Investigation of Elastomeric Materials for Bolus using Stereolithography Printing Technology in Radiotherapy. *Biomed Phys Eng Express*, 6:045014.
https://doi.org/10.1088/2057-1976/ab9425

85. Tack P, Victor J, Gemmel P, *et al.*, 2016, 3D-Printing Techniques in a Medical Setting: A Systematic Literature Review. *Biomed Eng Online*, 15:115.
https://doi.org/10.1186/s12938-016-0236-4

86. Thrasher CJ, Schwartz JJ, Boydston AJ, 2017, Modular Elastomer Photoresins for Digital Light Processing Additive Manufacturing. *ACS Appl Mater Interfaces*, 9:39708–16.
https://doi.org/10.1021/acsami.7b13909

87. Field J, Haycock JW, Boissonade FM, *et al.*, 2021, A Tuneable, Photocurable, Poly(Caprolactone)-Based Resin for Tissue Engineering-Synthesis, Characterisation and Use in Stereolithography. *Molecules*, 26:1199.
https://doi.org/10.3390/molecules26051199

REVIEW ARTICLE

Advances in Filament Structure of 3D Bioprinted Biodegradable Bone Repair Scaffolds

Chengxiong Lin[1], Yaocheng Wang[1,2], Zhengyu Huang[1,2], Tingting Wu[1], Weikang Xu[1], Wenming Wu[1], Zhibiao Xu[2]*

[1]National Engineering Research Center for Healthcare Devices, Guangdong Provincial Key Laboratory of Medical Electronic Instruments and Polymer Products, Guangdong Medical Device Research Institute, Guangzhou 510500, China
[2]School of Railway Tracks and Transportation, Wuyi University, Jiangmen 529020, China

Abstract: Conventional bone repair scaffolds can no longer meet the high standards and requirements of clinical applications in terms of preparation process and service performance. Studies have shown that the diversity of filament structures of implantable scaffolds is closely related to their overall properties (mechanical properties, degradation properties, and biological properties). To better elucidate the characteristics and advantages of different filament structures, this paper retrieves and summarizes the state of the art in the filament structure of the three-dimensional (3D) bioprinted biodegradable bone repair scaffolds, mainly including single-layer structure, double-layer structure, hollow structure, core-shell structure and bionic structures. The eximious performance of the novel scaffolds was discussed from different aspects (material composition, ink configuration, printing parameters, etc.). Besides, the additional functions of the current bone repair scaffold, such as chondrogenesis, angiogenesis, anti-bacteria, and anti-tumor, were also concluded. Finally, the paper prospects the future material selection, structural design, functional development, and performance optimization of bone repair scaffolds.

Keywords: Bone repair scaffolds; Filament structure; 3D printing; Mechanical properties

*Correspondence to: Zhibiao Xu, School of Railway Tracks and Transportation, Wuyi University, Jiangmen 529020, China; 544260221@qq.com

Received: August 9, 2021; **Accepted:** September 3, 2021; **Published Online:** October 13, 2021

Citation: Lin C, Wang Y, Huang Z, *et al*., 2021, Advances in Filament Structure of 3D Bioprinted Biodegradable Bone Repair Scaffolds. *Int J Bioprint*, 7(4):426. http://doi.org/10.18063/ijb.v7i4.426

1. Introduction

At present, the number of patients with bone defects caused by tumors, infections, aging populations, or accidental injuries shows an increasing trend. According to statistics, there are about 3 million new cases with bone injury worldwide every year, pointing to the huge development space in the market of bone repair materials[1]. Although bone tissue has the ability to recover and regenerate itself, bone defects such as fractures and microfractures that exceed a critical threshold (usually >2 cm, depending on the anatomical site) cannot renew itself[2-4]. Autologous bone transplantation is the "gold standard" for the treatment of bone defects in current clinical practice, but this treatment involves procedure that removes bone from patient which has the problem of limited sources of bone tissue and the second surgery that brings greater pain to the patient[5]. Compared with autologous bone grafts, allografts are prone to inactivation after ultraviolet (UV) irradiation or freeze-drying treatment, resulting in low osteoinductivity, the problem of treatment failure due to host immune response[6-8].

Bone repair scaffolds with wide source, easy fabrication and good osteogenic activity have provided new insight for bone defect treatment[9,10]. A good bone repair scaffold should have the following basic properties: (i) being biocompatible to avoid immune rejection after implantation in the patient[11]; (ii) having mechanical properties so that the scaffold can be a carrier in the defect site[12]; (iii) having interconnected pore structure and proper porosity[13] because bone formation requires not only a large amount of space to adhere to growth factors, but also connected pores to supply the necessary nutrients and oxygen[14] and provide channels for cell migration and blood vessel growth[15-17]; and (iv) being biodegradable so that the implanted scaffold will degrade

over time to make room for new bone tissue[18]. Traditional scaffold fabrication techniques, such as solvent casting, gas forming, membrane lamination, salt immersion, and fiber bonding, have limitations[19,20], including complex preparation processes, high costs, uncontrollable internal pore structure for scaffolds, incomplete matching of shape to host bone defects, and inability to load cells for bioprinting, which are difficult to meet the actual needs of patients. According to ASTM standard F2792[21], ASTM classifies three-dimensional (3D) printing technologies into the binding jetting, directed energy deposition, material extrusion, material jetting, powder bed fusion and sheet 3D printing techniques, which are increasingly used for product design[22]. Its layer-by-layer manufacturing method can precisely regulate the complex geometric structure to make the processed product highly optimized, reduce the weight of the product at the same time, reduce material loss and reduce the cost of expenditure[23]. 3D printing is also used for small production runs, such as model customization and print-on-demand, and can streamline the supply process through sub-station manufacturing[24]. In the field of bone repair, 3D printing technology, which is simple to operate and has fast molding speed as well as good control, can not only construct the complex shape matching the bone tissue defect, but also accurately regulate the internal pore structure, and it has become the first choice for the preparation of porous bone repair scaffolds[25,26].

The development of bone tissue engineering has resulted in different types of bone repair scaffold structures, materials, and properties to better serve human needs through the unremitting efforts of a large number of researchers. The purpose of this review is to summarize and review the current research progress of biodegradable extrudable bone repair scaffolds in terms of scaffold materials, filament structure, and scaffold function. The filament structure of the stent, that is, the line composition inside the stent, is particularly important to the overall performance of the stent and its scope of application. Therefore, this paper reviews the proposal, design, performance, and evaluation of the scaffold in five major directions, including classical structure, bilayer structure, core-shell structure, hollow structure, and bionic structure of the biodegradable bone repair scaffold, and in the end, the future development of the filament structure of the scaffold is prospected.

2. Materials

Bone tissue is a kind of connective tissue composed of a bone matrix and a variety of cells. The bone matrix contains organic and inorganic substances, the inorganic substances are mainly made of calcium and phosphorus in the form of hydroxyapatite (HA) crystals, compounds (sodium, potassium, magnesium, and fluoride) as well as salts (chloride and carbon) and some trace elements such as silicon, zinc, and copper[27]. Organic matter mainly refers to collagen (COL) fibers and calcium-binding protein gels such as osteocalcin and osteophosphoprotein[28].

In view of the composition of bone tissue, materials for 3D printed bone repair scaffolds mainly include bioceramics, polymers, cells, growth factors, and composites, with polymer materials being the most widely used (such as gelatin, COL, sodium hyaluronate, silk protein, polycaprolactone (PCL), polylactic acid (PLA), and polyethylene glycol)[29]. The bioceramic materials used in ceramic scaffolds for bone repair mainly include calcium-phosphorus-based bioactive materials and calcium-silica-based bioactive materials. Calcium-phosphorus-based bioactive materials include HA, β-type calcium phosphate (β-TCP), and biphasic calcium phosphate (BCP), while calcium-silica-based bioactive materials include bioactive glass, calcium silicate, tricalcium silicate, magnesium yellow feldspar, and white calcium silicate. This section consolidates the commonly used scaffold materials in the field of bone repair with examples of their material properties and research progress (**Table 1**).

2.1. Bioceramics

Bioceramic materials are widely used in bone repair engineering because of their similarity to the inorganic composition of bone tissue. The common bioceramic materials mainly include HA, β-TCP, silicate, and bioceramics. They have excellent osteoconductive properties, good bioactivity, biodegradability and strong compressive properties and have great potential for development in the treatment of bone defects[30].

Calcium phosphate materials have significant osteoinductive ability due to the release of calcium and phosphate ions, which contributes to a bone-like apatite layer that can adsorb osteogenic proteins on the material surface, with HA and tricalcium phosphate being the most widely used. HA is chemically similar to the minerals of natural bone and is considered a substitute with high bone repair potential[31]. Damien *et al*. and Oonishi *et al*.[32,33] found that HA scaffolds have better mechanical properties as well as strong osteoinductive and osseointegration ability and are less prone to deformation through *in vivo* experiments[34]. In contrast, HA prepared by hydrothermal liquid exchange method by Roy *et al*.[35], showed that HA has the defects of poor sintering properties and poor biodegradability. Tricalcium phosphate, with its ability to bind well to hard tissues, has become another class of calcium-phosphorus bioactive materials that have been widely studied and applied in the field of bone repair, generally in two forms: Low-temperature stable β-phase (β-TCP) and high-temperature stable α-phase (α-TCP)[34]. Li *et al*.[36] used the porous structure ceramic scaffold

Table 1. Summary of the characteristic of different materials in 3D bioprinted biodegradable bone repair scaffolds

Materials		Features	References
Bioceramics	Calcium phosphate	Excellent osteosimilarity, osteoinductive, biocompatibility, mechanical properties Hard to degrade, poor toughness	[27-33]
	Bioglass	Eximious osteogenic properties, biocompatibility Insufficient mechanical strength	[34-37]
	Silicate	High biocompatibility, osteoinductivity, pro-hard tissue regeneration ability Poor fracture toughness, too fast degradation	[38,39]
Polymers	Natural polymers	Good biocompatibility, degradability, printability, high modulus of elasticity Poor mechanical strength, fast degradation rate, single material function	[46-52]
	synthetic polymers	Wide range of material sources, gallows biocompatibility, high mechanical strength Some materials are difficult to degrade and have no obvious osteogenic properties	[53-54]
Composites		Functional diversity, combination of excellent performance of various materials, wide range of material selection	[62-72]

prepared by sintering β-TCP ceramic slurry to show good biocompatibility in biological experiments and provide richer calcium and phosphorus elements and growth space for new bone formation after implantation *in vivo*. However, β-TCP suffers from low mechanical strength and very rapid degradation, which limit its development in the field of bone repair[37].

Bioglass has good bioactivity, biocompatibility, and promotes bone and soft-tissue regeneration, making it an excellent material for bone defect repair. One of the most famous bioactive glass, 45S5, can rapidly bond to bone and promote bone growth away from the bone-implant interface[38]. Fujishiro *et al*.[39] observed 24 weeks after surgery in a rat femoral defect experiment and found that this bioactive glass accelerated the rate of bone regeneration compared to HA. On the other hand, bioglass has disadvantages such as high brittleness and poor mechanical strength, which limit its application for bone defects in load-bearing areas[40]. Li *et al*.[41] obtained porous BG scaffolds with controllable mechanical strength by modulating the molar ratio of SiO_2/CaO (90/5 – 60/35), and the characterization results showed that the high content of SiO_2 produced more uniform crystal particles and dense sintering to improve the mechanical strength of the scaffolds.

Compared to bioceramics such as calcium phosphate, calcium silicate-based biomaterials exhibit better biodegradability, and osteoinductive properties. Huang *et al*.[42] found that Si^{2+} release and calcium silicate-based materials accelerated the formation of bone-like apatite layers by printing hinokitiol-modified wollastonite slurry and that hinokitiol-modified scaffolds were also effective in suppressing cellular inflammatory responses. By adding different ratios of graphene to calcium silicate powder, Shie *et al*.[43] showed that the Young's modulus was increased by 47.1% with the addition of 1 wt% of graphene to calcium silicate, and the proliferation and expression of alkaline phosphatase (ALP), osteogenic, and osteogenic-related proteins in hMSCs were superior to the expression results of pure calcium silicate.

2.2. Polymers

Polymers are long-chain organic materials linked by covalent bonds[44], mainly including natural polymers and synthetic polymers such as COL, which are more hydrophilic and can form hydrogels with high water content[45-47]. The use of polymers in 3D printing not only achieves more precise customization of the scaffold geometry, but also minimizes processing costs compared to other traditional molding methods. At the same time, due to the lack of mechanical strength and single function of natural polymers, research in the field of bone repair has focused on material selection and preparation methods for advanced polymer composites[48,49].

Natural polymers are more widely used in 3D printing by virtue of their better bioactivity[50], mainly including COL, silk proteins, cellulose, and alginates[51]. COL is the most abundant protein in the human body, and different types of COL bodies are distributed in different tissues according to their structure and hierarchical organization. Its unique triple helix structure is the basis for the good stability and mechanical properties of COL

scaffolds[52]. In the past few years, researchers have developed COL-containing hybrid printing and sacrificial material printing methods to improve the rheological properties of bioink by improving the printability of the slurry[53,54]. Shim *et al*.[55] prepared a scaffold for application in cartilage tissue regeneration using COL, supramolecular hyaluronic acid and PCL loading (hTMSCs), bone morphogenetic protein 2 (BMP 2) and transforming growth factor-beta (TGF-β), and the results showed that the hydrogel/PCL layered printing method successfully prepared multilayer cell-carrying scaffolds with high mechanical stability, circumventing the negative effects of chemical cross-linking agents and physical cross-linking while showing higher bone repair performance than pure hydrogel scaffolds in animal experiments. Alginate, a natural polymer derived from algae, has properties similar to extracellular matrix with good biocompatibility and printability, and has many applications in the field of 3D printed bioinks. Almarza *et al*.[56] used scaffolds prepared by adding polyglycolic acid to natural alginate for culturing temporomandibular joint cells, and found that a large amount of COL was produced by the cells inside the scaffold after 4 weeks of incubation, confirming the good biocompatibility of alginate.

To date, polymer materials and their composites have been commonly used in clinical treatment of bone defective diseases. These materials are widely available and have good biocompatibility and excellent mechanical properties. Natural polymer materials are limited in clinical use because of different sources and forms. Their chemical structures are more complex, and their physicochemical properties are highly variable. Compared to natural polymer materials, many synthetic polymer materials have received attention due to their superior mechanical strength and processing flexibility. At present, the common synthetic polymer materials used in bone tissue engineering are poly (lactic acid-hydroxyacetic acid) (PLGA), PCL, PLA, silicone, polyurethane (PU), and so on. These materials have superior biocompatibility, biodegradability, and usually the degradation products which belong a class of green eco-polymers are non-toxic.

PCL has good biodegradability, biocompatibility, and non-toxicity and is typically used as a medical biodegradable material. It has high crystallinity and low melting point, and its excellent rheological and viscoelastic properties endow it with good melt printability. In addition, scaffolds prepared from PCL have high mechanical strength and are popular in bone tissue engineering systems. Li et al.[57] achieved simultaneous repair of bone and cartilage tissue defects by coating a self-assembled peptide hydrogel on a PCL scaffold and blank controls, and confirmed that PCL scaffolds lacked the ability to promote cell adhesion ability to promote cell adhesion. Mahdi et al.[58] modified the hydrophobicity and surface properties of PCL scaffolds by coating them with peptide hydrogel or polydopamine to improve cell adhesion. Another candidate bone tissue engineering material PLA is an aliphatic polyester, mainly derived from plant starch, with good biocompatibility and degradability, which survives in the human body as soluble lactic acid after hydrolysis. Its main advantages are low melting point, low-viscosity, and excellent mechanical properties, but there are problems such as high brittleness and high glossiness. Yi et al.[59] modified HA using poly(L-lactide)/β-cyclodextrin/citrate (PLA/β-CD/citrate), and the modified HA had significantly improved bioactivity and mechanical properties, with better cell adhesion and higher viability for rat bone marrow mesenchymal stem cells (MSCs). Silicone elastomer can be formulated to have low elastic modulus, high extensibility and toughness, excellent thermal and oxidative stability, and chemical inertness[60,61]. Luis et al.[62] used a two-part Ecoflex silicone resins for 3D printing a bionic scaffold for meniscus structure using a thermosetting extrusion method. The results of the quantitative cell proliferation test showed low cytotoxicity and good biocompatibility of silicone.

2.3. Composites

The structure of scaffolds prepared from any single material can be affected by the defects that exist in the material itself. For example, ceramic scaffolds may undergo very fast or difficult *in vivo* degradation and have poor sintering quality due to material differences, and polymer scaffolds have insufficient mechanical strength and may collapse during printing, resulting in low porosity[63,64]. The emergence of composite materials has provided a new strategy to solve this problem, and researchers have developed a series of composites with excellent properties through extensive experiments[65]. The results showed that the performance of composites is superior and more comprehensive than that of individual components, and they are rapidly attracting widespread attention in the field of bone repair[66,67]. Among them, bioceramic materials and polymeric materials are favored for their material properties; the former have good biocompatibility, excellent bone regeneration properties, and high mechanical strength, whereas the latter have high printability, notable toughness, and the ability to encapsulate cells for bioprinting[29].

Composites are constructed from two or more different materials (e.g. bioceramics and bioceramics, polymers and bioceramics, and polymers and polymers.)[68-70]. BCP, which is a new composite bioceramic material, was synthesized by HA and β-TCP. The degradation rate of β-TCP is too fast, resulting in the

inability to provide structural support for new bone after degradation, so it is especially important to control the degradation rate and mechanical strength by synthesizing two materials[71]. By comparing the compressive strength of BCP scaffolds with different ratios, Zyman *et al*.[72] showed that the compressive strength of the material increased with the increase of β-TCP content. Sánchez-Salcedo *et al*.[73,74] investigated the degradation rate of BCP slurry in an *in vitro* test by testing different ratios of BCP slurry and showed that the dissolution rate of BCP material was between HA and β-TCP, and the dissolution rate increased with increasing β-TCP content.

Polymer-ceramic composites combine the excellent properties of two different chemical compositions, including the high wear resistance of ceramic materials and the high toughness of polymers[75-78]. The incorporation of ceramic particles and bioglass particles into the initial material effectively enhances the mechanical strength of the composite, and its bioactivity gives the material the ability to regenerate bone[79]. This can also be applied in the fabrication of biphasic porous scaffolds to repair the regenerated damaged tissues. Inzana *et al*.[80] used Darvan821-A as a size controlling agent and dispersant for the 1st time during HA synthesis to prevent the formation of particle aggregates throughout the COL matrix, resulting in COL-nHA scaffolds with excellent rheological properties and great potential for precise tailoring of scaffold shape. Li *et al*.[81] incorporated COL into calcium phosphate slurry at low temperature to maximize the cytocompatibility and mechanical strength of the scaffold. Compared to the difficult degradation problem of conventional HA powder, nano-scale HA (nHA) possesses a faster degradation rate *in vivo* without affecting osteogenesis[82]. However, nHA single-phase materials are not able to mimic the composition, structure and properties of natural bone, and researchers need to compensate this deficiency by introducing another material. Wang *et al*.[83] prepared the scaffold by adding polyamide (PA) to HA which has excellent mechanical properties, and the addition of PA did not produce adverse effects in *in vitro* experiments. *In vivo* experiments showed that the nHA/PA composite scaffold had good biocompatibility and osteoconductivity with host bone. High water content, low-viscosity hydrogels provide a superior environment for cell growth, but the mechanical strength properties they provide are often insufficient to support *in vivo* analysis. Therefore, attempts have been made to create composite bioinks that can integrate the mechanical strength of viscous hydrogels with the biocompatibility provided by low-viscosity hydrogels.

3. Scaffold filament structure

With the development of technology and the demand of clinical applications, the overall performance requirements of 3D printed bone repair scaffolds are also increasing. In addition to the need for continuous improvement, mapping and configuration of printing materials, the spatial filament structure of 3D printed scaffolds which can directly affect the porosity and mechanical properties of the scaffolds has drawn much attention, indicating that the structure could be used in biomaterials. Therefore, it is important to design and develop microfilament structured scaffolds that are appropriately sized and meet clinical needs[84]. This section explores the latest state of research on the filament structure of 3D printed bone repair scaffolds and summarizes and lists the physical structure as well as the application characteristics of bone repair scaffolds (**Table 2**).

3.1. Classic structure

The classical scaffold structure defined in this paper is the most widely used 3D printed bone repair scaffold structure, in which the scaffold fibers are single cylindrical and cross-arrayed at a certain angle between layers, and assembled into a 3D scaffold after the printing parameters are regulated. The classical scaffold structure is characterized by easily adjustable printing parameters, simple scaffold preparation, high printability, high potential for secondary processing, and good development prospects. However, the classical structure of the scaffold type is single and cannot simulate the tissue structure more accurately. The printing slurry is mostly prepared by direct mixing, and thus, the performance of the material cannot be maximized, and it is still necessary to improve the scaffold performance by improving the printing technology.

Classical monolayer scaffold structures are mostly based on bioceramic materials with the auxiliary addition of certain binders or dispersants to the slurry. Shao *et al*.[85] conducted a detailed study of the composition-structure-strength relationship of the ceramic scaffold process using a one-step/two-step method (**Figure 1A**), which showed that the overall mechanical strength of the scaffold could be better balanced and the degradability could be adjusted using a two-step sintering method. Treatment of cartilage defects remains a great challenge in clinical practice, and Deng *et al*.[86] successfully prepared bioactive (BRT) scaffolds with controlled surface micro/nanostructures (**Figure 1B**), which significantly improved the scaffold's compressive strength and promoted the simultaneous regeneration of cartilage and subchondral bone tissue, providing a sensible strategy for inducing cartilage regeneration. Wei *et al*.[87] successfully constructed hexagonal microarrays on the surface of 3D printed HA porous scaffolds by hydrothermal reaction and added Sr^{2+} to replace the crystal phase of HA in the surface microarrays (**Figure 1C**) to improve the surface morphology and chemical properties of the scaffolds, and

Table 2. Summary of the characteristic of different structures in 3D bioprinted biodegradable bone repair scaffolds

Structure	Features	References
Classic Structure	Easy parameter adjustment, simple preparation process, secondary processing potential	[82-86]
Double layer structure	Effectively improve the mechanical strength of the stent and enrich the function of the stent	[5],[88-91]
Hollow structure	Large pore structure for nutrient delivery and drug loading, providing space for blood vessel growth	[92-97]
Core-shell structure	Ensures material independence, adjustable scaffold degradation rate	[98-101]
Bionic structures and others	Free shape customization based on defects, easy to load cells	[103-107]

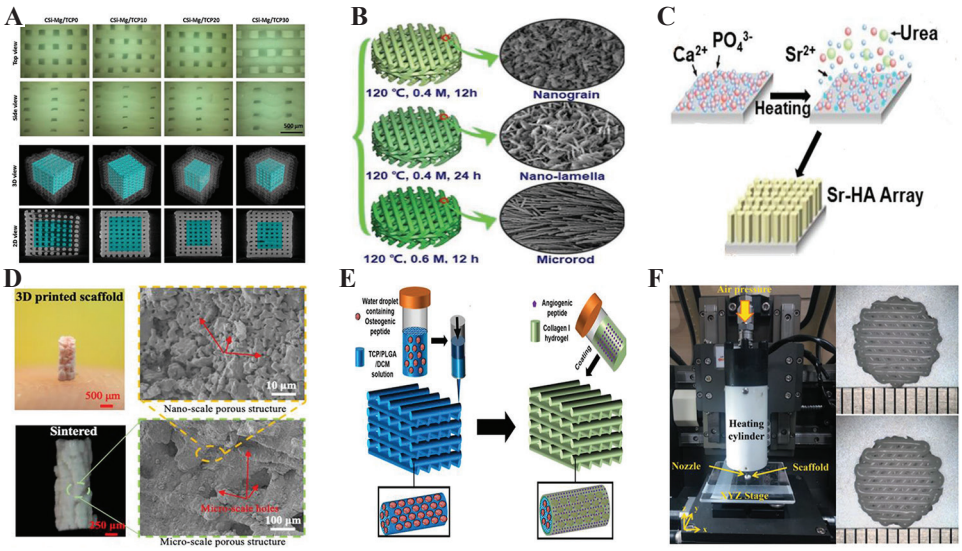

Figure 1. Schematic diagrams of classical scaffold structures. (A) Optical images and Micro-CT images of CSi-Mg/TCP scaffold after sintering[85]. (Reprinted from Journal of the European Ceramic Society, 36, Shao H, He Y, Fu J, *et al*., 3D printing magnesium-doped wollastonite/β-TCP bioceramics scaffolds with high strength and adjustable degradation, 1495-1503, Copyright (2016), with permission from Elsevier) (B) Schematic diagram of the micro-nanostructure surface fabrication process of BRT scaffold[86]. (Reprinted from Deng C, Lin R, Zhang M, *et al*., Advanced Functional Materials, Copyright© 1999-2021 John Wiley and Sons, Inc). (C) Schematic diagram of HA scaffold surface morphology[87]. (from ref[87] licensed under Creative Commons Attribution 4.0 license) (D) Local SEM images of bionic HA/TCP[88]. (Bio-Design and Manufacturing, 3D printing of hydroxyapatite/tricalcium phosphate scaffold with hierarchical porous structure for bone regeneration, 3, 2020, 15-29, Li X, Yuan Y, Liu L, *et al*., © 2021 Springer Nature Switzerland AG. With permission of Springer). (E) Schematic diagram of low-temperature 3D printed and AP and OP cross-linked TCP/PLGA scaffolds[89]. (from ref.[89] licensed under Creative Commons Attribution 4.0 license). (F) Finished PCL (left) and PCL/β-TCP (right) scaffolds[90]. (Reprinted from Pae H, Kang J, Cha J, *et al*., Journal of Biomedical Materials Research Part B: Applied Biomaterials, Copyright © 1999-2021 John Wiley and Sons, Inc).

cellular experiments showed that the early osteogenic gene expression level of the scaffolds modified by Sr^{2+} was much higher than that of the blank group, and significant osteogenic effects can be observed. Li *et al*.[88] developed a scaffold structure for stereographic projection lithography based on micro mask image of HA/TCP slurry (**Figure 1D**) and found that the HA/TCP scaffold with 30 wt% content exhibited superior mechanical properties and porosity with good biocompatibility in terms of biological characteristics and layered porosity. In their study, Wang *et al*.[89] prepared bone tissue engineering scaffolds (**Figure 1E**) with mechanical strength similar to that of human bone by cryogenic 3D printing of β-tricalcium phosphate and PLA/dichloromethane in osteogenic peptide (OP) emulsion slurry, and the angiogenic peptide (AP) containing COL type I hydrogel was coated on the scaffold surface to further provide angiogenic capability of the scaffold, and the sustained OP release significantly accelerated the rate of new bone formation. Pae *et al*.[90] investigated the biocompatibility and osteogenic effect of PCL scaffolds by adding β-TCP and COL membrane (M) to PCL material by high temperature printing (**Figure 1F**),

and *in vivo* experiments showed that new osteogenesis could be observed on PCL+β-TCP, PCL+ β-TCP+M scaffolds, and the largest area of new osteogenesis was observed on the PCL+β-TCP+M scaffolds.

3.2. Double layer structure

In contrast to the classic support structure in the previous section, the two-layer structure can be realized by adjusting the printing parameters based on single-layer printing. That is, the printhead prints two layers in the same direction and then switches the angle and repeats the print. Unlike the single-layer structure printing, multi-material can only be printed by the way of mechanical mixing of the paste before printing, and double-layer printing can be achieved through multi-jet printing or direct stacking method to avoid the degradation of material properties caused by the mixing of multiple pastes.

Lin *et al*.[5] prepared a COL-HA scaffold by low-temperature printing technique (**Figure 2A**) and analyzed to determine the optimal printing parameters, selecting a rod structure with a pore size at 600 μm to maintain the properties of most raw material, and the experimental results showed that the scaffold promoted the proliferation of bone marrow stromal cells *in vitro* and could be incubated for 7 days with significantly higher levels of osteogenic gene transcription than the blank control. Shao *et al*.[91] investigated the effect of one-step/two-step sintering method on the physicochemical properties of Mg ion-doped CS scaffolds on the basis of bilayer printing (**Figure 2B**), the bilayer scaffolds had increased degradation rate due to their large pore diameter but slightly weaker compressive properties than the monolayer scaffolds, and then the two-step sintering significantly improved the scaffold compressive strength (~25104 MPa) and flexural strength (~618 MPa). Jin *et al*.[92] doped calcium silicate powders with different mass fractions of Mg ions and used a bilayer printing (**Figure 2C**), and its compressive strength increased from 11.2 MPa to 39.4 MPa and 80 MPa with the increase of Mg ions content. To

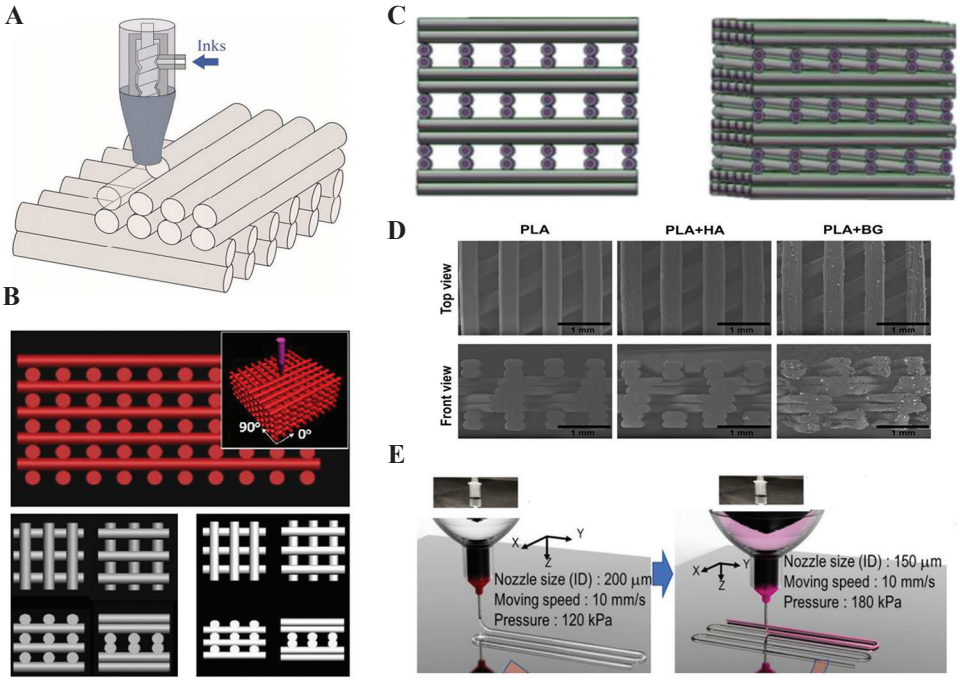

Figure 2. Schematic diagram of bilayer scaffold structure. (A) Schematic diagram of CHA scaffold printing[5]. (Reprinted with permission from Lin K F, He S, Song Y, *et al*. Low-Temperature Additive Manufacturing of Biomimic Three-Dimensional Hydroxyapatite/Collagen Scaffolds for Bone Regeneration. ACS Applied Materials and Interfaces. 2016; 8(11):6905-6916. Copyright© 2016 American Chemical Society). (B) Schematic diagram of scaffold printing by LBL method[91]. Reprinted with permission from Shao H, Ke X, Liu A, *et al*., Biofabrication,2017; 9(2):025003, ©Copyright 2021 IOP Publishing (C) Schematic diagram of cell-carrying α-TCP/collagen scaffold printing[92]. (Reprinted from Journal of the European Ceramic Society, 36, Shao H, He Y, Fu J, *et al*., 3D printing magnesium-doped wollastonite/β-TCP bioceramics scaffolds with high strength and adjustable degradation, 1495-1503, Copyright (2016) with permission from Elsevier). (D) Schematic diagram of CSi+PVA+Metal ion bilayer scaffold[93]. (Reprinted from Journal of the Mechanical Behavior of Biomedical Materials, 104, Alksne M, Kalvaityte M, Simoliunas E, *et al*. *In vitro* comparison of 3D printed polylactic acid/hydroxyapatite and polylactic acid/bioglass composite scaffolds: Insights into materials for bone regeneration, Copyright© 2021, with permission from Elsevier) (E) Schematic diagram of PLA/PLA+HA/PLA+BG bilayer scaffold[94]. (From ref.[94] licensed under Creative Commons Attribution 4.0 license).

achieve higher osteoinductivity of bioceramic materials, Alksne *et al*.[93] prepared two bilayer scaffolds, that is, PLA + HA and PLA + BG (**Figure 2D**); PLA + BG scaffolds were 15% more absorbent than other controls, provided better nutrient and protein uptake, and induced the earliest onset of ALP activity and the highest cellular activity, and a large amount of protein deposition was found on the surface of PLA + BG scaffold. Due to the high process ability of cell-carrying bioceramic scaffolds, Kim *et al*.[94] prepared α-TCP/COL scaffolds with ceramic volume fraction over 70% by modulating printing parameters using preosteoblasts (**Figure 2E**), which had a higher elastic modulus (~0.55 MPa) compared to the control group and a cell survival rate of over 91% (within 4 h), concluding that cell-laden ceramic scaffold is a potentially viable solution for bone regeneration.

3.3. Hollow structure

Compared with the conventional bone repair scaffolds with cylindrical filament structure or rectangular filament structure, the hollow structure scaffold possesses one or more pores that completely run through both sides of the scaffold, and the pores are usually distributed in parallel. The advantage of the hollow structure is that the scaffold has large porosity to facilitate the growth and flow of osteoblasts and growth factors, transport nutrients and load drugs, and its internal structure also provides a suitable space for the development of vascular growth.

Feng *et al*.[95] successfully prepared a lotus root-like bone repair scaffold with parallel multichannel structure (channel-struts-packed, 1-4CSP) using Mg yellow feldspar (**Figure 3A**). The porosity (80%) and specific surface area (~3.86 m^2g^{-1}) of the mimetic material were significantly higher, and micro-computed tomography results showed that the BV/TV values were significantly higher in the 3CSP group (12.6%) after 12 weeks of implantation. They found that the porous scaffold is more suitable for cell delivery and regeneration of large bone defects. The complexity of the hierarchical structure, the mechanical properties required and the diversity of bone resident cells are the major challenges in building bionic bone tissue engineering scaffolds. Zhang *et al*.[96] successfully fabricated a mimic havers bone scaffold with magnesium yellow feldspar as the raw material – an internal mesh structure with cylindrical pores, accompanied by multiple regularly distributed havers

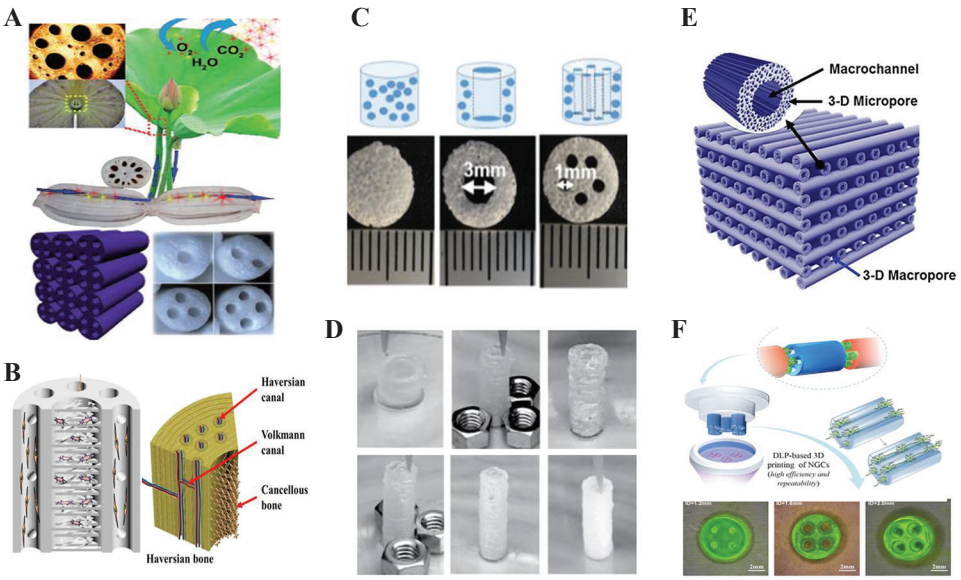

Figure 3. Schematic diagram of hollow structure scaffold. (A) Schematic diagram of Lotus-like structure scaffold[95]. (from ref.[95] licensed under Creative Commons Attribution 4.0 license). (B) Schematic diagram of Haversian-like bone scaffold structure[96]. (from ref.[96] licensed under Creative Commons Attribution Non-Commercial License 4.0 (CC BY-NC) (C) Schematic diagram of non-porous, monoporous and porous scaffold prepared from apatite material[97]. (Reprinted with permission from Wang X, Lin M, Kang Y. Engineering Porous β-Tricalcium Phosphate (β-TCP) Scaffolds with Multiple Channels to Promote Cell Migration, Proliferation, and Angiogenesis. ACS Applied Materials and Interfaces. 2019; 11(9):9223-9232. Copyright© 2019 American Chemical Society) (D) Schematic diagram of nut-like scaffold structure prepared from NICE bioink[98]. (Reprinted with permission from Chimene D, Miller L, Cross L M, *et al*. Nanoengineered Osteoinductive Bioink for 3D Bioprinting Bone Tissue. ACS Applied Materials and Interfaces. 2020; 12(14):15976-15988. Copyright© 2020 American Chemical Society) (e) Schematic diagram of scaffold composed of highly microporous hollow filament structure[99]. (Reprinted from Journal of the European Ceramic Society, 35(16), Moon Y W, Choi I J, Koh Y H, *et al*., Macroporous alumina scaffolds consisting of highly microporous hollow filaments using three-dimensional ceramic/camphene-based co-extrusion, 4623-4627., Copyright © 2015, with permission from Elsevier) (F) Schematic diagram of GelMA porous gel scaffold[100]. (From ref.[100] licensed under Creative Commons Attribution 4.0 license).

tubes (**Figure 3B**), and the compressive strength (9.67 – 26.72 MPa) and bending strength (15.21 – 21.12 MPa) of the scaffold could be well controlled by changing the parameters of the bone-mimicking structure to simulate the bone growth process, and the scaffold demonstrated the ability to induce new bone formation, angiogenesis and neurogenic differentiation and accelerate the growth of blood vessels in *in vitro* experiments, indicating that multi-cellular delivery has great potential. Wang *et al*.[97] prepared a porous β-tricalcium phosphate scaffolds with channel less, single-channel, and multi-channel structures based on a single-layer cylindrical scaffold (**Figure 3C**), which can achieve better cellular penetration and enhanced vascularization using interconnected channels and pores in the scaffold to facilitate nutrient transport. The macrostructure and microsurface topography of the implant play an important role in bone tissue regeneration. Chimene *et al*.[98] developed a gelatin methacrylate (GelMA) slurry based on nanoengineered ionic-covalent entanglement in a nut-like scaffold structure (**Figure 3D**). With the increasing GelMA concentration, the compressive strength and toughness also increases (103 kPa, 78 kJ/m^3 ⁽7.5 wt%). It also showed high printability, excellent enzymatic degradability (no more than 20% degradation in 60 days), and osteoinductive properties. Moon *et al*.[99] designed 3D printed scaffolds with hollow structures using alumina powder with a particle size of 0.3 μm and camphene (**Figure 3E**), and the scaffold had a compressive strength of approximately 5.4 MPa and a porosity of up to 86%, and the resulting alumina filaments exhibited a highly microporous structure that could effectively stimulate cell-matter interactions to induce new bone shapes. Ye *et al*.[100] prepared hollow-structured gel scaffolds using GelMA (**Figure 3F**) to assess biocompatibility and neuronal differentiation by culturing PC-12 cells and neural crest stem cells *in vitro*, and coculture experiments showed that the average cell viability of nerve guidance conduits with different inner diameters was 97.2%, 95.6%, and 95.1%, and close to 100%, respectively, and PC-12 cells on GelMA scaffolds did not show any cytotoxic effects.

3.4. Core-shell structure

Adopting a physical structure similar to that of fiber optic cables, the core-shell structure consists of two types of slurry – internal and external, and is divided in different tubes and extruded in the form of a shell material closely covering the core material. Most of the common core-shell structured supports are manufactured by coaxial dual-jet printing devices. The core-shell structure is characterized by the independence of the printing paste in the pre-printing process and inside the molded scaffold, which allows the scaffold to have degradability and bioactivity with adjustable fast and slow rates.

Ke *et al*.[101] prepared scaffolds with core-shell structure using β-tricalcium phosphate/β-calcium silicate (**Figure 4A**) with different combinations (CaSi@CaP, CaP@CaSi, CaSi, and CaP), and by adjusting the composition distribution, it was found that CaSi@CaP showed a faster degradation rate within 7 – 14 days (35%), while CaP@CaSi microspheres showed excellent surface bioactivity and osteogenic activity (BV/TV, 33%). Pistry *et al*.[102] used alginate gel or alginate/poly(ethylene glycol) diacrylate hybrid hydrogel as the scaffold shell in coaxial printing, and the core material was separately used in three hydrogels encapsulating different cells (3T3-GelMA, HepG2-COL, and human umbilical vein endothelial cells [HUVEC]-Matrigel) (**Figure 4B**). The experimental results showed that the scaffold had good mechanical properties (elastic modulus up to 500 kPa) after the addition of PRGDA to the alginate gel, and the cells on the scaffold as a whole exhibited high biological activity, which remained above 90% after 28 days of *in vitro* culture. Taymour *et al*.[103] developed a core-shell structure scaffold using alginate and methylcellulose to loaded hepatocytes through a 3D extrusion-based bioprinting method (**Figure 4C**), which effectively constructed a microenvironment that allowed coculture of hepatocytes with other liver-specific cells. Jin *et al*.[92] prepared a calcium silicate core-shell structure scaffold containing different mass fractions of Mg ions by a coaxially aligned bilayer nozzle device (**Figure 4D**), and the presence of Mg increased the compressive strength of the scaffold from 39.4 MPa (CSi-Mg4) to 80 MPa (CSi-Mg10), and the degradation rate of CSi-Mg10 after 6 weeks was only 4.3%. Hong *et al*.[104] prepared a gelatin-polyethylene glycol-tyrosamine-based core-shell structure based on a coaxial extrusion device using a one-step gel bioprinting method (**Figure 4E**), and achieved radial distribution of multiple vascular cells by loading HUVECs with human dermal fibroblasts in tyramine, demonstrating that one-step generation of the idea of vascular structures is feasible.

3.5. Bionic structures and others

In addition to the four main structures mentioned above, the overall structure of the scaffold can be customized to fit the shape of the defect or to simulate the organ contour, depending on the skeletal defect and the need for functionality of the scaffold. For example, to repair bone defects more efficiently and precisely, designers try to print scaffolds into bionic structures such as meniscus-shaped and ear-shaped. To address the defects in patients' bodies more specifically, scaffolds are often designed into special structures such as boat-shaped, spring-shaped, and scroll-shaped, which can easily encapsulate cells and growth factors or load other drugs[105].

Inspired by the rosette structure, Han *et al*.[106] prepared

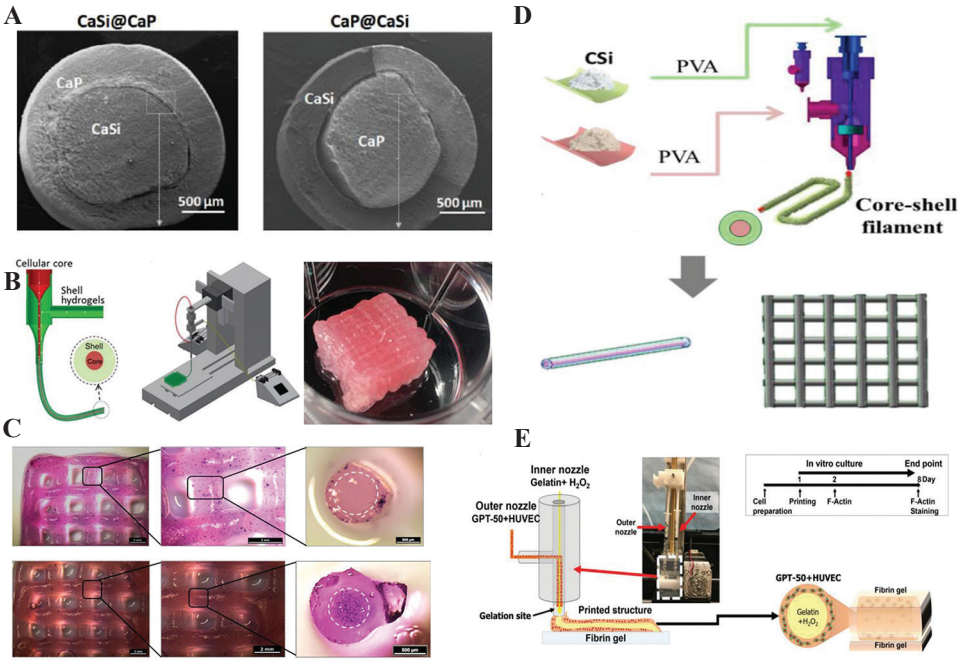

Figure 4. Schematic diagram of the core-shell structure scaffold. (A) SEM images of CaSi, CaP core-shell structure[101]. (Reprinted with permission from Ke X, Zhuang C, Yang X, *et al*. Enhancing the Osteogenic Capability of Core-Shell Bilayered Bioceramic Microspheres with Adjustable Biodegradation, ACS Applied Materials and Interfaces. 2017; 9(29):24497-24510, Copyright © 2017 American Chemical Society) (B) Schematic diagram of GPT-50 and HUVEC hybrid scaffold printing[102]. (Reprinted from Pistry P, Aied A, Alexander M, *et al*., Macromolecular Bioscience, Copyright © 1999-2021 John Wiley and Sons). (C) Printed schematic of the cell-loaded hydrogel core-shell structure scaffold[103]. (from ref.[103] licensed under Creative Commons Attribution 4.0 license). (D) Schematic diagram of the CSi+PVA+Metal ion core-shell structure scaffold[92]. (Reprinted from Journal of the European Ceramic Society, 36, Shao H, He Y, Fu J, *et al*., 3D printing magnesium-doped wollastonite/β-TCP bioceramics scaffolds with high strength and adjustable degradation, 1495-1503, Copyright (2016), with permission from Elsevier) (E) Printed schematic of the GelMA-loaded dual-cell scaffold[104]. Reproduced from ref.[104] with permission from The Royal Society of Chemistry.

a porous structures encapsulating deferoxamine (DFO) liposomal hydrogel microspheres using a combination of microfluidic and light-curing techniques (**Figure 5A**). About 36% of DFO was released within the first 6 h and 69% after 7 days, and the expression of osteogenesis-related proteins such as HIF1-α, CD31, OPN, and OCN in the rat femoral defect model were effectively promoted, thereby significantly cutting down the time of bone repair. Meanwhile, Gao *et al*.[107] attempted to prepare 3D hydrogel vascular structures with multi-level fluid channels by extruding hollow structured sodium alginate filaments loaded with fibroblasts and smooth muscle cells through a coaxial nozzle (**Figure 5B**), which improved the overall mechanical strength of the scaffold, and L929 mouse fibroblasts encapsulated in the structures attained over 90% survival within 1 week. In addition to the encapsulation of cells or drugs in the slurry, researchers have used different post-processing methods to explore the structural and performance aspects of 3D printed scaffolds. Ma *et al*.[108] developed a high-precision rapid 3D bioprinting technique using biohydrogel (GelMA) as a substrate to combine two types of cells in a complementary mode, and constructed a bionic 3D liver tissue model by photopolymerization of the hydrogel matrix (**Figure 5C**). The scaffolds exhibited good biocompatibility with only 9% reduction in cell survival after 1 week of printing. In addition, the liver genes in 3D cultivation mode were higher than two-dimensional (2D) monolayer culture. Xie *et al*.[109] prepared a complex 3D structure such as ear-like, nasal, and multi-hollow chamber-like using 3D bioluminescent printing (**Figure 5D**) that possesses higher biocompatibility and combines GelMA with conventional microfluidic chips in a double cross-linking method. In addition, scaffolds can also be used as suitable models for *in vitro* drug screening, cell interaction studies, etc. By encapsulating cells in a chip, Xue *et al*.[110] successfully prepared a graphene oxide/chitosan/calcium silicate (GO/CTS/CS) bioactive scaffold by a "bottom-up" approach (**Figure 5E**), and the interaction between the GO/CTS/CS laminar microstructure interfaces and the multilayer helical columnar structure of the calcium silicate biomaterials resulted in high bending strength, compressive strength, toughness, and specific strength. The expression level of osteogenic genes was higher than those of the blank group (~150%), and significant osteogenic effects could be seen after 8 weeks of *in vivo* experiments.

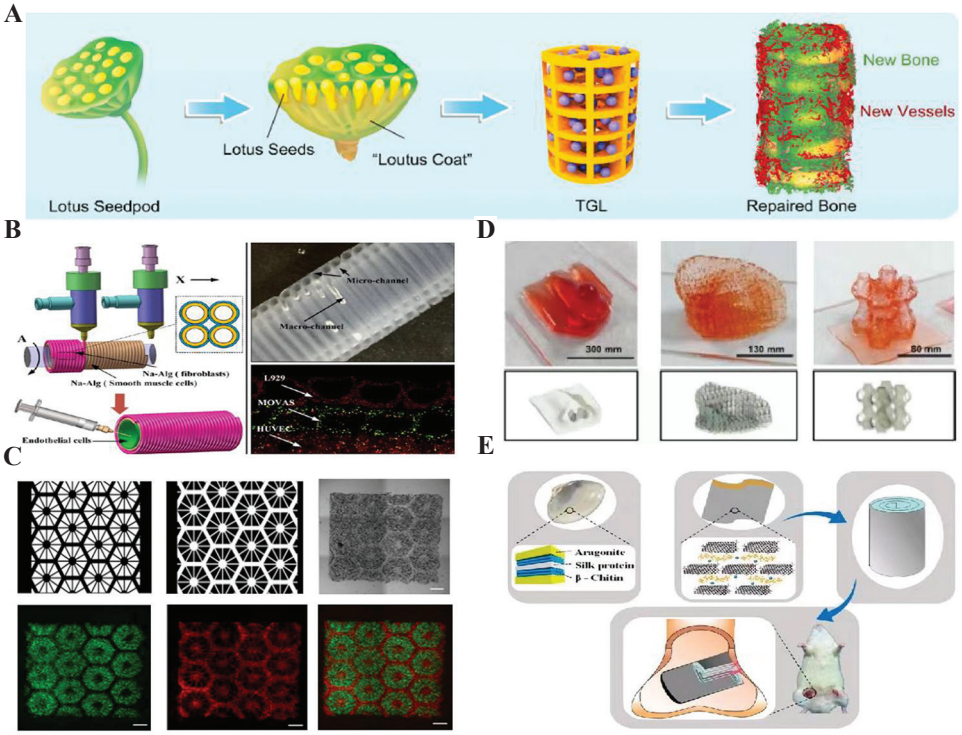

Figure 5. Schematic diagrams of other scaffold structures. (A) Schematic diagram of GML+TGL material mimic lotus pod scaffold structure[106]. (From ref.[106] licensed under Creative Common Attribution-NonCommercial-NoDerivatives 4.0 International (CC BY-NC-ND 4.0) (B) Schematic diagram of cell-carrying spring-like scaffold structure[107]. (Reprinted with permission from Gao Q, Liu Z, Lin Z, *et al.*, 3D Bioprinting of Vessel-like Structures with Multi-level Fluidic Channels, ACS Biomaterials Science and Engineering. 2017; 3(3):399-408. Copyright© 2017 American Chemical Society) (C) Schematic diagram of hexagonal mimic scaffold structure[108]. Reprinted with permission from Ma X, Xin Q, Wei Z, *et al*. Deterministically patterned biomimetic human iPSC-derived hepatic model via rapid 3D bioprinting. Proceedings of the National Academy of Sciences. 2016; 113(8):2206. (D) Light microscope images of multi-shape GelMA[109]. Adapted from Xie, M., Yu, K., Sun, Y., Shao, L., Nie, J., Gao, Q., Qiu, J., Fu, J., Chen, Z., He, Y. Protocols of 3D Bioprinting of Gelatin Methacryloyl Hydrogel Based Bioinks. J. Vis. Exp. (154), e60545, doi:10.3791/60545 (2019) (E) Schematic diagram of multi-layered helical cylindrical scaffold structure[110]. Reprinted with permission from Xue J M, Feng C, Xia LG, *et al*. Assembly Preparation of Multilayered Biomaterials with High Mechanical Strength and Bone-Forming Bioactivity. Chemistry of Materials. 2018; 30(14):4646-4657, Copyright© 2018 American Chemical Society.

4. Composite function

With the development of tissue engineering technology, biomedical scaffolds used in clinical practice are constantly updated[111-116]. 3D printed scaffolds are widely used in regenerating tissues and organs such as skin, nerve, bladder, bone, and blood vessels[117-119]. However, it is still difficult to prepare ideal 3D printable scaffolds that promote tissue regeneration[120]. 3D bioprinting, a recently developed biomanufacturing technology, addresses this challenge by providing unprecedented manufacturing precision by a highly controllable mechanical manufacturing mechanism[121]. Bioprinting technology is controlled by a computer-aided design system and can manufacture a variety of complex microstructures layer by layer. Cell printing is one of the more widely used 3D bioprinting methods that can overcome the drawbacks of conventional cell-free printed 3D scaffolds by loading cells in bioink. Using a cell-filled hydrogel as the bioink, cell printing can print any cells needed directly within the scaffold area to prepare 3D cell scaffold structures with cell proliferation and differentiation[122-127].

However, bioprinting of cellular structures faces significant obstacles, including the impact of different materials on maintaining mechanical properties at micro- and macro-scopic scales, achieving tissue designs with biological specificity, developing methods to obtain and expand functional cells from stem cells, and connecting bioprinted tissues to the physiological vascular system. The initial success of clinical applications of 3D bioprinting for the preparation of active tissues was attributed to the relatively simple geometry of the prepared active tissues. Based on this perspective, we provide an overview of recent advances in bio-3D printed active scaffolds and a generalized enumeration of their main functions.

4.1. Cartilage

The skeletal system consists primarily of bones, cartilage, and bands of fibrous connective tissue (i.e. tendons and ligaments). Cartilage is a highly specific tissue with no blood supply, nerve tissue, or lymphatic vessels, and once injured, it cannot regenerate spontaneously in the body[128]. Calcified cartilage is found in the deepest part of the natural cartilage tissue, connecting the cartilage to the underlying subchondral bone[129]. Cartilage defects usually include damage to surface articular cartilage, intermediate calcified cartilage, and deep subchondral bone[130]. Driven by the growing medical demand, the number of patients requiring functional bone grafting is also increasing, with at least 500,000 patients receiving bone defect repair annually worldwide[131]. Therefore, bioprinting of skeletal tissues such as cartilage is one of the main areas of interest in the field of tissue engineering and regenerative medicine. In contrast, traditional treatment methods are complicated and not only lead to a lack of biomechanical function of fibrocartilage, but also have limitations in terms of cost and side effects. With the development of cartilage engineering, the construction and grafting of cartilage composites is considered an effective method to treat osteochondral (OC) defects[132,133].

Recently, Chen *et al*.[134] designed and successfully fabricated a three-layer gradient cartilage scaffold by physical cross-linking, photo-cross-linking, and chemical cross-linking for the 1st time, and the addition of nHA effectively improved the tensile properties of the scaffold (up to 160 kPa). With the increase of nHA concentration, the compressive strength of the scaffold also increased, and the compressive strength of nHA scaffold with 70% nHA content can reach 0.65 MPa, which is about 5 times of 40% nHA content. The ICRS (International Cartilage Repair Society) score was the highest in the 70% nHA + BMSC group. Sun *et al*.[135] printed gradient scaffolds with PCL and wrapped BMP 4 and TGF-β3 into PLGA microspheres, and encapsulated them into hydrogels along with bone marrow MSCs (BMSCs), which were injected into the PCL fiber gap. To better simulate the full cartilage structure, the deepest layer was the hydrogel wrapped with BMP4, while the upper layer was the hydrogel wrapped with TGF-β3. The characterization results showed that the scaffold had well connectivity and biocompatibility, and the PCL support structure provided a suitable environment for cell distribution, nutrient supply, and proliferation and differentiation. In addition, the gradient scaffold formed bone-like tissue (4 times that of the non-gradient scaffold) in whole layers after 12 weeks of *in vitro* culture, and its Young's modulus and mechanical properties were close to those of normal cartilage tissue. Diloksumpan *et al*.[136] integrated hydrogel, ceramic, and polymer materials to fabricate a calcium phosphate-based bioceramic ink into a subchondral bone substitute using extrusion printing, followed by a near-field direct writing technique to prepare polymer meshes immobilized in the ceramic ink and embedded in cell-laden GelMA (**Figure 6C**). The several microfiber structures prepared as crosslinker resulted in more than 6.5-fold increase in bond strength at the hydrogel-ceramic interface, and the Melt Electrowriting lattices imparted cartilage structures with compressive properties close to those of natural cartilage (20 times that of the original hydrogel), in addition, cells remained viable within the microfiber reinforced GelMA and the deposition of cartilage-like extracellular matrix was observed in both structures after 6 weeks of culture. Kim *et al*. and Hong *et al*.[137,138] synthesized a light-curable bioink material, that is, glycidyl methacrylate modified silk protein (Sil-MA), for the 1st time. It was found that the compressive modulus increased about 2.6 times for every 10% increase in Sil-MA concentration, and the compressive breaking stress was up to 910 kPa and the tensile fracture stress was up to 50 kPa for a 30% concentration of Sil-MA hydrogel; an extended epithelial matrix was found around the Sil-MA hydrogel in rabbit tracheal defect experiments, confirming that the Sil-MA hydrogel replaced the defective part of the trachea part of the trachea and guided the regeneration of the trachea.

4.2. Vascular

Bone tissue repair requires nutrient and oxygen delivery and the ability to remove waste products in a timely manner to maintain necessary functions and nutrient supplies[139-141]. Therefore, the introduction of vascular-like structures is a prerequisite for the successful design of functional tissues suitable for regeneration and the construction in *in vitro* models[142]. Achieving a directed design of vascular growth structures remains a great challenge, and pre-creating microstructures with customized microtissues (e.g. interconnected microchannels) to mimic the vascular system that provides a survival environment for the surrounding stromal cells remains a feasible solution.

To achieve this goal, researchers have explored cell-laden printing techniques to ensure precise control of the spatial arrangement of vascular cells in the matrix. Jia *et al*.[143] used bioinks made of GelMA, sodium alginate and 4-arm poly(ethylene glycol)-tetra-acrylate to deposit implantable vascular structures with highly ordered arrangements in one step by a coaxial extrusion device. The percentage of surviving cells under UV experiments exceeded 80%, and longer UV irradiation reduced the scaffold degradation rate. Suntornnond *et al*.[144] designed and fabricated highly printable hydrogel composites using Planic-127 and GelMA to prepare mimic vascular-like scaffold structures by 3D extrusion-based printing method, and *in vitro* evaluation showed that after 7 days of co-culture, the highest number of cells survived

(nearly 20% more) at a Planic-GelMA ratio of 2:1, and the hydrogel composite with this ratio provided a good platform for cell attachment and proliferation. Non-scaffold vascular-like structures are evolving as potential vascular alternatives through 3D bio-direct printing technology. Zhang *et al*.[145] used sodium alginate solution as a printing ink and formed vascular-like structures through coaxial printing by physical cross-linking using calcium chloride solution. Compared to conventional scaffold structures with a 21% reduction in volume, the lubricin gene PRG-4 also showed over a twofold higher expression in hollow fibers after encapsulation of cartilage progenitor cells.

4.3. Drug-carrying antibacterial

Malignant bone tumors mainly include osteosarcoma, chondrosarcoma, and Ewing sarcoma[146-148]. At present, a combination of surgical resection, chemotherapy, and radiotherapy is often used for malignant bone tumors, and this treatment has significantly improved the overall survival rate of patients in the last 5 years[149]. However, surgical resection cannot completely eliminate tumor cells and can lead to bone defects, and chemotherapy and radiotherapy may induce side effects such as drug resistance and radiation resistance in normal tissues. To address these long-standing challenges for patients, researchers have worked to develop bone repair scaffolds that have antimicrobial properties and inhibit the growth of tumor cells.

Bioceramic materials are widely used in the repair of tissue defects in bone, teeth and skin due to their ability to induce tissue regeneration and regulate cell growth and functional differentiation. In recent years, it has been found that composite scaffolds made of bioceramic materials and materials which containing tumor growth inhibitors can not only keep the growth of tumor cells, but also further repair bone defects caused by surgery[150-152]. Mehdi *et al*.[153] prepared a gelatin/β-TCP composite scaffold, and *in vivo* experiments showed that the rate of new bone formation throughout the defective area was more than 75% after 3 – 4 months, the scaffold was further treated by adding zoledronic acid which inhibits tumor cell growth and the gelatin/β-TCP scaffold structure could modulate the release of drugs *in vivo* for therapeutic effect.

In recent years, photothermal therapy (PTT), a minimally invasive and highly effective antitumor approach, has been shown in numerous clinical trials to improve the effectiveness of tumor treatment and reduce side effects[154-156]. PTT requires ablation of tumor tissue by induced thermotherapy with the help of photothermal agents. Wang *et al*.[157] developed a new bifunctional biomaterial (MS-AKT scaffold) with photothermal therapeutic ability and bone regeneration ability, and based on the *in vivo* experiments, 89% of tumor cells in the MS-AKT group were necrotic, which was much higher than other controls. This bifunctional scaffold was able to treat tumors and promote bone growth, providing a promising clinical strategy for the treatment of tumor-induced bone defects. Liu *et al*.[158] used Darvan821-A as a size controlling agent and dispersant for the 1st time during HA synthesis to prevent the formation of particle aggregates throughout the COL matrix, resulting in COL-nHA scaffolds with excellent rheological properties and great potential for precise tailoring of scaffold shape. In addition, inhibition of tumor cell growth can also be achieved by incorporating materials with photothermal properties in the scaffold to control temperature changes under infrared irradiation. Wang *et al*.[159] prepared a series of black bioceramic powders with good biocompatibility by magnesium thermal reduction, and the presence of a large number of oxygen vacancies inside the crystals improved the degradation properties of the scaffold materials and the adhesion effect for osteoblasts and skin cells. Under low-power infrared irradiation, the black bioactive ceramic scaffolds demonstrated a significant photothermal warming effect, and the survival rate of LM8 cells was only 0.98% at 25 min after irradiation. Bo *et al*.[160] combined copper ion-ligated meso-Tetra(4-carboxyphenyl) porphine (Cu-TCPP) with tricalcium phosphate ceramic scaffold material to make Cu-TCPP-TCP composite scaffold, and based on the *in vitro* experiments on PTT, 20Cu-TCPP-TCP scaffold had only 10% bone tumor cell activity under near-infrared light irradiation.

5. Conclusions

In summary, this paper points out that the standard of bone repair scaffolds within the field of tissue engineering is getting higher. Conventional bone repair scaffolds can no longer meet the high standards and requirements of clinical applications in terms of preparation process and service performance. A wide range of researchers are dedicated to exploring the diversity of scaffold structures and functions and developing bioprinting technologies to improve the filament structure, material composition and scaffold functions in terms of printing paste, preparation process, and scaffold structure in order to build bone repair scaffolds that meet modern clinical requirements. In terms of material composition, bioceramics as the traditional bone repair scaffold material have been the first choice of researchers, but the unchanging ceramic scaffold cannot meet the clinical needs of contemporary society. The introduction of polymeric materials has greatly improved the biocompatibility and printability of scaffolds. Some materials in polymers, such as hydrogel, COL, and PLA, have good viscoelasticity as well as biocompatibility, and it can be introduced

into the scaffold as an outer membrane to wrap growth factors and functional cells with different functions. In terms of spatial structure, attempts were made to improve the classical structure by creating microporous or hydrothermally generating nano-layers on the scaffold surface; bilayer structure can improve the mechanical properties as well as ensure the independence of the slurry while printing multiple materials; core-shell structure can intelligently adjust the degradation rate of the scaffold materials; and hollow structure provides more space for the growth of blood vessels and nerve tissues on the basis of increasing the porosity. There were also some specific scaffolds designed on the basis of bionic, which can repair human bone defects more precisely and efficiently after implantation. In terms of biological functions, to meet the growing clinical demands, bone repair scaffolds are endowed with antibacterial, tumor suppressive, slow drug release, and tissue regenerative properties in addition to meeting the basic osteogenic requirements, which help facilitate maximal recovery while meeting the requirements of bone repair.

The market scale of bone repair devices sees a continuous expansion while the patients' requirements for post-operative living standards and the structural and functional diversity of bone repair scaffolds have gradually increased. The future development can be concluded in different aspects:

1. In future, the bone repair scaffold is not only similar to bone tissue in terms of chemical composition (e.g. bioceramics, polymers, cells, and growth factors), but also in terms of physical structure which can simulate the shape of bone defects and human tissue mechanism from a bionic perspective to achieve precise repair and shorten osteogenesis time (e.g. more microscopic Haver's canal, and vascular tract).
2. Building a balance between mechanical and biological properties of the scaffold. Scaffolds with good mechanical properties have a high specific gravity of bioceramics, which is detrimental to cell viability; scaffolds with eximious cell viability tend to be polymer-based and require sacrificing mechanical properties.
3. Composite materials have become the first choice for the preparation of bone repair scaffolds. With the gradual increase in the number of scaffold components, it remains a challenge to ensure that the advantageous properties of each material and the value of the material are maximized.
4. More functions are given to the bone repair scaffold according to sites and physiological regions. For example, the function of loading drugs can cure bone tumors with long-lasting stability; the function of scaffold can be expressed under microenvironmental changes such as pH, electric field, magnetic field, and temperature.
5. After continuous optimization and efforts to bring bone repair scaffolds into clinical treatment, a marketable clinical application of bone repair scaffolds will be of interest in the future in the field of tissue engineering.
6. The concept of four-dimensional (4D) printing, which gives the scaffold structure the property of changing over time, opens up a new vision of scaffold function from a new dimension, and the customized spatial arrangement of cells and the activity of cells during the printing process, will be the topics of future research.

Acknowledgments

This work was supported by China Post-doctoral Science Foundation (2020M682631), Guangdong Basic and Applied Basic Research Foundation (2020A1515011407), National Natural Science Foundation of China (52105202, 5210022045), Guangdong academy of science project (2019GDASYL-0103021, 2019GDASYL-0102004/0103018), Guangzhou Science and Technology Program (201904010280, 2018A050506056) and Guangdong Basic and Applied Basic Research Foundation (2020A1515011407).

Conflicts of interest

No conflict of interest is reported by the author.

References

1. Lan L, Fei Y, Shi J, *et al*., 2017, *In Situ* Repair of Bone and Cartilage Defects Using 3D Scanning and 3D Printing. *Sci Rep*, 7:9416. https://doi.org/10.1038/s41598-017-10060-3
2. Annamalai RT, Hong X, Schott NG, *et al*., 2019, Injectable Osteogenic Microtissues Containing Mesenchymal Stromal Cells Conformally Fill and Repair Critical-Size Defects. *Biomaterials*, 208:32–44. https://doi.org/10.1016/j.biomaterials.2019.04.001
3. Zhang X, Li Y, Chen YE, *et al*., 2016, Cell-free 3D Scaffold with Two-stage Delivery of miRNA-26a to Regenerate Critical-sized Bone Defects. *Nat Commun*, 7:10376. https://doi.org/10.1038/ncomms10376
4. Schemitsch EH, 2017, Size Matters: Defining Critical in Bone Defect Size! *J Orthop Trauma*, 31:S20–2. https://doi.org/10.1097/BOT.0000000000000978
5. Lin KF, He S, Song Y, *et al*., 2016, Low-Temperature Additive Manufacturing of Biomimic Three-Dimensional Hydroxyapatite/Collagen Scaffolds for Bone Regeneration. *ACS Appl Mater Interfaces*, 8:6905–16.

https://doi.org/10.1021/acsami.6b00815

6. Faldini C, Traina F, Perna F, *et al*., 2015, Surgical Treatment of Aseptic Forearm Nonunion with Plate and Opposite Bone Graft Strut. Autograft or Allograft? *Int Orthop*, 39:1343–9. https://doi.org/10.1007/s00264-015-2718-6
7. Arrington ED, Smith WJ, Chambers HG, *et al*., 1996, Complications of Iliac Crest Bone Graft Harvesting. *Clin Orthop Relat Res*, 329:300–9. https://doi.org/10.1243/09596518JSCE892
8. Lai Y, Cao H, Wang X, *et al*., 2018, Porous Composite Scaffold Incorporating Osteogenic Phytomolecule Icariin for Promoting Skeletal Regeneration in Challenging Osteonecrotic Bone in Rabbits. *Biomaterials*, 153:1–13. https://doi.org/10.1016/j.biomaterials.2017.10.025
9. Almubarak S, Nethercott H, Freeberg M, *et al*., 2016, Tissue Engineering Strategies for Promoting Vascularized Bone Regeneration. *Bone*, 83:197–209. https://doi.org/10.1016/j.bone.2015.11.011
10. Kim JA, Lim J, Naren R, *et al*., 2016, Effect of the Biodegradation Rate Controlled by Pore Structures in Magnesium Phosphate Ceramic Scaffolds on Bone Tissue Regeneration *In Vivo*. *Acta Biomater*, 44:155–67. https://doi.org/10.1016/j.actbio.2016.08.039
11. Williams DF, 2008, On the Mechanisms of Biocompatibility. *Biomaterials*, 29:2941–53. https://doi.org/10.1016/j.biomaterials.2008.04.023
12. Yao Y, Qin W, Xing B, *et al*., 2021, Highperformance Hydroxyapatite Ceramics and a Triply Periodic Minimum Surface Structure Fabricated by Digital Light Processing 3D printing. *J Adv Ceramics*, 10:39–48. https://doi.org/10.1007/s40145-020-0415-4
13. Rouwkema J, Rivior NC, Van CA, *et al*., 2008, Vascularization in Tissue Engineering. *Trends Biotechnol*, 26:434–41. https://doi.org/10.1016/j.tibtech.2008.04.009
14. Cao H, Kuboyama N, 2010, A Biodegradable Porous Composite Scaffold of PGA/beta-TCP for Bone Tissue Engineering. *Bone*, 46:386–95. https://doi.org/10.1016/j.bone.2009.09.031
15. Olszta M, Cheng X, Jee S, *et al*., 2007, Bone Structure and Formation: A New Perspective. *Mater Sci Eng R Rep*, 58:77–116. https://doi.org/10.1016/j.mser.2007.05.001
16. Bramfeldt H, Sabra G, Centis V, *et al*., 2010, Scaffold Vascularization: A Challenge for Three-Dimensional Tissue Engineering. *CMC*, 17:3944–67. https://doi.org/10.2174/092986710793205327
17. Jain RK, Au P, Tam J, *et al*., 2005, Engineering Vascularized Tissue. *Nat Biotechnol*, 23:821–3. https://doi.org/10.1038/nbt0705-821
18. Ma Y, Dai H, Huang X, *et al*., 2019, 3D Printing of Bioglass-reinforced β-TCP Porous Bioceramic Scaffolds. *J Mater*, 54:10437–46. https://doi.org/10.1007/s10853-019-03632-3
19. Woodfield T, Malda J, Wijn JD, *et al*., 2004, Design of Porous Scaffolds for Cartilage Tissue Engineering Using a Three-dimensional Fiber-deposition Technique. *Biomaterials*, 25:4149–61. https://doi.org/10.1016/j.biomaterials.2003.10.056
20. Hutmacher DW, 2001, Scaffold Design and Fabrication Technologies for Engineering Tissues State of the Art and Future Perspectives. *J Biomater Sci Polym Ed*, 12:107–24. https://doi.org/10.1163/156856201744489
21. ASTM F2792-12a, 2012, Standard Terminology for Additive Manufacturing Technologies. West Conshohocken, PA: ASTM International.
22. Shahrubudin N, Lee TC, Ramlan R, 2019, An Overview on 3D Printing Technology: Technological, Materials, and Applications. *Proc Manufact*, 35:1286–96. https://doi.org/10.1016/j.promfg.2019.06.089
23. Mahajan C, Cormier D, 2015, 3D Printing of Carbon Fiber Composites with Preferentially Aligend Fibers. Industrial and Systems Engineering Research Conference.
24. Yeong WY, Guo DG, 2020, 3D Printing of Carbon Fiber Composite: The Future of Composite Industry? *Materials*, 2:1361–3. https://doi.org/10.1016/j.matt.2020.05.010
25. Murphy SV, Coppi PD, Atala A, 2019, Opportunities and Challenges of Translational 3D Bioprinting. *Nat Biomed Eng*, 4:370–80. https://doi.org/10.1038/s41551-019-0471-7
26. Savage N, 2016, Technology: The Promise of Printing. *Nature*, 540:S56–7. https://doi.org/10.1038/540S56a
27. Boskey AL, 2015, Bone Composition: Relationship to Bone Fragility and Antiosteoporotic Drug Effects. *Bonekey Rep*, 4:710. https://doi.org/10.1038/bonekey.2015.79
28. Fu S, Zhu M, Zhu Y, 2019, Organosilicon Polymer-derived Ceramics: An Overview. *J Adv Ceramics*, 8:457–78. https://doi.org/10.1007/s40145-019-0335-3
29. Fahmy MD, Jazayeri HE, Razavi M, *et al*., 2016, Three-Dimensional Bioprinting Materials with Potential Application in Preprosthetic Surgery. *J Prosthodont*, 25:310–8. https://doi.org/10.1111/jopr.12431

30. Zhu W, Qu X, Zhu J, *et al*., 2017, Direct 3D Bioprinting of Prevascularized Tissue Constructs with Complex Microarchitecture. *Biomaterials*, 124:106–15. https://doi.org/10.1016/j.biomaterials.2017.01.042
31. Tang Z, Li X, Tan Y, *et al*., 2017, The Material and Biological Characteristics of Osteoinductive Calcium Phosphate Ceramics. Regener. Biomater. 5:43–59. https://doi.org/10.1093/rb/rbx024
32. Damien CJ, Parsons JR, 1991, Bone Graft Substitutes: A Review of Current Technology and Applications. Autumn (Fall). 2:187–208. https://doi.org/10.1002/jab.770020307
33. Oonishi H, 1991, Orthopaedic Applications of Hydroxyapatite. *Biomaterials*, 12:171–8. https://doi.org/10.1016/0142-9612(91)90196-H
34. Lowe B, Hardy JG, Walsh LJ, 2020, Optimizing Nanohydroxyapatite Nanocomposites for Bone Tissue Engineering. *ACS Omega*, 5:1–9. https://doi.org/10.1021/acsomega.9b02917
35. Desiraju GR, Hulliger J, 2001, Current Opinion in Solid State and Materials Science: Molecular Crystals and Materials. *Curr Opin Solid State Mater Sci*, 5:105–6. https://doi.org/10.1016/s1359-0286(01)00015-8
36. Li S, Liu Y, Zhang Q, *et al*., 2011, Microwave-assisted Co-precipitation Synthesis of High Purity β-tricalcium Phosphate Crystalline Powders. *Mater Chem Phys*, 129:1138–41. https://doi.org/10.1016/j.matchemphys.2011.05.075
37. Chen Z, Li Z, Li J, *et al*., 2018, 3D Printing of Ceramics: A Review. *J Eur Ceramic Soc*, 39:661–87. https://doi.org/10.1016/j.jeurceramsoc.2018.11.013
38. Jones JR, 2013, Review of Bioactive Glass: From Hench to Hybrids. *Acta Biomater*, 9:4457–86. https://doi.org/10.1016/j.actbio.2012.08.023
39. Fujishiro Y, Hench LL, Oonishi H, 1997, Quantitative Rates of *In Vivo* Bone Generation for Bioglass and Hydroxyapatite Particles as Bone Graft Substitute. *J Mater Sci Mater Med*, 8:649–52. https://doi.org/10.1023/A:1018527621356
40. Ducheyne P, 2010, Bioglass Coatings and Bioglass Composites as Implant Materials. *J Biomed Mater Res Part A*, 19:273–91. https://doi.org/10.1002/jbm.820190309
41. Li L, Hu H, Zhu Y, *et al*., 2019, 3D-printed Ternary SiO_2CaO P_2O_5 bioglass-Ceramic Scaffolds with Tunable Compositions and Properties for Bone Regeneration. *Ceramics Int*, 45:10997–1005. https://doi.org/10.1016/j.ceramint.2019.02.183
42. Huang MH, Shen YF, Hsu TT, *et al*., 2016. Physical Characteristics, Antimicrobial and Odontogenesis Potentials of Calcium Silicate Cement Containing Hinokitiol. *Mater Sci Eng C Mater Biol Appl*, 65:1–8. https://doi.org/10.1016/j.msec.2016.04.016
43. Shie M, Chiang W, Chen I, *et al*., 2017, Synergistic Acceleration in the Osteogenic and Angiogenic Differentiation of Human Mesenchymal Stem Cells by Calcium Silicate-Graphene Composites. *Mater Sci Eng C*, 73:726–35. https://doi.org/10.1016/j.msec.2016.12.071
44. Bittner SM, Guo JL, Melchiorri A, *et al*., 2018, Three-dimensional Printing of Multilayered Tissue Engineering Scaffolds. *Mater Today*, 21:861–74.
45. Sant S, Coutinho F, Gaharwar AK, *et al*., 2017, Self-Assembled Hydrogel Fiber Bundles from Oppositely Charged Polyelectrolytes Mimic Micro/Nanoscale Hierarchy of Collagen. *Adv Funct Mater*, 27:1606273. https://doi.org/10.1016/j.mattod.2018.02.006
46. Daniela L, Christoph M, Elke K, *et al*., 2016, Functionalization, Preparation and Use of Cell-laden Gelatin Methacryloyl-based Hydrogels as Modular Tissue Culture Platforms. *Nat Protoc Erec Res*, 11:727–46. https://doi.org/10.1038/nprot.2016.037
47. Ying G, Jiang N, Maharjan S, *et al*., 2018, Bioprinting: Aqueous Two-Phase Emulsion Bioink-Enabled 3D Bioprinting of Porous Hydrogels. *Adv Mater*, 30:1870382. https://doi.org/10.1002/adma.201805460
48. Wang X, Jiang M, Zhou Z, *et al*., 2017, 3D Printing of Polymer Matrix Composites: A Review and Prospective. *Comp Part B Eng*, 110:442–58. https://doi.org/10.1016/j.compositesb.2016.11.034
49. Takezawa A, Kobashi M, 2017, Design Methodology for Porous Composites with Tunable Thermal Expansion Produced by Multi-Material Topology Optimization and Additive Manufacturing. *Comp Part B Eng*, 131:21–9. https://doi.org/10.1016/j.compositesb.2017.07.054
50. Li J, Xing R, Bai S, *et al*., 2019 Recent Advances of Self-assembling Peptide-based Hydrogels for Biomedical Applications. *Soft Matter*, 30:1704–15. https://doi.org/10.1039/c8sm02573h
51. Pataky K, Braschler T, Negro A, *et al*., 2012, Microdrop Printing of Hydrogel Bioinks into 3D Tissue-Like Geometries. *Adv Mater*, 24:391–6. https://doi.org/10.1002/adma.201102800
52. Silva T, Moreira-Silva J, Marques A, *et al*., 2014, Marine Origin Collagens and its Potential Applications. *Mar Drugs*, 12:5881–901.

https://doi.org/10.3390/md12125881

53. Hinton TJ, Jallerat Q, Palchesko RN, *et al*., 2015, Three-dimensional Printing of Complex Biological Structures By Freeform Reversible Embedding of Suspended Hydrogels. *Sci Adv*, 1:e1500758. https://doi.org/10.1126/sciadv.1500758
54. Campos DF, Blaeser A, Korsten A, *et al*., 2015, The Stiffness and Structure of Three-dimensional Printed Hydrogels Direct the Differentiation of Mesenchymal Stromal Cells toward Adipogenic and Osteogenic Lineages. *Tissue Eng Part A*, 21:740–56. https://doi.org/10.1089/ten.TEA.2014.0231
55. Shim JH, Jang KM, Hahn SK, *et al*., 2016, Three-dimensional Bioprinting of Multilayered Constructs Containing Human Mesenchymal Stromal Cells for Osteochondral Tissue Regeneration in the Rabbit Knee Joint. *Biofabrication*, 8:014102. https://doi.org/10.1089/ten.TEA.2014.0231
56. Almarza AJ, Athanasiou KA, 2004, Seeding Techniques and Scaffolding Choice for Tissue Engineering of the Temporomandibular Joint Disk. *Tissue Eng Part A*, 10:1787–95. https://doi.org/10.1089/ten.2004.10.1787
57. Li L, Li J, Guo J, *et al*., 2019, 3D Molecularly Functionalized Cell-Free Biomimetic Scaffolds for Osteochondral Regeneration. *Adv Funct Mater*, 29:1807356. https://doi.org/10.1002/adfm.201807356
58. Hasani-Sadrabadi MM, Sarrion P, Nakatsuka N, *et al*., 2019, Hierarchically Patterned Polydopamine-Containing Membranes for Periodontal Tissue Engineering. *Acs Nano*, 13:3830–8. https://doi.org/10.1021/acsnano.8b09623
59. Yi WJ, Li LJ, He H, *et al*., 2018, Poly(L-lactide)/Cyclodextrin/Citrate Networks Modified Hydroxyapatite and its Role as Filler in the Promotion to the Properties of Poly(L-lactide) Biomaterials. *Polymer*, 145:1–10. https://doi.org/10.1016/j. olymer.2018.04.034
60. O'Bryan CS, Bhattacharjee T, Hart S, *et al*., 2017, Self-assembled Micro-Organogels for 3D Printing Silicone Structures. *Sci Adv*, 3:1602800. https://doi.org/10.1126/sciadv.1602800
61. Chow L, Yick KL, Kwan MY, *et al*., 2020, Customized Fabrication Approach for Hypertrophic Scar Treatment: 3D Printed Fabric Silicone Composite. *Int J Bioprint*, 6:70–81. https://doi.org/10.18063/ijb.v6i2.262
62. Luis E, Pan HM, Sing SL, *et al*., 2019, Silicone 3D Printing: Process Optimization, Product Biocompatibility, and Reliability of Silicone Meniscus Implants. *3D Print Addit Manufact*, 6:319–32. https://doi.org/10.1089/3dp.2018.0226
63. Rahmanian M, Seyfoori A, Dehghan MM, *et al*., 2019, Multifunctional Gelatin-Tricalcium Phosphate Porous Nanocomposite Scaffolds for Tissue Engineering and Local Drug Delivery: *In Vitro* and *In Vivo* Studies. *J Taiwan Inst Chem Eng*, 101:214–20. https://doi.org/10.1016/j.jtice.2019.04.028
64. Tibbits S, 2014, 4D Printing: Multi-Material Shape Change. *Arch Des*, 84:116–21. https://doi.org/10.1002/ad.1710
65. Lee JM, Yeong WY, 2016, Design and Printing Strategies in 3D Bioprinting of Cell-Hydrogels: A Review. *Adv Healthc Mater*, 5:2856–65. https://doi.org/10.1002/adhm.201600435
66. Vorndran E, Klammert U, Ewald A, *et al*., 2010, Simultaneous Immobilization of Bioactives During 3D Powder Printing of Bioceramic Drug-Release Matrices. *Adv Funct Mater*, 20:1585–91. https://doi.org/10.1002/adfm.200901759
67. Chia HN, Wu BM, 2015, Recent Advances in 3D Printing of Biomaterials. *J Biol Eng*, 9:4. https://doi.org/10.1186/s13036-015-0001-4
68. Liu X, Ma PX, 2004, Polymeric Scaffolds for Bone Tissue Engineering. *Biomaterials*, 32:9622–9. https://doi.org/10.1023/b: abme.0000017544.36001.8e
69. Peltola SM, Melchels F, Grijpma DW, *et al*., 2008, A Review of Rapid Prototyping Techniques for Tissue Engineering Purposes. Ann Med 40:268–80. https://doi.org/10.1080/07853890701881788
70. Bajpai I, Yang S, Lee S, *et al*., 2015, Compressive Strength and Biomineralisation Improvement by Water Glass Coating on Porous Calcium Phosphate Scaffolds. *Adv Appl Ceramics*, 115:243–8. https://doi.org/10.1179/1743676115Y.0000000028
71. Shuai CJ, Yuan X, Yang WJ, *et al*., 2021, Synthesis of a Mace-like Cellulose Nanosystem Via *In-Situ* Growth for Antibacterial Activities of Poly-L-lactide scaffold. *Carbohydr Polym*, 262:117937. https://doi.org/10.1016/j.carbpol.2021.117937
72. Zyman ZZ, Tkachenko MV, Polevodin DV, 2008, Preparation and Characterization of Biphasic Calcium Phosphate Ceramics of Desired Composition. *J Mater Sci Mater Med*, 19:2819–25. https://doi.org/10.1007/s10856-008-3402-9
73. de Wild M, Amacher F, Bradbury CR, *et al*., 2016,

Investigation of structural resorption behavior of biphasic bioceramics with help of gravimetry, μCT, SEM, and XRD. *J Biomed Mater Res Part B Appl Biomater*, 104:546–53. https://doi.org/10.1002/jbm.b.33419

74. Sánchez-Salcedo S, Balas F, Izquierdo-Barba I, *et al*., 2009, *In Vitro* Structural Changes in Porous HA/β-TCP Scaffolds in Simulated Body Fluid. *Acta Biomater*, 5:2738–51. https://doi.org/10.1016/j.actbio.2009.03.025
75. Diba M, Camargo WA, Brindisi M, *et al*., 2017, Composite Colloidal Gels Made of Bisphosphonate-Functionalized Gelatin and Bioactive Glass Particles for Regeneration of Osteoporotic Bone Defects. *Adv Funct Mater*, 27:1703438. https://doi.org/10.1002/adfm.201703438
76. Jakus AE, Rutz AL, Jordan SW, *et al*., 2016, Hyperelastic\ bone\: A Highly Versatile, Growth Factor-free, Osteoregenerative, Scalable, and Surgically Friendly Biomaterial. *Sci Transl Med*, 8:358ra127. https://doi.org/10.1126/scitranslmed. aaf 7704
77. Lei M, Qu X, Liu H, *et al*., 2019, Programmable Electrofabrication of Porous Janus Films with Tunable Janus Balance for Anisotropic Cell Guidance and Tissue Regeneration. *Adv Funct Mater*, 29:1900065. https://doi.org/10.1002/adfm.201900065
78. Du Y, Liu H, Qin Y, *et al*., 2017, Selective Laser Sintering Scaffold with Hierarchical Architecture and Gradient Composition for Osteochondral Repair In Rabbits. *Biomaterials*, 137:37–48. https://doi.org/10.1016/j.biomaterials.2017.05.021.
79. Zhai X, Ruan C, Ma Y, *et al*., 2018, 3D-Bioprinted Osteoblast-Laden Nanocomposite Hydrogel Constructs with Induced Microenvironments Promote Cell Viability, Differentiation, and Osteogenesis both *In Vitro* and *In Vivo*. *Adv Sci*, 5:1700550. https://doi.org/10.1002/advs.201700550
80. Inzana JA, Olvera D, Fuller SM, *et al*., 2014, 3D Printing of Composite Calcium Phosphate and Collagen Scaffolds for Bone Regeneration. *Biomaterials*, 35:4026–34. https://doi.org/10.1016/j.biomaterials.2014.01.064
81. Li X, Zou Q, Chen H, *et al*., 2019, *In Vivo* Changes of Nanoapatite Crystals During Bone Reconstruction and the Differences with Native Bone Apatite. *Sci Adv*, 5:eaay6484. https://doi.org/10.1126/sciadv. aay 6484
82. Montalbano G, Molino G, Fiorilli S, *et al*., 2020, Synthesis and Incorporation of Rod-like Nano-hydroxyapatite into Type I Collagen Matrix: A Hybrid Formulation for 3D Printing of Bone Scaffolds. *J Eur Ceramic Soc*, 40:3689–97. https://doi.org/10.1016/j.jeurceramsoc.2020.02.018
83. Wang H, Li Y, Zuo Y, *et al*., 2007, Biocompatibility and Osteogenesis of Biomimetic Nano-hydroxyapatite/ Polyamide Composite Scaffolds for Bone Tissue Engineering. *Biomaterials*, 28:3338–48. https://doi.org/10.1016/j.biomaterials.2007.04.014
84. Diao J, Yang JO, Deng T, *et al*., 2018, 3D-Plotted Beta-Tricalcium Phosphate Scaffolds with Smaller Pore Sizes Improve *In Vivo* Bone Regeneration and Biomechanical Properties in a Critical-Sized Calvarial Defect Rat Model. *Adv Healthc Mater*, 7:1800441. https://doi.org/10.1002/adhm.201800441
85. Shao H, He Y, Fu J, *et al*., 2016, 3D Printing Magnesium-doped Wollastonite/β-TCP Bioceramics Scaffolds with High Strength and Adjustable Degradation. *J Eur Ceramic Soc*, 36:1495–503. https://doi.org/10.1016/j.jeurceramsoc.2016.01.010
86. Deng C, Lin R, Zhang M, *et al*., 2019, Micro/Nanometer-Structured Scaffolds for Regeneration of Both Cartilage and Subchondral Bone. *Adv Funct Mater*, 29:1806068. https://doi.org/10.1002/adfm.201806068
87. Wei Y, Gao H, Hao L, *et al*., 2020, Constructing a Sr2+-Substituted Surface Hydroxyapatite Hexagon-Like Microarray on 3D-Plotted Hydroxyapatite Scaffold to Regulate Osteogenic Differentiation. *Nanomaterials*, 10:1672. https://doi.org/10.3390/nano10091672
88. Li X, Yuan Y, Liu L, *et al*., 2020, 3D Printing of Hydroxyapatite/ Tricalcium Phosphate Scaffold with Hierarchical Porous Structure for Bone Regeneration. *Biodes Manufact*, 3:15–29. https://doi.org/10.1007/s42242-019-00056-5
89. Wang C, Lai J, Li K, *et al*., 2020, Cryogenic 3D Printing of Dual-delivery Scaffolds for Improved Bone Regeneration with Enhanced Vascularization. *Bioact Mater*, 6:137–45. https://doi.org/10.1016/j.bioactmat.2020.07.007
90. Pae H, Kang J, Cha J, *et al*., 2019, 3D-printed Polycaprolactone Scaffold Mixed with β-Tricalcium Phosphate as a Bone Regenerative Material in Rabbit Calvarial Defects. *J Biomed Mater Res Part B Appl Biomater*, 107:1254–63. https://doi.org/10.1002/jbm.b.34218
91. Shao H, Ke X, Liu A, *et al*., 2017, Bone Regeneration in 3D Printing Bioactive Ceramic Scaffolds with Improved Tissue/ Material Interface Pore Architecture in Thin-wall Bone Defect. *Biofabrication*, 9:025003. https://doi.org/10.1088/1758-5090/aa663c
92. Jin ZW, Wu RH, Shen JH, *et al*., 2018, Nonstoichiometric Wollastonite Bioceramic Scaffolds with Core-shell Pore Struts and Adjustable Mechanical and Biodegradable

Properties. *Mech Behav Biomed Mater*, 88:140–9. https://doi.org/10.1016/j.jmbbm.2018.08.018

93. Alksne M, Kalvaityte M, Simoliunas E, *et al*., 2020, *In Vitro* Comparison of 3D Printed Polylactic Acid/Hydroxyapatite and Polylactic Acid/Bioglass Composite Scaffolds: Insights into Materials for Bone Regeneration. *J Mech Behav Biomed Mater*, 104:103641. https://doi.org/10.1016/j. jmbbm.2020.103641
94. Kim WJ, Yun HS, Kim GH, 2017, An Innovative Cell-laden α-TCP/Collagen Scaffold Fabricated Using a Two-step Printing Process for Potential Application in Regenerating Hard Tissues. *Sci Rep*, 7:3181. https://doi.org/10.1038/s41598-017-03455-9
95. Feng C, Zhang W, Deng C, *et al*., 2017, 3D Printing of Lotus Root-Like Biomimetic Materials for Cell Delivery and Tissue Regeneration. *Adv Sci*, 4:1700401. https://doi.org/10.1002/advs.201700401
96. Zhang M, Lin R, Wang X, *et al*., 2020, 3D Printing of Haversian Bone-Mimicking Scaffolds for Multicellular Delivery in Bone Regeneration. *Sci Adv*, 6:eaaz6725. https://doi.org/10.1126/sciadv.aaz 6725
97. Wang X, Lin M, Kang Y, 2019, Engineering Porous β-Tricalcium Phosphate (β-TCP) Scaffolds with Multiple Channels to Promote Cell Migration, Proliferation, and Angiogenesis. *ACS Appl Mater Interf*, 11:9223–32. https://doi.org/10.1021/acsami.8b22041
98. Chimene D, Miller L, Cross LM, *et al*., 2020, Nanoengineered Osteoinductive Bioink for 3D Bioprinting Bone Tissue. *ACS Appl Mater Interf*, 12:15976–88. https://doi.org/10.1021/acsami.9b19037
99. Moon YW, Choi IJ, Koh YH, *et al*., 2015, Macroporous Alumina Scaffolds Consisting of Highly Microporous Hollow Filaments Using Three-Dimensional Ceramic/Camphene-Based Co-extrusion. *J Eur Ceramic Soc*, 35:4623–7. https://doi.org/10.1016/j.jeurceramsoc.2015.08.017
100. Ye W, Li H, *et al*., 2020, 3D Printing of Gelatin Methacrylate-based Nerve Guidance Conduits with Multiple Channels. *Mater Des*, 192:108757. https://doi.org/10.1016/j.matdes.2020.108757
101. Ke X, Zhuang C, Yang X, *et al*., 2017, Enhancing the Osteogenic Capability of Core-Shell Bilayered Bioceramic Microspheres with Adjustable Biodegradation. *ACS Appl Mater Interf*, 9:24497–510. https://doi.org/10.1021/acsami.7b06798
102. Pistry P, Aied A, Alexander M, *et al*., 2017, Bioprinting Using Mechanically Robust Core–Shell Cell-Laden Hydrogel Strands. *Macromol Biosci*, 17:1600472. https://doi.org/10.1002/mabi.201600472
103. Taymour R, Kilian D, Ahlfeld T, *et al*., 2021, 3D Bioprinting of Hepatocytes: Core-shell Structured Co-cultures with Fibroblasts for Enhanced Functionality. *Sci Rep*, 11:5130. https://doi.org/10.1038/s41598-021-84384-6
104. Hong SY, Ji SK, Jung B, *et al*., 2019, Coaxial Bioprinting of Cell-laden Vascular Constructs Using a Gelatin-tyramine Bioink. *Biomater Sci*, 7:4578–87. https://doi.org/10.1039/c8bm00618k
105. Cui J, Wang H, Shi Q, *et al*., 2019, Multicellular Co-Culture in Three-Dimensional Gelatin Methacryloyl Hydrogels for Liver Tissue Engineering. *Molecules*, 24:1762. https://doi.org/10.3390/molecules24091762
106. Han X, Sun M, Chen B, *et al*., 2021, Lotus Seedpod-inspired Internal Vascularized 3D Printed Scaffold for Bone Tissue Repair. *Bioact Mater*, 6:1639–52. https://doi.org/10.1016/j.bioactmat.2020.11.019
107. Gao Q, Liu Z, Lin Z, *et al*., 2017, 3D Bioprinting of Vessel-like Structures with Multi-level Fluidic Channels. *ACS Biomater Sci Eng*, 3:399–408. https://doi.org/10.1021/acsbiomaterials.6b00643
108. Ma X, Xin Q, Wei Z, *et al*., 2016, Deterministically Patterned Biomimetic Human iPSC-Derived Hepatic Model Via Rapid 3D Bioprinting. *Proc Natl Acad Sci*, 113:2206. https://doi.org/10.1073/pnas.1524510113
109. Xie M, Yu K, Yuan K, *et al*., 2019, Protocols of 3D Bioprinting of Gelatin Methacryloyl Hydrogel Based Bioinks. *J Vis Exp*, 154:e60545. https://doi.org/10.3791/60545
110. Xue JM, Feng C, Xia LG, *et al*., 2018, Assembly Preparation of Multilayered Biomaterials with High Mechanical Strength and Bone-Forming Bioactivity. *Chem Mater*, 30:4646–57. https://doi.org/10.1021/acs.chemmater.8b01272
111. Mitsouras D, Liacouras P, Imanzadeh A, *et al*., 2015, Medical 3D Printing for the Radiologist. *Radiographics*, 35:1965–88. https://doi.org/10.1148/rg.2015140320
112. Hallem A, Javaid M, Saxena A, 2018, Additive Manufacturing Applications in Cardiology: A Review. *Egypt Heart J*, 70:433–41. https://doi.org/10.1016/j.ehj.2018.09.008
113. Odeh M, Levin D, Inziello J, *et al*., 2019, Methods for Verification of 3D Printed Anatomic Model Accuracy Using Cardiac Models as an Example. *3D Print Med*, 5:6. https://doi.org/10.1186/s41205-019-0043-1
114. Vukicevic M, Mosadegh B, Min JK, *et al*., 2017, Cardiac 3D Printing and its Future Directions. *Jacc Cardiovasc Imaging*, 10:171–84. https://doi.org/10.1016/j.jcmg.2016.12.001

115. Doucet G, Ryan S, Bartellas M, *et al*., 2017, Modelling and Manufacturing of a 3D Printed Trachea for Cricothyroidotomy Simulation. *Cureus*, 9:e1575. https://doi.org/10.7759/cureus.1575
116. Jin ZW, Li Y, Yu K, *et al*., 2021, 3D Printing of Physical Organ Models: Recent Developments and Challenges. *Adv Sci*, 2021:2101394. https://doi.org/10.1002/advs.202101394
117. Hollister SJ. Hollister SJ, 2005, Porous Scaffold Design for Tissue Engineering. *Nat Mater*, 4:518–24. https://doi.org/10.1038/nmat1421
118. Hutmacher DW, 2000, Scaffolds in Tissue Engineering Bone and Cartilage. *Biomaterials*, 21:2529–43. https://doi.org/10.1016/S0142-9612(00)00121-6
119. Vaz CM, Tuijl S V, Bouten C, *et al*., 2005, Design of Scaffolds for Blood Vessel Tissue Engineering Using a Multi-layering Electrospinning Technique. *Acta Biomater*, 1:575–82. https://doi.org/10.1016/j.actbio.2005.06.006
120. Ma PX, 2004, Scaffolds for Tissue Fabrication. *Mater Today*, 7:30–40. https://doi.org/10.1016/S1369-7021(04)00233-0
121. Zhang YS, Yue K, Aleman J, *et al*., 2017, 3D Bioprinting for Tissue and Organ Fabrication. *Ann Biomed Eng*, 45:148–63. https://doi.org/10.1007/s10439-016-1612-8
122. Yeo MG, Lee JS, Chun W, *et al*., 2016, An Innovative Collagen-Based Cell-Printing Method for Obtaining Human Adipose Stem Cell-Laden Structures Consisting of Core-Sheath Structures for Tissue Engineering. *Biomacromolecules*, 17:1365–75. https://doi.org/10.1021/acs.biomac.5b01764
123. Yeo MG, Ha JH, Lee HJ, *et al*., 2016, Fabrication of hASCs-laden Structures Using Extrusion-based Cell Printing Supplemented with an Electric Field. *Acta Biomater*, 38:33–43. https://doi.org/10.1016/j.actbio.2016.04.017
124. Xu T, Gregory CA, Molnar P, *et al*., 2006, Viability and Electrophysiology of Neural Cell Structures Generated by the Inkjet Printing Method. *Biomaterials*, 27:3580–8. https://doi.org/10.1016/j.biomaterials.2006.01.048
125. Xu F, Finley TD, Turkaydin M, *et al*., 2011, The Assembly of Cell-encapsulating Microscale Hydrogels Using Acoustic Waves. *Biomaterials*, 32:7847–55. https://doi.org/10.1016/j.biomaterials.2011.07.010
126. Koo Y W, Kim GH, 2016, New Strategy for Enhancing *In Situ* Cell Viability of Cell-printing Process Via Piezoelectric Transducer-assisted Three-Dimensional Printing. *Biofabrication*, 8:025010. https://doi.org/10.1088/1758-5090/8/2/025010
127. Koch L, Deiwick A, Chichkov B, 2014, Laser-based 3D Cell Printing for Tissue Engineering. *Bionanomaterials*, 15:71–8. https://doi.org/10.1515/bnm-2014-0005
128. Furukawa KS, Imura K, Tateishi T, *et al*., 2008, Scaffold-free Cartilage by Rotational Culture for Tissue Engineering. *J Biotechnol*, 133:134–45. https://doi.org/10.1016/j.jbiotec.2007.07.957
129. Keeney M, Pandit A, 2009, The Osteochondral Junction and its Repair via Bi-Phasic Tissue Engineering Scaffolds. *Tissue Eng Part B Rev*, 15:55–73. https://doi.org/10.1089/ten.teb.2008.0388
130. Zhang H, Huang H, Hao G, *et al*., 2020, 3D Printing Hydrogel Scaffolds with Nanohydroxyapatite Gradient to Effectively Repair Osteochondral Defects in Rats. *Adv Funct Mater*, 31:2006697. https://doi.org/10.1002/adfm.202006697
131. Amini AR, Laurencin CT, Nukavarapu SP, 2012, Bone Tissue Engineering: Recent Advances and Challenges. *Crit Rev Biomed Eng*, 40:363–408. https://doi.org/10.1615/critrevbiomedeng. v40. i5.10
132. Rezwan K, Chen QZ, Blaker JJ, *et al*., 2006, Biodegradable and Bioactive Porous Polymer/Inorganic Composite Scaffolds for Bone Tissue Engineering. *Biomaterials*, 27:3413–31. https://doi.org/10.1016/j. biomaterials.2006.01.039
133. Asadi N, Alizadeh E, Salehi R, *et al*., 2017, Nanocomposite Hydrogels for Cartilage Tissue Engineering: A Review. *Artif Cells Nanomed Biotechnol*, 46:465–71. https://doi.org/10.1080/21691401.2017.1345924
134. Chen J, Yang J, Wang L, *et al*., 2021, Modified Hyaluronic Acid Hydrogels with Chemical Groups that Facilitate Adhesion to Host Tissues Enhance Cartilage Regeneration. *Bioact Mater*, 6:1689–98. https://doi.org/10.1016/j.bioactmat.2020.11.020
135. Sun Y, You Y, Jiang W, *et al*., 2020, 3D Bioprinting Dual-factor Releasing and Gradient-structured Constructs Ready to Implant for Anisotropic Cartilage Regeneration. *Sci Adv*, 6:eaay1422. https://doi.org/10.1126/sciadv. aay 1422
136. Diloksumpan P, Castilho M, Gbureck U, *et al*., 2020, Combining Multi-Scale 3D Printing Technologies to Engineer Reinforced Hydrogel-ceramic Interfaces. *Biofabrication*, 12:025014. https://doi.org/10.1088/1758-5090/ab69d9
137. Kim SH, Yeon YK, Lee JM, *et al*., 2018, Precisely Printable and Biocompatible Silk Fibroin Bioink for Digital Light Processing 3D Printing. *Nat Commun*, 9:1620. https://doi.org/10.1038/s41467-018-03759-y

138. Hong H, Seo YB, Kim DY, *et al*., 2020, Digital Light Processing 3D Printed Silk Fibroin Hydrogel for Cartilage Tissue Engineering. *Biomaterials*, 232:119679. https://doi.org/10.1016/j.biomaterials.2019.119679
139. Bae H, Puranik A, Gauvin R, *et al*., 2012, Building Vascular Networks. *Sci Transl Med*, 4:160. https://doi.org/10.1126/scitranslmed.3003688
140. Nomi M, Atala A, Coppi PD, *et al*., 2003, Principals of Neovascularization for Tissue Engineering. *Mol Aspect Med*, 23:463–83. https://doi.org/10.1016/s0098-2997(02)00008-0
141. Novosel EC, Kleinhans C, Kluger PJ, 2011, Vascularization is the Key Challenge in Tissue Engineering. *Adv Drug Deliv Rev*, 63:300–11. https://doi.org/10.1016/j.addr.2011.03.004
142. Zhang YS, Khademhosseini A, 2015, Seeking the Right Context for Evaluating Nanomedicine: From Tissue Models in Petri Dishes to Microfluidic Organs-on-a-Chip. *Nanomedicine*, 10:685–8. https://doi.org/10.2217/nnm.15.18
143. Jia W, Gungor-Ozkerim PS, Yu SZ, *et al*., 2016, Direct 3D Bioprinting of Perfusable Vascular Constructs Using a Blend Bioink. *Biomaterials*, 106:58–68. https://doi.org/10.1016/j.biomaterials.2016.07.038
144. Suntornnond R, Tan E, An J, *et al*., 2017, A Highly Printable and Biocompatible Hydrogel Composite for Direct Printing of Soft and Perfusable Vasculature-like Structures. *Sci Rep*, 7:16902. https://doi.org/10.1038/s41598-017-17198-0
145. Zhang Y, Yu Y, Chen H, *et al*., 2013, Characterization of Printable Cellular Micro-fluidic Channels for Tissue Engineering. *Biofabrication*, 5:025004. https://doi.org/10.1088/1758-5082/5/2/025004
146. Isakoff MS, Bielack SS, Meltzer P, *et al*., 2015, Osteosarcoma: Current Treatment and a Collaborative Pathway to Success. *J Clin Oncol*, 33:3029–35. https://doi.org/10.1200/JCO.2014.59.4895
147. Italiano A, Mir O, Cioffi A, *et al*., 2013, Advanced Chondrosarcomas: Role of Chemotherapy and Survival. *Ann Oncol*, 24:2916–22. https://doi.org/10.1093/annonc/mdt374
148. Gaspar N, Hawkins DS, Dirksen U, *et al*., 2016, Ewing Sarcoma: Current Management and Future Approaches Through Collaboration. *J Clin Oncol*, 33:3036–46. https://doi.org/10.1200/JCO.2014.59.5256
149. Smeland S, Bielack SS, Whelan J, *et al*., 2019, Survival and Prognosis with Osteosarcoma: Outcomes in more than 2000 Patients in the EURAMOS-1 (European and American Osteosarcoma Study) Cohort. *Eur J Cancer*, 109:36–50. https://doi.org/10.1016/j.ejca.2018.11.027
150. Hu MC, Yao ZH, Liu XG, *et al*., 2018, Enhancement Mechanism of Hydroxyapatite for Photocatalytic Degradation of Gaseous Formaldehyde over TiO_2/Hydroxyapatite. *J Taiwan Inst Chem Eng*, 85:91–7. https://doi.org/10.1016/j.jtice.2017.12.021
151. Kebede MA, Asiku KS, Imae T, *et al*., 2018, Stereolithographic and Molding Fabrications of Hydroxyapatite-polymer Gels Applicable to Bone Regeneration Materials. *J Taiwan Inst Chem Eng*, 92:91–6. https://doi.org/10.1016/j.jtice.2018.01.034
152. Huang L, Lu W, Liu M, *et al*., 2017, Facile Preparation of Eu^{3+} and F co-Doped Luminescent Hydroxyapatite Polymer Composites via the Photo-RAFT Polymerization. *J Taiwan Inst Chem Eng*, 83:184–91. https://doi.org/10.1016/j.jtice.2017.12.006
153. Mehdi R, Amir S, Mohammad MD, *et al*., 2019, Multifunctional Gelatin Tricalcium Phosphate Porous Nanocomposite Scaffolds for Tissue Engineering and Local Drug Delivery: *In Vitro* and *In Vivo* Studies. *J Taiwan Inst Chem Eng*, 101:214–20. https://doi.org/10.1016/j. jtice.2019.04.028
154. Cheng L, Wang C, Feng L, *et al*., 2014, Functional Nanomaterials for Phototherapies of Cancer. *Chin J Clin Oncol*, 114:10869–939. https://doi.org/10.1021/cr400532z
155. Ma H, Jiang C, Dong Z, *et al*., 2016, A Bifunctional Biomaterial with Photothermal Effect forTumor Therapy and Bone Regeneration. *Adv Funct Mater*, 26:1197–208. https://doi.org/10.1021/cr400532z
156. Qu Y, Chu BY, Peng JR, *et al*., 2015, A Biodegradable Thermo-responsive Hybrid Hydrogel: Therapeutic Applications in Preventing the Post-operative Recurrence of Breast Cancer. *Npg Asia Mater*, 7:e207. https://doi.org/10.1038/am.2015.83
157. Wang X, Li T, Ma H, *et al*., 2017, A 3D-printed Scaffold with MoS2 Nanosheets for Tumor Therapy and Tissue Regeneration. *Npg Asia Mater*, 9:e376. https://doi.org/10.1038/am.2017.47
158. Liu HH, Lin ML, Liu X, *et al*., 2020, Doping Bioactive Elements into a Collagen Scaffold Based on Synchronous Self-assembly/Mineralization for Bone Tissue Engineering. *Bioactive Mater*, 5:844–58. https://doi.org/10.1016/j. bioactmat.2020.06.005
159. Wang XC, Xue JM, Ma B, *et al*., 2020, Black Bioceramics:

Combining Regeneration with Therapy. *Adv Mater*, 32:e2005140.
https://doi.org/10.1002/adma.202005140

160. Bo L, Wang X, Lei C, *et al*., 2018, Ultrathin Cu-TCPP MOF Nanosheets: A New Theragnostic Nanoplatform with Magnetic Resonance/Near-infrared Thermal Imaging for Synergistic Phototherapy of Cancers. *Theranostics*, 8:4086–96.
https://doi.org/10.7150/thno.25433

RESEARCH ARTICLE

Ecologically Friendly Biofunctional Ink for Reconstruction of Rigid Living Systems Under Wet Conditions

Alan Avila-Ramírez[1], Alexander U. Valle-Pérez[1], Hepi Hari Susapto[1], Rosario Pérez-Pedroza[1], Giuseppina R. Briola[1], Abdulelah Alrashoudi[1], Zainab Khan[1], Panayiotis Bilalis[1], Charlotte A. E. Hauser[1,2]*

[1]Laboratory for Nanomedicine, Division of Biological and Environmental Science and Engineering, King Abdullah University of Science and Technology, Thuwal 23955-6900, Saudi Arabia
[2]Computational Bioscience Research Center (CBRC), King Abdullah University of Science and Technology, Thuwal 23955-69900, Saudi Arabia

Abstract: The development of three-dimensional (3D)-printable inks is essential for several applications, from industrial manufacturing to novel applications for biomedical engineering. Remarkably, biomaterials for tissue engineering applications can be expanded to other new horizons; for instance, restoration of rigid living systems as coral reefs is an emergent need derived from recent issues from climate change. The coral reefs have been endangered, which can be observed in the increasing bleaching around the world. Very few studies report eco-friendly inks for matter since most conventional approaches require synthetic polymer, which at some point could be a pollutant depending on the material. Therefore, there is an unmet need for cost-effective formulations from eco-friendly materials for 3D manufacturing to develop carbonate-based inks for coral reef restoration. Our value proposition derives from technologies developed for regenerative medicine, commonly applied for human tissues like bone and cartilage. In our case, we created a novel biomaterial formulation from biopolymers such as gelatin methacrylate, poly (ethylene glycol diacrylate), alginate, and gelatin as scaffold and binder for the calcium carbonate and hydroxyapatite bioceramics needed to mimic the structure of rigid structures. This project presents evidence from 2D/3D manufacturing, chemical, mechanical, and biological characterization, which supports the hypothesis of its utility to aid in the fight to counteract the coral bleaching that affects all the marine ecosystem, primarily when this is supported by solid research in biomaterials science used for living systems, it can extend tissue engineering into new approaches in different domains such as environmental or marine sciences.

Keywords: Bioprinting; Biopolymers; Bioceramics; Rigid tissue; Crosslinking; Ecofriendly

*Correspondence to: Charlotte A. E. Hauser, Laboratory for Nanomedicine, Division of Biological and Environmental Science and Engineering, King Abdullah University of Science and Technology, Thuwal 23955-6900, Saudi Arabia; charlotte.hauser@kaust.edu.sa

Received: June 15, 2021; **Accepted:** July 21, 2021; **Published Online:** August 19, 2021

Citation: Avila-Ramírez A, Valle-Perez AU, Susapto HH, *et al.,* 2021, Ecologically Friendly Biofunctional Ink for Reconstruction of Rigid Living Systems Under Wet Conditions. *Int J Bioprint*, 7(4):398. http://doi.org/10.18063/ijb.v7i4.398

1. Introduction

Biomaterials have been essential elements in developing technologies that counteract the current issues in the biomedical field[1]. On the other hand, there is a strong interest from the industry to create new technologies based on eco-friendly biopolymers that can be cost-effective for the current needs in the market[2]. Therefore, several studies coming from the development of biomaterials are a trending topic for medical applications. Researchers commonly look for natural sources that could potentially be chemically and physically modified to surpass their ground state behavior[3]. A couple of examples are gelatin and alginate as one of the classic materials for tissue regeneration. Gelatin comes from inexpensive natural sources; on the other side, alginate has ionic-crosslinking behavior that permits crosslinking with cations such as calcium. Both biopolymers are used for cartilage

replacements, bone regeneration, drug delivery, and even exciting uses for molecular gastronomy. Gelatin usually works as a viscous platform to bind other elements of interest.

Nevertheless, to expand the functionality of these materials in tissue engineering, the methacrylation reaction has been studied; in this case, the functionalization of gelatin can be photo-crosslinked by different wavelengths, depending on the photoinitiator (PI) used. This physicochemical improvement has permitted the usage of novel biofrabrication techniques[4]. Besides applications in wound dressings and hard tissues, cartilages or bones have been implemented with gelatin methacrylate (GelMA), with reinforcements with bioceramics as hydroxyapatite and other sort of inorganic particles[5,6]. In addition, poly (ethylene glycol diacrylate) (PEGDA) has been widely implemented due to its fast end effective crosslinking behavior, which can work as a complement to other photo-cross-linkable polymers[7].

Innovation should not be stuck in just a particular direction; conversely, there are other biological issues that our world is currently facing. Therefore, it is crucial to take action to adopt eco-friendly applications that could counteract problems derived from climate change. Thus, we aim to expand tissue engineering applications into a broader range of goals in this project. For instance, one of the most significant burdens from the environmental and marine sciences is coral bleaching, that in other words can be considered the disruption of a symbiosis that consists of a robust and rigid system of calcium carbonate with the living beings, which are mainly species of polyps derived from heat wave and changes in the marine ecosystem that bleaches the colonies and have strong effects in the marine biota[8,9]. For this reason, many groups around the world has started to take an interest in creating and developing new formulations and taking advantage of new innovative materials to counteract environmental problems as a way of preventing more extensive problems that will jeopardize the lives of human beings in the future[10,11]. Therefore, in this project, biopolymers as gelatin, alginate, gelatin methacrylate (GelMA), and poly (ethylene glycol diacrylate) (PEGDA) are reinforced with bioceramics as calcium carbonate and hydroxyapatite. This unique formulation can assist the growth of hard-living systems, like corals, as an innovative technology that ionic/photo-crosslink, which makes it adaptable to new 3D manufacturing technologies and can withstand under wet conditions (**Figure 1**).

2. Materials and methods

The following materials and reactants are necessary for obtaining the biopolymer base and bioceramics to develop the final paste and subsequently realize the fundamental characterization. The final formulation is homogenized into two main parts. The initial one is the biopolymer base that works as a binder and crosslinking material. The second is the bioceramics side that will reinforce the paste and mimic the paste hard-living structure, a standard coral. The materials used include GelMA (synthesized), gelatin from porcine skin (Sigma-Aldrich), alginic acid (Merck), PEGDA (Sigma-Aldrich), lithium phenyl-2,4,6 trimethyl-benzoyl phosphinate (Sigma-Aldrich), milli-Q water, hydroxyapatite (Sigma-Aldrich), calcium carbonate (Sigma Aldrich), dimethyl sulfoxide (DMSO) (Sigma-Aldrich), Dialyzer Maxi, molecular weight cut off (MWCO) 12 – 14 kDa (Merck), 0.22 μm bottle top vacuum filter (Corning), DMSO for Nuclear Magnetic Resonance (NMR) (Sigma-Aldrich), phosphate-buffered saline (PBS), pH 7.4 (Sigma-Aldrich), and syringe pump (Harvard Apparatus).

2.1. High GelMA (H-GelMA) synthesis

For a high degree of methacrylation of GelMA (**Figure S1**), that is, 10 g of gelatin, 100 mL 1 × PBS (sterile) was added. The mixture was dissolved with the aid of a heating plate (~240 rpm at 50°C). 8 mL of methacrylic anhydride was added dropwise with the assistance of a syringe pump and let emulsion rotate (240 rpm) at 50°C for 2 h. 100 mL of sterile PBS (50°C) was preheated to dilute GelMA solution for 10 min at 50°C. The dialysis membrane (MWCO 12-14,000 kDa) was prepared at 40°C, and GelMA solution was inserted inside them; dialysis was allowed to go on for a minimum of 5 days with constant stirring. The water was changed from 1 to 2 times a day to eliminate the excess methacrylate ions and dispose of the residue in a regulated container. A sterile vacuum (0.22 μm) filtration cup was used to filter the liquid. Sterilized polymer was transferred into Falcon tubes. Semi-closed tubes were submerged in liquid nitrogen and freeze-dried for at least 5 days to get a sponge-like freeze-dried GelMA sample[12].

2.2. Biopolymer-base preparation

Depending on the volume required to prepare and the percentages stated in **Table 1**, freeze-dried H-GelMA, gelatin, alginate, and PEGDA were dissolved in Milli-Q with constant stirring to dissolve the final solution. Using a heath bath is recommended to melt the solution at a temperature of the maximum of 50°C. A higher temperature can modify the molecular behavior of the four polymer chains and jeopardize the accuracy of printability. Then, the PI was added (Lithium phenyl-2,4,6 trimethylbenzoylphosphinate) to the previous solution. To avoid the interaction with light that triggers crosslinking reaction, it is recommended to cover it with aluminum foil. This base can be kept at −20°C for more extended periods if there is no interaction with light that could trigger gelation.

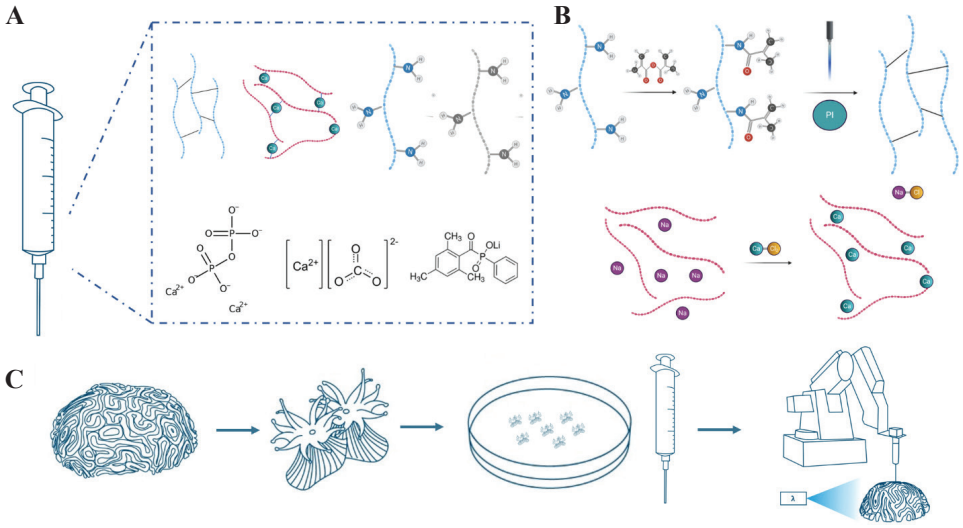

Figure 1. Explanation from the project's scope. (A) Integration of biopolymers gelatin, alginate, gelatin methacrylate, poly (ethylene glycol diacrylate), and bioceramics calcium carbonate and hydroxyapatite for potential rigid-living systems. (B) Schematics from the two primary sources of crosslinking to enhance printability, ionic-crosslinking with cations such as calcium and photo-crosslinking with a wavelength range from 365 nm to 405 nm. (C) The proposal for a potential future application with this material for rigid-living systems can be manufactured with extrusion-based 3D printing technologies.

Table 1. Formulation from the complete ink.

Biopolymer base	**Percentage W/W**	**Weight by cartridge sample**	**Purpose**
High gelatin methacrylate (H-GelMA)	2.50%	0.25 g.	Photo-crosslinking and printability
Poly (ethylene glycol diacrylate) (PEGDA) 700 MW	2.50%	0.25 g. ≈ 0.25 mL	Increase speed rate of photo-crosslinking
Alginic acid (Alg) Low MW	2.50%	0.25 g	Ionic-crosslinking with calcium
Gelatin (Gel)	2.50%	0.25 g	Viscosity for pre-crosslinked paste
Lithium phenyl-2,4,6 trimethylbenzoylphosphinate (LAP)	0.15%	0.015g	Photoinitiation 365(UV) – 405 (blue) nm
Bioceramics	**Percentage W/W**	**Weight in 10 mL.**	**Purpose**
Hydroxyapatite (HA)	40%	4 g	Density for under wet conditions
Calcium carbonate (CaCO3)	40%	4 g	Mimic coral chemical Structure
Solvent	**Quantity**	**Quantity**	**Purpose**
Milli-Q water	10 mL	10 mL	Dissolve

2.3. Bioceramics reinforcement

The quantity of bioceramics needed for the formulation is presented in **Table 1,** imbued at the biopolymer-based solution prepared previously. Solid and constant stirring with a thin spatula is crucial as the final homogenous product will be viscous, similar to a commercial bone paste. It is recommended to start 3D printing protocols with the fresh material to avoid premature crosslinking with the light or natural desiccation of water. The formulation is intended to be cost-effective because the biopolymer part from the formulation was designed at minimal concentrations without compromising its crosslinking properties and printing fidelity, relying on inexpensive materials for commercial 3D manufacturing technologies.

2.4. Manufacturing

Two methodologies were used for 3D manufacturing. The first one was molding of a flexible resin; it is designed in different designs derived from real branched and brain corals obtained in the red sea. The second one is 3D printing based on the implementation of two systems: A pressure-based bioprinter Inkredible from the Cellink company and the designed 6-°-of-freedom robotic arm system developed for bioprinting applications at our research group[13].

2.5. Image processing for 3D printing

The similarity structural index measurement (SSIM) was measured by comparing pixels between images (**Figure S2**); it can be visually seen how the comparison is made between two fixed figures to get this numerical value[14]. The response surface methodology (RSM) was applied to evaluate the effect of enhancing the developed ink with hydroxyapatite and calcium carbonate over the structural similarity index from the printed structure. According to the statistical modeling reported in recent studies[15,16], the elaboration of the RSM was performed with the MATLAB® software, and the model's constants were obtained with the Minitab 18 software (Minitab® LLC, USA). The general model is presented in **Equation 1**, and the simplified resulting model is shown in **Equation 2**.

$$\gamma = \delta_0 \pm \delta_1\alpha \pm \delta_2\beta \pm \delta_3\alpha^2 \pm \delta_4\beta^2 \pm \delta_5(\alpha\beta) + \varepsilon_{ijk} \quad (1)$$

Equation 1. A general model for the effect of hydroxyapatite and calcium carbonate over the structural similarity index of the printed structure; where Y is the response and α,β are the factors of the model, $\delta_{0,1,2,3,4,5}$ represent the constants of the model, and ε_{ijk} is the total error.

$$\gamma = \delta_0 + \delta_1\alpha - \delta_2\beta - \delta_3\alpha^2 + \delta_4\beta^2 \; ; \; \frac{\partial\gamma}{\partial i} = \varphi_i \quad (2)$$

Equation 2. A simplified model for the effect of hydroxyapatite and calcium carbonate over the structural similarity index of the printed structure; where Y is the response and α,β are the factors of the model, $\delta_{0,1,2,3,4}$ the constants of the model, i represents any of the two factors, and ϕ_i the solved values from the partial derivatives.

2.6. Morphological imaging

The scanning electron microscope FEI Magellan extreme-high-resolution imaging was applied to a grid of the 3D printed formulation, crosslinked, and dried overnight, with an accelerating voltage of 3 kV. The dried peptides were sputter-coated with 5 nm Ir before imaging. An optical microscope was used to obtain the macrography with a source of light in the upper side from the sample.

2.7. Chemical characterization

For Fourier-transform infrared (FTIR) spectroscopy, a Thermo Nicolet iS10 FTIR Spectrometer (Thermofisher) was used; the samples were prepared and crosslinked by two different sources individually compared to control with exposure at room conditions. For Solid-State NMR, the 13C Magic Angle Spinning (MAS) NMR spectra were recorded using Bruker Avance 400 MHz spectrometer (Bruker, USA) at room temperature. The sample was lyophilized. Bruker Topspin 3.5pl7 software (Bruker BioSpin, Rheinstetten, Germany) and MestReNova (Mestrelab Research, Spain) were used for data collection and analysis. In addition, Solution-State NMR, the NMR spectra (1H and 13C) of biopolymer-base were recorded using Bruker Avance 400 MHz spectrometer (Bruker, USA) at room temperature. The sample was prepared to dissolve 5 mg powder in 500 µl of d6-DMSO (Cambridge Isotope Laboratories, USA) and then transferred into 5 mm NMR tubes. Bruker Topspin 3.5pl7 and MestReNova software were used for data collection and processing, respectively, of NMR of H-NMR, C-NMR for the solid and liquid state, the PI was not added as it behaves similar to paramagnetic species; therefore, the equipment will not detect any significant signal. A complete sample of a printed coral was ground for X-ray diffraction compared with bioceramics spectra. For thermochemical characterization, both thermogravimetric analysis (TGA) and differential scanning calorimetry (DSC) (TA Instruments), the final printed inks were ground and analyzed by both instruments. Around 20 mg of material were used for each sample. The ranges of temperatures used, were 25-850°C for TGA and 25-400°C for DSC.

2.8. Viscoelastic characterization

The mechanical properties of non-crosslinked ink were analyzed using TA Ares-G2 Rheometer equipped with Advanced Peltier System. A freshly prepared ink was measured using an 8 mm parallel plate with a 1.8 mm gap at 25°C. The stiffness was analyzed through a time-sweep test for 5 min with angular frequency and one rad/s and 0.1% strain, respectively. A temperature sweep was subsequently performed on the sample by applying a gradual temperature increase from 25°C to 50°C with similar angular frequency and strain.

The viscosity of the ink before crosslinking was determined using 25 mm parallel plate geometry with a 0.5 mm gap at 25°C. Three replicate samples were measured using a 25 mm parallel plate geometry with a gap of 0.5 mm at 25°C. The flow experiment was set up by starting the shear rate from 0.001 to 300 s^{-1} for a 600-s duration. The value of the shear rate that we choose for our printing system was calculated using the equation below[17,18]:

$$\gamma = \frac{8Q}{\pi d^3} \quad (3)$$

Equation 3. γ: shear rate (s^{-1}); Q: flow rate (2 µL/s); d: diameter of needle (0.84 mm).

2.9. Biological assessments

Undifferentiated mesenchymal stem cells (MSCs) were seeded at a density of 15.5E3 cells/cm^2 and incubated for 7 days (5% CO_2, 37°C) in supplemented DMEM-F12

medium. The media were changed on the 4th day. Then, the treated cells were cultivated together with a droplet of 10 µL of crosslinked bioink. As a blank, a droplet was incubated in the same conditions, with no cells. As a control, cells were cultured without a droplet of bioink. The cells proliferation was measured using Alamar Blue (Invitrogen, CAT: DAL1025) by adding 1/10th of the volume directly to the cells, followed by 2 h of incubation. Fluorescence was read in a PheraStar plate reader (Ex/Em: 485/520). The cell viability was evaluated using the Live/Dead assay (Invitrogen, CAT: L3224).

3. Results and discussion

The ink was printed in an extrusion-based 3D printing at a pre-crosslinked state with the aid of the robotic arm system. In this example, several layers can be printed one over another without collapsing. Moreover, with the aid of blue light, crosslinking can aid in printing to invent more complex structures. For this case, we demonstrated that it could be done even at the ground state behavior from the formulation. For instance, with the incidence of blue light, the printed structure can be easier to manufacture and is more stable in the air or under wet conditions. An underwater printing test was done; a 2D structure of a grid and another at undersea water of the KAUST (**Figure 2C**) was printed and kept after 12 weeks in seawater. The printed structure did not have visible degradation and was derived from the photo-crosslinking of PEGDA and GelMA and ionic-crosslinking of alginate with calcium ions found in the filtered water obtained from the Red Sea, permitting the appliance of this material directly in damaged coral reefs.

In addition, as printing takes significant amounts of time, we established a 3D molding protocol. The ink was directly poured into the negative molds obtained from natural coral structures, where these samples were dried at room temperature overnight. These structures coming from the mold were rigid and complex. Consequently, this is a cost-effective methodology that does not require robust equipment.

During the formulation development, we noticed that the ink was enhanced by adding hydroxyapatite (to improve the under-water stability property) and calcium carbonate (to increase the stiffness from the

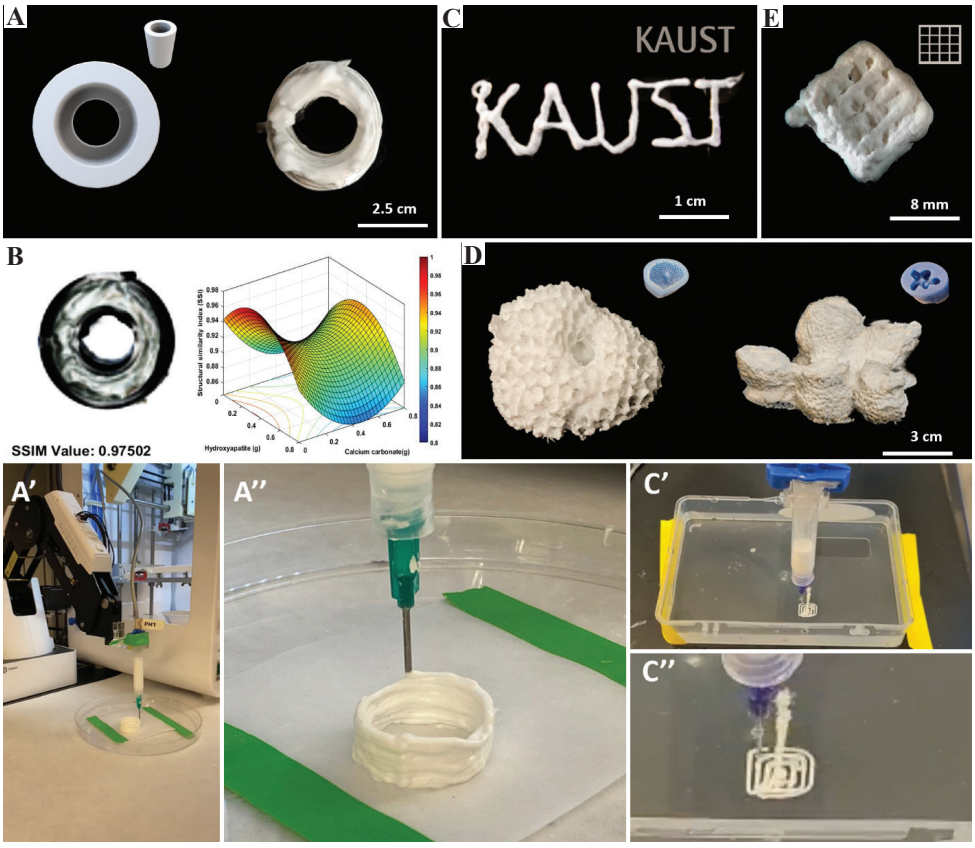

Figure 2. 2D/3D fabrication. (A-A") 3D printing of a 50-layer cylindric structure with the aid of an assembled 6-degree-of-freedom robotic arm system coupled with an extrusion-based bioprinter. (B) The image processing technique that is used to obtain a SSIM. (C-C") Manufacturing under wet conditions of structure KAUST one-layer structure and a squared-grid. (D) Molded structures dried at room temperature overnight. (E) Squared grid printed and details at millimetric scale after crosslinking and desiccation. Videos from A and C are included in the supplementary file.

printed or molded objects). It was observed that the integration of these two components to the original ink composition affected the overall structural definition of the printed objects (**Figure 2**). The contour plot representation of the surface response graph can be found as part of the supplementary material (**Figures S3 and S4**). The original ink exhibited a structural definition between 0.92 and 0.94; however, it was found that the definition could be improved (SSIM >0.95) by the addition of 0.1 g/cm^3 – 0.6 g/cm^3 of hydroxyapatite (**Figure 2**). On the other hand, the addition of calcium carbonate resulted in a lower structural definition (Soil-structure interaction [SSI] <0.92). Nevertheless, it was found that when adding both: calcium carbonate and hydroxyapatite, the structural definition from the printed object could be preserved (SSIM >0.92), even with the presence of the calcium carbonate in ink, possible when simultaneously adding 0.1 g/cm^3 – 0.2 g/cm^3 of calcium carbonate and 0.1 g/cm^3 – 0.6 g/cm^3 of hydroxyapatite (**Figure 2**). Similarly, the addition of 0.8 g/cm^3 ^{g} of calcium carbonate and 0.2 g/cm^3 – 0.6 g/cm^3 of hydroxyapatite resulted in a high structure definition. It is essential to highlight that adding beyond 0.7 g/cm^3 of hydroxyapatite in the presence of calcium carbonate reduces the structure definition (SSI <0.875) of the printed object (**Figure S3 and S4**). Therefore, the development of enhanced inks for under seawater printing without losing their printing definition can be carried by adding these two components to the original ink according to the previously described maximization conditions.

It is essential to clarify that due to the loss of solvent derived from room temperature desiccation, the structure was slightly deformed; however, as the solvent corresponds to a minimal portion compared to the rest of the constituents. For this reason, a fast image processing test was done, arrowing 97.5% similarity between a 3D printed cylinder of 50 layers after crosslinking and desiccation (**Figure 2B**). This analysis is an innovative way to characterize printing fidelity. Nevertheless, more improvements in the technique could be made in further studies to get more accurate results.

This ink was designed to a helpful a carrier for biological cargo in different orders of magnitude, depending on the biological species of interest that could go from 50 mm (corroborated at **Figure 7**) until the printing resolution of the assembled 3D printing system that experimentally was 1 mm (**Figure 3)**. In the scanning electron microscope images (**Figure 3B**), the binding from the polymer can be an attachment from the calcium carbonate and hydroxyapatite round crystals; GelMA and gelatin offer the porous platform to get the crystals incrusted due to its long polymer chains at a molecular level[19-21].

FT-IR corroborated the two crosslinking behaviors from the ink **(Figure 4A**); one clear result from the ionic-crosslinking comes from the OH peak observed at 3300 cm^{-1}, that states the covalent bonding between hydroxyl groups in alginic acid polysaccharides. The photo-crosslinked material and the exposure at room conditions are similar because the photoinitiation with a wavelength in the spectrum related to blue light can come from regular exposure to light; therefore, crosslinking occurs at a lower rate. Evidence from this is the peaks from N-H and C-H at 2950 cm^{-1} and 2990 cm^{-1}. Finally, carbonate

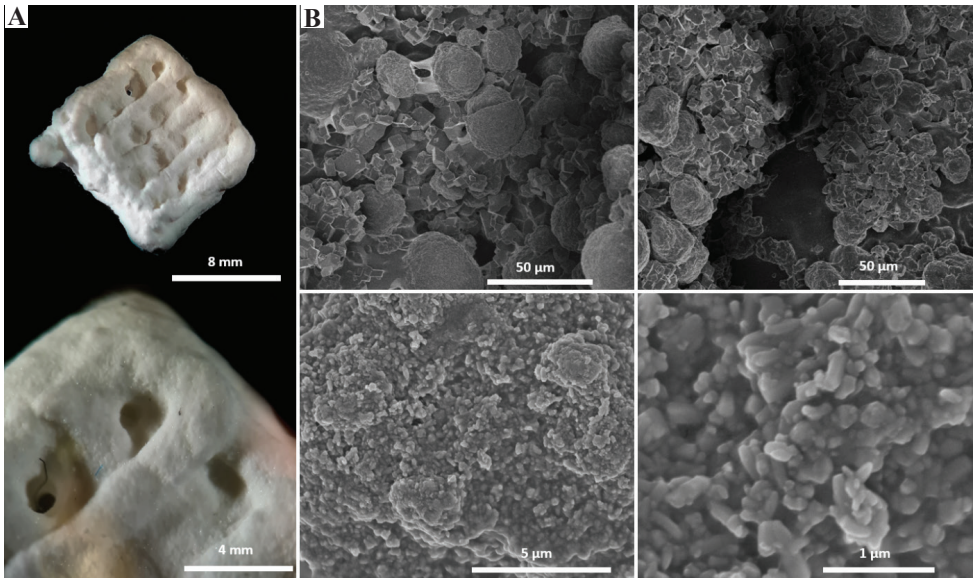

Figure 3. Morphological studies of a 3D dried printed grid. (A) Demonstration of the feasibility of printing at a resolution of approximately 1 mm, with the aid of a commercial extrusion-based bioprinter. (B) Scanning electron microscope (SEM) image of the same grid at the microscale at different sizes. To see the morphology of the surface and the binding from the bioceramics crystals to the polymer.

and phosphate ions appear in the 1400 cm^{-1} and 1000 cm^{-1} peaks, referring to bioceramics in the sample.

The peaks from XRD (**Figure 4B)** represent the mixture of bioceramics components from the ink. This study helped us understand ceramics' chemical interaction with the natural base polymer to corroborate its crosslinking behavior and binding with the polymer base[22,23]. Therefore, in the final formulation analysis, both calcium carbonate and hydroxyapatite peaks remained unaltered compared to the crystals from both bioceramics components, stating no crystal rearrangement or direct modification contact with the polymer source. Besides, the calcium carbonate peaks at 23°, 29°, 36°, 39°, 43°, 47°, 48°, and 58° correspond to a crystal structure reported in the literature as calcite, remarkably seen at the strong peak from 29°[24]. On the other side, hydroxyapatite's most representative signals appear at 26°, 32°, 39°, and 49° highlighting the intensity of the ones in between 30 and 35 that usually appears stronger according to the literature, and both of them can be observed in the supplementary measurements (**Figure S5)** where XRD was done just to each independent bioceramics[25].

The biopolymer structure was investigated using ^{13}C solid-state NMR spectroscopy. The differences between ^{13}C MAS NMR spectra (**Figure 4C)** of the sample without and with bioceramics can be distinguished. The most significant result is the double peak (blue box) appears between 155 and 135 ppm, which correspond to C=CH that result of the interaction of a C group from the polymer attached to carbonate ions from the sample[26].

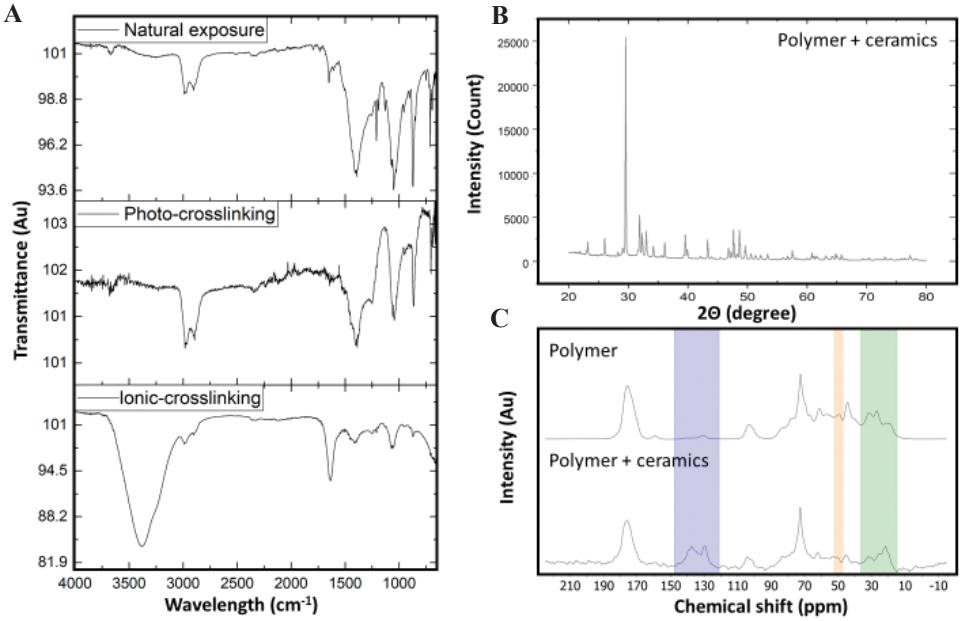

Figure 4. (A) Fourier-transform infrared spectra from the formulation under different crosslinking conditions, initially in room temperature conditions, with the incidence of blue-light at 405 nm and ionic-crosslinking with calcium chloride at 6% solution. (B) XRD-P spectra from ink formulation of the biopolymers and bioceramics. (C) ^{13}C magic angle spinning nuclear magnetic resonance spectra of biopolymers without (above) and with (below) bioceramics.

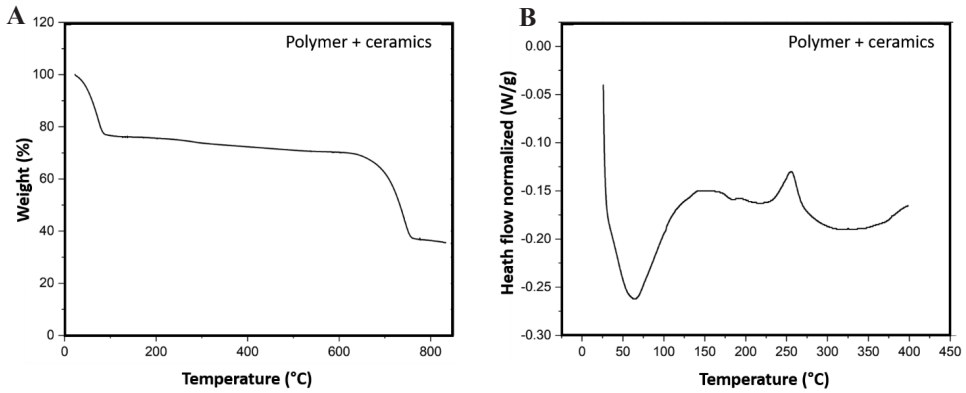

Figure 5. Thermal Analysis. (A) TGA and (B) DSC thermograms of bioceramics incorporated in the biopolymer base.

The rise in the orange box, at 50 ppm, and the green box, between 35 and 25 ppm, disappears when there are bioceramics; therefore, these signals are a piece of evidence from the interaction of binding from inorganic components of calcium, phosphate, and carbonate ions to the biopolymer side from the formulation. This data can be corroborated in future studies with ^{31}P MAS NMR and ^{43}Ca MAS NMR[27,28]. Besides, in ^{1}H-NMR (**Figure S6**), it can be complemented the presence of the methacrylation functionalization of the GelMA synthesis and PEGDA integration as the methacrylate ions can be observed between 6 and 6.5 ppm[28,29].

In the TGA (**Figure 5A**), there is a reduction of 13% of weight from 90°C to 100°C due to the loss of H_2O-coordinated ions remaining in the crystalline arrangements of ceramics compressed with the polymer. From 100°C to 642°C, there is a loss of 10% from the sample, equivalent to the biopolymers that were calcined under this procedure; this variation comes from the different polymeric ionic/photo-crosslinking behaviors

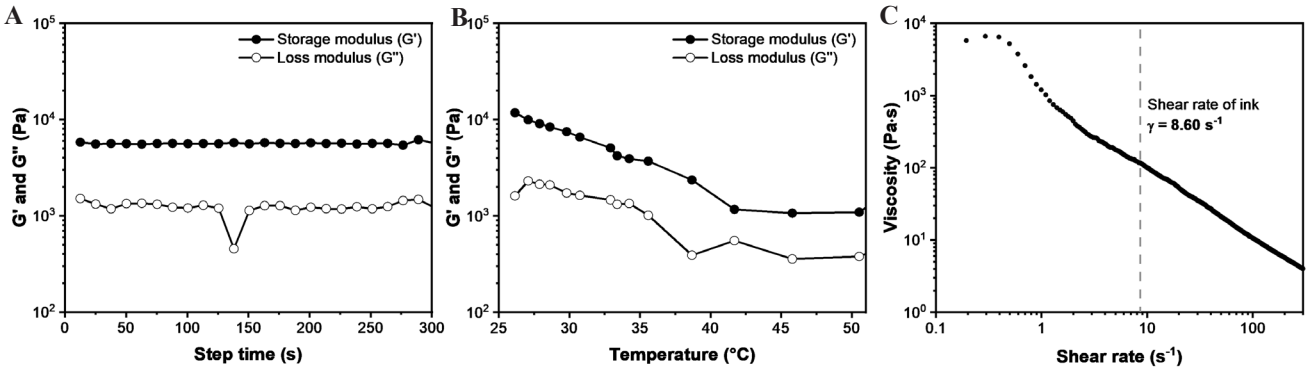

Figure 6. Rheological characterization of non-crosslinked ink. (A) Storage modulus (G') and loss modulus (G'') were measured for 5 min at 1 rad/s angular frequency, 0.1% strain, and 25°C. (B) Temperature sweep test at 1 rad/s and 0.1% strain. (C) Viscosity at different shear rates.

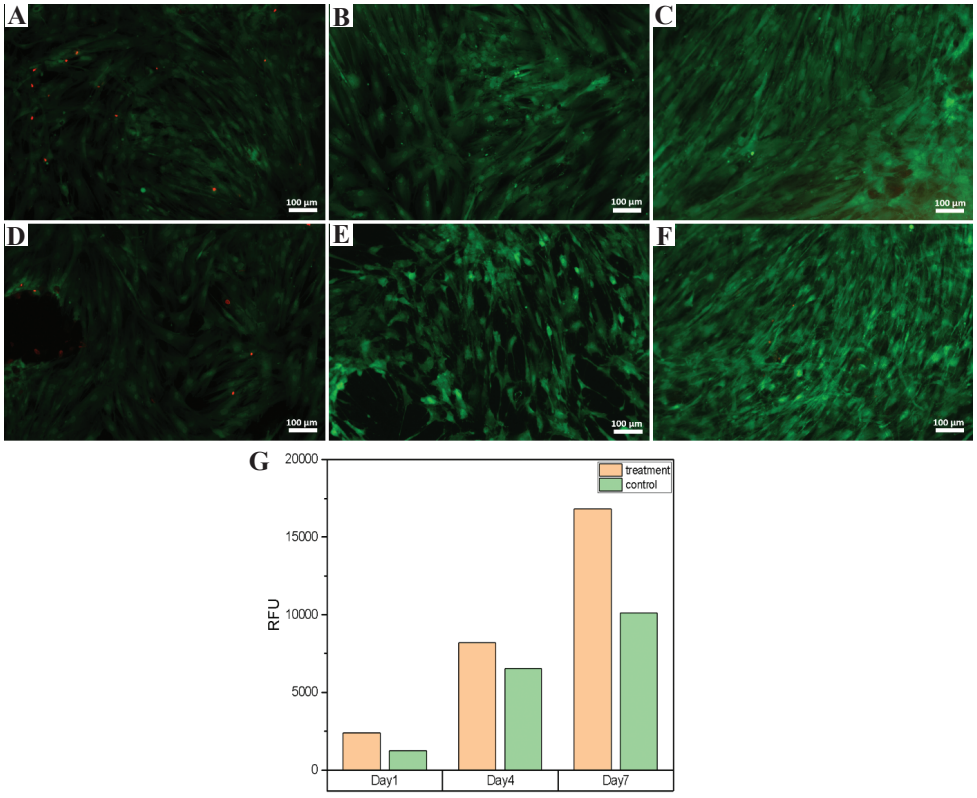

Figure 7. Biological assessments. Growth of MSCs cultured in direct contact with the developed ink during (A) 1, (B) 4, and (C) 7 days. The cells were also cultured in 2D for the same amount of time; (D), (E), and (F) served as the control. (G) Amount of metabolically active MSCs during 1, 4, and 7 days. These cells were cultured with the ink (treatment) and with growth media (control). The assay was quantified in terms of relative fluorescence units (RFU).

of the components. The final loss from the 39% of the material comes from the calcium carbonate in the sample; the rest comes from some residues from hydroxyapatite; which is the strongest component to decompose by heat in this formulation[23]. In the DSC (**Figure 5B**), as several distinct chemical behaviors are coming from different sources of crosslinking and the inorganic composition, the initial broad peak corroborates the TGA statement of dehydration. Furthermore, it can be stated that a glass transition (Tg) can be observed in the shoulder at 175°C, a slight crystallization point (Tc) can be observed at the exothermic downslide at 225°C, and finally a melting point (Tm), presumably all organic compounds coming from biopolymers, can be detected at 260°C in the endothermic peak[30].The viscoelastic properties of the ink were determined using an oscillatory rheology test. The mechanical stiffness of the non-crosslinked ink was found to be 5.80 kPa, which was assessed from the average of storage modulus (G') in 5 min measurement (**Figure 6A**). The ink with a higher G' value compared to the loss modulus (G'') usually provides good shape fidelity for the printed construct[18]. The thermal stability of the ink was also investigated using a temperature-dependent rheological test (**Figure 6B**). The result suggests that the stiffness of the ink can be tuned by increasing the temperature. The viscosity of the ink during the extrusion was found to be 117 Pa·s, which was determined from the calculated shear rate of the nozzle of 8.60 s^{-1} (**Figure 6C**).

The biological assessment results in **Figure 7A-F** show the biocompatibility of the developed ink with biological organisms, such as the MSCs. It was observed that during the initial 4 days of interaction with the developed ink, an accelerated growth was achieved by the MSCs when cultured in the presence of the ink, in comparison to when only being cultured in media. Moreover, after 7 days (**Figure 7G**), the amount of metabolically active cells was higher in the presence of the ink in comparison to using media. These findings demonstrate the excellent biocompatibility of the developed ink with biological entities and highlight the potential of this ink to be used in tissue engineering applications.

4. Conclusions

This project expanded the frontiers of biomaterials commonly used in regenerative medicine to assist in finding the solution for the latent problem in the marine environmental ecosystem – coral bleaching. Therefore, we developed an eco-friendly ink that can potentially be used to restore rigid living systems. Based on a wide range of previous investigations in biomaterials applied for bone and cartilage tissue regeneration, our ink is composed of biopolymers as gelatin, alginate, GelMA, and PEGDA with the integration of bioceramics as calcium carbonate and hydroxyapatite, which are fundamental for mimicking the structures of corals. We demonstrated the effectiveness of the ink to be manufactured by 3D molding and printing technologies, which is a crucial step to develop complex figures that could mimic a coral and serve as a scaffold for biological systems as polyps. Furthermore, we implemented an image processing and surface analysis to find a more accurate concentration of ceramics imbued in the biopolymers. This innovative analysis provides a new opportunity to mitigate the lack of characterization methods to improve the printability fidelity of novel bioinks. The photo-crosslinking behavior coming from GelMA, PEGDA, and ionic-crosslinking of alginate make the ink stable for complex physicochemical conditions, as the seawater ecosystem, in which there is an excess of cations are coming from calcium sources. This presents a possibility for *in situ* appliances in coral reefs with the aid of diverse 3D manufacturing technologies, as shown in the schematic overview in **Figure S7**.

Furthermore, the chemical characterization corroborates the interaction of the materials and the crosslinking behavior seen at the infrared spectra peaks for ionic-crosslinking at 3300 cm^{-1} and photo-crosslinking at 2950-90 cm^{-1}. In addition, X-Ray diffraction clearly shows the convergence of calcium carbonate and hydroxyapatite without altering its ground state crystal structure, corroborating that no other chemical or physical methods are needed for its preparation. Using this method, the product can be easily produce in a cost-effective manner. Moreover, NMR corroborates the interaction of calcium, phosphate, and carbonate ions from the bioceramics in the biopolymer matrix. Besides, thermochemical characterization with TGA and DSC gives us an initial insight into how the material works with the temperature appliance, which works perfectly for our final scope. In addition, discussion related to the mechanical properties of the ink, with different tests of rheology to evaluate storage/loss modulus in terms of time and temperature, and its viscosity versus shear rate, corroborates the potential printability of the precrosslinked ink for manufacturing complex structures. Finally, a biological assessment was done with MSCs to demonstrate the material's biocompatibility with living MSCs; we suggest that the material could potentially be used for different living systems. In conclusion, the material can withstand harsh conditions, and the degradation rate can be controlled with the specific behavior from each constituent of the ink. This formulation is the beginning of future investigations as it has potential use for rigid living systems with interesting tunable properties that could fulfill different directions regarding the final user's needs.

Acknowledgments

Team members of the group developed graphical abstract and technical assistance from the biotech artist Alma R.

García-Roche. In addition, supplementary figures were designed and created with the aid of http://biorender.com/. This work was financially supported by the King Abdullah University of Science and Technology.

Conflicts of interest

The authors declare that they do not have any competing interests.

Authors' Contributions

C.A.E.H. guided and supervised the project. A. A. R. designed and supervised the experiments. A. A. R., A.U.V.P., H.H.S., G.B., R.P.P., A. A., and Z. K. conducted experiments and contributed intellectually to the scientific design of the project. P.B. mentored the technical part of the project.

References

1. Chesterman J, Zhang Z, Ortiz O, *et al*., 2020, Biodegradable Polymers. In: Principles of Tissue Engineering. 5th ed., Ch. 18. Academic Press, United States, p317-342. https://doi.org/10.1016/j.matpr.2020.01.437
2. Biswal T, BadJena SK, Pradhan D, 2020, Sustainable Biomaterials and their Applications: A Short Review. *Mater Today*, 30:274–82.
3. Simionescu BC, Ivanov D, 2015, Natural and Synthetic Polymers for Designing Composite Materials. In: Handbook of Bioceramics and Biocomposites. Ch. 11-1. Wiley-VCH: Weinheim, Germany, p1–54. https://doi.org/10.1007/978-3-319-09230-0_11-1
4. Lee M, Rizzo R, Surman F, Zenobi-Wong M, 2020, Guiding Lights: Tissue Bioprinting Using Photoactivated Materials. *Chem Rev*, 120:10950–1027. https://doi.org/10.1021/acs.chemrev.0c00077
5. Chimene D, Miller L, Cross LM, *et al*., 2020, Nanoengineered Osteoinductive Bioink for 3D Bioprinting Bone Tissue. *ACS Appl Mater Interfaces*, 12:15976–88. https://doi.org/10.1021/acsami.9b19037
6. Zhou H, Lee J, 2011, Nanoscale Hydroxyapatite Particles for Bone Tissue Engineering. *Acta Biomater*, 7:2769–81.
7. Kelly BE, Bhattacharya I, Heidari H, *et al*, 2019, Volumetric Additive Manufacturing Via Tomographic Reconstruction. *Science*, 363:1075–9. https://doi.org/10.1126/science.aau7114
8. Leggat WP, Camp EF, Suggett DJ, *et al.*, 2019, Rapid Coral Decay is Associated with Marine Heatwave Mortality Events on Reefs. *Curr Biol*, 29:2723–30.e4. https://doi.org/10.1016/j.cub.2019.06.077
9. Mass T, *et al.*, 2017, Amorphous Calcium Carbonate Particles form Coral Skeletons. *Proc Natl Acad Sci*, 114:E7670–8. https://doi.org/10.1073/pnas.1707890114
10. Wangpraseurt D, You S, Azam F, *et al.*, 2020, Bionic 3D Printed Corals. *Nat Commun*, 11:1748.
11. Yu AC, Reinhart M, Hunter R, *et al.*, 2021, Seasonal Impact of Phosphate-Based Fire Retardants on Soil Chemistry Following the Prophylactic Treatment of Vegetation. *Environ Sci Technol*, 55:2316–23. https://doi.org/10.1021/acs.est.0c05472.s001
12. Loessner D, Meinert C, Kaemmerer E, *et al.*, Functionalization, Preparation and use of Cell-laden Gelatin Methacryloyl-based Hydrogels as Modular Tissue Culture Platforms. *Nat Protoc*, 11:727–46. https://doi.org/10.1038/nprot.2016.037
13. Khan Z, Kahin K, Rauf S, *et al.*, 2019, Optimization of a 3D Bioprinting Process Using Ultrashort Peptide Bioinks. *Int J Bioprint*, 5:173. https://doi.org/10.18063/ijb.v5i1.173
14. Gong J, Schuurmans CC, van Genderen AM, *et al.*, 2020, Complexation-induced Resolution Enhancement of 3D-Printed Hydrogel Constructs. *Nat Commun*, 11:1267.
15. Gonzalez-Rios JA, Valle-Pérez AU, Amaya-Delgado L, *et al*., 2021, A Quick Fed-batch Saccharification Strategy of Wheat Straw at High Solid Loadings Improving Lignocellulosic Ethanol Productivity. *Biomass Conversion Biorefinery*. https://doi.org/10.1007/s13399-021-01580-0
16. Valle-Pérez AU, Flores-Cosío G, Amaya-Delgado L, 2021, Bioconversion of Agave Bagasse to Produce Cellulases and Xylanases by *Penicillium citrinum* and *Aspergillus fumigatus* in Solid-State Fermentation. *Waste Biomass Valorization*. https://doi.org/10.1007/s12649-021-01397-y
17. Susapto HH, Alhattab D, Abdelrahman S, *et al.*, 2021, Ultrashort Peptide Bioinks Support Automated Printing of Large-Scale Constructs Assuring Long-Term Survival of Printed Tissue Constructs. *Nano Lett*, 21:2719–29. https://doi.org/10.1021/acs.nanolett.0c04426.s010
18. Theus AS, Ning L, Hwang B, *et al.*, 2020, Bioprintability: Physiomechanical and Biological Requirements of Materials for 3D Bioprinting Processes. *Polymers* (*Basel*), 12:2262. https://doi.org/10.3390/polym12102262
19. Doostmohammadi A, Monshi A, Salehi R, *et al.*, 2011, Cytotoxicity Evaluation of 63s Bioactive Glass and Bone-Derived Hydroxyapatite Particles Using Human Bone-marrow Stem Cells. *Biomed Pap Med Fac Univ Palacky Olomouc Czech Repub*, 155:323–6. https://doi.org/10.5507/bp.2011.028

20. Parvez S, Rahman MM, Khan MA, *et al.*, 2012, Preparation and Characterization of Artificial Skin Using Chitosan and Gelatin Composites for Potential Biomedical Application. *Polym Bull*, 69:715–31. https://doi.org/10.1007/s00289-012-0761-7
21. Guo X, Liu L, Wang W, *et al*., 2011, Controlled Crystallization of Hierarchical and Porous Calcium Carbonate Crystals Using Polypeptide Type Block Copolymer as Crystal Growth Modifier in a Mixed Solution. *Cryst Eng Commun*, 13:2011. https://doi.org/10.1039/c0ce00202j
22. Saarai A, Kasparkova V, Sedlacek T, *et al*., 2013, On the Development and Characterisation of Crosslinked Sodium Alginate/Gelatine Hydrogels. *J Mech Behav Biomed Mater*, 18:152–66. https://doi.org/10.1016/j.jmbbm.2012.11.010
23. Aldana AA, Malatto L, Rehman MA, *et al*., 2019, Fabrication of Gelatin Methacrylate (GelMA) Scaffolds with Nano- and Micro-Topographical and Morphological Features. *Nanomaterials*, 9:120. https://doi.org/10.3390/nano9010120
24. Kontoyannis CG, Vagenas NV, 2000, Calcium Carbonate Phase Analysis Using XRD and FT-Raman Spectroscopy. *Analyst*, 125:251–5. https://doi.org/10.1039/a908609i
25. Manafi SA, Yazdani B, Rahimiopour MR, *et al*., 2008, Synthesis of Nano-hydroxyapatite under a Sonochemical/ Hydrothermal Condition. *Biomed Mater*, 3:025002. https://doi.org/10.1088/1748-6041/3/2/025002
26. Duan P, Li X, Wang T, *et al.*, 2018, The Chemical Structure of Carbon Nanothreads Analyzed by Advanced Solid-State NMR. *J Am Chem Soc*, 140:7658–66. https://doi.org/10.1021/jacs.8b03733
27. Zhu M, Wang Y, Ferracci G, *et al*., 2019, Gelatin Methacryloyl and its Hydrogels with an Exceptional Degree of Controllability and Batch-to-Batch Consistency. *Sci Rep*, 9:6863. https://doi.org/10.1038/s41598-019-42186-x
28. Raveendran NT, Vaquette C, Meinert C, *et al*., 2019, Optimization of 3D Bioprinting of Periodontal Ligament Cells. *Dent Mater*, 35:1683–94. https://doi.org/10.1016/j.dental.2019.08.114
29. Tan F, Xu X, Deng T, *et al*., 2012, Fabrication of Positively Charged Poly(Ethylene Glycol)-Diacrylate Hydrogel as a Bone Tissue Engineering Scaffold. *Biomed. Mater*, 7:055009. https://doi.org/10.1088/1748-6041/7/5/055009
30. Gill P, Moghadam TT, Ranjbar B, 2010, Differential Scanning Calorimetry Techniques: Applications in Biology and Nanoscience. *J. Biomol. Technol*., 21:167–193.

RESEARCH ARTICLE

Fabrication of a Lateral Flow Assay for Rapid In-Field Detection of COVID-19 Antibodies Using Additive Manufacturing Printing Technologies

Abdulelah A. Alrashoudi[1†], Hamed I. Albalawi[1†], Ali H. Aldoukhi[1†], Manola Moretti[1], Panayiotis Bilalis[1], Malak Abedalthagafi[2,3], Charlotte A. E. Hauser[1,4*]

[1]Laboratory for Nanomedicine, Division of Biological and Environmental Science and Engineering, King Abdullah University of Science and Technology, Thuwal 23955-6900, Saudi Arabia
[2]King Abdulaziz City for Science and Technology, Riyadh, Saudi Arabia
[3]Department of Genomics Research, King Fahad Medical City and King Abdulaziz City for Science and Technology, Riyadh, Saudi Arabia
[4]Computational Bioscience Research Center, King Abdullah University of Science and Technology, Thuwal 23955-6900, Saudi Arabia
[†]*These authors contributed equally to this work.*

Abstract: The development of lateral flow immunoassay (LFIA) using three-dimensional (3D) printing and bioprinting technologies can enhance and accelerate the optimization process of the fabrication. Therefore, the main goal of this study is to investigate methods to speed up the developing process of a LFIA as a tool for community screening. To achieve this goal, an in-house developed robotic arm and microfluidic pumps were used to print the proteins during the development of the test. 3D printing technologies were used to design and print the housing unit for the testing strip. The proposed design was made by taking into consideration the environmental impact of this disposable medical device.

Keywords: Lateral flow immunoassay; COVID-19; Diagnostic tools; 3D Printing; Additive manufacturing technologies; Microfluidic pumps

*Correspondence to: Charlotte A. E. Hauser, Laboratory for Nanomedicine, Division of Biological and Environmental Science and Engineering, King Abdullah University of Science and Technology, Thuwal 23955-6900, Saudi Arabia; charlotte.hauser@kaust.edu.sa

Received: June 15, 2021; **Accepted:** July 29, 2021; **Published Online:** August 23, 2021

Citation: Alrashoudi AA, Albalawi HI, Aldoukhi AH, *et al.,* Fabrication of a Lateral Flow Assay for Rapid In-Field Detection of COVID-19 Antibodies Using Additive Manufacturing Printing Technologies. *Int J Bioprint*, 7(4):399. http://doi.org/10.18063/ijb.v7i4.399

1. Introduction

Severe acute respiratory syndrome coronavirus 2 (SARS-CoV-2) is the causative virus of coronavirus disease 2019 (COVID-19), and the first case was reported in China in December 2019[1]. SARS-CoV-2 is a RNA virus that belongs to the coronavirus family and has multiple structural proteins on its surface, including spike, nucleocapsid, membrane, and envelope proteins[2]. The virus causes severe respiratory symptoms requiring mechanical ventilation and intensive care unit admission, and contributes to high mortality rates[3]. Moreover, the virus had high transmissibility between humans, and for that, the World Health Organization declared COVID-19 as a pandemic on March 11, 2020[4]. Since then, huge efforts to identify people with active infection of SARS-CoV-2 were implemented in order to stop the spread of the virus. Detecting individuals with active infection require polymerase chain reaction testing in nasal or throat swab samples, and the test results are used to identify and isolate positive cases so as to limit the transmission of the virus[5]. Antibodies against the viral spike and nucleocapsid surface proteins are developed and can be detected in the serum of infected 14 days after the infection[6]. Thus, testing serum or blood samples for antibodies against the viral surface proteins, especially

IgG, would provide information about people who had a history of prior infection and have recovered from the disease[6]. Therefore, antibody testing has an important role in epidemiological assessment of community spread of the virus and to guide policy-makers when designing and introducing protective measures[7].

A recent study by Dan *et al*. reported that people who recovered from COVID-19 have immunity lasting for 6-8 months after the infection in which IgG antibodies could be detected by serology testing[8]. Screening for COVID-19 antibodies could provide valuable information about the level of immunity in the community. The screening can also be an important part in identifying who is immune and who is not when a majority of people return to work and transition to the new normal[7]. Furthermore, the detection of antibodies against SARS-CoV-2 can be used as a tool to monitor immunity against SARS-CoV-2 acquired through vaccines, which can be done using laboratory-based immunoassays such as chemiluminescence and enzyme-linked immunosorbent assay, or rapid tests such as lateral flow immunoassay (LFIA)[9]. Indeed, a cost-effective diagnostic tool would be beneficial for wide community screening. Rapid tests offer comparable outcomes to the laboratory-based tests and can be used when there is a need to identify people with immunity against the virus within a few minutes while having the advantages of being user-friendly, portable, and not requiring expensive instruments[10].

A LFIA is a point-of-care diagnostic device that offers a rapid and inexpensive test that targets analytes in the samples by providing qualitative or semi-quantitative results[11]. It consists of four essential parts, namely, the sample pad, conjugate pad, nitrocellulose membrane, and the absorption pad, which are assembled and placed in a housing cassette. One of the most predominant advantages of LFIA is the simplicity of the device as it can be used in the field without the need for any special equipment or sample processing. Moreover, since the beginning of the COVID-19 pandemic, there has been a tremendous effort to develop LFIA that can be used to detect viral antigens or serum antibodies for the identification of infected individuals or immune individuals, respectively[12,13]. As more research is being conducted to optimize and develop more accurate tests, there is a need for a rapid method to prototype and construct these LFIA.

Technologies such as three-dimensional (3D) printing and bioprinting can be used as tools to aid in the development of LFIA where time is of the essence such as global pandemic[14]. A material extrusion-based 3D bioprinting technique was utilized during the testing strip development where microfluidic pumps and a robotic arm were used to print different antibodies for screening. The microfluidic pump system was used to dispense the capturing material on the nitrocellulose membrane as it offers an easier and efficient way to test multiple proteins. Furthermore, the robotic arms provide fine control of the nozzle when dispensing the material, while the pumps ensure consistent volume of the material to be dispensed on the nitrocellulose membrane to capture antibodies against SARS-COV-2.

Another component of the LFIA is the cassette used to house and protect the testing strip from damage. Since the LFIA test can be used to detect different types of analytes, billions of LFIA tests and cassettes are manufactured annually[11]. Recently, there has been an increase in awareness regarding the environmental impact of medical devices, especially disposable devices[15-17]. Thus, the environmental impact should be taken into consideration when designing medical devices to limit this negative impact[16]. Since the LFIA cassette is made of polymers, it would be beneficial to consider how it can be designed in a way to decrease its environmental impact. Furthermore, using computer simulation for the 3D design, these iterations could be tested before the fabrication process. Furthermore, the simulation could be utilized to design and 3D print cassette with minimum polymeric material using different technologies.

In the past two decades, 3D printing technologies have been developed as essential prototyping techniques, industrially known as additive manufacturing technology, which are used as the primary prototyping technology in many applications today[18]. 3D printing provides an accessible method for fabrication of a customized design solution in a rapid controlled manner. Due to its high utility, it has developed tremendously in many fields, from aeronautics to sustainability, as well as medicine[19-21]. In this study, 3D printing was used to fabricate cassettes for rapid in-field assays. 3D printing technology provides the freedom to fabricate and prototype any designs in a standard laboratory setting, and saves the time and effort of many researchers. Overtime, different types of 3D technologies have been developed, including material extrusion 3D printing and vat photopolymerization 3D printing. These 3D technologies were used to prototype and print the housing unit.

During the pandemic, there has been a massive increase in the innovations and application of 3D printing technologies. 3D printing technologies offered a wide range of on-demand solutions during a time where supply chains were constrained. Some of the applications of 3D printing during COVID-19 pandemic include the production of medical devices, personal protective equipment, and other devices that aid in controlling the spread of the virus[22]. With the evolutionary mutations of SARS-CoV-2 virus, we are facing new variants such as Delta variant[23,24]. Since the virus is changing at a fast pace, we need to utilize technologies that allow us

to adapt to these changes and provide rapid solutions to protect our community.

The advantage of using 3D printing over the traditional methods, such as laser cutting, is that 3D printing offers a prototyping method to test multiple designs in short period of time. In addition, ease of accessibility to 3D printers makes them suitable for prototyping in a laboratory setting. Once the design is tested and finalized using 3D printing technology, it can be sent out for mass production.

Here, we developed a LFIA test using multiple technologies to efficiently optimize the testing strips. Bioprinting and 3D printing techniques were used during the development of a rapid test for the detection of antibodies against COVID-19. A material extrusion-based bioprinting setup utilizing a robotic arm was used during the construction of the strips to aid the dispensing of the capturing materials. In addition, an additive manufacturing technology was used to build a housing unit for the strip in a layer-by-layer manner using photopolymerization technique. The design of the cassette was modified as needed to adapt with the rapid changes in the testing strip during the optimization process. Using finite element analysis (FEA), we were able to simulate the physical strains on the designed cassette to determine its minimum thickness while ensuring the practicality of use and durability when conducting the test.

2. Materials and methods

2.1. Materials

Forty nanometers Gold NanoSpheres 2 mM citrate (OD=1) was purchased from nanohybrids. SARS-CoV-2 (2019-nCoV) Spike S1-His Recombinant Protein (HPLC-verified) (Cat. No.: 40591-V08H) and Normal Rabbit Control IgG (Cat. No.: CR1) were purchased from Sino Biological. SARS-CoV-2 Spike Protein (S-ECD/RBD) Monoclonal Antibody (bcb03) (Cat. No.: MA5-35950) and Goat Anti-Rabbit IgG (H+L) Superclonal Secondary Antibody (Cat. No.: A27033) were purchased from Fisher Scientific. Mouse monoclonal (JDC-10) Anti-Human IgG Fc (HRP) (Ab99759) was purchased from Abcam. 1×Phosphate-buffered saline (PBS), sucrose, TWEEN 20, and bovine serum albumin (BSA), potassium carbonate, and Tris buffer were purchased from Sigma-Aldrich. All chemicals were used as received, without purification or modification. Cellulose fiber sample pads, glass fiber conjugate pads, and high-flow nitrocellulose membrane were purchased from EMD Millipore Corporation. Sample pads, conjugate pads, and absorbent pads of different sizes were purchased from Ahlstrom-Munksjo. Backing cards KN-2211 were purchased from Kenosha. FormLabs Photopolymer Resin White (FLGPWH04) was purchased from FormLabs.

2.2. Conjugation of the gold nanoparticles

To conjugate the gold nanoparticles (AuNP) with S1 spike protein (40591-V08H, Fisher) and Rabbit antibody, as shown in **Figure 1A**, 1 ml of 1 OD AuNP solution was used and the pH was adjusted to 8.5-9 using potassium carbonate (K_2CO_3). The protein was added to the AuNP suspension at a ratio of protein solution: AuNP solution of 1:100 (v: v) with a final protein concentration of 10 µg/ml, and the suspension was incubated for 2 h while mixing. Then, 250 µl of 5% BSA in TRIS buffer was added and mixed for an additional 15 min. Afterward, 100 µl of 1% TWEEN 20 in TRIS buffer was added to the suspension and centrifuged for 10 min at 8000×*g* and 4°C. The supernatant was removed, and the precipitate was resuspended in 1 ml of Tris buffer (pH 8.5) + 1% BSA + 1% TWEEN 20 and centrifuged as before. Finally, the precipitate was resuspended in 100 µl of Tris buffer (pH 8.5) + 1% BSA + 1% TWEEN 20 + 20% sucrose to achieve a conjugated AuNP concentration of 10 OD. The same process was used when conjugating the S1 spike protein and rabbit antibodies to the AuNP.

To confirm the conjugation of the protein to the gold nanoparticles, UV–Vis Spectrometer (PerkinElmer Lambda 1050) was used to compare the UV–Vis spectra of the conjugated AuNP with ligand-free AuNP. We assessed the red shift in peak absorbance between the conjugated AuNP and ligand-free AuNP which can be used to confirm the conjugation. The sample was scanned from 800 nm to 250 nm with a data interval of 1 nm and a scanning speed of 266.75 nm/min. To assess

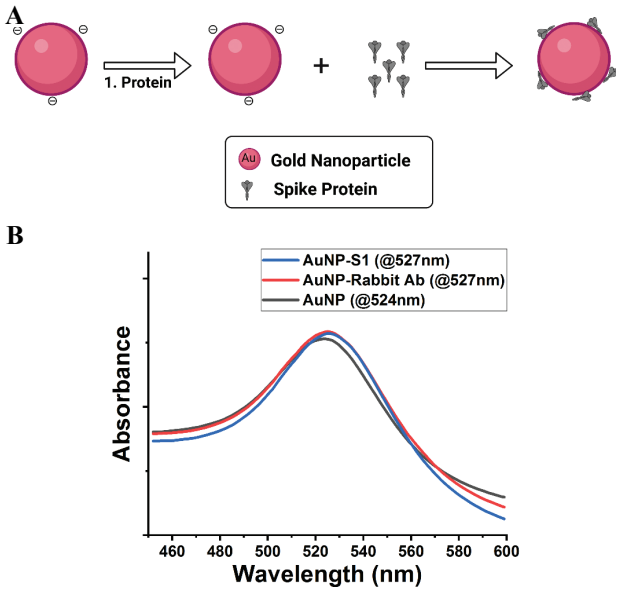

Figure 1. (A) Schematic representation of the physical conjugation process between the gold nanoparticles and the proteins of interest. (B) Detection of conjugated AuNP with antibodies and proteins by UV/VIS spectroscopy.

the attachment of the proteins to the gold nanoparticles, we performed UV–VIS absorption scan in which we compared AuNP-S1, AuNP-rabbit antibody conjugates to ligand-free AuNP. The conjugated nanoparticles showed a 3 nm shift compared to the ligand-free nanoparticles, as shown in **Figure 1B**, indicating the success of the functionalization of the 1 mL gold nanoparticles to the 10 µg of the S1 protein, and rabbit antibody[25]. The red shift in peak absorbance is an indication of the enlargement of the gold nanoparticle size from the attachment of the proteins to the nanoparticle[26].

2.3. Assembly of the strip

To assemble the strip, first, the high-flow nitrocellulose membrane was mounted on the backing cards. Dispensing of the antibodies to the nitrocellulose membrane was done using a setup consisting of a robotic arm (Dobot Magician, Dobot, China) and a microfluidic pump (ExiGo, Cellix, Ireland), as depicted in **Figure 2**; this setup could be considered as material extrusion-based bioprinting. Dispensing of the antibodies onto the nitrocellulose membrane was done using a 21 G needle attached to the robotic arm. The antibodies were dispensed at a rate of 200 µl/min and the robotic arm was programmed to move at a speed of 17 mm/s; antibodies were diluted in 1×PBS to be dispensed at a concentration of 200 µg/ml. These parameters ensured that antibodies were dispensed in a thick and continuous line. In particular, two antibody lines were printed on the nitrocellulose membrane. A test line was printed with anti-human antibodies (Abcam, Ab99759) and a control line was printed with anti-rabbit antibodies (Fisher, A27033). A video demonstrating the printing process is provided as the supplementary file. The strip was then dried at room temperature for 1 h. Then, the absorption pad was added to the backing card with a 2-3 mm overlap with the nitrocellulose membrane. Finally, the assembled backing card, nitrocellulose membrane, and absorbent pad were cut into 5 mm wide strips.

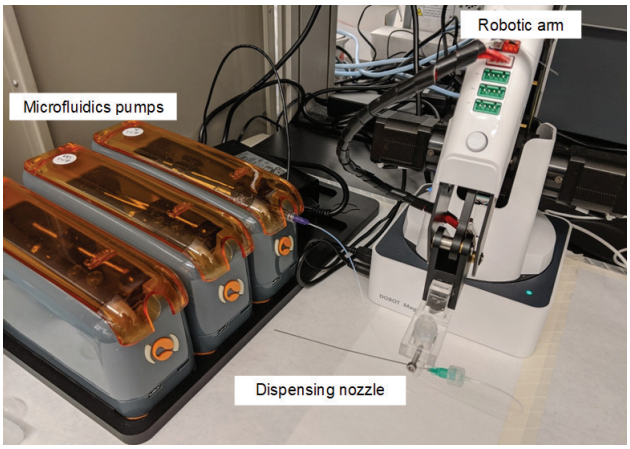

Figure 2. The printing setup consists of a robotic arm, microfluidics pumps, and dispensing nozzle.

2.4. Designing and 3D printing of the LFIA strip cassettes

NX computer-aided design (CAD) software was used in designing the housing units, along with SolidWorks as a supporting program. NX CAD was mainly used to design several iterations due to its capability in designing small features. NX CAD provided the simulation tools needed to test the assembly of the design before printing; the simulation of the designed structure was needed to design the locking mechanism as it requires a precise sizing to ensure proper locking after printing.

Multiple 3D printing technologies were used to ensure the design's maximum potential in prototyping these small housing units. Material extrusion 3D printing is the traditional 3D printing method, and vat photopolymerization 3D printing was used in prototyping the cassette designs. Using vat photopolymerization, 3D printing was about its ability to print a small housing unit with fine features in a short period of time. Furthermore, cassettes were printed with FormLabs white liquid resin and commercially available thermoplastic filament to keep the housing unit price reasonable. The vat photopolymerization 3D printer, FormLabs (Form 3), which was used in printing the housing unit, is capable of printing a hundred units a day.

We have devolved several design iterations to complement the rapid changes that we encounter during the test development. The first iteration of the designs started with mimicking the commercially available rapid tests[27]. While modifying the test, the cassette design was modified as well leading to the final iteration design. Using different 3D printing technologies allowed us to try and change different features while developing the test.

2.5. FEA simulation for the final iteration of the cassette

LFIA test strips are usually single-use tests, and the housing units are there to protect the strip. Our aim during the designing process was to reduce the amount of material needed to build the cassette, thus reducing wasted and discarded material from each cassette used. FEA simulation was used to study the proposed design before printing to ensure that the design can sustain handling forces without breaking. The durability of the cassette is not essential in single-use devices; however, a minimum thickness for the proposed cassette is required to prevent it from breaking during the test and handling when polyethylene is used as a material for the designed cassette.

The FEA simulation was conducted using NX software. As NX was the CAD software used to design the

cassette, it was also used to perform the FEA simulation to ensure accurate simulations results for the proposed design. Furthermore, before FEA simulation, the two sides of the cassette were assembled without restricting the locking mechanisms to mimic the printing assembly. This setting gave a better understanding of the behavior of the dipsticks while exerting force (F). The type of element applied during this simulation was tetrahedral, with an element size equal to 1.43 mm. During the simulation, one side of the cassette was fixed, while the other side was the location of the applied force to the negative z-axis **(Figure S1)**.

2.6. Testing of the assembled strip

The assembled strip was added to the cassette. A solution of AuNP-S1 and AuNP-rabbit antibody at a concentration of 10 OD was mixed together at a ratio of 1:1. The solution was then used by adding 10 µl of the mixture into an Eppendorf tube, as shown in **Figure 3**. Afterward, a 1 µl sample was added to the mixture and vortexed for 5 s. Here, we used SARS-CoV-2 Spike Protein Monoclonal Antibody (MA5-35950) at a concentration of 200 ug/ml as a positive sample and 1×PBS was used as a negative sample. Then, the strip was submerged into the AuNP mixture until the strip fully absorbed the solution. Finally, it was submerged into another tube that contains 1×PBS as a running buffer to wash strips from any remaining particles.

3. Results and discussion

Here, we developed by assembling all the components a successful LFIA test that detects IgG antibodies. First, we conjugated SARS-CoV-2 spike protein to gold nanoparticles to capture SARS-CoV-2 antibodies in the sample tube. Then, the testing lines consisting of secondary antibodies were printed on the nitrocellulose membrane to capture primary antibodies, and the strip was placed in a 3D-printed housing cassette after careful design and strain simulation.

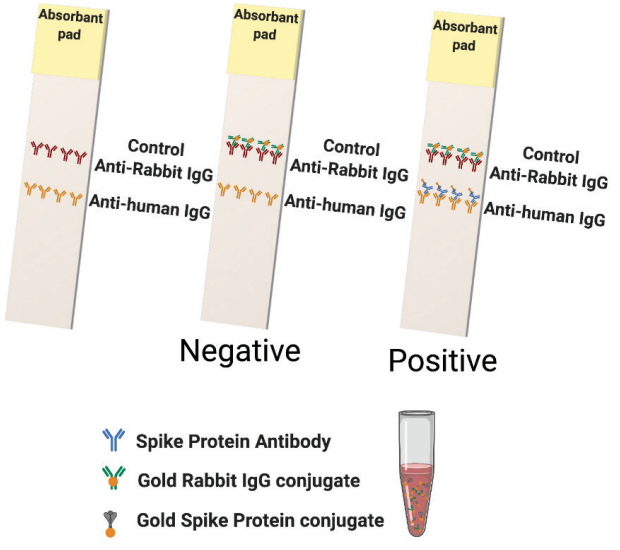

Figure 3. Illustration of an assembled dipstick test using the conjugated gold nanoparticles.

3.1. LFIA cassette designs and 3D printing

The housing unit design went through different iterations for adapting the changes and requirements for the test. These iterations were designed, fabricated, and assembled in the laboratory using specific requirements. The first two iterations are illustrated in the supplemental documents **(Figures S2 and S3)**. These designs were made for testing using a full strip setup which includes the conjugate pad. Alternatively, the third iteration was a dipstick design which was made to house a strip that does not contain a conjugate pad. This provides a faster way to test the strip by removing an extra step that adds the conjugated AuNP to the conjugate pad.

In this study, we used two 3D printing technologies to print the proposed cassettes. Material extrusion 3D printing technology using thermoplastic filament was developed in the early 1990's[28]. In the material extrusion 3D printing technique, a thermoplastic filament is fused using a mounted motor, which heats and melts the filament to be extruded during the printing process. On the other hand, vat photopolymerization technique uses a liquid photopolymer resin as a printing material, which is subjected to polymerization initiated by a projected laser. This process would selectively solidify the liquid resin against the platform, creating a 3D construct in a layer-by-layer fashion[29]. The advantages of using vat photopolymerization over material extrusion 3D printing are the higher printing resolution and smoother finish surface[30]. **Table 1** provides a summary comparing the two 3D printing technologies. **Figure 4** demonstrates a schematic of the process used to fabricate our cassettes using these two printing methods.

3.2. Dipstick housing unit

The dipstick housing unit design consists of a smaller unit with an opening from one side to be used for dipping the strip in the test solution as demonstrated in **Figure 5A**. This unit was engineered and designed by taking into consideration the security of the testing strip, as shown in **Figure 5B**. Since this design has a wide opening, it was essential to secure the strip, especially during the testing process. Therefore, a pressing locking mechanism was designed inside the housing unit, as shown in **Figure 5C**. Furthermore, the dipstick design was 3D printed using Form 3 printer (FormLabs) while taking into consideration the resolution of the used material.

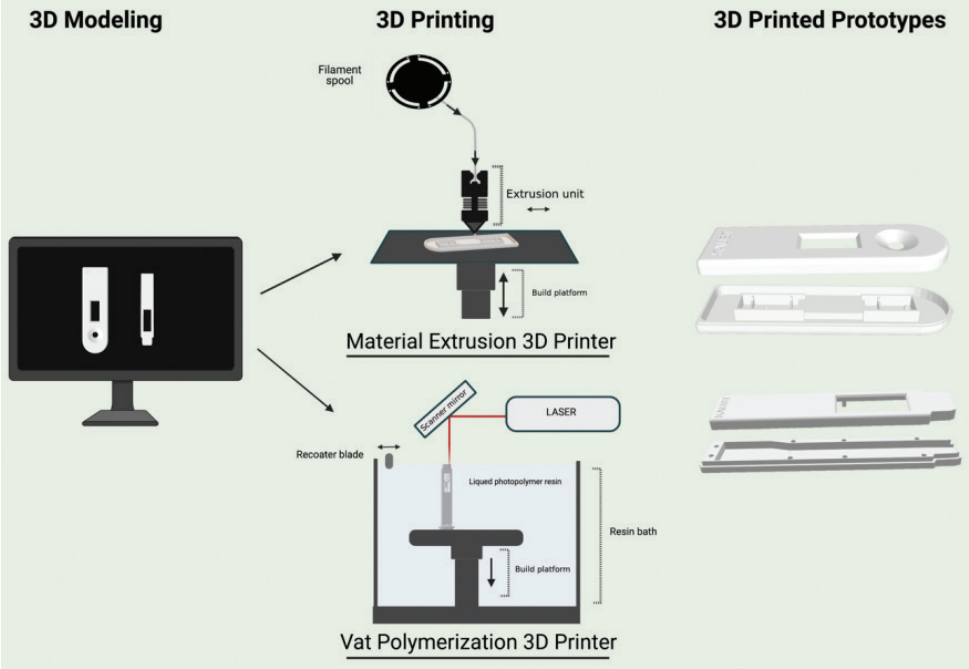

Figure 4. Schematic demonstration of the process used to fabricate the cassettes printed using material extrusion and vat polymerization 3D printing.

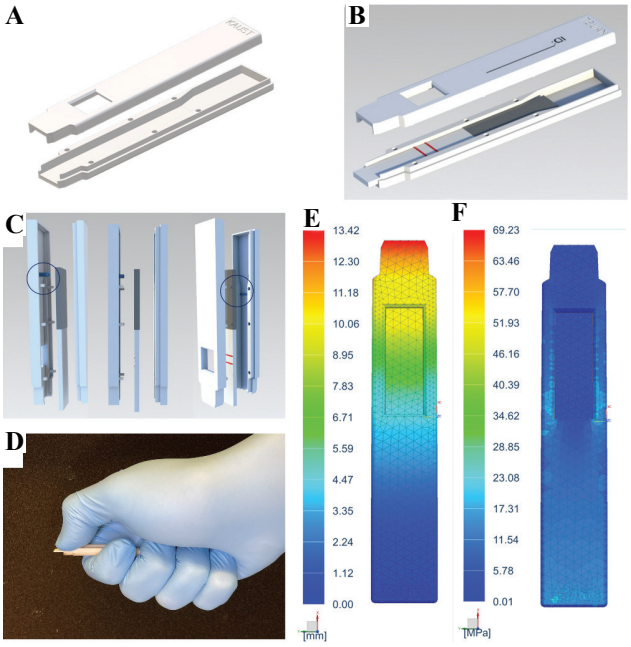

Figure 5. (A and B) CAD of the dipstick housing unit design. (C) CAD of the housing unit design with the bed pressing locking mechanism for securing the bed, the dipstick housing unit was 3D printed using vat photopolymerization. (D) The assumption and location of the applied force used in the simulation. (E) Simulation of the displacement for the dipstick cassette measured in mm when 5 N force was applied. (F) Simulation of the von Mises stress measured in MPa on the dipstick cassette when 5 N force was applied.

3.3. FEA simulation for the final iteration of the cassette

As the simulation was conducted on the same software, it made the process of changing and modifying the design more straightforward. During this experiment, we have changed the thickness of the dipstick several times to reduce the use of any unnecessary material in the printing process. We concluded that a cassette with thickness of 0.8 mm can be used and printed, and is the minimum thickness needed considering the simulation result.

The mass applied on the edge of the cassette during the simulation was set to be twice the normal handling force, where the normal handling force was assumed to be 2.5N. The assumption and location of the applied force were selected based on the actual state of a person applying pressure using one hand **(Figure 5D)**. **Figure 5E** illustrates the dipstick cassette deformation for the pressing simulation. The maximum deformation value was observed to be 13.4 mm. Comparing the deformation result to the dimension of the model, the value range of the deformation is acceptable. **Figure 5F** illustrates the von Mises distribution of stress in the pressing simulation of the dipstick. From this result, it can be seen that the maximum stress of von Mises was 69.2 MPa. This is slightly lower than the yield strength of the material used in 3D printing which was approximately 70 MPa. Under these conditions, the results suggest that our dipstick design will tolerate the expected use.

Table 1. Summary of the differences between material extrusion and vat photopolymerization 3D printing technologies.

Additive manufacturing technologies	Materials	Speed	Average cost of materials (kg)	Printing resolution	Limitation
Material extrusion[31,32]	Plastic filaments (PLA, ABS, ASA, PETG, and nylon)	Fast	Affordable; $40	Low	Support material
Vat photo polymerization[32,33]	Liquid photopolymers and resins	Slow	Average; $100	High	Support material and post-curing required

PLA: Polylactic acid; ABS: Acrylonitrile butadiene styrene; ASA: Acrylonitrile styrene acrylate; PETG: Polyethylene terephthalate glycol

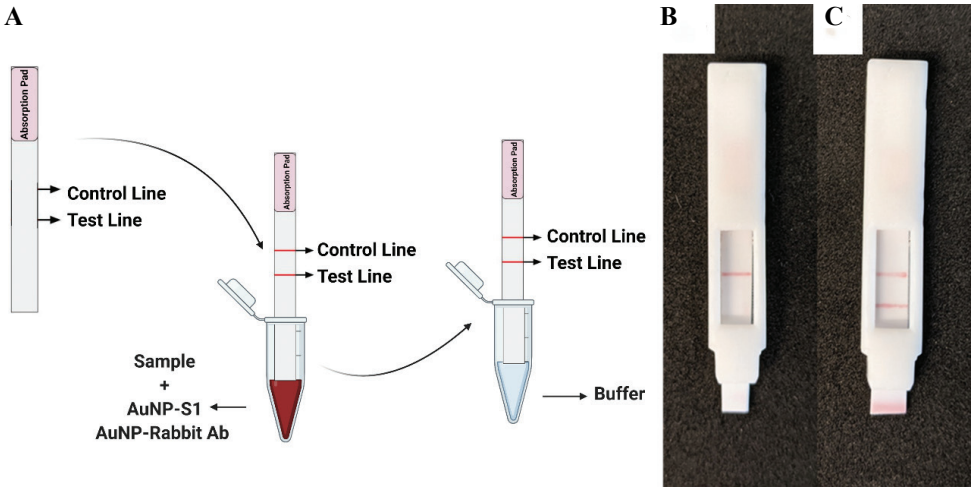

Figure 6. (A) Schematic of the dipping test without the housing cassette. (B) A lateral flow immunoassay (LFIA) showing a negative signal. (C) A LFIA showing a positive signal.

3.4. Testing of the assembled strip

LFIA dipstick strips were assembled to be tested with commercial SARS-CoV-2 antibodies to simulate positive or negative tests. **Figure 6A** shows a schematic of the test without the housing cassette. In this setup, if only the control line shows a red signal, then the sample is negative. If both control line and test line show a red signal, then the sample is positive. **Figures 6B** and **6C** depict two LFIA strips that were used as a dipstick in our testing. **Figure 6**B shows a negative sample in which a clear band is visible on the control line and no band is visible on the test line. On the other hand, **Figure 6C** demonstrates a positive sample containing anti-spike antibodies in which both the test and control lines are visible.

Using a dipstick design in prototyping, the LFIA provides a faster way to assess the test and ensure that all the test components are working as desired. When designing a new protein or modifying an existing one to enhance the sensitivity of the test, it is time-efficient to test the conjugated material using a dipstick LFIA before proceeding with further optimization processes to be used as a standard LFIA.

4. Conclusions

In this study, we demonstrated that the prototyping, printing, and assembly of an LFIA test are feasible using an in-house developed setup. We showed that the test cassette could be prototyped to sustain mechanical stress applied to it by hand even if it was designed to be printed with minimum thickness to reduce material. To support the full functional capabilities of the device, we also demonstrated that bioprinting of the test lines with a robotic arm and microfluidic pump was accurate enough to detect IgG antibodies, when tested with protein-conjugated AuNP and commercially available antibodies.

Additive manufacturing technologies can be a great tool for prototyping and fabricating medical devices and diagnostics tools. These technologies can accelerate the optimization process by quickly adjusting to the designs and then 3D printing the device as needed. During the development phase of a new medical device and diagnostic tools, 3D printing can provide on-demand solutions despite the challenges.

Acknowledgments

This work was financially supported by King Abdullah University of Science and Technology (KAUST) and by King Abdulaziz City for Science and Technology (KACST) with a funded grant (4419-KACST COVID -19).

Conflicts of interest

The authors declare no conflict of interest.

Author contributions

C.A.E.H. proposed the research direction and guided the project. A.A.A., H.I.A., A.H.A. designed and performed the majority of the experimental parts. M.M., P.B. contributed to the experimental design and supervised the experimental work. A.A.A., H.I.A., A.H.A. wrote the manuscript. M.M. P.B. M.A. revised the manuscript. The authors have given approval to the final version of the manuscript.

References

1. Guan WJ, Ni ZY, Hu Y, *et al.*, 2020, Clinical Characteristics of Coronavirus Disease 2019 in China. *N Engl J Med*, 382:1708–20.
2. Chan JF, Kok KH, Zhu Z, *et al.*, 2020, Genomic Characterization of the 2019 Novel Human-pathogenic Coronavirus Isolated from a Patient with Atypical Pneumonia after Visiting Wuhan. *Emerg Microbes Infect*, 9:221–36. https://doi.org/10.1080/22221751.2020.1719902
3. Huang C, Wang Y, Li X, *et al.*, 2020, Clinical Features of Patients Infected with 2019 Novel Coronavirus in Wuhan, China. *Lancet*, 395:497–506.
4. Cucinotta D, Vanelli M, 2020, WHO Declares COVID-19 a Pandemic. *Acta Biomed*, 91:157–60.
5. Zou L, Ruan F, Huang M, *et al.*, 2020, SARS-CoV-2 Viral Load in Upper Respiratory Specimens of Infected Patients. *N Engl J Med*, 382:1177–9. https://doi.org/10.1056/nejmc2001737
6. To KK, Tsang OT, Leung WS, *et al.*, 2020, Temporal Profiles of Viral Load in Posterior Oropharyngeal Saliva Samples and Serum Antibody Responses during Infection by SARS-CoV-2: An Observational Cohort Study. *Lancet Infect Dis*, 20:565–74. https://doi.org/10.3410/f.737608898.793574123
7. Winter AK, Hegde ST, 2020, The Important Role of Serology for COVID-19 Control. *Lancet Infect Dis*, 20:758–59. https://doi.org/10.1016/s1473-3099(20)30322-4
8. Dan JM, Mateus J, Kato Y, *et al.*, 2021, Immunological Memory to SARS-CoV-2 Assessed for up to 8 Months after Infection. *Science*, 371:eabf4063. https://doi.org/10.1126/science.abf4063
9. Martín J, Tena N, Asuero AG, 2021, Current State of Diagnostic, Screening and Surveillance Testing Methods for COVID-19 from an Analytical Chemistry Point of View. *Microchem J*, 167:106305. https://doi.org/10.1016/j.microc.2021.106305
10. Schuler CF, Gherasim C, O'Shea K, *et al.*, 2021, Accurate Point-of-care Serology Tests for COVID-19. *PLoS One*, 16:e0248729. https://doi.org/10.1371/journal.pone.0248729
11. Banerjee R, Jaiswal A, 2018, Recent Advances in Nanoparticle-based Lateral Flow Immunoassay as a Point-of-care Diagnostic Tool for Infectious Agents and Diseases. *Analyst*, 143:1970–96. https://doi.org/10.1039/c8an00307f
12. Adams E, Ainsworth M, Anand R, *et al.*, 2020, Antibody Testing for COVID-19: A Report from the National COVID Scientific Advisory Panel. *Wellcome Open Res*, 5:139.
13. Dinnes J, Deeks JJ, Berhane S, *et al.*, 2021, Rapid, Point-of-care Antigen and Molecular-based Tests for Diagnosis of SARS-CoV-2 Infection. *Cochrane Database Syst Rev*, 3:CD013705. https://doi.org/10.1002/14651858.cd013705
14. Ozbolat IT, Hospodiuk M, 2016, Current Advances and Future Perspectives in Extrusion-based Bioprinting. *Biomaterials*, 76:321–43. https://doi.org/10.1016/j.biomaterials.2015.10.076
15. Eckelman MJ, Sherman JD, 2018, Estimated Global Disease Burden From US Health Care Sector Greenhouse Gas Emissions. *Am J Public Health*, 108:S120–2. https://doi.org/10.2105/ajph.2017.303846
16. Leiden A, Cerdas F, Noriega D, *et al.*, 2020, Life Cycle Assessment of a Disposable and a Reusable Surgery Instrument Set for Spinal Fusion Surgeries. *Resour Conserv Recycl*, 156:104704. https://doi.org/10.1016/j.resconrec.2020.104704
17. Unger SR, Hottle TA, Hobbs SR, *et al.*, 2017, Do Single-use Medical Devices Containing Biopolymers Reduce the Environmental Impacts of Surgical Procedures Compared with their Plastic Equivalents? *J Health Serv Res Policy*, 22:218–25. https://doi.org/10.1177/1355819617705683
18. Gebhardt A, 2011, Understanding Additive Manufacturing. In: Understanding Additive Manufacturing. Hanser Pub Inc., Cincinnati, OH. https://doi.org/10.3139/9783446431621.fm
19. Joshi SC, Sheikh AA, 2015, 3D Printing in Aerospace and its Long-term Sustainability. *Virtual Phys Prototyp*, 10:175–85. https://doi.org/10.1080/17452759.2015.1111519
20. Ng WL, Chua CK, Shen YF, 2019, Print Me An Organ! Why We Are Not There Yet. *Prog Polym Sci*, 97:101145.

https://doi.org/10.1016/j.progpolymsci.2019.101145

21. Pant A, Lee AY, Karyappa R, *et al.*, 2021, 3D Food Printing of Fresh Vegetables Using Food Hydrocolloids for Dysphagic Patients. *Food Hydrocolloids*, 114:106546. https://doi.org/10.1016/j.foodhyd.2020.106546
22. Choong YY, Tan HW, Patel DC, *et al.*, 2020, The Global Rise of 3D Printing during the COVID-19 Pandemic. *Nat Rev Mater*, 5:637–9. https://doi.org/10.1038/s41578-020-00234-3
23. Harvey WT, Carabelli AM, Jackson B, *et al.*, 2021, SARS-CoV-2 Variants, Spike Mutations and Immune Escape. *Nat Rev Microbiol*, 19:409–24. https://doi.org/10.1038/s41579-021-00573-0
24. World Health Organization, 2021, Tracking SARS-CoV-2 Variants, World Health Organization, Geneva. Available from: https://www.who.int/en/activities/tracking-SARS-CoV-2-variants. [Last accessed on 2021 Jul 25]. https://doi.org/10.12659/msm.933622
25. Jazayeri MH, Amani H, Pourfatollah AA, *et al.*, 2016, Enhanced Detection Sensitivity of Prostate-specific Antigen via PSA-Conjugated Gold Nanoparticles Based on Localized Surface Plasmon Resonance: GNP-coated Anti-PSA/LSPR as a Novel Approach for the Identification of Prostate Anomalies. *Cancer Gene Ther*, 23:365–9. https://doi.org/10.1038/cgt.2016.42
26. Pollitt MJ, Buckton G, Piper R, *et al.*, 2015, Measuring Antibody Coatings on Gold Nanoparticles by Optical Spectroscopy. *RSC Adv*, 5:24521–7. https://doi.org/10.1039/c4ra15661g
27. Yetisen AK, Akram MS, Lowe CR, 2013, Paper-based Microfluidic Point-of-care Diagnostic Devices. *Lab Chip*, 13:2210–51. https://doi.org/10.1039/c3lc50169h
28. Stansbury JW, Idacavage MJ, 2016, 3D Printing with Polymers: Challenges among Expanding Options and Opportunities. *Dent Mater*, 32:54–64. https://doi.org/10.1016/j.dental.2015.09.018
29. Infuehr R, Pucher N, Heller C, *et al.*, 2007, Functional Polymers by Two-photon 3D Lithography. *Appl Surface Sci*, 254:836–40. https://doi.org/10.1016/j.apsusc.2007.08.011
30. Milovanović A, Milošević M, Mladenović G, *et al.*, 2019, Experimental Dimensional Accuracy Analysis of Reformer Prototype Model Produced by FDM and SLA 3D Printing Technology. Springer International Publishing, Cham, p84–95. https://doi.org/10.1007/978-3-319-99620-2_7
31. Gibson I, Rosen D, Stucker B, *et al.*, 2021, Material Extrusion. In: Additive Manufacturing Technologies. Springer International Publishing, Cham, p171–201. https://doi.org/10.1007/978-3-030-56127-7_6
32. Kun K, 2016, Reconstruction and Development of a 3D Printer Using FDM Technology. *Proc Eng*, 149:203–211. https://doi.org/10.1016/j.proeng.2016.06.657
33. Gibson I, Rosen D, Stucker B, 2015, Vat Photopolymerization Processes. In: Additive Manufacturing Technologies: 3D Printing, Rapid Prototyping, and Direct Digital Manufacturing. Springer New York, p63-106. https://doi.org/10.1007/978-1-4939-2113-3_4

RESEARCH ARTICLE

3D Bioprinting of Biomimetic Bilayered Scaffold Consisting of Decellularized Extracellular Matrix and Silk Fibroin for Osteochondral Repair

Xiao Zhang†, Yang Liu†, Qiang Zuo†, Qingyun Wang, Zuxi Li, Kai Yan, Tao Yuan, Yi Zhang, Kai Shen, Rui Xie, Weimin Fan*

Department of Orthopedics, The First Affiliated Hospital of Nanjing Medical University, Nanjing, China
†*These authors contributed equally to this work*

Abstract: Recently, three-dimensional (3D) bioprinting technology is becoming an appealing approach for osteochondral repair. However, it is challenging to develop a bilayered scaffold with anisotropic structural properties to mimic a native osteochondral tissue. Herein, we developed a bioink consisting of decellularized extracellular matrix and silk fibroin to print the bilayered scaffold. The bilayered scaffold mimics the natural osteochondral tissue by controlling the composition, mechanical properties, and growth factor release in each layer of the scaffold. The *in vitro* results show that each layer of scaffolds had a suitable mechanical strength and degradation rate. Furthermore, the scaffolds encapsulating transforming growth factor-beta (TGF-β) and bone morphogenetic protein-2 (BMP-2) can act as a controlled release system and promote directed differentiation of bone marrow-derived mesenchymal stem cells. Furthermore, the *in vivo* experiments suggested that the scaffolds loaded with growth factors promoted osteochondral regeneration in the rabbit knee joint model. Consequently, the biomimetic bilayered scaffold loaded with TGF-β and BMP-2 would be a promising strategy for osteochondral repair.

Keywords: Tissue engineering; Three-dimensional bioprinting; Osteochondral repair; Extracellular matrix; Silk fibroin; Polycaprolactone

*Correspondence to: Weimin Fan, Department of Orthopaedics, The First Affiliated Hospital of Nanjing Medical University, Nanjing 210029, China; fanweimin1959@vip.sina.com

Received: July 8, 2021; **Accepted:** August 20, 2021; **Published Online:** September 14, 2021

Citation: Zhang X, Liu Y, Zuo Q, *et al.,* 2021, 3D Bioprinting of Biomimetic Bilayered Scaffold Consisting of Decellularized Extracellular Matrix and Silk Fibroin for Osteochondral Repair. *Int J Bioprint*, 7(4):401. http://doi.org/10.18063/ijb.v7i4.401

1. Introduction

Osteochondral defects, which occur due to inflammation, trauma or aging, involve lesions of cartilage and subchondral bone and constitute a significant healthcare burden[1,2]. Current treatment strategies include microfracture, autologous chondrocyte implantation, and mosaicplasty. Nonetheless, there are still failures and undesirable complications in the above-mentioned treatment strategies[3-6]. In recent years, tissue engineering that provides suitable biomaterials to support the growth and differentiation of cells provides a promising strategy for osteochondral regeneration[7,8]. The application of bilayered scaffolds that concerned physical structure of osteochondral tissue has been the focus of osteochondral regeneration research[9,10]. Ideal bilayered scaffolds should be equipped with biological and physical properties that can match the native tissues[11,12]. However, traditional tissue engineering strategies have not been able to develop a bilayered scaffold with anisotropic structural properties to mimic a native osteochondral tissue[13]. Furthermore, each layer of the current bilayered scaffolds is usually fabricated separately and then joined together, resulting in a poor integration between two layers of the bilayered construction[11,14,15]. Recently, 3D bioprinting has emerged as a continuous way to fabricate biomimetic and complex tissue structure, such as osteochondral bilayered structure[11,13,16]. Three-dimensional (3D) bioprinting technology integrates equipment manufacturing industry, biomaterial science, and computer aided to fabricate

"living" engineered tissue or organ using bioink containing living cells, and thus has great potential in regeneration medicine[17-20].

3D bioprinting techniques can be classified into three distinct process categories: (i) Material extrusion[21], (ii) material jetting[22], and (iii) vat polymerization bioprinting[23]. Of these, extrusion-based bioprinting is the most prevalent employed research approach to fabricate 3D cell-laden scaffolds due to its accessibility, cost-effectiveness, and capacity to replicate tissue complexity[21]. For extrusion-based bioprinting, various biomaterials, such as gelatin, HA, or alginate, have been extensively used as bioink sources[24-28]. However, some problems remain, such as the cell toxicity of the chemical cross-link process, poor cell-material interactions, and inferior tissue formation[29,30]. In addition, only a small percentage of cells in these materials could drive cell differentiation towards target cell lineage[30,31]. Moreover, these materials cannot represent the complexity of extracellular matrices of repaired natural tissue. Therefore, there is an urgent need to develop a bioink that is sufficient to create a tissue-specific microenvironment with 3D cellular organization and cell-to-cell/cell-to-matrix communication that are typical of natural tissues.

Decellularized extracellular matrix (dECM) has been developed as bioink to fabricate 3D bioprinted tissues and organs[32,33]. Both biologically and functionally, dECM is more representative of the natural extracellular matrix (nECM) than other kinds of biomaterials. dECM provides a native-mimicking microenvironment for the migration, proliferation, and differentiation of bone marrow-derived mesenchymal stem cells (BMSCs)[34,35]. Furthermore, BMSCs encapsulated in cartilage dECM (DCM) or bone dECM (DBM) hydrogel can recognize and interact with surrounding matrix that specifically enhanced chondrogenic/osteogenic differentiation and tissue maturation[36]. However, the mechanical strength of DCM and DBM is insufficient because of the loss of cartilage/bone native tissue structure during the homogenization and solubilization process[36,37]. Silk fibroin (SF) is a natural biopolymer that is widely investigated for various 3D bioprinting and tissue engineering applications due to its remarkable mechanical properties, biocompatibility and biodegradation nature[38,39]. In our previous study, we reported the use of a cross-linker-free DCM-SF bioink in printing 3D construct which had similar mechanical properties compared with native cartilage tissue[37].

Since dECM-based bioink most likely retain endogenous growth factors than other kinds of bioink, it will lead to enhancement of osteochondral regeneration that incorporates additional exogenous growth factors in dECM bioink. The previous studies have shown that dECM acts as an excellent growth factor delivery system since the extracellular matrix (ECM) itself is a natural reservoir for growth factors which have a natural affinity to ECM[40,41]. Transforming growth factor-beta (TGF-β) is regarded as a highly efficient chondrogenic factor[42]. Bone morphogenetic protein-2 (BMP-2) plays a key role in driving osteogenesis of BMSCs[43]. Hence, the combination of such a bioink with TGF-β and BMP-2 is effective to enhance osteochondral regeneration.

Therefore, on the basis of our previous study, we employed dECM-SF bioink to fabricate 3D-printed bilayered constructs. First, polycaprolactone (PCL) was first extruded to print frame of bone layer, and the DBM bioink was printed to fill the space. The DCM bioink was used to print the cartilage layer on the bone layer. Next, we evaluated the mechanical strength and degradation rate of the two layers to confirm the properties of constructs. Furthermore, the delivery capacity of growth factors and the potential of constructs for chondrogenesis or osteogenesis were measured *in vitro*. Finally, we implanted bilayered constructs containing TGF-β1 and BMP-2 into the osteochondral defect and determined the osteochondral regeneration efficacy *in vivo*.

2. Materials and methods

All experimental procedures involving animals have been approved and implemented in accordance with the animal use guidelines outlined by the Medical College of Nanjing Medical University (IACUC-2005033). All animal subjects were treated in accordance with the National Laboratory guidelines for Laboratory Animal Nursing.

2.1. Preparation of decellularized cartilage/bone ECM

Decellularized DCM and DBM were prepared based on our previously reported method[37]. Briefly, articular cartilage and cancellous bone segments were harvested from female goats (n = 12) within 6 h after sacrifice. These cartilage and bone segments were washed, freeze-dried, and immersed in liquid nitrogen and cut into small pieces (1~2 mm^3). The cartilage pieces were rinsed with phosphate-buffered saline (PBS), while the bone pieces were demineralized using an adaptation of previously reported methods by submerging in 0.5 M hydrochloric (HCL) under agitation for 24 h, and then degreased with 1:1 mixture of chloroform and methanol for 2–3 h[44]. Cartilage and demineralized bone pieces were washed thoroughly with PBS and lyophilized before decellularization. The cartilage and bone pieces were homogenized, milled, and soaked in PBS containing 0.1% w/v ethylenediaminetetraacetic acid (EDTA; Sigma-Aldrich, St. Louis, MO, USA) and 3.5% w/v phenylmethyl sulfonylfluoride (PMSF; Beyotime, Shanghai, China) for 24 h to inhibit protease activity. These cartilage and bone granules were treated with a 1%

solution of Triton X-100 in a protease inhibitor cocktail (0.1% w/v EDTA, 3.5% w/v PMSF in Tris-HCl, pH = 7.5) for 24 h. Next, the cartilage and bone granules were washed and digested with 50 U/mL deoxyribonuclease and 1 U/mL ribonuclease (Sigma-Aldrich, St. Louis, MO, USA) for 12 h. To obtain DCM and DBM, the granules were lyophilized and solubilized using a previously reported protocol with modifications[30]. In brief, 10 mg decellularized granules were mixed with 1 mL of 0.1 mol HCl containing 1 mg of pepsin powder (Sigma-Aldrich, St. Louis, MO, USA) at room temperature for 2 days. After solubilization, 1 Mol NaOH was added to adjust the pH to 7.4. The solution was centrifuged at 10,000 ×*g* for 3 min to remove undigested particles and the supernatant was lyophilized and stored at −80℃ for longer storage.

2.2. Preparation of TGF-β1-loaded DCM/SF bioink

Solubilized and lyophilized SF protein (SF, molecular weight >100 kDa) was purchased from Simatech Inc. (Suzhou, China). Polyethylene glycol (PEG 400; molecular weight 380~420 Da) was provided by Aladdin Inc. (Shanghai, China). About 10% w/v of SF, 5% w/v DCM, and 4 μg/mL of TGF-β1 (PeproTech, Rocky Hill, USA) were dissolved in PBS to prepare SF/DCM blends. The blends were then mixed with an equal volume of 80% v/v PEG for gelation of the DCM/SF bioinks (5% w/v final SF concentration; 2.5% w/v final DCM concentration; and 2 μg/mL final TGF-β1 concentration).

2.3. Preparation of BMP-2-loaded DBM/SF bioink

About 10% w/v of SF, 5% w/v DBM, and 4 μg/mL of BMP-2 (PeproTech, Rocky Hill, USA) were dissolved in PBS to prepare SF/DBM blends. The blends were then mixed with an equal volume of 80% PEG for gelation of the DBM/SF bioinks (5% w/v final SF concentration; 2.5% w/v final DBM concentration; and 2 μg/mL final BMP-2 concentration).

2.4. Cell isolation and encapsulation

BMSCs were harvested and isolated as we previously described[45,46]. Briefly, bone marrow aspirate was isolated from the medullary cavity of femur bone in New Zealand rabbits. The mixture of cells was separated by gradient density centrifugation in 1.073 g/ml lymphocyte separation solution (Gibco, NY, USA). The mononuclear fraction interphase was collected and washed twice in sterile PBS. The cells were resuspended in low-glucose DMEM containing 100 U/ml penicillin, 100 U/ml streptomycin, and 10% fetal bovine serum (HyClone, UT, USA), and subsequently incubated at 37°C with 5% CO_2. The culture medium was changed to remove suspension cells after 48 h, and the adherent cells were expanded up to passage 3. To encapsulate cells for 3D bioprinting, BMSCs were trypsinized after reaching approximately 80% confluence and then washed with low-glucose DMEM containing 10% fetal bovine serum. After centrifugation at 1200 rpm for 5 min, BMSCs were resuspended in bioinks at a density of 1.0×10^7 cells mL^{-1}.

2.5. Fabrication of bilayered scaffolds

3D bioprinting system (3D Discovery, Regenhu, Villaz-St-Pierre, Switzerland) provided by Bioexcellence Inc. (Beijing, China) was used to fabricate the bilayered scaffolds. DBM bioink and DCM bioink were prepared and loaded into 10 mL plastic containers at room temperature. FDA-approved PCL (molecular weight 70–90 Kda) provided by Polysciences Inc. (PA, USA) was loaded into metal container with temperature control, and the container temperature was set to 60°C. The parameters related to the process of printing are listed in **Table 1**.

For the fabrication of the bone layer (4 mm in diameter, 4.5 mm in height), PCL was first extruded to print outline, and then, the DBM/SF bioink was printed to fill the space. DCM/SF bioink was used to print the cartilage layer (4 mm in diameter, 0.5 mm in height) on the bone layer (**Figure 1**). The thicknesses of cartilage layer and bone layer were adjusted to 2 mm for *in vitro* investigation.

2.6. Fourier-transform infrared (FTIR) spectroscopy

The infrared spectra of DCM/SF and DBM/SF hydrogels were evaluated using Thermo Scientific Nicolet iS5 FT-IR Microscope (Waltham, MA, USA). The samples were prepared by lyophilization for FTIR analysis. Scanning was conducted in the spectral range from 1000 cm^{-1} to 2200 cm^{-1}.

Table 1. Parameters of the designed construct and 3D bioprinting.

Parameters	Cartilage layer	Bone layer	
	DCM/SF bioink	DBM/SF bioink	PCL
Container temperature	**15°C**	**15°C**	**60°C**
Nozzle diameter	0.25 mm	0.25 mm	0.25 mm
Size (length * width * height)	4 mm* 4 mm*0.5 mm	4 mm*4 mm*4.5 mm	
Interlayer spacing	0.25 mm	0.25 mm	0.25 mm
Line spacing	0.20 mm	0.20 mm	2 mm
Printing speed	4 – 7 mm/s	3 – 5 mm/s	1.8 ~ 2.7 mm/s
Print pressure	0.20–0.30 MPa	0.20 – 0.30 MPa	0.50~0.60 MPa

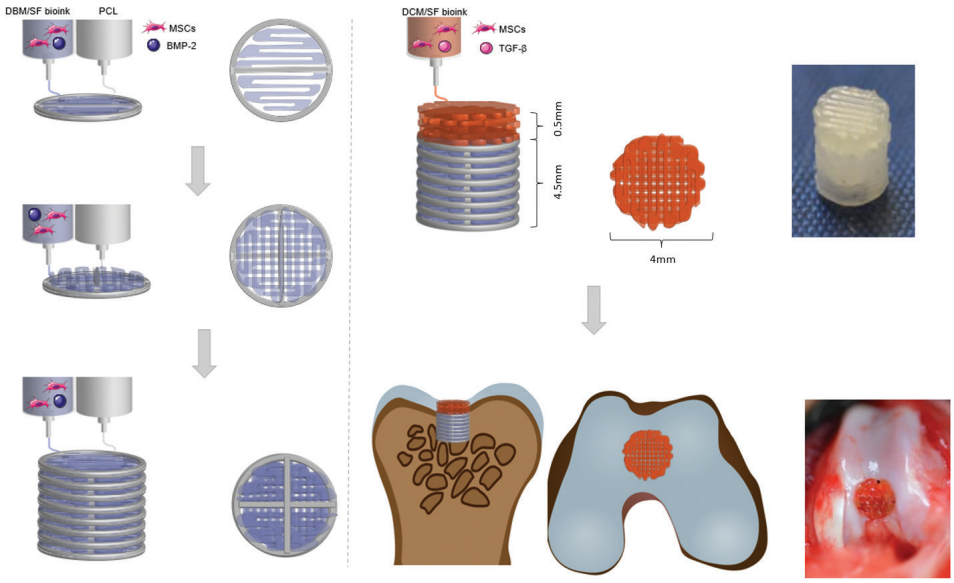

Figure 1. Schematic illustration of the bilayered scaffold loaded with transforming growth factor-β and bone morphogenetic protein-2 for osteochondral repair.

2.7. Rheological analysis

Thermo Scientific HAAKE MARS 40 Rheometer (Waltham, MA, USA) was used to investigate rheological properties fitted with 25 mm parallel geometry. Frequency-dependent loss modulus (G''), storage modulus (G'), and dynamic viscosity of DCM/SF and DBM/SF hydrogels were determined by the frequency sweep in the shear rate range of 0.1~100 Hz at 15℃.

2.8. Growth factor releasing

To investigate release of growth factors, cartilage layer and bone layer construct samples were encapsulated with 2 μg/mL TGF-β1 and 2 μg/mL BMP-2, respectively. To evaluate the release rate of TGF-β1, pre-weighed cartilage layer samples were rinsed with 2 ml PBS solutions containing 0.05% EDTA, 0.1% heparin, 0.02% sodium azide, and 0.1% BSA at 37°C. The PBS solution was replenished and harvested every 48 h for 21 days. The harvested PBS samples were then assessed by TGF-β1 ELISA Kit assay (PeproTech, RH, USA). To evaluate the release rate of BMP-2, pre-weighed bone layer samples were rinsed with 2 ml PBS solutions containing 0.05% EDTA, 0.1% heparin, 0.02% sodium azide, and 0.1% BSA at 37°C. The PBS solution was replenished and harvested every 48 h for 14 days. The harvested PBS samples were then assessed by BMP-2 ELISA Kit assay (PeproTech, Rocky Hill, USA). All samples were analyzed in triplicate.

2.9. Cell viability

For the observation of cell viability, LIVE/DEAD cell staining kit (Molecular Probes, OR, USA) was used to stain cells. Cell-scaffold construct samples were incubated in low-glucose DMEM containing 2 μM calcein AM (live) and 4 μM ethidium homodimer-1 (dead) reagents at 37°C for 45 min. Fluorescence images were obtained from a fluorescence microscope (Zeiss, Nanjing, China). Calcein AM (green) and ethidium homodimer-1 (red) were detected by excitation wavelengths of 495 nm and 560 nm, respectively. The cell survival rate at 1 and 3 days was analyzed using ImageJ software. Cell proliferation and viability in construct samples were examined using CCK8 assay (Beyotime, Nanjing, China) after 1, 4, and 7 days of culture.

2.10. Degradation of 3D bilayered scaffolds

For the analysis of degradation of bilayered scaffolds, the rates of weight loss were performed with treatment of protease XIV enzyme at several time points over 24 days. The weight loss test of cartilage layer and bone layer was conducted separately. The initial dry printed scaffold was weighed as W0 and the enzyme solution was changed every day. Scaffolds were taken out from the enzyme solution and weighed at dry state at each time point (Wd). The degradation rate was defined as $100\% \times (W0 - Wd)/W0$.

2.11. Comprehensive stress

For the investigation of comprehensive properties, cartilage layer and bone layer construct samples were loaded on an Instron Tensile Force Tester (Instron, HW, UK). A displacement rate of 0.1 mm/min was set to obtain stress-strain curve. The compression modulus was determined from the linear region of the stress-strain curve.

2.12. mRNA expression

For mRNA expression analysis, cell-scaffold construct samples were cultured for 7 and 14 days (n = 3). For mRNA extraction, the samples were homogenized and lysed in TRIzol (Yeasen, Shanghai, China) before being centrifuged at 12,000 rpm at 4°C. Subsequently, a cDNA reverse transcription kit (Yeasen, Shanghai, China) was used to reverse-transcribed total RNA into cDNA. The expression levels of cartilage-related markers (COL II, type-2 collagen; ACAN, aggrecan; SOX-9, SRY-box transcription factor 9) and osteogenic-related markers (COL I, type-1 collagen; OCN, osteocalcin; ALP, alkaline phosphatase; RNUX2, runt-related transcription factor 2) were analyzed by real-time qPCR system (Applied Biosystems, CA, USA). The target mRNA was normalized to a housekeeping control (glyceraldehyde 3-phosphate dehydrogenase mRNA) and determined using the ΔΔCt method. The sequences are listed in **Table S1**.

2.13. *In vivo* surgical operation

To determine the osteochondral regeneration effect *in vivo*, New Zealand white rabbits weighted 2.0 – 3.0 kg were chosen to create osteochondral defect models. After general anesthesia, osteochondral defects (diameter: 4 mm, depth: 5 mm) were caused on the patellar groove of right knee joints. In the control group (n = 6), the defect was left blank without material added. In the pristine-bilayered construct group (PB group) (n = 6), the constructs without bioactive growth factors were implanted into the defects. In the GF-bilayered construct group (GB group) (n = 6), bilayered constructs containing TGF-β1 and BMP-2 were implanted in the osteochondral defect (**Figure S2A and B**). The rabbits were anesthetized and executed 3 months after operation.

2.14. Histological and immunohistochemical analysis

For histological assessment, rabbit femurs were fixed overnight in 4% paraformaldehyde at 4°C and then decalcified with decalcification solution for about 30 days. The decalcified constructs were dehydrated with a graded series of ethanol and embedded in paraffin for sectioning. The deparaffinized paraffin sections were stained with safranin O and Masson's trichrome, and imaged with an Olympus microscope. To further observe the expression of COL II and OCN, immunohistochemical staining was performed as we previously described[47]. The ICRS Visual Histological Assessment Scale was carried out to score the morphology and the degree of metachromatic staining, respectively. The total score ranged from 0 to 18, including semi-quantitative scales to rate the surface, matrix, cell distribution, viability of the cell population, subchondral bone, and cartilage mineralization.

2.15. Biochemical analysis

We analyzed the contents of collagen and sulfated-glycosaminoglycan (sGAG) of samples. Samples were dissolved in papain digestion (125 μL/mL papain, 100 mM EDTA, and 5 mM L-cysteine; Sigma-Aldrich, MO, USA) at pH 6.5 at 60°C under rotation for 18 h. Collagen content was examined by quantifying hydroxyproline concentration. Briefly, the hydroxyproline content of the solution was determined by the chloramine-T assay after acidic hydrolyzation in 38% HCl for 18 h at 110°C. Collagen content was calculated by assuming a hydroxyproline: collagen ratio of 1:7.69. The total sGAG content was analyzed by the 1,9-dimethylmethylene blue (DMMB; Sigma-Aldrich, MO, USA) assay. The sGAG and collagen content were normalized by dry weight of construct.

2.16. Statistical analysis

All data are expressed as the mean ± standard deviation (SD), and $P < 0.05$ was considered statistically significant. For statistical analysis, intergroup differences were calculated by analysis of variance (ANOVA) after testing for homogeneity of variance. All statistical analysis was performed using Statistical Package for the Social Sciences (SPSS) version 19.0 software (IBM SPSS Statistics for Windows, Armonk, NY, USA).

3. Results and discussion

3.1. Preparation and characterization of DCM/SF and DBM/SF bioinks

To estimate the ECM component change, we determined the collagen and glycosaminoglycans (GAGs) contents before and after decellularization (**Figure S1A and B**). A significant loss of collagen and GAGs in DCM and DBM was observed after decellularization. The reason behind the reduction of the collagen and GAGs is the treatment with the enzymes during the trypsinization and decellularization including deoxyribonuclease , ribonuclease and pepsin[30,48]. Quantification of DNA content from native ECM (NCM and NBM) and dECM (DCM and DBM) revealed the significant reduction (~96%) in the case of dECM as compared to the native ECM before decellularization.

We investigated rheological behavior to explore flow properties of DCM/SF and DBM/SF bioinks. The frequency sweep indicated that viscosity of DCM/SF and DBM/SF bioinks decreased in response to linearly increasing shear rate (**Figure 2A**), indicated that the bioinks exhibited shear-thinning flow behavior, which are similar to most polymer gels[36]. Furthermore, the G' values exceeded the G'' values over the whole angular frequency range (G' > G''; **Figure 2B**), indicating the formation of a typical gel structure[49].

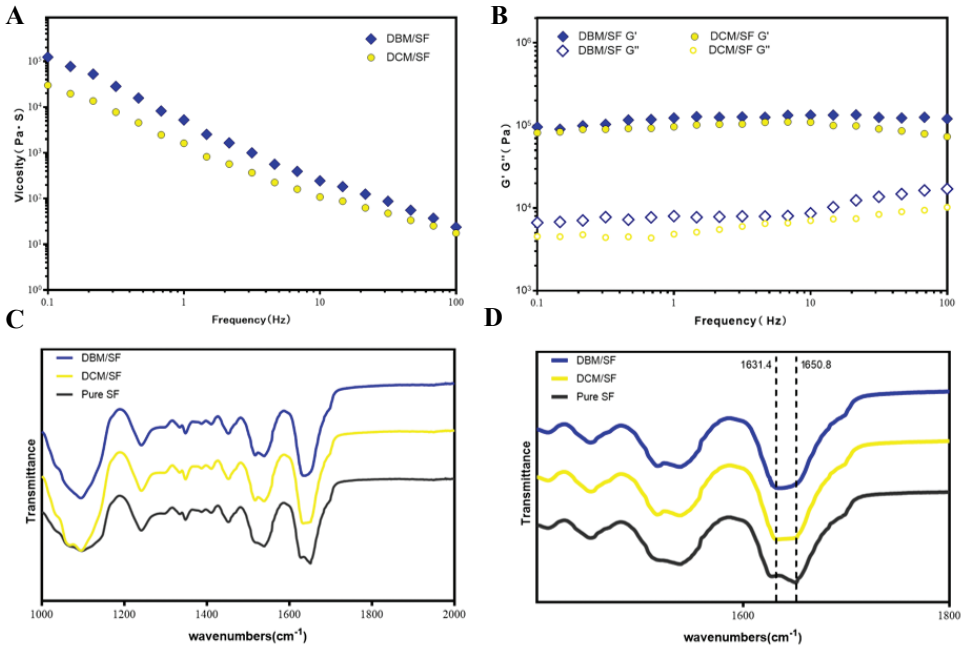

Figure 2. (A) Frequency sweep of the DCM/SF and DBM/SF bioinks. (B) Dynamic viscosity measurement of the DCM/SF and DBM/SF bioinks. (C, D) FTIR absorption spectra of the DCM/SF and DBM/SF bioinks.

FTIR spectroscopy was done to analyze the crystallization of SF in DCM/SF and DBM/SF bioinks (**Figure 2C**). The pure SF control group showed a major peak at 1,650.8 cm^{-1} in the amide I region (C=O stretch), suggesting the presence of a higher proportion of random coils than β-sheet structure[50]. The major peak of DCM/SF and DBM/SF bioinks in the amide-I region shifted to a lower wavelength at 1628–1632 cm^{-1} (**Figure 2D**), indicating that the mixture was dominated by β-sheet structure[51].

3.2. One-step 3D-bioprinting and characterization of a bilayered scaffolds

We printed the bilayered scaffolds as shown in **Figure 3A**. PCL was first extruded to print frame of bone layer, and the DBM bioink was printed to fill the space. The DCM bioink was used to print the cartilage layer on the bone layer. The PCL frame not only provided a mechanical support in the bone layer but it is also favorable for the cell migration and exchange of nutrients because the DCM/SF hydrogel take up more space than PCL frame in the bone layer.

For the analysis of degradation of bilayered scaffolds, the rates of weight loss were performed with treatment of protease XIV enzyme at several time points over 24 days (**Figure 3B**). Bone layer constructs showed a significantly lower degradation rate than cartilage layer constructs. The reason lies in the slow degradation characteristics of PCL frame in the bone layer. For measurement of compressive strength, 3D-printed constructs were subjected to mechanical tests. We performed the stress-strain curve to investigate the relation between compressive stress and strain (**Figure 3C**). The compressive stress finally reached the maximum before yielding for bone layer construct, bone layer construct without PCL frame, and cartilage layer construct at the compressive stress of 310 kpa, 47 kPa, and 44 kPa, respectively. The compressive modulus was significantly higher in bone layer construct than in the bone layer construct without PCL and cartilage construct, with about 9-fold enhancement (**Figure 3D**). Ding *et al*. reported that the difference in compressive modulus is approximately 5–20 times between natural cartilage and bone[52].

We then observed the viability of BMSCs in printed cartilage and bone layers by live/dead staining assay (**Figure 4A and B**). The survival rates of BMSCs in the printed cartilage and bone layer were over 80% (**Figure 5C**). CCK8 cell proliferation assay was also carried out to ascertain the viability of BMSCs in both layers at different time points (**Figure 5D**). The optical density (OD) value increased over the 7 days of culture and did not differ significantly between cartilage and bone layer. The results indicated that the cartilage and bone layers promoted the proliferation of BMSCs and exhibited low cytotoxicity.

3.3. Release of growth factors from the scaffolds promoted differentiation of BMSCs *in vitro*

Growth factors such as TGF-β and BMP-2 play an important role in promoting directed differentiation of

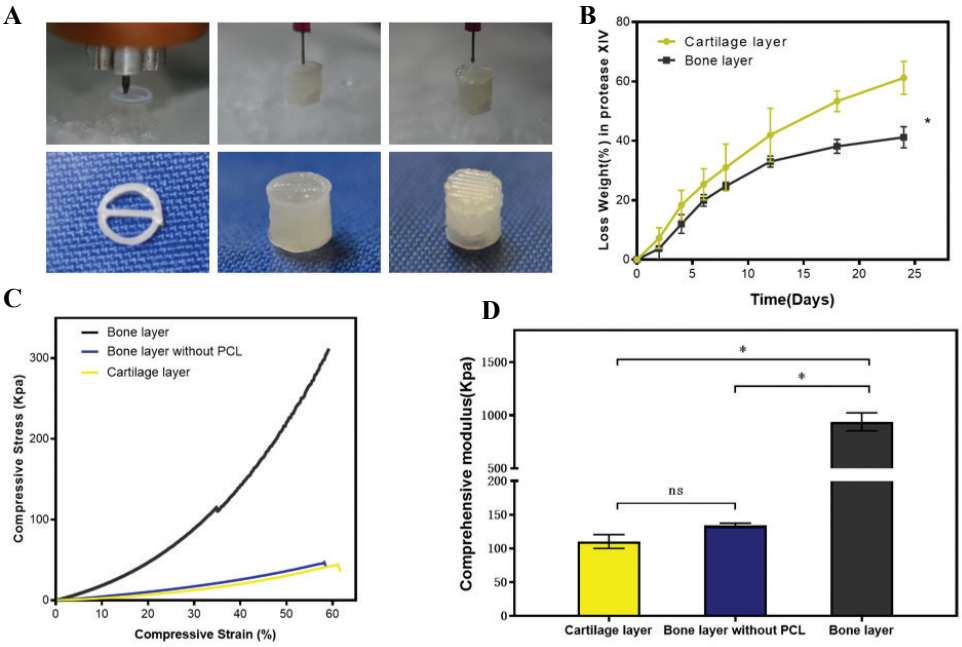

Figure 3. (A) PCL was first extruded to print frame of bone layer, and the DBM bioink was printed to fill the space. The DCM bioink was used to print the cartilage layer on the bone layer. (B) Degradation rate of cartilage layer and bone layer in protease XIV. (C) Stress-strain curve that was used to investigate the relation between compressive stress and strain. (D) Comprehensive modulus calculated by linear region of the stress-strain curve ($n = 3$; $^*P < 0.05$).

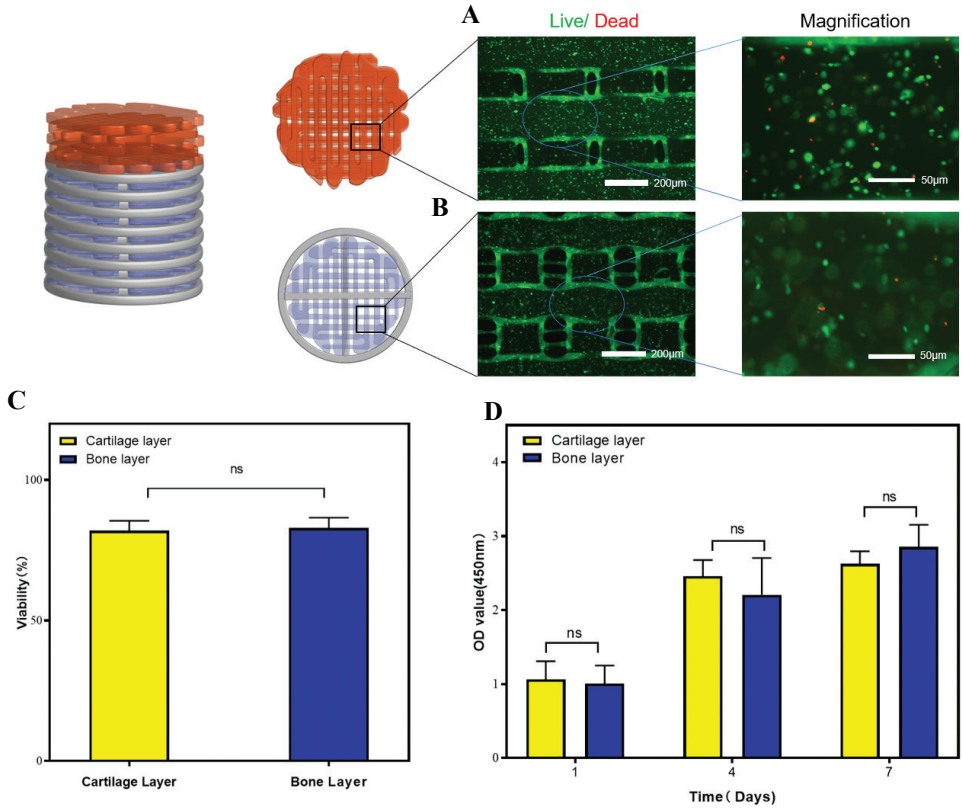

Figure 4. Viability of BMSCs in the printed constructs. Fluorescence microscopy findings of the LIVE/DEAD assay of BMSCs cultured in the (A) cartilage layer and (B) bone layer. (C) Quantification of cell viability. (D) Cell viability results obtained by the CCK-8 assay on 1, 4, and 7 days of cell culture ($n = 3$; $^*P < 0.05$).

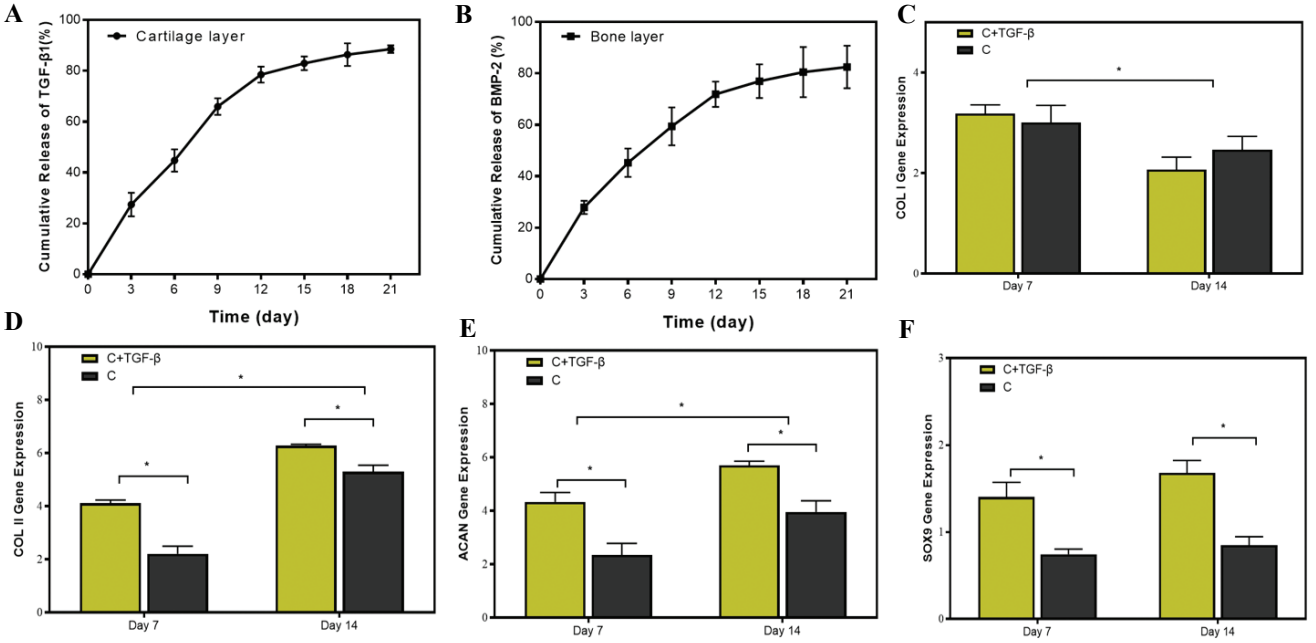

Figure 5. (A) Release kinetics of TGF-β1 from printed cartilage layer. (A) Release kinetics of TGF-β1 from printed cartilage layer. (B) Release kinetics of BMP-2 from printed bone layer. mRNA expression level of cartilage-related genes, including (C) collagen type I (*COL I*, a fibrotic marker gene), (D) collagen type II (*COL II*), (E) aggrecan (*ACAN*), and (F) *SOX-9* in cartilage layer group (C group) and cartilage layer loaded with TGF-β1 group (C+TGF-β group) on days 7 and 14 ($n = 3$; $^*P < 0.05$).

BMSCs[53,54]. Although dECM-based bioink most likely retain endogenous growth factors than other kinds of bioink, the pure dECM is always insufficient for the effective treatment of osteochondral defects due to the loss of bioactive factors during decellularized process. Datta *et al*. reported the reduction of BMP-2 in decellularized bone matrix due to decellularization[55]. Almeida *et al*. reported that the addition of exogenous TGF-β in dECM promoted the chondrogenesis of fat pad-derived stromal cells[41]. Moreover, the previous studies have shown that dECM acts as an excellent growth factor delivery system since the ECM itself is a natural reservoir for growth factors which have a natural affinity to ECM[40,41]. In this study, we developed a controlled release system by encapsulating TGF-β1 and BMP-2 into the bilayered construct.

We evaluated the TGF-β1 and BMP-2 release using ELISA to determine the capacity of scaffolds to support the controlled release of growth factors. The printed cartilage layer suggested a relatively fast release of TGF-β1 about 65.91 ± 3.29% in the beginning 9 days, with a slow release reached to 88.51 ± 1.51 % in the following days (**Figure 5A**). BMP-2 in the printed bone layer displayed an initial burst release to 59.39 ± 7.36% within the first 9 days (**Figure 5B**). BMP-2 exhibited a sustained release profile after being released for more than 12 days. The cumulative release of BMP-2 reached to 82.45 ± 8.26% after being released for 21 days. The results indicated that the bilayered construct exhibited sustained long-term release of growth factors.

Next, we investigated whether the release of TGF-β has an effect on chondrogenic differentiation potential of BMSCs in cartilage layer *in vitro*. To answer this question, we examined the mRNA expression levels of collagen I (COL I), collagen II (COL II), aggrecan (ACAN), and SOX-9 by real-time quantitative polymerase chain reaction (qPCR) on days 7 and 14 of culture (**Figure 5C-F**). The reverse transcription polymerase chain reaction (RT-PCR) analysis showed that the mRNA expression levels of COL I in C+TGF-β group were comparable to that in C group. The mRNA expression levels of COL I were significantly decreased from day 7 to day 14. The expression of COL II and ACAN in the C+TGF-β group was significantly higher than that in the C group at 2 time points. In addition, the expressions of COL II and ACAN in the C+TGF-β group and C group at day 14 were significantly increased as compared with day 7. SOX-9, a member of the Sry-type HMG box (SOX) gene family, is expressed to activate the expression of cartilage ECM-related gene (COL II and ACAN) and suppress the expression of fibrotic-related gene (COL I)[56]. SOX-9 plays a key role in the chondrogenic differentiation process of stem cells. The previous studies reported that SOX-9 is activated during very early events in chondrogenesis of BMSCs, and directly or indirectly maintains its regulation during the differentiation and maturation of chondrocytes[57]. The RT-PCR analysis showed that the SOX-9 transcription level was similar at the 2 time points. Significantly higher SOX-9 transcription occurred in the C+TGF-β group

than in the C group, suggesting that a higher extent of signaling cascade was activated during the chondrogenic differentiation of BMSCs over the C+TGF-β group than C group.

Furthermore, to investigate the osteogenic differentiation of BMSCs in the bone layer, the expression levels of COL I, RUNX2, OCN, and ALP were measured by RT-PCR (**Figure 6A-D**). The result showed that mRNA expression levels of COL I, RUNX2, and OCN for B+BMP-2 group were obviously higher than those for B group after culture for 14 days. The mRNA expression levels of ALP did not differ significantly between the B+BMP-2 group and the B group at day 7. On the other hand, the expression of ALP in the B+BMP-2 group was significantly higher than that in the B group at day 14. As a transcription factor, RUNX2 is expressed to activate the expression of bone-related gene (COL I, OCN, and ALP). The activation and expression of RUNX2 peak in the early stage of osteogenic differentiation of BMSCs[11]. The RT-PCR suggested that the RUNX2 expression level showed no significantly difference at the 2 time points. Meanwhile, the RUNX2 transcription level was significantly higher in the B+BMP-2 group than in the B group at days 7 and 14, indicating that a higher extent of signaling cascade was activated during the osteogenic differentiation of BMSCs in the B+BMP-2 group than in the B group. The result indicated that the B+BMP-2 constructs were able to enhance osteoinductive abilities *in vitro*.

3.4. The scaffolds loaded with growth factors promoted osteochondral regeneration *in vivo*

To investigate whether the composite constructs stimulate osteochondral regeneration *in vivo*, regenerative efficacy was further observed in a rabbit osteochondral defect model. No deaths occurred during the whole observational period. The grafts were sampled 3 months after operation. The gross macroscopic observations suggested that the regenerated tissues of the PB and GB groups seemed smooth and similar to the surrounding normal tissues (**Figure 7A**). The defects of the PB and GB groups were completely covered with excellent integration, whereas the repaired tissues of the control group only partially filled the defect and showed incomplete integration with the native cartilage tissues.

Histological and immunohistochemical staining analyses were conducted to evaluate repair efficacy. Compared to the control group and PB group, the GB group had smoother and more homogeneous neocartilage which had a considerable number of typical cartilage lacunae structures (**Figure 7B**). The cells in neocartilage of GB group were in a typical linear arrangement and similar to normal chondrocytes. Masson (blue staining) and safranin O (red staining) staining were carried out to evaluate the proportion of collagen and proteoglycan content, respectively (**Figure 7C and D**). Compared to other groups, the collagen and proteoglycan deposition in the neocartilage of GB group was abundant and uniform.

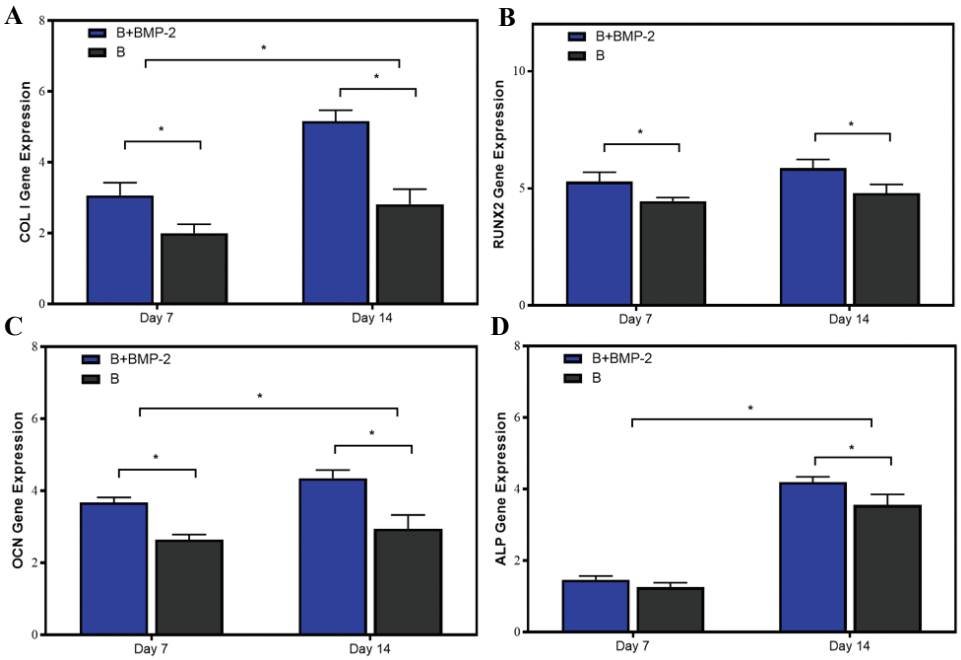

Figure 6. mRNA expression level of bone-related genes, including (A) collagen type I (*COL I*, a fibrotic marker gene), (B) RUNX family transcription factor 2 (*RUNX2*), (C) osteocalcin (*OCN*), and (D) alkaline phosphatase (*ALP*) in bone layer group (B group) and cartilage layer loaded with BMP-2 group (B+BMP-2 group) on days 7 and 14 ($n = 3$; $*P < 0.05$).

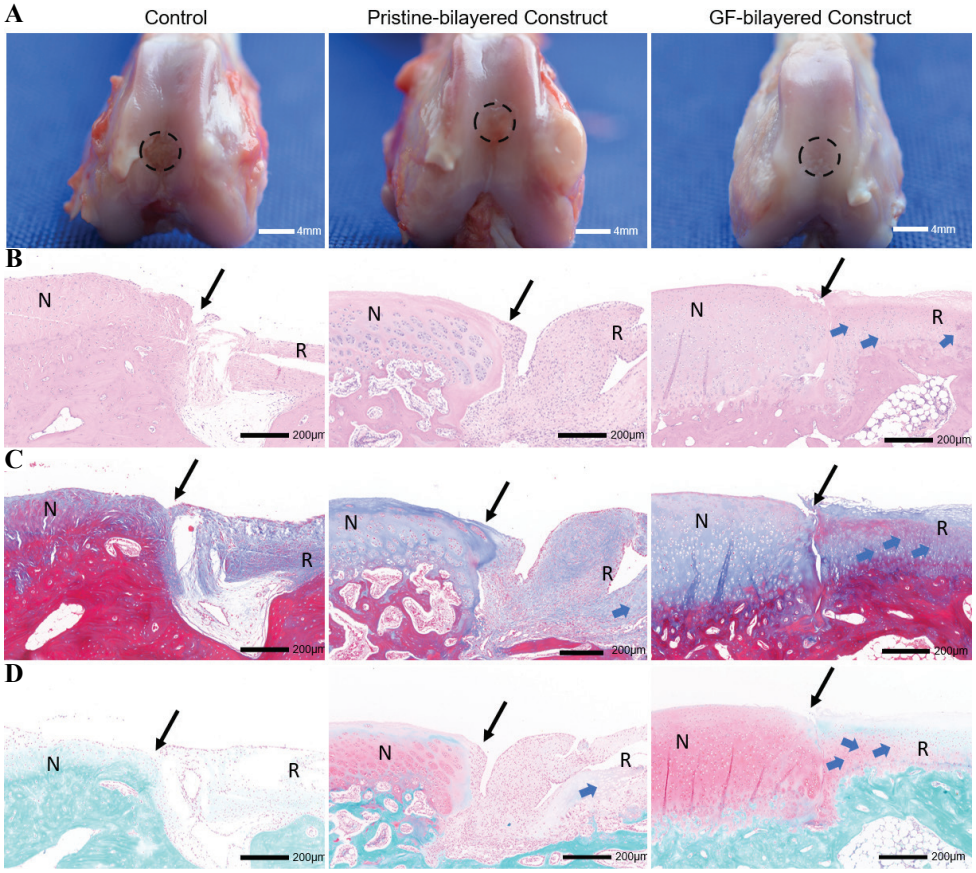

Figure 7. The bilayered constructs facilitated the regeneration of osteochondral tissues *in vivo* (n = 6). The grafts were sampled 3 months after operation. (A) Gross observations of defect repair at 3 months for the control group, pristine-bilayered construct group, and GF-bilayered construct group (scale bar: 4 mm). (B) Hematoxylin and eosin (H & E) staining of repaired cartilage at 3 months (N, normal cartilage; R, repair cartilage; blue arrows, typical cartilage lacunae structures; black arrows, the repair boundary of the cartilage surface; scale bar: 200 μm). (C) Masson staining of repaired cartilage at 3 months (scale bar: 200 μm). (D) Safranin-O/fast green staining of repaired cartilage at 3 months (scale bar: 200 μm).

Coll II immunohistochemical staining demonstrated more intense staining in the GB group compared to other two groups (**Figure 8A**). A high expression of Coll II surrounding the chondrocytes could be observed in the neocartilage of GB group. Neovascularization, trabecula structure (**Figure 8B and C**), and higher intensity of staining of OCN **(Figure 8D)** could be observed in the neo-bone of GB group. While in the control group, incompletely calcified cancellous bone could be found in the bone layer. Furthermore, we performed a histologic score according to the ICRS Visual Histological Assessment Scale (**Figure S2C**). The histologic score was significantly higher in the GB group than in the PB and control groups.

Regenerated cartilage was further investigated by quantifying sGAG and collagen contents. The sGAG content of neocartilage was 9.36 ± 1.279 μg/mg in control group, 16.03 ± 0.784 μg/mg in PB group, and 24.83 ± 1.866μg/mg in GB group, with statistically significant differences ($P < 0.05$). The collagen content of neocartilage was 72.95 ± 5.82 μg/mg in control group, 106.50 ± 7.84 μg/mg in PB group, and 115.50 ± 11.28 μg/mg in GB group. The collagen content of GB group and PB group was significantly higher than that of control group. There was no significant difference between collagen content in the GB group and PB group.

In the current study, we demonstrated that a 3D bioprinted bilayered scaffolds can be used as a controlled released system, which leads to the reconstruction of osteochondral tissue. Each layer of bilayered scaffolds had a suitable mechanical strength and degradation rate. Furthermore, the scaffolds encapsulating TGF-β1 and BMP-2 can act as a controlled release system and promote osteochondral regeneration. Although the mechanical strength of the bilayered scaffolds needs to be further enhanced, this method does provide a novel strategy for osteochondral regeneration.

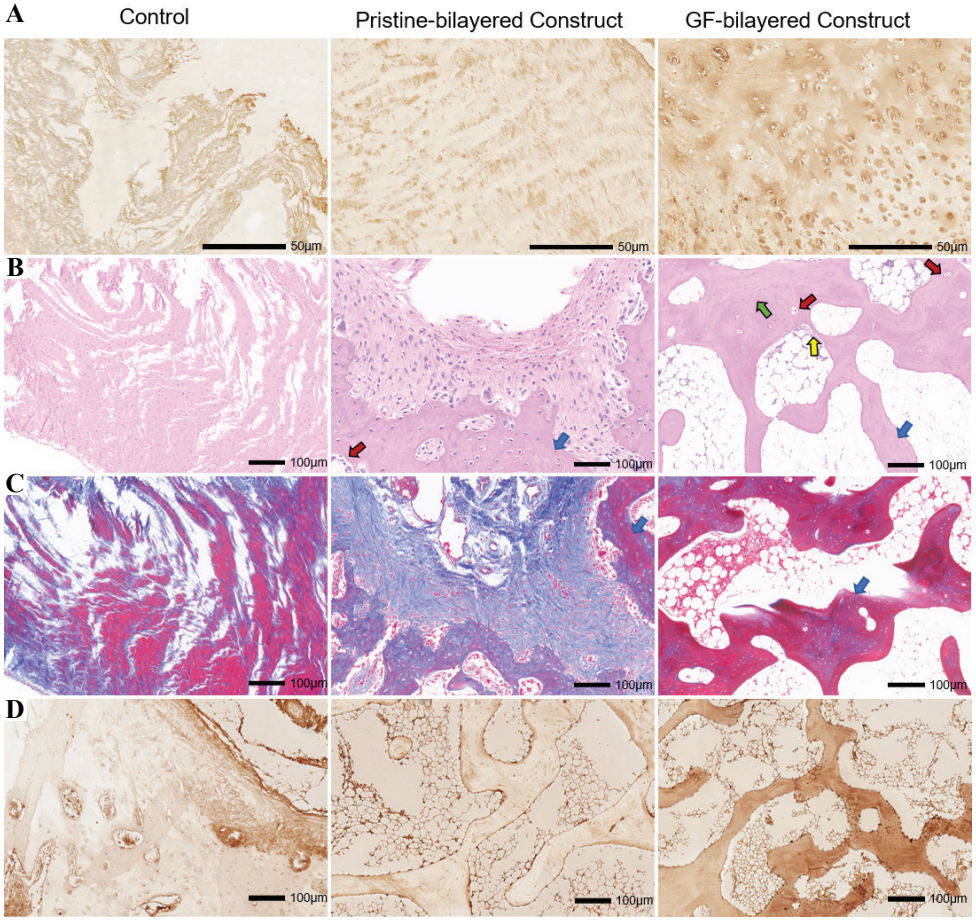

Figure 8. (A) Immunohistological staining for collagen type II of neocartilage at 3 months for the control group, pristine-bilayered construct group, and GF-bilayered construct group (scale bar: 50 μm). (B) H & E staining and imaging of neo-bone at high magnification at 3 months (blue arrows, trabecular structures; green arrows, typical osteoblasts; yellow arrows, osteocytes; red arrows, vascularization; scale bar: 100 μm). (C) Masson staining of neo-bone at 3 months (scale bar: 100 μm). (D) Immunohistological staining for OCN of neo-bone at 3 months (scale bar: 100 μm).

4. Conclusions

The present study has shown that each layer of scaffolds had a suitable mechanical strength and degradation rate. Furthermore, the scaffolds encapsulating TGF-β1 and BMP-2 can act as a controlled released system and promote directed differentiation of BMSCs. The *in vivo* experiments suggested that the scaffolds loaded with growth factors promoted osteochondral regeneration in the rabbit knee joint model. Altogether, the biomimetic bilayered scaffolds offer a novel option for application in osteochondral regeneration.

Acknowledgments

We would like to thank the Core Faility of Jiangsu Provincial People's Hospital for its help in the detection of experimental samples.

Funding

This work was supported by the National Natural Science Foundation of China (No. 81974332).

Conflicts of interest

There are no conflicts of interest to declare.

Authors' contributions

WM. F. planned the experiments; Q. Z. and Y. L. supervised the project; X. Z., ZX. L., R. X. and T. Y. carried out the experiments; Y. L. and Q. Z. performed the data analyses; X. Z. wrote the manuscript; QY. W., K. S., Y. Z., and K. Y. discussed the results, and reviewed and edited the manuscript.

References

1. Lewis PB, McCarty LP 3rd, Kang RW, et al., 2006, Basic Science and Treatment Options for Articular Cartilage Injuries. *J Orthop Sports Phys Ther*, 36:717–27.
2. Kilian D, Ahlfeld T, Akkineni AR, *et al*., 2020, 3D Bioprinting of Osteochondral Tissue Substitutes *in Vitro*-Chondrogenesis in Multi-layered Mineralized Constructs. *Sci Rep*, 10:8277.

3. Hu J, Zou WZ, Li L, *et al*., 2020, Overexpressing Runx2 of BMSCs Improve the Repairment of Knee Cartilage Defects. *Curr Gene Ther*, 20:395–404.
4. Stefani RM, Barbosa S, Tan AR, *et al*., 2002, Pulsed Electromagnetic Fields Promote Repair of Focal Articular Cartilage Defects with Engineered Osteochondral Constructs. *Biotechnol Bioeng*, 117:1584–96.
5. Levingstone TJ, Ramesh A, Brady RY, *et al*., 2016, Cell-free Multi-layered Collagen-based Scaffolds Demonstrate Layer Specific Regeneration of Functional Osteochondral Tissue in Caprine Joints. *Biomaterials*, 87:69–81.
6. Khanarian NT, Haney NM, Burga RA, *et al*., 2012, A Functional Agarose-hydroxyapatite Scaffold for Osteochondral Interface Regeneration. *Biomaterials*, 33:5247–58.
7. Abdollahiyan P, Oroojalian F, Mokhtarzadeh A, *et al*., 2002, Hydrogel-Based 3D Bioprinting for Bone and Cartilage Tissue Engineering. *Biotechnol J*, 2020:e2000095.
8. Abasalizadeh F, Moghaddam SV, Alizadeh E, *et al*., 2020, Alginate-based Hydrogels as Drug Delivery Vehicles in Cancer Treatment and their Applications in Wound Dressing and 3D Bioprinting. *J Biol Eng*, 14:8.
9. Zuo Q, Cui W, Liu F, *et al*., 2016, Utilizing Tissue-engineered Cartilage or BMNC-PLGA Composites to Fill Empty Spaces during Autologous Osteochondral Mosaicplasty in Porcine Knees. *J Tissue Eng Regen Med*, 10:916–26.
10. Cui W, Wang Q, Chen G, *et al*., 2011, Repair of Articular Cartilage Defects with Tissue-engineered Osteochondral Composites in Pigs. *J Biosci Bioeng*, 111:493–500.
11. Qiao Z, Lian M, Han Y, *et al*., 2021, Bioinspired Stratified Electrowritten Fiber-reinforced Hydrogel Constructs with Layer-specific Induction Capacity for Functional Osteochondral Regeneration. *Biomaterials*, 266:120385.
12. Cao R, Zhan A, Ci Z, *et al*., 2021, A Biomimetic Biphasic Scaffold Consisting of Decellularized Cartilage and Decalcified Bone Matrixes for Osteochondral Defect Repair. *Front Cell Dev Biol*, 9:639006.
13. Ashammakhi N, Ahadian S, Xu C, *et al*., 2019, Bioinks and Bioprinting Technologies to Make Heterogeneous and Biomimetic Tissue Constructs. *Mater Today Bio*, 1:100008.
14. Antich C, de Vicente J, Jimenez G, *et al*., 2002, Bio-inspired Hydrogel Composed of Hyaluronic Acid and Alginate as a Potential Bioink for 3D Bioprinting of Articular Cartilage Engineering Constructs. *Acta Biomater*, 106:114–23.
15. Zhang W, Ling C, Zhang A, *et al*., 2020, An All-silk-derived Functional Nanosphere Matrix for Sequential Biomolecule Delivery and *In Situ* Osteochondral Regeneration. *Bioact Mater*, vol. 5, no. 4, pp. 832-843, 2020.
16. Ng WL, Chua CK, Shen YF, 2019, Print Me An Organ! Why We Are Not There Yet. *Prog Polym Sci*, 97:101145.
17. Liu N, Ye X, Yao B, *et al*., 2021, Advances in 3D Bioprinting Technology for Cardiac Tissue Engineering and Regeneration. *Bioact Mater*, 6:1388–401.
18. Osidak EO, Kozhukhov VI, Osidak MS, *et al*., 2020, Collagen as Bioink for Bioprinting: A Comprehensive Review. *Int J Bioprint*, 6:270.
19. Lee JM, Sing SL, Yeong WY, 2002, Bioprinting of Multimaterials with Computer-aided Design/Computer-aided Manufacturing. *Int J Bioprint*, 6:245.
20. Gantumur E, Nakahata M, Kojima M, *et al*., 2002, Extrusion-Based Bioprinting through Glucose-Mediated Enzymatic Hydrogelation. *Int J Bioprint*, 6:250.
21. Askari M, Naniz MA, Kouhi M, *et al*., 2020, Recent Progress in Extrusion 3D Bioprinting of Hydrogel Biomaterials for Tissue Regeneration: A Comprehensive Review with Focus on Advanced Fabrication Techniques. *Biomater Sci*, 9:535–573.
22. Li X, Liu B, Pei B, *et al*., 2020, Inkjet Bioprinting of Biomaterials. *Chem Rev*, 120:10793–833.
23. Ng WL, Lee JM, Zhou M, *et al*., 2002, Vat Polymerization-based Bioprinting-process, Materials, Applications and Regulatory Challenges. *Biofabrication*, 12:022001.
24. Vurat MT, Ergun C, Elcin AE, *et al*., 2002, 3D Bioprinting of Tissue Models with Customized Bioinks. *Adv Exp Med Biol*, 1249:67–84.
25. Ning L, Mehta R, Cao C, *et al*., 2020, Embedded 3D Bioprinting of Gelatin Methacryloyl-Based Constructs with Highly Tunable Structural Fidelity. *ACS Appl Mater Interfaces*, 12:44563–577.
26. Bicho D, Ajami S, Liu C, *et al*., 2019, Peptide-biofunctionalization of Biomaterials for Osteochondral Tissue Regeneration in Early Stage Osteoarthritis: Challenges and Opportunities. *J Mater Chem B*, 7:1027–44.
27. Gan D, Xu T, Xing W, *et al*., 2019, Mussel-inspired Dopamine Oligomer Intercalated tough and Resilient Gelatin Methacryloyl (GelMA) Hydrogels for Cartilage Regeneration. *J Mater Chem B*, 7:1716–25.
28. Mishbak HH, Cooper G, Bartolo PJ, 2019, Development and Characterization of a Photocurable Alginate Bioink for Three-dimensional Bioprinting. *Int J Bioprint*, 5:189.
29. Chang R, Nam J, Sun W, 2008, Effects of Dispensing Pressure and Nozzle Diameter on Cell Survival from Solid Freeform Fabrication-based Direct Cell Writing. *Tissue Eng Part A*, 14:41–8.
30. Pati F, Jang J, Ha DH, *et al*., 2014, Printing Three-dimensional Tissue Analogues with Decellularized Extracellular Matrix

Bioink. *Nat Commun*, 5:3935.

31. Fedorovich NE, De Wijn JR, Verbout AJ, *et al*., 2008, Three-dimensional Fiber Deposition of Cell-laden, Viable, Patterned Constructs for Bone Tissue Printing. *Tissue Eng Part A*, 14:127–33.
32. Abaci A, Guvendiren M, 202, Designing Decellularized Extracellular Matrix-Based Bioinks for 3D Bioprinting. *Adv Healthc Mater*, 2020:e2000734.
33. Shin YJ, Shafranek RT, Tsui JH, *et al*., 3D Bioprinting of Mechanically Tuned Bioinks Derived from Cardiac Decellularized Extracellular Matrix. *Acta Biomater*, 1;119:75–88.
34. Lee H, Yang GH, Kim N, *et al*., 2018, Fabrication of Micro/Nanoporous Collagen/dECM/Silk-fibroin Biocomposite Scaffolds Using a Low Temperature 3D Printing Process for Bone Tissue Regeneration. *Mater Sci Eng C Mater Biol Appl*, 84:140–7.
35. Yang Q, Peng J, Guo Q, *et al*., 2008, A Cartilage ECM-derived 3-D Porous Acellular Matrix Scaffold for *In Vivo* Cartilage Tissue Engineering with PKH26-labeled Chondrogenic Bone Marrow-derived Mesenchymal Stem Cells. *Biomaterials*, 29:2378–87.
36. Jang J, Kim TG, Kim BS, *et al*., 2016, Tailoring Mechanical Properties of Decellularized Extracellular Matrix Bioink by Vitamin B2-Induced Photo-Crosslinking. *Acta Biomaterialia*, 33:88–95.
37. Zhang X, Liu Y, Luo C, *et al*., 2002, Crosslinker-free Silk/Decellularized Extracellular Matrix Porous Bioink for 3D Bioprinting-based Cartilage Tissue Engineering. *Mater Eng C*, 2020:111388.
38. Li Z, Zhang X, Yuan T, *et al*., 2020, Addition of Platelet-Rich Plasma to Silk Fibroin Hydrogel Bioprinting for Cartilage Regeneration. *Tissue Eng Part A*, 26:886–95.
39. Gupta S, Alrabaiah H, Christophe M, *et al*., 2020, Evaluation of Silk-based Bioink during Pre and Post 3D Bioprinting: A Review. *J Biomed Mater Res B Appl Biomater*, 109:279–93.
40. Almeida HV, Liu Y, Cunniffe GM, *et al*., 2014, Controlled Release of Transforming Growth Factor-beta3 from Cartilage-extra-cellular-matrix-derived Scaffolds to Promote Chondrogenesis of Human-joint-tissue-derived Stem Cells. *Acta Biomater*, 10:4400–9.
41. Almeida HV, Cunniffe GM, Vinardell T, *et al*., 2015, Coupling Freshly Isolated CD44(+) Infrapatellar Fat Pad-Derived Stromal Cells with a TGF-beta3 Eluting Cartilage ECM-Derived Scaffold as a Single-Stage Strategy for Promoting Chondrogenesis. *Adv Healthc Mater*, 4:1043–53.
42. Dickman CT, Russo V, Thain K, *et al*., 2002, Functional Characterization of 3D Contractile Smooth Muscle Tissues Generated Using a Unique Microfluidic 3D Bioprinting Technology. *FASEB J*, 34:1652–64.
43. Stanco D, Boffito M, Bogni A, *et al*., 2002, 3D Bioprinting of Human Adipose-Derived Stem Cells and Their Tenogenic Differentiation in Clinical-Grade Medium. *Int J Mol Sci*, 21:8694.
44. Sawkins MJ, Bowen W, Dhadda P, *et al*., 2013, Hydrogels Derived from Demineralized and Decellularized Bone Extracellular Matrix. *Acta Biomater*, 9:7865–73.
45. Zhang X, Zhai C, Fei H, *et al*., 2018, Composite Silk-Extracellular Matrix Scaffolds for Enhanced Chondrogenesis of Mesenchymal Stem Cells. *Tissue Eng Part C Methods*, 24:645–58.
46. Chenjun Z, Qiang Z, Kai S, *et al*., 2002, Utilizing an Integrated Tri-layered Scaffold with Titanium-Mesh-Cage Base to Repair Cartilage Defects of Knee in Goat Model. *Mater Des*, 193:108766.
47. Zhai C, Fei H, Hu J, *et al*., 2018, Repair of Articular Osteochondral Defects Using an Integrated and Biomimetic Trilayered Scaffold. *Tissue Eng Part A*, 24:1680–92.
48. Crapo PM, Gilbert TW, Badylak SF, 2011, An Overview of Tissue and Whole Organ Decellularization Processes. *Biomaterials*, 32:3233–43.
49. Schacht K, Jungst T, Schweinlin M, *et al*., 2015, Biofabrication of Cell-loaded 3D Spider Silk Constructs. *Angew Chem Int Ed Engl*, 54:2816–20.
50. Ni T, Liu M, Zhang Y, *et al*., 2002, 3D Bioprinting of Bone Marrow Mesenchymal Stem Cell-Laden Silk Fibroin Double Network Scaffolds for Cartilage Tissue Repair. *Bioconjug Chem*, 31:1938–47.
51. Chawla S, Midha S, Sharma A, *et al*., 2018, Silk-Based Bioinks for 3D Bioprinting. *Adv Healthc Mater*, 7:e1701204.
52. Ding C, Qiao Z, Jiang W, *et al*., 2013, Regeneration of a Goat Femoral Head Using a Tissue-specific, Biphasic Scaffold Fabricated with CAD/CAM Technology. *Biomaterials*, 34:6706–16.
53. Cals FL, Hellingman CA, Koevoet W, *et al*., 2012, Effects of Transforming Growth Factor-beta Subtypes on *In Vitro* Cartilage Production and Mineralization of Human Bone Marrow Stromal-derived Mesenchymal Stem Cells. *J Tissue Eng Regen Med*, 6:68–76.
54. Freeman FE, Pitacco P, van Dommelen LH, *et al*., 2002, 3D Bioprinting Spatiotemporally Defined Patterns of Growth Factors to Tightly Control Tissue Regeneration. *Sci Adv*, 6:eabb5093.
55. Datta S, Rameshbabu AP, Bankoti K, *et al*., 2021,

Decellularized Bone Matrix/Oleoyl Chitosan Derived Supramolecular Injectable Hydrogel Promotes Efficient Bone Integration. *Mater Sci Eng C Mater Biol Appl*, 119:111604.

56. Das S, Pati F, Chameettachal S, *et al*., 2013, Enhanced Redifferentiation of Chondrocytes on Microperiodic Silk/Gelatin Scaffolds: Toward Tailor-made Tissue Engineering. *Biomacromolecules*, 14:311–21.
57. Huh JE, Koh PS, Seo BK, *et al*., 2014, Mangiferin Reduces the Inhibition of Chondrogenic Differentiation by IL-1beta in Mesenchymal Stem Cells from Subchondral Bone and Targets Multiple Aspects of the Smad and SOX9 Pathways. *Int J Mol Sci*, 15:16025–42.

RESEARCH ARTICLE

3D Printing of Tricalcium Phosphate/Poly Lactic-co-glycolic Acid Scaffolds Loaded with Carfilzomib for Treating Critical-sized Rabbit Radial Bone Defects

Ye Li[1†], Kegong Xie[1†], Chong Wang[2†], Chengliang Yang[1], Ke Huang[1], Feng Li[1], Chuanchuan Zheng[1], Jian Chen[1], Shujun Dong[3], Guangfeng Deng[4], Gege Huang[4], Qiaoyan Lu[4], Jia Liu[1*], Kai Li[5*], Yujin Tang[1*], Liqiang Wang[6]

[1]Department of Orthopaedics, Affiliated Hospital of Youjiang Medical University for Nationalities, Baise, Guangxi, PR China
[2]School of Mechanical Engineering, Dongguan University of Technology, Songshan Lake, Dongguan, Guangdong, PR China
[3]Department of Rehabilitation medicine, Affiliated Hospital of Youjiang Medical University for Nationalities, Baise, Guangxi, PR China
[4]Youjiang Medical University for Nationalities, Baise, Guangxi, PR China
[5]The Third Affiliated Hospital of Southern Medical University, Guangzhou, Guangdong, PR China
[6]State Key Laboratory of Metal Matrix Composites, School of Material Science and Engineering, Shanghai Jiao Tong University, Shanghai, 200240, China
[†]*These authors contributed equally to this work*

Abstract: The rapid development of scaffold-based bone tissue engineering strongly relies on the fabrication of advanced scaffolds and the use of newly discovered functional drugs. As the creation of new drugs and their clinical approval often cost a long time and billions of U.S. dollars, producing scaffolds loaded with repositioned conventional drugs whose biosafety has been verified clinically to treat critical-sized bone defect has gained increasing attention. Carfilzomib (CFZ), an approved clinical proteasome inhibitor with a much fewer side effects, is used to replace bortezomib to treat multiple myeloma. It is also reported that CFZ could enhance the activity of alkaline phosphatase and increase the expression of osteogenic transcription factors. With the above consideration, in this study, a porous CFZ/β-tricalcium phosphate/poly lactic-co-glycolic acid scaffold (designated as "cytidine triphosphate [CTP]") was produced through cryogenic three-dimensional (3D) printing. The hierarchically porous CTP scaffolds were mechanically similar to human cancellous bone and can provide a sustained CFZ release. The implantation of CTP scaffolds into critical-sized rabbit radius bone defects improved the growth of new blood vessels and significantly promoted new bone formation. To the best of our knowledge, this is the first work that shows that CFZ-loaded scaffolds could treat nonunion of bone defect by promoting osteogenesis and angiogenesis while inhibiting osteoclastogenesis, through the activation of the Wnt/β-catenin signaling. Our results suggest that the loading of repositioned drugs with effective osteogenesis capability in advanced bone tissue engineering scaffold is a promising way to treat critical-sized defects of a long bone.

Keywords: Bone defect; Cryogenic 3D printing; Bone regeneration; β-tricalcium phosphate; Carfilzomib

*Correspondence to: Jia Liu, Department of Orthopedics, Affiliated Hospital of Youjiang Medical University for Nationalities, Baise, Guangxi, 533000, China: liujia0111@live.cn; Kai Li, The Third Affiliated Hospital of Southern Medical University, Guangzhou, Guangdong Province, 510000, China: lk516433415@smu.edu.cn; Yujin Tang, Department of Orthopedics, Affiliated Hospital of Youjiang Medical University for Nationalities, Baise, Guangxi, 533000, China: tangyujin1967@163.com

Received: July 12, 2021; **Accepted:** August 2, 2021; **Published Online:** September 14, 2021

Citation: Li Y, Xie K, Wang C, *et al.,* 2021, 3D Printing of Tricalcium Phosphate/Poly Lactic-co-glycolic Acid Scaffolds Loaded with Carfilzomib for Treating Critical-sized Rabbit Radial Bone Defects. *Int J Bioprint*, 7(4):405. http://doi.org/10.18063/ijb.v7i4.405

1. Introduction

To date, regeneration of long bone with critical-size defects induced by steroid-induced osteonecrosis, tumor resection, osteoporotic fractures, or accidental trauma is still challenging. Among various bone regeneration therapies, autologous bone transplantation is recognized as the gold standard[1,2]. However, its mass application is severely restricted due to insufficient donor sources. In the past decade, scaffold-based tissue engineering has gained increasing attention in treating bone defects[4-7]. In addition to the required biocompatibility, biodegradability and appropriate mechanical properties, capability of promoting osteogenesis and angiogenesis should also be imparted to the bone tissue engineering scaffolds[3].

Calcium phosphate has been widely used for the producing artificial protheses with a dense structure due to its high compositional similarity to bone apatite and high bioactivity[4]. Animal studies and clinical experiments have shown that calcium phosphates have excellent repair effects on bone regeneration[5-7]. To improve the repair capability of calcium phosphates, porous scaffolds made of calcium phosphate/biodegradable polyester composites which are structurally similar to native cancellous bone tissue have been developed[8]. The porous structure of scaffolds facilitates cell growth, migration, and transportation of nutrients and metabolites[9]. To further improve the osteogenic capability of bone tissue engineering scaffolds, growth factors and drugs related to osteogenesis and/or angiogenesis can be incorporated[10].

Additive manufacturing has gained increasing attention in making bone tissue engineering scaffolds as it is advantageous in producing scaffolds with customized shape, pore size, porosity, and interconnectivity[11]. Cryogenic 3D printing is a new type of additive manufacturing technology that uses polymeric water-in-oil emulsions as printing inks to deposit three-dimensional (3D) patterns below 0°C[12]. The emulsion inks immediately solidify when they contact the cryogenic substrate, allowing a layer-by-layer material deposition. After cryogenic 3D printing, as-printed 3D patterns are lyophilized to remove solvents to obtain stabilized scaffolds with a hierarchical structure[10].

The success of scaffold-based bone tissue engineering not only relies on the employment of advanced scaffolds but also depends on the use of newly discovered functional drugs. However, creation of new drug and its clinical approval cost a long time and a lot of money. Therefore, producing advanced scaffolds loaded with repositioned conventional drugs with effective osteogenesis capability, whose biosafety has been verified clinically, has gained increasing attention in the treatment of critical-sized defect in long bone. Carfilzomib (CFZ) is an approved clinical proteasome inhibitor with a much fewer side effects, replacing bortezomib in the treatment of multiple myeloma by inhibiting osteoclast activity and pathological bone destruction through the disruption of receptor activator for Nuclear factor kappa B [NF-κB] ligand (RANKL)-induced NF-κB signaling[13]. It is also reported that CFZ could induce increased alkaline phosphatase activity and upregulated expression of the osteogenic transcription factors such as osterix, osteopontin, and osteocalcin (OCN) through Wnt pathway by activating the β-catenin/T-cell factor (TCF) pathway[14-16].

The Wnt pathway is a complex signaling system involving the mutual regulation of multiple factors, and can interact with other signaling pathways and various cytokines. It is known that β-catenin protein in the Wnt pathway enters the nucleus and binds to TCF/lymphoid enhancer factor transcription factors to regulate the expression of genes related to cell proliferation, migration and differentiation, which are related to bone formation[17]. The Wnt pathway not only indirectly inhibits osteoclasts through osteoprotection in osteoblasts but can also directly regulate the function of osteoclasts by activating its own pathway[18,19]. Activation of the Wnt/β-catenin signaling is not only related to aging or directed differentiation of mesenchymal stem cells into osteoblasts[20], but also involved in the development, maturation, and function of osteoblasts[21].

To elucidate the combination effect of CFZ and 3D printed bony environment on the bone regeneration in long bone with defect and the underlying mechanism, in this study, a porous β-tricalcium phosphate/poly lactic-co-glycolic acid (TCP/PLGA) scaffold incorporated with CFZ was fabricated through cryogenic 3D printing. The morphological and physical properties of scaffolds and release behavior of CFZ were investigated. The positive effects of drug CFZ/TCP/PLGA scaffolds on the osteogenesis and angiogenesis and the inhibitory effect of CFZ on osteoclasts were studied *in vivo*. Significantly improved new bone formation and enhanced vascularization were observed in the regenerated tissue in radial defects of rabbits. This study suggests that the employment of 3D printed porous bone tissue engineering scaffolds incorporated with CFZ can effectively treat long bone defects by activating the Wnt/β-catenin signaling.

2. Materials and methods

2.1. Scaffold fabrication

The formulation of printing inks and the fabrication process of the 3D printed bone tissue engineering scaffolds (designated as "cytidine triphosphate [CTP]") are shown in **Figure 1**. The CTP material was prepared by in situ incorporation of CFZ in TCP/PLGA (TP) scaffolds using cryogenic 3D printing based on TCP/PLGA (TP) material. First, 3 g of PLGA (Shandong Medical Device Company,

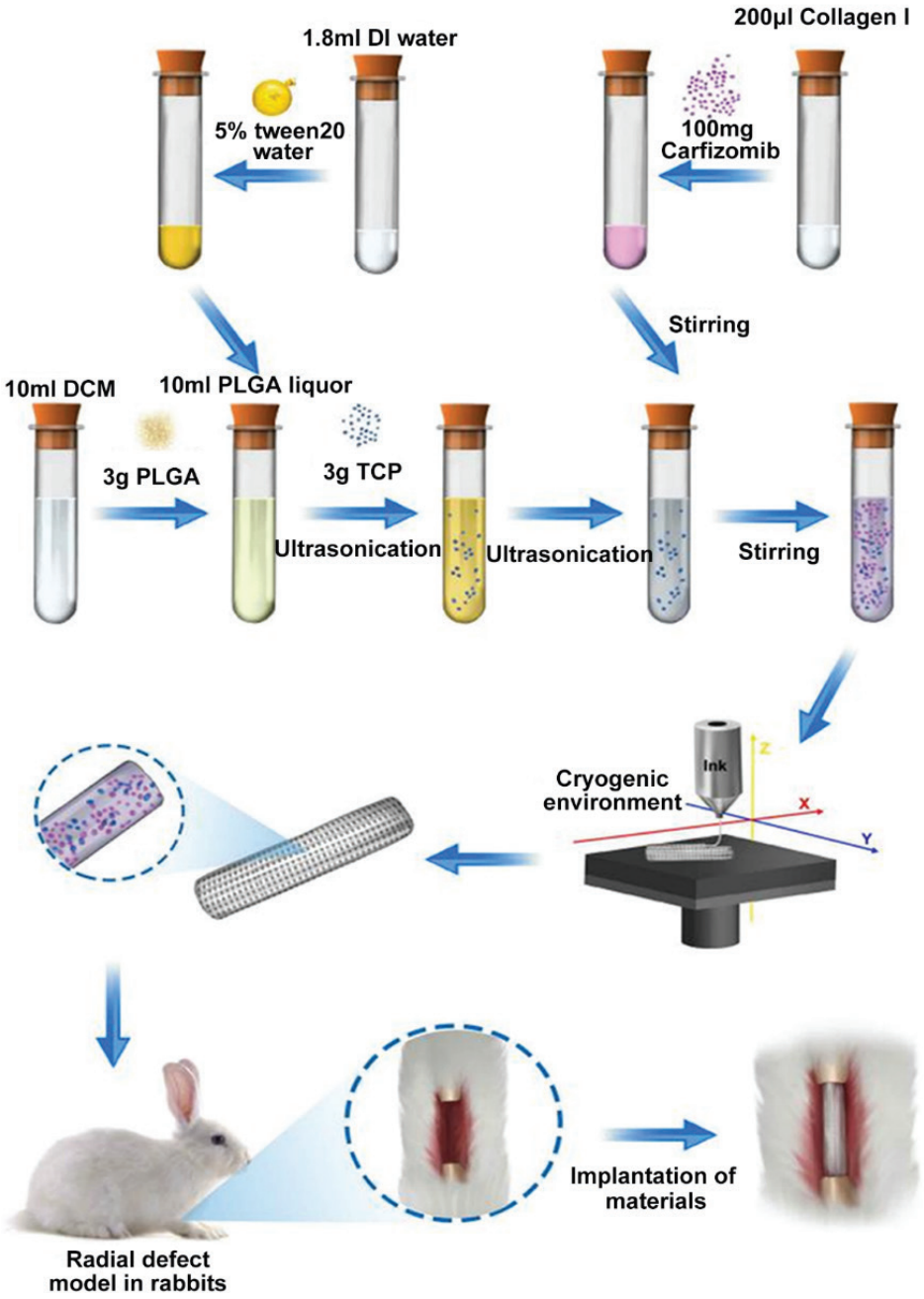

Figure 1. Schematic diagram depicting the fabrication of the 3D-printed β-tricalcium phosphate/poly lactic-co-glycolic acid carfilzomib-loaded scaffolds.

P.R. China) was dissolved in 10 mL of dichloromethane (DCM) and vortex-stirred for 15 min until the PLGA was fully dissolved. Then, 1.8 mL of deionized (DI) water and 50 μL of Tween 20 water were added to the PLGA to prepare 10 mL of PLGA organic solution. Afterward, 3 g of β-TCP powder mixture was mixed in the solution by ultrasonic vibration for 15 min to form TCP/DI water/PLGA/DCM composite emulsion inks (designated as "TP"). To load CFZ in TP inks, 100 mg of CFZ and 4.6 μL of NaOH (1 N, to neutralize the acidic collagen I solution) were dissolved in 200 μL of collagen I solution (9 mg/mL) at 4°C, and the CFZ/collagen I solution was homogeneously mixed with TP inks to obtain CFZ/TCP/PLGA/DCM emulsion ink (designated as "CTP"). The as-formulated CTP inks were added into a 20 mL syringe which was connected to a V-shaped plastic nozzle (inner diameter: 0.4 mm) and further loaded into a cryogenic 3D printer (Shenzhen Creality 3D Technology Co., Limited, P.R. China). Following the CAD file (a cylinder with a diameter of 4 mm and a height of 15 mm), porous 3D

cylindrical scaffolds were drawn (each layer consists of seven parallel struts, and struts in adjacent layers had a cross angle of 90°, Figure S1-A). The printing process is shown in Figure S1-B. The emulsion mixture was extruded by pushing the plunger of the syringe via an electromechanical screw, and the as-printed pattern was frozen in 2 s due to the existence of the cryogenic environment (−30°C). The printing speed is 6 mm/s and the feeding rate of the plunger was set as 0.008 mm/s. After the cryogenic 3D printing, the as-fabricated scaffolds were freeze-dried to remove water and DCM. Thus, a stable cylindrical bone tissue engineering scaffold with a diameter of 3 – 4 mm and a height of 15 mm was obtained.

2.2. Morphology observation and structural characterization analysis

The surface morphology was observed by scanning electron microscopy (SEM) (Gemini, Zeiss, Germany). Before SEM, a thin layer of gold was sprayed on the surface of the material to improve its electrical conductivity. The average pore size of the specimen was measured by SEM. On the basis of TP material, TCP/PLGA slow-release CFZ was prepared by cryogenic 3D printing to make CTP material. Micro-CT and SEM were used to evaluate the structure of the CTP.

2.3. Mechanical properties of the scaffold

The scaffolds were 15 mm thick, 3.4 mm wide, and 2.3 mm high. TP and CTP materials were tested by an electronic universal testing machine (SUNS, Shenzhen, China). The test and load-displacement curve were carried out at a speed of 1 mm/min and 40 s. Finally, the corresponding values of compressive strength, compression modulus, and compressive strain were obtained according to the GB/T 1041-92 calculation standard.

2.4. *In vitro* release of the scaffold

To study CFZ release *in vitro*, preweighed stent samples were placed in tubes containing phosphate-buffered saline (PBS) solution (0.02% sodium azide for CFZ test). The test tube was placed in an oscillating water bath at 37°C, the test solution was taken out at a predetermined interval, and the concentration of CFZ was determined using the CFZ Determination Kit (US Biological, USA) and the release time was determined.

2.5. Cell culture

Mouse mesenchymal stem cells C3H10T1/2 were cultured in Dulbecco's Modified Eagle Medium (DMEM) medium supplemented with 10% fetal bovine serum (FBS), 100 U/mL penicillin G, and 100 mg/mL streptomycin under standard conditions. To induce osteogenesis, this medium was added with 0.1 mM dexamethasone (Sigma-Aldrich, St. Louis, MO. USA), 100 μg/mL ascorbic acid (Sigma-Aldrich), and 10 mM β-glycerol phosphate (Sigma-Aldrich). RAW264.7 cell line (ATCC) was maintained in DMEM containing 10% FBS. The medium was changed every 2 days. For osteoclastic differentiation, cells were incubated with medium containing 50 ng/ml RANKL (R and D Systems, Minneapolis, MN, USA) for 7 days. In the control group and CFZ group, the cells were stimulated with dimethylsulfoxide (DMSO) and the extracts of scaffolds, respectively.

2.6. Western blot analysis

The cells were lysed in 2% sodium dodecyl sulfate (SDS), 2 M urea, 10% glycerol, 10 mM Tris-HCl (pH 6.8), 10 mM dithiothreitol, and 1 mM phenylmethylsulfonyl fluoride. Proteins were separated by 10% SDS-polyacrylamide gel electrophoresis. After electrophoresis, the proteins were transferred to the membrane by wet transfer (Bio-Rad Laboratories, Hercules, CA, USA). Each membrane was incubated with TBST (100 mM Tris-HCl pH 7.5, 150 mM NaCl, 0.05% Tween 20) and 5% non-fat blocking milk powder at room temperature for 1 h, and then incubated overnight with the primary antibody in a shaking bottle at 4°C. The membrane and HRB-conjugated secondary antibody were incubated at room temperature for 1 h. The membrane was then treated with enhanced chemiluminescence reagent (ECL Kit, Amersham Biosciences, Piscataway, NJ, USA), and the proteins were detected using chemiluminescence technology.

2.7. Gene expression and real-time polymerase chain reaction (PCR) analysis

The expression of osteogenesis genes, such as Alkaline Phosphatase (ALP), bone morphogenetic protein 2 (BMP2), collagen type I, Osteocalcin (OCN), transcription factor SP7 (Osterix), and Runt-related transcription factor 2 (Runx2) in C3H10T1/2 cells, and of osteoclastogenic genes, such as Cathepsin K (CTSK), Matrix metalloproteinase-9 (MMP9), c FBJ osteosarcoma oncogene (c-fos), Nuclear factor of activated T cells cytoplasmic 1 (NFATC1) in Raw264.7 cells cultured in different treatments was detected by PCR. Total RNA was extracted from the cells with Trizol reagent (Life Technologies, Carlsbad, CA, USA). The concentration of RNA was determined by a NanoDrop spectrophotometer (Thermo Fisher Scientific, USA). Primers for real time PCR (RT-PCR) are listed in **Table 1**.

2.8. Alizarin red S staining

C3H10T1/2 cells were seeded into 48-well plates (three wells per group). After osteogenic induction for 14 days, the cells were fixed in 4% paraformaldehyde, and then rinsed twice in PBS. Afterwards, they were stained at room temperature

Table 1. Primer sequences of osteogenic and osteoclastic genes

Genes	Primer sequences
ALP	Forward: 5'-CGG ATC CTG ACC AAA AAC C-3'
	Reverse: 5'-TCA TGA TGT CCG TGG TCA AT-3'
OCN	Forward: 5'-CAC CAT GAG GAC CCT CTC TC-3'
	Reverse: 5'-TGG ACA TGA AGG CTT TGT CA-3'
Osterix	Forward: 5'-TCT CCA TCT GCC TGA CTC CT-3'
	Reverse: 5'-AGC GTA TGG CTT CTT TGT GC-3'
Runx2	Forward: 5'-GAC TGT GGT TAC CGT CAT GGC-3'
	Reverse: 5'-ACT TGG TTT TTC ATA ACA GCG GA-3'
CTSK	Forward: 5'- CCA GGA AAT GAG CTT GAC AAA-3'
	Reverse: 5'- ATA ATT CTC AGT CAC ACA GTC CAC A -3'
MMP9	Forward:5'- CAC TCC CAC CCT GAG ATT TGT-3'
	Reverse: 5'- CCCC AGA GAC ATG ATG AAG TCA -3'
c-fos	Forward: 5'- TGT CTG TGG CTT CCC TTG AT -3'
	reverse: 5'- ATC AAA GGG CTC GGT CTT CA -3'
NFATc1	Forward:5'- CCG TTG CTT CCA GAA AAT AAC A -3'
	Reverse: 5'- TGT GGG ATG TGA ACT CGG AA -3'
GAPDH	Forward:5'-CAT GTA CGT TGC TAT CCA GGC-3'
	Reverse: 5'-CTC CTT AAT GTC ACG CAC GAT-3'

in 40 mM alizarin red S staining solution for 10 min, rinsed twice in PBS, and visualized under a light microscope.

2.9. Immunofluorescence analysis

For immunofluorescence analysis, cells were incubated first with primary antibodies and then with Alexa Fluor 594 donkey anti-mouse IgG1 (Life Technologies, Carlsbad, CA, USA) and Alexa Fluor 488 goat anti-mouse IgG2b (Life Technologies) secondary antibodies. Cells were washed 3 times in PBS, after which nuclei were counterstained with 4',6-diamidino-2-phenylindole (Life Technologies). Images were obtained on a confocal laser scanning microscope (Olympus, Tokyo, Japan).

2.10. Animal model and material implantation

Fifteen New Zealand white rabbits (2.5 ± 0.5 kg) were provided by the Scientific Experimental Center of Youjiang Medical University for Nationalities (YYFY-TYJ-20200225). The animal experiments were approved by the Research Ethics Committee of Youjiang Medical College for Nationalities. Pentobarbital sodium (20 mg/kg) with a volume fraction of 3% was injected through an ear vein, and ketamine was injected with 50% ketamine mg/kg through intramuscular injection for anesthesia. After successful anesthesia, the rabbit was fixed on the operating table in the prone position. The bilateral forelimbs were facing upward, and the rabbit hair of both forearms was removed. The operation area was disinfected with a tincture of iodine and alcohol, and laid with a sterile towel. The skin, subcutaneous tissue, and deep fascia were cut through to the middle and upper radial forearm, and the muscle space was separated to expose the radius. A section of the radius and periosteum at 2.5 – 3.0 cm below the radial head was cut off, together with the periosteum. The ulnar and radial interosseous membrane and the periosteum on both sides of the broken end were removed. The broken end of the defect was flattened as far as possible with a file. A syringe was filled with 50 mL normal saline and used to wash the bone debris and related congestion scab and bone marrow tissue in the bone marrow cavity. On the experimental side, the CTP material was implanted between the broken ends. Corresponding control groups (TP group, blank group) were set up. The muscle membrane and subcutaneous tissue were sutured with 4-0 absorbable sutures, and the skin incision was sutured with 0 braided suture to disinfect the wound. After the operation, the bilateral forelimbs were not fixed. Penicillin 40 kU (1.6 million units, QD) was immediately injected intramuscularly. Intramuscular injection of penicillin 40 kU/D was performed for 3 consecutive days after the operation. The animals were fed by the same feeder in separate cages. After the operation, the feeding condition of the animals, the appearance of the limbs on the operation side, the infection of the surgical incision, and the activity function were observed. At 12 weeks after the operation, the animals were killed and the original incision was opened to observe the formation of local callus and growth of the bone defect.

2.11. Micro-computed tomography (CT) scan and 3D reconstruction

At 8 and 12 weeks after implantation, the rabbits were sacrificed by injecting air into the auricular vein. Specimens of the radial defects were collected and fixed for 1 week in 10% formalin. Then, micro-CT (Scanco Medical, Bassersdorf, Zurich, Switzerland) with a spatial resolution of 12 μm and 55 kVp and 145 μA was used

to scan the radial defects in the rabbits. The regions of interest were selected and reconstructed. Then, 510 axial images were reconstructed into 3D images. In the bone tunnel, the residual scaffolds could be distinguished from the newly formed bone in the tunnel by setting different gray levels. The gray threshold from 40 hu to 60 hu represented the implanted composite scaffold, and the gray threshold from 80 to 255 represented new bone. The changes in stent volume after implantation were analyzed.

2.12. Microfil angiography and micro-CT imaging

After the New Zealand white rabbits had been anesthetized, their abdomen was fixed on the plate with the abdomen facing upward. The skin and muscle layers were cut along the midline of the abdomen. The xiphoid process was lifted, the diaphragm was cut open, and the heart was exposed. The heart was fixed with hemostatic forceps, a 23 G needle was inserted into the left ventricle, and the right auricle was cut with ophthalmic scissors. The perfusion pump was opened. The perfusion pump was irrigated with normal saline until no red liquid flowed out and was then changed to 4% paraformaldehyde. After the muscle tissue was fixed, 40 – 50 ml of mixed microfil liquid (solvent: solute = 4:5 and 1 – 2% coagulant) was infused. At the end of the perfusion, the small mesenteric vessels turned yellow. The rabbit carcass was kept in a 4°C refrigerator overnight. After the contrast medium was fixed, the rabbits' upper limbs were taken for micro-CT scanning to observe the vascular development.

2.13. Histology analysis

At 12 weeks, the rabbits were sacrificed by injecting air into the ear edge vein. The skin and muscle tissues were removed, and the radial specimens were obtained. The specimens were fixed in 4% PFA solution for 2 weeks and then decalcified with 10% EDTA solution for 4 – 6 weeks. The decalcification was continued until the needle could be easily inserted into the bone tissue. Gradient concentrations of ethanol solution were used for dehydration, and a xylene soak for 30 min was used to clear the tissue. This was repeated twice. The treated tissues were immersed in paraffin for 30 min, and the paraffin was replaced 3 times. After paraffin solidification, the embedded specimens were taken out and cut into 5-μm slices. They were then put in distilled water, pasted to a slide, and baked at 60°C overnight. The prepared paraffin sections were used for hematoxylin and eosin staining.

2.14. Statistical analysis

All quantitative data were obtained from four or five independent experiments. The results are expressed as the mean ± standard deviation. One-way analysis of variance (ANOVA) was used for statistical analysis, and the data are indicated with * if the probability is <0.05 ($P < 0.05$).

3. Results and discussion

3.1. Scaffold characterization, mechanical properties and drug release behavior

The morphology and structure of CTP scaffolds were evaluated by SEM. As shown in **Figure 2A-D**, both scaffolds had a porous structure in both the horizontal and vertical (cross-sectional) directions, and the interconnected gridded pores had a side length of 200 ± 50 μm. Compared to TP scaffolds, CTP scaffolds had a rougher strut surface on which a number of micropores and numerous TCP particles with a diameter around 200 nm can be seen **(Figure 2E** and **F)**. The mechanical properties of the TP and CTP scaffolds were measured through compression testing and the results are shown in **Table 2** and **Figure 2G** and **2H**. The compressive strengths of TP and CTP were 1.20 MPa and 1.34 MPa, respectively, which are in the low range of trabecular bone (1.3 – 4.4 MPa)[22], and hence is suitable for treating bone defects. The *in vitro* release behavior of CTP scaffold was also studied. As shown in **Figure 2I**, 55% level of released CFZ was observed on day 5, and the release profile achieved a plateau after 10 days of incubation. The survival rate of C3H10T1/2 cultured on the TP and CTP scaffolds for 3 days (as shown in **Figure 2J**) was more than 90%, indicating that the TP and CTP scaffolds were a biocompatible platform for C3H10T1/2 culture.

3.2. CTP scaffolds promote osteogenic differentiation of C3H10T1/2 cells

To analyze the effect of CTP scaffold on osteogenesis, we treated the mouse mesenchymal cells line C3H10T1/2 with osteogenic media supplemented with extracts of the scaffold. **Figure 3A** shows the mRNA expression of the osteogenic genes in C3H10T1/2 cells stimulated with control or CFZ for 7 days. It was seen that the expression of osteogenic genes, including *ALP*, *BMP2*, *Col1α1*, *OCN*, *Osterix,* and *Runx2*, was all upregulated in CFZ group compared with control group. With Western blot analysis, we confirmed that the protein level of OCN, Col1α1, and Runx2 was increased, and the expression of *Runx2* and *Col1α1* was more pronounced in the CFZ group **(Figure 3B)**, which were accordant with the

Table 2. Compression mechanical results of TP and CTP scaffolds

Scaffold	Young modulus (E)	Ultimate tensile strength (UTS)	Strain
TP	31.52	1.20MPa	9.69%
CTP	33.13	1.34MPa	11.90%

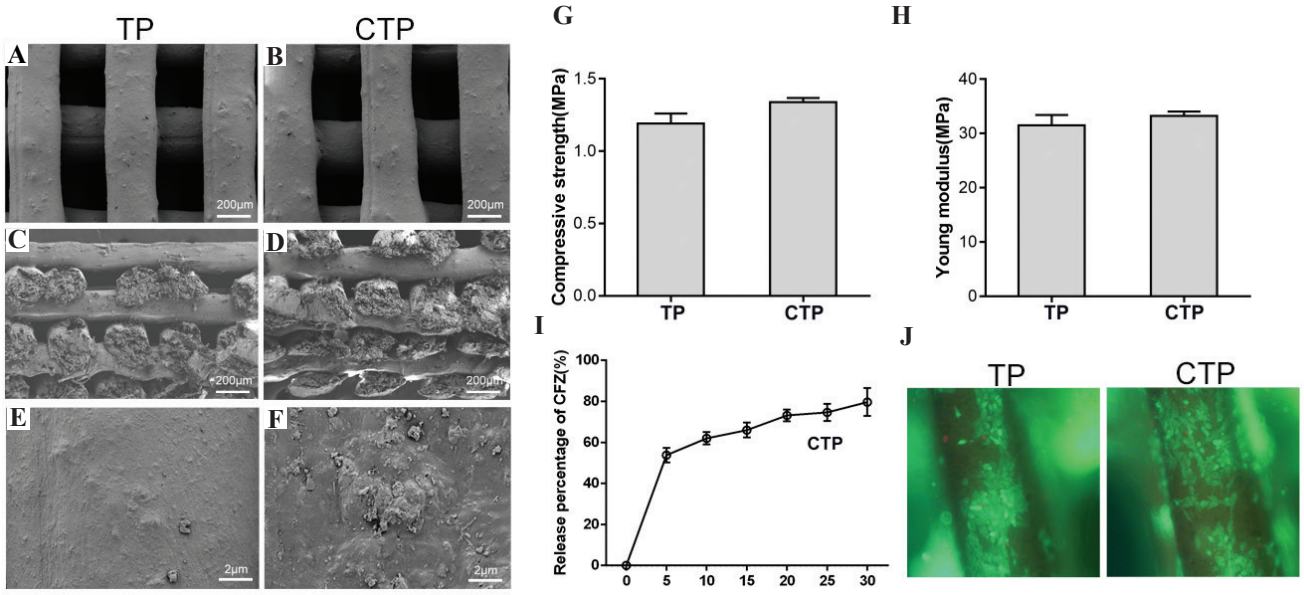

Figure 2. Fabrication of a 3D-printed β-tricalcium phosphate/poly lactic-co-glycolic acid scaffold loaded with carfilzomib (CFZ). (A-F) Scanning electron microscopy micrographs of different scaffolds at different magnification. (G) Compressive strengths of cytidine triphosphate (CTP) scaffolds and TP controls. (H) Young modulus of the CTP scaffolds and TP controls. (I) Release behavior of CFZ from CTP scaffolds in a 30-day test period. (J) Cell viability after seeding C3H10T1/2 in the scaffolds for 3 days.

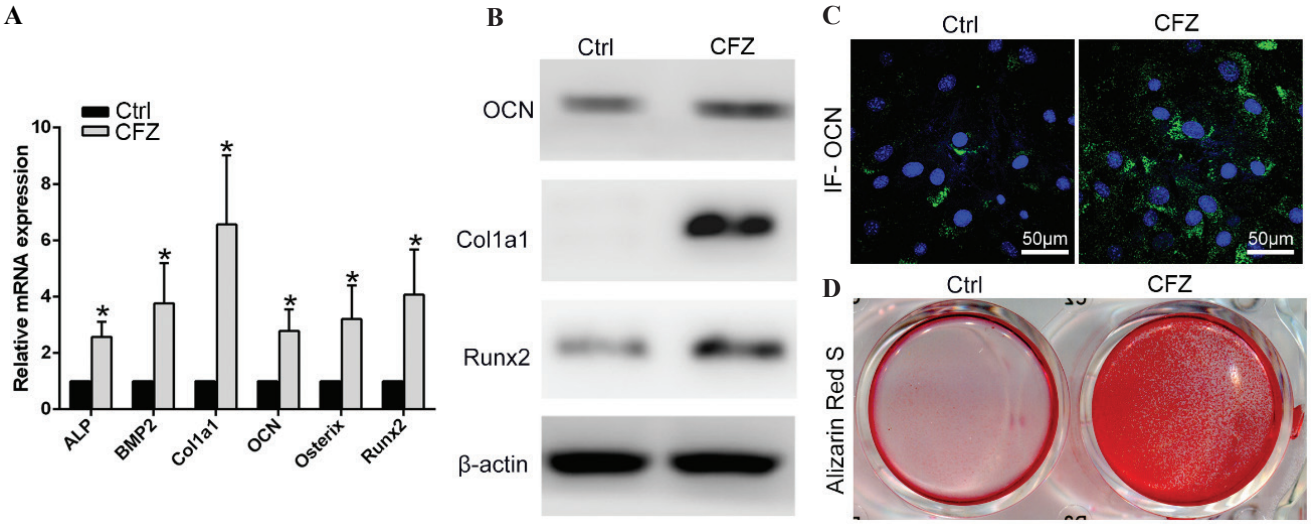

Figure 3. Cytidine triphosphate (CTP) scaffolds promote osteogenic differentiation in C3H10T1/2 mesenchymal cells. (A) mRNA expression of osteogenic genes in C3H10T1/2 cells stimulated with osteogenic medium supplemented with (carfilzomib [CFZ] group) or without (control group) extracts of the CTP scaffold for 7 days. (B) Western blot results of osteogenic proteins in C3H10T1/2 cells from control and CFZ group. (C) Immunofluorescence staining of osteocalcin in C3H10T1/2 cells from control and CFZ group. (D) Alizarin red S staining of C3H10T1/2 cells stimulated with osteogenic medium supplemented with (CFZ group) or without (control group) extracts of the CTP scaffold for 14 days. Scale bar = 50 μm. *$P < 0.05$.

mRNA expression levels. In addition, we performed immunofluorescence staining of OCN in C3H10T1/2 cells from control and CFZ groups. As shown in **Figure 3C,** OCN expression in CFZ group was remarkably enhanced compared to control group. And within 14 days, alizarin red staining confirmed enhanced mineralization of the extracellular matrix in CFZ group **(Figure 3D)**. Therefore, these data suggest that CTP scaffolds have good osteogenic capabilities *in vitro*.

3.3. CTP scaffolds inhibit osteoclast formation *in vitro*

The role of CFZ in osteoclast activity has been mentioned in the previous studies. In this study, we also investigated

the effect of CTP scaffolds on osteoclast formation in cultured cells. The mouse leukemic monocyte cell line RAW264.7 was stimulated with RANKL and supplemented with or without extracts of the scaffold. As shown in **Figure 4A,** mRNA expression of osteoclast differentiation marker genes (*Ctsk* and *Mmp9*), key transcription factors (*c-fos* and *NFATc1*), and osteoclast fusion-related genes (*β3-integrin*) were all dramatically downregulated in CFZ group compared to the control group. We ascertained the decreased protein level of CTSK, NFATc1, and MMP9 in CFZ group with Western blot analysis **(Figure 4B)**. RANKL induces macrophages to differentiate into osteoclast through the induction of multiple regulatory transcription factors, such as NF-κB and NFATc1. Our results suggested that CFZ had an inhibitory effect on osteoclastogenesis through the RANKL-related pathway. To better understand the potential role of CTP scaffolds on actin ring formation in osteoclasts, we conducted immunofluorescence staining of phalloidine (F-actin) and CTSK in raw264.7 cells. Our data showed that in control group, CTSK-positive cells, multinucleated osteoclasts, and well-polarized F-actin ring were observed, while all these were inhibited in cells of CFZ group (**Figure 4C**)**.** These data indicate that CTP scaffolds inhibit osteoclast formation partially through RANKL-related pathway and destroy the actin ring formation, which was consistent with the finding of a previous study[15].

3.4. CTP scaffolds activate Wnt/β-catenin signaling

To determine the underlying mechanism of CTP scaffolds on osteogenesis and osteoclast formation, we analyzed the effect of CTP scaffolds on the Wnt/β-catenin signaling in C3H10T1/2 cells. Western blot analysis indicated that the total expression of β-catenin was slightly elevated while the increased expression of active β-catenin was more pronounced in CFZ group compared to control group (**Figure 5A**). TOP/FOP-Flash luciferase reporter assay also confirmed the activity of Wnt/β-catenin signaling was significantly upregulated in CFZ group (**Figure 5B**). Next, we detected the expression of β-catenin in C3H10T1/2 cells with immunofluorescence staining. As shown in **Figure 5C**, cells in CFZ group exhibited enhanced total and nuclear expressions of β-catenin in comparison with control. All these results indicated that CTP scaffolds may enhance the activity of the Wnt/β-catenin signaling *in vitro*. We speculated that the effect of CFZ on osteogenesis and osteoclast formation may be mediated through the activation of Wnt/β-catenin signaling.

3.5. CTP scaffolds promote bone regeneration in a rabbit long bone defect model

Next, we analyzed the effect of CTP scaffold in a rabbit long bone (radius) defect model. After surgery and stent implantation **(Figure 6A)**, the specimens of each group were taken out after 12 weeks of cage feeding. With micro-CT scan, we noticed that the degree of bone formation in the CTP scaffolds group was significantly higher than in the TP group and the control group (**Figure 6B**). **Figure 6C** and **D** shows the bone volume/total volume (BV/TV) ratio and bone mineral density of different groups. It can be seen that CTP scaffolds induced the highest level of BV/TV ratio and bone mineral density value. These data suggest that the sustained release of CFZ significantly improved bone mineralization. In the process of bone regeneration, blood vessel formation is essential because vascularization can also facilitate

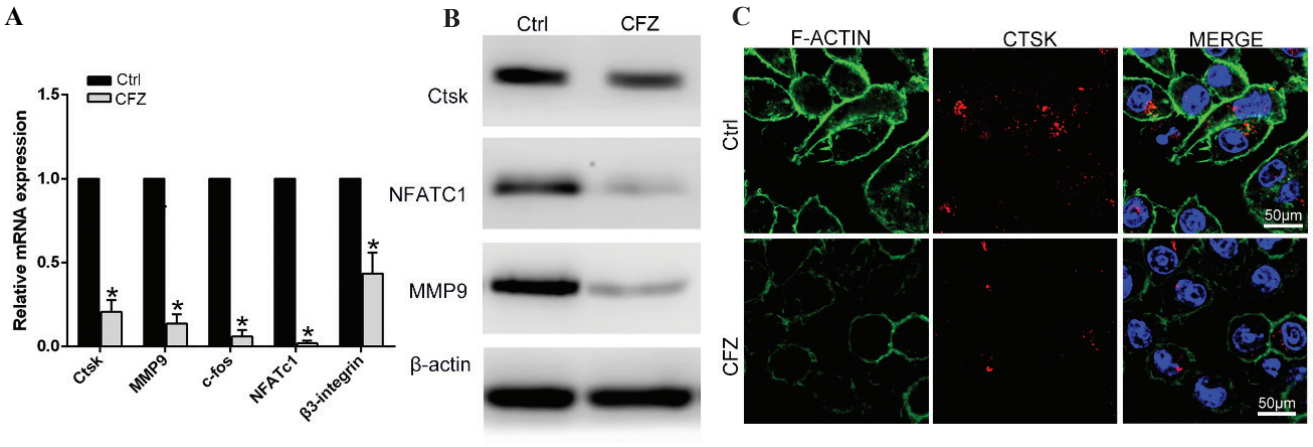

Figure 4. Cytidine triphosphate (CTP) scaffolds inhibit osteoclast formation in RAW264.7 cells. (A) mRNA expression of osteoclast formation genes in RAW264.7 cells stimulated with RANKL and supplemented with (carfilzomib [CFZ] group) or without (control group) extracts of CTP scaffold for 7 days. (B) Western blot results of Ctsk, MMP9 and NFATC1 in raw264.7 cells from control and CFZ group. (C) Immunofluorescence staining of F-actin and CTSK in raw264.7 cells stimulated with RANKL and supplemented with (CFZ group) or without (control group) extracts of CTP scaffold for 14 days. Scale bar = 50 μm. *$P < 0.05$.

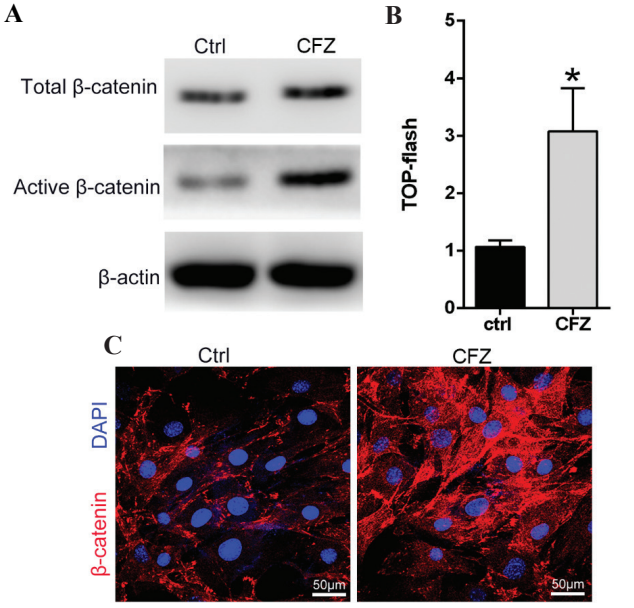

Figure 5. Cytidine triphosphate (CTP) scaffolds activate Wnt/β-catenin signaling. (A) Western blot results of β-catenin in C3H10T1/2 cells cultured with medium supplemented with (carfilzomib [CFZ] group) or without (control group) extracts of the CTP scaffold. (B) TOP/FOP-Flash luciferase reporter assay was used to analyze the effect of CTP scaffolds on the activity of Wnt/β-catenin signaling in C3H10T1/2 cells. (C) Immunofluorescence staining of β-catenin in C3H10T1/2 cells from control and CFZ group. Scale bar = 50 μm. **P* < 0.05.

bone formation. The 3D image of the neovascularization structure in the scaffold area is shown in **Figure 6E**. Neovascularization was significantly enhanced in CTP stents in CFZ group compared to the control group, which was at least 2 times more than TP stents, and at least 4 times more than the blank group. Thus, our data indicated that CTP scaffolds can significantly promote bone regeneration and neovascularization by showing significantly improved vessel length and vessel density **(Figure 6F** and **G)**.

Subsequently, animals were sacrificed and we performed H and E staining to examine the formation of bone in orthotropic segmental defects of each group. As shown in **Figure 7A**, CTP scaffolds showed a better effect in new bone formation and blood vessel formation compared to others, while the control and TP groups showed more fibrous tissue formation than mature bones. Next, we labeled the osteoclasts through immunofluorescence staining of CTSK in bone samples from each group. Compared to the other two groups, CTP scaffolds group showed a reduced level of CTSK on the surface of the trabecular bone (**Figure 7B** and **E**), indicating that CTP scaffolds inhibited osteoclasts formation *in vivo*. We also labeled the vessel with immunofluorescence staining of CD31 in bone sections from all groups, and as expected, the number of vessels around the new formation bone in CTP group was more than that in other two

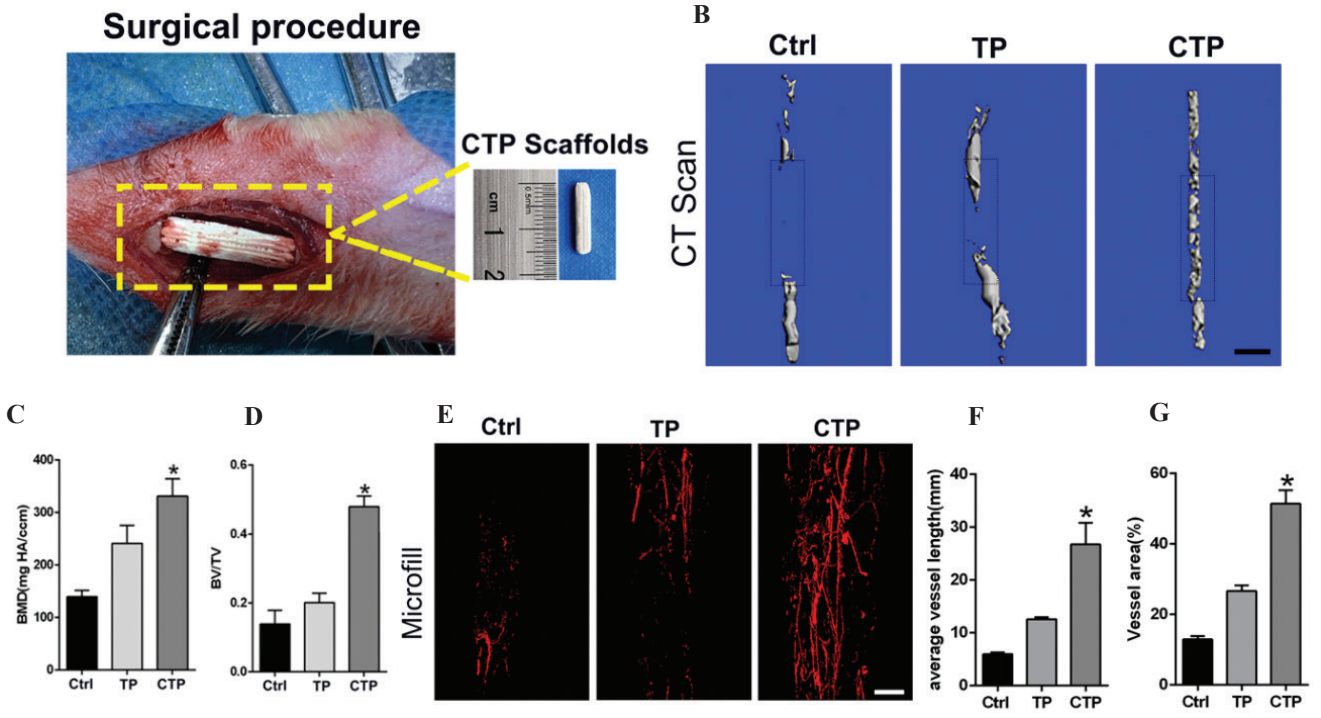

Figure 6. Imaging results show cytidine triphosphate scaffolds promote bone regeneration in a rabbit long bone defect model. (A) Surgical procedure in rabbits with the scaffolds. (B) Micro-CT scan images of the defect area at 12 weeks post-surgery. (C) Bone mineral density of regenerated bone tissue. (D) BV/TV ratio of regenerated tissue. (E) Microfil angiography and micro-CT imaging results of the experimental animals. (F) Quantification of average vessel length and vessel area (G) of the experimental animals **P* < 0.05.

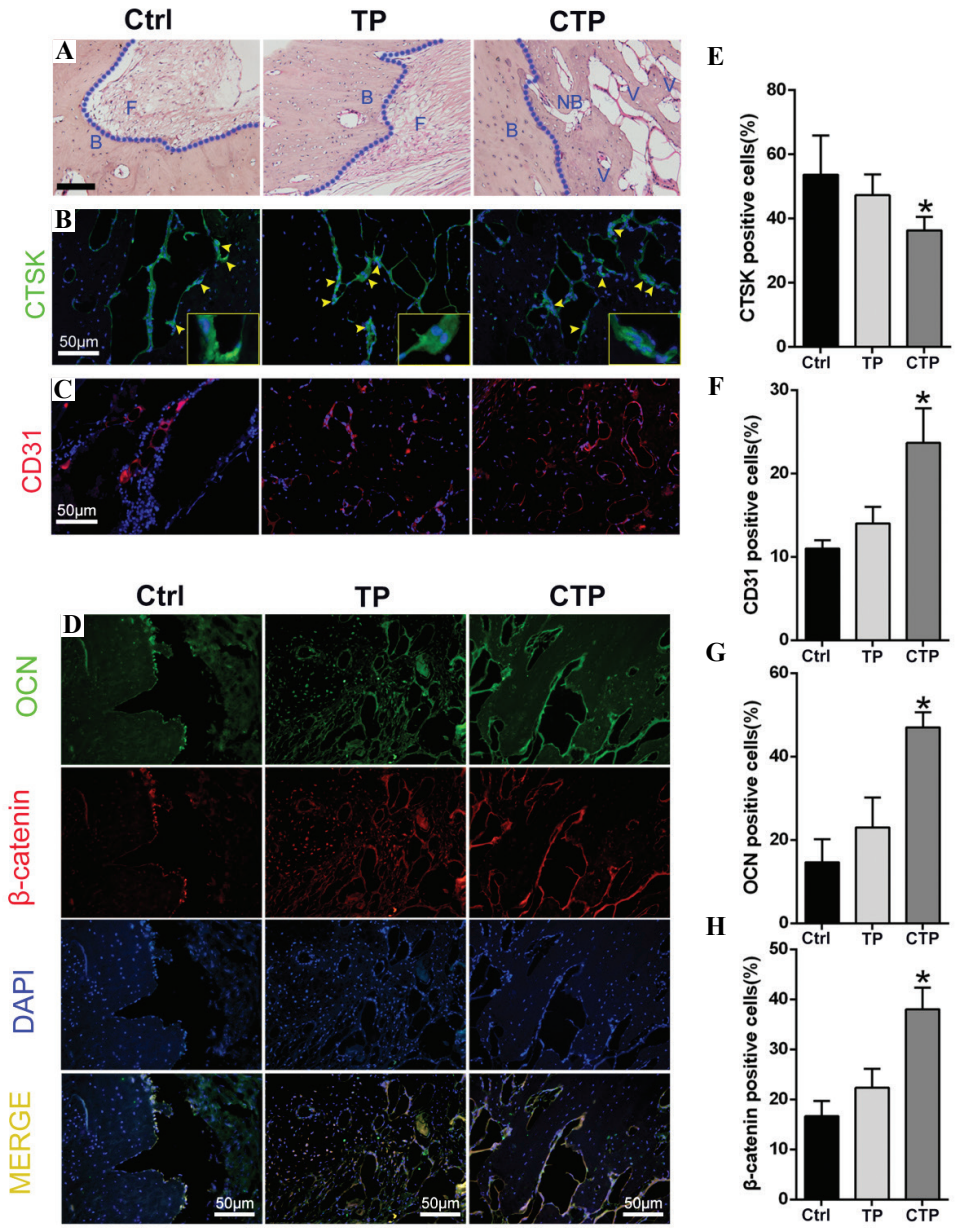

Figure 7. Histological results show that cytidine triphosphate scaffolds promote bone regeneration in a rabbit long bone defect model. (A) H&E staining of the defect area at 12 weeks post-surgery. B: bone, F: Fibrous tissue, NB: New bone; V: Vessel). (B and E) IF analysis and quantification of CTSK in bone sections from different groups. (C and F) Immunofluorescence analysis and quantification of CD31 in bone sections from all groups. (D, G, and H) Immunofluorescence analysis and quantification of OCN and β-catenin in bone sections from different groups. Scale bar = 50 μm. *$P < 0.05$.

groups (**Figure 7C and F**), indicating that the released CFZ promoted angiogenesis in the defected area. Further, expression of ontogenetic marker OCN and β-catenin was detected. We noticed that OCN and β-catenin co-localized in the cytoplasm and nucleus. In the CTP scaffolds, the expression of both OCN and β-catenin was higher than in other groups, suggesting that CTP scaffolds promoted osteogenesis and possibly via the activation of the β-catenin signaling (**Figure 7D**, **G**, and **H**).

Treatment for large bone defects resulting from trauma, tumor, or other diseases is still a major clinical challenge. Autologous bone or autograft is still the most effective therapeutic approaches for bone regeneration in large bone defect[23]. In recent years, bone graft scaffolds combined with various growth factors, such as BMPs, mesenchymal stem cells, and other agents, have been used in the repair of bone defects[24]. The most ideal bone graft scaffold should be biocompatible, osteogenic, and

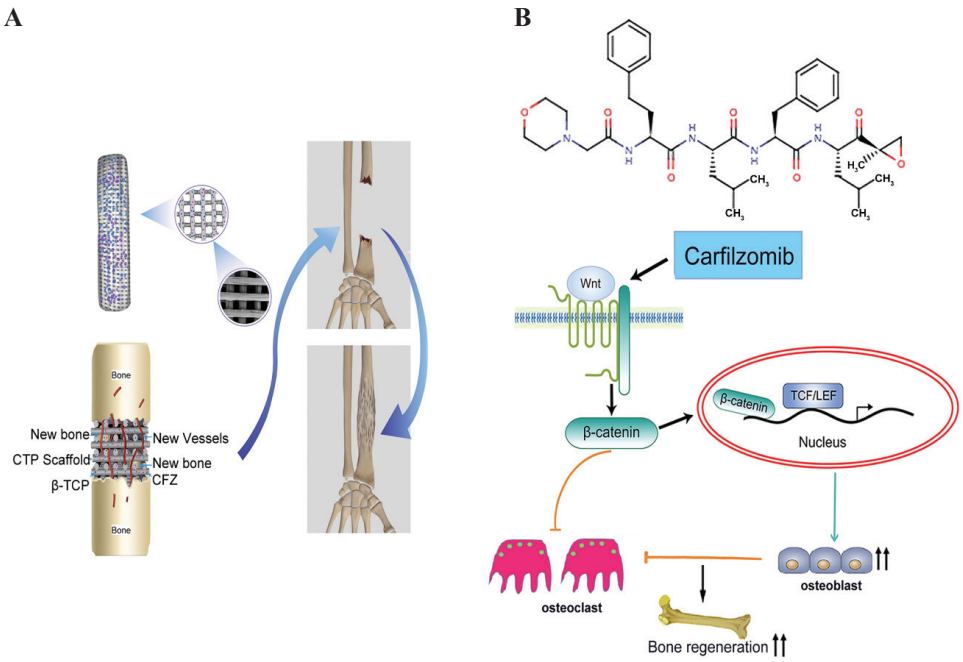

Figure 8. Schematic diagram of cytidine triphosphate (CTP) scaffolds promoting bone regeneration via activating Wnt/β-catenin pathway. (A) Schematic diagram of the preparation process of the CTP scaffold and its effect on angiogenesis and osteogenesis in the bone defect. (B) Chemical structure of carfilzomib and mechanism of carfilzomib on the canonical Wnt/β-catenin signaling.

angiogenic and have mechanical properties similar to those of bone at the implant site[25].

CFZ, an clinically approved proteasome inhibitor, is used to replace bortezomib to treat multiple myeloma, due to fewer side effects it causes[26]. The previous studies had reported the effect of CFZ in inhibiting osteoclasts formation and bone resorption, while enhancing osteogenic differentiation and matrix mineralization *in vitro*[15]. In our study, with sustained release of CFZ from CTP scaffolds, we confirmed the promotion of osteogenesis in cultured mouse mesenchymal cells and inhibition of osteoclastogenesis in mouse leukemic monocyte cell line. The canonical Wnt/β-catenin pathway has been found to be tightly linked to bone formation. Herein, after being treated with CTP scaffolds, the mesenchymal cells exhibited an increased expression of active β-catenin, and we noticed that β-catenin was translocated into the nucleus. Activation of canonical WNT/β-catenin signaling not only promotes differentiation of osteoblasts and bone production but also suppresses RANKL expression to inhibit osteoclasts formation[27]. Thus, we speculated that the effect of CFZ on osteogenesis and osteoclastogenesis may be mediated through activation of the WNT/β-catenin signaling.

During the progression of bone defect repair, osteoclast precursors are attracted from the invading blood vessels that are adjacent to the newly formed bone trabeculae[28]. The new bone tissue is continuously remodeled through the balancing activities of bone-forming osteoblasts and of bone-resorbing osteoclasts[29]. Since the CTP scaffolds showed good biomechanical properties and biocompatibility, we consider that the CTP scaffolds could be suitable for bone regeneration. In *in vivo* study, the CTP scaffolds-treated animals showed increased osteogenesis, decreased osteoclastogenesis, and notably improved bone formation. It was interesting to note that the vascularization was also enhanced in CTP-treated group. Osteogenesis and angiogenesis are two closely related processes in bone regeneration; the newly formed vessels transport nutrient to the cells and metabolic wastes away from the cells, thereby improving bone formation[30]. In summary, CTP scaffolds promoted osteogenesis, inhibited osteoclastogenesis through activation of WNT/β-catenin signaling, and also enhanced angiogenesis, thus improving bone regeneration in large bone defect (**Figure 8A** and **B**).

4. Conclusions

In this study, a porous CTP scaffold was generated by cryogenic 3D printing. The sustained release of CFZ from CTP scaffolds led to the induction of osteoblastic differentiation and inhibition of osteoclast formation *in vitro*, which may be mediated by an underlying mechanism where the CFZ activates the Wnt/β-catenin signaling. In the treatment of rabbit radius bone defects, CTP scaffolds improved new bone formation and promoted the growth of new blood vessels in the regenerated tissues. Overall, this study provides a theoretical basis for

CFZ-incorporated scaffolds, which are produced by 3D printing, in promoting bone regeneration in critical-sized bone defects.

Acknowledgments

This work was supported by Guangxi Science and Technology Program (2018GXNSFAA294116, 2018GXNSFAA138074,2018GXNSAA294091), Guangxi key R & D Project (Guike AB18050008), Scientific Research Project of High-level talents in the affiliated Hospital of Youjiang Medical College for nationalities (R20196301, R20196306), High-level Innovation team and Outstanding Scholars Program of Colleges and Universities in Guangxi: innovative team of basic and Clinical Comprehensive Research on Bone and Joint degenerative Diseases.

Conflicts of interest

The authors have no conflict of interest to declare.

Author contributions

K L., J L. and YJ T. conceived the project. Y L. KG X. and C W. conducted the scaffold fabrication, characterization. CL Y., GF D., GG H. and K H. conducted the *in vitro* release/degradation test and in vitro cell culture. F L., CC Z., SJ D. and J C. conducted the *in vivo* experiments in rat cranial defects and analyzed the related data. QY L., J L. and LQ W. contributed to the writing of the manuscript.

References

1. Sharif F, Ur Rehman I, Muhammad N, *et al*., 2016, Dental Materials for Cleft Palate Repair. *Mater Sci Eng C Mater Biol Appl*, 61:1018–28. https://doi.org/10.1016/j.msec.2015.12.019
2. Marx RE, 2007, Bone and Bone Graft Healing. *Oral Maxillofac Surg Clin North Am*, 19:455–66.
3. Agarwal R, García AJ, 2015, Biomaterial Strategies for Engineering Implants for Enhanced Osseointegration and Bone Repair. *Adv Drug Deliv Rev*, 94:53–62. https://doi.org/10.1016/j.addr.2015.03.013
4. Pilliar RM, Filiaggi MJ, Wells JD, *et al*., 2001, Porous Calcium Polyphosphate Scaffolds for Bone Substitute Applications-*In Vitro* Characterization. *Biomaterials*, 22:963–72. https://doi.org/10.1016/s0142-9612(00)00261-1
5. Lai Y, Li Y, Cao H, *et al*., 2019, Osteogenic Magnesium Incorporated into PLGA/TCP Porous Scaffold by 3D Printing for Repairing Challenging Bone Defect. *Biomaterials*, 197:207–19. https://doi.org/10.1016/j.biomaterials.2019.01.013
6. Lee JY, Son SJ, Son JS, *et al*., 2016, Bone-Healing Capacity of PCL/PLGA/Duck Beak Scaffold in Critical Bone Defects in a Rabbit Model. *Biomed Res Int*, 2016:2136215. https://doi.org/10.1155/2016/2136215
7. Walsh WR, Vizesi F, Michael D, *et al*., 2008, Bruceβ-TCP Bone Graft Substitutes in a Bilateral Rabbit Tibial Defect Model. *Biomaterials*, 29:266–71. https://doi.org/10.1016/j.biomaterials.2007.09.035
8. Huang J, Liu W, Liang Y, *et al*., 2018, Preparation and Biocompatibility of Diphasic Magnetic Nanocomposite Scaffold. *Mater Sci Eng C Mater Biol Appl*, 87:70–7.
9. Ji C, Annabi N, Khademhosseini A, *et al*., 2011, Fabrication of Porous Chitosan Scaffolds for Soft Tissue Engineering using Dense Gas Co_2. *Acta Biomater*, 7:1653–64. https://doi.org/10.1016/j.actbio.2010.11.043
10. Hartgerink JD, Beniash E, Stupp SI, 2002, Peptide-Amphiphile NanofibersA Versatile Scaffold for the Preparation of Self-Assembling Materials. *Proc Natl Acad Sci USA*, 99:5133–8. https://doi.org/10.1073/pnas.072699999
11. Green JD, Tollemar V, Dougherty M, *et al*., 2015, Multifaceted Signaling Regulators of ChondrogenesisImplications in Cartilage Regeneration and Tissue engineering. *Genes Dis*, 2:307–27.
12. Gaasbeek RD, Toonen HG, van Heerwaarden RJ, *et al*., 2005, Mechanism of Bone Incorporation of β-TCP Bone Substitute in Open Wedge Tibial Osteotomy in Patients. *Biomaterials*, 26:6713–9. https://doi.org/10.1016/j.biomaterials.2005.04.056
13. Michalicka M, Boisjoli G, Jahan S, *et al*., 2017, Human Bone Marrow Mesenchymal Stromal Cell-Derived Osteoblasts Promote the Expansion of Hematopoietic Progenitors Through Beta-Catenin and Notch Signaling Pathways. *Stem Cells Dev*, 26:1735–48. https://doi.org/10.1089/scd.2017.0133
14. Zhang C, Hu B, Chen Y, *et al*., 2013, Characterization of the Molecular Mechanism of the Bone-Anabolic Activity of Carfilzomib in Multiple Myeloma. *PLoS One*, 8:e74191. https://doi.org/10.1371/journal.pone.0074191
15. Hurchla MA, Garcia-Gomez A, Hornick MC, *et al*., 2012, The Epoxyketone-Based Proteasome Inhibitors Carfilzomib and Orally Bioavailable Oprozomib Have Anti-Resorptive and Bone-Anabolic Activity in Addition to Anti-Myeloma Effects. *Leukemia*, 27:430–40. https://doi.org/10.1038/leu.2012.183
16. Yang Y, Blair HC, Shapiro IM, *et al*., 2015, The Proteasome Inhibitor Carfilzomib Suppresses Parathyroid Hormone-induced Osteoclastogenesis through a RANKL-Mediated

Signaling Pathway. *J Biol Chem*, 290:16918–28. https://doi.org/10.1074/jbc.m115.663963

17. Maeda K, Kobayashi Y, Koide M, *et al*., 2019, The Regulation of Bone Metabolism and Disorders by WNT Signaling. *Int J Mol Sci*, 20:5525.
18. Wei W, Zeve D, Suh JM, *et al*., 2011, Biphasic and Dosage-Dependent Regulation of Osteoclastogenesis by β-Catenin. *Mol Cell Biol*, 31:4706–19. https://doi.org/10.1128/mcb.05980-11
19. Coffin JD, Homer-Bouthiette C, Hurley MM, *et al*., 2018, Fibroblast Growth Factor 2 and Its Receptors in Bone Biology and Disease. *J Endocr Soc*, 2:657–71. https://doi.org/10.1210/js.2018-00105
20. Zhou H, Mak W, Zheng Y, *et al*., 2008, Osteoblasts Directly Control Lineage Commitment of Mesenchymal Progenitor Cells through Wnt Signaling. *J Biol Chem*, 283:1936–45. https://doi.org/10.1074/jbc.m702687200
21. Barbosa MA, Yao D, Xie XH, *et al*., 2012, Icaritin, an Exogenous Phytomolecule, Enhances Osteogenesis but Not Angiogenesis-An *In Vitro* Efficacy Study. *PLoS One*, 7:e41264. https://doi.org/10.1371/journal.pone.0041264
22. Guzzo CM, Nychka JA, 2020, Bone 'Spackling' Paste: Mechanical Properties and *In Vitro* Response of a Porous Ceramic Composite Bone Tissue Scaffold. *J Mech Behav Biomed Mater*, 112:103958. https://doi.org/10.1016/j.jmbbm.2020.103958
23. Roddy E, DeBaun MR, Daoud-Gray A, *et al*., 2017, Treatment of Critical-Sized Bone Defectsclinical and Tissue Engineering Perspectives. *Eur J Orthop Surg Traumatol*, 28:351–62. https://doi.org/10.1007/s00590-017-2063-0
24. Ho-Shui-Ling A, Bolander J, Rustom LE, *et al*., 2018, Bone Regeneration Strategies: Engineered Scaffolds, Bioactive Molecules and Stem Cells Current Stage and Future Perspectives. *Biomaterials*, 180:143–62. https://doi.org/10.1016/j.biomaterials.2018.07.017
25. Polo-Corrales L, Latorre-Esteves M, Ramirez-Vick JE, 2014, Scaffold Design for Bone Regeneration. *J Nanosci Nanotechnol*, 14:15–56. https://doi.org/10.1166/jnn.2014.9127
26. McBride A, Klaus JO, Stockerl-Goldstein K, 2015, Carfilzomib: A Second-Generation Proteasome Inhibitor for the Treatment of Multiple Myeloma. *Am J Health Syst Pharm*, 72:353–60. https://doi.org/10.2146/ajhp130281
27. Glass DA, Bialek P, Ahn JD, *et al*., 2005, Canonical WNT Signaling in Differentiated Osteoblasts Controls Osteoclast Differentiation. *Dev Cell*, 8:751–64. https://doi.org/10.1016/j.devcel.2005.02.017
28. Wang Y, Li M, Li P, *et al*., 2019, Progress and Applications of Polyphosphate in Bone and Cartilage Regeneration. *Biomed Res Int*, 2019:5141204.
29. Hadjidakis DJ, Androulakis II, 2006, Bone Remodeling. *Ann N Y Acad Sci*, 1092:385–96.
30. Grosso A, Burger MG, Lunger A, *et al*., 2017, It Takes Two to Tango: Coupling of Angiogenesis and Osteogenesis for Bone Regeneration. *Front Bioeng Biotechnol*, 5:68. https://doi.org/10.3389/fbioe.2017.00068

RESEARCH ARTICLE

Cellulose Nanocrystal-Enhanced Thermal-Sensitive Hydrogels of Block Copolymers for 3D Bioprinting

Yuecheng Cui[1], Ronghua Jin[2], Yifan Zhang[3], Meirong Yu[2], Yang Zhou[1], Li-Qun Wang[1,4]*

[1]MOE Key Laboratory of Macromolecular Synthesis and Functionalization, Department of Polymer Science and Engineering, Zhejiang University, Hangzhou 310027, P. R. China
[2]Second Affiliated Hospital of Medical College, Zhejiang University, Hangzhou 310009, P. R. China
[3]Hangzhou Regenovo Biotechnology Co. Ltd, Hangzhou Economic and Technological Development Area, Hangzhou 310018, P. R. China
[4]Hangzhou Medsun Biological Technology Co., Ltd, Hangzhou Economic and Technological Development Area, Hangzhou 310018, P. R. China

Abstract: The hydrogel formed by polyethylene glycol-aliphatic polyester block copolymers is an ideal bioink and biomaterial ink for three-dimensional (3D) bioprinting because of its unique temperature sensitivity, mild gelation process, good biocompatibility, and biodegradability. However, the gel forming mechanism based only on hydrophilic-hydrophobic interaction renders the stability and mechanical strength of the formed hydrogels insufficient, and cannot meet the requirements of extrusion 3D printing. In this study, cellulose nanocrystals (CNC), which is a kind of rigid, hydrophilic, and biocompatible nanomaterial, were introduced to enhance the hydrogels so as to meet the requirements of extrusion 3D printing. First, a series of poly(ε-caprolactone/lactide)-*b*-poly(ethylene glycol)-*b*-poly(ε-caprolactone/lactide) (PCLA-PEG-PCLA) triblock copolymers with different molecular weights were prepared. The thermodynamic and rheological properties of CNC-enhanced hydrogels were investigated. The results showed that the addition of CNC significantly improved the thermal stability and mechanical properties of the hydrogels, and within a certain range, the enhancement effect was directly proportional to the concentration of CNC. More importantly, the PCLA-PEG-PCLA hydrogels enhanced by CNC could be extruded and printed through temperature regulation. The printed objects had high resolution and fidelity with effectively maintained structure. Moreover, the hydrogels have good biocompatibility with a high cell viability. Therefore, this is a simple and effective strategy. The addition of the hydrophilic rigid nanoparticles such as CNC improves the mechanical properties of the soft hydrogels which made it able to meet the requirements of 3D bioprinting.

Keywords: Poly(ε-caprolactone/lactide)-b-poly (ethylene glycol)-*b*-poly(ε caprolactone/lactide); Thermal-sensitive hydrogels; Three-dimensional bioprinting; Cellulose nanocrystal

*Correspondence to: Li-Qun Wang, Department of Polymer Science and Engineering, Zhejiang University, Hangzhou 310027, P. R. China; lqwang@zju.edu.cn

Received: June 02, 2021; **Accepted:** August 03, 2021; **Published Online:** August 27, 2021

Citation: Cui Y, Jin R, Zhang Y, *et al.,* 2021, Cellulose Nanocrystal-Enhanced Thermal-Sensitive Hydrogels of Block Copolymers for 3D Bioprinting. *Int J Bioprint*, 7(4):397. http://doi.org/10.18063/ijb.v7i4.397

1. Introduction

Three-dimensional (3D) bioprinting is a rapid additive manufacturing technology which is used in the field of tissue engineering[1,2]. As an emerging research direction, it has attracted widespread attention. The printing methods in this technology are diverse, and material jetting, material extrusion, and vat polymerization bioprinting are commonly used[3-7]. Among them, material extrusion bioprinting is capable of fabricating more scaled bio-scaffold compared with the other two technologies, exhibiting more potential and prospect in

tissue engineering and other biomedical fields. For the extrusion-based printing, the inks in the cylinder can be extruded under pressure through the nozzle and deposited on a substrate layer by layer. Therefore, the ink not only can be extruded smoothly but also can be set quickly after deposition. The fact that a printable biomaterial is required to have the properties of shear thinning, fast curing and good biocompatibility presents a huge challenge in broadening extrudable biomaterial inks[2,8].

Hydrogels are water-swellable 3D crosslinking network with adaptable mechanical strength. Therefore, under the premise of retaining the original excellent properties of the hydrogel, enhancing its mechanical strength to meet the needs of 3D printing is one of the focuses in this field[9,10]. Nevertheless, the diverse and complex gelation mechanisms of hydrogels are reciprocally restricted with technology condition of extrusion-based printing, thereby restraining the application in 3D bioprinting. Thus, it is an application prospect to develop more extrudable hydrogels with easy gelation mechanism[11,12]. Temperature-responsive hydrogels are the soft materials that can reversibly transit between gel and sol by regulating temperature, which are the ideal printable and extrudable materials[13]. Unfortunately, the crosslinking network of this type of hydrogels is often based on hydrogen bonds or hydrophilic-hydrophobic interactions. The weaker forces lead to poor structural stability and low mechanical strength of the cross-linked networks. Extrusion swelling and even structural collapse will occur during printing[14-16]. Therefore, the present research focuses on enhancing the mechanical strength of the hydrogels while retaining the original excellent properties.

At present, the introduction of carbon-carbon double bonds in the chemical structure of the materials, and subsequently photo-curing is the main means. Among them, methacryloyl gelatin (GelMA) is a representative of this strategy. In this approach, the chemical modification is easy and convenient. The degree of substitution of the double bond can be adjusted while the structure of the gelatin will not change significantly. The printed GelMA object can be fast photo-crosslinking by adding a photoinitiator. The mechanical strength of the cured hydrogel is remarkably enhanced[17-20]. However, the introduction of photoinitiator and its free radical species caused by UV irradiation that causes damage to the cells affect the cell survival rate[21-23]. We previously reported an alternative approach: introducing a crystalline poly(*ε*-caprolactone) (PCL) block into the molecular structure to construct poly(*ε*-caprolactone)-*b*-poly(ethylene glycol)-*b*-poly(*ε*-caprolactone) triblock copolymer. The results showed that the crosslinked network of the copolymers could partially crystalize in water. Compared with the amorphous control group, it showed significantly improved strength and thermal stability, which meets the requirements of extrusion 3D printing[12]. However, the limitation of this method is that the amorphous materials do not have the ability to crystallize. Therefore, it is necessary to develop more extensive mechanical enhancement strategies.

In this study, cellulose nanocrystals (CNC), kind of rigid nanoparticles, were introduced to strengthen the amorphous block copolymer hydrogels. CNC is a rod-shaped rigid nanomaterial made of natural polymers, which has a good biocompatibility and can be stably dispersed into nanoparticles in an aqueous medium[24-27]. As previously reported[28-30], the introduction of CNC could mechanically enhance the hydrogels. Therefore, we hope to introduce such rigid nanomaterials as reinforcing fillers to improve the mechanical strength and printability of amorphous hydrogels. Thus, triblock copolymers, poly(*ε*-caprolactone/lactide)-*b*-poly(ethylene glycol)-*b*-poly(*ε*-caprolactone/lactide) (PCLA-PEG-PCLA), were chosen for the study. A series of PCLA-PEG-PCLA copolymers with different molecular weight were prepared; subsequently, different amounts of CNC were introduced, and the mechanical improvement effect on the hydrogels was evaluated. It is found that the addition of CNC significantly improved the thermal stability and mechanical strength of the hydrogels. Within a certain concentration range, the improvement of hydrogel performance was proportional to the increase of CNC concentration. In addition, when a certain amount CNC was added, the sol system that cannot form a gel state at room temperature has a significant "liquid-solid transition" phenomenon. More importantly, the CNC-enhanced hydrogels could form effectively maintained 3D structural objects with high resolution and fidelity during the printing process, and no extrusion swelling or structural collapse was observed. The strategy of introducing rigid nanoparticles such as CNC to the mechanically weak hydrogels meets the demand of 3D bioprinting, and is a simple and effective way to improve the comprehensive performance of the thermal-sensitive hydrogels.

2. Materials and methods

2.1. Materials

CNC (11 wt%) was purchased from Beijing North Tianchen Technology Co., Ltd. (Beijing, China). *ε*-caprolactone (98%) was received from Shanghai Aladdin Biochemical Technology Co., Ltd. and dehydrated by CaH_2 for more 2 weeks. PEG ($\boldsymbol{M}_n$ = 6 000, 8 000 and 10 000 Da) was purchased from Sigma-Aldrich (98%) and dehydrated by lyophilization. L-lactide (LLA) was synthesized in our lab and recrystallized from ethyl acetate and dried in a vacuum oven at room temperature over 3 days. Stannous octoate ($Sn(Oct)_2$, 95%) and $CDCl_3$ (99.9%) were also obtained from Sigma-Aldrich. All other chemicals were obtained from Shanghai Chemical Reagent Co.

(Shanghai, China) and used without further purification, unless otherwise specified.

2.2. Synthesis of the triblock copolymer

The PCLA-PEG-PCLAs were all synthesized through ring-opening polymerization. Taking PCA_1 as an example, 3 g dihydroxyl PEG (M_n = 6 000 Da, 0.5 mmol), 1.14 g ε-CL (1.11 mL, 10 mmol), 1.44 g LLA (10 mmol), and 3% Sn $(Oct)_2$ were added into a blank round-bottom flask. The mixture was melted at 60°C and then purified with argon under stirring for 3 times. The polymerization was conducted under vacuum at 160°C for 8 h. The reaction was terminated at –20°C. The obtained crude product was dissolved in around 5 mL CH_2Cl_2 and precipitated in over 100 mL diethyl ether for 3 times. The solid product was then dried in a vacuum oven overnight.

2.3. Characterization of copolymer structure

^{1}H NMR spectra of triblock copolymers were recorded using a Brucker Avance-400 nuclear magnetic resonance instrument. The solvent was $CDCl_3$. The gel permeation chromatography (GPC) was determined through Waters PL-GPC-50 instrument. The eluent was THF with a flow rate of 1.0 mL/min.

2.4. Vial-inverting test

The enhancement effect of CNC on phase transition of hydrogels was evaluated by vial-inverting test. The hydrogels of the copolymers were prepared at the concentration of 20 wt% while 0, 2.2, 4.4, and 8.8 wt% CNC were used. The vials were incubated in a water bath. The temperature was regulated from 25 to 70°C with an increment of 1°C per step. Each sample was equilibrated for 5 min at each temperature and the state was evaluated. Once a flowable or dehydrated state was observed after inverting the vial, the transition temperature would be recorded.

2.5. Rheological experiments

The rheological properties of hydrogels were characterized through a TA ARES-G2 instrument using a 25 mm parallel plate geometry. The samples were loaded on the Peltier platform. Temperature sweep experiments were conducted at 1 Hz from 25 to 75°C with a ramp rate of 3°C/min. Frequency sweep experiments were carried out at 25°C from 0.1 to 100 rad/s with a strain value of 0.5%. Strain sweep experiments (25°C) were performed at a strain ranging from 0.01% to 1000% with a frequency value of 1 Hz. Shear thinning tests was carried out at 37°C with a frequency value of 1 Hz. The shear rates were from 0.01 to 100 rad/s. The thixotropy experiments (25°C) were performed at an alternating strain of 0.01% and 100% for 100 s, respectively, per cycle.

2.6. Scanning electron microscopy (SEM)

The copolymers-formed hydrogels (20 wt%) were lyophilized at -50°C under 10 Pa (Vacuum freeze dryer, FD-1A-50, BiLon, Shanghai, China) overnight, which was followed by metal-spraying using an MSP-2S, an ion sputtering instrument (EIKO Corporation, Japan) for 1 min. The SEM images were obtained through a Hitachi S-4800 SEM instrument.

2.7. Degradation properties

20 wt% PCA_2 hydrogel was chosen to study the degradation properties. 0.5 g of PCA_2 was added to a vial and 1 mL phosphate buffer (PB) containing 0.1 mg lipase (Aladdin, Shanghai, China) was subsequently added. The experiments were conducted in triplicates at 37°C and the buffer was refreshed every day. The residual samples were taken out and lyophilized at specific time intervals. The weight of each sample was recorded and the average value of weight ratio of weight loss and the original weight before incubation was calculated as the degradation rate for the analysis.

2.8. 3D printability of hydrogels

The extrusion-based 3D printing was carried out with an instrument of Bio-Architect® PRO (Regenovo). The hydrogels were filled into the barrels and then placed into an oven at 37°C overnight to eliminate the bubbles. The corresponding GCodes and software were supported by Regenovo. The filament collapse experiments and micro-extrusion were performed by adjusting the nozzle size, the pneumatic pressure value, and translational speed. Taking the 20 wt% PCA_2+4.4 wt% CNC gel with the 0.41 mm of nozzle as an example, the thickness was set as 0.4 mm and the 3D constructs were printed at 37°C under 0.3 MPa of air pressure with 10 mm/s of transitional speed.

2.9. *In vitro* cytotoxicity assay

Primary human fibroblasts (HDFs) were used for evaluation. HDFs were obtained from discarded human foreskin and used until 4–6th passage. The cell seeding density was 500/well. The Dulbecco's modified Eagle's medium, Sigma, USA was used as culture medium.

The cytocompatibility of the copolymers with different concentrations was evaluated through staining with cytotoxicity assay kit (KeyGEN BioTECH, China). The culture medium was removed and washed with PB saline (PBS) for 3 times. The work solution (0.5 μL propidium iodide (PI) + 0.5 μL calcein acetoxymethyl ester (AM) in 1 mL PBS) was added into the samples and then incubated for 45 min at room temperature. The fluorescent images were observed through fluorescence microscope (Leica, Germany); the living and dead cells showed as green and red regions, respectively.

The cytocompatibility of hydrogels was also investigated. 20 wt% PCA_2+4.4 wt% hydrogel was chosen for the investigation while cells were seeded on its surface. The following process was identical to the previous procedure. The fluorescent images were captured after 12-h co-incubation.

(c) The cell viability was also carried out using Cell Counting Kit-8 (CCK-8) cell viability assay. The CCK-8 stock solution (Dojindo, Kumamoto, Japan) was diluted (1:10) in culture medium to form a working solution. The human primary fibroblasts and copolymer at a given concentration were submerged for 2 h. 100 μL of the submerged solution was extracted and transferred into a plate of 96 wells. The measurements were conducted using a microplate reader (BioTek Instrument, USA) with the absorbance at 450 nm. The samples were washed with PBS until the working solution was totally removed; and fresh medium was added subsequently for incubation.

3. Results and discussion

3.1. Synthesis and properties of the copolymers

According to our previous study, dihydroxy terminated PEGs with different molecular weight (6, 8, and 10 kDa) were chosen as the macroinitiator. By regulating the feed ratio, the molecular weight of polyester was controlled around 2 kDa. Thus, three PCLA-PEG-PCLA copolymers with different chain lengths, named, respectively, as PCA_1, PCA_2 and PCA_3, were prepared via ring-opening polymerization using $Sn(Oct)_2$ as the catalyst (**Figure 1**). To ensure the elimination of the intrinsic crystallinity of polyester, the constitutional repeating unit between caprolactone (CL) and lactide (LA) were adjusted to the same molar number. The obtained samples were characterized through ^{1}H NMR and GPC, which is shown in **Table 1**. Through the calculation of integral area in ^{1}H NMR spectra (**Figure 2A**), the chain length of each polyester block was around 2000 Da. That means the block ratio of polyester decreased with the increase of PEG chains. Meanwhile, the molar ratio of the constitutional repeating unit between CL and LA was calculated, respectively, as 0.98, 0.9, and 1.08, which were close to the equal distribution of 1:1, ensuring the amorphous state of the hydrophobic block. In addition, the GPC results illustrated that the molecular weight of all copolymers was narrowly distributed (**Figure 2B**).

3.2. Gel-sol transition of the CNC-enhanced copolymer gels

The hydrogels formed by these copolymers exhibited thermal-sensitive properties with gel-sol transition, that is, these gels have a lower critical gelation temperature (LCGT). As the temperature is lower than LCGT, the system is in a gel state. When the temperature is above LCGT, lower concentration gels transform into a flowable sol state and the gels of higher concentration will dehydrate and precipitate. Therefore, LCGT can effectively reflect the thermal stability of the hydrogels. Since the polyester block is an amorphous block formed by the copolymerization of two monomers, the formed hydrogel often has a low LCGT and is not as stable as a gel formed by a crystalline copolymer with the same molecular weight. Thus, CNCs with different concentrations were introduced to the hydrogels (20 wt%) to evaluate the enhancement effect (**Figure 3A**). It can be seen that the overall LCGT was at a relatively low level in the absence of CNC, and as the molecular weight of PEG increases, the LCGT gradually decreases. The reduction of hydrophobic block ratio will be detrimental to the thermal stability of gels, which is consistent with our previous study[16]. The thermal stability of the hydrogels is improved to varying degrees when different concentrations of CNC

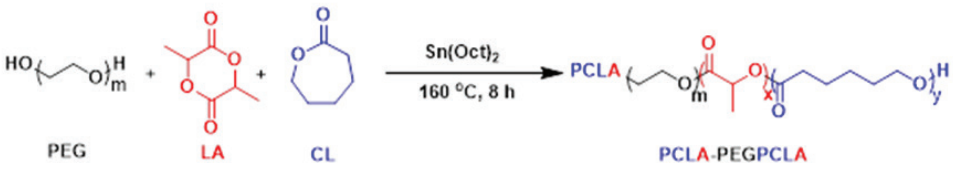

Figure 1. The synthesis strategy of PCLA-PEG-PCLA triblock copolymers.

Table 1. Properties of PCLA-PEG-PCLA triblock copolymers

Samples	$M_{n,NMR}$ [a,c]	$M_{n,GPC}$ [b]	M_w/M_n [b]	Polyester/PEG[a] (M_n/M_n)	CL/LA[a] (mol/mol)
PCA_1	2 170-6 000-2 170	10 500	1.01	0.72	0.98
PCA_2	1 820-8 000-1 820	13 400	1.11	0.46	0.9
PCA_3	1 880-10 000-1 880	16 100	1.25	0.38	1.08

[a]$M_{n,NMR}$, polyester/PEG ratios and CL/LA ratios of the copolymers were calculated from 1H NMR spectra. [b]$M_{n,GPC}$ and M_w/M_n of copolymers were calculated by GPC. [c]The difference among the PCA_1, PCA_2 and PCA_3 was the molecular weight of PEG, which was 6, 8, and 10 kDa, respectively, while the hydrophobic block was kept at around 2 kDa for the convenience of subsequent comparison

(2.2, 4.4, and 8.8 wt%, respectively) were added to the hydrogels. Among them, the effect on PCA_3 is the most remarkable. When the concentration of CNCs reaches 8.8 wt%, the LCGT of PCA_3 increased by about 15°C, showing a notable promotion effect.

This enhancement effect on phase transition with different concentrations of CNC also shows a similar result in tan δ (**Figure 3B**). Taking PCA_2 samples (20 wt%) as an example, temperature sweep was conducted ranging from 25 to 75°C. It can be found that tan δ of four samples increased from gel state (tan δ < 1, G' > G'') to sol state (tan δ > 1, G' < G'') with the increment of temperature, exhibiting a typical thermal-sensitive effect. As the temperature increased further (T >60°C), tan δ decreased due to the dehydration of hydrogels at elevated temperature. Compared with the PCA_2 without CNC, the tan δ reduced to varying degrees after different concentrations of CNC were added. As 8.8 wt% CNC was added, the values of tan δ became far below 1, showing a strong elastic effect. These results demonstrate that the introduction of CNCs can effectively improve the thermal stability of the crosslinked network of the copolymers.

3.3. Rheological properties of the CNC-enhanced hydrogels

Considering that the addition of different concentrations of CNCs has an effect on the thermal stability of the hydrogels to varying degrees, it is thereby predictable that the mechanical strength of the hydrogels may be similarly enhanced by CNC. Therefore, the rheological properties of the copolymers were investigated. Frequency sweep was conducted (**Figure 4**). For PCA_1 and PCA_2, the addition of CNCs significantly improved the modulus of the hydrogel, and with the increase of CNC concentration, the increased effect on the hydrogel strength becomes more prominent. For PCA_3 samples, the gel modulus is substantially improved after adding CNCs. From the results, it can be seen that the PCA_3 without CNC showed a high degree of frequency dependence. That is, the storage modulus (G') < loss modulus (G'') in the low frequency range (0.1~10 rad/s), and in the high frequency range (10~100 rad/s), it became G' > G'', indicating that PCA_3 (~20 wt%) can hardly form a stable hydrogel at room temperature, which is consistent with the above phase diagram (**Figure 3A**). Longer PEG chain is detrimental to gel formation. As the CNC concentration increase to 2.2 wt% in the gel system, the gel point moves to lower frequency, from 10 rad/s to 2 rad/s. Broader frequencies range was facilitated for gel formation. When the CNC concentration reached 4.4 wt%, a typical "gel-sol transition" could be observed where G' > G'' within the whole given frequencies range, but the sample still showed a significant frequency dependence. When the CNC concentration reached 8.8 wt%, the gel modulus was further improved, and the variation of gel modulus on frequency became inconspicuous, exhibiting a more elastic effect.

According to the results of frequency sweep, the addition of CNCs remarkably improves the gel modulus, and the improvement effect is proportional to the CNC concentration. For those samples which cannot form stable gels under conventional conditions, the addition of CNC can facilitate the gel point to shift to lower frequencies, exhibiting an elastic effect at a wider frequency range. When the CNC concentration reaches a certain extent, "gel-sol" transition effect will occur. According to our previous research, the hydrophilic block ratio of copolymers was higher within a certain range, and the hydrophobic cores were smaller while the hydrophilic chains were longer. Thus, the effective crosslinking points between micelles would reduce. The crosslinking network would thereby become unstable and exhibit frequency dependence, especially in the lower frequencies range. Due to the hydrophilic group (e.g. hydroxyl group) on the CNC surface, more hydrogen bonds would be generated between CNC and PEG chain. Thus, the effective crosslinking points increase remarkably, leading to a more stable structure of the network. That is, the CNC enhanced hydrogels show more independent on the frequency compared with the unmodified gels. Thereby, the stability of gels would improve[30-35].

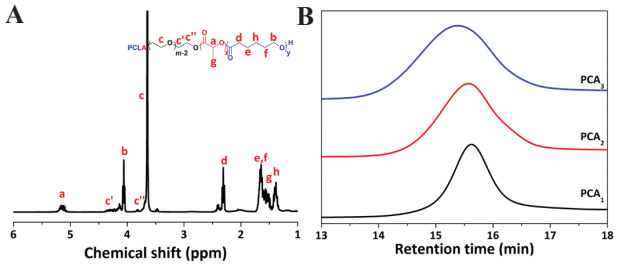

Figure 2. (A) $_1$H NMR spectra of PCLA-PEG-PCLA. The solvent used was D_2O. (B) GPC spectra of PCA_1, PCA_2 and PCA_3. The solvent used was THF.

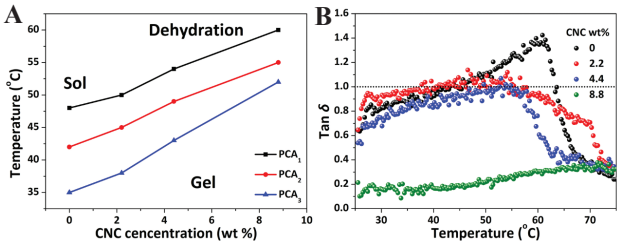

Figure 3. Enhancement effect of CNC on phase transition. (A) Phase diagram of PCLA-PEG-PCLA hydrogels (20 wt%) with CNC of different concentrations. (B) Tan δ of PCA_2 hydrogels added with different concentrations of CNC as a function of temperature with a ramp rate of 3°C/min.

The strain sweep was subsequently conducted and the results are shown in **Figure 5**. Abiding by the rule of normal crosslinking system, all the samples of the three groups had a linear viscoelastic regime in which the gel modulus had no significant change and $G' > G''$, showing a typical elastic effect. When the strain reached a certain extent, the hydrogel yields and modulus drop abruptly, and $G' < G''$, exhibiting a liquid-like state. Moreover, we observed that there were significant changes between before and after the addition of CNC under the large amplitude oscillatory strain (LAOS). The system with added CNC at the LAOS produced an obvious weak strain overshoot (WSO) phenomenon, that is, when the gel yielded, G'' experienced a sharp rise first and then abruptly decrease. We believe that this is due to the destruction and reorganization of the cross-linked network structure in the process of increasing strain amplitude, resulting in a sudden increase in energy dissipation. The system without CNC has no significant WSO phenomenon, and with the increase of CNC concentration, the WSO phenomenon becomes more obvious, indicating that this phenomenon is attributed to the addition of CNC, and the copolymer itself has an amorphous structure in the water phase. The energy dissipation in the LAOS process is not obvious, and WSO does not occur. However, the introduced CNC itself is a rigid and crystalline material. The energy dissipation required for the destruction and reorganization of its structure in the same LAOS process rises sharply, and with the increase of CNC content, the WSO phenomenon becomes more apparent. The addition of CNC significantly increases the modulus of the system, and the modulus increases with the increase of CNC concentration, which is consistent with the previous results[16,36-39].

The rheological results effectively illustrate that the introduction of CNC can not only increase the effective crosslinking chains of the hydrogels but also enhance the structural stability of the network due to its rigid crystal particles. Thus, enhanced hydrogels will weaken the frequency dependence and simultaneously strengthen the mechanical properties.

3.4. Printability of CNC-enhanced hydrogel

According to the thermodynamic and rheological results, the addition of CNCs effectively improves the thermal stability and mechanical strength of hydrogels. It is thereby believed that printability can also be improved. Thus, 20 wt% PCA_2+4.4 wt% CNC was chosen for the investigation of the feasibility in 3D bioprinting (**Figure 6**). Extrudability was first evaluated. As mentioned above, materials with shear-thinning properties can be extruded. Thus, the viscosity variation of the hydrogel ranging from 0.01 to 100 rad/s was investigated and the result is shown in **Figure 6A**. It is found that the viscosity of the sample experienced a

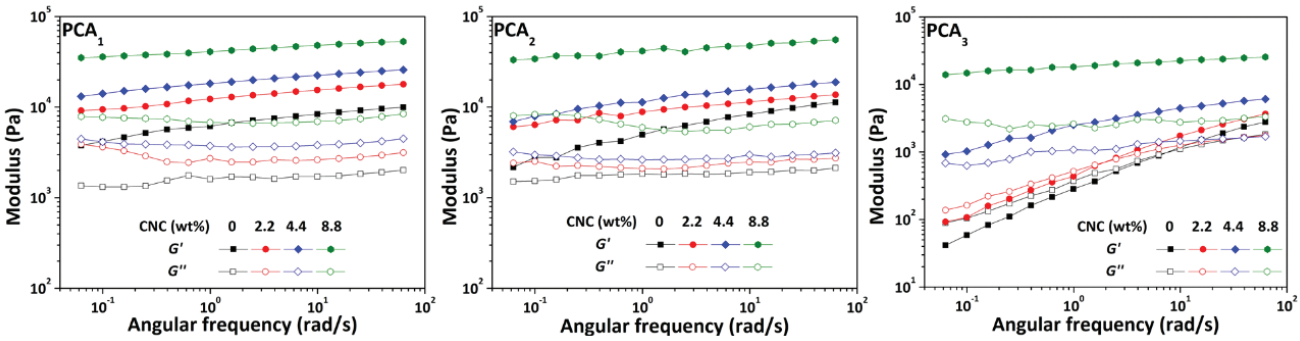

Figure 4. Frequency sweep of PCA_1, PCA_2 and PCA_3 (20 wt%) with CNC of different concentrations.

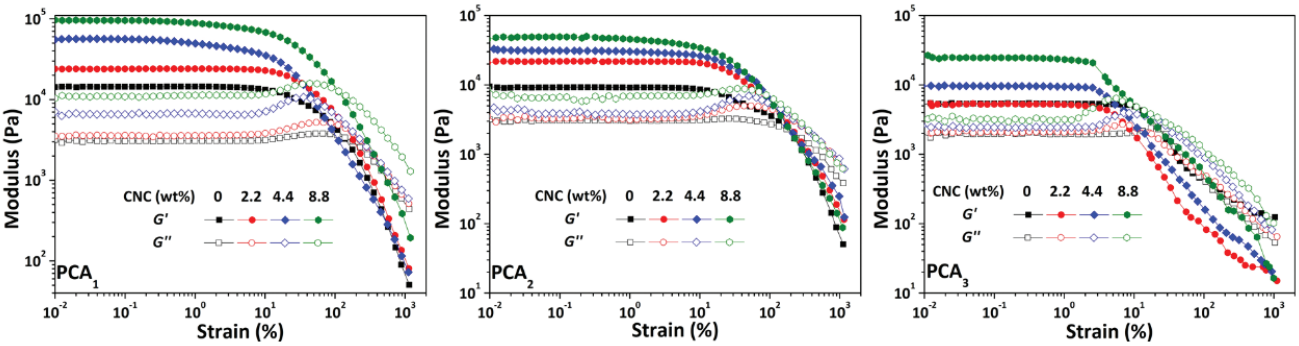

Figure 5. Strain sweep of PCA_1, PCA_2 and PCA_3 (20 wt%) with CNC of different concentrations

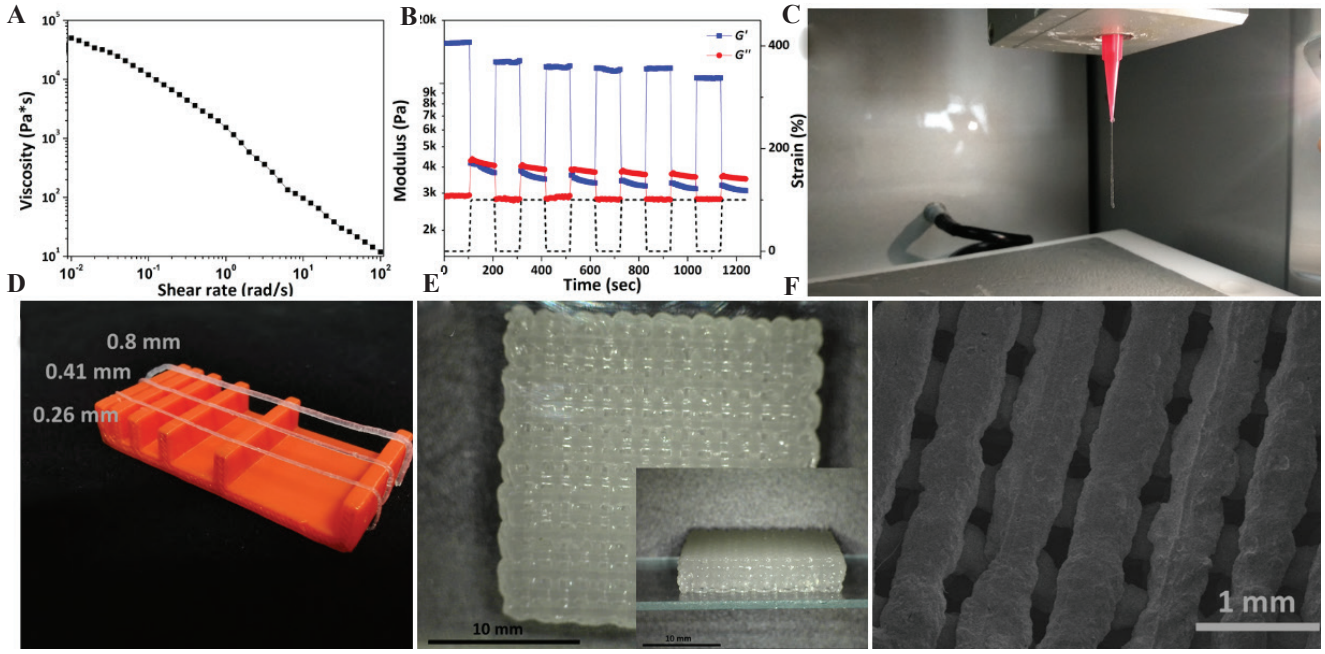

Figure 6. 3D printing results of hydrogels (20 wt% PCA_2+4.4 wt% cellulose nanocrystals). (A) Shear-thinning tests with the shear rate from 0.01 to 100 rad/s. (B) Shear recovery experiments with alternating strain of 0.01% and 100% (black dot line). (C) The extrusion effect. (D) Filament strength and stability with different size of nozzles. (E) The optical microscopic image of printed object and (F) The SEM image of printed object after lyophilization.

linear decline with the increase of the shear rate at 37°C. In addition, thixotropy, another critical parameter for the printable estimation, was also conducted to measure the recovery of the mechanical properties of materials under a large amplitude oscillatory force. The result (**Figure 6B**) indicated that this material has a typical elastic effect (***G'*** > ***G''***) under a small amplitude strain (γ=0.01%). When the strain is increased to a larger amplitude (γ=100%), ***G'*** decreases from 11 kPa to 3.6 kPa while ***G''*** increases from 2.8 kPa to 4.0 kPa, exhibiting a quasi-liquid state. Moreover, the gel modulus varied reciprocally with the variation of strain amplitude, showing that this material had a favorable irreversibility, that is, thixotropy.

Based on these results, extrusion-based 3D printing was conducted using Bio-architect®-PRO of Regenovo for further evaluation. Through adjusting the temperature in the cylinder to 37°C, the hydrogels could be extruded fluently as a filament rather than flowed as droplets (**Figure 6C**), intuitively demonstrating that the enhanced hydrogel has a required strength to be extruded. Then, filament collapse experiment was conducted using nozzles of syringe needles of different sizes for further confirmation (**Figure 6D**). It is seen that different thickness of filaments could hanged straight on different gap distance of scaffold, and no significant collapse can be observed, proving the favorable mechanical strength. By regulating the printing parameters (including size dimension, spacing distance, and translational speed), the material could be extruded and printed as a 3D hydrogel construct, as shown in **Figure 6E**. Under the optical microscope, the printed pattern showed relatively high resolution and fidelity with high layers (~4 mm), in which each filament was clearly visible without any obvious extrusion-swell or even collapse. Moreover, the details of printed constructs with different concentrations of inks are presented in **Table S1**. Meanwhile, the SEM image of the lyophilized 3D printed pattern clearly exhibited the intact structure and framework (**Figure 6F**). For the unmodified PCA_2 hydrogel (**Figure S1**), the printed structure was totally collapsed and lumped within 20 min based on our previous research[16]. So far, the results illustrate that the introduction of CNCs can effectively enhance the mechanical properties of the amorphous copolymers hydrogels, thereby significantly improving the extrudability and printability of the material.

3.5. *In vitro* cytotoxicity analysis

PCLA-PEG-PCLA-formed hydrogels were originally widely used as injectable hydrogels for drug delivery[40]. These materials show a good biocompatibility and biodegradability. Thus, fibroblasts were used to verify the former properties while lipase was used for the latter. The enzymatic degradation properties were displayed in **Figure S2**. The weight percent of hydrogel reduced linearly in 7-day incubation, showing a favorable biodegradability of the hydrogels. The *in vitro* cytotoxicity during the 3-day cultivation was characterized and estimated by live/dead staining assay. Under the fluorescent microscope

(**Figure 7**), it is found that the addition of PCLA-PEG-PCLA (5 mg/mL) did not influence the growth of fibroblasts and showed a similar growth tendency compared with blank control. Furthermore, CCK-8 assay was also used for the quantitative evaluation of the cell viability, as shown in **Figure 8**. Setting the absorbance result of blank control each day as 100%, it can be found that over 80% of viability of fibroblasts was maintained at a PCA_2 concentration of 5 mg/mL after co-cultivation for 24 h, and the viability increased further with a decrease

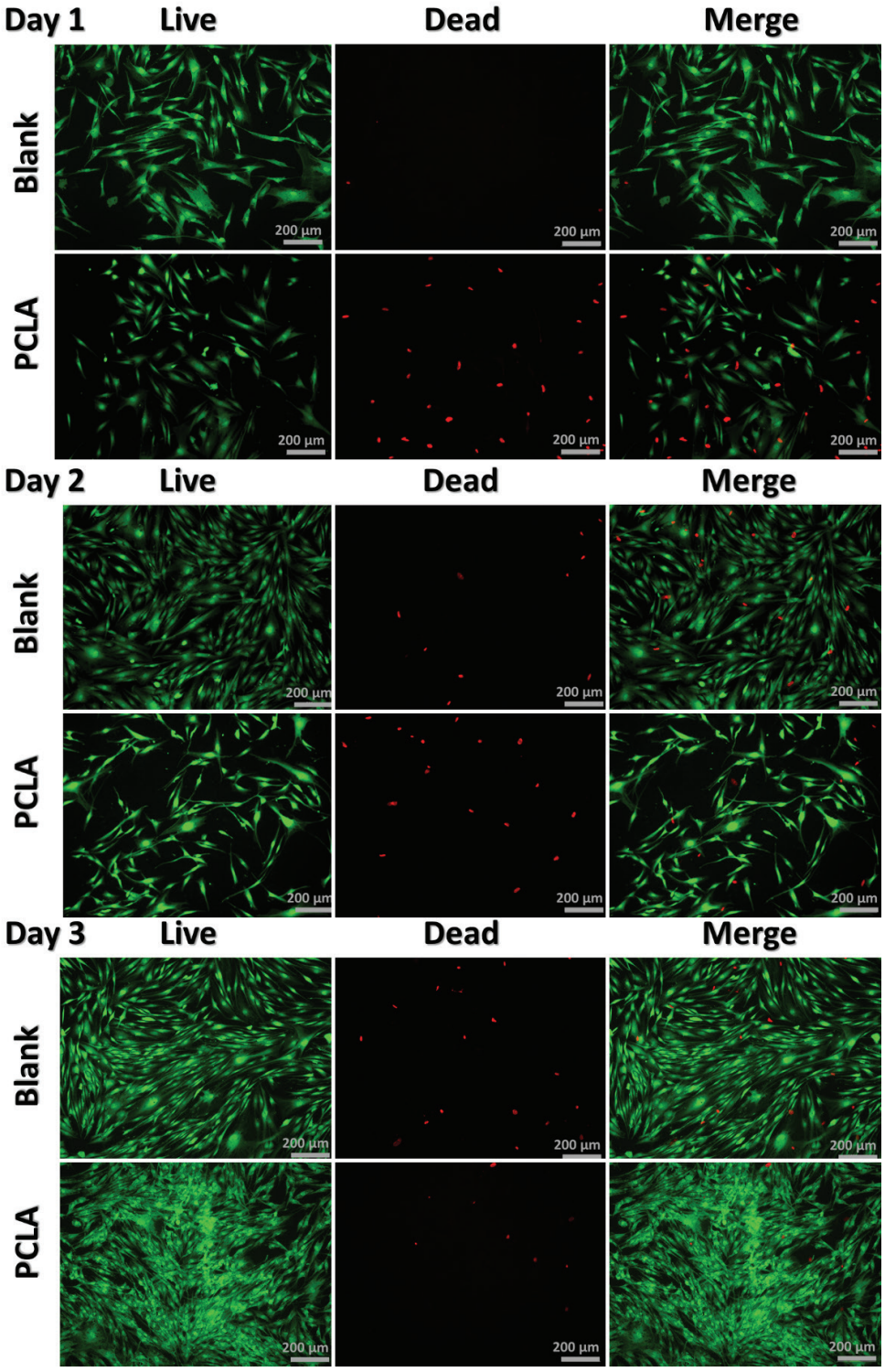

Figure 7. Fluorescent microscopic images of fibroblasts cultured with PCA_2 (5 mg/ml) and with medium only for 3 days.

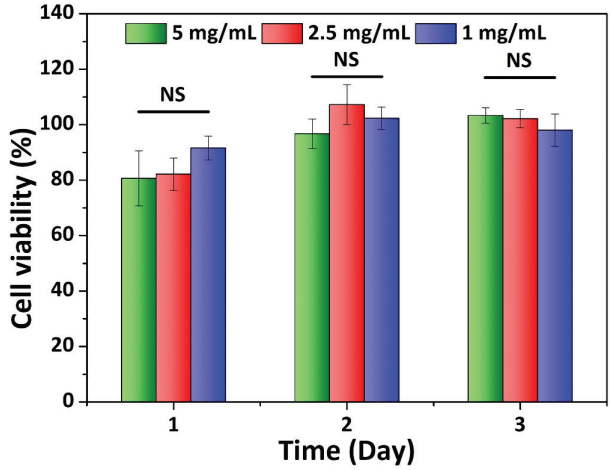

Figure 8. Cell viability of fibroblasts in the culture media after addition of PCA_2 at given concentrations as a function of days. The blank control with only culture medium each day was set as 100%. *n*=3.

of copolymer concentration. In the following 2 days, there was no significant difference between the additional PCA_2 of three different concentrations and blank control, showing around 100% cell viability. Meanwhile, the co-cultivation of hydrogel (20 wt% PCA_2+4.4 wt% CNC) with fibroblasts, which were seeded on the surface of the hydrogel, was also evaluated (**Figure S3**). The results exhibited a considerable cell compatibility after 12 h incubation and few dead cells were observed. All these results indicated that the addition of copolymers did not significantly affect the cell growth. However, none of living cells was observed in the encapsulated materials (unpublished data). It is speculated that the high printing pressure required for material with high viscosity may be detrimental to the cells. Therefore, we believe that as a bio-ink, the proper printing viscosity is as important as the biocompatibility of the material itself.

4. Conclusions

In this work, a series of PCLA-PEG-PCLA triblock amorphous block copolymers with different molecular weights and hydrophilic-hydrophobic ratios were prepared through ring-opening polymerization. CNCs of different concentrations were subsequently introduced into the copolymers formed hydrogels to investigate the improvement effect of the printability of the hydrogels. The results of thermodynamic and rheological studies show that the addition of CNC not only effectively enhances the thermal stability, forming a gel state at wider range of temperature, but also significantly increases the mechanical properties of hydrogels. When the CNC concentration reaches a certain level, the "sol-gel transition" presents at the sol system which cannot form a stable gel state at room temperature. The enhancement effect was proportional to CNC concentration within certain range. The printed 3D construct of CNC-enhanced copolymer formed hydrogels have strong mechanical properties to maintain the shape with high resolution and precision. These results proved that for the amorphous hydrogels, the printability of materials can be improved by adding rigid nanocrystals such as CNC. This method provides an effective approach of enhancing the comprehensive performance of materials for 3D bioprinting and other additive manufacturing technologies.

Acknowledgments

This work was financially supported by the National Key R&D Program of China (2017YFC1103400)..

Conflicts of interest

All authors declare that they have no conflict of interest.

Author contributions

Y. C. designed the experiments. Y. C., R. J., Y. Z., M. Y. and Y. Z. performed the experiments and analyzed the results. Y. C. wrote the manuscript. L. W. supervised the work and revised themanuscript.

References

1. Ng WL, Chua CK, Shen YF, 2019, Print Me An Organ! Why We Are Not There Yet. *Prog Polym Sci*, 97:101145. https://doi.org/10.1016/j.progpolymsci.2019.101145
2. Matai I, Kaur G, Seyedsalehi A, *et al.*, 2020, Progress in 3D Bioprinting Technology for Tissue/Organ Regenerative Engineering. *Biomaterials*, 226:119536. https://doi.org/10.1016/j.biomaterials.2019.119536
3. Murphy SV, Atala A, 2014, 3D Bioprinting of Tissues and Organs. *Nat Biotechnol*, 32:773–85. https://doi.org/10.1038/nbt.2958
4. Malda J, Visser J, Melchels FP, *et al.*, 2013, 25th Anniversary Article: Engineering Hydrogels for Biofabrication. *Adv Mater*, 25:5011–28. https://doi.org/10.1002/adma.201302042
5. Bedell ML, Navara AM, Du Y, *et al.*, 2020, Polymeric Systems for Bioprinting. *Chem Rev*, 120:10744–92.
6. Li X, Liu B, Pei B, *et al.*, 2020, Inkjet Bioprinting of Biomaterials. *Chem Rev*, 120:10793–833.
7. Valot L, Martinez J, Mehdi A, *et al.*, 2019, Chemical Insights Into Bioinks for 3D Printing. *Chem Soc Rev*, 48:4049–86. https://doi.org/10.1039/c7cs00718c
8. Zhang M, Vora A, Han W, *et al.*, 2015, Dual-Responsive Hydrogels for Direct-Write 3D Printing. *Macromolecules*,

48:6482–8.

9. Hoffman AS, 2012, Hydrogels for Biomedical Applications. *Adv Drug Deliv Rev*, 64:18–23.
10. Sponchioni M, Palmiero UC, Moscatelli D, 2019, Thermo-Responsive Polymers: Applications of Smart Materials in Drug Delivery and Tissue Engineering. *Mater Sci Eng C*, 102:589–605. https://doi.org/10.1016/j.msec.2019.04.069
11. Jungst T, Smolan W, Schacht K, *et al.*, 2016, Strategies and Molecular Design Criteria for 3D Printable Hydrogels. *Chem Rev*, 116:1496–539. https://doi.org/10.1021/acs.chemrev.5b00303
12. Nikolova MP, Chavali MS, 2019, Recent Advances in Biomaterials for 3D Scaffolds: A review. *Bioact Mater*, 4:271–92.
13. Zarrintaj P, Jouyandeh M, Ganjali MR, *et al.*, 2019, Thermo-Sensitive Polymers in Medicine: A Review. *Eur Polym J*, 117:402–23.
14. Drzewiecki KE, Parmar AS, Gaudet ID, *et al.*, 2014, Methacrylation Induces Rapid, Temperature-Dependent, Reversible Self-Assembly of Type-I Collagen. *Langmuir*, 30:11204–11. https://doi.org/10.1021/la502418s
15. Kajave NS, Schmitt T, Nguyen TU, *et al.*, 2020, Dual Crosslinking Strategy to Generate Mechanically Viable Cell-Laden Printable Constructs using Methacrylated Collagen Bioinks. *Mater Sci Eng C*, 107:110290. https://doi.org/10.1016/j.msec.2019.110290
16. Cui Y, Jin R, Zhou Y, *et al.*, 2021, Crystallization Enhanced Thermal-Sensitive Hydrogels of PCL-PEG-PCL Triblock Copolymer for 3D Printing. *Biomed Mater*, 16:035006. https://doi.org/10.1088/1748-605x/abc38e
17. Wang Z, An G, Zhu Y, *et al.*, 2019, 3D-Printable Self-Healing and Mechanically Reinforced Hydrogels With Host-Guest Non-Covalent Interactions Integrated into Covalently Linked Networks. *Mater Horiz*, 6:733–42. https://doi.org/10.1039/c8mh01208c
18. Yue K, Trujillo-de Santiago G, Alvarez MM, *et al.*, 2015, Synthesis, Properties, and Biomedical Applications of Gelatin Methacryloyl (GelMA) Hydrogels. *Biomaterials*, 73:254–71. https://doi.org/10.1016/j.biomaterials.2015.08.045
19. van den Bulcke AI, Bogdanov B, de Rooze N, *et al.*, 2000, Structural and Rheological Properties of Methacrylamide Modified Gelatin Hydrogels. *Biomacromolecules*, 1:31–8. https://doi.org/10.1021/bm990017d
20. Heinrich MA, Bansal R, Lammers T, *et al.*, 2019, 3D-Bioprinted Mini-Brain: A Glioblastoma Model to Study Cellular Interactions and Therapeutics. *Adv Mater*, 31:1806590. https://doi.org/10.1002/adma.201806590
21. Lim KS, Galarraga JH, Cui X, *et al.*, 2020, Fundamentals and Applications of Photo-Cross-Linking in Bioprinting. *Chem Rev*, 120:10662–94.
22. Billiet T, Gevaert E, de Schryver T, *et al.*, 2014, The 3D Printing of Gelatin Methacrylamide Cell-Laden Tissue-Engineered Constructs with High Cell Viability. *Biomaterials*, 35:49–62. https://doi.org/10.1016/j.biomaterials.2013.09.078
23. Colosi C, Shin SR, Manoharan V, *et al.*, 2016, Microfluidic Bioprinting of Heterogeneous 3D Tissue Constructs Using Low-Viscosity Bioink. *Adv Mater*, 28:677–84. https://doi.org/10.1002/adma.201503310
24. Moon RJ, Martini A, Nairn J, *et al.*, 2011, Cellulose Nanomaterials Review: Structure, Properties and Nanocomposites. *Chem Soc Rev*, 40:3941–94. https://doi.org/10.1039/c0cs00108b
25. Kargarzadeh H, Mariano M, Gopakumar D, *et al.*, 2018, Advances in Cellulose Nanomaterials. *Cellulose*, 25:2151–89. https://doi.org/10.1007/s10570-018-1723-5
26. Kontturi E, Laaksonen P, Linder MB, *et al.*, 2018, Advanced Materials through Assembly of Nanocelluloses. *Adv Mater*, 30:1703779. https://doi.org/10.1002/adma.201703779
27. Almeida AP, Canejo JP, Fernandes SN, *et al.*, 2018, Cellulose-Based Biomimetics and Their Applications. *Adv Mater*, 30:1703655. https://doi.org/10.1002/adma.201703655
28. Yang J, Han CR, Duan JF, *et al.*, 2012, Studies on the Properties and Formation Mechanism of Flexible Nanocomposite Hydrogels from Cellulose Nanocrystals and Poly (Acrylic Acid). *J Mater Chem*, 22:22467–80. https://doi.org/10.1039/c2jm35498e
29. Siqueira G, Kokkinis D, Libanori R, *et al.*, 2017, Cellulose Nanocrystal Inks for 3D Printing of Textured Cellular Architectures. *Adv Funct Mater*, 27:1604619. https://doi.org/10.1002/adfm.201604619
30. Yang J, Han CR, Duan JF, *et al.*, 2013, Mechanical and Viscoelastic Properties of Cellulose Nanocrystals Reinforced Poly (Ethylene Glycol) Nanocomposite Hydrogels. *ACS Appl Mater Interfaces*, 5:3199–207. https://doi.org/10.1021/am4001997
31. Ching YC, Ershad Ali M, Abdullah LC, *et al.*, 2016, Rheological Properties of Cellulose Nanocrystal-Embedded Polymer Composites: A Review. *Cellulose*, 23:1011–30.

https://doi.org/10.1007/s10570-016-0868-3

32. Ma T, Yang R, Zheng Z, *et al.*, 2017, Rheology of Fumed Silica/Polydimethylsiloxane Suspensions. *J Rheol*, 61:205–15. https://doi.org/10.1122/1.4973974
33. Song Y, Zheng Q, 2015, Linear Rheology of Nanofilled Polymers. *J Rheol*, 59:155–91.
34. Song Y, Zheng Q, 2016, A Guide for Hydrodynamic Reinforcement Effect in Nanoparticle-Filled Polymers. *Crit Rev Solid State Mater Sci*, 41:318–46. https://doi.org/10.1080/10408436.2015.1135415
35. Song Y, Zheng Q, 2016, Concepts and Conflicts in Nanoparticles Reinforcement to Polymers Beyond Hydrodynamics. *Prog Mater Sci*, 84:1–58.
36. Fan X, Xu H, Zhang Q, *et al.*, 2019, Insight into the Weak Strain Overshoot of Carbon Black Filled Natural Rubber. *Polymer*, 167:109–17. https://doi.org/10.1016/j.polymer.2019.01.076
37. Lu HD, Charati MB, Kim IL, *et al.*, 2012, Injectable Shear-Thinning Hydrogels Engineered with a Self-Assembling Dock-and-Lock Mechanism. *Biomaterials*, 33:2145–53. https://doi.org/10.1016/j.biomaterials.2011.11.076
38. Wang Q, Mynar JL, Yoshida M, *et al.*, 2010, High-Water-Content Mouldable Hydrogels by Mixing Clay and a Dendritic Molecular Binder. *Nature*, 463:339. https://doi.org/10.1038/nature08693
39. Olsen BD, Kornfield JA, Tirrell DA, 2010, Yielding Behavior in Injectable Hydrogels from Telechelic Proteins. *Macromolecules*, 43:9094–9. https://doi.org/10.1021/ma101434a
40. Zhang Z, Ni J, Chen L, *et al.*, 2011, Biodegradable and Thermoreversible PCLA-PEG-PCLA Hydrogel as a Barrier for Prevention of Post-Operative Adhesion. *Biomaterials*, 32:4725–36. https://doi.org/10.1016/j.biomaterials.2011.03.046

RESEARCH ARTICLE

Toward Mass Customization Through Additive Manufacturing: An Automated Design Pipeline for Respiratory Protective Equipment Validated Against 205 Faces

Shiya Li[1], Yongxuan Tan[1], Samuel Willis[1], Mohanad Bahshwan[2,3], Joseph Folkes[1], Livia Kalossaka[1], Usman Waheed[1], Connor Myant[1]*

[1]Dyson School of Design Engineering, Imperial College London, London, SW7 1AL, United Kingdom
[2]Department of Mechanical Engineering, Imperial College London, London, SW7 1AL, United Kingdom
[3]Department of Mechanical and Materials Engineering, University of Jeddah, Jeddah, Saudi Arabia

Abstract: Respiratory protective equipment (RPE) is traditionally designed through anthropometric sizing to enable mass production. However, this can lead to long-standing problems of low-compliance, severe skin trauma, and higher fit test failure rates among certain demographic groups, particularly females and non-white ethnic groups. Additive manufacturing could be a viable solution to produce custom-fitted RPE, but the manual design process is time-consuming, cost-prohibitive and unscalable for mass customization. This paper proposes an automated design pipeline which generates the computer-aided design models of custom-fit RPE from unprocessed three-dimensional (3D) facial scans. The pipeline successfully processed 197 of 205 facial scans with <2 min/scan. The average and maximum geometric error of the mask were 0.62 mm and 2.03 mm, respectively. No statistically significant differences in mask fit were found between male and female, Asian and White, White and Others, Healthy and Overweight, Overweight and Obese, Middle age, and Senior groups.

Keywords: Respiratory Protective Equipment; Design Automation; Mass Customization; Additive Manufacturing; 3D Graphics

*Correspondence to: Connor Myant, Dyson School of Design Engineering, Imperial College London, London, SW7 1AL, United Kingdom; connor.myant@imperial.ac.uk

Received: July 15, 2021; **Accepted:** August, 2021; **Published Online:** October 13, 2021

Citation: Li S, Tan Y, Willis S, *et al*., 2021, Toward Mass Customization Through Additive Manufacturing: An Automated Design Pipeline for Respiratory Protective Equipment Validated Against 205 Faces. *Int J Bioprint*, 7(4):417. http://doi.org/10.18063/ijb.v7i4.417

1. Introduction

Respiratory protective equipment (RPE) is routinely mandated across a wide range of industries to protect millions of workers worldwide from inhaling harmful airborne particles, gases or vapors that are present in the environment. Some examples of respirator masks are disposable N95/FFP3 used in the healthcare sector, or re-usable elastomeric half-mask RPE commonly used in construction, mining, firefighting, and manufacturing. The performance of RPE depends on three factors: (i) compliance, (ii) comfort, and (iii) effective seal. The coronavirus (COVID-19) pandemic has brought the world's attention to RPE's long-standing but often neglected problem of poor fit and its associated issues such as device-related pressure ulcers. High incidence (97%) of skin damage over the nasal bridge and cheeks among frontline health-care personnel wearing standard-sized RPE has been reported as a serious occupational hazard[1]. These skin damages are likely caused by excessive strap pressure applied on poorly fitted masks to improve seal at the skin/mask interface[2]. Excessive strap pressure can result in user discomfort, which is often cited as a major factor for non-compliance[3]. Thus, improving fit will improve the effectiveness of RPE across all three success factors.

Users must pass a fit test to ensure an effect seal is achieved before they are deployed in high-risk environment. Despite its importance, there is clear evidence that current commercially available disposable RPE[4] or reusable elastomeric RPE[5] are inadequate at creating an effective seal for all demographic user groups. There are numerous reports of demographic bias in RPE fit test failure rates. It has been found that female users were nearly twice as likely to fail a fit test compared to male users[6-10]. Fit test failure rates were also found to be skewed across different ethnic groups. Asian users have failure rate as high as 54%[11] and African users at 86%[12] as compared to about 5 – 10% among Caucasian users[7,8,13]. Other than gender and ethnicity, age has also been reported as another factor that affects fit test failure rate[14]. More importantly, it was found that certain combination of subdemographic groups will lead to a higher fit test failure rate. For example, McMahon *et al*.[7] reported statistical significant difference ($P < 0.05$) in fit test passing rates among age groups in women (19 – 71 years old with an average 10 years increment for each age group), but not in men. Sandkovsky *et al*.[15] also found that only females with body mass index (BMI) >25 are at higher risk of failing a fit test, but not males.

These demographically biased fit test failure rates are potentially caused by the limitations associated with design methodologies employed for mass producing wearables. The conventional design method is based on anthropometric sizing, which are anthropometric surveys that collect body dimensions from a sample population and statistically analyze them to suggest a sizing system (e.g. three-size system that consists of small, medium, and large) to cover majority of the population[16,17]. For RPE masks, respirator fit test panels (two-Dimensional charts) are typically developed from analyzing 1-Dimensional facial dimensions collected from thousands of subjects to provide an objective tool for selecting a few representative human test subjects based on their facial characteristics for use in research, product development, testing, and certification[18]. The panel is built with the aim to cover about 95% facial variation of a population and can be segmented into a few broad categories to inform a sizing system to guide the design of RPE. One of the earliest and most referenced respirator fit test panels was developed based on bivariate distribution of face length and lip length (for half-face piece RPE) or face length and face width (for full-face piece RPE) data from an anthropometric survey of 4000 male subjects in the US Air Force by Los Alamos National Laboratory[19] in the early 1970s. Recently in 2007, the National Institute for Occupational Safety and Health (NIOSH) recognized the unsuitability of using outdated military data for the design of civilian RPE, and developed a new fit test panel using data (3997 subjects) from a 2001 anthropometric survey of civilian respirator users[20]. Despite having a more updated dataset, several large-scale comparative anthropometric studies have reported statistically significant differences ($P < 0.05$) in key face dimensions (e.g. face width, length, and nose protrusion) between males and females, different ethnic groups (Asian, White, African, Hispanic, etc.), and age groups (18 – 29 years old and above 45 years old)[21-24] in the updated panel. Respirator manufacturers may create different product sizes based on demographic-specific anthropometric sizing to accommodate such differences. However, each additional size will incur additional tooling costs for mass production, therefore making it economically undesirable. The anthropometric sizing-based design methodology was developed decades ago to enable affordable mass customization (MC) of wearables through conventional mass production methods, such as injection molding, and it had been shown to result in design bias toward certain demographic groups and higher failure rates in protective equipment as mentioned above. With the maturation of advanced manufacturing techniques such as additive manufacturing (AM) which can create custom-fit product at near-zero tooling cost, it is time to re-think and develop new design methods to facilitate the use of such new manufacturing methods to provide well fitted masks for people from all backgrounds, regardless of their gender, ethnicity, age, or BMI.

AM has been identified as the next generation agile manufacturing system that enables the MC of custom-fit products[25-29]. A key strength of AM is its near-zero tooling cost associated with every new design, which greatly reduces the per part manufacturing cost as compared to mass production processes such as injection molding. AM has been widely adopted to produce custom-fit products including traditionally custom-made medical devices such as maxillofacial prosthetics[30-32], foot orthosis[33,34], removable partial denture[35], or mass-produced ergonomic products such as shoe insoles[36,37], and aircrew seats[25]. In recent years, AM has been explored to produce custom-fit specialty masks, such as Bi-level/Continuous Positive Airway Pressure (BiPAP/CPAP) masks[38-40], where they have been shown to have less leakage and better comfort as compared to conventional generically designed masks. For RPE, custom-fit face seals have been shown to distribute contact pressure more evenly across the contact area, reducing the occurrence of high pressure imposed by commercial mass-produced RPE masks on areas such as the nose bridge, upper cheek, middle cheek and lower cheek and chin[41]. There are also ongoing investigations on whether three-dimensional (3D) printed tailored RPE can improve fit test passing rate and provide better sustained comfort than conventional RPE[42,43]. AM can also serve as an agile supply chain solution during an emergent public health crisis[44-48]. During the earlier days of the COVID-19 pandemic, various government

agencies, local communities, and individual makers have used AM as a supply chain response to de-centralize production and combat supply chain disruption for RPE and other protective equipment[48-57].

Despite the promises of AM in producing custom fit RPE, major cost barriers exist in adopting AM for large-scale production. One key cost contributor stems from a highly manual and time-consuming customization process, which can add up to 20 – 30% of the overall AM production cost[25,34,37,58]. Sporadic efforts have been made over the past few decades to simplify and shorten the AM design process. The most utilized method has been parametric geometric modeling, where a generic parametric computer-aided design (CAD) model is created with control points that can be automatically updated based on the shape of an input scan. Such approach has been applied to customizable medical devices, such as protective face masks, wrist splits, ankle-foot orthotics[59-61], and recently to BIPAP/CPAP masks[38,40]. However, these are semi-automated modeling processes where a technician with CAD modeling knowledge is needed to perform manual operations such as aligning the generic model to a raw scan. Studies demonstrating a fully automated customization process for traditionally mass-produced body-fitted products are rare. Ellena *et al*.[62] proposed a design process for customizing bicycle helmets, where a statistical shape model was utilized to classify a head scan into one out of four helmet sizes before cropping away the inner lining of the helmet with a generic B-Spline head surface adapted to the shape of the head scan using an iterative genetic algorithm[63]. While it is a fully automated process, it essentially uses a sizing-based approach where the statistical shape model was built by analyzing 222 head scans that may be representative of the Australian cyclist population, but not other demographic groups. For RPE designs, the sample size required could be much larger (e.g. the US NIOSH panel used almost 4000 subjects) for a particular demographic group. The amount of resources and time needed to collect a large-scale 3D anthropometric database and to build a statistical shape model for each applicable demographic group defeats the purpose of lowering design cost for tailor-fit products. Sela *et al*.[64] proposed a fully automated pipeline to generate customized CPAP masks based on a 3D scan or depth image of a person's face. The shape of the mask model was customized by updating 256 control points on a generic mask model made up with Non-uniform Rational Basis Spline (NURBS) surfaces. However, automatically deforming a generic NURBS-based geometric model with organic shape can be problematic, particularly given the complexity and high variability of facial shapes. The pipeline was only validated against one subject; therefore, its robustness against a larger dataset remains unknown. To the best of authors' knowledge, there has not been a study demonstrating a completely automated process for customizing respirator masks and validated against a 3D face dataset.

Recently, the authors[65] proposed a new automated respirator mask customization process which reduced design time from hours to minutes. While it is a promising pipeline, the pipeline has yet to be seamlessly integrated, neither has it been validated against a reasonable dataset. This study builds upon this previous work[65] and integrates a CAD Application Programming Interface (API) with the rest of the pipeline to present a seamless and automated design pipeline for generating custom-fitted respirator masks ready to be manufactured using AM techniques.

To investigate whether this pipeline can be universally applied to people from different demographic backgrounds, an online portal was created to recruit participants during the COVID-19 lockdown periods in the UK, where their facial scans and demographic information were collected. Success rate, computational run time, and fit (how well a mask fits to a face) were evaluated. Furthermore, fit results were compared across subcategories of demographics to investigate whether the pipeline can produce respirator mask models that fit equally well to people across different age (young, middle aged, senior), gender (male or female), ethnic (Asian, White, and Others), or BMI groups (healthy, overweight, and obese).

2. Methods

2.1. RPE design pipeline

An automated MC design pipeline, shown in **Figure 1**, was employed for this study. This pipeline is based on our previous study which employs a series of alignment and template fitting processes[65] to represent user-submitted 3D facial scans using a universal 3D face template mesh. This removes heterogeneity across different raw facial meshes in terms of orientation, location, and mesh structure (vertex indexing and triangulation), thereby enabling the subsequent automatic extraction of topographical data from a large facial dataset. Using a set of predefined vertices on the template mesh as landmarks, 200 points on two egg-shaped loops based on those landmark locations were projected onto the fitted template

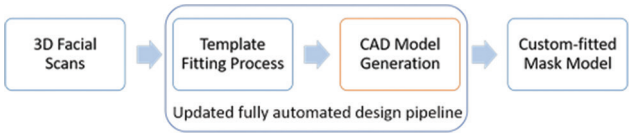

Figure 1. Pipeline overview, the computer-aided design model generation step (highlighted) is now integrated into the design pipeline.

mesh, forming the contact region between the mask and the user's face, greater details can be found in Li *et al*.[65]. These points together with the set of landmarks act as the reference geometry in the CAD model generation step.

In the previous study[65], Autodesk Fusion 360 API was employed. However, as it cannot be readily integrated with the rest of the pipeline which was written in MATLAB, a Python based Blender script is now utilized to seamlessly interface the CAD API into the pipeline such that the whole pipeline can run in a headless mode. Blender builds polygonal 3D models from successive addition of vertices, edges, and faces through functions with defined rules and constraints. This polygon-based generative geometric modeling approach can robustly handle the complexity and high variation of facial topographies, particularly around the nasal regions, making it well suited to the requirements of a MC pipeline for RPE. The design of the respirator mask (**Figure 2**) remained the same[65] with three standard components (grey) and a modifiable component (blue) that will be updated geometrically in blender to achieve custom-fit.

2.2. Participants

Participants were recruited from mid-July 2020 to mid-October 2020. Due to travel restrictions during the COVID-19 pandemic, a dedicated online portal[66] was created to collect 3D facial scans remotely. This way of data collection transcends geographical boundaries, thereby enabling us to reach a wider demographics. Recruitment was advertised on mainstream media platforms such as the BBC[67], as well as on various social media platforms. As a token of appreciation to each participant, a custom-fitted mask model generated from the pipeline was emailed to the participant with assembly and manufacturing instructions so that he/she can manufacture the mask at home (if a 3D printer is available) or through commercial 3D printing services. This also served as a supply chain response to the global mask shortage at that time, as the 3D printed mask could be used as a face covering or face shield.

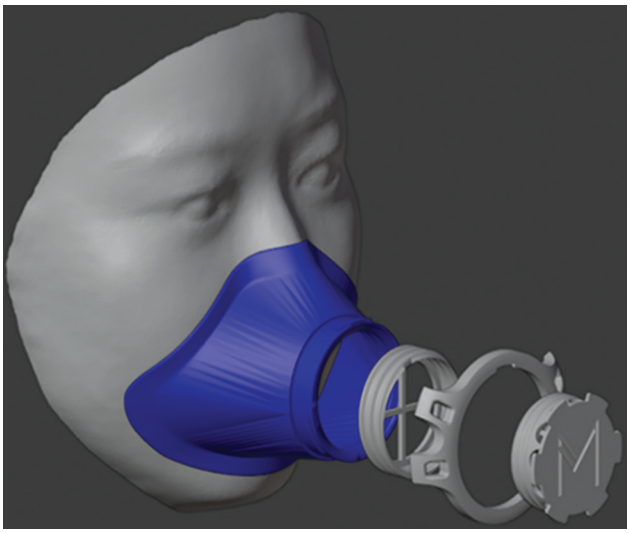

Figure 2. Custom-fitted mask body generated using Blender with standard FFP3 filter components.

As facial scans are sensitive biometric data, Data Protection Impact Assessment has been carefully conducted and approved by Imperial College London to ensure all data-associated activities, including online data collection, transfer, storage, and analyses, are secure and compliant with relevant data protection regulations. The study protocol (19IC5167) was approved by the Science Engineering Technology Research Ethics Committee, Imperial College London.

Eligible participants were adults (≥18 years) regardless of gender, ethnicity, or BMI. Before scanning, participants were asked to read through a Participant Information Sheet to understand the project, how their data will be utilized and to clarify any questions. Written instructions[68] were also provided on the online portal to instruct participants to prepare for scanning by doing the followings: clean shave their face, remove any glasses, and pin/tie all hair if it is obstructing the face. Video instructions[68] were provided to ensure that facial data were acquired under the same conditions. Participants were recommended to use an iPhone X or newer versions (Apple Inc., Cupertino, California, USA) with a TrueDepth camera to acquire their facial scans. However, facial scans obtained from other acquisition devices were also accepted. If an iPhone was used, software applications recommended for creating and exporting 3D facial scans were ScandyPro (Scandy, New Orleans, USA) and Bellus3D (Bellus3D, Campbell, California, USA). Participants were also instructed to remain in a neutral expression during the data acquisition process. Once a scan had been acquired, participants were instructed to upload their scans through the online portal. Demographic information including age, gender, ethnicity, weight, and height were collected through a short survey in the submission process. Before the final submission, permission was sought from each participant to use their data anonymously through an Adult Consent Form. Details of the survey and consent form can be found in the online portal[69].

2.3. Scan exclusion

Facial data acquisition is not a trivial task and will require the user to have a good level of understanding of the acquisition device and software to obtain 3D facial data with minimal noise and obstruction. While written and video instructions were provided to guide the participants on data acquisition, it cannot be assumed that all participants have followed the instructions diligently

and were able to produce good quality scans. Therefore, each scan was manually checked against the following set of exclusion criteria to ensure that all scans were of similar quality before submitted to the pipeline:

i. Being duplicates, that is, having two or more submissions containing the same face
ii. Having any obstruction on the face that may interfere with the mask, including beard, moustache, glasses, and piercing.
iii. Having poor quality, including poor reconstruction of facial geometry, corrupted file, scan resolution at >0.5 mm
iv. Having been modified by the participant to remove any holes/defects
v. Having non-neutral facial expression
vi. Not human faces, that is, scans of other objects
vii. Being manifold, that is, enclosed to form a solid volume, instead of being an open surface

A total of 322 submissions were received at the end of recruitment, of which 117 were excluded based on the above criteria. **Figure 3** shows a summary of the excluded scans.

2.4. Computational time evaluation

All 205 included scans were processed through the pipeline on a remote Linux workstation (Intel® XEON® 4114 2.2 2400MHz 10-Core CPU, 256 GB DDR4 2666 DIMM Memory, Nvidia Quadro P1000 4GB GFX). For each input scan, a solid respirator mask CAD model was generated by the pipeline described in Section 2.1. The total run time for processing a scan and generating a CAD model was recorded.

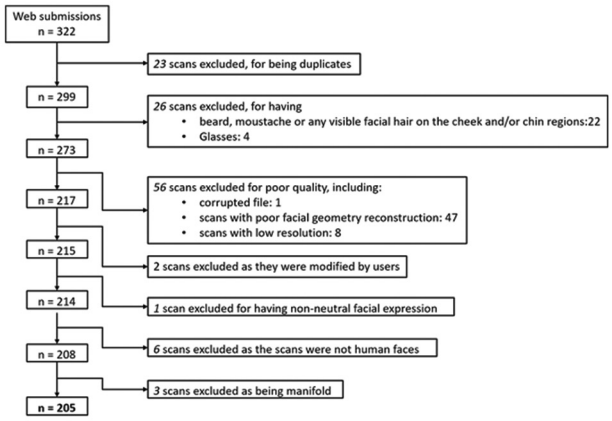

Figure 3. Facial scans exclusion.

2.5. Fit evaluation

Euclidean distance was used to computationally evaluate fit between the mask surface and the aligned face mesh (**Figure 4**). A nearest neighbor search[70] was performed through a space-partitioning method called K-dimensional tree[71] to pair each vertex on the mask surface with its nearest neighboring vertex on the aligned mesh. The nearest neighbor search was defined as: given a set of points $u \in U$ (the aligned mesh), and a set of query points $v \in V$ (the mask surface), for all v, find the closest points to U. The Euclidean distance was computed for each closest pair. Subsequently, the maximum and root mean square error (RMSE) of the Euclidean distances of were computed. The Maximum Euclidean distance indicates the maximum gap between a mask and its corresponding face mesh, whereas the RMSE Euclidean distance indicates the average gap between the mask and the face.

Maximum and RMSE Euclidean distance results were grouped into age, gender, ethnicity, and BMI subcategories according to demographic data reported by participants. For age, results have been grouped into three subcategories: Young (18 – 39 years old), Middle aged (40 – 54 years old), and Seniors (55 years old and above). There is not an international standard on age classification according to craniofacial shape change; however, various studies have shown evidence of craniofacial change as a result of aging[72-75]. Therefore, it is important to investigate whether the current pipeline can deliver similar fit results across different age groups. Age has generally been grouped into three categories (young, middle aged, and senior), and the cutoff points are approximately 15 – 25, 35 – 45, and 55 – 65 years old. In this study, the author, therefore, used 18 – 39 years old for young adults, 40 – 54 years old for middle aged adults, and 55 years and above for seniors. For gender, results were grouped into male and female categories. BMI grouping was based on the

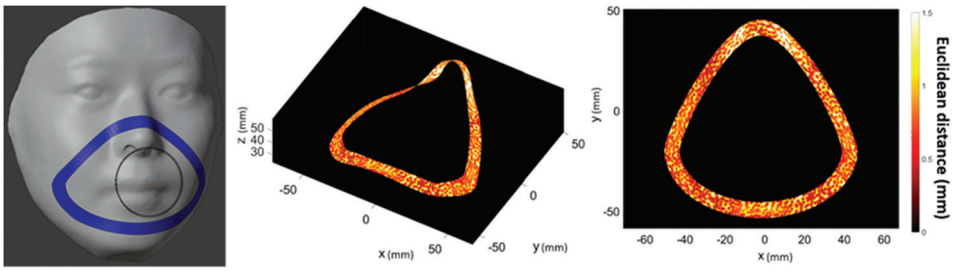

Figure 4. Euclidean distance between mask surface and a aligned face scan.

standard adult BMI classification[76]: underweight (BMI < 18.5), healthy (18.5 < BMI ≤ 24.9), overweight (25.0 < BMI < 29.9), and obese (BMI > 30.0). For ethnicity, participants were grouped into the broad categories of Asian, White, and Others (including Black, Arabs, and any other ethnicity) as reported by participants.

3. Results and discussion

Using our pipeline, 197 of the 205 included scans returned a valid CAD model and 8 scans were rejected by the alignment checking algorithms in the pipeline (misalignment between input scan and template mesh), which gives an overall processing success rate of 96.1%. **Table 1** shows the respective average run time for the processed 197 scans obtained from Bellus3D, ScandyPro and Lightstage. Compared to a manual process the pipeline has achieved significant time-savings. The average run time for processing a single scan was <2 min (104.4) that a significant portion of which time was consumed by the template fitting sub-process. The underlying code for this sub-process has not been optimized for the graphics processing unit (GPU) computation; hence, further time savings may be attained through GPU rather than CPU computation. This is a significant improvement from earlier manual process studies. This time saving is crucial to scale up the production for mass-customizing respirator masks, which has a much higher demand than conventionally customized orthotics or prosthetics. In addition, the customisation process is now completely automated which eliminates labor cost. Cazon *et al*.[61] have reported that labor cost can take up to 80% of the entire AM design cost; therefore, such savings is significant for making AM a more viable production method for the MC of respirator masks. Notably, the average run time per scan for ScandyPro scans was the longest (at almost 4 min/scan) compared to Bellus3D (<1 min/scan) and Light stage scans (<1.5 min/scan). This extended runtime is owed to the fact that ScandyPro scans contained significantly greater number of vertices than the other two. In addition, the ScandyPro scans included noisier data, including large neck/shoulder parts and many disconnected regions scattered around the face. Collectively, these resulted in longer time to perform the template fitting process.

Table 2 shows participants' profiles grouped into the demographic categories, and their corresponding Maximum and RMSE Euclidean distances. The majority of the participants were male (80.7%), or White (76.1%), or having BMI more than 25 (85.8%). The average RMSE Euclidean distance between a mask surface and a face is 0.62 ± 0.20 mm (mean ± sd) for all 197 scans. This means that the mask model was able to achieve an average sub-millimeter accuracy. The Maximum Euclidean distance is 2.03 ± 0.75 mm (mean ± sd), located on nasal sidewalls. Lee *et al*.[77] used a virtual fit testing method on 3D facial data of 336 Korean Air Force men and found that the gap between a pilot oxygen mask (similar to a reusable elastomeric half-face respirator) at the nasal bridge is approximately 6 mm when pressing the mask tightly onto a face (10 mm into the cheek). A maximum 2 mm gap at the nasal sidewalls instead of the nasal bridge, which has been reported as the most commonly injured site for respirator users[1], is a significant improvement from the mass-produced RPE. In addition, contrary to the design bias in current commercially available RPE, where fit was poorer among females and Asians, the Maximum Euclidean distance was slightly lower for females (1.82 mm) as compared to males (2.08 mm), and Asians (1.80 mm) as compared to the others (White: 2.05 mm and others: 2.33 mm).

Table 1. Average run time.

Acquisition method	Average run time, mean (sd)
All	104.4 (95.2)
Bellus3D	52.5 (25.7)
ScandyPro	235.5 (89.9)
Lightstage	133.3 (56.8)

To investigate if the proposed pipeline could produce respirator masks that fit equally well to people with different demographic backgrounds, the following hypothesis was tested: there will be no difference between the maximum or RMSE Euclidean distance across each subcategory under age, gender, ethnicity or BMI. Choice of an appropriate statistical test is dependent on the nature of the Euclidean distance results. Before deciding on an appropriate statistical test, Shapiro–Wilk tests were conducted to check for normality of the distributions for each grouped RMSE and maximum Euclidean distances. Most of the demographic groups rejected the null hypothesis ($P < 0.05$) that the data is normally distributed with unspecified mean and variance, except for the Maximum Euclidean Distance in Female group ($P = 0.12$), RMSE Euclidean distance in Other Ethnicity group ($P = 0.31$), and RMSE Euclidean distance in Healthy BMI group ($P = 0.23$). Nonetheless, for these groups, the sample size is small (≤30). Therefore, the nonparametric Wilcoxon Rank Sum Test (confidence level at 95%) was used to compare outcomes between each pair of subcategories in age, gender, ethnicity and BMI. The underweight group was excluded as the sample size is too small ($n = 1$).

Wilcoxon Rank Sum test results (**Table 3**) showed that there is no statistically significant difference for RMSE and maximum Euclidean distances between Male and Female, Asian and White, White and others, healthy and overweight, overweight and obese, Middle age, and senior groups. This suggests that the pipeline produced mask models that fit equally well across these groups. This

Table 2. Participants' profile and Euclidean distance results.

	Total (*n*=197)	RMSE Euclidean distance (mm), mean (sd)	Maximum Euclidean distance (mm), mean (sd)
Overall		0.62 (0.20)	2.03 (0.75)
Gender, *n* (%)			
Male	159 (80.7)	0.62 (0.20)	2.08 (0.77)
Female	30 (15.2)	0.64 (0.21)	1.82 (0.61)
No response	8 (3.1)	-	-
Ethnicity, *n* (%)			
Asian	27 (13.7)	0.59 (0.18)	1.80 (0.62)
White	150 (76.1)	0.62 (0.20)	2.05 (0.75)
Others	14 (7.1)	0.63 (0.24)	2.33 (0.86)
No response	6 (3.1)	-	-
BMI, mean (sd)			
Underweight (<18.5)	−(0.5)	-	-
Healthy (18.5 – 24.9)	23.1±1.8 (10.7)	0.59 (0.17)	1.76 (0.67)
Overweight (25.0 – 29.9)	27.4±1.3 (42.1)	0.61 (0.19)	2.02 (0.70)
Obese (>30.0)	36.6±9.3 (43.7)	0.64 (0.21)	2.12 (0.79)
No response	−(3.0)	-	-
Age, mean (sd)			
Young (18 – 39)	29.3±6.3 (30.5)	0.56 (0.20)	1.71 (0.64)
Middle aged (40 – 54)	48.5±4.1 (33.5)	0.62 (0.18)	2.06 (0.72)
Senior (55 and above)	61.3±5.3 (32.5)	0.68 (0.20)	2.32 (0.75)
No response	−(3.6)	-	-

BMI; Body mass index, sd; Standard deviation

Table 3. Wilcoxon Rank Sum test results.

		RMSE Euclidean Distance (mm)		Maximum Euclidean distance (mm)	
		H	*P* value	H	*P* value
Category 1	**Category 2**				
Gender					
Male	Female	0	0.814	0	0.061
Ethnicity					
Asian	White	0	0.375	0	0.061
Asian	Others	0	0.711	1	0.035
White	Others	0	0.941	0	0.120
BMI					
Healthy	Overweight	0	0.740	0	0.100
Healthy	Obese	0	0.580	1	0.035
Overweight	Obese	0	0.673	0	0.394
Age					
Young	Middle age	0	0.078	1	0.002
Young	Senior	1	0.005	1	0.000
Middle age	Senior	0	0.165	0	0.051

is a significant improvement compared to conventional anthropometric sized RPE where failure rates were found to be as high as double among females compared to male colleagues[6-8], or 16% – 54% among Asians[11,13]. The same analyses have been conducted for just the Bellus3D scans and just the ScandyPro scans respectively (Light stage scans were not used due to its small sample size), and similar results were found. This shows that the pipeline can produce demographically non-biased mask models regardless of acquisition methods.

There are statistically significant differences between the Young and the Senior groups for RMSE Euclidean distance, and between the Asian and Others, Healthy and Obese, Young and Middle-age, and Young and Senior for Maximum Euclidean distance. Nonetheless, all differences in their absolute values (**Table 2**) were <1 mm. The Maximum Euclidean distance is 1.7 mm – 2.3 mm for each of these groups, which are significantly smaller than the 6 mm gap reported in similar commercial masks[78]. With a much smaller gap to fill, users can potentially apply less strap pressure onto the mask to create a good seal, reducing chances of skin trauma.

This study may be under-powered as the current sample is skewed towards male, White, and high BMI populations, whereas the sample size for female, non-White and normal BMI populations were small. Future studies should look to collect a more evenly distributed gender, BMI and ethnicity sample with a larger sample size to further validate the universality of this pipeline. Nonetheless, initial results show great potential to produce customized RPE products that can fit equally well across different demographic and demographic subgroups. This contrasts current anthropometric sizing methodologies which contain inherent biases due to the sample populations they were cased on.

The proposed pipeline was deployed as an online application which promoted decentralized manufacturing during the period when there was a global shortage of RPE. However, the pipeline's main contribution is to quickly create custom-fitted RPE models that offer superior fit to commercial masks, making it a viable tool to produce RPE products in the healthcare and construction industry where good fit and comfort are required. This pipeline can be deployed quickly in the extent of future pandemics.

The pipeline was validated computationally to demonstrate that it is possible to rapidly produce RPE design models that fit well to a user's face. The pipeline offers a route to lower product unit costs by automating the design phase, thus removing that barrier for mass customizing wearables. It also shows a novel and promising design methodology that is not inherently biased towards specific demographic group as it is in the traditional anthropometric sizing approach. The mask model presented in this pipeline had been shown to be successfully fabricated through the stereolithography (SLA) process in our previous study[65], taking an average of 8 h and using 40 mL of resin to fabricate the mask body. A fit test study is currently being conducted to evaluate the performance of the 3D printed custom-fitted masks against commercial masks. Future studies can build upon our previous and current work to investigate other factors affecting the manufacturing of the mask, including the impact of different AM build processes, such as SLA, fused deposition modeling and selective laser sintering, and post-processing techniques on the surface finish of the mask/face contact area, and Young's Modulus, biocompatibility and sterilizability of the print materials. Different filter materials with different levels of particle filtration capabilities can also be evaluated to Filter materials, with different levels of particle filtration capabilities, can also be investigated to determine their performance and impact on custom fitted masks.

4. Conclusions

This study presented a fully automated design pipeline to enable MC of RPE via AM. The pipeline was validated against 205 facial scans to generate custom fit respirator mask CAD models. The pipeline achieved 96% processing success rate with <2 min/scan processing time. When virtually fitted, the mean RMSE and Maximum Euclidean distance between the masks and faces were 0.62 mm and 2.03 mm, respectively. It was found that there was no statistically significant difference in goodness of fit between different age, gender, ethnicity, and BMI subgroups. When combined with appropriate AM processes and materials, it could be a promising route towards the true MC of RPE or even other body-fitted products.

Acknowledgments

The authors would like to thank Lara Lewington and the team from the BBC, and Kristie Lu Stout from the CNN, for featuring this study - the Mensura Mask project. These media exposures have greatly helped us with volunteer recruitment around world so that we can build a dataset with better demographic distribution. The authors would also like to thank Mike Westlake from the Autodesk for connecting us with the CNN. Finally, the authors would like to thank all volunteers who have participated in this study.

Funding

This work was funded by Community Jameel and Imperial College London under the award of the Community Jameel Imperial College COVID-19 Excellence Fund, and the Imperial College President's PhD Scholarship Fund.

Conflicts of interest

The authors declare no conflict of interest.

References

1. Lan J, Song Z, Miao Z, *et al*., 2020, Skin Damage among Health Care Workers Managing Coronavirus Disease-2019. *J Am Acad Dermatol*, 82:1215-6.
2. Gefen A, Alves P, Ciprandi G, *et al*., 2020, Device-related

Pressure Ulcers: SECURE Prevention. *J Wound Care*, 29:S1-52.

3. Gosch, M.E., Shaffer RE, Eagan AE, *et al*., 2013, B95: A New Respirator for Health Care Personnel. *Am J Infect Control*, 41:1224-30.
4. O'Kelly E, Arora A, Pirog S, *et al*., 2021, Comparing the Fit of N95, KN95, Surgical, and Cloth Face Masks and Assessing the Accuracy of Fit Checking. *PLoS One*, 16:e0245688. https://doi.org/10.1371/journal.pone.0245688
5. Pompeii LA, Kraft CS, Brownsword EA. *et al*. Training and Fit Testing of Health Care Personnel for Reusable Elastomeric Half-Mask Respirators Compared With Disposable N95 Respirators. *JAMA*, 323:1849-52. https://doi.org/10.1001/jama.2020.4806
6. Han DH, Choi KL, 2003, Facial Dimensions and Predictors of Fit for Half-mask Respirators in Koreans. *Aiha J*, 64:815-22. https://doi.org/10.1080/15428110308984877
7. McMahon E, Wada K, Dufresne A, 2008, Implementing Fit Testing for N95 Filtering Facepiece Respirators: Practical Information from a Large Cohort of Hospital Workers. *Am J Infect Control*, 36:298-300. https://doi.org/10.1016/j.ajic.2007.10.014
8. Ascott A, Crowest P, de Sausmarez E, *et al*., 2020, Respiratory Personal Protective Equipment for Healthcare Workers: Impact of Sex Differences on Respirator Fit Test Results. *Br J Anaesth*, 126:e48-e49. https://doi.org/10.1016/j.bja.2020.10.016
9. Regli A, Sommerfield A, von Ungernd.org/10.1 B, 2021, The Role of Fit Testing N95/FFP2/FFP3 Masks: A Narrative Review. *Anaesthesia*, 76:91-100. https://doi.org/10.1111/anae.15261
10. Lam S, Lee JK, Yau SY, *et al*., 2011, Sensitivity and Specificity of the User-seal-check in Determining the Fit of N95 Respirators. *J Hosp Infect*, 77:252-256. https://doi.org/10.1016/j.jhin.2010.09.034
11. Yu Y, Jiang L, Zhuang Z, *et al*. 2014, Fitting Characteristics of N95 Filtering-facepiece Respirators Used Widely in China. *PLoS One*, 9:e85299. https://doi.org/10.1371/journal.pone.0085299
12. Spies A, Wilson KS, Ferrie R, 2011, Respirator Fit of a Medium Mask on a Group of South Africans: A Cross-sectional Study. *Environ Health*, 10:1-7. https://doi.org/10.1186/1476-069x-10-17
13. Wilkinson IJ, Pisaniello D, Ahmad J, *et al*., 2010, Evaluation of a Large-scale Quantitative Respirator-fit Testing Program for Healthcare Workers: Survey Results. *Infect Control Hosp Epidemiol*, 31:918-25. https://doi.org/10.1086/655460
14. Zhuang Z, Bergman M, Brochu E, *et al*., 2016, Temporal Changes in Filtering-facepiece Respirator Fit. *J Occup Environ Hyg*, 13:265-74.
15. Sandkovsky U, Schwedhelm M, Grayer S, *et al*., 2017, Small changes make a big difference in the fit of N95 respirators. *Open Forum Infect Dis*, 4:S166. https://doi.org/10.1093/ofid/ofx163.292
16. Roebuck JA, 1995, Anthropometric Methods: Designing to Fit the Human Body. In: Human Factors and Ergonomics Society. Santa Monica, California: Humanoid Factors and Ergonomics Society. https://doi.org/10.1177/106480469500300309
17. Pheasant S, 2014, Bodyspace: Anthropometry, Ergonomics and the Design of Work: Anthropometry, Ergonomics and the Design of Work. Boca Raton, Florida: CRC Press. https://doi.org/10.1201/9781482272420
18. Chen W, Zhuang Z, Benson S, *et al*., 2009, New Respirator Fit Test Panels Representing the Current Chinese Civilian Workers. *Ann Occup Hyg*, 53:297-305. https://doi.org/10.1093/annhyg/men089
19. Hack A, Hyatt EC, Held BJ, *et al*., 1973, Selection of Respirator Test Panels Representative of US Adult Facial Sizes. New Mexico: Los Alamos Scientific Lab., N. Mex, (USA). https://doi.org/10.2172/4335046
20. Zhuang Z, Bradtmiller B, 2005, Head-and-Face Anthropometric Survey of US Respirator Users. *J Occup Environ Hyg*, 2:567-576. https://doi.org/10.1080/15459620500324727
21. Zhuang Z, Landsittel D, Benson S, *et al*., 2010, Facial Anthropometric Differences among Gender, Ethnicity, and Age Groups. *Ann Occup Hyg*, 54:391-402.
22. Kim H, Han DH, Roh YM, *et al*., 2003, Facial Anthropometric Dimensions of Koreans and their Associations with Fit of Quarter-mask Respirators. *Ind Health*, 41:8-18. https://doi.org/10.2486/indhealth.41.8
23. Du L, Zhuang Z, Guan H, *et al*., 2008, Head-and-face Anthropometric Survey of Chinese Workers. *Ann Occup Hyg*, 52:773-782.
24. Yang L, Shen H, Wu G, 2007, Racial Differences in Respirator Fit Testing: A Pilot Study of Whether American Fit Panels are Representative of Chinese Faces. *Ann Occup Hyg*, 51:415-421. https://doi.org/10.1093/annhyg/mem005
25. Tuck CJ, Hague RJ, Ruffo M, *et al*., 2008, Rapid Manufacturing Facilitated Customization. *Int J Comput Integr Manufact*, 21:245-258. https://doi.org/10.1080/09511920701216238
26. Tan HW, An J, Chua CK, *et al*., 2019, Metallic Nanoparticle Inks

for 3D Printing of Electronics. *Adv Electron Mater*, 5:1800831. https://doi.org/10.1002/aelm.201800831

27. Choong YY, Maleksaeedi S, Eng H, *et al*., 2020, High Speed 4D Printing of Shape Memory Polymers with Nanosilica. *Appl Mater Today*, 18:100515. https://doi.org/10.1016/j.apmt.2019.100515
28. Tan HW, Saengchairat N, Goh GL, *et al*., 2020, Induction Sintering of Silver Nanoparticle Inks on Polyimide Substrates. *Adv Mater Technol*, 5:1900897. https://doi.org/10.1002/admt.201900897
29. Ng WL, Chua CK, Shen YF, 2019, Print me an Organ! Why we are not there yet. *Prog Polym Sci*, 97:101145. https://doi.org/10.1016/j.progpolymsci.2019.101145
30. Bibb R, Eggbeer D, Evans P, 2010, Rapid Prototyping Technologies in Soft Tissue Facial Prosthetics: Current State of the Art. *Rapid Prototyp J*, 16:25852. https://doi.org/10.1108/13552541011025852
31. Eggbeer D, Evans PL, Bibb R, 2006, A Pilot Study in the Application of Texture Relief for Digitally Designed Facial Prostheses. *Proc Inst Mech Eng Part H*, 220:705-14. https://doi.org/10.1243/09544119jeim38
32. Kai CC, Meng CS, Ching LS, *et al*., 2000, Facial prosthetic model fabrication using rapid prototyping tools. *Integr Manuf Syst*, 11:42-53. https://doi.org/10.1108/09576060010303668
33. Pallari J, Dalgarno K, Munguia J, *et al*. 2010, Design and Additive Fabrication of Foot and Ankle-foot Orthoses. In: Proceedings of the 21st Annual International Solid Freeform Fabrication Symposium an Additive Manufacturing Conference. https://doi.org/10.32656/2018_29sff_symposium
34. Pallari JH, Dalgarno KW, Woodburn J, 2001, Mass Customization of Foot Orthoses for Rheumatoid Arthritis Using Selective Laser Sintering. *IEEE Trans Biomed Eng*, 57:1750-6. https://doi.org/10.1109/tbme.2010.2044178
35. Eggbeer D, Bibb R, Williams R, 2005, The Computer-aided Design and Rapid Prototyping Fabrication of Removable Partial Denture Frameworks. *Proc Inst Mech Eng Part H*, 219:195-202. https://doi.org/10.1243/095441105x9372
36. Salles AS, Gyi DE, 2013, Delivering Personalised Insoles to the High Street Using Additive Manufacturing. *Int J Comput Integr Manuf*, 2013. 26:386-400. https://doi.org/10.1080/0951192x.2012.717721
37. Salles AS, Gyi DE, 2012, The Specification of Personalised Insoles Using Additive Manufacturing. *Work*, 41:1771-4. https://doi.org/10.3233/wor-2012-0383-1771
38. Wu YY, Acharya D, Xu C, *et al*., 2018, Custom-Fit Three-dimensional-printed BiPAP Mask to Improve Compliance in Patients Requiring Long-term Noninvasive Ventilatory Support. *J Med Dev*, 12:0310031-8. https://doi.org/10.1115/1.4040187
39. Ma Z, Hyde P, Drinnan M, *et al*., 2021, Custom Three-Dimensional-Printed CPAP Mask Development, Preliminary Comfort and Fit Evaluation. *J Med Dev*, 15:024501. https://doi.org/10.1115/1.4050201
40. Martelly E, Rana S, Shimada K, 2021, Design and Fabrication of Custom-Fit BiPAP and CPAP Masks Using Three-Dimensional Imaging and Three-Dimensional Printing Techniques. *J Med Dev*, 15:024502. https://doi.org/10.1115/1.4049981
41. Cai M, Li H, Shen S, *et al*., 2018, Customized Design and 3D Printing of Face Seal for an N95 Filtering Facepiece Respirator. *J Occup Environ Hyg*, 15:226-34. https://doi.org/10.1080/15459624.2017.1411598
42. Finne H, Liacouras P, Wilsnack AR, *et al*., Custom Fit N95 Respirator Acceptability and Fit. Bethesda, Maryland, United States: Walter Reed National Military Medical Center.
43. Stokes AA, 2021, 3DPPE: Rapid 3D Printing of Personalised Protective Facemasks and Visors to WHO Standard for Healthcare Workers Treating SARS-CoV-2 Patients.
44. Choong YY, Tan HW, Patel DC, *et al*., 2002, The Global Rise of 3D Printing during the COVID-19 Pandemic. *Nat Rev Mater*, 5:637-639. https://doi.org/10.1038/s41578-020-00234-3
45. Sherborne C, Claeyssens F, 2021, Considerations Using Additive Manufacture of Emulsion Inks to Produce Respiratory Protective Filters against Viral Respiratory Tract Infections Such as the COVID-19 Virus. *Int J Bioprint*, 7:316. https://doi.org/10.18063/ijb.v7i1.316
46. Shpichka A, *et al*., 2020, Engineering a Model to Study Viral Infections: Bioprinting, Microfluidics, and Organoids to Defeat Coronavirus Disease 2019 (COVID-19). *Int J Bioprint*, 6:302. https://doi.org/10.18063/ijb.v6i4.302
47. Bishop EG, Leigh SJ, 2020, Using Large-scale Additive Manufacturing as a Bridge Manufacturing Process in Response to Shortages in Personal Protective Equipment during the COVID-19 Outbreak. *Int J Bioprint*, 6:281. https://doi.org/10.18063/ijb.v6i4.281
48. Celik HK, Kose O, Ulmeanu ME, *et al*., 2020, Design and Additive Manufacturing of Medical Face Shield for Healthcare Workers Battling Coronavirus (COVID-19). *Int J*

Bioprint, 6:286.
https://doi.org/10.18063/ijb.v6i4.286

49. Flanagan ST, Ballard DH, 2020, 3D Printed Face Shields: A Community Response to the COVID-19 Global Pandemic. *Acad Radiol*, 27:905.
https://doi.org/10.1016/j.acra.2020.04.020
50. Wesemann C, Pieralli S, Fretwurst T, *et al*., 2020, 3-d Printed Protective Equipment during covid-19 Pandemic. *Materials*, 13:1997.
https://doi.org/10.3390/ma13081997
51. Cavallo L, Marcianò A, Cicciù M, *et al*., 2020, 3D Printing beyond Dentistry during COVID 19 Epidemic: A Technical Note for Producing Connectors to Breathing Devices. *Prosthesis*, 2:46-52.
https://doi.org/10.3390/prosthesis2020005
52. Clifton W, Damon A, Martin AK, 2020, Considerations and Cautions for Three-Dimensional-Printed Personal Protective Equipment in the COVID-19 Crisis. *3D Print Addit Manuf*, 7:97-9.
https://doi.org/10.1089/3dp.2020.0101
53. Novak JI, Loy J, 2020, A Critical Review of Initial 3D Printed Products Responding to COVID-19 Health and Supply Chain Challenges. *Emerald Open Res*, 2:24.
https://doi.org/10.35241/emeraldopenres.13697.1
54. Swennen GR, Pottel L, Haers PE, 2020, Custom-made 3D-printed Face Masks in Case of Pandemic Crisis Situations with a Lack of Commercially Available FFP2/3 Masks. *Int J Oral Maxillofac Surg*, 49:673-7.
https://doi.org/10.1016/j.ijom.2020.03.015
55. Novak JI, Loy J, 2020, A Quantitative Analysis of 3D Printed Face Shields and Masks during COVID-19. *Emerald Open Res*, 2:42.
https://doi.org/10.35241/emeraldopenres.13815.1
56. Provenzano D, Rao YJ, Mitic K, *et al*., 2020, Rapid Prototyping of Reusable 3D-printed N95 Equivalent Respirators at the George Washington University. *Preprints*, 2020:2020030444.
https://doi.org/10.20944/preprints202003.0444.v1
57. Greig P, Carvalho C, El-Boghdadly K, *et al*., 2020, Safety Testing Improvised COVIDng IPersonal Protective Equipment Based on a Modified Full-odifiSnorkel Mask. *Anaesthesia*, 75:970-1.
https://doi.org/10.1111/anae.15085
58. Rogers B, Bosker GW, Crawford RH, *et al*., 2007, Advanced Trans-tibial Socket Fabrication Using Selective Laser Sintering. *Prosthet Orthot Int*, 31:88-100.
https://doi.org/10.1080/03093640600983923
59. Schrank ES, 2011, Dimensional Accuracy of Ankle-Foot Orthoses Constructed by Rapid Customization and Manufacturing Framework. *J Rehabil Res Dev*, 48:31.
https://doi.org/10.1682/jrrd.2009.12.0195
60. Paterson AM, Donnison E, Bibb RJ, *et al*., 2014, Computer-aided Design to Support Fabrication of Wrist Splints Using 3D Printing: A Feasibility Study. *Hand Ther*, 19:102-13.
https://doi.org/10.1177/1758998314544802
61. Cazon A, Aizpurua J, Paterson A, *et al*., 2014, Customised Design and Manufacture of Protective Face Masks Combining a Practitioner-friendly Modelling Approach and Low-cost Devices for Digitising and Additive Manufacturing: This Paper Analyses the Viability of Replacing Conventional Practice with AM Method to Make Customized Protective Face Masks. *Virtual Phys Prototyp*, 9:251-261.
https://doi.org/10.1080/17452759.2014.958648
62. Ellena T, Mustafa H, Subic A, *et al*., 2018, A Design Framework for the Mass Customisation of Custom-fit Bicycle Helmet Models. *Int J Ind Ergon*, 64:122-33.
https://doi.org/10.1016/j.ergon.2018.01.005
63. Galvez A, Iglesias A, Puig-Pey J, 2012, Iterative Two-step Genetic-algorithm-Based Method for Efficient Polynomial B-spline Surface Reconstruction. *Inf Sci*, 182:56-76.
https://doi.org/10.1016/j.ins.2010.09.031
64. Sela M, Toledo N, Honen Y, *et al*., 2016, Customized Facial Constant Positive Air Pressure (CPAP) Masks. *arXiv*, 2016:07049.
65. Li S, Waheed U, Bahshwan M, *et al*., 2021, A Scalable Mass Customisation Design Process for 3D-printed Respirator Mask to Combat COVID-19. *Rapid Prototyp J*, 27:1302-17.
https://doi.org/10.1108/rpj-10-2020-0231
66. Mensura M, 2020, Mensura Mask Website. Available from: Available from: https://www.mensuramask.com [Last accessed on 2021 Feb 04].
67. BBC, 2020, What is it Like to Wear a Customised Face Mask? Available from: https://www.bbc.co.uk/programmes/p08ky38x [Last accessed on 2021 Feb 04].
68. Mensura M, 2020, How to Perform a Face Scan. Available from: https://www.mensuramask.com/instructions [Last accessed on 2021 Jun 26].
69. Mensura M, 2020, Participate in the Study. Available from: https://imperial.eu.qualtrics.com/jfe/form/SV_8jC7fcmYEOT6aMt [Last accessed on 2021 Jun 26].
70. Yianilos PN, 1993, Data Structures and Algorithms for Nearest Neighbor Search in General Metric Spaces. In: Proceedings of the fourth annual ACM-SIAM Symposium on Discrete algorithms.

71. Bentley, J.L., 1975, Multidimensional Binary Search Trees Used for Associative Searching. *Commun ACM*, 18:509-517. https://doi.org/10.1145/361002.361007

72. Richard MJ, Morris C, Deen BF, *et al*., 2009, Analysis of the Anatomic Changes of the Aging Facial Skeleton Using Computer-assisted Tomography. *Ophthalmic Plast Reconstr Surg*, 25:382-386. https://doi.org/10.1097/iop.0b013e3181b2f766

73. Kahn DM, Shaw RB Jr., 2008, Aging of the Bony Orbit: A Three-dimensional Computed Tomographic Study. *Aesthet Surg J*, 28:258-64.

74. Mendelson BC, Hartley W, Scott M, *et al*., 2007, Age-related Changes of the Orbit and Midcheek and the Implications for Facial Rejuvenation. *Aesthet Plast Surg*, 31:419-423. https://doi.org/10.1007/s00266-006-0120-x

75. Zadoo VP, Pessa JE, 2000, Biological Arches and Changes to the Curvilinear form of the aging Maxilla. *Plast Reconstr Surg*, 106:460-6. https://doi.org/10.1097/00006534-200008000-00036

76. World Health Organization. Body Mass Index BMI. Available from: https://www.euro.who.int/en/health-topics/disease-prevention/nutrition/a-healthy-lifestyle/body-mass-index-bmi [Last accessed on 2021 Fe b 04]. https://doi.org/10.1007/springerreference_179795

77. Lee W, Kim H, Jung D, *et al*., 2013, Ergonomic Design and Evaluation of a Pilot Oxygen Mask. In Proceedings of the Human Factors and Ergonomics Society Annual Meeting. Los Angeles, CA: SAGE Publications Sage CA. https://doi.org/10.1177/1541931213571371

78. Lee W, Jung D, Park S, *et al*., 2012, Development of a Methodology to Design a Pilot Oxygen Mask Based on Virtual Fit Testing Method. In: Proceedings of the 2012 Spring Conference of the Korean Institute of Industrial Engineers.

RESEARCH ARTICLE

3D-Printed Degradable Anti-Tumor Scaffolds for Controllable Drug Delivery

Yucheng Mei[1†], Chengzu He[2†], Chunxia Gao[1], Peizhi Zhu[1*], Guanming Lu[3*], Hongmian Li[4*]

[1]Institute of Biomedical Research and Tissue Engineering, Yangzhou University, Yangzhou 225002, PR China
[2]Department of Oncology, the People's Hospital of Binyang County, Binyang 530405, Guangxi, China
[3]Department of Breast and Thyroid Surgery, Affiliated Hospital of Youjiang Medical University for Nationalities, Baise 533000, Guangxi, China
[4]Research Center of Medical Sciences, The People's Hospital of Guangxi Zhuang Autonomous Region and Guangxi Academy of Medical Sciences, Nanning 530021, China
[†]*These authors contributed equally to this work*

Abstract: In this study, porous polylactic acid/methotrexate (PLA/MTX) scaffolds were successfully fabricated by three-dimensional (3D) printing technology as controllable drug delivery devices to suppress tumor growth. Scanning electron microscopy and energy-dispersive spectrometer confirmed that MTX drug was successfully incorporated into the PLA filament. 3D-printed PLA/MTX scaffolds allow sustained release of drug molecules *in vitro* for more than 30 days, reducing systemic toxic side effects caused by injection or oral administration. *In vitro* cytotoxicity assay revealed that PLA/MTX scaffolds have a relatively high inhibitory effect on the tumor cells (MG-63, A549, MCF-7, and 4T1) and relatively low toxic effect on the normal MC3T3-E1 cells. Furthermore, results of *in vivo* experiments confirmed that PLA/MTX scaffolds highly suppressed tumor growth and no obvious side effects on the organs. All these results suggested that 3D-printed PLA/MTX scaffolds could be used as controllable drug delivery systems for tumor suppression.

Keywords: 3D printing; Polylactic acid; Methotrexate; Anti-tumor

*Correspondence to: Peizhi Zhu, Institute of Biomedical Research and Tissue Engineering, Yangzhou University, Yangzhou 225002, PR China; pzzhu@yzu.edu.cn; Guanming Lu, Department of Breast and Thyroid Surgery, Affiliated Hospital of Youjiang Medical University for Nationalities, Baise 533000, Guangxi, China; luguanming@ymcn.edu.cn; Hongmian Li, Medical Laboratory Center, People's Hospital of Guangxi Zhuang Autonomous Region and Guangxi Academy of Medical Science, Nanning, Guangxi, 530021, China; lihongmian@gxmu.edu.cn

Received: July 20, 2021; **Accepted:** September 1, 2021; **Published Online:** October 1, 2021

Citation: Mei Y, He C, Gao C, *et al*., 2021, 3D-Printed Degradable Anti-Tumor Scaffolds for Controllable Drug Delivery. *Int J Bioprint*, 7(4):418. http://doi.org/10.18063/ijb.v7i4.418

1. Introduction

The mainstream treatment strategy for tumor is to remove the tumor tissue, supplemented by post-operative chemotherapy or radiation therapy. Despite the great progress in treatment for tumor, many adverse post-operative side effects, including the limited distribution of chemotherapy drugs at the target site and severe toxicity after radiotherapy, are unavoidable[1-3]. Therefore, developing a new drug delivery system that can overcome these limitations has become the focus of cancer research.

4-Amino-10-methylfolate (methotrexate [MTX]), an antitumor drug[4], has been widely used to treat various cancer diseases, such as head-and-neck tumors, breast cancer, and lung cancer[5-8]. In spite of its wide application in clinical practice, the treatment with MTX through injection or oral administration is still accompanied by some disadvantages, including non-tissue selectivity, the need for high dose, and high toxicity. In addition, MTX is resistant to bone marrow suppression and gastrointestinal cytotoxicity.

To avoid the shortcomings of injection and oral administration, it is necessary to design a drug delivery system to deliver MTX into the diseased area to achieve the optimal therapeutic effect[9]. Various strategies have been developed to control drug delivery using materials

such as hydrogels, polymer micelles, and stimulus-responsive materials[10-12]. Three-dimensional (3D) printing technology, known as additive manufacturing (AM), has great potential in fabricating the personalized scaffolds[13-15]. Based on the patient's computed tomography (CT) or magnetic resonance imaging (MRI), 3D models can be quickly and accurately established, making it possible to accurately print irregular models[16,17]. Moreover, the drug-loaded scaffolds made by 3D printing technology have unique advantages in personalization, spatial structure, drug components diversity, drug loading accuracy, and drug release sustainability[18-22].

Among various 3D printing technologies, fused deposition modeling (FDM), which was launched by Stratasys in 1992, has become one of the most popular technologies[23]. The technical advantages of FDM include the selectivity of a variety of applicable materials, customized high precision, and low cost[18]. As a typical heat dissipation technology for scaffolding, FDM uses a thermoplastic polymer filament, which is heated to the melting point, and then extruded from the nozzle, and deposited layer by layer to create a scaffold[20,24-27]. The thermoplastic materials used in FDM technology include polylactic acid (PLA), poly(ε-caprolactone) (PCL), poly (methyl methacrylate) (PMMA), polycarbonate (PC), and acrylonitrile butadiene styrene (ABS)[28-35]. Among these thermoplastic materials, PLA has been approved by the FDA as biomedical material due to its excellent biocompatibility[36,37]. Studies demonstrated that 3D printing is a powerful tool for manufacturing personalized scaffolds with specific geometries. Fouladian *et al*. reported that 3D-printed stents loaded with 5-fluorouracil (5-FU) drug were used to treat esophageal cancer. Incorporating anti-cancer drugs into endoluminal stents can provide a sustained release of drugs to esophageal malignant tissues while prolonging the retention of the stent and relieving dysphagia[38].

The purpose of this research is to prepare porous PLA/MTX scaffold with a controllable MTX release. PLA/MTX filaments with different MTX concentrations (MTX mass fraction: 0.5 wt%, 1.5 wt%, and 2.5 wt%) were prepared by melt mixing and extruding method. PLA/MTX scaffolds were printed by FDM using prepared PLA/MTX filament. The morphology, composition, and structure of printed PLA/MTX scaffold were investigated by scanning electron microscopy (SEM) and energy-dispersive spectrometer (EDS). The biocompatibility of printed PLA/MTX scaffolds and the inhibitory effect on tumor cells were evaluated *in vitro* by mouse embryo osteoblast precursor cells (MC3T3-E1), human osteosarcoma cells (MG-63), human breast cancer cells (MCF-7), human lung cancer cell lines (A549), and mouse breast cancer cells (4T1). In addition, the subcutaneous xenograft model was used to explore the inhibitory effect on tumor tissues and the toxicity to normal tissues and organs.

2. Materials and methods

2.1. Materials

PLA (MW: 500 kDa) was purchased from Sigma-Aldrich (Darmstadt, Germany), and MTX was purchased from Bio Basic Inc. (Markham, Ontario, Canada). Cell counting kit-8 (CCK-8) was purchased from Dojindo (Japan). LIVE/DEAD® Viability/Cytotoxicity Kit (Live/Dead) was purchased from Thermo Fisher Scientific (L-3224). The fetal bovine serum (FBS), Dulbecco's Modified Eagle Medium (DMEM), RPMI-1640, penicillin-streptomycin, and trypsin-ethylenediaminetetraacetic acid (EDTA) were purchased from Grand Island (New York, USA). All the reagents were used without further treatment.

2.2. Preparation of the PLA and PLA/MTX composite filaments

The mixture of PLA and MTX was melted and extruded using granulators. PLA/MTX and PLA filament were prepared by the 3D printing consumable extruder (SHSJ, Songhu Machinery Co., Ltd., Dongguan, China) with a 1.75 ± 0.05 mm constant diameter at 220°C and cooled by water, and the screw speed was 45 rpm.

2.3. Fabrication of PLA/MTX scaffolds

The 3D printing bracket was designed using Mimics software and SolidWorks2015 software. STL files were converted to a format (gcode) recognizable by 3D printer (ShanRui DK2, Guangzhou, China) using CURA software. An ink cartridge was added to the 3D printer to transport the PLA/MTX composite filaments, and the filaments were drawn and melted (210°C) and extruded through a nozzle (0.4 mm) to print layer by layer.

2.4. Characterization of PLA/MTX scaffolds

The structures and aperture sizes of PLA/MTX scaffold were characterized using field emission SEM (SEM, Zeiss_Supra55, Germany). Energy-dispersive X-ray analysis (JXA-8230, JEOL, Japan) was then used to perform elemental analysis of the PLA/MTX scaffold surfaces to assess the distribution of MTX in the PLA matrix.

The high-precision digital density meter (ED-1000, Shanghai Tuxin Electronic Technology Co., Ltd.) was used to measure the porosity. The porosity calculation formula is as follows:

$$\text{Porosity } (\%) = (1-(m/\rho)/V) \times 100\%$$

Where, V: outer volume, m: mass, and ρ: density.

2.5. Drug loading capacity and drug release

The 500 mg of PLA/MTX scaffolds were placed in a beaker containing 3 mL $CHCl_3$ to fully dissolve, and then, phosphate-buffered saline (PBS) was used to extract the drug. The absorbance of the PBS was determined by ultraviolet (UV) spectrophotometer at 305 nm.

The 500 mg of scaffold was placed in a 5 mL centrifuge tube containing 3 mL PBS and then shaken at 37°C with a speed of 100 r/min. The absorbance of the scaffolds was determined by UV spectrophotometer at 305 nm and calculated by the following formula.

Loading efficiency % (LE%) = (Weight of encapsulated drug/total mass of the PLA/ MTX scaffold) ×100%

Entrapment efficiency % (EE%) = (Weight of encapsulated drug / Weight of total added drug) × 100%.

2.6. *In vitro* experiments

(1) Cell lines

Mouse embryo osteoblast precursor cells (MC3T3-E1), human osteosarcoma cells (MG-63), human breast cancer cells (MCF-7), human lung cancer cell lines (A549), and mouse breast cancer cells (4T1) were purchased from Shanghai Cell Bank of the Chinese Academy of Sciences (Shanghai, China), and cultured in DMEM (or RPMI) containing 10% FBS and 100 U/mL penicillin-streptomycin.

(2) Cytotoxicity assay

Cells were cultured using 24-well plates with a density of 1×10^4 cells/well. When the cells adhered and spread in plates, the scaffolds were immersed into the culture medium. The CCK-8 assay was performed on days 1, 3, and 5. Briefly, the culture medium of the sample was replaced with 100 μL DMEM (RPMI) and incubated at 37°C for 2.5 h. The absorbance was measured at 450 nm in the Multiskan FC enzyme labeling instrument (Thermo, Waltham, USA). The cell viability was evaluated by live/dead staining. After incubation in the medium for 12 h, 24 h, 72 h, and 120 h, 4 μM Calcein-AM and 2 μM ethidium homodimer-1 were added to stain living cells and dead cells, respectively. After incubated at 37°C for 15 min, the cells were examined using fluorescence microscope (Olympusix53, Tokyo, Japan).

2.7. *In vivo* anti-tumor effect

(1) Subcutaneous xenograft model

The 4T1 cells (2×10^5) were subcutaneously injected into the back of the BALB/c mice to establish the subcutaneous xenograft model. After surgery, celecoxib (Dalian Meilun Biotechnology, China) was given to relieve postoperative pain (10 mg/kg, gavage, q.d./2 days) and ceftriaxone sodium (Dalian Meilun Biotechnology, China) to prevent post-operative infection (20 mg/kg, tail vein injection, q.d./2 days). The mice were housed under the standard conditions.

(2) In vivo antitumor efficacy and mechanism studies

When tumor volume reached approximately 62.50 ± 10 mm^3 (5 mm×5 mm×5 mm), mice bearing 4T1 tumors were randomly assigned to four groups with five mice in each group. The injection group was administered an intraperitoneal injection of drugs every 2 days of MTX at 4 mg/kg. The PLA/MTX scaffolds printed from filament were implanted near the tumors. The tumor size and the weight of mice were recorded every day. The animals were euthanized at the end point (21 days), and the major organs (heart, liver, spleen, lung, and kidney) were collected for weighing to calculate organ coefficient and then fixed in 4% paraformaldehyde for histopathological examination. The animal research was approved by the Experimental Animal Ethics Committee of Yangzhou University (NSFC2020-HXXY-4).

2.8. Statistical analysis

All the experiments were performed in triplicate. Results were expressed as mean ± standard deviation (SD). Bonferroni post-test was performed to assess statistical significance. Statistical analysis was performed using non-parametric Kruskal–Wallis tests. $P < 0.05$ was considered statistically significant.

3. Results

3.1. Morphological, composition, and structural analysis

The morphology, microstructure, and compositions were investigated by SEM and EDS (**Figure 1**). According to **Figure 1A-1**, SEM image of the PLA/MTX scaffold showed a relatively smooth surface and had open big pores in uniform size with integrated lines (755 ± 0.7 μm) among the big pores. Moreover, the printed PLA/MTX scaffolds were porous, with the porosity and pore size at 29.7% and 309 ± 0.5 μm, respectively.

The EDS spectra are shown in **Figure 1B**, and the peaks of C, N, and O were observed in the spectrum of PLA/MTX scaffold. The appearance of N peak confirmed that MTX was introduced into PLA matrix. The color map obtained from EDS analysis in **Figure 1A** shows the N (blue) distribution in the scaffold structure, which proves that MTX was well distributed in the PLA matrix. The evenly dispersion of MTX in the scaffold provides the possibility for MTX to be released along with PLA degradation.

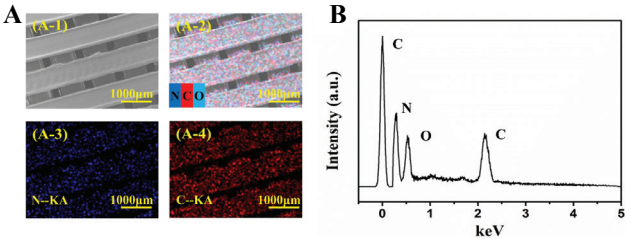

Figure 1. The morphology, composition, and structure of printed polylactic acid/methotrexate (PLA/MTX) and PLA scaffolds. (A) Scanning electron microscopy images of PLA/MTX scaffolds. Scale bars represent 1 mm for A. Element mapping of C, N, and O for the PLA/MTX scaffold. Scale bars represent 1 mm. (B) Energy-dispersive spectrometer of porous printed PLA/MTX composite scaffolds.

3.2. Characterization of drug loading (LE%) and encapsulation efficiency (EE%) in PLA/MTX scaffolds and drug release profiles *in vitro*

Before assessing the release profiles of MTX from PLA/MTX scaffolds with different drug concentrations, the LE% and EE% were calculated by measuring the concentration of drug absorbance in the PBS. The EE% of MTX was 98.1% and the LE% of MTX was controlled at 0.5%, 1.5%, and 2.5%.

The release profiles of MTX from PLA/MTX scaffolds are shown in **Figure 2**. Approximately 25% of MTX was released within the first 24 h, and about 50% of MTX was released within the first 7 days. 3D-printed PLA/MTX scaffolds allow sustained release of drugs *in vitro* more than 30 days. In addition, with the increase of drug content, the release trend of MTX is basically similar. Therefore, the drug release could be controlled by adjusting MTX content in scaffolds. This result proved that PLA/MTX scaffolds had a sustained release effect.

Figure 3 shows the comparison of MTX release profiles of 3D-printed PLA/MTX scaffolds of varying drug contents and cast PLA/MTX with 0.5% of MTX over 5 days. The drug release pattern of cast PLA/MTX sample is similar to that of 3D-printed porous PLA/MTX scaffold. However, the drug release rate of the cast PLA/MTX sample is slower than that of 3D-printed PLA/MTX scaffold. In cast PLA/MTX sample, the MTX drug molecules were wrapped tightly by PLA material to obstruct the release of drug molecules from the polymer matrix. The release of MTX from 3D-printed porous PLA/MTX scaffold is more stable than cast sample.

3.3. In vitro cytotoxicity

Figure 4 shows the *in vitro* inhibitory effect of PLA/MTX scaffolds on human lung cancer cell lines (A549), human osteosarcoma cells (MG-63), human breast cancer cells (MCF-7), and normal mouse embryo

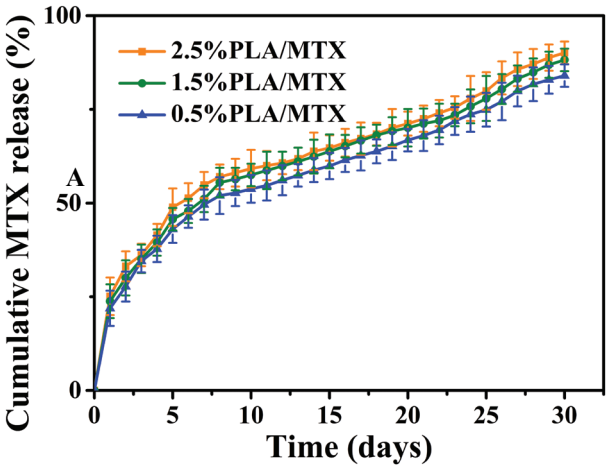

Figure 2. Methotrexate (MTX) release profiles of polylactic acid/MTX (PLA/MTX) scaffolds of varying drug content over 7 and 30 days.

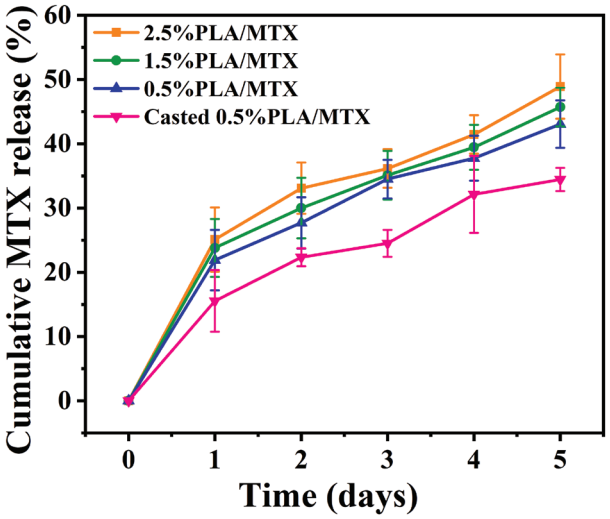

Figure 3. Methotrexate (MTX) release profiles of polylactic acid/MTX (PLA/MTX) scaffolds of varying drug contents and cast PLA/MTX with 0.5% of MTX over 5 days.

osteoblast precursor cells (MC3T3-E1). As shown in **Figure 4A-C**, the inhibitory effect increases as the drug content increases. The growth of tumor cells (A549, MG-63, and MCF-7) has been significantly inhibited at 24 h. At the same time, the inhibitory effect increased as the administration time was extended to the third and 5th days. Each PLA/MTX scaffold has a 95% inhibition rate of tumor cells at the 120 h. The above results indicate that the implantable PLA/MTX scaffold showed strong anti-tumor efficacy compared with PLA group and control group. The toxicity of PLA and PLA/MTX scaffolds on normal MC3T3 cells was also investigated (**Figure 4D**). The results showed that PLA scaffold had little effect on the growth of normal cells,

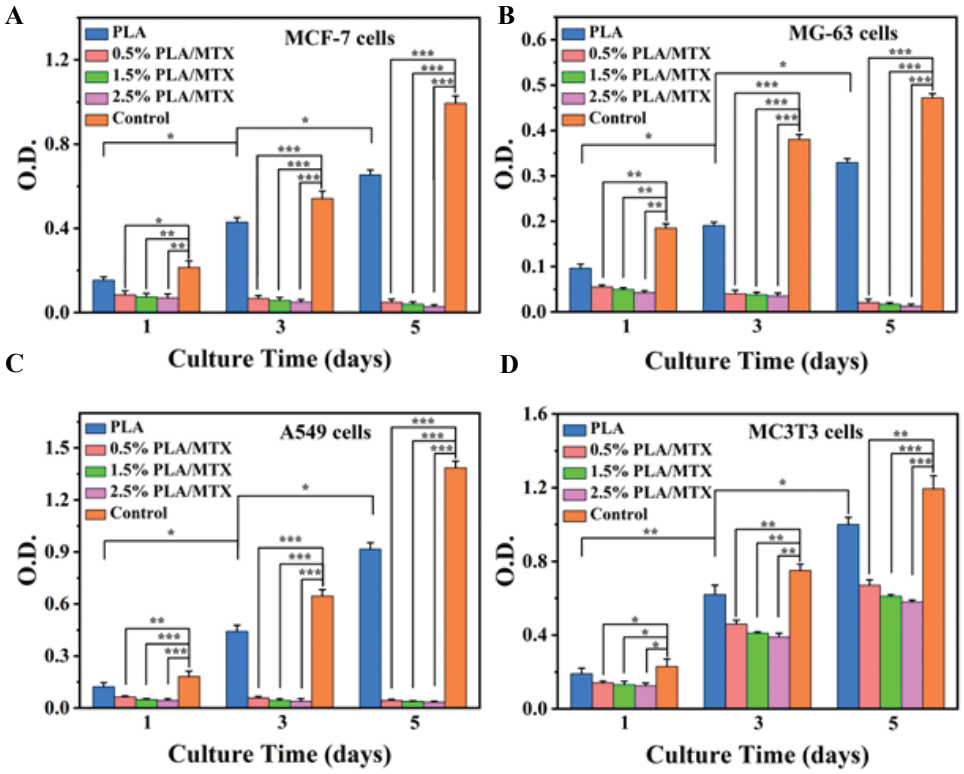

Figure 4. Evaluation of anticancer effect *in vitro*. *In vitro* proliferation of MCF-7(A), MG- 63 (B), A549 (C), and MC3T3 (D) cells after culturing in the polylactic acid/methotrexate (0.5%, 1.5%, and 2.5%) scaffolds and the tissue culture plate substrate (as control) for 1, 3, and 5 days.

while PLA/MTX scaffold had some effect on normal cells, but the effect was limited.

As shown in **Figure 5**, the toxicity of PLA and PLA/MTX scaffolds on cancer cells was also investigated by Live/Dead fluorescence staining of mouse breast cancer 4T1 cells. Due to its excellent biocompatibility, PLA scaffold group has low cytotoxicity within 120 h. The PLA/MTX scaffold groups showed a lower cell survival rate compared with PLA group and control group, and the inhibitory effect increased with the prolonged culture time. With the gradual release of MTX from the scaffold, the cell viability in the PLA/MTX scaffold group decreased. With the increase of drug concentration and culture time, the number of living cells gradually decreased and the number of dead cells gradually increased. The total induction of apoptosis of 4T1 cells by PLA/MTX scaffolds increased from 52.89% to 99.63% (**Figure 4C**). Thus, compared with the PLA and control groups, the PLA/MTX scaffolds showed strong inhibitory effect on tumor 4T1 cells.

3.4. *In vivo* anti-tumor effect

As shown in **Figure 6**, the anti-tumor effects of PLA/MTX scaffolds were evaluated by subcutaneous xenograft model of 4T1 tumor-bearing Balb/c mice compared with intraperitoneal drug injection of MTX. The minor body weight changes in implant groups (**Figure 6A**) proved that the implanted scaffolds were well tolerated by the mice. Weight loss occurred in the 0.5% PLA/MTX and 2.5% PLA/MTX groups at the beginning due to surgical anesthesia, surgical implantation, and other operations, but the growth status in the middle and later stages was the same as the control group (**Figure 6A**). Throughout the experiment, the overall growth of mice in the negative control group was good, but one mouse in the control group was paralyzed due to excessive compression of the spine by the tumor. In the early stage, the growth state of the injection group was the same as that of the control group. In the later stage, there were some adverse phenomena, such as weight loss, bad hair, small and sticky stool, and scorched yellow urine. There was no significant difference in organ coefficient of heart, liver, lung, and kidney among groups. The organ coefficient of spleen in injection group was much lower than the other three groups, which was found at the time of dissection (**Figure 6B**). The tumor sizes in **Figure 6C** can directly show that PLA/MTX scaffold implantation significantly inhibited the tumor growth compared with control group. The anti-tumor effects of 0.5% PLA/MTX scaffold with low concentration of drug are similar to

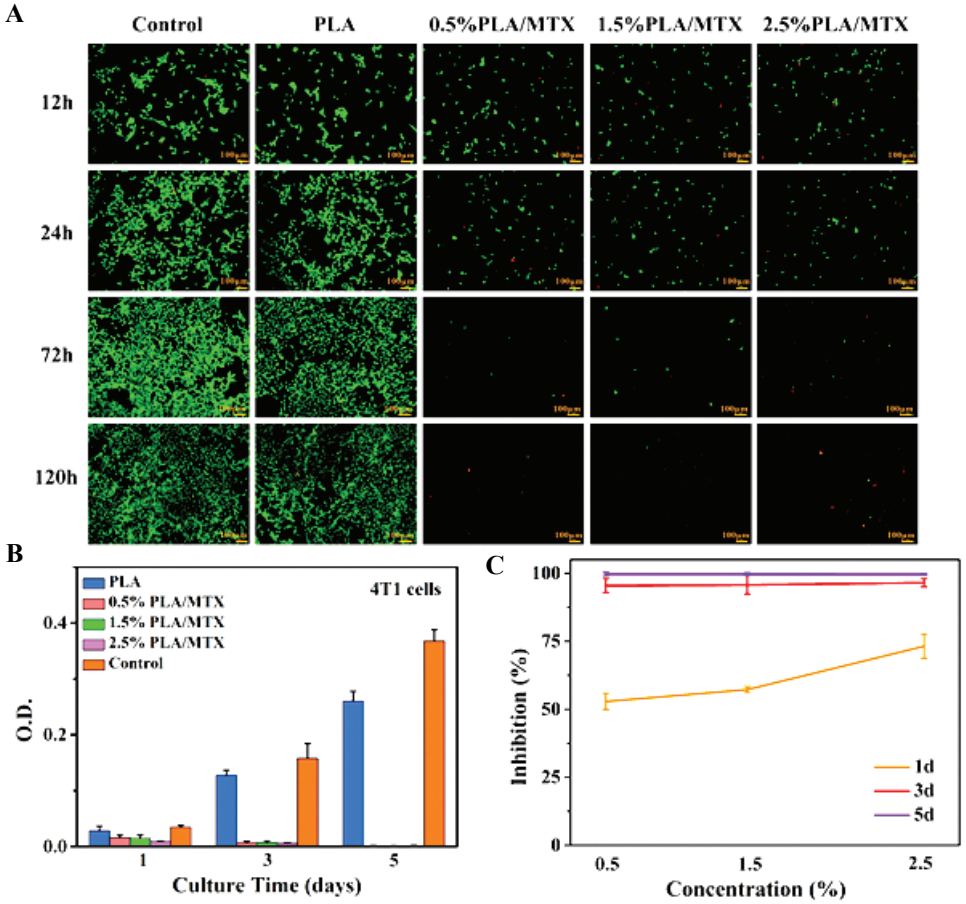

Figure 5. Evaluation of anticancer effect *in vitro*. (A) Live/Dead fluoresce staining of 4T1 cells on polylactic acid/methotrexate (PLA/MTX). The cells were cultured in DMEM for 12 h, 24 h, 72 h, and 120 h. Viable cells are stained green while dead cells red. (B) *In vitro* proliferation of 4T1 cells after culturing in the PLA/MTX (0.5%, 1.5%, and 2.5%) scaffolds and the tissue culture plates substrate (as control) for 1, 3, and 5 days. (C) Inhibition rate at different MTX concentrations.

that of injection group. The anti-tumor effects of 2.5% PLA/MTX scaffold with high concentration of drug were relatively better than that of 0.5% PLA/MTX scaffold with low concentration of drug (**Figure 6D**). The mean tumor volume of the control group was above 1300 mm^3, which was much larger than tumor volume in the 0.5% PLA/MTX and 2.5% PLA/MTX groups (<400 mm^3).

As shown in **Table 1**, PLA/MTX scaffold groups were more effective than the MTX injection in controlling tumor growth. The anti-tumor effect of the 2.5% PLA/MTX scaffold group was also significantly different from that of the 0.5% PLA/MTX group ($P < 0.05$). The main reason is that the injected drug is eliminated by renal metabolism in a short time, resulting in a short plasma half-life (5-8 h) and low drug concentration in target tissues. The tumor growth inhibition value (TGI) of high concentration group could reach 89.26%, which was higher than 74.04% in injection group. The results indicated that PLA/MTX scaffold had a better therapeutic effect than the intraperitoneal injection of drugs.

Table 1. Tumor weight and tumor growth inhibition value (TGI) of each group

Group	Tumor weight (g)	TGI
2.5% PLA/MTX	0.1557±0.024	89.26%
0.5% PLA/MTX	0.33524±0.042	76.88%
Injection	0.3763±0.018	74.04%
Control	1.45±0.3	-

TGI, tumor growth inhibition value.

The hematoxylin and eosin (H and E) staining results in **Figure 7** showed that some area of tumor necrosis appeared in the sections of 0.5% PLA/MTX group, 2.5% PLA/MTX group, and injection group. The nuclei of cancer cells enlarged, produced cavities and the cells showed apoptosis and necrosis. Eventually, the nucleus breaks, creating a "ghost" area. There was no obvious tumor necrosis in the control group. No obvious metastasis and inflammatory were found in the 0.5% PLA/MTX group and 2.5% PLA/MTX group, while the control group showed metastases. The H and E staining

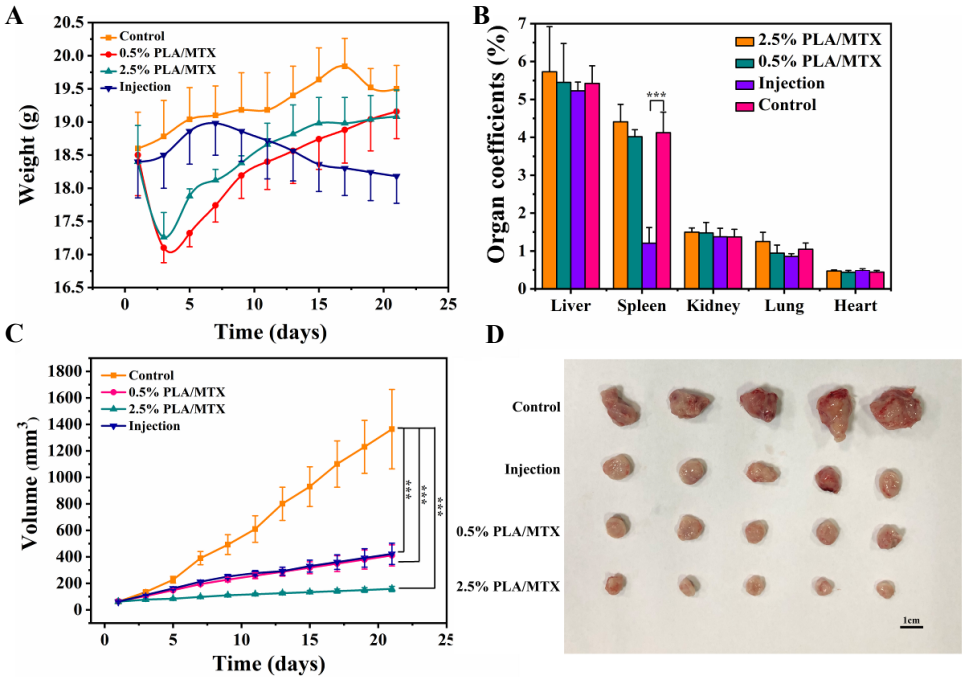

Figure 6. Evaluation of therapeutic efficiency of scaffolds *in vivo*. (A) Time-dependent body weight of the mice after different treatments. (B) Organ coefficients. (C) Time-dependent tumor growth curves of the mice with different treatments. (D) Photographs of the harvested tumors on day 21 from mice with different treatments.

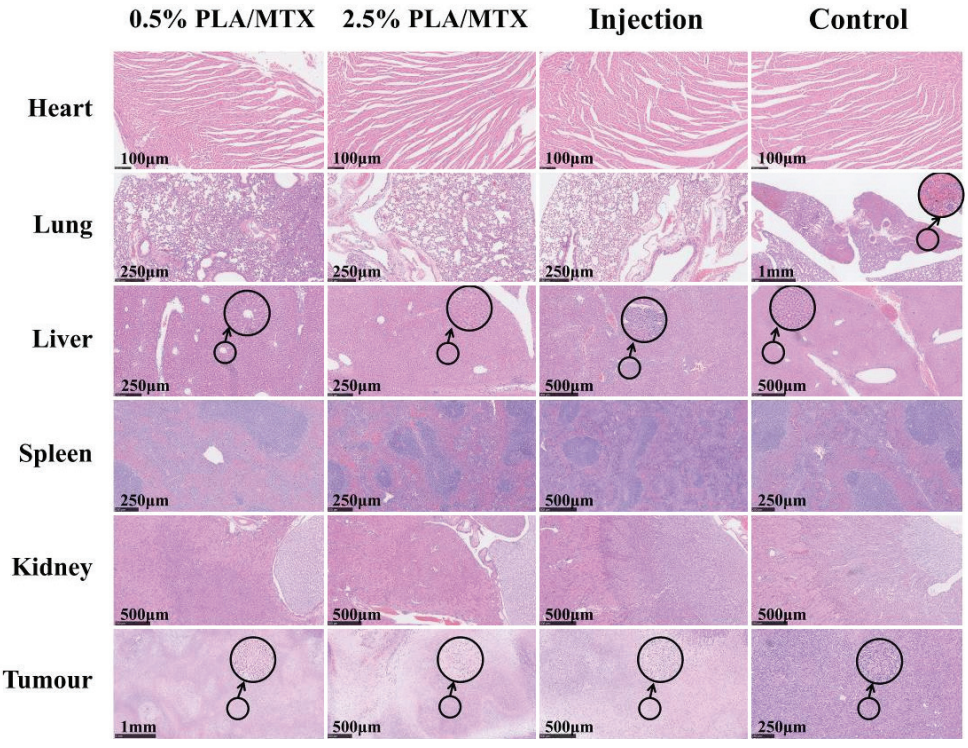

Figure 7. H &E staining results of experimental endpoint. The representative H and E staining images of the tumor, heart, liver, spleen, lung, and kidney from Balb/c mice with indicated treatment. Explanation about the circled area: In the tumor slices of 0.5% polylactic acid/methotrexate (PLA/MTX), 2.5% PLA/MTX, and injection group, the circled area indicates that tumor necrosis occurred in some areas, forming a "ghost" area. In the control group, the structure of tumor cells in the circled area was stable, the nuclei were clearly visible and arranged regularly. In the control group, metastases and increased inflammatory cells appeared in the circled area of lung sections. There were more inflammatory cells (lymphocytes, leukocytes and monocytes, etc.) in the liver slices of injection group. Scale bars represent 100, 250, 500, and 1000 μm.

of the spleen showed that the injection group had obvious white hyperplasia and more inflammatory cells (B-cell monocytes, etc.). There was no obvious nephrotoxicity found in all four groups.

4. Discussion

As shown in **Figure 8**, under the guidance of computer-aided design (CAD) and 3D printing technology, PLA/MTX drug-loaded scaffold was prepared by FDM printer. Then, PLA/MTX drug-loaded scaffold was implanted into the mouse body. With the release of MTX, the growth and reproduction of tumor cells were inhibited. The drug release from the PLA/MTX scaffold showed a sustained and slow process due to the degradation process of PLA[39]. The CCK-8 assay demonstrated that the PLA material did not exert severe cytotoxic effects on 4T1, A549, MCF-7, MG-63, and MC3T3 cells. *In vitro* cellular experiments revealed that the printed PLA/MTX scaffolds have a relatively high inhibitory effect on the tumor cells MG-63, A549, MCF-7, and 4T1, and lower toxic effect on the normal cells MC3T3-E1. The inhibition rates of three different concentrations of PLA/MTX scaffolds on cancer cells were more than 95% after cultured for 5 days.

After 3 weeks of observation, PLA/MTX scaffold with different MTX concentrations group had a higher tumor inhibition rate. We found that PLA/MTX scaffold was better than MTX injection in controlling tumor growth. This was attributed to an enrichment of the released MTX around the tumor tissue and lasting therapeutic MTX levels for prolonged time. The intraperitoneal delivery of MTX needed injection of drug every 2 days while PLA/MTX scaffold was implanted only once for the treatment, indicating that the PLA/MTX drug delivery system was more efficient than traditional injection method.

In a word, 3D-printed PLA/MTX scaffolds maintained a high tumor inhibition rate and significantly reduced systemic drug toxicity compared with intraperitoneal injection. The implanted PLA/MTX scaffolds can release and maintain therapeutic drug levels at the tumor site for prolonged time while reducing systemic drug exposure to healthy tissues. Moreover, this implantable scaffold only requires 1 time implantation, which greatly reduces the frequency of drug administration. Therefore, PLA/MTX scaffold as a controllable drug delivery system has great potential for suppressing tumor growth.

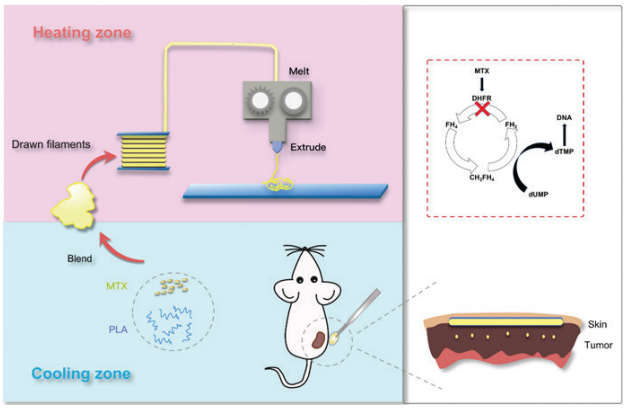

Figure 8. Schematic illustration of the fabrication and application of PLA/methotrexate scaffolds for tumor therapy.

5. Conclusions

We developed a novel 3D-printed drug delivery scaffold for tumor therapy. Morphological and structural analysis results showed that MTX was successfully incorporated into the PLA filament. PLA/MTX scaffolds can maintain MTX release for more than 30 days. *In vitro* cytotoxicity experiments confirmed that PLA/MTX scaffolds have a relatively high inhibitory effect on tumor cells while showing less toxicity to normal cells. In addition, *in vivo* results demonstrated that the PLA/MTX scaffolds highly suppressed tumor growth with negligible side effects on the normal tissues and organs. 3D-printed PLA/MTX scaffolds could be used as a controllable drug delivery system and have the great potential for suppressing tumor growth.

Funding

This research was supported by Technology Department of Yangzhou City (YZ2019073) from Jiangsu Huadong Medical Device Industrial Co., Ltd., China. A project funded by the Priority Academic Program Development of Jiangsu Higher Education Institutions, Guangxi Natural Science Foundation (2019JJA140071), and the First Batch of High-level Talent Scientific Research Projects of the Affiliated Hospital of Youjiang Medical University for Nationalities in 2019 (Contract No. R20196307).

Conflicts of interest

The authors declare that they have no conflicts of interest.

Authors' contributions

P.Z., C.H., and Y.M. conceived the project. Y.M. and C.H. conducted the scaffold fabrication and characterization. C.H. and C.G. conducted the cell and animal study. P.Z. reviewed the experimental results and advised the organization of the main contents. P.Z., G.L., H.L, C.G., and Y.M. wrote the manuscript.

References

1. O'Reilly M, Mellotte G, Ryan B, 2020, Gastrointestinal Side Effects of Cancer Treatments. *Ther Adv Chronic Dis*, 11:1-7. https://doi.org/10.1177/2040622320970354
2. Nandini D B, Rao R S, Hosmani J, *et al*., 2020, Novel

Therapies in the Management of Oral Cancer: An Update. *Dis Mon*, 66:101036.
https://doi.org/10.1016/j.disamonth.2020.101036

3. van Kaick G, Delorme S, 2008, Therapy-Induced Effects in Normal Tissue. *Radiologe*, 48:871–80.
https://doi.org/10.1007/s00117-008-1729-3
4. Fiehn C, 2011, The Future of Methotrexate Therapy and Other Folate Inhibitors. *Z Rheumatol*, 70:129–34.
https://doi.org/10.1007/s00393-010-0688-z
5. Sparano JA, Gray RJ, Makower, D, *et al*., 2020, Clinical Outcomes in Early Breast Cancer With a High 21-Gene Recurrence Score of 26 to 100 Assigned to Adjuvant Chemotherapy Plus Endocrine Therapy: A Secondary Analysis of the TAILORx Randomized Clinical Trial. *JAMA Oncol*, 6:367–74.
https://doi.org/10.1001/jamaoncol.2019.4794
6. Cohen EE, Soulieres D, Le Tourneau C, 2019, Pembrolizumab Versus Methotrexate, Docetaxel, or Cetuximab for Recurrent or Metastatic Head-and-Neck Squamous Cell Carcinoma (KEYNOTE-040): A Randomised, Open-Label, Phase 3 Study. *Lancet*, 393:156–67.
https://doi.org/10.1016/S0140-6736(18)31999-8
7. Bielack SS, Smeland S, Whelan JS, *et al*., 2015, Methotrexate, Doxorubicin, and Cisplatin (MAP) Plus Maintenance Pegylated Interferon Alfa-2b Versus MAP Alone in Patients With Resectable High-Grade Osteosarcoma and Good Histologic Response to Preoperative MAP: First Results of the EURAMOS-1 Good Response Randomized Controlled Trial. *J Clin Oncol*, 33:2279–87.
https://doi.org/10.1200/JCO.2014.60.0734
8. Suksiriworapong J, Taresco V, Ivanov DP, *et al*., 2018, Synthesis and Properties of a Biodegradable Polymer-Drug Conjugate: Methotrexate-Poly(Glycerol Adipate). *Colloids Surf B Biointerfaces*, 167:115–25.
https://doi.org/10.1016/j.colsurfb.2018.03.048
9. Zhong SH, Liu P, Ding JS, *et al*., 2021, Hyaluronic Acid-Coated MTX-PEI Nanoparticles for Targeted Rheumatoid Arthritis Therapy. *Crystals*, 11:321.
https://doi.org/10.3390/cryst11040321
10. Ghobashy MM, Elbarbary AM, Hegazy DE, 2021, Gamma Radiation Synthesis of a Novel Amphiphilic Terpolymer Hydrogel pH-Responsive Based Chitosan for Colon Cancer Drug Delivery. *Carbohydr Polym*, 263:117975.
https://doi.org/10.1016/j.carbpol.2021.117975
11. Fu YP, Ding Y, Zhang LT, *et al*., 2021, Poly Ethylene Glycol (PEG)-Related Controllable And Sustainable Antidiabetic Drug Delivery Systems. *Eur J Med Chem*, 217:113372.
https://doi.org/10.1016/j.ejmech.2021.113372
12. Song FY, Gong JW, Tao YH, *et al*., 2021, A Robust Regenerated Cellulose-Based Dual Stimuli-Responsive Hydrogel as an Intelligent Switch for Controlled Drug Delivery. *Int J Biol Macromol*, 176:448–58.
https://doi.org/10.1016/j.ijbiomac.2021.02.104
13. Koons GL, Diba M, Mikos AG, 2020, Materials Design for Bone-Tissue Engineering. *Nat Rev Mater*, 5:584–603.
14. Lepowsky E, Tasoglu S, 2018, 3D Printing for Drug Manufacturing: A Perspective on the Future of Pharmaceuticals. *Int J Bioprint*, 4:119.
https://doi.org/10.18063/IJB.v4i1.119
15. Jimenez M, Romero L, Dominguez I A, *et al*., 2019, Additive Manufacturing Technologies: An Overview about 3D Printing Methods and Future Prospects. *Complexity*, 2019:9656938.
https://doi.org/10.1155/2019/9656938
16. Bozo II, Deev RV, Smirnov IV, *et al*., 2020, 3D Printed Gene-activated Octacalcium Phosphate Implants for Large Bone Defects Engineering. *Int J Bioprint*, 6:275.
https://doi.org/10.18063/ijb.v6i3.275
17. Gatenholm B, Lindahl C, Brittberg M, *et al*., 2020, Collagen 2A Type B Induction after 3D Bioprinting Chondrocytes *In Situ* into Osteoarthritic Chondral Tibial Lesion. *Cartilage*, 2020:1-15.
https://doi.org/10.1177/1947603520903788
18. Zhang B, Cristescu R, Chrisey DB, *et al*., 2020, Solvent-based Extrusion 3D Printing for the Fabrication of Tissue Engineering Scaffolds. *Int J Bioprint*, 6:211.
https://doi.org/10.18063/ijb.v6i1.211
19. Wang H, Vijayavenkataraman S, Wu Y, *et al*., 2021, Investigation of process Parameters of Electrohydro-Dynamic Jetting for 3D Printed PCL Fibrous Scaffolds with Complex Geometries. *Int J Bioprint*, 2:63–71.
20. An J, Teoh JE, Suntornnond R, *et al*., 2015, Design and 3D Printing of Scaffolds and Tissues. *Engineering*, 1:261–8.
21. Long JJ, Gholizadeh H, Lu J, *et al*., 2017, Application of Fused Deposition Modelling (FDM) Method of 3D Printing in Drug Delivery, *Curr Pharm Des*, 23:433–9.
22. Tappa K, Jammalamadaka U, 2018, Novel Biomaterials Used in Medical 3D Printing Techniques. *J Funct Biomater*, 9:17.
https://doi.org/10.3390/jfb9010017
23. Daminabo SC, Goel S, Grammatikos SA, *et al*., 2020, Fused Deposition Modeling-Based Additive Manufacturing (3D Printing): Techniques for Polymer Material Systems. *Mater Today Chem*, 16:100248.
https://doi.org/10.1016/j.mtchem.2020.100248
24. Ranjan N, Singh R, Ahuja IP, *et al*., 2020, On 3D Printed

Scaffolds for Orthopedic Tissue Engineering Applications. *SN Appl Sci*, 2:192.

25. Nurulhuda A, Aqmaliah SH, Ali R, *et al*., 2019, Multi-Layered ABS Scaffold Fabrication via Fused Deposition Modelling (FDM) 3D Printing. *J Mech Contin Math Sci*, 4:131–8. https://doi.org/10.26782/jmcms.spl.4/2019.11.00013
26. Wang ZZ, Yang Y, 2021, Application of 3D Printing in Implantable Medical Devices. *Biomed Res Int*, 2021:6653967. https://doi.org/10.1155/*2021*/6653967
27. Limongi T, Susa F, Allione M, *et al*., 2020, Drug Delivery Applications of Three-Dimensional Printed (3DP) Mesoporous Scaffolds. *Pharmaceutics*, 12:851. https://doi.org/10.3390/pharmaceutics12090851
28. Zhang B, Seong B, Nguyen V, *et al*., 2016, 3D Printing of High-Resolution PLA-Based Structures by Hybrid Electrohydrodynamic and Fused Deposition Modeling Techniques. *J Micromech Microeng*, 26:025015. https://doi.org/10.1088/0960-1317/26/2/025015
29. Hedayati SK, Behravesh AH, Hasannia S, *et al*., 2020, 3D Printed PCL Scaffold Reinforced with Continuous Biodegradable Fiber Yarn: A Study on Mechanical and Cell Viability Properties. *Polym Test*, 83:106347.
30. Babu NV, Venkateshwaran N, Rajini N, *et al*., 2021, Influence of Slicing Parameters on Surface Quality and Mechanical Properties of 3D-Printed CF/PLA Composites Fabricated by FDM teChnique. *Mater Technol*, 2021:1-18. https://doi.org/10.1080/10667857.2021.1915056
31. Viidik L, Vesala J, Laitinen R, *et al*., 2021, Preparation and Characterization of Hot-Melt Extruded Polycaprolactone-Based Filaments Intended for 3D-Printing of Tablets. *Eur J Pharm Sci*, 158:105619.
32. Solorio-Rodriguez LE, Vega-Rios A, 2019, Filament Extrusion and Its 3D Printing of Poly(Lactic Acid)/ Poly(Styrene-co-Methyl Methacrylate) Blends. *Appl Sci*, 9:5153.
33. Chen PC, Chou CC, Chiang CH, Systematically Studying Dissolution Process of 3D Printed Acrylonitrile Butadiene Styrene (ABS) Mold for Creation of Complex and Fully Transparent Polydimethylsiloxane (PDMS) Fluidic Devices. *BioChip J*, 15:144–51.
34. Andrzejewski J, Marciniak-Podsadna L, 2020, Development of Thermal Resistant FDM Printed Blends. The Preparation of GPET/PC Blends and Evaluation of Material Performance. *Materials*, 13:2057. https://doi.org/10.3390/ma13092057
35. Baran EH, Erbil HY, 2019, Surface Modification of 3D Printed PLA Objects by Fused Deposition Modeling: A Review. *Colloid Interface*, 3:43. https://doi.org/10.3390/colloids3020043
36. Singhvi MS, Zinjarde SS, Gokhale DV, 2019, Polylactic Acid: Synthesis and Biomedical Applications. *J Appl Microbiol*, 127:1612–26. https://doi.org/10.1111/jam.14290
37. Lasprilla AJ, Martinez GA, Lunelli BH, *et al*., 2012, Poly-Lactic Acid Synthesis for Application in Biomedical Devices-a Review. *Biotechnol Adv*, 30:321–8. https://doi.org/10.1016/j.biotechadv.2011.06.019
38. Fouladian P, Kohlhagen J, Arafat M, *et al*., 2020, Three-Dimensional Printed 5-Fluorouracil Eluting Polyurethane Stents for the Treatment of Oesophageal Cancers. *Biomater Sci*, 8:6625–36. https://doi.org/10.1039/d0bm01355b
39. Gorrasi G, Pantani R, 2018, Hydrolysis and Biodegradation of Poly (Lactic Acid). *Adv Polym Sci*, 279:119–51.

RESEARCH ARTICLE

Development of a Multi-Material 3D Printer for Functional Anatomic Models

Laszlo Jaksa[1,2]*, Dieter Pahr[2,3], Gernot Kronreif[1], Andrea Lorenz[1]

[1]Austrian Center for Medical Innovation and Technology (ACMIT Gmbh), Viktor-Kaplan-Strasse 2/A, 2700 Wiener Neustadt, Austria
[2]Technical University of Vienna, Institute of Lightweight Design and Structural Biomechanics, Object 8, Gumpendorfer Strasse 7, 1060 Vienna, Austria
[3]Karl Landsteiner University of Health Sciences, Department of Anatomy and Biomechanics, Dr.-Karl-Dorrek-Strasse 30, 3500 Krems an der Donau, Austria

Abstract: Anatomic models are important in medical education and pre-operative planning as they help students or doctors prepare for real scenarios in a risk-free way. Several experimental anatomic models were made with additive manufacturing techniques to improve geometric, radiological, or mechanical realism. However, reproducing the mechanical behavior of soft tissues remains a challenge. To solve this problem, multi-material structuring of soft and hard materials was proposed in this study, and a three-dimensional (3D) printer was built to make such structuring possible. The printer relies on extrusion to deposit certain thermoplastic and silicone rubber materials. Various objects were successfully printed for testing the feasibility of geometric features such as thin walls, infill structuring, overhangs, and multi-material interfaces. Finally, a small medical image-based ribcage model was printed as a proof of concept for anatomic model printing. The features enabled by this printer offer a promising outlook on mimicking the mechanical properties of various soft tissues.

Keywords: Silicone 3D printing; Multi-material 3D printing; Anatomic models; Soft tissues

*Correspondence to: Laszlo Jaksa, Austrian Center for Medical Innovation and Technology, Viktor-Kaplan-Strasse 2/A, 2700 Wiener Neustadt, Austria; laszlo.jaksa.official@gmail.com

Received: July 20, 2021; **Accepted:** September 1, 2021; **Published Online:** October 12, 2021

Citation: Jaksa L, Pahr D, Kronreif G, *et al*., 2021, Development of a Multi-Material 3D Printer for Functional Anatomic Models. *Int J Bioprint*, 7(4):420. http://doi.org/10.18063/ijb.v7i4.420

1. Introduction

1.1. Anatomic models

In medical practice and education, anatomic models are provided through using human donors, animal models, or artificial technical solutions that range from hand-crafted training models to mass-produced commercial products. In the former case of using real biological tissues, progress is often hindered by the lack of available human donors, strict regulations regarding animal and human testing, and problems in experiment repeatability due to the anatomical uniqueness of every human or animal specimen[1,2]. Using advanced artificial anatomical models has the potential to ease these problems, especially in case of anatomy or surgical education, pre-operative planning, or development of novel medical devices[3,4]. Studies show that the use of physical anatomic models improves medical education from various aspects due to the additional haptic and spatial information students could not receive through books or screen visualizations[5-7]. In the surgical domain, anatomical models can aid the planning of complicated surgeries in a wide range of surgical specialties, since rehearsing the steps of the operation on a patient-specific model can reveal upcoming intra-operative complications[2,8-11]. This can significantly reduce the risk and duration of certain operations, which may result in the lower risk of complication and higher patient satisfaction[12]. Moreover, patient-specific models help the development of various customized implants and other medical instruments[12-14].

Traditionally, artificial anatomical models are mass-produced through casting or molding techniques,

often based on population-averaged geometries[3,13]. The materials used in such models are usually different hard and soft polymers, such as thermoplastics, waxes, or rubbers. With casting and molding techniques, the mechanical properties of various represented tissues can be matched mainly through material selection as these traditional technologies produce fully dense parts. This level of matching is often sufficient for certain mass-produced educational models[6], but the requirements of medical product development and testing, as well as preoperative planning may benefit from a better mechanical fidelity[3,14-17].

1.2. Additive manufacturing (AM) of anatomic models

AM, also called three-dimensional (3D) printing, has become an increasingly influential group of technologies in the field of anatomic models and other medically relevant areas in recent years[12,18,19]. Achieving better geometric and mechanical fidelity is possible with the combination of medical imaging technologies and AM[20]. For polymeric materials, the two dominant groups of AM techniques are based on photopolymerization and on extrusion[3]. In an extrusion-based technique called fused filament fabrication (FFF), a thermoplastic filament is pushed into a heated extruder, and deposited through a nozzle[21]. This is mostly used for bone modeling and mold making in the field of anatomic models[3,9]. FFF is cheaper than most other AM technologies due to its relative simplicity and fierce competition between several manufacturers. These systems can process a large variety of hard thermoplastic filaments but are limited in their ability to handle soft materials. A large proportion of available medical image-based anatomic models are made of hard plastic using FFF[20].

Liquid photopolymers can be deposited and solidified in small droplets via material jetting, which is called inkjet printing (IJP). Among others, it has been used to create surgical training models of aortic aneurysms, kidney tumors, skulls and fetuses[15,22,23]. IJP can also use multi-colored inks to make full-color objects[9,20] and even use multiple hard and soft materials in a single print job[14,16,17,24,25]. The deposited droplets can be understood as voxels. Given the proper printhead, this allows multiple voxels of multiple materials to be deposited simultaneously[26]. While changing or mixing materials in a single droplet generator unit is difficult, IJP can easily achieve anisotropic properties by creating inclusions of various materials[16,17,27], or even seemingly gradient composition change[28]. However, IJP is limited in creating hollow and completely closed cavities because droplets need support underneath them. Therefore, internal structuring is only possible if the support material can be washed or cut out after printing without damaging the printed object. From the standpoint of anatomic models, a relevant IJP printer on the market is the J750 Digital Anatomy Printer by Stratasys Ltd. (Eden Pairie, MI) [24,29]. This offers an outstanding performance concerning geometric representation and the number of materials and colors used, including soft materials[30,31]. However, the mechanical realism of soft tissue representing materials is still criticized[15].

Using soft materials is an intensely researched direction of AM[32]. Besides IJP, thermoset, photoreactive or chemically cured materials like certain silicones, resins or hydrogels may be deposited through extrusion as well, which is also called direct ink writing (DIW)[3,33-35]. This is used to print models of various soft structures[3,36-38]. Most of these operate with pressurized material reservoirs with controllable valves or syringe extruders to deposit soft materials. The rheological properties of the printed material, such as viscosity or thixotropy, are decisive for maintaining the shape of the printed object. Creating closed air inclusions is theoretically possible with FFF and certain DIW techniques[20].

Silicone rubbers offer a range of mechanical properties that may be ideal to represent soft tissues in anatomic models[33]. Certain silicone AM (SAM) technologies are already being applied to anatomical models in some research endeavors and early-stage commercial services[33,39-47]. These are summarized in **Table 1**. The collaboration of Wacker Chemie AG (Munich, Germany) with ACEO (Burghausen, Germany) led to a droplet-based silicone printing technology, which relies on curing each layer of silicone with UV light, in a similar fashion to IJP[39,48]. Dow Inc. (Midland, MI) and German RepRap GmbH (Feldkirchen, Germany) created an extrusion-based technology called Liquid AM (LAM) which deposits silicone with extrusion and cures it layer-wise using a heat source[40,49]. Another SAM process is

Table 1. Summary of relevant commercial soft material printing technologies

Group name	Process name	Principle	Material
Stratasys Ltd.	J750	Droplet jetting	Photopolymers
Wacker Chemie AG	ACEO	Droplet jetting	Silicone rubbers
Dow Inc./GermanRepRap GmbH	LAM	Extrusion	Silicone rubbers
Fripp Design Ltd.	Picsima	Extrusion	Silicone rubbers
Spectroplast AG	Spectroplast	Vat photo-polymerization	Silicone rubbers

developed by Spectroplast AG (Zürich, Switzerland), a spinoff company of ETH Zürich. This method uses layer-wise photopolymerization in a liquid silicone bath[43]. Another method called Picsima by Fripp Design Ltd. (Rotherham, UK) represents a different bath-based printing approach, namely extruding the catalyst component of a two-part silicone into a bath of the base component[41]. SAM may also utilize a non-planar coordinate system. Coulter *et al*. developed a printing method specialized on rotating printing surfaces, which offers unique advantages in realizing certain geometries[44,45]. Despite the promising development that these technologies represent, almost all focus on single-material printing. Therefore, the capabilities to tune mechanical properties are limited to realizing porous structures with internal cavities[32].

1.3. Problems in mechanical realism

These AM technologies (IJP, FFF, and DIW) are highly applicable to create personalized anatomic models that are geometrically unique[3]. However, geometric or color fidelity alone do not satisfy all possible needs of medical device development, surgical education, or preoperative planning. For more advanced applications, models should behave realistically under physical manipulation with hands or surgical instruments[20]. To achieve such surgical realism, the materials used to represent various biological tissues need to have similar mechanical properties to the tissues, such as density, elastic modulus, hardness, tensile strength, or viscoelasticity[15-17]. While matching hard tissues like bone with AM is already a mature field, there are still many unsolved problems regarding soft tissues[20]. Most biological tissues – unlike technical materials – exhibit multi-level hierarchic structures of various functional building blocks, which often results in anisotropic and viscoelastic mechanical properties[15,50]. This behavior could be approximated with soft-hard multi-material structures[14,16,17], but to date, there are no AM technologies available that can approximate a multitude of tissues[15]. Therefore, two major areas for improvement could be printing both hard and soft materials simultaneously, and tuning local mechanical properties through multi-material structuring. These should happen simultaneously to produce high quality anatomic models that resemble real tissues from a mechanical standpoint[15].

1.4. Research aims

Combining extrusion-based AM technologies such as FFF and DIW may be helpful for making more realistic anatomic models. While using FFF to produce the whole model is ineffective regarding mechanical realism, thermoplastics may be used as fiber reinforcement if printed into a softer matrix material, like a silicone rubber that is deposited by a DIW printhead. Such a concept may also work with having both the soft matrix and a harder reinforcement being deposited through DIW[51]. In any case, this strategy would allow the hardening, toughening (further referred to as "up-tuning") of bulk mechanical properties compared to the original matrix material. Since both FFF and extrusion-based DIW can print closed and empty cavities, the weakening, and softening (further referred to as "down-tuning") of mechanical properties would also be possible[15].

Therefore, the main aim of this research was to design, build and test a 3D printer based on the concept of combining hard and soft materials for printing more realistic anatomic models. As a proof of concept, the printer should be capable of printing at least one soft and one hard material, and thus achieve both up-tuning and down-tuning to influence mechanical properties. Moreover, the printer should also realize thin-walled structures and closed internal cavities with the soft material since these are relevant features in anatomic models. In this study, a 3D printer with these features was built, and its abilities were evaluated through qualitative analysis of various printed proof-of-concept objects, including a small ribcage model based on a medical image. The applicability of the system in the field of anatomic models and the future direction of research are also discussed.

2. Materials and methods

2.1. Technology definition

The design process of this novel AM system started with a comparison of various AM technologies and their specifications, as clarifying differences is critical for choosing the right printing concept. The fact that IJP, DIW, and FFF can handle different materials in the same print is a required feature to produce multi-material structures. Other technologies based on material jetting or vat photopolymerization, such as binder jetting (BJ), stereolithography (SLA), and digital light processing (DLP) all use a single-material bath (or "vat") of liquid resin or powder[21]. This prevents multi-material printing, and the creation of closed air inclusions. For IJP, DIW, and FFF, changing materials simply requires switching to a different filament, cartridge, or printhead. Mimicking the macroscopic mechanical properties of biological tissues through up- and down-tuning requires printing both soft and hard materials. Extrusion is the preferred method to create closed internal cavities and support structures, if needed. The mentioned technologies are compared considering our construction preferences in **Table 2**. Further descriptions and schematics of these technologies are available in other literature[21,32].

Table 2. A survey of features considering various additive manufacturing technologies

Technology	Principle	Soft materials	Multi-material	Material deposition	Support structures	Closed cavities
SLS	Powder bed fusion	Limited	No	Spreading	Powder or printed	No
BJ	Material jetting	Limited	No	Spreading and droplets	Powder or printed	No
IJP	Material jetting	Yes	Yes	Droplets	Printed	Limited
SLA	Vat photo-polymerization	Limited	No	Spreading	Liquid or printed	No
DLP	Vat photo-polymerization	Limited	No	Spreading	Liquid or printed	No
FFF	Extrusion	Limited	Yes	Heated extrusion	Printed	Yes
DIW	Extrusion	Yes	Yes	Extrusion or droplets	Liquid or printed	Yes
*Ideal for anatomic models	Extrusion	Yes	Yes	Extrusion	Printed	Yes

*An imaginary technology which we found ideal for anatomic models if mechanical realism is desirable.

Concerning the printing material, some silicone rubbers exhibit ideal mechanical properties to mimic various soft tissues. This also makes them a popular casting material for certain anatomic models, where a casting mold of the desired anatomy is first printed with FFF or SLA, and then filled with a two-component addition-cured silicone rubber[7,9]. However, in multi-material printing, the adhesion of the various printing materials is important, unlike in casting. Certain single-component condensation-cured silicone rubbers may exhibit an adhesive behavior to some thermoplastic polymer materials, which makes these a promising combination in a multi-material printing scenario. Therefore, the printer should employ an FFF printhead for printing thermoplastics, and a continuous extrusion-based DIW printhead to print single-component silicone rubbers.

2.2. Printer system

For an extrusion-based DIW printhead, various extrusion mechanisms, such as syringes, peristaltic pumps and screw extruders, are available. However, for high-viscosity and high-precision applications, screw extruders were preferred. The final choice fell on a Vipro-HEAD 3/3 two-component printhead by Viscotec GmbH (Töging am Inn, Germany)[52], which enables processing either one or two single-component silicones, or a two-component silicone. In this study, only one single-component silicone rubber was used.

Regarding printer mechanics from the standpoint of printing soft and flexible materials, it is important that the building platform only moves in the axis of the building direction (usually labeled "Z"), so that it does not shake the printed objects horizontally during printing. The printer kinematics which fulfills this criterion are the so-called XY-Core and the Delta kinematics. Hardware and software formed another important aspect in the component selection. An FFF printer which does not only apply Delta or XY-Core kinematics, but also employs a control board that is open-source and easily extended with the chosen Viscotec extruder was considered highly desirable.

Finally, a Railcore II 300 ZL open-source FFF 3D printer system[53] was chosen and modified (**Figure 1**). On this printer, the original E3D V6 FFF printhead was extended with the Viscotec Vipro-HEAD 3/3 (**Figure 2**)[52]. Silicones and other high-viscosity materials can be fed into this screw extruder with pressurized air up to 6 bars, from 55 mL cartridges, which are also mounted on the printhead. If necessary, these can be moved to the frame, which removes their volume and mass limitations, enabling a large material supply to the printhead given that the feed pressure is sufficient. The silicone printing nozzle is connected to the outlet of the extruder through a Luer-thread and is secured against unscrewing with a retainer part. These white Luer-adapters and retainers were custom-made for the extruder (**Figure 2A**). A nozzle with 0.33 mm outlet diameter was selected for silicone extrusion. The original E3D V6 FFF printhead on the other side of the carriage (**Figure 2B**) is capable of melting and depositing thermoplastic filaments through a 0.4 mm diameter nozzle.

The printer is controlled by the Duet 2 Wi-Fi control electronics, extended with a Duex 5 extension board, operating with RepRap v1.18 firmware[54]. The system can be connected to a personal computer (PC) through a Wi-Fi network, and print jobs can be started through the Duet Web Interface, which is accessible through an internet browser running on the PC. The general printer configuration, including the printhead definitions and dosing calibration settings are done by modifying a file stored on the Duet 2 Wi-Fi board. The slicing software used to generate G-codes for printing objects is Prusa Slicer (version 2.1), an open-source slicer originally made for filament-based printers[55]. The user can easily

define a multi-material printhead and generate G-codes for multi-material FFF-DIW print jobs. No post-processing of the generated G-code files is necessary, and an extrusion correction factor can also be set to fine-tune dosing accuracy, when necessary. To start a print job, the generated G-code files must be uploaded to the Duet 2 Wi-Fi board through the Duet Web Interface. This way, the printer is likely also compatible with other popular slicing software, such as Cura or Simplify3D.

2.3. Materials

The selected silicone material is a high-viscosity single-component condensation-crosslinking liquid silicone rubber called Elkem AMSil 20101 (Elkem Silicones, Oslo, Norway), which was used with the Viscotec DIW printhead. This material is intended for cold extrusion; therefore, no heating or other means of energy input is required during printing. Moreover, a 1.75 mm diameter poly-lactic acid (PLA) filament from Fillamentum Manufacturing (Hulín, Czech Republic) was used with the E3D V6 FFF printhead in case of prints that demonstrate the multi-material capabilities. PLA was chosen as it is an easily accessible and popular FFF material.

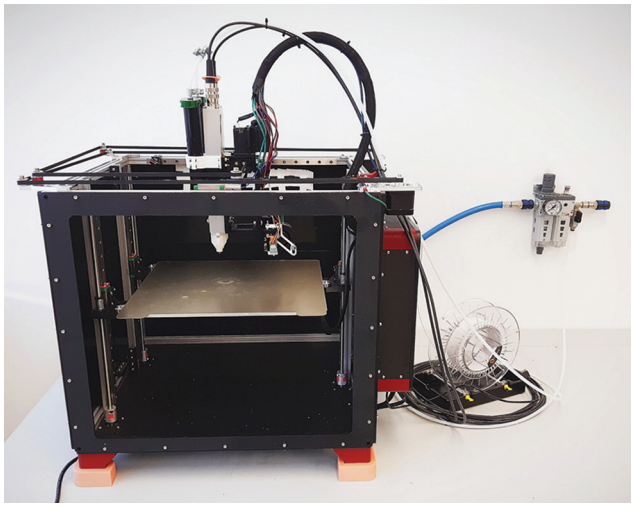

Figure 1. The modified Railcore II 300 ZL printer, extended with a Viscotec Vipro-HEAD 3/3 extruder.

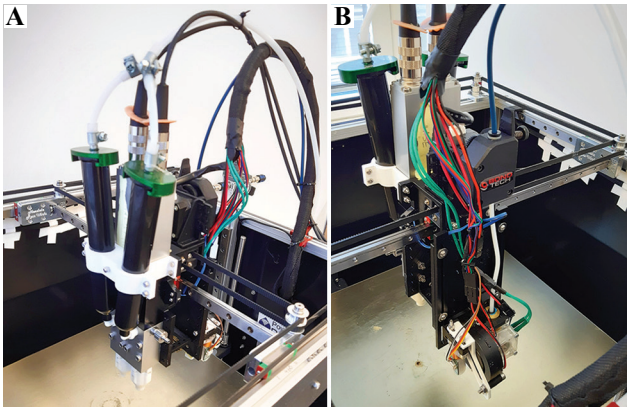

Figure 2. The Viscotec Vipro-HEAD 3/3 extruder with custom Luer-compatible endpieces (A), and the original E3D V6 filament extruder on the opposite side of the printhead carriage (B).

2.4. Printing tests

For accurate dosing, the silicone printhead was calibrated for the chosen material using a KERN PES 42002M scale (Kern & Sohn GmbH, Balingen, Germany). After this, 15 × 15 × 10 mm silicone blocks were printed with various speeds and layer thicknesses to find reasonable settings for further printing tests. The integrity of the printed cubes was qualitatively evaluated by observing them and then slicing them with a blade to see if there are any internal faults (**Figure 3**).

Based on the calibration prints, a printing speed of 15 mm/s and a layer thickness of 0.3 mm were chosen for further trials. Furthermore, every printed object was left on the building platform untouched for 24 h to ensure sufficient crosslinking before any manipulation or inspection. After calibration, the system's ability to print silicone objects with closed internal cavities, infill structuring and thin walls as well as to combine silicone DIW and thermoplastic FFF was assessed by conducting six printing tests:

1. In the first test, a thin-walled shell was printed based on the same 15 × 15 × 10 mm cuboid that was used for the calibrations. In this case, only two lines of outer contour were used, resulting in approximately 0.7 mm shell wall thickness (**Figure 4**). This is relevant to anatomic models in case of printing vessels or membranes, which feature thin walls.
2. The second test involved a silicone block of the same dimensions as in the first test, but with 40% volume fraction gyroid infill structuring to simulate down-tuning (**Figure 5**).

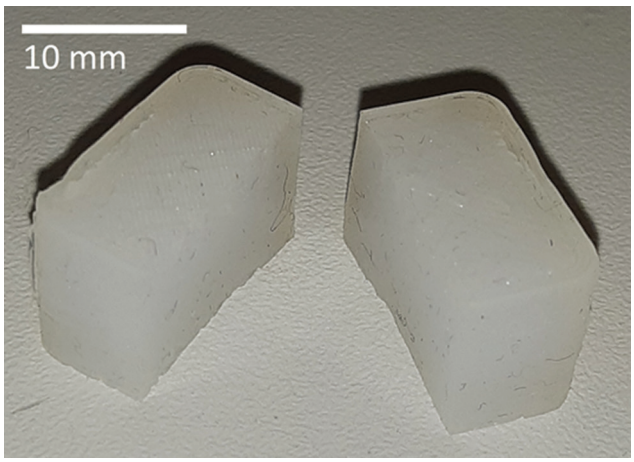

Figure 3. A 15 × 15 × 10 mm test block that was printed after calibration and cut in half after printing.

3. In the third test, a 50% downscaled version of a human bladder was printed based on a 3D model segmented from a computed tomography (CT) image earlier. To test the feasibility of such a large internal cavity with overhanging areas, no support was used inside. The envelope dimensions of this downscaled bladder were approximately 35 × 30 × 25 mm, and the wall thickness was changing between 1.5 and 2 mm (**Figure 6**).
4. The fourth test involved a pair 15 × 15 × 3 mm square silicone and PLA multi-material chips on top of each other. The silicone was printed on top of the PLA to simulate a situation of printing hard plastic support under a silicone structure (**Figure 7A**).
5. In the fifth test, the same model was used as in the fourth test, but now the PLA was printed on top of the silicone to simulate laying the filament as an inclusion into the silicone matrix (**Figure 7B**).
6. The sixth test was planned to give some synthesis of the features investigated through the previous tests. The ribcage and the surrounding soft tissues were segmented from the CT image of a newborn using 3D-Slicer, and the model was printed (**Figure 8**). The ribs and the support structures were printed from PLA and the surrounding soft tissue was printed from silicone. To mimic bone structure, the ribs were printed with a 30% gyroid infill, while 80% infill was used for the soft tissue.

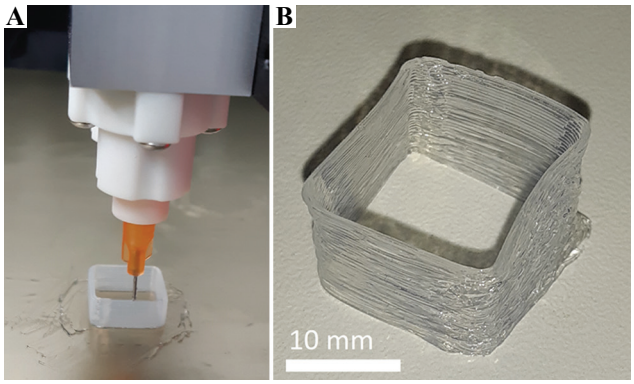

Figure 4. Thin-walled silicone rubber shell during (A) and after printing (B).

3. Results

All test objects were successfully printed. The thin-walled shell of the first test (**Figure 4**) did not collapse during or after printing, despite having only 0.7 mm wall thickness.

The 40% gyroid block of the second test (**Figure 5**) was cut in half with a blade after crosslinking to reveal the internal structure (**Figure 5C**).

The downscaled bladder in the third test (**Figure 6**) had minor material integrity errors at the top due to the

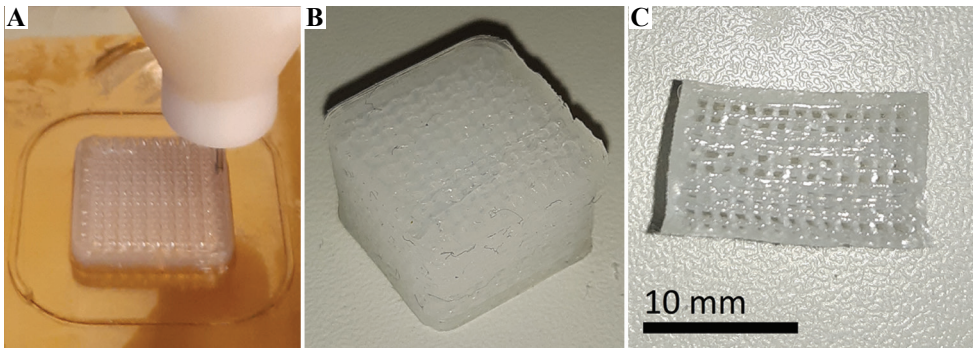

Figure 5. Silicone block with 40% volume fraction gyroid infill during (A) and after printing (B), and after slicing with a blade (C) to reveal the internal structure.

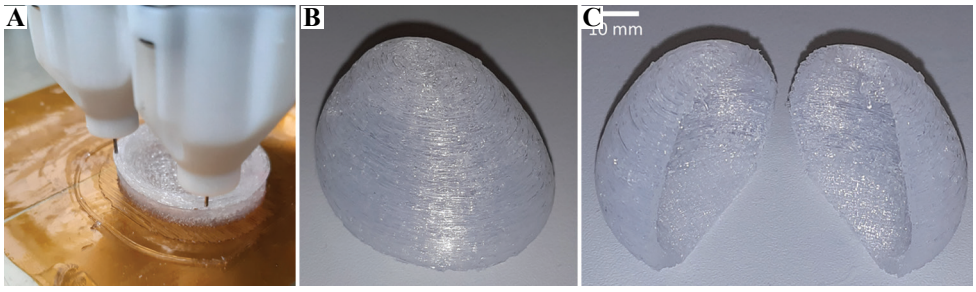

Figure 6. A downscaled human bladder with no internal support during (A) and after printing (B), and after slicing with a blade (C) to reveal the internal cavity.

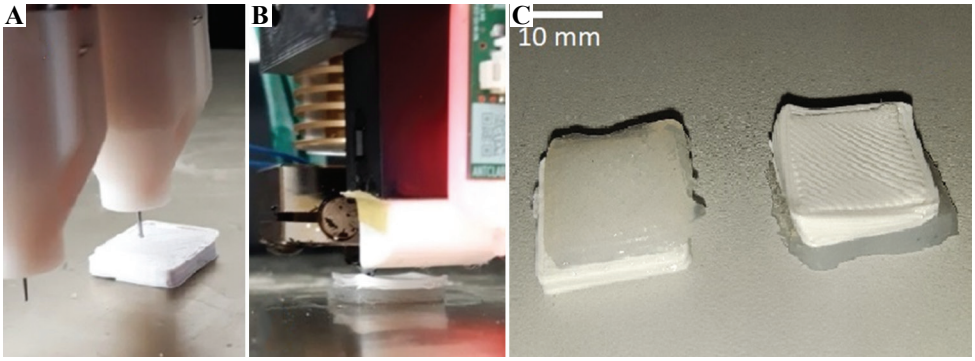

Figure 7. Printing silicone rubber on top of PLA (A), then PLA on top of silicone rubber (B), and the resulting multi-material chips from both tests (C) .

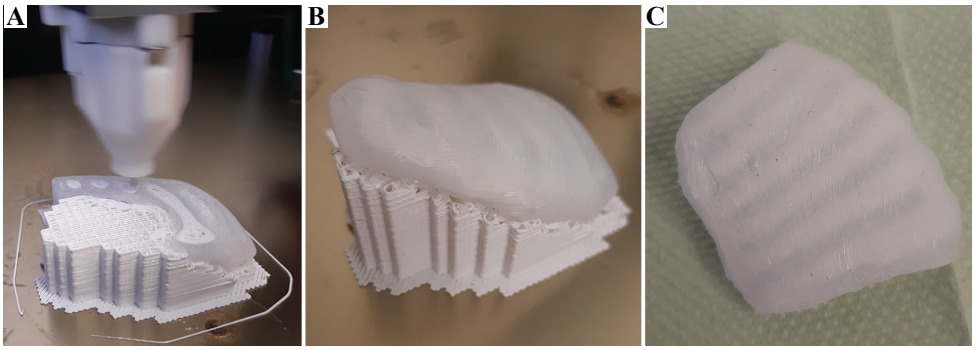

Figure 8. Silicone-PLA multi-material ribcage model based on a medical image of a newborn during printing (A), with support after printing (B), and after support removal (C).

lack of internal support, but the external geometry stayed intact. This bladder was also cut in half after printing to reveal the internal cavity (**Figure 6C**).

The multi-material chips from the fourth (**Figure 7C**) and fifth (**Figure 7B**) tests were also printable. Moreover, in case of the fifth test, the PLA top was deformed, presumably due to printing on a soft and unstable silicone surface. After printing, the adhesion between the silicone and the PLA in the multi-material chips was evaluated by trying to manually separate the materials. The silicone was considered adhesive enough to resist this manual peeling, since the bulk silicone material was damaged before the interface.

After seeing the success of the five previous tests, the ribcage model of the sixth test was printed to demonstrate the applicability of the printer to produce medical image-based anatomic models (**Figure 8**). No complications were experienced during the printing process, although the manual removal of the support structures was challenging due to the adhesion between the silicone and the PLA.

4. Discussion

4.1. Overview of aims and results

The aim of this study was to build and test a 3D printer that enables features necessary for producing more realistic anatomic models in the future. The specifications stemming from this goal were printing multi-material structures out of at least one hard and one soft material, while also being capable of printing empty cavities, infill structures and thin-walled features. Considering the advantages and drawbacks of various AM methods and their applicable materials, a printer was built that combines FFF and DIW technologies to print with a single-component silicone rubber and a thermoplastic PLA filament.

The printing trials demonstrated that the established technology is capable of printing objects of both materials and can print silicone with a weakened internal structure (down-tuning) or combine silicone with PLA (up-tuning). An unsupported internal cavity and a thin-walled structure were also printable with the silicone. It was shown that the FFF printhead can create hard support structures. The strong adhesion between the PLA and the silicone that was experienced during the tests suggests that this material combination can be applied to create more complex multi-material structures, and that the silicone must be cut away from the PLA in case of using PLA for printing support structures under the silicone. These assumptions were confirmed through the last test, where the ribcage was indeed printable with PLA support and sufficient adhesion between the silicone and the PLA.

These promising outcomes imply that the technology could be used to approximate the mechanical properties

of various soft biological tissues through up- and down-tuning strategies. Using the other half of the Viscotec printhead as a third extruder, the system could easily be extended to introduce a viscous fluid into printed internal cavities. Such a method used in parallel with up- and down-tuning strategies could possibly increase viscoelasticity[15] in anatomic models. This means that with the further development of our technology, a significant increase in anatomic model realism may be delivered, accelerating the development of certain medical instruments and improve medical education and preoperative planning.

4.2. Comparison with other technologies

From the perspective of down-tuning, the greatest limitation of concurrent technologies such as IJP, BJ, SLA, and DLP is their difficulty to realize completely closed and empty cavities, either because of an inherent need for support (IJP) or because of a leveled slurry or powder bath (BJ, SLA, DLP)[21]. This also applies to the Picsima silicone printing process[41], as well as the technology used by Wacker and ACEO[39], and by Spectroplast[43]. In our case, this limitation is overcome by utilizing extrusion-based DIW and FFF, even though the LAM process of Dow and GermanRepRap[40] is also free of this problem.

Considering up-tuning, IJP has a better resolution and a larger variety of applicable materials than our presented technology[14,16,17]. Our process can use up to three materials and can be extended to handle two more without changing the electronics. The LAM process of Dow and GermanRepRap[40] along with the one of Wacker and ACEO[39] could theoretically also be extended to work with multiple materials. Meanwhile, the other methods (BJ, SLA, DLP, Picsima, and Spectroplast) are more confined to single material printing[21,41,43].

The various available IJP printer models from Stratasys (including the J750 dedicated for anatomic models)[24] are frequently used in literature for producing soft multi-material tissue models[15-17]. However, the biological realism of the materials that are printable with these printers is often criticized, and IJP technologies are inherently limited in terms of printing unsupported overhangs. We have demonstrated that our system can print steeply overhanging structures, which (combined with other relevant features) may enable more accurate tissue approximation than what is possible with IJP systems.

Differentiating our system from other self-built silicone rubber printers, we can note that some are specialized on printing on curved surfaces[44,45], while others use two-component silicones on a heated building platform[46,47] and do not feature additional printheads for thermoplastics or other fluids.

4.3. Limitations and outlook

In case of DIW and FFF, spatial resolution, printing quality, and printing speed are tightly connected process parameters; therefore, the presented technology is slow compared to the shower-like droplet generation of IJP or BJ, or the scanning laser or full-layer projector of SLA or DLP. Moreover, despite the successful first prints, the system suffers from certain other limitations in its current state. If used in more complex geometries, the removal of PLA supports might damage the contact surface of the silicone. This adverse effect may be minimized by careful support design in the future. The difficulties with removing the silicone parts from the building platform may be eased by choosing a different printing surface. It must also be pointed out that the printing abilities were only demonstrated with one silicone and one thermoplastic material, and the general applicability to other materials is so far untested.

A decisive factor in the compatibility of a silicone-thermoplastic combination is the adhesion between them. Qualitatively testing the adhesion strength between the silicone and PLA or other thermoplastics remains an interesting direction for further research, along with the qualitative testing of the effects of infill structuring on the mechanical properties of silicone objects. Finally, the extent of applicability to the field of anatomic models depends not only on mechanical property tuning but also on geometric limitations. To succeed at printing complex anatomic geometries, an optimization method should first be developed to find the ideal printing parameters. This may be done in a follow-up study by printing various basic features at different printing settings and then analyzing the integrity and accuracy of the printed features. In addition, using the other available DIW extruder to deposit a high-viscosity filler liquid into internal cavities may provide a way to modify viscoelastic mechanical properties.

5. Conclusions

In this study, a novel multi-material AM technology targeted at facilitating the production of more realistic anatomical models was established and tested. The printable features enabled by this technology offer promising possibilities in the field of functional anatomic models. Analyzing geometric limitations, along with an evaluation of feasible mechanical properties, are needed before this technology could make a significant impact in the field of medical education, device testing, and pre-operative planning. However, a medical image-based anatomic model was already successfully printed in this study, implying a long-term applicability for the presented system. Moreover, besides anatomic models, the system may also have potential applications in the

field of soft robotics, wearable electronic devices, or sports equipment.

Funding

This work was supported by the Provincial Government of Lower Austria (Land Niederösterreich) under grant assignment number WST3-F2-528983/005-2018.

Conflicts of interest

Concerning the manufacturing technology described in Materials and Methods subsections 2.1, 2.2 and 2.3, a patent application has been filed by the Austrian Center for Medical Innovation and Technology (ACMIT Gmbh) at the European Patent Office under applicant reference number 51241. The inventors are Laszlo Jaksa, Andrea Lorenz and Dieter Pahr.

Author contributions

L. J. designing and assembling the 3D-printer, conducting all tests, writing the manuscript D. P. consulting and supervising the design and publication processes G. K. consulting and supervising the design and publication processes A. L. consulting and supervising the design, assembly, testing and publication processes, managing component procurement and research budget.

References

1. Ventola CL, 2014, Medical Applications for 3D Printing: Current and Projected Uses. *P T*, 39:704–11.
2. Rengier F, Mehndiratta A, von Tengg-Kobligk H, *et al*., 2010, 3D Printing Based on Imaging Data: Review of Medical Applications. *Int J Comput Assist Radiol Surg*, 5:335–41. https://doi.org/10.1007/s11548-010-0476-x
3. Wang K, Ho CC, Zhang C, *et al*., 2017, A Review on the 3D Printing of Functional Structures for Medical Phantoms and Regenerated Tissue and Organ Applications. *Engineering*, 3:653–62. https://doi.org/10.1016/j.eng.2017.05.013
4. Pietrabissa A, Marconi S, Negrello E, *et al*., 2019, An Overview on 3D Printing for Abdominal Surgery. *Surg Endosc*, 34(1):1–13. https://doi.org/10.1007/s00464-019-07155-5
5. Preece D, Williams SB, Lam R, *et al*., 2013, Let's Get Physical: Advantages of a Physical Model Over 3D Computer Models and Textbooks in Learning Imaging Anatomy. *Anat Sci Educ*., 6:216–24. https://doi.org/10.1002/ase.1345
6. Khot Z, Quinlan K, Norman GR, *et al*., 2013, The Relative Effectiveness of Computer-based and Traditional Resources for Education in Anatomy. *Anat Sci Educ*., 6:211–5.
7. Sulaiman A, Boussel L, Taconnet F, *et al*., 2008, *In vitro* Non-rigid Life-size Model of Aortic Arch Aneurysm for Endovascular Prosthesis Assessment. *Eur J Cardiothorac Surg*, 33:53–7. https://doi.org/10.1016/j.ejcts.2007.10.016
8. Giesel FL, Hart AR, Hahn HK, *et al*., 2009, 3D Reconstructions of the Cerebral Ventricles and Volume Quantification in Children with Brain Malformations. *Acad Radiol*, 16:610–7. https://doi.org/10.1016/j.acra.2008.11.010
9. Golab A, Smektala T, Kaczmarek K, *et al*., 2017, Laparoscopic Partial Nephrectomy Supported by Training Involving Personalized Silicone Replica Poured in Three-Dimensional Printed Casting Mold. *J Laparoendosc Adv Surg Tech A*, 27:420–2. https://doi.org/10.1089/lap.2016.0596
10. Mavili ME, Canter HI, Sağlam-Aydinatay B, *et al*., 2007, Use of Three-Dimensional Medical Modeling Methods for Precise Planning of Orthognathic Surgery. *J Craniofac Surg*, 18:740–7. https://doi.org/10.1097/scs.0b013e318069014f
11. Poukens J, Haex J, Riediger D, 2003, The Use of Rapid Prototyping in the Preoperative Planning of Distraction Osteogenesis of the Cranio-maxillofacial Skeleton. *Comput Aided Surg*, 8:146–54. https://doi.org/10.3109/10929080309146049
12. Tack P, Victor J, Gemmel P, *et al*., 2016, 3D-Printing Techniques in a Medical Setting: A Systematic Literature Review. *Biomed Eng Online*, 15:115. https://doi.org/10.1186/s12938-016-0236-4
13. Yan Q, Dong H, Su J, *et al*., 2018, A Review of 3D Printing Technology for Medical Applications. *Engineering*, 4:729–42.
14. Qian Z, Wang K, Liu S, *et al*., 2017, Quantitative Prediction of Paravalvular Leak in Transcatheter Aortic Valve Replacement Based on Tissue-Mimicking 3D Printing. *JACC Cardiovasc Imaging*, 10:719–31. https://doi.org/10.1016/j.jcmg.2017.04.005
15. Ratinam R, Quayle M, Crock J, *et al*., 2019, Challenges in Creating Dissectible Anatomical 3D Prints for Surgical Teaching. *J Anat*, 234:419–37. https://doi.org/10.1111/joa.12934
16. Wang K, Wu C, Qian Z, *et al*., 2016, Dual-material 3D Printed Metamaterials with Tunable Mechanical Properties for Patient-specific Tissue-mimicking Phantoms. *Addit Manuf*, 12:31–7. https://doi.org/10.1016/j.addma.2016.06.006

17. Wang K, Zhao Y, Chang YH, *et al*., 2016, Controlling the Mechanical Behavior of Dual-material 3D Printed Meta-materials for Patient-specific Tissue-mimicking Phantoms. *Mater Des*, 90:704–12. https://doi.org/10.1016/j.matdes.2015.11.022
18. Goh GL, Zhang H, Chong TH, *et al*., 2021, 3D Printing of Multilayered and Multimaterial Electronics: A Review. *Adv Electron Mater*, 2021:2100445. https://doi.org/10.1002/aelm.202100445
19. Yap YL, Sing SL, Yeong WY, 2020, A Review of 3D Printing Processes and Materials for Soft Robotics. *Rapid Prototyp J*, 26:1345–61. https://doi.org/10.1108/rpj-11-2019-0302
20. Qiu K, Haghiashtiani G, McAlpine MC, 2018, 3D Printed Organ Models for Surgical Applications. *Annu Rev Anal Chem*, 11:287–306. https://doi.org/10.1146/annurev-anchem-061417-125935
21. Ngo TD, Kashani A, Imbalzano G, *et al*., 2018, Additive Manufacturing (3D Printing): A Review of Materials, Methods, Applications and Challenges. *Compos B Eng*, 143:172–96. https://doi.org/10.1016/j.compositesb.2018.02.012
22. Pugliese L, Marconi S, Negrello E, *et al*., 2018, The Clinical Use of 3D Printing in Surgery. *Updates Surg*, 70:381–8. https://doi.org/10.1007/s13304-018-0586-5
23. Dorweiler B, Baqué PE, Chaban R, *et al*., 2021, Quality Control in 3D Printing: Accuracy Analysis of 3D-Printed Models of Patient-Specific Anatomy. *Materials*, 14:1021. https://doi.org/10.3390/ma14041021
24. Stratasys Ltd. Available from: https://stratasys.com/medical/advanced-medical-models. [Last accessed on 2021 Jan 10].
25. Mirzaali MJ, Nava AH, Gunashekar D, *et al*., 2020, Mechanics of Bioinspired Functionally Graded Soft-hard Composites Made by Multi-material 3D Printing. *Composit Struct*, 237:111867. https://doi.org/10.1016/j.compstruct.2020.111867
26. Ionita CN, Mokin M, Varble N, *et al*., 2014, Challenges and Limitations of Patient-specific Vascular Phantom Fabrication Using 3D Polyjet Printing. *Proc SPIE Int Soc Opt Eng*, 9038: 90380M. https://doi.org/10.1117/12.2042266
27. Reiter M, Major Z, 2011, A Combined Experimental and Simulation Approach for Modelling the Mechanical Behaviour of Heterogeneous Materials Using Rapid Prototyped Microcells. *Virtual Phys Prototyp*, 6:111–20. https://doi.org/10.1080/17452759.2011.586949
28. Hiller J, Lipson H, 2010, Tunable Digital Material Properties for 3D Voxel Printers. *Rapid Prototyp J*, 16:241–7. https://doi.org/10.1108/13552541011049252
29. Patent, 2019, Additive Manufacturing of Rubber-like Materials. Patent US2019224914A1.
30. Slesarenko VY, 2017, Towards Mechanical Characterization of Soft Digital Materials for Multimaterial 3D-Printing. *Int J Eng Sci*, 123:62–72. https://doi.org/10.1016/j.ijengsci.2017.11.011
31. Goh GL, Agarwala S, Yong WI, 2016, 3D Printing of Microfludic Sensor for Soft Robots: A Preliminary Study in Design and Fabrication. In: Proceedings of the 2nd International Conference on Progress in Additive Manufacturing (Pro-AM 2016). p177–81.
32. Truby RL, Lewis JA, 2016, Printing Soft Matter in Three Dimensions. Nature, 540:371–8. https://doi.org/10.1038/nature21003
33. Yeo J, Koh J, Wang F, *et al*., 2020, 3D Printing Silicone Materials and Devices. In: Silicon Containing Hybrid Copolymers. Germany: Wiley-VCH Verlag GmbH & Co. KGaA; 2020, p. 239–63. https://doi.org/10.1002/9783527823499.ch9
34. Zhao Y, Yao R, Ouyang L, *et al*., 2014, Three-dimensional Printing of Hela Cells for Cervical Tumor Model *In Vitro*. *Biofabrication*, 6:035001. https://doi.org/10.1088/1758-5082/6/3/035001
35. Lee JM, Sing SL, Yeong WY, 2020, Bioprinting of Multimaterials with Computer-aided Design/Computer-aided Manufacturing. *Int J Bioprint*, 6:245. https://doi.org/10.18063/ijb.v6i1.245
36. Liu W, Zhang YS, Heinrich MA, *et al*., 2016, Rapid Continuous Multimaterial Extrusion Bioprinting. *Adv Mater*, 29:1604630.
37. Hardin JO, Ober TJ, Valentine AD, *et al*., 2015, Microfluidic Printheads for Multimaterial 3D Printing of Viscoelastic Inks. *Adv Mater*, 27:3279–84. https://doi.org/10.1002/adma.201570145
38. Skylar-Scott MA, Mueller J, Visser CW, *et al*., 2019, Voxelated Soft Material Via Multimaterial Multinozzle 3D Printing. *Nature*, 575:330–4. https://doi.org/10.1038/s41586-019-1736-8
39. Wacker Chemie AG, 2021, Avaialble from: https://www.aceo3d.com/3d-printing [Last accessed on 2021 Jan 10].
40. GermanRepRap GmbH, 2021, Avaialble from: https://www.germanreprap.com/material-de/SILASTIC-3D-3335.aspx [Last accessed on 2021 Jan 10].
41. Fripp Design Ltd., 2021, Avaialble from: https://www.picsima.com [Last accessed on 2021 Jan 10].

42. Deltatower GmbH, 2021, Avaialble from: https://www.deltatower.ch/en/home-2 [Last accessed on 2021 Jan 10].
43. Spectroplast AG, 2021, Avaialble from: https://www.spectroplast.com [Last accessed on 2021 Jan 10].
44. Coulter F, 2021, Avaialble from: http://www.fergalcoulter.eu [Last accessed on 2021 Jan 10].
45. Coulter F, Schaffner M, Faber J, *et al*., 2019, Bioinspired Heart Valve Prosthesis Made by Silicone Additive Manufacturing. *Matter*, 1:266–79. https://doi.org/10.1016/j.matt.2019.05.013
46. Luis E, Pan HM, Sing SL, *et al*., 2019, Silicone 3D Printing: Process Optimization, Product Biocompatibility, and Reliability of Silicone Meniscus Implants. *3D Print Addit Manufact*, 6:319–32. https://doi.org/10.1089/3dp.2018.0226
47. Luis E, Pan HM, Sing SL, *et al*., 2020, 3D Direct Printing of Silicone Meniscus Implant Using a Novel Heat-Cured Extrusion-Based Printer. *Polymers*, 12:1031. https://doi.org/10.3390/polym12051031
48. Patent, 2017, 3D-printing Device and Process for Producting an Object with Use of a 3D-Printing Device, Patent WO2017108208A1.
49. Patent, 2017, 3D Printing Method Utilizing Heat-curable Silicone Composition, Patent WO2017040874A1.
50. Studart AR, 2016, Additive Manufacturing of Biologically-inspired Materials. *Chem Soc Rev*, 45:359–76. https://doi.org/10.1039/c5cs00836k
51. Bakarich SE, Gorkin R, Panhuis M, *et al*., 2014, Three-Dimensional Printing Fiber Reinforced Hydrogel Composites. *ACS Appl Mater Interfaces*, 6:15998–16006. https://doi.org/10.1021/am503878d
52. Viscotec GmbH, 2021, Avaialble from: https://www.viscotec.de/produkte/3d-druckkoepfe [Last accessed on 2021 Jan 10].
53. White JS, Akens T, 2021, Avaialble from: https://railcore.org [Last accessed on 2021 Jan 10].
54. Duet3D Advanced 3D Printing Electronics, 2021, Avaialble from: https://www.duet3d.com/DuetWifi [Last accessed on 2021 Jan 10].
55. Prusa Research, 2021, Avaialble from: https://www.prusa3d.com/prusaslicer [Last accessed on 2021 Jan 10].

RESEARCH ARTICLE

Three-Dimensional Printing of Food Foams Stabilized by Hydrocolloids for Hydration in Dysphagia

Amelia Yilin Lee[1,2], Aakanksha Pant[1,2], Kanitthamniyom Pojchanun[2], Cheng Pau Lee[1,3], Jia An[2], Michinao Hashimoto[1,3], U-Xuan Tan[1], Chen Huei Leo[4], Gladys Wong[5], Chee Kai Chua[1], Yi Zhang[2]*

[1]Pillar of Engineering Product Development, Singapore University of Technology and Design, Singapore
[2]Singapore Centre for 3D Printing, School of Mechanical and Aerospace Engineering, Nanyang Technological University, Singapore
[3]SUTD-MIT International Design Centre (IDC), Singapore University of Technology and Design, Singapore
[4]Science, Math and Technology, Singapore University of Technology and Design, Singapore
[5]Department of Nutrition and Dietetics, Khoo Teck Puat Hospital, Singapore

Abstract: Three-dimensional food printing offers the possibility of modifying the structural design, nutrition, and texture of food, which may be used for consumers with special dietary requirements such as dysphagic patients. One of the food matrices that can be used for liquid delivery to dysphagic patients is food foams. Foams are widely used in different food products to adjust food density, rheological properties, and texture. Foams allow the food to stay in the mouth for sufficient time to provide hydration while minimizing the danger of choking. Our work studies the foam properties and printability of both egg white foams and eggless foams with a strong focus on their foaming properties, rheological properties, printability, and suitability for dysphagic patients. Food hydrocolloid, xanthan gum (XG), is added to improve foam stability and rheological properties so that the inks are printable. Rheological and syneresis properties of the pre-printed foam inks are examined. The texture profile and microstructure properties are studied post-printing. International dysphagia diet standardization initiative tests are carried out to assess the inks' potential for dysphagic diets. Inks with XG performed better with minimal water seepage, better foam stability, and excellent printability. This suggests that hydrocolloids lead to more stable food foams that are suitable for 3DFP and safe for hydration delivery to dysphagic patients.

Keywords: Additive manufacturing; 3D food printing; Dysphagia; Hydrocolloids; Food foams' Food inks

*Correspondence to: Yi Zhang, Singapore Centre for 3D Printing, School of Mechanical and Aerospace Engineering, Nanyang Technological University, Singapore; yi_zhang@ntu.edu.sg

Received: May 11, 2021; **Accepted:** June 14, 2021; **Published Online:** July 26, 2021

Citation: Lee AY, Pant A, Pojchanun K, *et al.,* 2021, Three-Dimensional Printing of Food Foams Stabilized by Hydrocolloids for Hydration in Dysphagia. *Int J Bioprint*, 7(4):393. http://doi.org/10.18063/ijb.v7i4.393

1. Introduction

With the introduction of Industry 4.0, additive manufacturing has been growing in focus as it opens up many possibilities for smart production. It has progressed from a mere prototyping tool to a practical manufacturing solution[1,2]. The improvements in design, materials, hardware, and controller software of additive manufacturing printers have resulted in time- and cost-efficient parts, opening up additive manufacturing to various applications for mass customization.

With the advances of three-dimensional (3D) printing technology, many different industries are increasingly utilizing 3D printing for manufacturing, such as aerospace[3], construction[4], dentistry[5], and regenerative medicine[6,7]. In the recent decade, there has been a rising interest in 3D food printing (3DFP)[8,9]. 3DFP provides benefits that include structural design of the food[10], customized nutrition[11], modified food texture[12], and reduced need for skilled cook[13]. For example, it can be used for designing diets for individuals with special nutritional requirements such as dysphagic patients[14] or athletes[15]. 3DFP may also target prosumers such as high-end restaurants in producing aesthetically beautiful meals and products[16].

Foams are a type of food that consists of a liquid or continuous phase in which air bubbles are dispersed[17]. They are widely applied to food products such as ice creams, mousse, and baked goods[18,19]. The primary purposes for foam products are food density and caloric density reduction, modification of texture, and improved rheological properties[20]. Foams are also used to enhance sensory features, such as enhanced texture and flavors of food. More importantly, food foams are used to deliver liquid in a more easy-to-swallow form, especially for dysphagic patients[21]. For example, the aeration of water or milk into foams changes their texture and improves nutrients delivery to dysphagic patients. These foods could stay in the mouth for a certain duration, thereby providing prolonged hydration for dysphagic patients[22].

The main characteristics of food foams are foaming ability, foam stability, and water leakage[23]. The foaming ability dictates how much the volume increases after foaming, and the foam stability measures how long the foam maintains its shape without disintegrating. The water leakage (syneresis) determines the ability of the foam to hold its shape. This provides an early indication if the printed part is able to sustain its shape. The criteria for the ideal ink for food foam should be decently high foaming ability, high foam stability of more than an hour (sufficient time for printing), and low/no syneresis. Foaming ability indicates whether the food matrix is suitable for the creation of food foam. One of the most widely studied food foams is egg white (EW) food foam. It is the most commercially used foaming ingredient due to its high foaming ability and its ability to create an irreversible semi-stable foam[24]. Most of the foam-based food, such as meringues, pavlova, macarons, and mousse, are made from EW food foams[25,26]. 3D printing of EW foam was demonstrated by Kouzani *et al.,* achieved through printing a pavlova using an EW foam-based batter[27]. However, the foam stability and rheological properties, which were key properties to the printability of foams, were not characterized and controlled. Food foams have yet to be studied in depth for 3DFP. Without the characterization of foam properties and rheological properties, it is unclear if these foams are suitable for patients with dysphagia. Therefore, there is a need to study the foam inks for 3DFP.

Foam stability is a unique aspect of food foam that is different from other types of food matrices and strongly influences printability. Unlike other food matrices, the thermodynamic instability causes the disintegration of foams, and it is vital to ensure that the foam remains stable while undergoing printing. Therefore, it is crucial to increase the foam stability for 3DFP purposes with additives such as hydrocolloids[28,29] while ensuring that the texture meets the standard of the dysphagic diet set by the international dysphagia diet standardization initiative (IDDSI) framework. In addition, food foams generally have a lower viscosity, making them harder to print than other food matrices.

In this study, we used EW and alternative food ingredients, Methocel F50 and Foam Magic, which are commercial products available to create food foams. The hydrocolloid included in this study is xanthan gum (XG). XG is a thickener that is commonly used in food products, such as mayonnaise and ice cream[30]. XG provides high viscosity even at low concentrations[31]. Its highly shear-thinning properties[32] make it an ideal choice as a thickener to improve the printability of low-viscosity food foams and enhance the stability of foams[33]. XG was added to the foaming agent to formulate printable food foam inks. The foam properties, such as foaming ability, foam stability, foam density, and syneresis, were studied to provide an in-depth understanding of how the foam properties affect the printability of the respective foam inks. The rheological properties, printability, microstructures, and texture profiles of the food foams were characterized extensively in this study. IDDSI[34] tests were also conducted to examine the suitability of the foam inks for hydration to dysphagic patients.

2. Materials and method

2.1. Formulation of foam inks

The materials used were commercially available pasteurized eggs from a local supermarket (N & N Egg Story, Singapore), Foam Magic from Modernist Pantry (SKU:1214-25), Methocel F50 from Modernist Pantry (SKU:1056-50), XG from Diabetic Food Delivery Singapore - Better4U.sg and Honeydew Extract Powder from RunDeKang BioTechnologies.

For the egg-based foams, the EW were separated from the egg yolks and weighed. They were then beaten using an electronic whip (Kenwood, 800W) for 5 min to foam. 12.5 wt% of honeydew extract powder was then added, and the mixture was whipped for another minute.

For eggless foams, 2 wt% of Foam Magic and/or 2 wt% Methocel F50 were added to water, and the mixture was beaten using an electronic whip for 5 min. Foam Magic is a proprietary formulation of maltodextrin, methylcellulose, and XG designed to create foams when whipped with either a hand blender or iSi whipper. Methocel F50 is a food-grade hydroxyl propyl methylcellulose (HPMC).

The pH of EW is approximately 9.2 in the normal state. The EW used in Inks 1 and 2 were not treated; therefore, Ink 1 has a pH close to pure EW's (**Table 1**). The presence of XG brought down the pH of Ink 2. The pH of XG in an aqueous solution is 7 which brought down the overall pH of the solution. Tap water was used to produce Inks 3 – 5. The pH of tap water was tested to be approximately 8.40. Therefore, the pH of Inks 3 – 5 is approximately similar to that of tap water.

Table 1. Formulation for each foam ink

Sample	Ingredients	pH
Ink 1	• Egg white 87.5 wt% • Honeydew extract 12.5 wt%	9.19
Ink 2	• Egg white 85.5 wt% • Honeydew extract 12.5 wt% • Xanthan gum 2 wt%	8.91
Ink 3	• Methocel F50 2 wt% • Water • Honeydew extract 12.5 wt%	8.33
Ink 4	• Foam Magic 2 wt% • Water • Honeydew extract 12.5 wt%	8.16
Ink 5	• Methocel F50 2 wt% • Foam Magic 2 wt% • Water • Honeydew extract 12.5 wt%	8.20

2.2. Foaming characteristics

(1) Foaming ability

The foams were prepared at room temperature by whipping 50 mL of respective suspensions in a 500-mL beaker using a multi-quick hand blender (Kenwood, 800W) at a constant turbo speed for 5 min. The foaming ability, which is also known as the overrun, is the percentage of volume increase after the whipping process. Three replicates were used for each type of foam, and the averages from the results were reported.

(2) Foam stability

Foam stability was characterized by the half-life of the foam, which was measured as the time required to lose 50% of the volume of the foam. Three replicates of 30 mL of foams were placed in a 50-mL Falcon tube. The volume of the foam was recorded over time to determine the time required for the volume of the foam to reduce to half. Only the volume of the foam, not including the volume of the liquid formed as foams burst, was measured in this study.

(3) Foam density

The foams were prepared as mentioned in part *(1)* of section 2.2. Then, 50 mL of each foam ink was placed in a 50-mL Falcon tube and weighed using an electronic balance. Each ink was measured in three replicates. The average density was calculated by dividing the average mass from the volume of 50 mL.

(4) Syneresis of foam inks

Syneresis was analyzed by placing 0.2 g of the foam ink at the center of a piece of Whatman Grade 4 filter paper. The foams were spread evenly to cover a circle of 1 cm in radius. The filter paper was left to stand for 30 min to allow the liquid to spread before the filter paper was photographed. The area covered by the fluid was measured using a Python program that detects the edge of the foam inks and the edge of the spread fluid. An 1×1 cm^2 red square was included in the photograph as a reference for image analysis. Each sample was carried out in replicates of three.

2.4. Rheological characterization of the foams

The rheological properties of the foam inks were tested using an oscillatory rheometer (Discovery Hybrid Rheometer DHR-3, TA Instruments, Delaware, USA). The measurements were conducted using stainless steel parallel plates with a diameter of 40 mm and a truncation gap of 500 μm. Viscosity shear-thinning tests were performed on the foam inks by applying a stepwise shear ramp rate from 0.001 s^{-1} to 100 s^{-1}. Stress sweep measurements were carried out with a logarithmically increasing shear stress at a constant frequency of 1 Hz from 0.1 to 2000 Pa to study the viscoelastic properties of the inks. A recovery test was done to mimic the three phases the ink experienced – before extrusion, during extrusion, and after extrusion from the nozzle. A multiple stepped flow ramp (peak hold) test was conducted wherein the initial shear rate of 0.1 s^{-1} – 0.2 s^{-1} was applied for 20 s, followed by a rapid increase in shear rate from 0.2 s^{-1} to 200.0 s^{-1} in 1 s. The shear rate was held at 200.0 s^{-1} for 5 s before reducing the shear rate from 200.0 s^{-1} to 0.1 s^{-1} in 1 s and held for 20 s.

2.5. 3D printing of foams

Wiiboox Sweetin 3D Food Printer (Wiiboox, China), an extrusion-based 3D food printer, was used to print the 3D samples of different foam inks. The nozzle size used for these experiments was 1.5 mm. The foams were printed into a six-pointed star with a length and width of 3 cm and a height of 0.5 cm to assess its printability. The star was used to assess if the ink was able to handle sharp curves. Three replicates were printed with each foam ink. Photographs of the printed samples were taken after the printing and assessed visually. The first three prints of the inks were rated visually from 1 (poorest) to 5 (best) on two categories, self-supporting structure and shape, with a maximum total score of 10. The smallest observation for each category was given a score of 1.

The foams were printed at a print speed of 25 mm/s with an initial layer thickness of 0.8 mm and subsequent layer thickness of 1 mm. The fill density was set to 80% with a flow of 80%.

2.6. Scanning electron microscopy (SEM)

The micromorphological structure of the printed parts was observed by using SEM. All samples were gold-

coated with 10 mA current using JEOL JFC-1600 Auto Fine Coater machine. The images were viewed and taken under 10 – 13 kV condition under a JEOL JSM-5600LV SEM.

2.7. Texture profile analysis

Texture Pro CT V1.3 Build 15 (Brookfield Engineering Labs, Inc) was used for double-cycle compression tests to obtain force-time curves. The foams were prepared and filled into a 20-mm deep tray of aluminum foil for testing. Both as-printed and baked foam inks were tested. The baked foam samples were printed and baked at 70°C for 2 h before being tested at the height of 20 mm. The test parameters were as follows: Block probe with a trigger load of 5 g, pre-test, test and return speed at 2.0 mm/s, and the compressive strain was set to 45% for two cycles. Each ink was tested in triplicates. Hardness, chewiness, adhesiveness, gumminess, stringiness, and springiness were measured. The averages of the three replicates were represented in a radar graph. They were also normalized to the highest value obtained among the food inks and represented in another radar graph for ease of comparison.

2.8. Data analysis

Data were plotted by using the OriginLab software. The results were analyzed using unpaired student's *t*-test with $n = 3$. The significance of the results is denoted on top of the columns where * represents $P \leq 0.1$, ** $P \leq 0.01$, *** $P \leq 0.001$, and **** $P \leq 0.0001$. The results were compared within the groups of EW and non-EW inks on whether XG affects the properties of food foams. The first group (EW-based) was compared between Inks 1 and 2, and the second group (HPMC-based) was compared between Ink 3 and Inks 4,5.

3. Results and discussion

3.1. Foam properties

(1) Foaming ability of the inks

Both EW[23] and HPMC[35] are known to have excellent foaming abilities. The overrun quantitatively measures the foaming ability of each foam ink. **Figure 1A** shows that all the food ink formulations can foam more than 300% of their original volume.

Ink 1 is based on EW, and Ink 3 is based on methylcellulose without the addition of hydrocolloids. They were able to foam more than their counterparts with added XG. The inclusion of XG makes the foam denser and more sticky, thus less able to hold more air bubbles. The reduced foaming ability may be attributed to the increase in density, as seen from the difference between Inks 3 and 4. While Ink 5 contains Methocel F50, a component present in Ink 3 which is able to foam to a massive extent of over 700% of its original volume, it has an overrun that is even lower than Ink 4. While inks with XG have reduced overrun, the overall increase in Methocel F50 and Foam Magic mass, contributing to the increase in density that made it difficult to hold the air bubbles without bursting too. The EW foam ink generally has a lower overrun compared to the eggless foams.

(2) Foam stability of the inks

The foam inks' stability is a critical factor as the food inks have to retain the foams after being printed. The viscosity of the continuous fluid phase is one of the main factors affecting foam stability[36]. The higher viscosity of the continuous fluid phase delays the movement of the liquid through the network of films that enclose the air bubble, hence slowing the formation of larger bubbles and the liquid drainage.

As shown in **Figure 1B**, the foam inks without XG have much poorer foam stability. The significant difference in the half-life of foams shows that XG plays an important role in foam stability for both groups (EW and HPMC). Ink 3 with only HPMC is unable to retain the foam for more than 15 min. The poor foam stability is due to the lack of foam stabilizer in the mixture. HPMC generally stabilizes the hydration layer when it is heated and sets into a gel at a specific temperature. However, this ink was prepared at room temperature. Therefore, while it was able to foam, it was unable to retain the foam and stabilize the foam at room temperature. As for the EW-based Ink 1, it has the foam stability of over 80 min. While its stability is not as high as inks that contain XG, it is stable enough to be printed within a certain duration immediately after preparation. EW contains globulins that facilitate foam formation, and also contains ovomucin that stabilizes the foam[37]. During the whipping, the EW proteins adsorb at the interface of air bubbles and the liquid through the hydrophobic areas. The partially unfolded proteins (denatured through whipping) stabilize the protein films formed. The foam collapses when large gas bubbles grow at the expense of tiny bubbles. These films counteract the growth of the large bubbles, thus stabilizing the foam. However, the EW foams, without additives, tend to destabilize too[28].

Inks with the inclusion of XG have a significant improvement in foam stability of more than 1000% in terms of half-life. With the use of Foam Magic which has a proprietary mix of HPMC and XG, Inks 4 and 5 have a foam stability of 158 min and 104 min, respectively. An inclusion of 2 wt% of XG in the EW-based foam allows Ink 2 to have long half-life of 1200 min. XG is widely used as a food thickener. It thickens the inks and retains the liquid phase in foam structures against gravitational force[29]. The fixation of the liquid phase due to the presence of XG makes it harder for small bubbles to grow

into larger bubbles, which stabilize the foams. However, the increase in density also makes it harder for the foams to form, resulting in a lower overrun.

(3) Foam density

The EW foams (Inks 1 and 2) are generally denser than the HPMC foams. The HPMC forms a light foam as a result of the large overrun. The XG increases the density as shown in **Figure 1C**, where there is a slight increase in density from Ink 1 to Ink 2 and from Ink 3 to Ink 4. The density affects the foaming ability inversely; as discussed previously, the overrun is lower when the density is higher. Ink 5 has a higher density than Ink 3 and 4 as it contains more HPMC, thus making it more difficult to be aerated and leading to a denser foam.

(4) Water retention

Syneresis refers to the undesired leakage of water from food. This study investigates the ability of the foam ink to retain water. In the case of foams, the spreading of water affects the integrity of the printed structures, causing the print to spread and collapse due to instability. In this study, the amount of water leakage from the foam inks was obtained by measuring the area wetted on a piece of filter paper.

Inks that do not have XG (Inks 1 and 3) had a large amount of spreading compared to the inks containing XG (**Figure 1D**), and the difference was statistically significant. The spreading was caused by both foam instability and lack of ability to retain water. XG thickened the foams by increasing the viscosity of the liquid phase and forming a hydrogel phase[31]. This prevented water from spreading on the filter paper, greatly reducing water spreading of Inks 2, 4, and 5. Without XG, while Ink 1 had the protein films to hold the air bubbles and water migrated to the filter paper due to strong capillary force. Likewise, for Ink 3, water between the air bubbles migrated from the food ink to the filter paper. Over time, the area of wetting increased when the foam collapsed. For Inks 4 and 5, XG prevented the water from leaking onto the filter paper. Over time, water evaporated, thus resulting in a slight shrinkage of the area of the foam.

3.3. Rheological properties of the inks

All the five inks displayed a shear-thinning or pseudoplastic property **(Figure 2A)**. Shear-thinning properties were preferred for extrusion printing as they suggested that the food ink could be easily extruded and held its shape after extrusion. The printability and self-supporting structure depended on the viscosity and yield stress, respectively[33]. The low viscosity of the inks allowed them to be printed easily through extrusion. When the shear rate increased, the viscosity of the ink decreased, allowing the ink to flow out smoothly. The EW

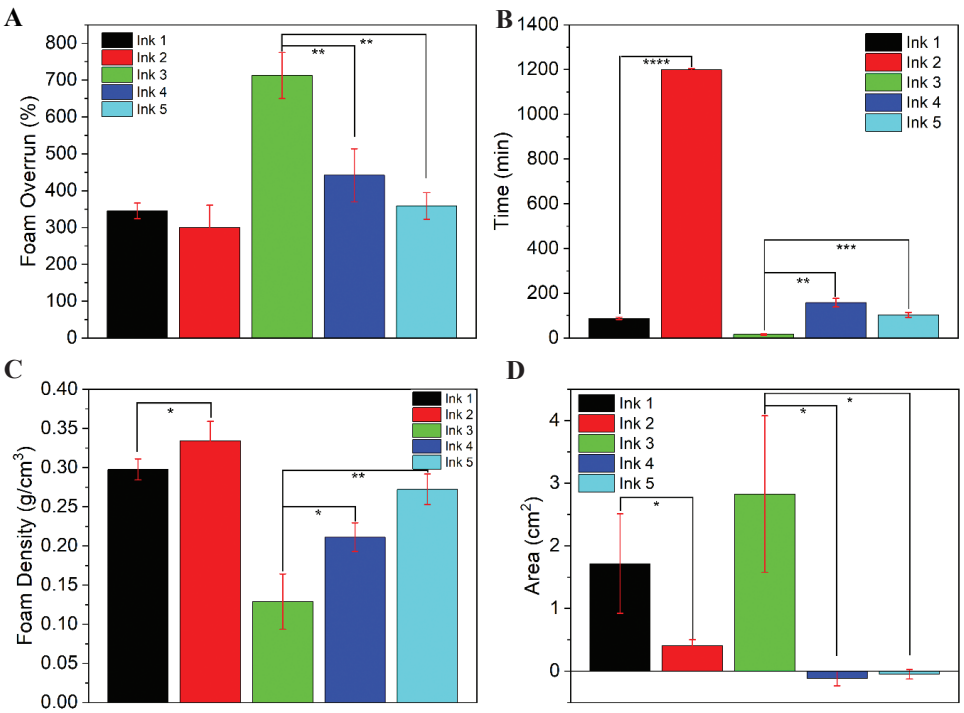

Figure 1. Foam properties (A). The foaming ability of each foam ink based on their overrun. (B) The foam stability of each foam ink. (C) The density of each foam ink. (D) The syneresis results of each ink. *$P \leq 0.1$, **$P \leq 0.01$, ***$P \leq 0.001$, ****$P \leq 0.0001$ for the *t*-test results (n=3).

inks (Inks 1 and 2) had a higher viscosity than the HPMC inks (Inks 3 – 5), which accounted for the slightly better foam stability explained in part *(2)* of Section 3.1. As XG allowed the liquid phase to form a hydrogel-like phase with increased viscosity, Ink 3 had the lowest viscosity compared to the ones with XG. While XG generally increases the viscosity of the foam inks, similar to the comparison between XG containing HPMC inks (Inks 4 and 5) and non-XG containing HPMC ink (Ink 3) the viscosity of Ink 2 was lower than that of Ink 1.

All foams displayed characteristics of linear viscoelasticity at low oscillation frequencies, where storage modulus (G') was higher than loss modulus (G") (**Figure 2B**). Having a G' that was higher than the G" in the linear viscoelastic range also suggests that the ink has the potential to form gel-like self-supporting structure after it was printed[33]. In the non-linear range, the G' fell below G", indicating a more liquid-like behavior. The foams tend to flow like liquids, and are easier to extrude.

The average yield stresses of the inks are displayed in **Figure 2C**. Yield stress determined the ability to form a self-supporting structure[33]. Higher yield stress allowed better self-supporting ability. The EW inks (Inks 1 and 2) have higher yield stresses than the HPMC inks (Inks 3-5). This suggests that they can undergo higher stress before plastic deformation. This allowed Inks 1 and 2 to form better self-supporting structures and higher leniency under the pressure used for the extrusion of the inks during printing. Ink 3 exhibited low yield stress <10 Pa. This suggests that the foam from Ink 3 might not survive the pressure from extrusion printing. Ink 4 has significantly higher yield stress than Ink 3 ($P < 0.01$). XG does not significantly change the yield stress of egg-based foam inks but shows a significant effect in eggless foams. Inks 1 and 5 have significant errors due to the poorer foam stability, which caused some foam to collapse in later tests, changing the rheological properties slightly.

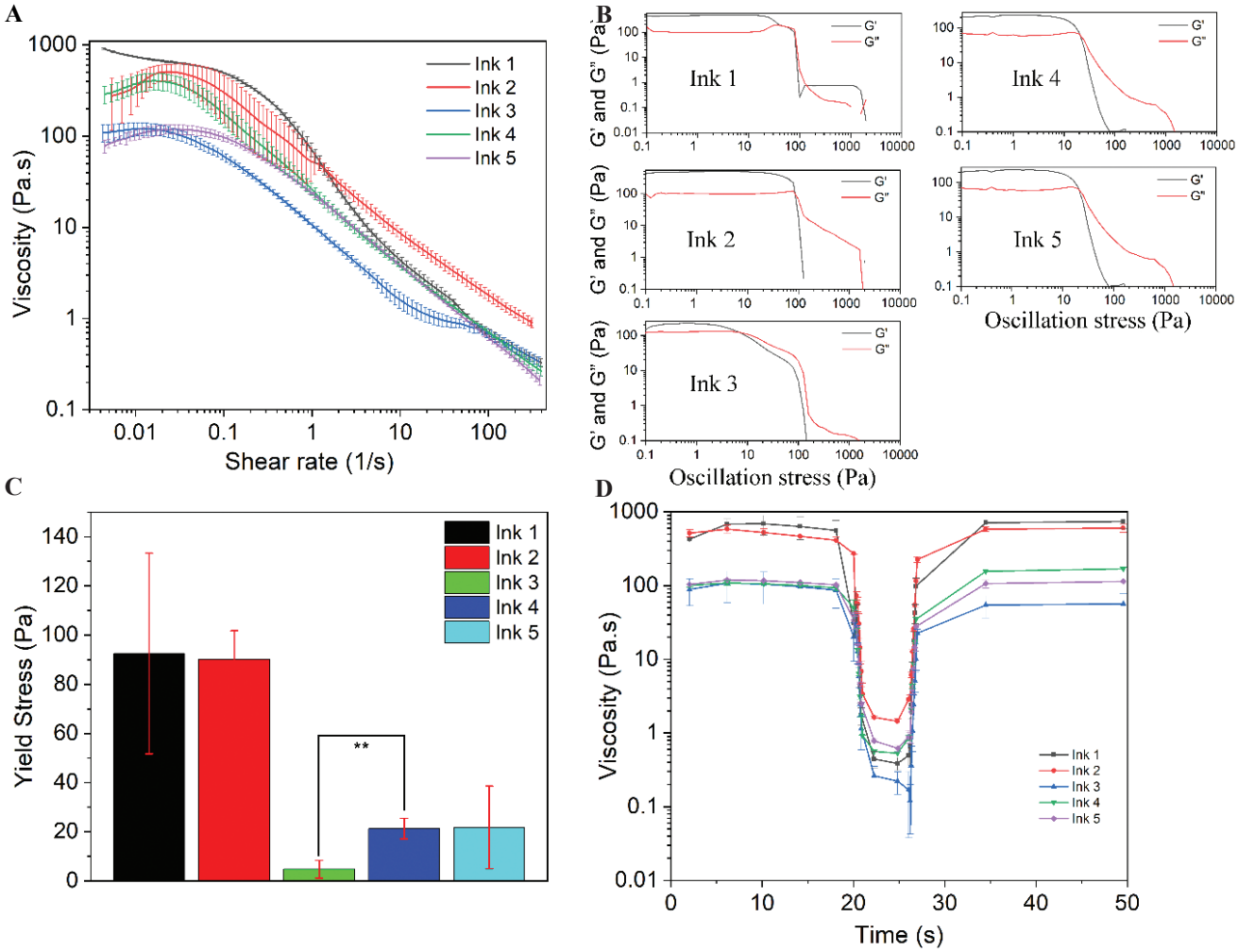

Figure 2. Rheological properties of the foam inks. (A) Flow ramp study of each foam ink. (B) Stress sweep of each ink in triplicates. (C) Yield stress of each foam ink. (D) Peak hold study of each ink simulating before, during, and after extrusion printing. *$P \leq 0.1$, **$P \leq 0.01$, ***$P \leq 0.001$, ****$P \leq 0.0001$ for the *t*-test results ($n = 3$).

Figure 2D shows the peak hold study of the inks. Under low a shear rate from 0.1 to 1 s^{-1}, all the inks gradually reduced their viscosities, which is in line with the flow ramp study that depicts the inks as shear thinning. When the inks experienced a spike in shear rate, the viscosity dropped drastically. This suggests that the viscosities of the foam inks reduced during printing, and inks flowed effortlessly out of the nozzle, allowing smooth printing. Once the shear stress was removed, simulating the shear rate after printing, the viscosities of the inks recovered quickly. This implies that the inks were able to return to their original rheological properties after printing and held their structures.

3.4. Printability of the inks

The printability is dependent on the rheology and the stability of the inks. Out of all the inks, Ink 3 was not printable at all as shown in **Figure 3** where the printed ink was a pool of liquid and it has an average printability score of 2. The foam stability, as described earlier, was very low for Ink 3 as it collapsed too quickly. While in the foam stability test, the half-life of Ink 3 was 15 min under atmospheric pressure, the stability within the syringe and during printing was lower due to significantly higher pressure. Therefore, Ink 3 was extruded as a liquid instead of foams. This was also seen in Ink 1 (**Figure S1**). While it was printable in the first print and was able to form self-support structures, the foam bubbles grew in size in the cartridge and became unstable in the subsequent second and third print. Even though the viscosity of Ink 1 was the highest amongst all the inks, but its stability was not high enough. This was also observed in Ink 5. While the first print was good, it was less able to self-support and spread more in the later prints. The best prints were from Inks 2 and 4 with scores of approximately 9, where they consistently presented good self-supporting structures in three consecutive prints.

The effect of XG on the printability of the inks within the EW and HPMC groups was compared. The first three prints of the inks were rated visually from 1 (poorest) to 5 (best) on two categories, self-supporting structure and shape fidelity. The printability of inks with XG shows significant improvement regardless of the base ingredients. XG is an important factor to achieve a good printable structure for the foam inks.

3.5. Microstructure of the baked inks

The scanning electron micrographs in **Figure 4** show the microstructure of the EW foams and the HPMC foams. Only the printable inks (*i.e.* Inks 1, 2, 4, and 5) were assessed. The pure EW or Foam Magic only foam samples were included for comparison.

Comparing the foam formed by EW and by Foam Magic only (**Figure 4A** & **D**), the EW foam had a

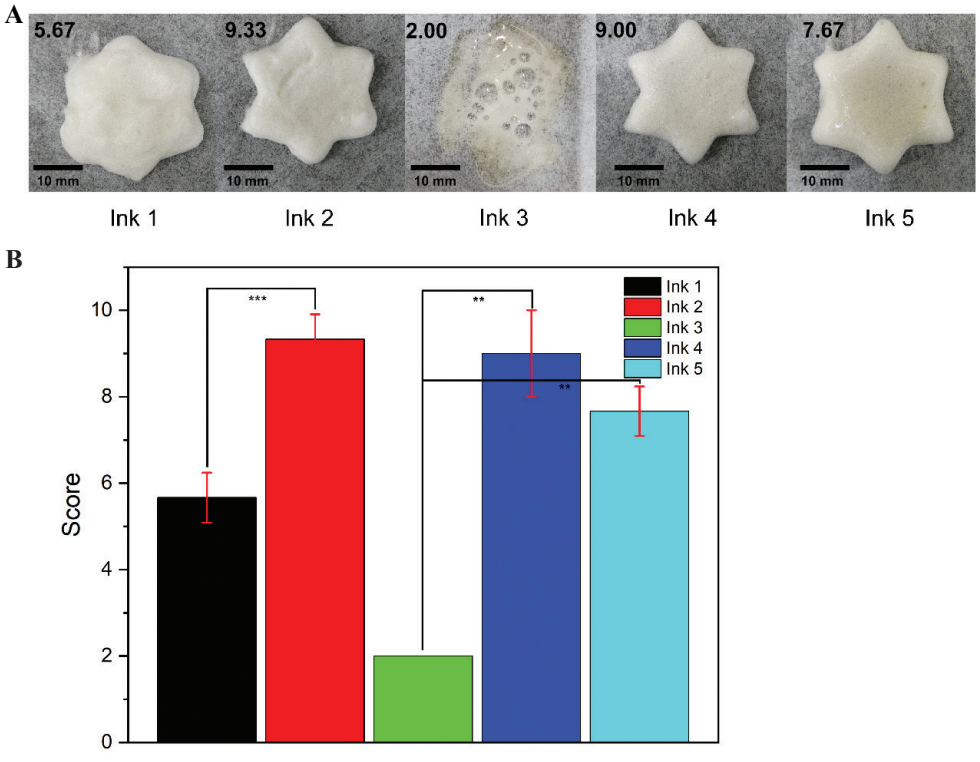

Figure 3. (A) Six-pointed star (first) prints with Inks 1 – 5 with the average score in each frame. (B) The printability scores for each ink. *$P \leq 0.1$, **$P \leq 0.01$, ***$P \leq 0.001$, ****$P \leq 0.0001$ for the *t*-test results ($n = 3$).

microstructure with thicker films between each bubble. It also explains why the EW inks were denser than the HPMC inks.

Comparing the EW only foam to Inks 1 and 2, the baked EW foam was flakier and had more disconnected sections as shown in the blue boxes in column I for A, B, and C. The honeydew extract, which contained a large portion of small polysaccharide[38], seemed to increase the adhesiveness of the liquid phase of the foams. Even after the foams were baked, most bubbles retained their shapes for Inks 1 and 2. In Inks 1 and 2, thin films covered most of the bubbles. More bubbles were intact in Ink 2 than Ink 1 (red boxes of B and C in column II); suggesting that the XG kept the foams from collapsing, especially at elevated temperature during baking, and the gas bubbles tend to grow larger. Furthermore, in Ink 2, the films over the bubbles were more wrinkled, suggesting that the liquid phase with XG was stretched when hydrated to prevent the bubbles from bursting and the foam from collapsing.

Comparing Control 2 to Inks 4 and 5, the pores in Control 2 were larger and exhibited a thinner layered interface between pores pointed out in blue arrows in column IV. Most of the bubbles in Control 2 were torn or burst after being dehydrated by baking. The honeydew extract increased the adhesion between each bubble and thickened the interfaces. In Ink 4, the film over the larger bubbles was intact, whereas the film over smaller bubbles was torn slightly as seen in column IV **(Figure 4E)**. In comparison, Ink 5 had more burst or torn bubbles than Ink 4. Ink 5 also showed more small- and medium-sized bubbles than Ink 4 as shown in the red box in column IV. This could be attributed to the higher density of Ink 5, which made it harder for foam formation and reduced its ability to trap air.

3.6. Texture profile of foam inks

From **Figure 5A**, all the inks have relatively low hardness and gumminess ranging from 0 to 2 N. The adhesiveness of all inks is below 5 mJ. Adhesiveness helps increase the ability of the foam to self-support. A good combination of slightly higher hardness and good adhesiveness of Ink 2 as well as Inks 4 and 5 resulted in better printability than inks without XG, such as Inks 1 and 3. While Ink 1 had a higher hardness, it had poor adhesiveness. Hence, while it could be extruded, it was unable to maintain a good shape, resulting in poor printability. Ink 5 had a lower adhesiveness than Inks 2 and 4 but higher than Ink 1. This explains the better printability of Ink 5 than Ink 1 as it can retain shape better than Ink 1.

While Inks 1, 2, 4, and 5 were all printable and retained their shapes after baking, Ink 5 could not maintain the height of 20 mm after baking and collapsed. Hence, it was not included in the texture profile analysis in the baked form (B is added to the ink names to differentiate baked samples). After baking, all the printed inks became meringue-like after dehydration by baking. This increased the hardness as reflected in **Figure 5C**. The chewiness of the printed inks increased too. However, the springiness and adhesiveness reduced. The other parameters remained similar. The lack of water made the

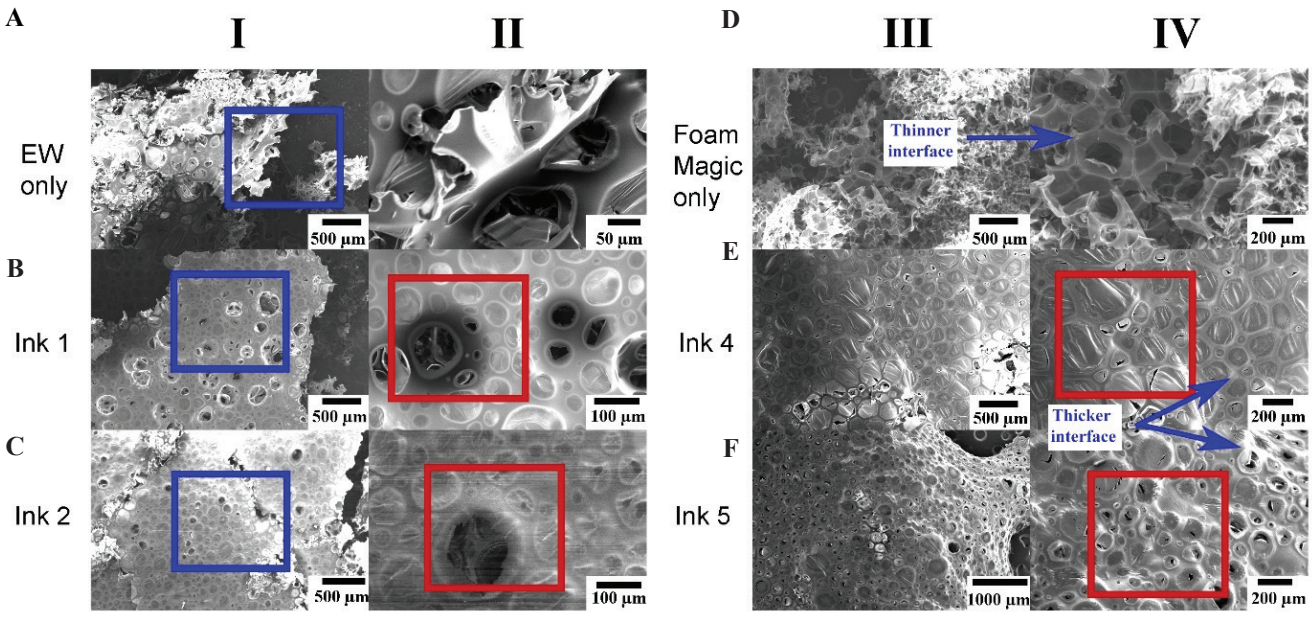

Figure 4. Microstructure of foam inks after baking for 1 h at 70°C. (A) Control 1: Egg white only foam. (B) Ink 1. (C) Ink 2. (D) Control 2: Foam Magic only foam. (E) Ink 4. (F) Ink 5.

inks less sticky and leads to a fall in adhesiveness and springiness. In absolute values, Ink 2B and Ink 4B had similar performance to Ink 1B. This suggests that the XG added to EW foam increases printing performance. Furthermore, the use of HPMC inks as a replacement for EW foams does not significantly affect the textural performance due to the similar texture profiles.

Considering that foams are to be consumed by dysphagic patients as a safe way of hydration, IDDSI tests, including the fork pressure test (**Figure 6A**) and the spoon tilt test (**Figure 6B**), was carried out. These two tests were recommended test in the IDDSI framework for food of level 4-5 (pureed, minced, and moist). The results are shown in **Figure 6**. The fork pressure tests food hardness. Inks 2, 4, and 5 show a clear indent pattern, suggesting that they are soft enough to be consumed by dysphagic patients. For the spoon tilt test, the spoon was tilted and flicked once to check if the inks slid off the spoon. It is used to determine the adhesiveness and cohesiveness. According to the framework, the food is considered safe for consumption by dysphagic patients as long as the spoon is visible after flicking, even though a thin food film may remain on the spoon[34]. Most inks allow a large portion of the inks to slide off the spoon, except Ink 5, suggesting that most inks would not stick to the oral cavity. Out of all the inks, Ink 2 had the best performance.

3.7. Demonstration of 3D-printed food foam

Out of the three inks tested for textural properties, Inks 2 and 4 had better printability. Both inks were used to print various 3D structures. The structures were created without overhang or with only small overhang due to the lack of support. The four structures printed were an octopus, lobster, turtle, and hammerhead shark, as shown in **Figure 7.**

The lighter Ink 4 provided better and smoother prints than Ink 2, (**Figures 7A and B**), with the octopus head bearing clunks and a smooth spherical shape as

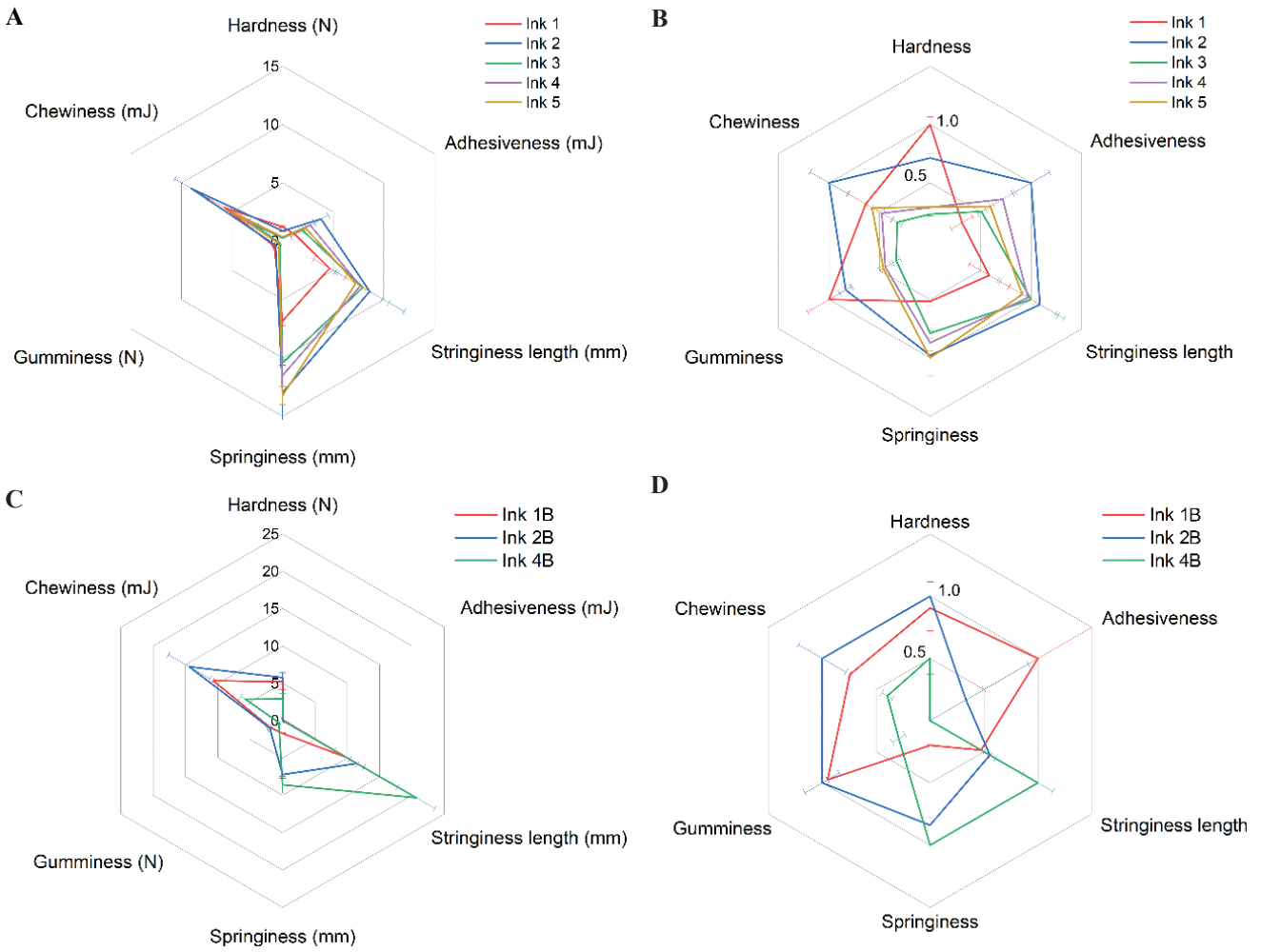

Figure 5. Texture profile of the foam inks in (A) absolute values, (B) normalized values and its baked samples (B represents baked), (C) absolute values, and (D) normalized values.

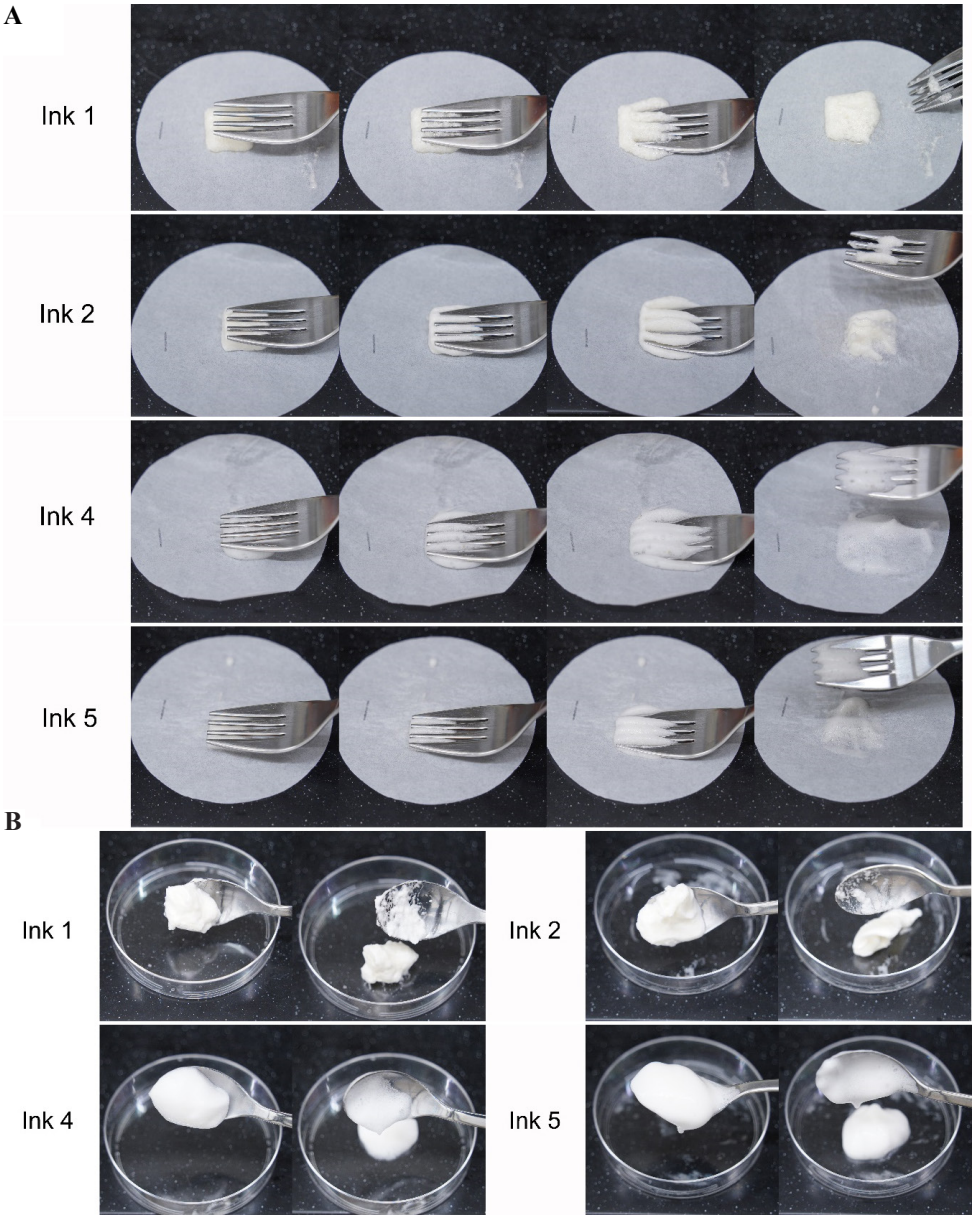

Figure 6. IDDSI tests. (A) Fork pressure test on a 20 × 20 × 10 mm^3 sized 3D-printed samples of the foam inks. (B) Spoon tilt test on the foam inks.

shown in **Figure 7A and B**. However, these 3D structures were larger than the prints used in the printability test. The lower foam stability is visible in the one printed by Ink 4. The surface of the prints was getting moist and shrank over time. The lobster and octopus were printed first. Hence, the surfaces were getting watery and causing them to lose their structure ahead of all the other prints. This suggests that the printed parts of Ink 4 had an even lower storage time than the foam stability test's time, as the printing process reduces the stability due to higher pressure. It should be served or baked once printed. Ink 2 was able to produce stable structures with a half-life foam stability of 30.6 h at room temperature. When refrigerated, it was possible to be stored longer. Ink 2 also performed better in the spoon tilt test. These properties suggest that Ink 2 is ideal as food foam for hydration delivery.

Most meringues are produced with EW and sugar. The presence of honeydew powder was to enhance the taste and flavor of the foams. Similar fruit extract powders such as strawberry and papaya could be used to achieve similar results. Fruits provide a sweet taste that replaces sugar as a flavor enhancer[39]. These foams can function as a flavor and sensory booster in addition to mere water delivery systems to dysphagic patients.

Figure 7. Demonstration of 3D food foam printing. (A) Top profile of the 3D printed structures of an octopus, lobster, turtle and hammerhead shark (from left to right) using Ink 2. (B) Top profile of the 3D printed structures of an octopus, lobster, turtle, and hammerhead shark (from left to right) using Ink 4.

4. Conclusions

The structures in **Figure 7** show that 3D printing can provide more creative and esthetically pleasing, and complex structures of food foams by computer-aided design (CAD) designs and a 3D food printer. Silicone molds cannot accomplish the shaping of foams because it is almost impossible to de-mold the foam. 3DFP with foam allows artists to freely express their ideas and designs using food, enhancing visual appeal of the food, hence, elevating palatability. Moreover, 3DFP provides a simple way of modifying the food texture, giving chefs more freedom to work with the different food and cooking methods. However, food foams are volatile and delicate to work with due to the instability of foams. In this study, the foam properties of the foam inks (with and without XG) proposed were investigated. The inclusion of XG in this study stabilized food foams for high printability. XG provided additional foam stability, which aided in producing better prints and permitted longer storage of the printed food, as displayed by Inks 2 and 4. The texture properties were also studied to understand the difference between the EW foam and HPMC foam and their XG counterparts. The improvements to the EW ink provide an alternative approach to creating artisan meringues. In this case of 3DFP, the sugar is replaced with fruit extract to provide a fruity and sweet taste. Several 3D shapes were printed with the optimal Inks 2 and 4 to demonstrate the 3D printing of food foams. This form of 3DFP may also be used as a flavor and visual enhancer as foams are widely used for dish plating. Vegans do not consume egg-based products, so the eggless Ink 4 may be an alternative to EW in creating 3D-shaped meringues and icing. The excellent performance of Inks 1, 2, and 4 in the IDDSI tests shows that these food foams (without baking) are well suited for medical applications such as hydration for dysphagic patients as EW consists of mainly 90% of water[40] and the formulation in Ink 4 has approximately 87% of water. This study has shown the possibility of 3DFP of stable food foams and their applications for hydration delivery for dysphagic patients. In the future, robotic arm-based printers may be used over cartesian printers as they allow both printings of the foam and assembling the foams in 3D, using a similar concept by Awa Taccino machine from Takara Tomy[41].

Funding

Authors would like to thank National Additive Manufacturing Innovation Cluster (Project ID 2019048) and Singapore University of Technology and Design (SUTD) Growth Plan, Healthcare Sector Thrust 3-3 3DFP (SGPHCRS1907) for the funding support. This work is also supported by Singapore Centre for 3D Printing, which is funded by the Singapore National Research Foundation under its Medium-Sized Centre funding scheme

Conflicts of interest

The authors declare no known conflict of interest.

Author contributions

A.Y.L., A.P., and Y.Z. conceptualized the idea. Y.Z. and C.K.C. supervised the project. A.Y.L., Y.Z., and A.P. planned the experiments. A.Y.L., K.P., and C.P.L. carried out the experiments. A.Y.L. wrote the manuscript. J.A., M.H., U.X.T, C.H.L., C.P.L., C.K.C., G.W., and Y.Z. discussed the results, and reviewed and edited the manuscript. All authors contributed to the final manuscript.

References

1. Haleem A, Javaid M, 2019, Additive Manufacturing Applications in Industry 4.0: A Review. *J Ind Inf Integr*, 4:1930001.
2. Chua CK, Fai K, 2017, 3D printing and Additive Manufacturing: Principles and Application. In: Rapid Prototyping: Principles and Applications. 5th ed. Singapore: World Scientific Publishing Co Inc.
3. Najmon J, Raeisi S, Tovar A, 2019, Review of Additive Manufacturing Technologies and Applications in the Aerospace Industry. Amsterdam, Netherlands: Elsevier. https://doi.org/10.1016/b978-0-12-814062-8.00002-9
4. Ahmed ZY, Bos FP, van Brunschot MC, *et al*., 2020, On-demand Additive Manufacturing of Functionally Graded Concrete. *Virtual Phys Prototyp*, 15:194–210. https://doi.org/10.1080/17452759.2019.1709009
5. Khorsandi D, Fahimipour A, Abasian P, *et al.*, 2021, 3D and 4D Printing in Dentistry and Maxillofacial Surgery: Printing Techniques, Materials, and Applications. *Acta Biomaterialia*, 122:26–49. https://doi.org/10.1016/j.actbio.2020.12.044
6. Ng WL, Chua CK, Shen YF, 2019, Print Me An Organ! Why We Are Not There Yet. *Progress in Polymer Science*, 97:101145. https://doi.org/10.1016/j.progpolymsci.2019.101145
7. Ng WL, Chan A, Ong YS, *et al*., 2020, Deep Learning for Fabrication and Maturation of 3D Bioprinted Tissues and Organs. *Virtual Phys Prototyp*, 15:340–58.
8. Chua CK, 2020, Publication Trends in 3D Bioprinting and 3D Food Printing. *Int J Bioprint*, 6:257. https://doi.org/10.18063/ijb.v6i1.257
9. Voon SL, An J, Wong G, *et al*., 2019, 3D Food Printing: A Categorised Review of Inks and their Development. *Virtual Phys Prototyp*, 14:203–18.
10. Severini C, Azzollini D, Albenzio M, *et al*., 2018, On Printability, Quality and Nutritional Properties of 3D Printed Cereal Based Snacks Enriched with Edible Insects. *Food Res Int*, 106:666–76. https://doi.org/10.1016/j.foodres.2018.01.034
11. Lee CP, Karyappa R, Hashimoto M, 2020, 3D Printing of Milk-based Product. *RSC Adv*, 10:29821–8. https://doi.org/10.1039/d0ra05035k
12. Derossi A, Caporizzi R, Paolillo M, *et al*., 2021, Programmable Texture Properties of Cereal-based Snack Mediated by 3D Printing Technology. *J Food Eng*, 289:110160. https://doi.org/10.1016/j.jfoodeng.2020.110160
13. Tomašević I, Putnik P, Valjak F, *et al.*, 2021, 3D Printing as Novel Tool for Fruit-Based Functional Food Production. *Curr Opin Food Sci*, 41:138–45. https://doi.org/10.1016/j.cofs.2021.03.015
14. Pant A, Lee AY, Karyappa R, *et al.*, 2021, 3D Food Printing of Fresh Vegetables Using Food Hydrocolloids for Dysphagic Patients. *Food Hydrocolloid*, 114:106546. https://doi.org/10.1016/j.foodhyd.2020.106546
15. Godoi FC, Prakash S, Bhandari BR, 2016, 3d Printing Technologies Applied for Food Design: Status and Prospects. *J Food Eng*, 179:44–54. https://doi.org/10.1016/j.jfoodeng.2016.01.025
16. Baiano A, 2020, 3D Printed Foods: A Comprehensive Review on Technologies, Nutritional Value, Safety, Consumer Attitude, Regulatory Framework, and Economic and Sustainability Issues. *Food Rev Int*, 2020:1–31. https://doi.org/10.1080/87559129.2020.1762091
17. Perez AA, Sánchez CC, Patino JM, *et al*., 2012, Foaming Characteristics of β-Lactoglobulin as Affected by Enzymatic Hydrolysis and Polysaccharide Addition: Relationships with the Bulk and Interfacial Properties. *J Food Eng*, 113:53–60. https://doi.org/10.1016/j.jfoodeng.2012.05.024
18. Mardani M, Yeganehzad S, Ptichkina N, *et al.*, 2019, Study on Foaming, Rheological and Thermal Properties of Gelatin-free Marshmallow. *Food Hydrocolloid*, 93:335–41. https://doi.org/10.1016/j.foodhyd.2019.02.033
19. Licciardello F, Frisullo P, Laverse J, *et al*., 2012, Effect of Sugar, Citric Acid and Egg white Type on the Microstructural and Mechanical Properties of Meringues. *J Food Eng*, 108:453–62. https://doi.org/10.1016/j.jfoodeng.2011.08.021
20. Żmudziński D, Ptaszek P, Kruk J, *et al.*, 2014, The Role of Hydrocolloids in Mechanical Properties of Fresh Foams Based on Egg White Proteins. *J Food Eng*, 121:128–34. https://doi.org/10.1016/j.jfoodeng.2013.08.020
21. de Villiers M, Hanson B, Moodley L, *et al*., 2020, The Impact of Modification Techniques on the Rheological Properties of Dysphagia Foods and Liquids. *J. Texture Stud*, 51:154–68.

https://doi.org/10.1111/jtxs.12476

22. Belardi L, 2014, Bringing Dignity Back to Modified Meals. United States: Intermedia Group.
23. Alavi F, Emam-Djomeh Z, Mohammadian M, *et al*., 2020, Physico-chemical and Foaming Properties of Nanofibrillated Egg White Protein and its Functionality in Meringue Batter. *Food Hydrocolloid*, 101:105554. https://doi.org/10.1016/j.foodhyd.2019.105554
24. Gharbi N, Labbafi M, 2019, Influence of Treatment-induced Modification of Egg White Proteins on Foaming Properties. *Food Hydrocolloid*, 90:72–81. https://doi.org/10.1016/j.foodhyd.2018.11.060
25. Li X, Li J, Chang C, *et al.*, 2019, Foaming Characterization of Fresh Egg White Proteins as a Function of Different Proportions of Egg Yolk Fractions. *Food Hydrocolloid*, 90:118–25. https://doi.org/10.1016/j.foodhyd.2018.12.014
26. Özer C, Ağan C, 2020, The Influence of Aging Egg on Foaming Properties of Different Meringue Types. *J Culin Sci Technol*, 2020:1–10. https://doi.org/10.1080/15428052.2020.1790073
27. Kouzani AZ, Adams S, Oliver R, *et al*., 2016, 3D Printing of a Pavlova. In: 2016 IEEE Region 10 Conference (TENCON), p2281–5. https://doi.org/10.1109/tencon.2016.7848435
28. Ptaszek P, Kabziński M, Ptaszek A, *et al*., 2016, The Analysis of the Influence of Xanthan Gum and Apple Pectins on Egg White Protein Foams Using the Large Amplitude Oscillatory Shear Method. *Food Hydrocolloid*, 54:293–301. https://doi.org/10.1016/j.foodhyd.2015.10.010
29. Dabestani M, Yeganehzad S, 2019, Effect of Persian Gum and Xanthan Gum on Foaming Properties and Stability of Pasteurized Fresh Egg White Foam. *Food Hydrocolloid*, 87:550–60. https://doi.org/10.1016/j.foodhyd.2018.08.030
30. Milani J, Maleki G, 2012, Hydrocolloids in Food Industry. IntechOpen, DOI: 10.5772/32358. Available from: https://www.intechopen.com/books/food-industrial-processes-methods-and-equipment/hydrocolloids-in-food-industry.
31. Sworn G, 2009, Xanthan Gum. In: Phillips GO, Williams PA, editors. Handbook of Hydrocolloids. 2nd ed. Sawston, United Kingdom: Woodhead Publishing, p186–203.
32. Saha D, Bhattacharya S, 2010, Hydrocolloids as Thickening and Gelling Agents in Food: A Critical Review. *J Food Sci Technol*, 47:587–97. https://doi.org/10.1007/s13197-010-0162-6
33. Jiang H, Zheng L, Zou Y, *et al*., 2019, 3D Food Printing: Main Components Selection by Considering Rheological Properties. *Crit Rev Food Sci*, 59:2335–47. https://doi.org/10.1080/10408398.2018.1514363
34. IDDSI Framework Testing Methods 2.0, (2021), Available from: https://www.iddsi.org. [Last accessed on 2021 Mar 01].
35. Karlsson K, Schuster E, Stading M, *et al*., 2015, Foaming Behavior of Water-soluble Cellulose Derivatives: Hydroxypropyl Methylcellulose and Ethyl Hydroxyethyl Cellulose. *Cellulose*, 22:2651–64. https://doi.org/10.1007/s10570-015-0669-0
36. Renpu W, 2011, Measures for Putting a Well into Production. In: Renpu W, editor. Advanced Well Completion Engineering. 3rd ed., Ch. 8. Gulf Professional Publishing, p417–523. https://doi.org/10.1016/b978-0-12-385868-9.00011-7
37. Belitz HD, Grosch W, Schieberle P, editors, 2009, Amino Acids, Peptides, Proteins. In: Food Chemistry. Berlin, Heidelberg: Springer Berlin Heidelberg, p8–92. https://doi.org/10.1007/978-3-662-07279-0_2
38. Simandjuntak V, Barrett DM, Wrolstad RE, 1996, Cultivar and Maturity Effects on Muskmelon (*Cucumis melo*) Colour, Texture and Cell Wall Polysaccharide Composition. *J Sci Food Agric*, 71:282–90. https://doi.org/10.1002/(sici)1097-0010(199607)71:3<282:aid-jsfa576>3.0.co;2-5
39. Hutchings SC, Low JY, Keast RS, 2019, Sugar Reduction without Compromising Sensory Perception. An Impossible Dream? *Crit Rev Food Sci*, 59:2287–307. https://doi.org/10.1080/10408398.2018.1450214
40. Réhault-Godbert S, Guyot N, Nys Y, 2019, The Golden Egg: Nutritional Value, Bioactivities, and Emerging Benefits for Human Health. *Nutrients*, 11:684. https://doi.org/10.3390/nu11030684
41. Moynihan T. 2014, This Gadget Fires Foamy 3-D Pandas into your Lattes.

RESEARCH ARTICLE

Custom Shoe Sole Design and Modeling Toward 3D Printing

Ali Zolfagharian[1], Mohammad Lakhi[2], Sadegh Ranjbar[3], Mahdi Bodaghi[4]

[1]School of Engineering, Deakin University, Geelong, Australia
[2]Department of Mechanical Engineering, University of Birjand, Birjand, Iran
[3]Department of Mechanical Engineering, Birjand University of Technology, Birjand, Iran
[4]Department of Engineering, School of Science and Technology, Nottingham Trent University, Nottingham NG11 8NS, UK

Abstract: This study introduces a design procedure for improving an individual's footwear comfort with body weight index and activity requirements by customized three-dimensional (3D)-printed shoe midsole lattice structure. This method guides the selection of customized 3D-printed fabrications incorporating both physical and geometrical properties that meet user demands. The analysis of the lattice effects on minimizing the stress on plantar pressure was performed by initially creating various shoe midsole lattice structures designed. An appropriate common 3D printable material was selected along with validating its viscoelastic properties using finite element analysis. The lattice structure designs were analyzed under various loading conditions to investigate the suitability of the method in fabricating a customized 3D-printed shoe midsole based on the individual's specifications using a single material with minimum cost, time, and material use.

Keywords: Customization; Shoe; Sole; 3D printing; 4D printing; Viscoelastic, Polyurethane

*Correspondence to: Ali Zolfagharian, School of Engineering, Deakin University, Geelong, Australia; a.zolfagharian@deakin.edu.au

Received: June 1, 2021; **Accepted:** June 25, 2021; **Published Online:** July 23, 2021

Citation: Zolfagharian A, Lakhi M, Ranjbar S, *et al.*, 2021, Custom Shoe Sole Design and Modeling Towards 3D Printing. *Int J Bioprint*, 7(4):396. http://doi.org/10.18063/ijb.v7i4.396

1. Introduction

The use of additive manufacturing and three-dimensional (3D) printers is very popular these days[1-3], and they have various applications in various industries, including aerospace[4], automotive[5], soft robotics[6], construction[7], food printing[8], and tissue engineering[9,10]. One of these is the custom manufacturing of products. 3D printing opens the way to novel footwear items by integrating new materials and digital production. At present, the technology now makes it easier to produce high-performance sports shoes and customized sandals using 3D printed shoe components. This enables shoe manufacturers to join the market rapidly by exploring new designs and offering more personalization options. Despite these benefits, the use of 3D printing in footwear remains limited, as the technology currently is yet to enable mass customization incorporating high-level nonlinear materials behavior and geometrical designs to accommodate the intensive and high productivity needs of individuals in the market. However, the development of footwear 3D printing is driven by trends in digital production and desire for personalized experience. Considering midsoles, they are typically constructed throughout the shoe as a solid component with the same level of support. The designers may optimize cushioning properties throughout the whole shoe by adjusting various sections of a midsole, producing better performance footwear. The present study shows an approach to improve the efficiency of shoes in different uses through the optimal geometry design of a 3D printing material tailoring different purposes.

Due to unhealthy lifestyle, like high fat diet and lack of enough exercises due to working from home, a higher number of people are nowadays prone to various types of diseases, which lead to obesity, which in turn increases body mass index (BMI). People with high BMI frequently suffers from the problems of foot ulceration due to excessive walking or standing for a long time.

The need is to have a perfect shoe which will not only provide comfort, but also maintain the functionality in diverse daily activities[11]. It can also be inferred from the open literature that shoe sole plays a critical role in rehabilitation of lower limb[12] while it improves walking function[13] and reduces foot lesions. Patients often complain of foot pain and fatigue after prolonged walking, followed by pain in the knee and ankle that generally deteriorates the quality of life[14]. The effects of custom-made sole on the life quality of individuals both physically and mentally are proven[15]. Due to difference in foot structures of people, customizable midsole has come into picture, which provides more comfort as compared to prefabricated counterparts. One solution is 3D printing of custom shoe midsole, where 3D scanning techniques helps in getting the exact shape and size of the foot which act as input to design. Custom soles are more suitable for plantar structure of patient[16] and can further be improved if traditional support structure is optimized; therefore, further damage reduction at a lower cost, material waste, and fabrication time[17,18].

In the past years, there has been considerable amount of research in footwear industry to provide best comfort shoes for different walks of people from various fields, such as the sports or health sector; many researchers continue to deliver crucial information based on the experimental and theoretical works[19]. The stiffness reported as a crucial factor accounts for 70% of the comfort for diabetic users[20]. High plantar pressure generated on foot can be impacted by changing the stiffness of the shoe sole material[21,22]. A study has shown the efficacy of customized sole in reducing the peak of load by 40% at metatarsal region[23]. Custom-made insoles have proven to provide considerably better stress distribution and much less maximum stress (around 40%) compared to flat insoles, which is very important in fabrication and selection of comfortable insoles[24]. Furthermore, the effect of custom-made 3D-printed foot orthoses in the treatment of pain result in the foot of workers due to prolonged standing has been studied[25]. Analysis of the participants' test results revealed that after wearing customized 3D printing orthoses, feeling of discomfort, pain, and heavy legs were reduced significantly.

Increase of thickness makes the stress distribution more uniform and decreases the maximum stress value up to 10%. However, simply increasing the thickness does not necessarily lead to less maximum stress after a certain thickness of the insole[26] that is where more sophisticated lattice design from 3D printing could play a significant role. 3D printing has been recently focused as the most flexible technology in making midsoles due to its unit features in designing and developing variable density and stiffness products with changing the infill pattern in two and three dimensions, changing the infill across the sole, changing wall thickness of infill walls and changing infill density and height of each voxel. Hence, the midsole designed could not only be customized to the individual's foot, but also is customized to the types of activity, such as walking, running, or jumping. The same level of performance will be hard to do or impossible with machining and conventional subtractive manufacturing.

Recent studies were conducted on different lattice structures by changing its unit cell size and shape to check the behavior of their mechanical property, deformation behavior, and compressive property[27-29]. Different lattice structures with closed and open unit cells of same size were investigated in these studies and found that lattice structure with a closed unit cell has higher stiffness compared to the open lattice. A comparison analysis of lattice structures made from different unit cells by additive manufacturing were conducted[30]. The compression tests were performed on four different topologies such as Diamond, Grid, X shape, and Vintiles to investigate the mechanical property of all four topologies. It has been found that the Grid lattice delivered the highest stiffness compared to others which can be helpful to use in heel part of the insole as it requires stiffer material. Diamond shape lattice structure has shown the most uniform stress distribution property which can be helpful for reducing the plantar pressure.

Shoe firms have been moving away from leather to shoes that are almost entirely polymeric. Thermoplastic urethane (TPU) is a soft material that is highly resistant to wear and abrasion, and is already used widely in many industries, including footwear. The visco-hyper-elastic property of TPU is preferred due to their elasticity property and resistance they offer when subjected to compression. The TPU also meets the requirements for medical devices with regard to cytotoxicity and skin sensitization in accordance with the DIN EN ISO 10993-5 and 10993-10 standards. The major advantage of soft-filament materials is the flexibility that makes them deformed under a load and its ability to revert back to their original state when the load is removed. This property makes it possible to fabricate durable 3D objects with high deformation stability. In addition to its softness and flexibility, TPU is also known for its functional properties of being durable and being able to withstand ambient temperatures up to 80°C. TPU is therefore practical for both consumer and industrial use.

The fast print speeds and compatibility with springy and flexible materials such as TPU, silicone, and elastic polyurethane, common for athletic shoes, have made resin-based 3D printing technology a sustainable manufacturing option. At present, vat photopolymerization is the most popular category of 3D printing methods for footwear manufacturing[31]. This category includes resin-based technologies, such as stereolithography and digital

light processing, and Carbon's digital light synthesis (DLS)[32]. These methods are based on a similar technique, in which a light source (laser, light-emitting projector or diodes) is applied to a liquid resin layer by layer, thereby consolidating it. Besides resin-based technology, shoe manufacturers also employ powder-based technologies, such as Multi Jet Fusion (MJF) from HP and Selective Laser Sintering (SLS)[33]. The MJF and SLS are more frequently utilized in the manufacture of insoles, as opposed to resin-based technologies used in midsoles.

In this study, we present three different lattice patterns designed with same wall thickness and amount of a DLS 3D printing-based material. The midsoles were positioned according to the foot sole to create a specific design taking into consideration the visco-hyper-elastic material effects as per individual specifications. The type of lattice depends on the required demands of the individual applications. These patterns were also compared in different loading scenarios under different input loads simulating the type of activities to judge the efficiency of viscoelastic lattice design in distributing the stress. The results of the conducted simulations showed that the physical properties of customized 3D-printed midsoles are affected by the pattern type with the same amount of material and properties. The contribution of our study is as follows:

a) The 3D-printed grade TPU material properties were validated in ABAQUS finite element analysis (FEA) platform.
b) A specific design for the customized 3D printing was introduced along with flexible patterns, considering the viscoelasticity property of material.
c) A procedure was presented to design and 3D print a customized midsole in terms of specific individual features, such as body weight and type of activity, using merely one type of material at minimum cost and material use.

The rest of this paper is organized as follows: Section 2 is dedicated to the detailed methodology of 3D-printed customized midsole design and the materials characterizations; Section 3 provides the description of the FEA and simulation results and discussion; and Section 4 summarizes the study.

2. Methodology

2.1. Custom midsole design workflow

The pressure distribution is practically consistent in ordinary people. Originally, the body mass appeared on the heel area than that on the middle foot as it transitioned to the forefoot and then was received by that of the toe region in the end[34]. In ordinary humans, the maximum pressure is located on the second metatarsal. The variation of the plantar pressure in normal individuals is from region of heel contact to area off toe. **Figure 1** shows an image[35] where ground reaction forces generated on the foot are derived by foot movement using an experimental gait analysis.

To build an individual shoe sole for a person, plantar pressure needs to be lower which is possible using different lattice structures and a single 3D printing material. As midsole is subjected to low velocity impact test, visco-hyper-elastic materials are most suitable as they offer high elasticity and show positive results on dynamics humans' body.

The effects of sole designs on the plantar pressure and the ground reaction force over a period of time have been studied[36]. The results revealed the reaction force value changes by changing the stiffness and damping structure. It was also observed that both elastic and viscos properties of sole give torque to ankle and knee joints and make the body propulsion. The aim of midsole design is to reduce plantar pressure generated on different areas of foot and give more relaxation to the person's body while they do activities in footwear.

Therefore, in the present work, the shoe sole was designed by considering different activities of person, such as walking, running and jumping, and for this trend, viscoelastic material was selected and subjected to low-velocity impact test that results in a graph of load over time. This load versus time graph gives the idea about how shoe midsole is helpful to reduce the plantar pressure in people based on their specific activity. The novelty of the present study compared to other currently commercial models is the investigation of functional customization that does more than just geometry consideration with the incorporation of viscoelastic material properties into performance evaluation for specific user demand.

A detailed workflow of design and simulation proposed in this study is illustrated in **Figure 2**. The

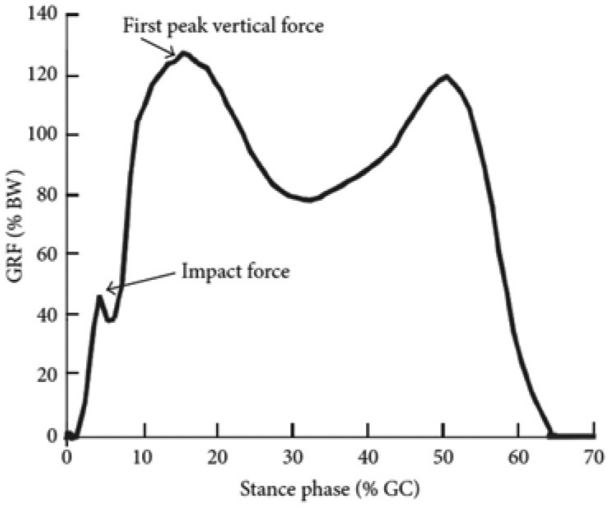

Figure 1. Reaction force generated on feet (from ref.[35] licensed under Creative Commons Attribution 4.0 License).

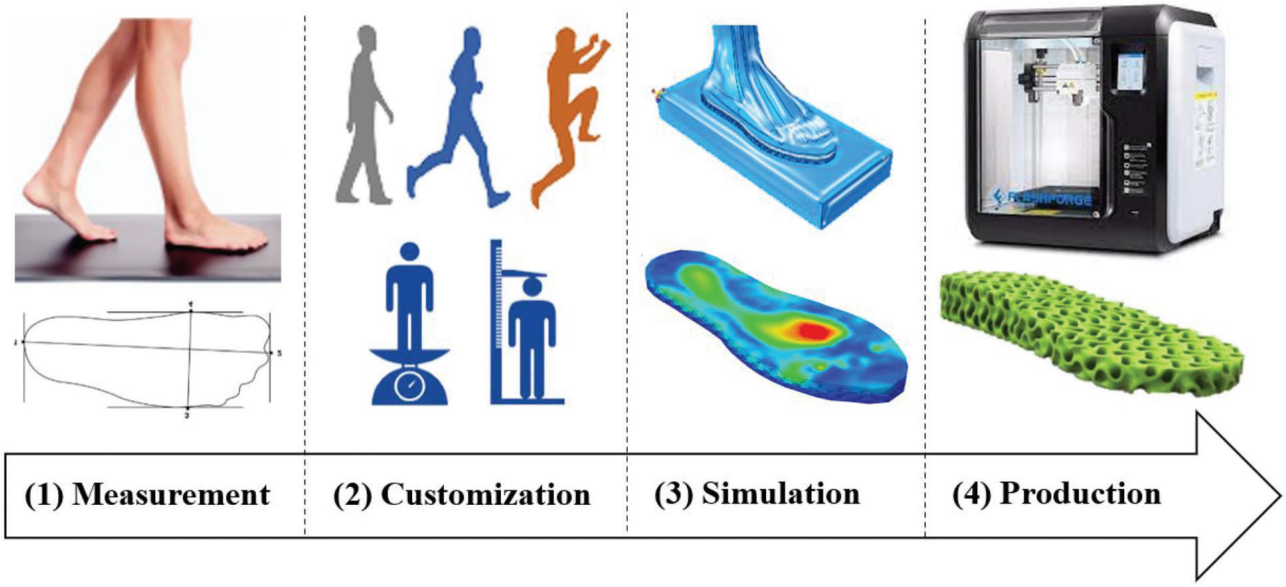

Figure 2. A schematic workflow of custom 3D-printed midsole production.

process starts with receiving the foot shape of an individual using scan or even the shoe size. Then, the lattice of different shapes, for example, three here, are designed and generated in computer-aided design (CAD) software. It should be noted that the cell size of lattices is chosen arbitrarily while their effect is considerable for a further study to deliver more regional stiffness in sole as per individual specifications, such as diabetic patients. Next, a simulation is carried out in an FEA platform called ABAQUS, considering the nonlinearity and viscoelastic properties of the 3D printing material to reflect the stress distribution on the midsole surface in contact with plantar subjected to increasing, downward-directed displacement, which leads to contact with the rigid ground surface and compression of the lattice. Finally, the desired lattice providing less stress compatible to the user application, that is, walking or running, are suggested for 3D printing.

2.2. Materials preparation and characteristics

DLS technology is a new printing method for 3D printing of soft polymers. Elastomeric polyurethane (EUP40) is a type of soft polymer that can be printed by this method. This material has an elongation length of about 275%, shear strength 23 kN.m, shore hardness 68A, and T_g (glass transition temperature) 8°C[37]. These properties have led to EUP40 being classified as a rubber-like viscoelastic material. For this reason, the neo-Hookean and Yeoh's rubber-like model as well as Carol are used to study the behavior of the material as:

$$W = \sum_{i=0}^{s} C_i (I_{1i} - 3)^3 + \sum_{i=s+1}^{n} D_i (I_{1i} - 3) \quad (1)$$

$$W = aI_1 + bI_1^4 + c\sqrt{I_2} \quad (2)$$

The viscoelastic behavior of EPU40 for 3D printing of midsole is characterized at different strain rates and it was used in this work to simulate the results having validated using FEA in ABAQUS. To find the stress-strain relationship in quasi-static state, homogeneous uniaxial tensile test with low strain rate were conducted[37]. Furthermore, to confirm the ability of traction, that is, high elongation in the failure of EUP40 in the set of experiments, the strain rates of 0.032/s, 0.128/s, and 0.576/s at speeds of 50 mm/min, 200 mm/min, and 900 mm/min were conducted, respectively, to achieve high elongation.

The validation of stress-strain results at different strain rates are shown in **Figure 3**. According to this figure, increasing the strain rate has increased the stress in the same strain by 100%. This behavior of material indicates that models (1) and (2) are suitable to use to understand the behavior of the midsole material. Finally, after performing quasi-static tests, cyclic tests, relaxation tests, and experimental study of material behavior, the parameters of the two models are presented in **Table 1**.

3. Results and discussion

Three lattice designs with the same amount of materials for the sake of comparisons were created in the CAD software and converted into step format before being imported into ABAQUS (Dassault, France) for the FEA study. Different elements were used for ground, foot, and midsole where ground block and foot were meshed by 5 mm R3D4 and R3D3, respectively, and midsoles were meshed by 3 mm C3D4 tetrahedral elements as shown in **Figure 4**. The boundary conditions of different parts are shown in **Figure 5**, where the ground block is constrained in all directions. The input force was defined for three different scenarios of walking, running, and jumping of an individual with 1820 mm height, 84.6 kg weight, and equivalent BMI of 25.3 in **Figure 6**[35]. A dynamics/explicit solver with time steps corresponding to input force was used for calculating the simulation results in various individual specifications during walking, running, and jumping. According to the simulation of ordinary walking[12], the stresses of plantar were within the linear elastic range of EPU40 material. The properties of the foot and the ground were assumed rigid, and for shoe midsole, the EPU40 properties were defined (**Figure 3**).

The impact forces representing the individual specifications in walking, running, and jumping were applied for the three lattices, and stress and displacement distributions results are shown in **Figures 7 and 8**, respectively. It is observed that the highest-pressure peaks

Table 1. Elastic and viscous parameters for Carroll's, neo-Hookean, and Yeoh's models

Carrol model	a	b	c	-
	2.868e-01	1.4183e-07	7.846e-01	-
Neo-Hookean+ Yeoh's model	C_1	D_1	D_2	D_3
	8.201e-01	5.792e-01	4.464e-01	3.382e+00

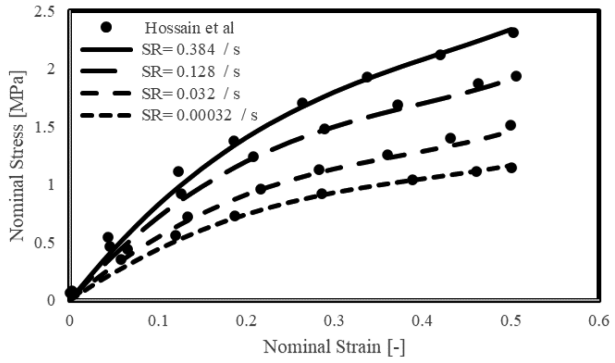

Figure 3. Viscoelastic 3D-printed EPU40 stress-strain results.

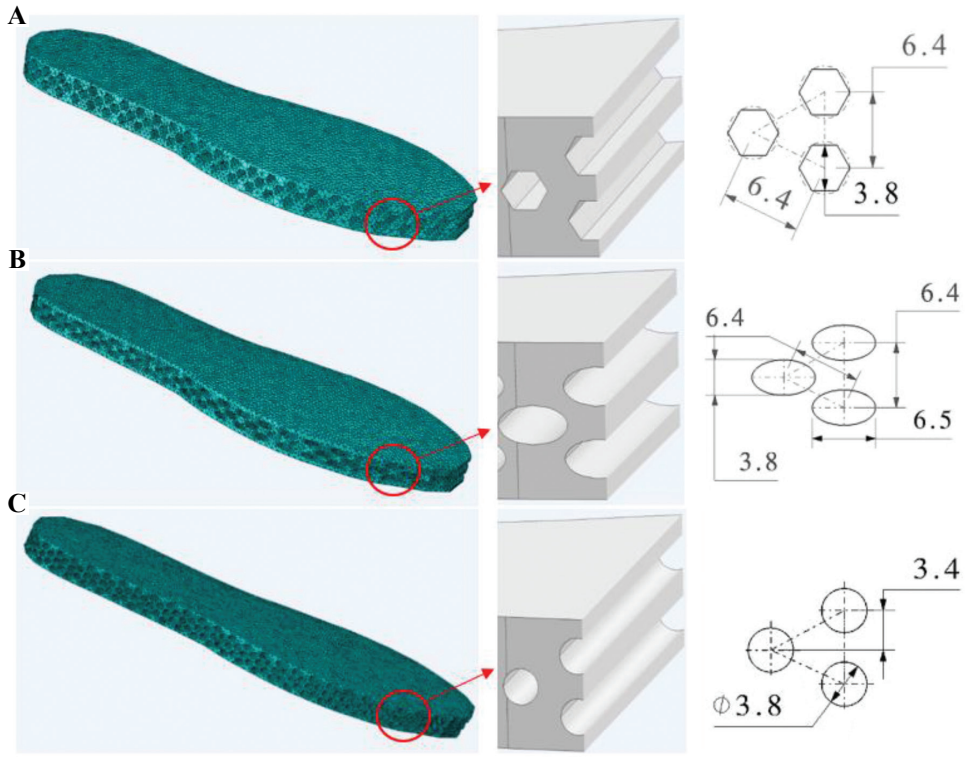

Figure 4. Different lattice meshes of midsole designs: (A) hexagonal, (B) elliptical, and (C) circular.

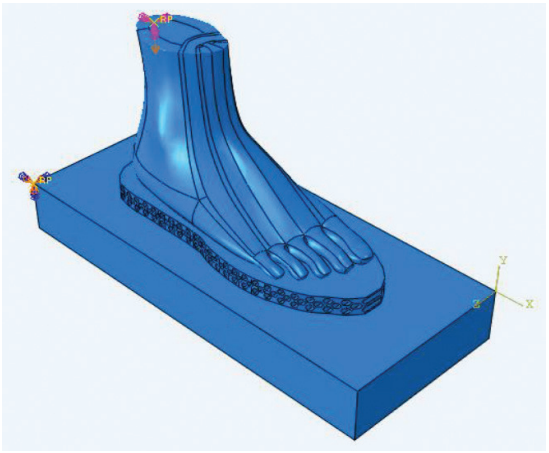

Figure 5. The boundary conditions and contact illustration of foot on midsole.

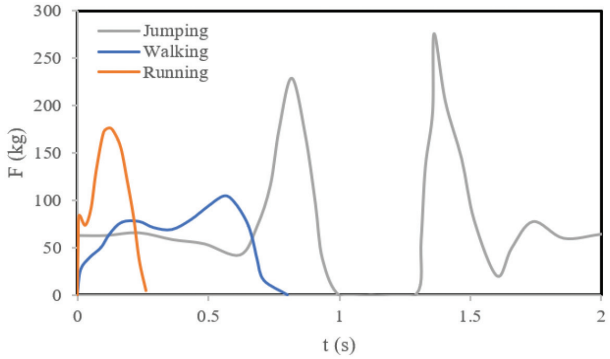

Figure 6. Input forces representing the individual specifications.

were at the heel and medial forefoot for all modes of walking, running, and jumping. From the data, it is clear that the medial forefoot and heel absorbed the maximum pressure during the jumping activity in comparison to the other two activities. The absolute peak data represent the maximum pressure at a specific point in the segmented area. For running, the peak pressure at medial forefoot and heel meaning both the regions are high pressure peak areas.

Furthermore, the results revealed the elliptical lattice has the highest stress, which accordingly undergoes higher displacement. This is due to the different structure in the shape of the lattice compared to the circular and hexagonal ones. According to **Figure 9**, it can be concluded that as the number of polygonal sides decreases or the ratio of large diameter to small diameter (in horizontal geometry) increases, the amount of stress and displacement increases.

Figures 10 and **11** show the changes in strain energy and viscous energy loss over time, respectively. According to these results, in each of the stepping specifications, the highest energy is related to the elliptical geometry. The greater effect of the elliptical geometry is due to the topology of this structure that is more prone to crushing and consequently undergoing a higher amount of displacement, stress, and energy. According to **Figures 10** and **11**, the maximum values of strain energy and viscous energy loss are observed in elliptical, hexagonal, and circular lattices,

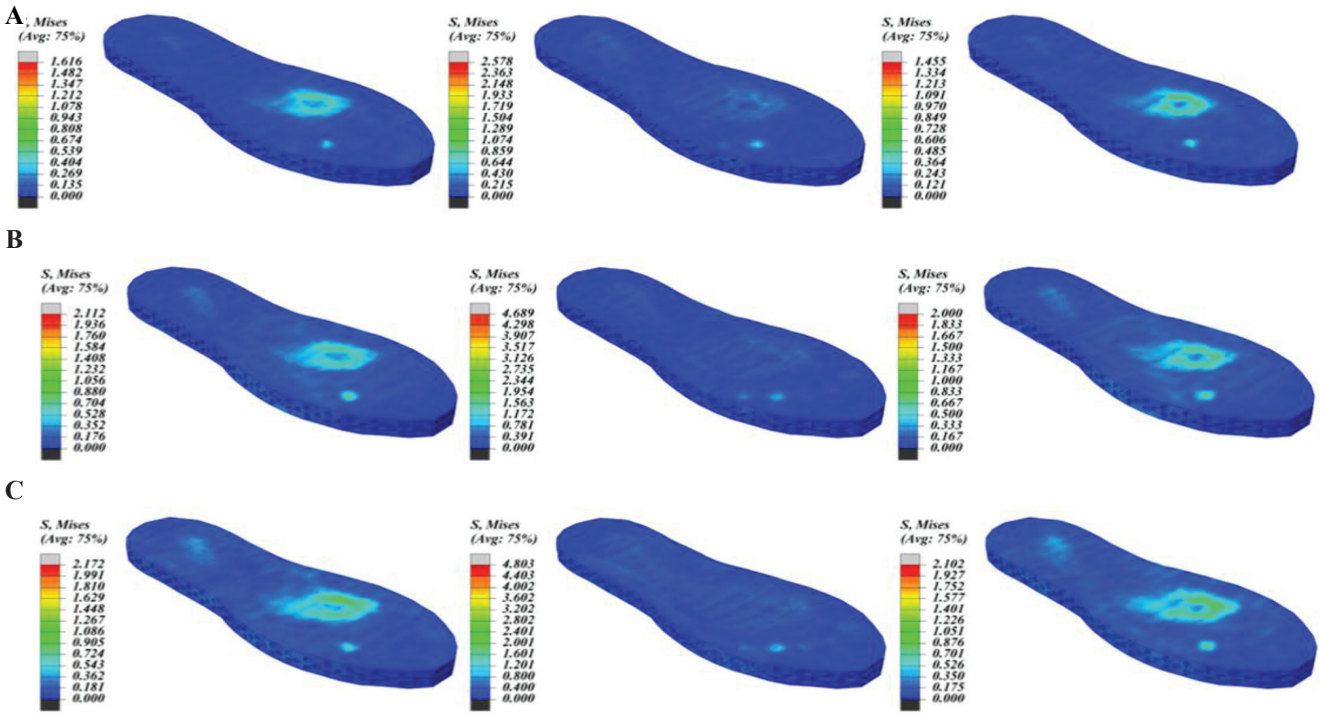

Figure 7. Maximum stress distributions of midsoles for different lattices (circular, elliptical, and hexagonal, from the left to right, respectively) at different scenarios of (A) walking, (B) running, and (C) jumping.

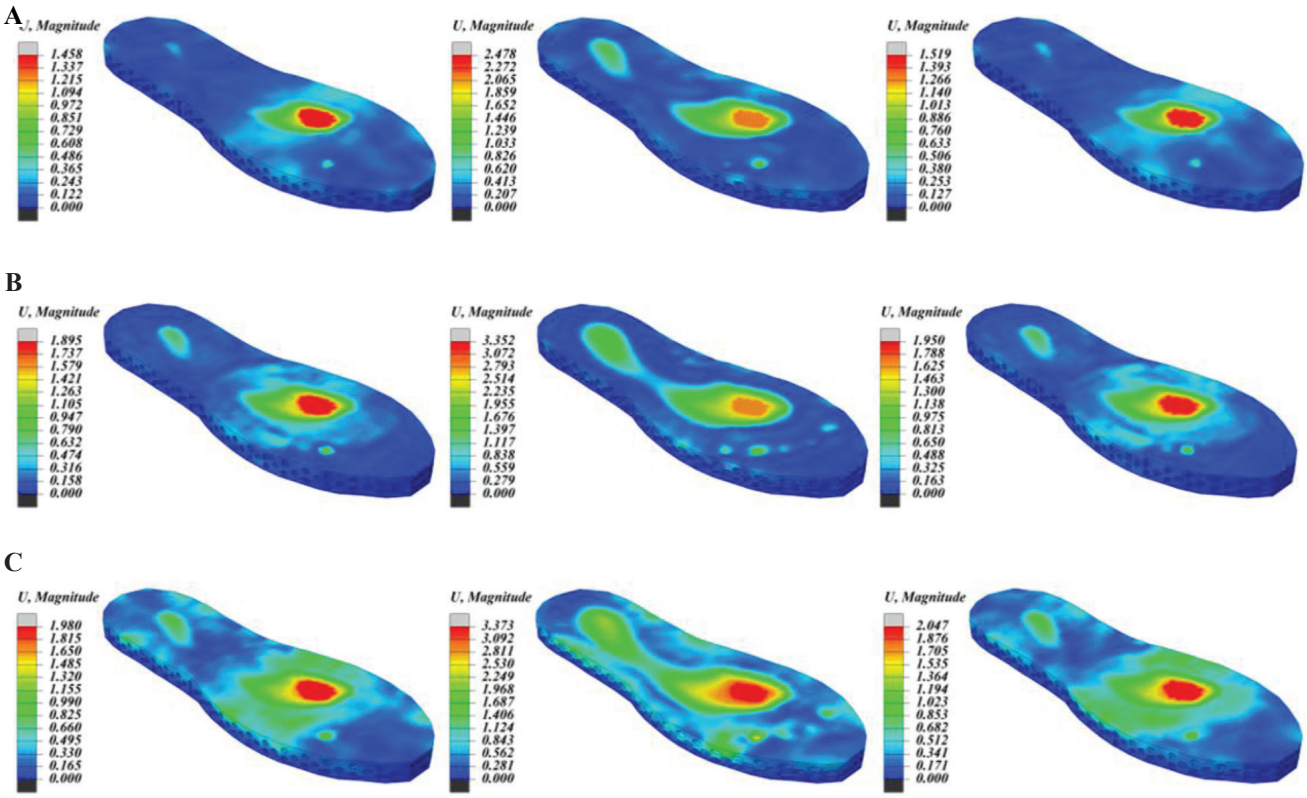

Figure 8. Maximum displacements of midsoles for different lattices (circular, elliptical, and hexagonal, from left to right, respectively) at different scenarios of (A) walking, (B) running, and (C) jumping.

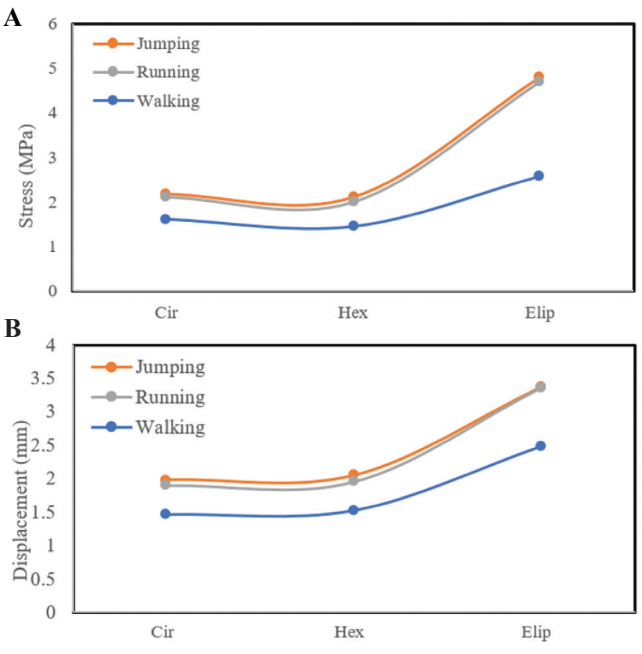

Figure 9. Maximum (A) stress and (B) displacement of midsoles in different scenarios of walking, running, and jumping.

respectively. This result is also arguable according to **Figure 9**, where with increasing displacement values in different lattices and consequently increasing amount of stress applied to the midsole, higher dissipation energy occurs with the same trend. As a result, the elliptical lattice experiences the highest amount of energy dissipation.

In general, hexagonal grids under non-planar loading have a higher energy absorption capacity than in-plane loading. The hexagonal lattice could be useful when the merely energy absorption of non-planar loading is the goal. Yet, the impact force duration is one of the important parameters in energy absorption. When the goal is to protect the human body from injury in walking, running, and jumping under the impact load, the importance of the impact time dominates so as with extending the time of impact its magnitude and the risk of damage it causes to the human body reduces accordingly. By applying the input forces of different gaits of an individual according to **Figure 6**, it can be seen that the amount of energy in **Figures 10** and **11** for jumping mode is much higher than running and walking

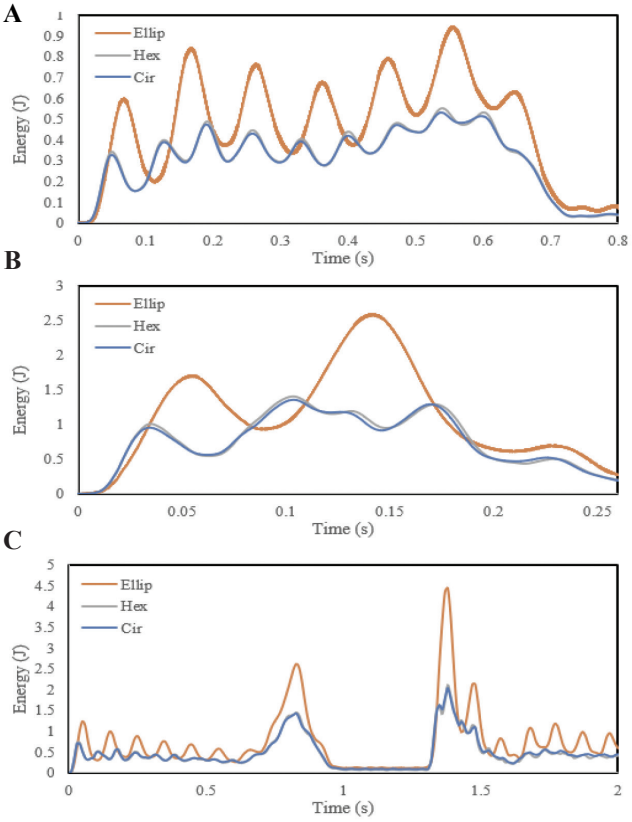

Figure 10. (A-C) Strain energy comparisons.

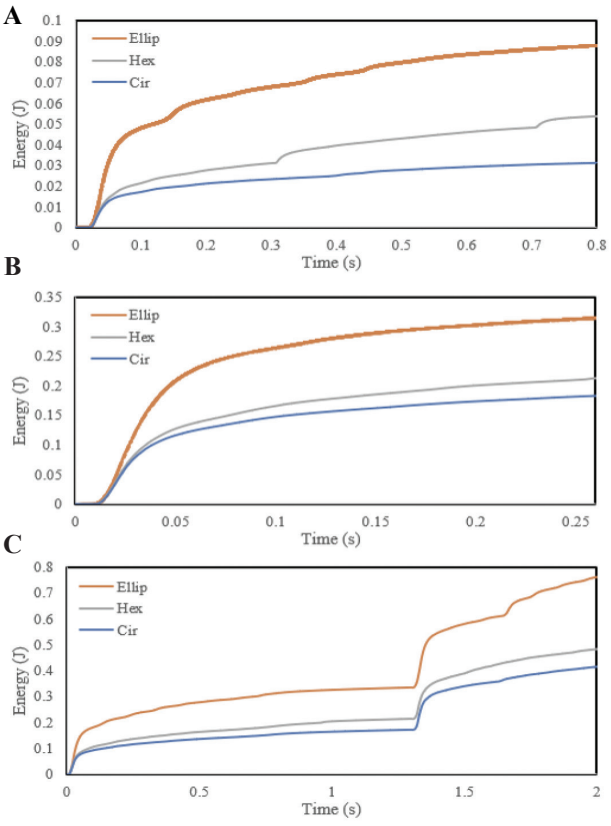

Figure 11. (A-C) Energy dissipation due to viscosity comparisons.

mode due to the effects of the magnitude and time of impact force on the shoe midsole.

It is an undeniable that denser infill patterns supply stronger support to a fabrication to absorb more energy or less the crushing. However, they consume more printing time, energy, material, and subsequent waste. Therefore, this method of customizing the shoe midsole in terms of individual's specifications but using the same amount of materials is efficiency in the reduction of material usage and time of 3D printing. This study proves the feasibility of an adaptive infill patterns application in stiffness and damping tuning required in custom shoes industry. Further clinical and experimental measurements are required as future directions.

4. Conclusions

In this work, various shoe midsoles were designed by considering different activities of person, such as walking, running, and jumping, and for this trend, a 3D printable viscoelastic material was selected and subjected to low velocity impact test that resulted in a graph of load over time. This load versus time graph gives the idea about how shoe midsole is helpful to reduce the plantar pressure on people based on their specific activity. The novelty of the present study compared to other currently commercial models is investigation of functional customization that does more than just geometry consideration with incorporating the viscoelastic material properties into performance evaluation for specific user need. The models with different thicknesses and materials were not considered here and our focus was merely on the interior pattern of 3D-printed midsoles that delivers various functionalities with considerations on cost reduction and the use of a common 3D printer and a single material. The study proved that the 3D printing is effective in making a midsole that caters to requirements of different individuals based on the infill patterns design. This study brings new innovation into customized 3D-printed shoes industries by providing these meaningful insights into the design process.

The results of this study also provide scope of using combination of lattice structure to increase the energy absorption capacity or elasticity, or providing more local support and comfort as per individual requirements, such as diabetic injuries or sports. The midsoles could see evolving improvements through 4D printing that redirects these vertical impact forces into horizontal forward motion, thus delivering a running economy or varying the stiffness to serve at various environmental conditions, such as different relative humidities and temperatures.

Acknowledgments

The work was supported by Faculty of Science, Engineering and Built Environment, Deakin University, Australia.

Funding

The work was funded by Faculty of Science, Engineering and Built Environment, Deakin University, Australia, under 2021 Mini ARC Analog Program (MAAP)–Discovery 25310 and Peer-Review, ECR Support Scheme PRESS) 2021.

Conflicts of interest

The authors declare that they have no conflict of interest.

Author contributions

A.Z. conceived the ideas and drafted the manuscript. M.B. revised the manuscript, reviewed the simulation results, and advised the organization of the main contents. S.R. and M.L. collected the detailed research results.

References

1. Khosravani MR, Zolfagharian A, 2020, Fracture and Load-carrying Capacity of 3D-Printed Cracked Components. *Extreme Mech Lett*, 37:100692. https://doi.org/10.1016/j.eml.2020.100692
2. Zolfagharian A, Denk M, Bodaghi M, *et al*., 2019, Topology-optimized 4D Printing of a Soft Actuator. *Acta Mech. Solida Sin*, 33:418–30. https://doi.org/10.1007/s10338-019-00137-z
3. Shirzad M, Zolfagharian A, Matbouei A, *et al*., 2021, Design, Evaluation, and Optimization of 3D Printed Truss Scaffolds for Bone Tissue Engineering. *J Mech Behav Biomed Mater*, 120:104594. https://doi.org/10.1016/j.jmbbm.2021.104594
4. Joshi SC, Sheikh AA, 2015, 3D Printing in Aerospace and its Long-term Sustainability. *Virtual Phys Prototyp*, 10:175–85.
5. Nichols MR, 2019, How does the Automotive Industry Benefit from 3D Metal Printing? *Metal Powder Rep*, 74:257–8. https://doi.org/10.1016/j.mprp.2019.07.002
6. Zolfagharian A, Durran L, Gharaie S, *et al*., 2021, 4D Printing Soft Robots Guided by Machine Learning and Finite Element Models. *Sens Actuators A Phys*, 328:112774. https://doi.org/10.1016/j.sna.2021.112774
7. Tay YW, Panda B, Paul SC, *et al*., 2017, 3D Printing Trends in Building and Construction Industry: A Review. *Virtual Phys Prototyp*, 12:261–76.
8. Liu Z, Zhang M, Bhandari B, *et al*., 2017, 3D Printing: Printing Precision and Application in Food Sector. *Trends Food Sci Technol*, 69:83–94. https://doi.org/10.1016/j.tifs.2017.08.018
9. Ng WL, Chua CK, Shen YF, 2019, Print me an Organ! Why we are not there yet. *Prog Polym Sci*, 97:101145. https://doi.org/10.1016/j.progpolymsci.2019.101145
10. Askari M, Naniz MA, Kouhi M, *et al*., 2021, Recent Progress in Extrusion 3D Bioprinting of Hydrogel Biomaterials for Tissue Regeneration: A Comprehensive Review with Focus on Advanced Fabrication Techniques. *Biomater Sci*, 9:535–73. https://doi.org/10.1039/d0bm00973c
11. Ma Z, Lin J, Xu X, *et al*., 2019, Design and 3D Printing of Adjustable Modulus Porous Structures for Customized Diabetic Foot Insoles. *Int J Lightweight Mater Manuf*, 2:57–63. https://doi.org/10.1016/j.ijlmm.2018.10.003
12. Cha YH, Lee KH, Ryu H, *et al*., 2017, Ankle-foot Orthosis Made by 3D Printing Technique and Automated Design Software. *Appl Bionics Biomech*, 2017:9610468. https://doi.org/10.1155/2017/9610468
13. Munteanu SE, Scott LA, Bonanno DR, *et al*., 2015, Effectiveness of Customised Foot Orthoses for Achilles Tendinopathy: A Randomised Controlled Trial. *Br J Sports Med*, 49:989–94. https://doi.org/10.1136/bjsports-2014-093845
14. Pita-Fernandez S, Gonzalez-Martin C, Alonso-Tajes F, *et al*., 2017, Flat Foot in a Random Population and its Impact on Quality of Life and Functionality. *J Clin Diagn Res*, 11:LC22. https://doi.org/10.7860/jcdr/2017/24362.9697
15. Kusumoto A, Suzuki T, Yoshida H, *et al*., 2007, Intervention Study to Improve Quality of Life and Health Problems of Community-living Elderly Women in Japan by Shoe Fitting and Custom-made Insoles. *Gerontology*, 53:348–56. https://doi.org/10.1159/000104252
16. Linberg BH, Mengshoel AM, 2018, Effect of a Thin Customized Insole on Pain and Walking Ability in Rheumatoid Arthritis: A Randomized Study. *Musculoskelet Care*, 16:32–8. https://doi.org/10.1002/msc.1199
17. Rasenberg N, Riel H, Rathleff MS, *et al*., 2018, Efficacy of Foot Orthoses for the Treatment of Plantar Heel Pain: A Systematic Review and Meta-analysis. *Br J Sports Med*, 52:1040–6. https://doi.org/10.1136/bjsports-2017-097892
18. Zhu Y, Joralmon D, Shan W, *et al*., 2021, 3D Printing Biomimetic Materials and Structures for Biomedical Applications. *Biodes Manuf*, 4:1–24.
19. Low JH, Chee PS, Lim EH, *et al*., 2020, Design of a wireless smart insole using stretchable microfluidic sensor for gait monitoring. *Smart Mater Struct*, 29:065003. https://doi.org/10.1088/1361-665x/ab802c

20. Begg L, Burns J, 2008, A Comparison of Insole Materials on Plantar Pressure and Comfort in the Neuroischaemic Diabetic Foot. *Clin Biomech*, 23:710–11. https://doi.org/10.1016/j.clinbiomech.2008.03.055
21. Chatzistergos PE, Naemi R, Healy A, *et al*., 2017, Subject Specific Optimisation of the Stiffness of Footwear Material for Maximum Plantar Pressure Reduction. *Ann Biomed Eng*, 45:1929–40. https://doi.org/10.1007/s10439-017-1826-4
22. Chatzistergos P, Farrugia K, Wright M, *et al*., 2019, Patient Specific Optimisation of the Stiffness of 3D Printed Orthoses for People with Diabetic Foot Syndrome. The Hague, The Netherlands: 8th International Symposium on Diabetic FootAt: World Forum.
23. Cheung JT, Zhang M, Leung AK, *et al*., 2005, Three-dimensional Finite Element Analysis of the Foot during Standing a Material Sensitivity Study. *J Biomech*, 38:1045–54.
24. Sarikhani A, Motalebizadeh A, Asiaei S, *et al*., 2016, Studying Maximum Plantar Stress Per Insole Design Using Foot CT-Scan Images of Hyperelastic Soft Tissues. *Appl Bionics Biomech*, 2016:8985690. https://doi.org/10.1155/2016/8985690
25. Tarrade T, Doucet F, Saint-Lô N, *et al*., 2019, Are Custom-made Foot Orthoses of any Interest on the Treatment of Foot Pain for Prolonged Standing Workers? *Appl Ergon*, 80:130–5. https://doi.org/10.1016/j.apergo.2019.05.013
26. Kim JS, Fell DW, Cha YJ, *et al*., 2012, Effects of Different Heel Heights on Plantar Foot Pressure Distribution of Older Women During Walking. *J Phys Ther Sci*, 24:1091–4. https://doi.org/10.1589/jpts.24.1091
27. Kumar A, Collini L, Daurel A, *et al*., 2020, Design and Additive Manufacturing of Closed Cells from Supportless Lattice Structure. *Addit Manuf*, 33:101168. https://doi.org/10.1016/j.addma.2020.101168
28. Zolfagharian A, Gregory TM, Bodaghi M, *et al*., 2020, Patient-specific 3D-printed Splint for Mallet Finger Injury. *Int J Bioprint*, 6:259. https://doi.org/10.18063/ijb.v6i2.259
29. Kolan KC, Huang YW, Semon JA, *et al*., 2020, 3D-printed Biomimetic Bioactive Glass Scaffolds for Bone Regeneration in Rat Calvarial Defects. *Int J Bioprint*, 6:274. https://doi.org/10.18063/ijb.v6i2.274
30. Dong G, Tessier D, Zhao Y, 2019, Design of Shoe Soles Using Lattice Structures Fabricated by Additive Manufacturing. *Proc Des Soc*, 1:719–28. https://doi.org/10.1017/dsi.2019.76
31. Ng WL, Lee JM, Zhou M, *et al.*, 2020, Vat Polymerization-based Bioprinting-Process, Materials, Applications and Regulatory Challenges. *Biofabrication*, 12:022001. https://doi.org/10.1088/1758-5090/ab6034
32. Redmann A, Oehlmann P, Scheffler T, *et al*., 2020, Thermal Curing Kinetics Optimization of Epoxy Resin in Digital Light Synthesis. *Addit Manuf*, 32:101018. https://doi.org/10.1016/j.addma.2019.101018
33. Sillani F, Kleijnen RG, Vetterli M, *et al*., 2019, Selective Laser Sintering and Multi Jet Fusion: Process-induced Modification of the Raw Materials and Analyses of Parts Performance. *Addit Manuf*, 27:32–41. https://doi.org/10.1016/j.addma.2019.02.004
34. Rai D, Aggarwal L, 2006, The Study of Plantar Pressure Distribution in Normal and Pathological Foot. *Pol J Med Phys Eng*, 12:25–34.
35. Nandikolla V, Bochen R, Meza S, *et al*., 2017, Experimental Gait Analysis to Study Stress Distribution of the Human Foot. *J Med Eng*, 2017:3432074. https://doi.org/10.1155/2017/3432074
36. Koike S Okina S, 2012, A Modeling Method of Sport Shoes for Dynamic Analysis of Shoe-body Coupled System. *Proc Eng*, 34:272–7. https://doi.org/10.1016/j.proeng.2012.04.047
37. Hossain M, Navaratne R, Perić D, 2020, 3D Printed Elastomeric Polyurethane: Viscoelastic Experimental Characterizations and Constitutive Modelling with Nonlinear Viscosity Functions. *Int J Nonlinear Mech*, 126:103546. https://doi.org/10.1016/j.ijnonlinmec.2020.103546

RESEARCH ARTICLE

Evaluation of Printing Parameters on 3D Extrusion Printing of Pluronic Hydrogels and Machine Learning Guided Parameter Recommendation

Zhouquan Fu[1†], Vincent Angeline[1†], Wei Sun[1,2*]

[1]Department of Mechanical Engineering and Mechanics, Drexel University, Philadelphia, PA 19104, USA
[2]Department of Mechanical Engineering, Tsinghua University, Beijing 100084, People's Republic of China
†*These authors contributed equally to this work*

Abstract: Bioprinting is an emerging technology for the construction of complex three-dimensional (3D) constructs used in various biomedical applications. One of the challenges in this field is the delicate manipulation of material properties and various disparate printing parameters to create structures with high fidelity. Understanding the effects of certain parameters and identifying optimal parameters for creating highly accurate structures are therefore a worthwhile subject to investigate. The objective of this study is to investigate high-impact print parameters on the printing printability and develop a preliminary machine learning model to optimize printing parameters. The results of this study will lead to an exploration of machine learning applications in bioprinting and to an improved understanding between 3D printing parameters and structural printability. Reported results include the effects of rheological property, nozzle gauge, nozzle temperature, path height, and ink composition on the printability of Pluronic F127. The developed Support Vector Machine model generated a process map to assist the selection of optimal printing parameters to yield high quality prints with high probability (>75%). Future work with more generalized machine learning models in bioprinting is also discussed in this article. The finding of this study provides a simple tool to improve printability of extrusion-based bioprinting with minimum experimentations.

Keywords: 3D printing; Bioprinting; Printability; Machine learning; Support vector machine; Pluronic

*Correspondence to: Wei Sun, Department of Mechanical Engineering and Mechanics, Drexel University, Philadelphia, PA 19104, USA; sunwei@drexel.edu

Received: August 19, 2021; **Accepted:** September 3, 2021; **Published Online:** October 15, 2021

Citation: Fu Z, Angeline V, Sun W, 2021, Evaluation of Printing Parameters on 3D Extrusion Printing of Pluronic Hydrogels and Machine Learning Guided Parameter Recommendation. *Int J Bioprint*, 7(4):434. http://doi.org/10.18063/ijb.v7i4.434

1. Introduction

Three-dimensional (3D) bioprinting is a developing technique in the biomedical field for creating a wide range of biological 3D structures, including cell-laden constructs and scaffolds[1]. The bioprinting technique includes several processes, for example, computer-aided design (CAD), 3D printing, and the synthesis of biomaterial and living material[2]. Bioprinting has found widespread applications such as tissue engineering[3,4], reconstructive surgery[5], and drug delivery and screening[6,7]. Bioprinting methods can be generally divided as extrusion, material jetting, and vat polymerization. Vat polymerization utilizes stereolithography or digital light processing to cure polymers of cell-hydrogel suspensions into 3D structures. This method can achieve high resolution but is limited to use with photo responsive bioinks[8]. In ink jetting, droplets of material containing cells are deposited to form printed structures. Variation of droplet sizes and cell concentrations allows for control over concentrations within structures and high resolution. However, low viscosity of the bioinks is often required for the jetting process[9]. Extrusion bioprinting is a bioprinting method derived from traditional thermoplastic 3D printing, incorporating a reservoir and nozzle through which material is extruded layer-by-layer onto a platform. It is unable to reach the resolutions achieved by other methods due to limitations based on nozzle size, but it is low-cost,

versatile, and can be used with bioinks having a much wider range of viscosities[10]. Extrusion bioprinting can be further characterized by two types of printers: pneumatic-based and displacement-based[11]. In a pneumatic-based printer, pressure in the reservoir is manipulated to force material through the nozzle onto the print bed. They allow for precise pressure control which is important to maintaining cell-viability during printing. Motor-based printers utilize a motor to push material down the reservoir and through the nozzle. Despite less precise pressure control, motor-based printers provide better spatial, and flow control and are therefore a better choice when using high viscosity materials[12] such as those in this study.

The overarching type of material used in biofabrication is the bioink. Bioinks are soft materials which contain living cells that are essential for prospective applications[13,14]. A common type of bioink is the hydrogel, which is a highly hydrated cross-linked polymer network capable of providing a tissue-like environment for cells[13,15]. Because of their high hydration and ability to form 3D structures, hydrogels are an ideal candidate for bioprinting which allows cells to survive and grow[13]. Thermo-responsive hydrogels are of interest in 3D bioprinting due to the opportunity to manipulate their properties through temperature control to assist in printing. Among this group of hydrogels is materials such as gelatin, methylcellulose, and PEO-PPO-PEO block copolymers (trade named Pluronic)[11]. Pluronic F127 (PL 127) is of particular interest due to its success for uses as a sacrificial material[3] which can be printed along with other materials then easily removed or washed away leaving other materials intact[11,16].

To characterize outcomes, the term printability is often used. Printability is defined as the geometrical difference between the designed print and the experimental print[15]. Printability is often characterized quantitatively (termed print fidelity[15]) using numerical indices of a print's dimensions and pores[17-19] or qualitatively through visual inspection for tears, breakage, or overall performance. Before testing, printability may also be evaluated on the basis of material properties and performance[15,20]. For this experiment and PL 127's applications in bioprinting, manipulating parameters to create a high-fidelity print is desirable. To simplify and apply experimental results, width index is used as the primary indicator for printability in this experiment. Four parameters were selected for testing based on the hypothesis that they would have a significant impact on the width index and therefore printability of PL 127.

Printing parameters are the wide range of variables which can be adjusted to impact printing outcomes. Printing parameters can be separated into two categories. Process parameters are factors which are set by the printer, such as the height of the nozzle, printing speed, and extrusion speed. Material parameters are related to properties of the material being used, such as its composition, viscosity, and storage or loss modulus. To encompass both types of parameters, nozzle gauge and path height were selected for process parameters, and composition and nozzle temperature were selected for material parameters. Nozzle temperature may be considered as falling under both categories due to thermoresponsive viscosity change of PL 127.

Machine learning (ML) is currently the most rapid developing field and has tremendous potential in 3D printing in terms of developing materials and processes. ML is a tool that establishes statistical models to analyze underling behaviors of a system and give predictions based on training data[21]. There have been several studies trying to fast-track optimal bioprinting parameters and predict printing outcome based on ML algorithms. Conev *et al*. used Random Forest (RF) classifier and regressor to identify suitable printing conditions to recommend for 3D extrusion printing of poly (propylene fumarate). The authors trained the two RF models using a previous factorial design datasets and explored the significance of each parameter based on the feature weights[22]. Menon *et al*. used hierarchical ML (HML) to predict 3D printing of silicone elastomer. A physical modeling layer was integrated in the HML framework, and the model was trained on 38 data points. Previously unseen data were discovered by the HML with high print fidelity and 2.5 times higher printing speed[23]. Ruberu *et al*. employed Bayesian Optimization (BO) to find the optimal printing parameters for 3D extrusion printing of gelatin methacrylate and methacrylated hyaluronic acid composite bioink. The number of experiments required to reach global optima ranged up to 47 with different bioink composition, which was greatly reduced compared with full factorial design (6000 – 10,000)[24]. However, these ML models still require quite large amount of training data points. Considering the cost of biomaterials, living cells, and biofactors, we are looking to adopt an algorithm with a minimal requirement on the number of training data that can still perform well.

The objective of this study is two-fold. The first objective is to evaluate the effects of printing parameters on the printability of PL 127 **(Figure S1)**. The previous research has been conducted on other thermoresponsive hydrogels, including gelatin and alginate[2,17,19,25], or has used pneumatic-based printers which allow for manipulation of pressure which is often studied due to its significant impact on print outcomes[26]. The first study focuses on establishing the understanding of how each parameter affects the outcome of extrusion printing of PL 127. The second objective of this study is to utilize Support Vector Machine (SVM) algorithm to select

sets of optimal printing parameters which have higher (>75%) probability to generate high fidelity PL 127 filaments. Traditional factorial experimental design is time-consuming, and the cost increases exponentially with increasing number of parameters and levels. Building physical models for the bioprinting process are also challenging due to the complex relationship between disparate printing parameters (e.g., biomaterial properties and process parameters) and print outcome. The SVM process optimization methodology was inspired by Aoyagi *et al*[27]. In this study, we selected biomaterial concentration, nozzle temperature, and printing path height as three key parameters. A space-filling Design of Experiment technique was used to select only 12 training data. A 3D process map was generated by the pairwise probability prediction based on SVM model and the validation on the unseen data points showed the model generalized well on the parameter space.

2. Materials and methods

2.1. Preparation of materials

Solutions of PL 127 were prepared by first cooling deionized (DI) water in a 4°C refrigerator, adding Pluronic F-127 (Sigma-Aldrich, St. Louis, MO) powder to create a large 30 w/v% sample, stirring using a magnetic stirrer, and then allowing the sample to homogenize fully in a 4°C refrigerator. Calculations for composition were based on the final solution volume. For lower compositions, the same sample of 30 w/v% PL 127 was then diluted down using DI water, mixed, and again allowed to homogenize fully in a 4°C refrigerator before testing began. This method was used to prevent any false affects appearing in the data due to variations between batches of material.

2.2. Printing and measurement

For all tests, an extrusion-based Bioprinter (BioMaker, SunP Biotech, Cherry Hill, NJ) was used along with the samples synthesized wit PL 127 powder (Sigma-Aldrich, St. Louis, MO). This printer uses motor-based extrusion, as opposed to the also-common pressure-based extrusion used in bioprinting. All CAD designs and slicing are included in the software for this printer, and as such these were the only software used to create and slice a grid design for testing in this experiment. Measurements from microscope images of each print were taken using Fiji/ImageJ.

2.3. Parameter selection for evaluation

Four parameters were selected for testing: two in the material property category and two in the printing parameter category. The material parameters selected were printing temperature and material composition, and process parameters selected were path height and nozzle gauge. Material composition refers to the weight/volume percentage (w/v %) of the PL 127 solution used during testing. This parameter will likely have an effect on print outcomes due to its impact on the viscosity of the material. Nozzle temperature is the temperature that the nozzle and material inside it is held at while printing. It will likely affect prints due to the relation between PL 127 temperature and viscosity. While this parameter is controlled by the printer, its impacts relate to the structure and material properties of PL 127. Therefore, it has been placed under the "material" category of parameter, even though it may be seen as both a "printing" and "material" parameter. Path height is the vertical offset between the printing nozzle and the print bed. During printing the material is stretched by different amounts depending on how high the path height is set. Nozzle gauge refers to the gauge number of the printing nozzle being used. Each nozzle has a different inner and outer diameter.

2.4. Rheological evaluation of PL 127

The viscosities of Pluronic inks were tested by a rheometer (R/S-CPS+, Brookfield, USA). The rheometer is equipped with a temperature control Peltier (0 – 135°C). A P50 plate (radius 25 mm) with 1 mm gap was used in the plate/plate measuring system for all tests. For each test, 2 mL sample was loaded on 4°C plate to fill the gap completely. Viscosities for all concentrations of Pluronic inks were first measured at temperature ramp from 40°C to 4°C for 15 min and constant shear rate at 1/s. The viscosities of all Pluronic inks at 23°C against shear rate ramp were also tested from 0.01 to 100/s for 5 min.

2.5. Variable testing

Baseline values were selected for each variable to be held constant while one category was varied independently. The selected values were a path height of 0.3 mm, nozzle gauge of 25, room temperature (23°C), and a composition of 30% PL 127. Values were varied in one category at a time while all other categories were kept at their baseline values.

2.6. Model grid for printing

The model grid used for printing was designed in the built-in software for the SunP Biotech Bioprinter. The grid was a 0.6 mm tall square with three 0.2 mm layers and a 6 mm side length. Theoretical line width of the infill lines was 0.4 mm.

2.7. Data collection

Before printing, material was pulled from the samples stored in a 4°C refrigerator into a 5 mL syringe. Syringes were allowed to come to room temperature for 10 min

then loaded into the printer for testing. In all temperature tests, the material was given an additional 10 min in the printer to reach the set temperatures before printing. For each combination of parameters, three samples were printed. On each sample, five horizontal line width measurements were taken at random around the grid. Data on vertical lines and pore width were also taken in the same manner. These were taken by imaging the grids under a microscope, then importing the images into Fiji for assessment. Images were converted to 8-bit (black and white) and then sharpened automatically using Fiji's automatic threshold adjustment. After sharpening, the previously mentioned measurements were taken using the line and automatic area selection tools. For each set of parameter tests, data from all three samples were then combined into one larger, 15-item set to calculate the mean and standard deviation.

For a few variables, printing the originally selected grid was not possible due to the effects of the parameters. The 21G nozzle and 20% PL 127 were unable to form a three-layer grid and were instead printed as a one-layer set of lines. In addition, 15% PL 127 was not viscous enough to form any kind of grid and produced no useful data.

2.8. Quantifying prints quality

To characterize prints a line width index was assigned to each print using a method similar to prior research[17]. This allowed for an easy view of how accurate a print was and what kind of error occurred in it. All averaged line values were divided by the theoretical line width, following the formula:

$$\text{Width index} = \frac{\frac{\textit{Experimental Line}}{\textit{Width}}}{\textit{Theoretical}} = \frac{\frac{\textit{Experimental Line}}{\textit{Width}}}{0.4\,mm} \quad (1)$$

2.9. SVM implementation

Uniform Design (UD) technique[28] was used to select 12 experiment data points (**Table 1**) based on a three parameter four level data space $U_{12}(P_3^4)$. Concentration of PL 127 was set at 15, 20, 25, and 30 w/v%. The temperature of the nozzle was selected at 16, 23, 30, and 37°C, and the path height as 0.3, 0.35, 0.4, and 0.45 mm. Twelve data points were normalized before being used as training set.

Table 1. Uniform design with three parameters and four levels

Concentration (Parameter 1)	1	1	1	2	2	2	3	3	3	4	4	4
Temperature (Parameter 2)	4	2	1	3	1	3	4	2	2	1	3	4
Path height (Parameter 3)	4	3	1	3	1	2	2	4	3	2	4	1

A Gaussian kernel was used in the model to transform the feature parameters into high dimensional space so that the nonlinear probability hyperplanes can be constructed. Given m data set $(x^{(i)}, y^{(i)})$, $y^{(i)} = \{-1,1\}$, $i=1,2,\ldots m$, for a certain data sample $x^{(i)}$, the transformation is done by:

$$f_i = exp\left(-\frac{\left\|x^{(i)} - x^{(j)}\right\|^2}{2\sigma^2}\right) \quad (2)$$

so that $x^{(i)}$ is constructed as $(f_1^{(i)}, f_2^{(i)}), f_3^{(i)})$. Here, σ is a scaling parameter and also a hyperparameter to tune in the SVM model. The optimization objective is to maximize the geometric margins of the hyperplane that separates the two classes. The optimization problem is to find the weight w and bias b that minimizes:

$$\min_{w,b,\xi} \frac{1}{2}\|w\|^2 + C\sum_i^m \xi^{(i)} \quad (3)$$

subject to

$$y^{(i)}\left(w^T f^{(i)} + b\right) \geq 1 - \xi^{(i)} \; for\, i = 1\ldots m \quad (4)$$

where ξ is a slack variable and C is the regularization parameter[29].

In this study, an open source SVM software LIBSVM was used on MATLAB to train the model and acquire the parameters w and b[30]. A grid search on two hyperparameters (C and g) was conducted with a threefold cross-validation. C is the regularization parameter applied on the slack variable SVM and g is the gamma parameters in Gaussian kernel ($1/(2\sigma^2)$). The data set is labeled as "1" class (good print) if the calculated width index in method 2.8 is between 0.9 and 1.1, while labeled as "−1" class (bad print) otherwise (**Table 2**). 3D process map was generated based on the pairwise probability estimates on a 3D parameter space[31].

2.10. Statistical analysis

n = 3 prints were made for each parameter test, with n = 5 line measurements taken from each. Mean and standard deviation were measured, and statistical analysis was performed based on original line data. Statistical significance was investigated using data analysis tools within Microsoft Excel. A t-test for two samples assuming equal variances was applied where $P < 0.05$ showed a significant difference between tests. Results displayed in **Figure 2** are of line index data for clarity and insight. A * symbol denotes significance.

Table 2. UD parameter selection and labeling

Concentration w/v %	15	15	15	20	20	20	25	25	25	30	30	30
Temperature (°C)	37	23	16	30	16	30	37	23	23	16	30	37
Path Height (mm)	0.45	0.4	0.3	0.4	0.3	0.35	0.35	0.45	0.4	0.35	0.45	0.3
Label	−1	−1	−1	−1	−1	1	1	−1	−1	1	−1	1

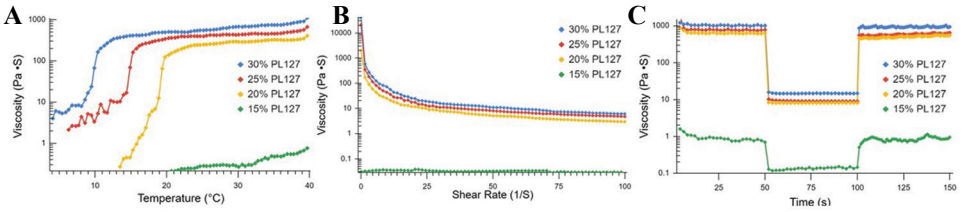

Figure 1. Rheological properties of PL 127 at 30, 25, 20, and 15% concentrations. (A) Temperature sweep of PL 127. Temperature ramp was set from 4 °C to 40 °C over a period of 15 min. (B) Shear rate sweep from 0-100 1/s in 296 s. (C) Thixotropic properties of PL 127 at 23°C. Shear rate stages were set as 0.5/50/0.5 1/s and 50 s for each stage.

3. Results

3.1. Rheological characterization of PL 127

A temperature sweep of the selected concentrations (**Figure 1A**) displayed the differences in viscosity reaction to temperature. Higher concentration resulted in a sharp increase in viscosity at a lower temperature than at lower concentrations. About 30% saw a sharp increase in viscosity at approximately 11°C, 25% at around 15°C, and 20% at around 19°C. Viscosity of 15% concentration was not affected by the temperature change in the same manner and maintained a very low viscosity throughout the temperature sweep process. A decrease in viscosity with respect to increasing shear rate (shear thinning) was observed for all concentrations except 15%, which had no viscosity response to shear rate (**Figure 1B**). PL 127 showed pronounced viscosity recovery for all concentrations (**Figure 1C**). All groups showed prompt decrease in viscosity when the shear rate increased from 0.5 1/s to 50 1/s. Rapid viscosity recovery was also observed when the shear rate decreased back to 0.5 1/s.

3.2. Effects of path height on width index

Path height tests revealed an inverse relationship between path height and line width. A significant difference was found between all tested line widths (0.3, 0.35, and 0.4 mm) (**Figure 2A**). The 0.45 mm test was unable to form a print with cohesive lines for measurement. These tests confirmed the previous hypothesis. Future testing may benefit from expanding intervals at the expense of time and material to find the exact point at which prints begin to fail.

3.3. Effects of nozzle gauge on width index

Nozzle gauge tests revealed no significant difference in line width for all test groups. All tests performed similarly with no significant differences appearing (**Figure 2B**). It is worthwhile to note that due to a difference in stretching effects during printing, 21G tests were only able to form a single layer print. As a result, three-layer tests could not be used to compare the effects of nozzle gauge. Therefore, single layer prints were used for all nozzle gauge tests to accurately determine its effects resulting in line widths below the ideal value for all tests. This is denoted in **Figure 2B** and further considered in the discussion.

3.4. Effects of concentration on width index

Material composition tests yielded results similar to expectations but included more failures than predicted. About 15% tests failed and were unable to form any cohesive structure (**Figure 2C**). The material was not viscous enough to form any type of structure and only bubbled and spread on the print bed. About 20% prints were able to retain some structural integrity but could only produce a single layer print similar to the 21G nozzle. It produced significantly thicker lines than 25% or 30%. A significant difference was not found between 25% and 30%.

3.5. Effects of nozzle temperature on width index

16°C tests produced significantly thicker line widths than all other tests far above the theoretical line width. At above room temperature (23°C, 30°C, and 37°C), all produced similar results which were closer to the theoretical line width (**Figure 2D**). Results of higher temperatures were unexpected given the relationship between PL 127 viscosity and temperature. Higher viscosity was expected to lead to thinner lines, but in these tests, that was not the case. However, 23°C tests did have a higher standard deviation (0.032) than 30 and 37°C tests (0.199 and 0.022, respectively). This indicates that a temperature increase was of use in reducing error in prints and creating more consistent lines.

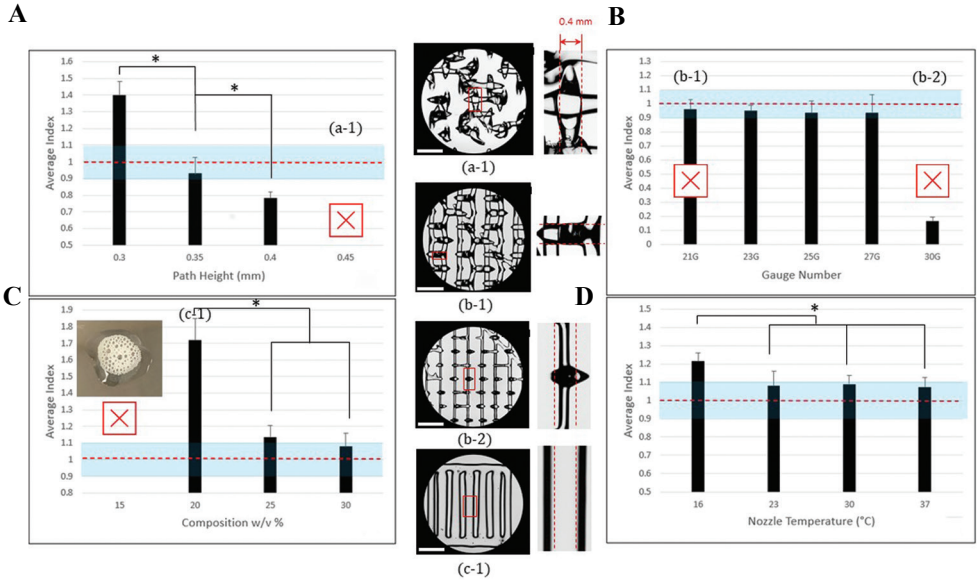

Figure 2. Index representation of parameters. (A) Effects of path height on width index of PL 127 printing. (B) Effects of nozzle gauge. (C) Effects of PL 127 concentration. (D) Effects of nozzle temperature during printing. Horizontal line indicates ideal index value of 1, * denotes statistical significance ($P < 0.05$). Pictures indicate tests which were unable to form the standard three-layer grid. Baseline parameters: 0.3 mm, 25G, 30%, 23°C. Scale bar is 1.87 mm. Distance between two dashed lines is 0.4 mm.

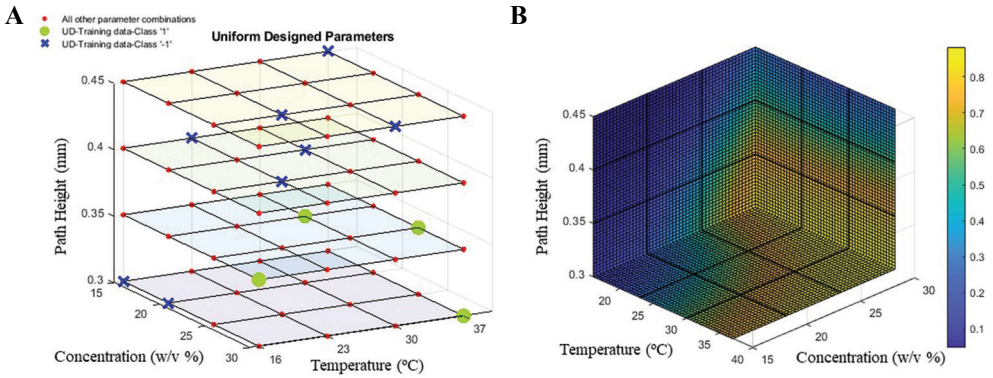

Figure 3. Parameter selection and construction of process map based on SVM prediction. (A) Training data points selection based on UD with three parameters and four levels and 12 tests ($U_{12}(P_3^4)$). (B) 3D process map generated by support vector machine classifier libsvm with regularization parameter $C = 10$ and Gaussian kernel scale parameter $g = 0.1$.

3.6. Parameter selection based on SVM

Training data and its label are shown in **Table 2**. There are totally 12 data points with four good prints and eight bad prints. In the 3D parameter space, all possible combinations of the parameters are labeled in **Figure 3A** which is 4*4*4 = 256 in total. "−1" class data points were labeled in blue cross, "1" class data points were labeled in green circle, and the rest were in red circle. Three-fold cross validation was conducted on the 12 data points and an average 83.3% accuracy score was reached with C taking 10 and g taking 0.1. The generated 3D process map reflects the probability for each data point in the parameter space (concentration, nozzle temperature, and path height) to be classified as good print (class "1"). The higher the color map value, the higher the probability of data point can yield good print.

4. Discussion

4.1. Effect of printing parameters on width index

A common factor between multiple parameters is their connection with the viscosity of PL 127. Viscosity is defined as the ratio of shear stress to shear rate[12]. PL 127 viscosity is dependent on the formation of micelles, which are a formation of connected individual polymer chains[11]. For micelles to form, the material must have reached a certain concentration (critical micelle concentration) and be above the lower critical solution temperature

(LCST)[32]. Micelle formation generally begins at 18-20 w/v %, which is therefore the lowest concentration at which PL 127 can form a cohesive gel capable of printing[11,32]. If the material is above the lower critical solution temperature, micelles will begin to become insoluble in the solution. As temperature increases, micelles will pack together, increasing viscosity, and forming a gel[32]. The temperature where this transition begins (the LCST) is dependent on concentration, with a higher concentration leading to a lower LCST due to the higher rate of polymer interactions[32]. This is shown in **Figure 1**, where 30% PL 127 has a sharp increase in viscosity at 11°C, whereas 25% and 20% do not have the same increase until 15°C and 19°C, respectively.

An understanding of how each print parameter effects printability is an essential basis to optimizing their effects. Material composition's effects result from the viscosity changes between samples. Adding PL 127 will create more viscous material which can improve structural integrity, prevent spreading on the print bed, and improve structural fidelity. At the lowest, concentration must also be high enough that micelle formation begins, and the material gains enough viscosity at certain temperature to form cohesive lines. However, the material cannot be too viscous, otherwise it will require too much force to be extruded and extrudability could be impeded. Therefore, a balance must be struck to achieve the best print outcome. The standard printing range for PL 127 is 25-40%, and at the lowest 18-20% due to micelle formation requirement[11]. This follows from this experiment's data, where 15% was unable to form a print, 20% was just able to form a print in single lines, and 25 and 30% formed a full print. While the differences between 25% and 30% were not found to be significant, the influence of other parameters could make the choice between them relevant.

Nozzle temperature also affects viscosity because of increased micelle packing and formation in the material. As follows, experimental results showed a significant increase in accuracy from 16°C to all higher temperatures. Because of the relationship between micelle formation, temperature, and material composition, an interaction between temperature and composition could be used to further improve accuracy and differentiate parameters. At higher concentrations, micelle formation begins at a lower temperature due to polymer interactions[32]. This is shown by the temperature sweep in **Figure 1**, where higher concentrations saw a sharp increase in viscosity at a lower temperature than lower concentrations. Therefore, at higher temperatures the difference between 25% and 30% PL 127 may become more apparent as 30% will have begun micelle formation before 25% and have accumulated more micelles and maintained a higher viscosity. Because initial tests were both conducted at room temperature, this discrepancy may not have originally been shown. In **Figure 1**, 25% and 30% viscosity are closer at room temperature than at higher temperatures. This possibility could warrant further experimentation to optimize the interplay between parameters when effects would otherwise have reached their individual limits.

Path height impacts printability and width index due to shearing effects during printing. The red region in **Figure 4A** represents the area of the material which is stretched between the print bed and nozzle during printing. The inner region is put under compressive stress, while the outer region is put under tensile stress. As path height increases the stress in the red region also increases, leading to thinly stretched prints and breakage (**Figure 4C and D**). In addition, higher path heights introduce a higher lag time between material leaving the nozzle and reaching the print bed. This may cause material to not follow the printing path correctly and lead to errors, particularly on sharp corners of prints where

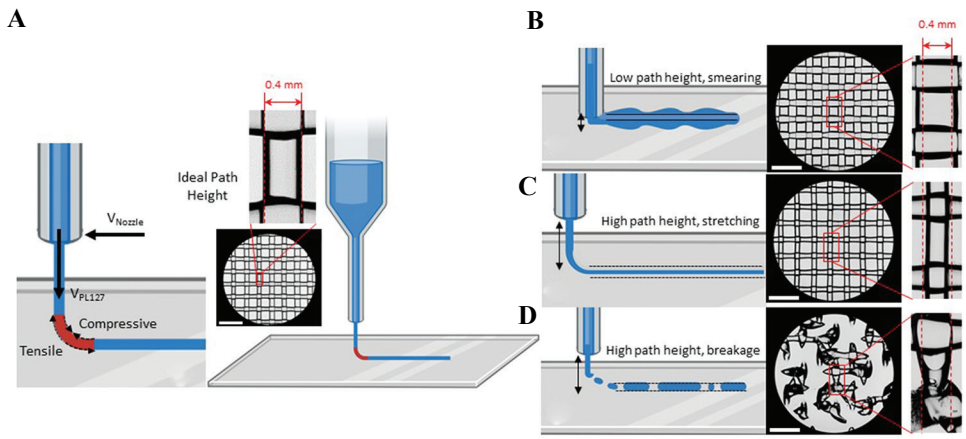

Figure 4. Path height effect representation with experimental examples. (A) Correct path height with stress region highlighted. (B) Low path height leading to interference and smearing. (C) High path height leading to stretching, thin lines. (D) High path height leading to breakage. Correct line width represented by dashed line. Scale bar is 1.87 mm. Created with BioRender.com

material would cut across rather than form a proper corner[25]. Low path heights can have the opposite affect due to the nozzle interfering and spreading the material out into over-deposited thick lines (**Figure 4B**).

Nozzle gauge was not found to have a significant impact on width index, but some other differences were observed between tests. A 21G nozzle corresponds to an inner diameter of 0.58 mm and an outer diameter of 0.81 mm, 23G to an inner/outer diameter of 0.43 and 0.635 mm, 25G to an inner/outer diameter of 0.3 and 0.5 mm, and 27G to an inner/outer diameter of 0.2 and 0.4 mm. It is expected that a change in nozzle diameter will not affect line width as the flow rate out of the nozzle should not be affected if the bioink is considered incompressible. With all other parameters held constant (particularly print speed and extrusion speed) the flow rate out of the nozzle is also constant, and line width therefore cannot change since the same amount of material is being deposited. A difference was noted in the second layer performance of tests. When using wider nozzles, the second layer is stretched more and may tear or fail completely. This can lead to thinner first-layer width as surface tension and the weight of the second layer are absent, leading to less spreading in single-layer prints. 21G tests were unable to form a second layer, 23G tests could form a second layer some errors, and 25G and 27G were able to form a consistent second layer. This problem necessitated single-layer prints for an accurate comparison of how nozzle gauge effects purely line width. However, a complete approach to defining a "best" nozzle gauge would require these problems with certain nozzles be considered.

Effects could be seen if nozzle diameter is small enough to cause a large pressure buildup inside the nozzle tip resulting in a push back on the printer motor. Pressure effects would then impede motor function and extrusion speed would be effectively lowered. To describe this issue a mathematical model of flow rate in the nozzle tip (Eq. 5) can be examined[33]:

$$Q = \left(\frac{n}{3n+1}\right)\pi\gamma_0^{\frac{n-1}{n}}\left(\frac{\partial P/\partial z}{2\eta_0}\right)R^{\frac{3n+1}{n}} \quad (5)$$

where Q represents flow rate, n is the power law index of the fluid, γ is the shear rate, P is pressure, z is the direction in the nozzle axis, η_0 is the limited viscosity, and R is the nozzle radius. If the flow rate (Q) out of the nozzle is to remain constant while the nozzle gauge (R) decreases, then pressure (P) must increase to balance the equation as no other variables will change. In smaller nozzles, this pressure increase could be high enough as to unintentionally lower extrusion speed because of push-back. This is a possible drawback of motor-based printers which is avoided with pressure-based pneumatic printers. To confirm that this effect did not impact testing, a short second experiment was conducted. 21, 23, 25, 27, and 30G nozzles were used with a room temperature sample of 30% PL 127 and extruded for 2 min each **(Figure 2S)**. The amount of material was then weighed and compared, revealing that all nozzles did extrude the same amount of material. Additional testing revealed that effects are seen at nozzle gauges higher than 27G such as 30G (**Figure 2B**).

4.2. Optimal parameter selection based on SVM

We selected two locations on the parameter space; one having higher than 75% probability, the other having lower than 25% probability (**Figure 5**). The scaffold printed with the parameters from low probability region cannot form continuous and stable structure and has a low printability. The printed cube and grid 3D structure were not able to form uniform and accurate shape as desired (**Figure 5A**). While the scaffold printed with the parameter from high printability region was able to generate high printability stable scaffold with multiple test prints having width index evaluated at 0.998 ± 0.049 (mean ± standard deviation). The printed cube and pyramid structure maintained good fidelity and uniformity (**Figure 5B**).

There exists a complex interplay between various printing parameters to achieve desired printability of the scaffold. The impact on the scaffold printability caused by changing one parameter can always be compensated by adjusting another. For example, when printing with a low concentration of PL 127, the low viscosity of the material could be compensated for with a high printing temperature which would increase viscosity. Understanding these relations creates the possibility of any number of "best" parameter combinations which create high fidelity prints. The SVM process optimization method provides a solution to analyze the sophisticated 3D bioprinting black box. Using a minimal preselected training data points can assist construct SVM prediction on a volumetric parameter space so that the optimal printing parameter combinations can be acquired directly without tedious trial and error experiments.

We only used three parameters that were hypothesized to have a significant impact on printability. In fact, a plethora of parameters, such as blend ratio (composite bioink), extrusion pressure (for cell encapsulated printing), and crosslinking strategies (e.g. duration and timing), should also be included. In addition, utilizing governing equations to make more physically informed choice on the parameters is also promising to build a more generalized model.

There were various quantification methods reported on the printability of a scaffold, which significantly affects the generalization of ML model since the label

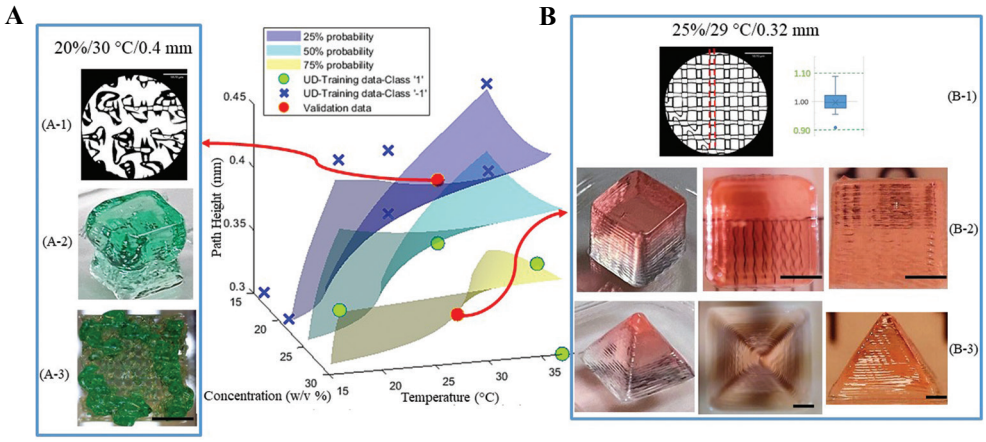

Figure 5. Validation on probability space. Three probability hyperplanes, 25%, 50%, and 75%, were illustrated based on Figure 3B. (A) Validation point selected at 20 w/v% concentration, 30°C nozzle temperature, and 0.4 mm path height. (A-1) Microscopic image evaluating the filament width. (A-2) Printing cube structure (5 × 5 × 5 mm^3). (A-3) Top view of the printed grid structure (5 × 5 × 5 mm^3). (B) Validation point at 25 w/v% concentration, 29°C nozzle temperature, and 0.32 mm path height. (B-1) Microscopic image evaluating the filament width index. (B-2) Printing cube structure (5 × 5 × 5 mm^3) with top view and side view. (B-3) Printing pyramid structure (10 mm × 10 mm × 8 mm) with top and side view. Scale bar for (A-1) and (B-1) is 1.87 mm and 2 mm for the rest.

of a scaffold is a critical information in supervised ML. This problem raises the importance of a standardized metric for printability within the bioprinting community. With a standard evaluation method, ML models could be more generalized and applied across different materials, printers, and applications. This expansion would greatly increase the usefulness of ML in bioprinting and allow for high fidelity prints using new materials without the labor-intensive testing required to continuously build new ML models.

5. Conclusions

In this paper, the effects of path height, nozzle temperature, nozzle gauge, and composition on printability were determined for PL 127 inks. Path height was shown to have an significant impact on printability, while nozzle temperature and composition affect the rheological properties of PL 127, and thus, affect the printability. Nozzle gauge alone was shown to have no effect. Rheological data and an investigation into how these parameters affect printability revealed the importance of viscosity in optimizing parameters and their interactions.

Based on 12 UD training data, a ML model was then built and validated to create a recommendation for optimal combinations of specific printing parameters for extrusion printing of acellular PL 127 bioink. This is our first step and a preliminary study to explore the application of ML toolkit to extrusion-based 3D bioprinting. Future work includes standardizing the quantification of "printability," incorporation of cell viability into the metric (ML labeling), and selection of higher dimensional feature space with more relevant parameters. Building a more generalized ML model creates the continuity between bioprinters and can be used to eliminate the need for mass testing when optimizing the bioprinting of new bioinks.

Acknowledgments

We acknowledge the financial support from SunP Biotech company research grant (Drexel University–260676).

Conflicts of interest

We declaration no conflict of interest.

Author contributions

Z.F. conceptualized the study, wrote the ML section, performed SVM and visualization, reviewed and edited the manuscript. V.A. conducted experiments, wrote the sections related to evaluation printing parameters on print outcome, reviewed and edited the manuscript. W.S. conceptualized the study, reviewed, and edited the manuscript

References

1. Sun W, Starly B, Daly AC, *et al.*, 2020, The Bioprinting Roadmap. *Biofabrication*, 12:022002. http://doi.org/10.1088/1758-5090/ab5158
2. Suntornnond R, Tan EY, An J, *et al.*, 2017, A highly Printable and Biocompatible Hydrogel Composite for Direct Printing of Soft and Perfusable Vasculature-Like Structures. *Sci Rep*, 7:16902. https://doi.org/10.1038/s41598-017-17198-0
3. Kolesky DB, Truby RL, Gladman AS, *et al.*, 2014, 3D

Bioprinting of Vascularized, Heterogeneous Cell-Laden Tissue Constructs. *Adv Mater*, 26:3124–30. https://doi.org/10.1002/adma.201305506

4. An J, Teoh JE, Suntornnond R, *et al.*, 2015, Design and 3D Printing of Scaffolds and Tissues. *Engineering*, 1:261–8. http://doi.org/10.15302/j-eng-2015061
5. Jessop ZM, Al-Sabah A, Gardiner MD, *et al.*, 2017, 3D Bioprinting for Reconstructive Surgery: Principles, Applications and Challenges. *J Plast Reconstr Aesthet Surg*, 70:1155–70. https://doi.org/10.1016/j.bjps.2017.06.001
6. Kondiah PJ, Kondiah PP, Choonara YE, *et al.*, 2020, A 3D Bioprinted Pseudo-Bone Drug Delivery Scaffold for Bone Tissue Engineering. *Pharmaceutics*, 12:166. https://doi.org/10.3390/pharmaceutics12020166
7. Ma X, Liu J, Zhu W, *et al.*, 2018, 3D Bioprinting of Functional Tissue Models for Personalized Drug Screening and *In Vitro* Disease Modeling. *Adv Drug Deliv Rev*, 132:235–51. https://doi.org/10.1016/j.addr.2018.06.011
8. Ng WL, Lee JM, Zhou M, *et al.*, 2020, Vat Polymerization-Based Bioprinting-Process, Materials, Applications and Regulatory Challenges. *Biofabrication*, 12:022001. https://doi.org/10.1088/1758-5090/ab6034
9. Lee JM, Sing SL, Zhou M, *et al.*, 2018, 3D Bioprinting Processes: A Perspective on Classification and Terminology. *Int J Bioprint*, 4:151. https://doi.org/10.18063/ijb.v4i2.151
10. Ouyang L, Yao R, Zhao Y, *et al.*, 2016, Effect of Bioink Properties on Printability and Cell Viability for 3D Bioplotting of Embryonic Stem Cells. *Biofabrication*, 8:035020. https://doi.org/10.1088/1758-5090/8/3/035020
11. Suntornnond R, An J, Chua CK, 2017, Bioprinting of Thermoresponsive Hydrogels for Next Generation Tissue Engineering: A Review. *Macromol Mater Eng*, 302:1600266. https://doi.org/10.1002/mame.201600266
12. Malda J, Visser J, Melchels FP, *et al.*, 2013, 25th Anniversary Article: Engineering Hydrogels for Biofabrication. *Adv Mater*, 25:5011–28. https://doi.org/10.1002/adma.201302042
13. Hospodiuk M, Dey M, Sosnoski D, *et al.*, 2017, The Bioink: A Comprehensive Review on Bioprintable Materials. *Biotechnol Adv*, 35:217–39. https://doi.org/10.1016/j.biotechadv.2016.12.006
14. Gungor-Ozkerim PS, Inci I, Zhang YS, *et al.*, 2018, Bioinks for 3D Bioprinting: An Overview. *Biomater Sci*, 6:915–46. https://doi.org/10.1039/c7bm00765e
15. Fu Z, Naghieh S, Xu C, *et al.*, 2021, Printability in Extrusion Bioprinting. *Biofabrication*, 3:033001. https://doi.org/10.1088/1758-5090/abe7ab
16. Gioffredi E, Boffito M, Calzone S, *et al.*, 2016, Pluronic F127 Hydrogel Characterization and Biofabrication in Cellularized Constructs for Tissue Engineering Applications. *Procedia CIRP*, 49:125–32. https://doi.org/10.1016/j.procir.2015.11.001
17. Kang KH, Hockaday LA, Butcher JT, 2013, Quantitative Optimization of Solid Freeform Deposition of Aqueous Hydrogels. *Biofabrication*, 5:035001. https://doi.org/10.1088/1758-5082/5/3/035001
18. Soltan N, Ning L, Mohabatpour F, *et al.*, 2019, Printability and Cell Viability in Bioprinting Alginate Dialdehyde-Gelatin Scaffolds. *ACS Biomater Sci Eng*, 5:2976–87. https://doi.org/10.1021/acsbiomaterials.9b00167
19. Naghieh S, Sarker MD, Sharma NK, *et al.*, 2019, Printability of 3D Printed Hydrogel Scaffolds: Influence of Hydrogel Composition and Printing Parameters. *Appl Sci*, 10:292. https://doi.org/10.3390/app10010292
20. Paxton N, Smolan W, Bock T, *et al.*, 2017, Proposal to Assess Printability of Bioinks for Extrusion-Based Bioprinting and Evaluation of Rheological Properties Governing Bioprintability. *Biofabrication*, 9:044107. https://doi.org/10.1088/1758-5090/aa8dd8
21. Yu C, Jiang J, 2020, A Perspective on Using Machine Learning in 3D Bioprinting. *Int J Bioprint*, 6:253. http://doi.org/10.18063/ijb.v6i1.253
22. Conev A, Litsa EE, Perez MR, *et al.*, 2020, Machine Learning-Guided Three-Dimensional Printing of Tissue Engineering Scaffolds. *Tissue Eng Part A*, 26:1359–68. https://doi.org/10.1089/ten.tea.2020.0191
23. Menon A, Póczos B, Feinberg AW, *et al.*, 2019, Optimization of Silicone 3D Printing with Hierarchical Machine Learning. *3D Print Addit Manuf*, 6:181–9. https://doi.org/10.1089/3dp.2018.0088
24. Ruberu K, Senadeera M, Rana S, *et al.*, 2021, Coupling Machine Learning with 3D Bioprinting to Fast Track Optimisation of Extrusion Printing. *Appl Mater Today*, 22:100914. https://doi.org/10.1016/j.apmt.2020.100914
25. Holzl K, Lin SM, Tytgat L, *et al.*, 2016, Bioink Properties Before, during and after 3D Bioprinting. *Biofabrication*, 8:032002. https://doi.org/10.1088/1758-5090/8/3/032002
26. Suntornnond R, Tan EY, An J, *et al.*, 2016, A Mathematical Model on the Resolution of Extrusion Bioprinting for the

Development of New Bioinks. *Materials*, 9:756. https://doi.org/10.3390/ma9090756

27. Aoyagi K, Wang H, Sudo H, *et al.*, 2019, Simple Method to Construct Process Maps for Additive Manufacturing using a Support Vector Machine. *Addit Manuf*, 27:353–62. https://doi.org/10.1016/j.addma.2019.03.013
28. Fang KT, Lin DK, Winker P, *et al.*, 2000, Uniform Design: Theory and Application. *Technometrics*, 42:237–48. https://doi.org/10.1080/00401706.2000.10486045
29. Boser BE, Guyon IM, Vapnik VN, 1992, A Training Algorithm for Optimal Margin Classifiers. In: Proceedings of the Fifth Annual Workshop on Computational Learning Theory, p144–52. https://doi.org/10.1145/130385.130401
30. Chang CC, Lin CJ, 2011, LIBSVM: A Library for Support Vector Machines. *ACM Trans Intell Syst Technol*, 2:1–27. https://doi.org/10.1145/1961189.1961199
31. Wu TF, Lin CJ, Weng RC, 2004, Probability Estimates for Multi-Class Classification by Pairwise Coupling. *J Mach Learn Res*, 5:975–1005. https://doi.org/10.5555/1005332.1016791
32. Matanović MR, Kristl J, Grabnar PA, 2014, Thermoresponsive Polymers: Insights Into Decisive Hydrogel Characteristics, Mechanisms of Gelation, and Promising Biomedical Applications. *Int J Pharm*, 472:262–75. https://doi.org/10.1016/j.ijpharm.2014.06.029
33. Khalil S, Sun W, 2007, Biopolymer Deposition for Freeform Fabrication of Hydrogel Tissue Constructs. *Mater Sci Eng C*, 27:469–78. https://doi.org/10.1016/j.msec.2006.05.023

INTERNATIONAL JOURNAL OF BIOPRINTING

ISSN (print): 2424-7723

ABOUT THE JOURNAL

International Journal of Bioprinting is a biannual, double-blind peer-reviewed, open access journal. This journal focuses on the use of 3D printing technology with materials that incorporate viable living cells or biological elements to produce tissue or biotechnological products. Further discourses and technological advancements in bioprinting are the goals behind acceptance of high-quality basic and applied research: from concept creation to fabrication of the bioprinting process, associated clinical applications as well as social implications.

Whioce Publishing, official publisher for the journal welcomes researchers to submit their papers relevant to bioprinting for consideration via **http://ijb.whioce.com/** For general enquiries and order for prints and reprints, please write in to **IJB@whioce.com** for a fast response.

SUBMIT YOUR PAPERS HERE

WHIOCE
PUBLISHING PTE. LTD.

ABOUT THE PUBLISHER

Whioce Publishing in Singapore is a registered publisher of excellent quality academic journals for an international readership. We deliver exceptional editorial support for the advancement and dissemination of scientific research by linking readers and researchers with networks and industries. We have ambitions to get our journals indexed in prominent databases such as EI, SCI, SSCI and AHCI, thereby aiming to be a first-class knowledge platform for researchers worldwide.

Whioce Publishing also engages in publishing e-books, organizing academic conferences and educational trainings, and providing translational services.

International Journal of Bioprinting is an
independent open access journal published
by Whioce Publishing Pte.Ltd.

WHIOCE PUBLISHING PTE. LTD.
PROVIDING
FIRST-CLASS SCIENTIFIC INFORMATION
FOR TOP SCHOLARS

Whioce Publishing Pte.Ltd.
7030 Ang Mo Kio Avenue 5
#04-15 Northstar@AMK
Singapore 569880
Tel: +65 65702707/65702718
Fax: +65 65702803

See **www.whioce.com/contact** for a full list of offices and contact information.

Whioce Publishing Pte.Ltd. is a company registered in Singapore (No. 201427293E), whose registered office is at 7030 Ang Mo Kio Avenue 5 #04-15 Northstar@AMK Singapore 569880